Reservoir characterization of super-hot unconventional geothermal systems, Mexico

Dissertation

Doctoral thesis approved in fulfillment of the requirements

for the degree of Doctor rerum naturalium (Dr. rer. nat.)

at the

Department of Material and Earth Sciences,

Technische Universität Darmstadt

TECHNISCHE UNIVERSITÄT DARMSTADT

Submitted by

Leandra Maren Weydt, M.Sc.

born on 14. August, 1990 in Oberhausen, Germany

Supervisor: Prof. Dr. Ingo Sass

Co-supervisor: Prof. Dr. Domenico Liotta

Darmstadt 2022

Submitted on: 31.08.2022

Date of viva voce: 18.11.2022

Board of examiners

Head:	Prof. Dr. Andreas Henk
First assessor:	Prof. Dr. Ingo Sass
Second assessor:	Prof. Dr. Domenico Liotta
Examiner:	Prof. Dr. David Bruhn
Examiner:	Prof. Dr. Moritz Bigalke

Technical University of Darmstadt

Institute of Applied Geosciences

Schnittspahnstraße 9

64287 Darmstadt

Germany

Declaration

I hereby declare that this presented dissertation is based on original research, and is the result of my own work. I certify that this dissertation contains no material which has been accepted for the award of any other degree in my name, at any university or other tertiary institution and, to the best of my knowledge and belief, contains no material previously published or written by another person, except where due reference has been made in the text.

Name	Location and Date

Abstract

Super-hot unconventional geothermal systems (> 350 °C) possess enormous potential for geothermal power and heat generation that could be harnessed in the future. Due to their high temperature fluids, they could provide significantly more energy per well than existing conventional wells. However, the development of such systems is challenging and their controlling factors are not fully understood yet. The high temperatures and often aggressive reservoir fluids have led to numerous drilling problems and eventual abandonments of wells in the past. Overcoming these challenges requires a deeper understanding of these reservoirs and the development of innovative exploration and drilling technologies. As part of the GEMex H2020 project, this thesis focuses on the reservoir characterization of super-hot unconventional geothermal systems linked to volcanic settings in Mexico. Two caldera complexes located in the northeastern Trans-Mexican Volcanic Belt, the Acoculco and Los Humeros caldera, were selected as demonstration sites. Sound knowledge of the reservoir units, their rock properties, and spatial heterogeneities in the subsurface is crucial for the interpretation of geophysical data as well as the parametrization of numerical models, and thus, forms the basis for an economic reservoir assessment and management. To improve the geological understanding of the caldera complexes, identify potential reservoirs, and obtain information on the physiochemical and mechanical characteristics of the reservoir rocks, a comprehensive outcrop analogue and wellbore core study was performed.

An innovative multi-method approach was used to create a comprehensive rock property database with more than 31000 data entries on 34 petrophysical and mechanical rock parameters, facilitating the application of the data for different disciplines and modeling approaches at different scales (local to super-regional). All relevant key units from the basement to the cap rock of the geothermal fields were characterized and distinct parameter ranges were defined for each unit. The results highlight the geological complexity of volcanic systems, which leads to high variability in rock properties that must be individually considered for each parameter and unit in a 3D reservoir model. Using the Los Humeros caldera as an example, a step-by-step guide for the parametrization of a 3D geothermal model was proposed. Subsequently, processes that affect the rock parameters were investigated. Fluid flow and fluid-rock interactions of the Los Humeros geothermal field are predominantly fracture-controlled and have significantly altered the physiochemical rock properties and their relationships. The investigation of alteration facies indicates that the reservoir rocks were affected by multiple hydrothermal events over time and that the geothermal reservoir is most likely fed by multiple heat sources. A new chemical discrimination approach was proposed for Los Humeros, which helped to relate the subsurface units to the corresponding formations in the outcrops. Based on the new findings, recommendations for the update of the static 3D geological model were defined.

Finally, the results of this work were used to create a local density model using gravity data obtained in the central collapse zone of the caldera complex to better characterize the shallow structures of the geothermal reservoir. Different parametrization approaches were tested including assumed average densities, weighted densities and a multimodal density distribution for each model unit, respectively. By using the multimodal density approach the misfit can be significantly reduced allowing for a more precise mapping of the different lithologies in the subsurface. The results highlight the importance of a profound rock property characterization and the correct estimation of the properties at reservoir depth during reservoir characterization.

Preface

During my time as a PhD candidate in the working group Geothermal Science and Technology at the Institute of Applied Geosciences, TU Darmstadt, I was involved in three international research projects: (1) the MalVonian project, (2) the Horizon 2020 GEMex project, and additionally, (3) the DOE EDGE project as part of my research stay at Oregon State University, USA. All three projects focused on improving the understanding of deep geothermal systems covering low-enthalpy to high-enthalpy geothermal reservoirs in various geological settings. As important steps in geothermal reservoir characterization, my work predominantly comprised the petrophysical and mechanical characterization of reservoir rocks, geothermal assessment studies, and well data analyses resulting in several peer-reviewed articles and conference contributions (Fig. 1; for a complete list of publications see page XXIV).
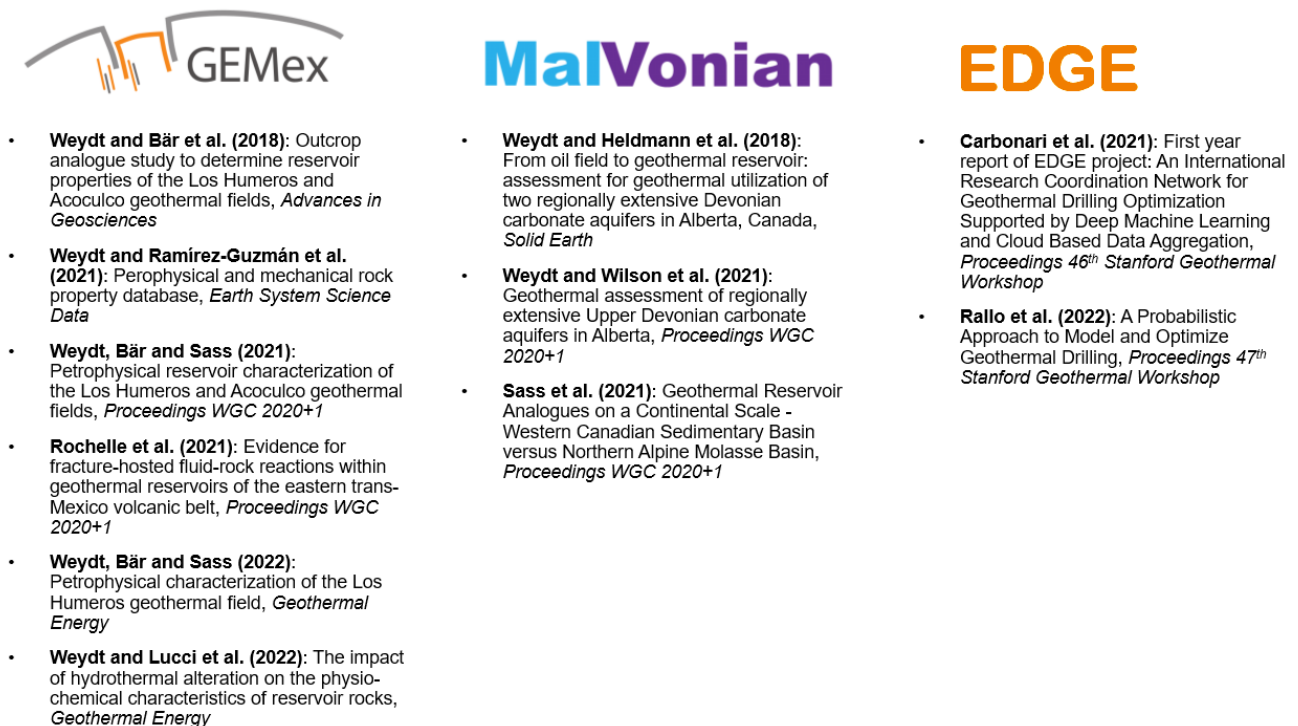

GEMex

- **Weydt and Bär et al. (2018)**: Outcrop analogue study to determine reservoir properties of the Los Humeros and Acoculco geothermal fields, *Advances in Geosciences*

- **Weydt and Ramírez-Guzmán et al. (2021)**: Perophysical and mechanical rock property database, *Earth System Science Data*

- **Weydt, Bär and Sass (2021)**: Petrophysical reservoir characterization of the Los Humeros and Acoculco geothermal fields, *Proceedings WGC 2020+1*

- **Rochelle et al. (2021)**: Evidence for fracture-hosted fluid-rock reactions within geothermal reservoirs of the eastern trans-Mexico volcanic belt, *Proceedings WGC 2020+1*

- **Weydt, Bär and Sass (2022)**: Petrophysical characterization of the Los Humeros geothermal field, *Geothermal Energy*

- **Weydt and Lucci et al. (2022)**: The impact of hydrothermal alteration on the physio-chemical characteristics of reservoir rocks, *Geothermal Energy*

MalVonian

- **Weydt and Heldmann et al. (2018)**: From oil field to geothermal reservoir: assessment for geothermal utilization of two regionally extensive Devonian carbonate aquifers in Alberta, Canada, *Solid Earth*

- **Weydt and Wilson et al. (2021)**: Geothermal assessment of regionally extensive Upper Devonian carbonate aquifers in Alberta, *Proceedings WGC 2020+1*

- **Sass et al. (2021)**: Geothermal Reservoir Analogues on a Continental Scale - Western Canadian Sedimentary Basin versus Northern Alpine Molasse Basin, *Proceedings WGC 2020+1*

EDGE

- **Carbonari et al. (2021)**: First year report of EDGE project: An International Research Coordination Network for Geothermal Drilling Optimization Supported by Deep Machine Learning and Cloud Based Data Aggregation, *Proceedings 46th Stanford Geothermal Workshop*

- **Rallo et al. (2022)**: A Probabilistic Approach to Model and Optimize Geothermal Drilling, *Proceedings 47th Stanford Geothermal Workshop*

Figure 1: Overview of the projects and the resulting peer-reviewed articles and conference proceedings.

The cumulative dissertation presented here focuses exclusively on my work performed within the GEMex project and includes content from four peer-reviewed publications as well as conference proceedings, project reports, and unpublished results. The GEMex project aims to improve the understanding of so-called 'super-hot' unconventional geothermal systems and the development of new transferrable exploration approaches and exploitation technologies that withstand high temperatures and challenging reservoir conditions. For this purpose, the Acoculco and Los Humeros caldera complexes located in the Trans-Mexican Volcanic Belt in Mexico were selected as demonstration sites.

The objective of this thesis is to perform an in-depth characterization of super-hot unconventional systems by applying a multi-method and multi-scale approach, which is integrated within a large-scale research project and links different disciplines and their results. The workflow presented here focuses on the physiochemical characterization of target units in the subsurface, recommendations for conceptual and computational 3D reservoir modeling, and their application in a local gravity model to improve the geological understanding of super-hot unconventional geothermal reservoirs linked to volcanic systems.

The first chapters of this thesis introduce the reader to super-hot unconventional geothermal systems, the GEMex project as well as the geological setting of the study area. Content from Weydt and Bär et al. (2018), published in Advances in Geosciences, Weydt and Bär et al. (2021), Proceedings World Geothermal Congress 2020+1, and GEMex deliverables are included in chapters 1 and 2.

Following the general introduction presented in the first chapters, chapter 3, published in Earth System Science Data, describes the various laboratory experiments conducted within the GEMex project to characterize all key lithologies of the Los Humeros and Acoculco geothermal fields. The chapter presents a comprehensive workflow starting with joint field work over sample identification using chemical and petrographic analyses to petrophysical and mechanical rock characterization and the creation of an extensive, ready-to-use relational rock property database. Unlike other databases, all data points are comparable with each other since each parameter was determined in the same way and all parameters were measured on each sample. Due to the joint approach in the field, this work can be linked to mineralogical, structural, and shallow geophysical investigations carried out in other work packages within the GEMex project.

From here on, the thesis predominantly focuses on the Los Humeros geothermal field. However, within the GEMex project, the methods and workflows presented in this thesis have been applied to both caldera complexes.

Chapter 4, published in Geothermal Energy, takes a closer look at the geological units of the Los Humeros caldera complex, which were sampled in outcrops during different field campaigns. This chapter describes all steps from outcrop investigation over petrophysical measurements to statistical evaluation of the results that are required for a profound and accurate petrophysical parametrization of a 3D reservoir model. In addition, this work provides T/P- corrected reservoir properties modeled for all reservoir units of the Los Humeros geothermal field and recommendations for future stochastic or numeric modeling approaches.

Chapter 5, submitted to Geothermal Energy, includes an in-depth characterization of wellbore core samples retrieved from the Los Humeros geothermal field. The aim was to identify the main processes occurring within the reservoir and to quantify their impact on the chemical and petrophysical characteristics of the reservoir rocks. For this purpose, alteration facies, mineralogical changes, and petrophysical and chemical properties (major, trace, and rare earth elements) were analyzed on the wellbore core samples and their results were compared with data from outcropping analogues. Chemical discrimination methods were identified to relate the wellbore core samples to the units in the outcrops. The integrated field-based approach enabled unraveling the complexity of geothermal reservoir rocks in active volcanic settings and updating the conceptual geological model of the Los Humeros geothermal field.

Chapter 6 discusses the results of the previous chapters and the observed differences between outcrop analogues and the respective subsurface units, applications and limitations of the generated database, and the predictability of reservoir properties. Furthermore, the findings from the physiochemical investigations of the different rock units are discussed in the context of other recent studies carried out within the GEMex project such as geophysical surveys, volcanological studies, and reservoir simulations. Based on the previous findings, implications for an updated conceptual model of the Los Humeros field and the respective reservoir properties are presented and implemented in a local gravity model of the central part of the Los Humeros caldera. The latter is part of a modeling approach performed by Cornejo-Triviño et al. (2022, in preparation) to improve the understanding of the internal architecture of the Los Humeros geothermal field, and to map lithological changes/alteration zones and structural feeding zones.

Acknowledgement

Table of Contents

List of Figures

List of Tables

List of Formulas

List of Symbols

A	Cross-sectional area of the sample [mm²]
c	Cohesion [-]
cf	Formation compaction factor [PSI]
c_p or cp	Specific heat capacity [J kg^{-1} K^{-1}]
cp sat	Saturated specific heat capacity [J kg^{-1} K^{-1}]
d	Sample diameter [mm]
E	Static E-Modulus [N mm^{-2}] or [MPa]
E_{dyn}	Dynamic E-Modulus [N mm^{-2}] or [MPa]
F	Load at failure [MPa]
F	Formation factor [-]
G	Static G-Modulus [N mm^{-2}] or [MPa]
G_{dyn}	Dynamic G-Modulus [N mm^{-2}] or [MPa]
K	Bulk Modulus [N mm^{-2}] or [MPa]
K	Permeability [m²]
K_0	Initial permeability [m²]
K_{Ic}	Fracture toughness [MPa]
l	Sample length [mm]
M	Estimated average thickness [m]
P	Pressure at reservoir depth in [bar] or [MPa]
P_0	Atmospheric pressure in [bar] or [MPa]
Q_1	25% quartile
Q_3	75% quartile
T	Temperature [K] or [°C]
VHC	Volumetric heat capacity [J m³ K^{-1}]
VHC sat	Saturated volumetric heat capacity [J m³ K^{-1}]
v_P or V_P	P-wave velocity [m s^{-1}]
v_S or V_S	S-wave velocity [m s^{-1}]
$V_{P\,sat}$	Saturated P-wave velocity [m s^{-1}]
$V_{S\,sat}$	Saturated S-wave velocity [m s^{-1}]
z	Depth [m]
α or α dry	Thermal diffusivity [m² s^{-1}]
α sat	Saturated thermal diffusivity [m² s^{-1}]
ß	Compressibility [PSI]
λ or λ dry	Thermal conductivity [W m^{-1} K^{-1}]

λ sat	Saturated thermal conductivity [W m^{-1} K^{-1}]
λ(0)	Normalized thermal conductivity at 0 °C [W m^{-1} K^{-1}]
λ(25)	Measured thermal conductivity at 25 °C [W m^{-1} K^{-1}]
λ(T)	Thermal conductivity at temperature T at reservoir depth [W m^{-1} K^{-1}]
λ(P)	Thermal conductivity at pressure P at reservoir depth [W m^{-1} K^{-1}]
λ(T,P)	Thermal conductivity at a specific temperature and pressure at reservoir depth [W m^{-1} K^{-1}]
μ	Poisson ratio [-]
μ_{dyn}	Dynamic Poisson ratio [-]
ρ	Density [kg m^{-3}]
ρ_B or ρB	Bulk density [kg m^{-3}]
ρB sat	Saturated bulk density [kg m^{-3}]
ρ_P or ρP	Particle density [kg m^{-3}]
ρ_F or ρF	Fluid density [kg m^{-3}]
σ_n	Normal stress [N mm^{-2}] or [MPa]
σ_1	Vertical stress [N mm^{-2}] or [MPa]
σ_3	Confining pressure [N mm^{-2}] or [MPa]
σ_t	Tensile strength [MPa]
σ_U	Measured UCS [MPa]
$\sigma_{U(2)}$	Corrected UCS [MPa]
τ	Shear stress [N mm^{-2}] or [MPa]
ф	Porosity [%]
ф$_0$	Initial porosity [%]
φ	Friction angle [°]
X	Magnetic susceptibility [SI]

Abbreviations

AC	Acoculco caldera
AGS	Advanced geothermal systems
AI	Ishikawa Alteration Index
BSEM	Back-scattered electron microscopy
bgl	Below ground level
BGS	British Geological Survey
CCPI	Chlorite Carbonate Pyrite Index
CFE	Comisíon Federal Electricidad
CIA	Chemical Index of Alteration
CIW	Chemical Index of Weathering
CV	Coefficient of variance
CWI	Chemical Weathering Indices
DC	Direct current resistivity
EDS	Energy Dispersive Spectrometry
EGS	Enhanced Geothermal Systems
HREE	Heavy rare earth elements
HP/HT	High-pressure/high-temperature
ICP-MS	Inductively coupled plasma mass spectrometry
LH	Los Humeros
LHGF	Los Humeros geothermal field
LHVC	Los Humeros Volcanic Complex
LREE	Light rare earth elements
m a. s. l.	Meters above sea level
MD	Measured depth
MSCL	Multi-sensor core logger
MT	Magnetotelluric method
PIA	Plagioclase Index of Alteration
PLM	Polarized light microscopy
REE	Rare earth elements
SEM	Scanning electron microscope
SHGS	Super-hot geothermal systems
SMT	San Miguel Tenango
TC	Thermal conductivity
TEM	Transient electromagnetic method

TD	Thermal diffusivity
TDS	Total dissolved solid
TMVB	Trans-Mexican Volcanic Belt
UNAM	Universidad Nacional Autónoma de México
XRF	X-ray fluorescence
XRD	X-ray diffraction

1. Introduction

The world energy demand is constantly increasing and it has never been more important to provide baseload and environmentally friendly energy to ensure economic viability, tackle climate change, and reduce geopolitical dependencies on fossil fuels. While renewable electricity generation in 2021 set new records in the fastest year-to-year growth (+ 8%), particularly for electricity generated from solar and wind power systems, much more effort is needed to reach Net Zero Emission targets by 2050 (IEA, 2021). Among renewable energy sources, only geothermal energy has the potential to contribute long-term baseload energy to the energy mix. Geothermal energy is defined as thermal energy generated and stored in the Earth's crust, which is used for electricity production, and the cooling and heating of buildings (Huenges, 2010). Despite steady growth over the past decades (plus 200 MW in 2021), geothermal energy only accounts for a fraction of the renewable energy capacity (< 0.1%), and the pace is falling below the required average annual capacity expansion of 3.6 GW per year to meet the target of 330 TWh in 2030 (IEA, 2021). While countries like Turkey, Indonesia, or Kenya with abundant untapped conventional geothermal resources are responsible for most of the current geothermal capacity growth, geothermal energy could theoretically be used everywhere. So-called 'unconventional' geothermal systems such as deep high-temperature hydrothermal systems or deep hot dry rock have the largest potential worldwide for deep geothermal energy utilization (Huenges, 2010). According to Lu (2018), fossil fuels could be replaced completely by exploiting the high energy reserves in the upper 10 km of the Earth's crust (approximately 1.3×10^{27} J). The development and exploitation of such systems would allow harnessing geothermal energy almost everywhere, also in areas with geological conditions that were previously considered less favorable for geothermal energy utilization. However, the controlling mechanisms of these deep high-temperature resources are not understood yet and comprehensive and detailed exploration, as well as new drilling technologies are required to provide safe and scalable energy that is economically competitive compared to fossil fuels.

Accurate reservoir characterization is crucial for reservoir development, operation, and monitoring (Aminzadeh and Dasgupta, 2013). Commonly, reservoir characterization starts with a simple conceptual geological model of the reservoir and the acquisition of comprehensive datasets from different disciplines such as geophysical surveys, well logs, structural data, production data, or information on the fluid and rock properties. The incoming data is used to derive reservoir properties such as reservoir thickness, number of reservoir units, hydraulic and thermal properties at reservoir conditions, pressure and fracture distribution, and subsequently, the static model is constantly updated based on the new knowledge. The improved static model will then be used to create numerical reservoir models for the simulation of e.g., subsurface temperature distribution, heat transport, and fluid flow, which form the basis for advanced resource and risk assessments.

During reservoir characterization, it is crucial to depict the geological conditions in the subsurface as accurately as possible. Especially for hydrothermal systems the economical success of geothermal projects highly depends on the correct identification of spatial heterogeneities and petrophysical anisotropies that might influence the fluid flow (Linsel et al., 2020). The current state of the reservoir is the result of diagenetic, tectonic, hydrothermal or metamorphic processes as well as reservoir production that alter the reservoir rocks and their properties over time and space. Therefore, the investigation of the controlling processes within the reservoir and the identification of lithological units with similar physiochemical characteristics that can depict the geological heterogeneity of the reservoir at different scales is essential for a profound reservoir assessment and the creation of reservoir models.

Starting with comparatively shallow (< 3 km depth) and easily accessible high-temperature resources, this thesis focuses on the reservoir characterization of super-hot unconventional geothermal systems linked to volcanic settings in Mexico. For this purpose, the already well-developed Los Humeros

geothermal field, and the Acoculco caldera, which is currently under exploration for geothermal energy utilization, were selected as demonstration sites. By applying an innovative multi-scale and multi-method approach, this work aims to improve the geological understanding of super-hot unconventional geothermal resources and help to accelerate their development for future use.

1.1. Deep Geothermal Systems

Deep geothermal energy resources are usually classified into conventional and unconventional systems. The term 'conventional geothermal systems' typically refers to easily accessible, naturally occurring steam or hot-water-dominated hydrothermal reservoirs, which are often restricted to areas with active volcanism or tectonic activity (Huenges, 2010). These systems are commonly characterized by sufficiently permeable reservoir rocks, an impermeable cap rock that traps the heat, and a sufficiently large recharge area allowing for sustainable utilization of the resource and fluids with temperatures that can range from a few degrees above ambient temperature to greater than 375 °C. In volcanic settings, these systems often reveal themselves on the surface through hot springs or fumaroles. The worldwide largest and most well-explored geothermal reservoirs (Table 1) are hydrothermal systems located in the USA (Geysers), Indonesia (Darajat), Philippines (Makban), Turkey (Kizildere), Kenya (Olkaria), New Zealand (Wairakei), Mexico (Cerro Pietro), Italy (Larderello), Iceland (Hellisheidi), and Japan (Kakkonda; Huttrer, 2021).

Table 1: Top 10 countries having the most installed geothermal power generation in 2020 after Huttrer (2021)

Country	MW_e installed in 2020
1. USA	3,700
2. Indonesia	2,289
3. Philippines	1,918
4. Turkey	1,549
5. Kenya	1,193
6. Mexico	1,105
7. New Zealand	1,064
8. Italy	916
9. Iceland	755
10. Japan	550

Unconventional geothermal systems include hot dry rock or enhanced geothermal systems (EGS), super-hot geothermal reservoirs, and advanced geothermal systems (Huenges, 2010; Stober and Bucher, 2021; Malek et al., 2021). To exploit unconventional resources innovative tools and engineering technologies are required. EGS often comprise promising high temperatures but lack the necessary initial rock permeability or reservoir fluids to transfer sufficient heat to the surface. Thus, reservoir stimulation is required to enhance or connect existing fracture zones in the subsurface to enable the fluid flow. Super-hot geothermal systems contain temperatures above 350°C, which would provide more energy per well than common geothermal installations (AltaRock, 2022), but also require specific drilling technologies and materials that can withstand the harsh reservoir conditions and corrosion caused by aggressive reservoir fluids (Stober and Bucher, 2021). In contrast, advanced geothermal systems use a

closed-loop system to circulate fluids in sealed pipes and boreholes completely relying on conductive heat transport in the deep subsurface (Malek et al., 2021). This approach requires precise lateral drilling to connect a horizontally arrayed series of lateral wells for the creation of the closed loop system.

Since conventional geothermal systems are restricted to a few sites worldwide, these energy resources are limited and not scalable. Unconventional systems have the worldwide largest potential for deep geothermal energy utilization (Huenges, 2010; AltaRock, 2022) and the development of advanced exploration, drilling, and exploitation technologies is required to make deep geothermal resources accessible on a large scale and economically competitive compared to existing energy resources such as coal and fossil fuels.

1.2. Super-Hot Unconventional Geothermal Systems

In this thesis, the term 'super-hot geothermal systems' (SHGS) refers to geothermal systems with high reservoir temperatures above 350 °C as defined in the GEMex project.

In the past, the terms 'super-hot' or 'super-heated' were often used synonymously with 'supercritical' and a clear temperature/pressure definition does not exist so far (Dobson et al., 2017; Kruszewski and Wittig, 2018; Heřmanská et al., 2019). Supercritical fluids are often defined as single-phase fluids exceeding the critical temperature and pressure. Beyond the critical point, the differences between the thermodynamic properties of the liquid and the vapor phase disappear (Suárez-Arriaga, 2019; Fig. 2). Considerable disagreement exists in the scientific community about whether the term 'supercritical' applies only to fluids with both temperature and pressure above the critical point of the fluids or also includes fluids exceeding the critical temperature but not the critical pressure (Heřmanská et al., 2019). For pure water, the critical properties are obtained at temperatures of > 374 °C and pressures of > 221 bar, which corresponds to a drilling depth of approximately 3500 m (Kruszewski and Wittig, 2018). However, the critical temperature and pressure of fluids increase with salinity. For seawater with 3.5% NaCl this point is reached at 405 °C and 302 bar, which corresponds to a drilling depth of about 5300 m. According to Elders et al. (2014), these conditions can already be reached for saline fluids between 2300 m and 3000 m depth in low-permeable systems (a sealing horizon that allows the pressure to exceed hydrostatic conditions is required; Dobson et al., 2017).

In contrast to subcritical fluids, supercritical fluids are characterized by a significant increase in fluid enthalpy, but reduced fluid density, fluid viscosity, and fluid thermal conductivity (Suárez-Arriaga, 2019; Fig. 2). Due to the high fluid enthalpies and reduced fluid viscosities, geothermal wells would have much higher productivity and higher mass transport (higher ratio of buoyancy forces relative to viscous forces; Elders et al., 2014), which make drilling into supercritical conditions very attractive. Assuming that a conventional high-temperature geothermal well (200 °C) produces about 3–5 MW_e, recent studies claim that the extraction of supercritical fluids increases the productivity by a factor of ten compared to conventional wells due to five times the energy content of the fluid and two times the conversion efficiency of the thermal heat to electricity (Cladouhos et al., 2018; Friðleifsson et al., 2014a, 2014b). According to Cladouhos et al. (2018) three very deep wells that reach supercritical conditions (~ 400 °C) could replace 42 EGS wells (200 °C) and reduce the costs of deep geothermal projects dramatically.

Super-hot geothermal reservoirs are commonly associated with active volcanic systems with high-temperature gradients and high heat flows due to shallow intrusions (Dobson et al., 2017). Thereby, super-critical fluids are thought to be located at great depth near the brittle-ductile zone close to an intrusive body representing the deep root of the geothermal system (Heřmanská et al. 2019). However, in volcanic settings temperatures exceeding the critical temperature can occur at comparatively shallow depths (< 2 km; e.g., Geysers, Los Humeros, Larderello). The worldwide largest and most efficient geothermal fields as described above (Table 1) are super-hot geothermal systems related to magmatic systems. However, supercritical conditions can theoretically be reached everywhere close to the brittle-

ductile zone, but require much deeper wells (AltaRock, 2022). Watanabe et al. (2017) infer that even though permeability generally decreases with reservoir depth, sufficient permeability remains in the brittle-ductile zone, and potentially exploitable resources could exist at 2–6 km depth in the granitic crust reaching temperatures between 375 and 400 °C.
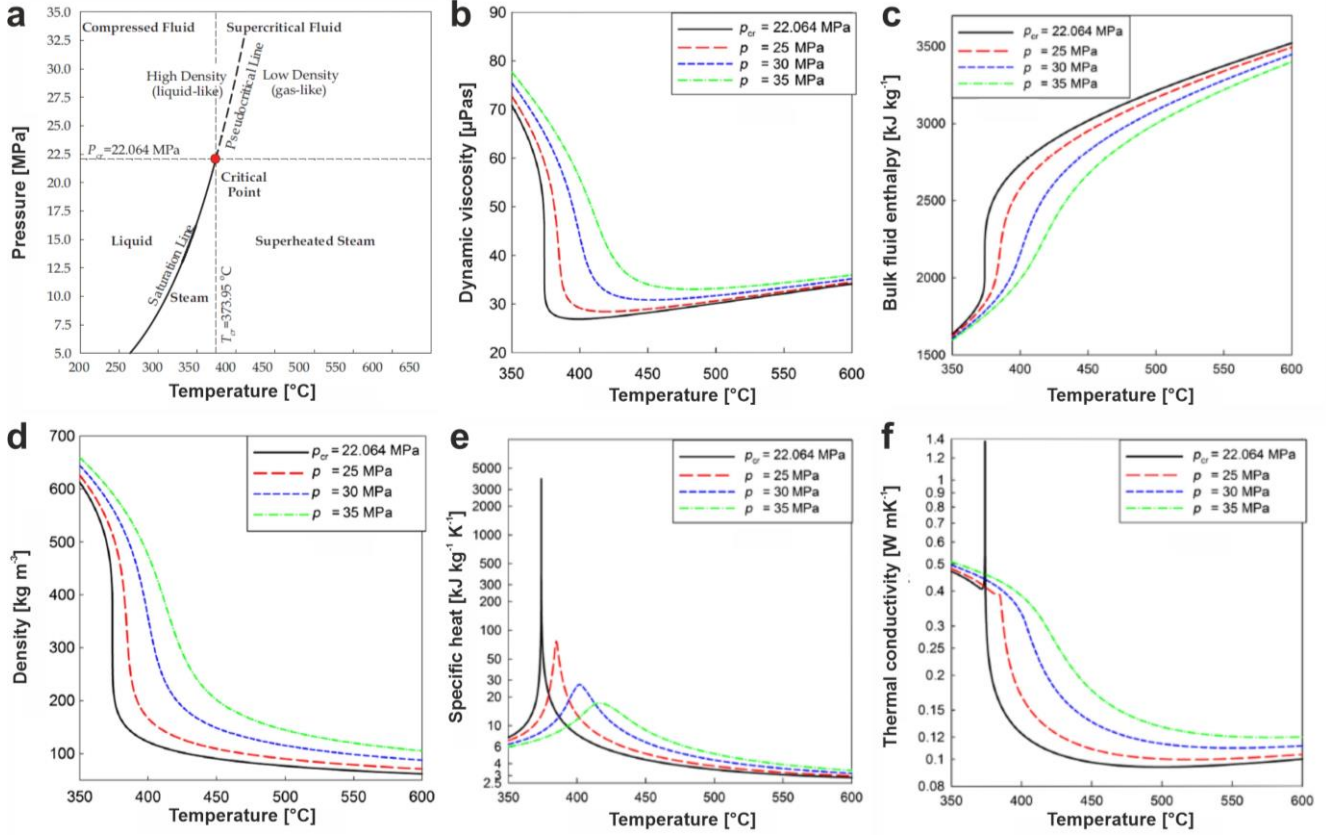
Figure 2: Pressure-temperature diagram for pure water (a), and fluid properties plotted against temperature (b-f) modified from Pioro (2014): dynamic viscosity vs. temperature (b), enthalpy vs. temperature, density vs. temperature (d), specific heat vs. temperature (e), and thermal conductivity vs. temperature (f).

Up to now, no geothermal power plant is producing fluids from reservoirs that exceed the respective critical temperature and critical pressure. However, about 25 wells have been drilled in the past that reached supercritical conditions (Kruszewski and Wittig, 2018), e.g., Reykjanes in Iceland, Geysers, Salton Sea, and Puna, Hawaii in the USA or Los Humeros in Mexico (Fig. 3). The majority of these wells are associated with active magmatic systems and several problems occurred during the drilling process such as casing failure, cementing failure, handling of loss circulation zones, risks of blow-outs and difficulties in cooling the well, damage to the wellhead assembly and drill string as well as heavy corrosion caused by acidic fluids and silica scaling (Kruszewski and Wittig, 2018).

Figure 3: Geothermal fields where temperatures > 374 °C were recorded (Bromley et al., 2021).

To overcome these challenges and to harness these resources in the future, innovative exploration and drilling technologies as well as a much better understanding of super-hot geothermal systems in general are required. Therefore, several international research projects have been or are currently conducted: IDDP (Reykjanes, Iceland), DESCRAMBLE and DEEPEGS (Larderello, Italy), Japan Beyond Brittle Project JBBP (Kakkonda, Japan), HADES (Hotter and Deeper) and The Next Generation (Taupo volcanic zone, New Zealand), ENN (Longfang, China), GEMex (Acoculco and Los Humeros, Mexico), and Newberry Deep Drilling project (Newberry, USA). Most of these projects target super-hot geothermal systems related to active volcanic systems because supercritical conditions could be reached at a comparatively shallow depth to reduce drilling costs. However, projects such as DOE FORGE (Utah, USA) and Super-hot EGS (Newberry, USA, AltaRock, 2022) focus on drilling into the brittle-ductile zone of crystalline rocks with up to 10 km deep wells to develop technologies that could make deep geothermal resources independent from specific geological sites (such as active volcanoes) and scalable for worldwide implementation.

Although significant improvements have been made during the past years regarding new drilling materials and technologies that can withstand the harsh conditions at reservoir depth (Petty et al., 2020), future research needs to focus on high-temperature cement and casing, high-temperature materials for bits and directional control systems as well as cooling of the wellbore. The current methods rely on cooling the wellbore drastically during drilling, which puts enormous stress on the downhole equipment (bits, BHA), casing, connections, and particularly cement as soon as the cooling stops (several heat cycles due to e.g., problems during drilling or when drilling is completed), which often causes stress-induced cracks. Thus, current research is developing e.g., non-metal materials, self-healing cement, new ultra-deep drilling technologies (plasma drilling, pressure-controlled drilling) using aerated water or nitrogen for cooling, high-temperature mud motors with liquid nitrogen cooling, CO_2-based stimulation methods or high-temperature logging tools (AltaRock, 2022).

According to Petty et al. (2020), the perhaps greatest improvements are needed in reservoir creation and management. The behavior of rock under high T/P conditions and the long-term fluid-rock interactions under in-situ conditions are not well understood which in turn are essential to predict the behavior of the reservoir formations during reservoir stimulation and operation. So far, high T/P laboratory experiments are scarce (Kummerow and Raab, 2015; Wanatabe et al., 2017), time-consuming, and very expensive. Supercritical EGS laboratories are under development in Japan and China. Furthermore, simulating a super-hot geothermal reservoir requires advanced modeling tools, which can incorporate the flow of single-phase, two-phase or supercritical fluids, fluid-rock interactions with gases and brines, and conductive and convective heat transport (Bromley et al., 2021). Recent efforts focused on tackling multiphase flow modeling and energy extraction (Feng et al., 2021), boiling and condensation above magmatic intrusions (Scott et al., 2017), or the reinjection into supercritical geothermal systems (Parisio et al., 2019).

1.3. Geothermal Energy Production in Mexico

Mexico hosts numerous subaerial and submarine hydrothermal systems (Prol-Ledesma and Morán-Zeteno, 2019) predominantly related to active volcanic areas (Fig. 4). Heat flow ranges between 40 mW m^{-2} in the southern and north-eastern coast plains and > 200 mW m^{-2} in the central part of Mexico within the Trans-Mexican Volcanic Belt (TMVB). Prol-Ledesma and Morán-Zeteno (2019) defined eleven geothermal provinces based on the play-type concept presented in Moeck (2014). The majority of these provinces contain convection-dominated magmatic and plutonic heat sources and to a lesser extent hydrothermal systems associated with oil deposits.

Although Mexico consists of numerous potential areas for geothermal energy production, geothermal energy utilization is still underdeveloped (Romo-Jones et al., 2021). Mexico's electricity generation relies about 80% on coal, oil, and gas (IEA, 2020), while geothermal power production contributes only 1.6% to the annual electricity generation. Direct uses of geothermal heat are predominantly limited to swimming facilities and recreational purposes and make up 156.1 Wth in Mexico (Romo-Jones et al., 2021). However, recent studies also highlight the enormous potential for geothermal heat utilization. Iglesias et al. (2015) estimated that there are more than 900 geothermal systems in Mexico of which 50% have a temperature between 62–100 °C, 40% have temperatures between 100–149 °C, and 5% have temperatures above 149 °C.

Up to now, five geothermal fields with a total electrical capacity of 947.8 MW$_e$ are under operation in Mexico (Romo-Jones et al., 2021): Cerro Pietro (Baja California), Los Azufres (Michoacán), Los Humeros (Puebla), Las Tres Vírgenes (Baja California Peninsula), and Domo de San Pedro (Nayarit). Thereby, the total electricity generated in Mexico was 5.375 GWh in 2018 (Romo-Jones et al., 2019; Table 2). Except for Domo San Pedro, all geothermal fields are owned and operated by the governmental institution Comisíon Federal Electricidad (CFE).

Numerous sites are currently under exploration for geothermal energy production in Mexico. Within the TMVB about 15 potential geothermal fields were identified including Acoculco and Las Derrumbadas (Prol-Ledesma and Morán-Zeteno, 2019).
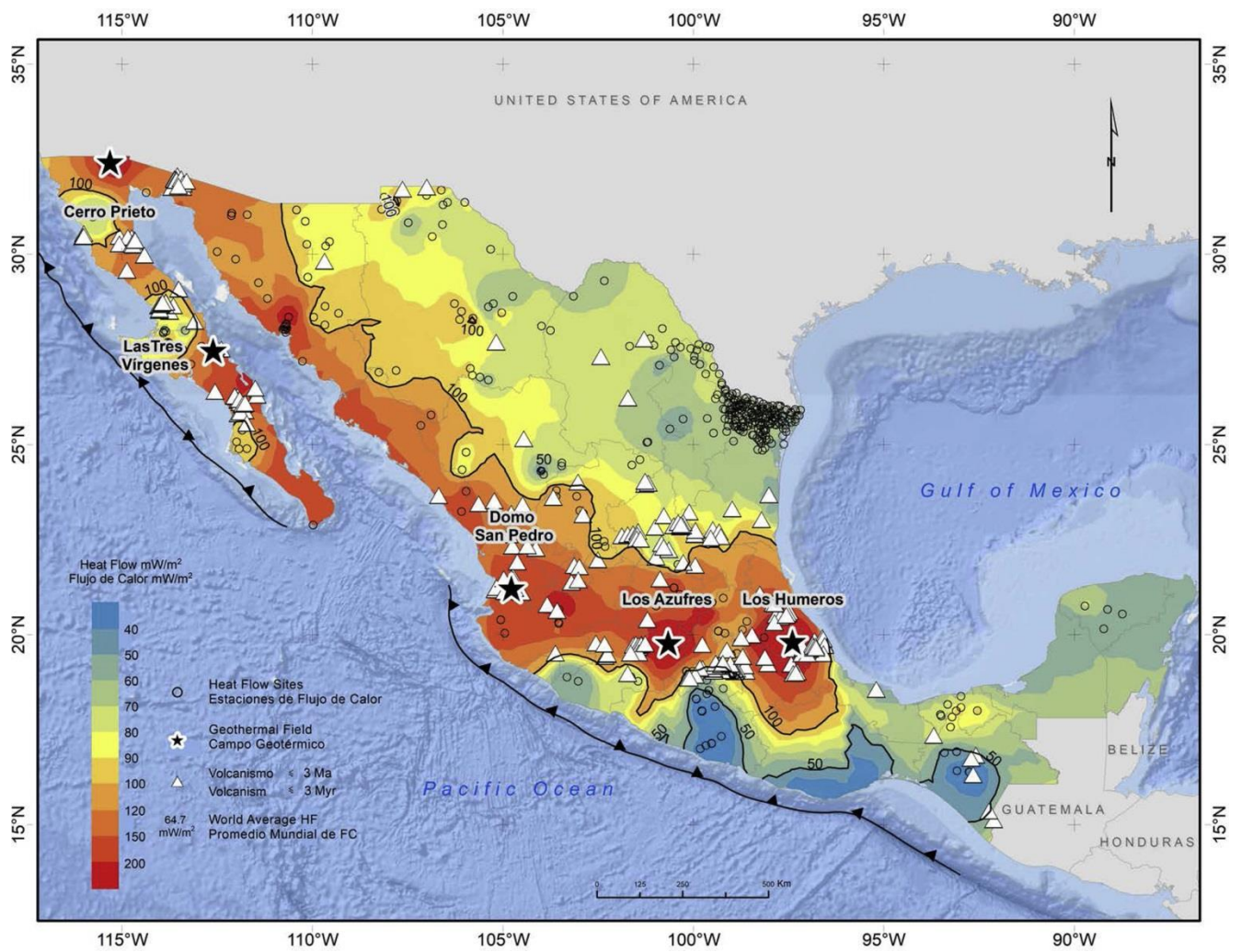
Figure 4: Heat flow map of Mexico including the five geothermal fields under operation (Prol-Ledesma and Morán-Zeteno, 2019).

Table 2: Geothermal fields in operation in Mexico in 2018 (Romo-Jones et al., 2019)

Geothermal field	Installed capacity (MWₑ)	Effective capacity (MWₑ)	Production wells	Injection wells	Year
Cerro Prietro	570.0	570.0	142	28	1973
Los Azufres	244.0	221.0	48	6	1982
Los Humeros	119.8	94.8	28	3	1990
Las Tres Vírgenes	10.0	10.0	3	1	2001
Domo de San Pedro	35.5	25.5	4	3	2015

1.3.1. The Los Humeros Geothermal Field

Exploration of the Los Humeros Volcanic Complex (LHVC; at ~ 2800 m above sea level (m a.s.l.); Fig. 5) for geothermal utilization started already in the late '60s to '80s and the first well was drilled in 1981 (Bienkowski, 2003; Pinti et al., 2017). However, geothermal energy production started in 1990 with the first 5 MW$_e$ power plant. Up to now, 65 wells have been drilled of which 28 are still productive and three wells are used as injection wells. Today the geothermal field consists of three condensing flash units of 26.6 MW$_e$ and eight backpressure units 5 MW$_e$ each (although 5 backpressure units are currently out of operation; Romo-Jones et al., 2019).

Figure 5: Geothermal power plant inside of the Los Humeros caldera.

The wells produce mainly steam (5.35 million tons in 2018) with high enthalpies of > 2400 kJ kg^{-1} except for well H1 which produces water (1500–1700 kJ kg^{-1}, Pinti et al., 2017). The wells produce between 6 and 56 t of steam per hour and the extracted heat ranges between 0.5 and 41 PJ (González-García et al., 2021). The majority of the boreholes target deep Miocene to Pleistocene andesites at ~ 1500–3000 m depth where temperatures between 300 °C and 400 °C occur (Fig. 6). The most profitable areas are in the central collapse zone (north of Los Humeros; central to the northern sector of the geothermal field) and along the Los Humeros–Maztaloya faults (Gutiérrez-Negrín and Izquíerdo-Montalvo, 2010). Several hydrothermal manifestations like Loma Blanca can be found in this area. The most productive wells are H9 (northwestern sector of the central collapse zone), H12 (close to the Xalapazco crater), H6 (along the Maztaloya fault), and H7 (close to the Los Humeros fault; Fig. 7), which have a large spatial distance to each other. According to CFE, most of the wells encountered more than one feeding zone within the andesites (except for H9, which produces from the underlying carbonate basement; Fig. 7).

Until recently, the conceptual geological models from Cedillo (2000) and Arellano et al. (2003) were used for reservoir management and development. These studies assume two andesitic reservoirs (upper reservoir = Teziutlán augite andesites, lower reservoir = Hornblende andesite), which feature different reservoir properties and are separated by a thick tuff aquitard (Humeros vitric tuff, Fig. 6). The

shallower reservoir in the Teziutlán andesites (1600–1000 m a.s.l.) is considered liquid-dominated with temperatures between 300 and 330 °C and the deeper aquifer (900–100 m a.s.l.) is considered a two-phase reservoir with temperatures of up to 400 °C (Portugal et al., 2002). It was assumed that the geothermal field is fed by one large magma chamber located between 5 and 11 km depth (Verma, 1985; Verma et al., 2011) and that fluid recharge takes place within the caldera (Cedillo, 2000).
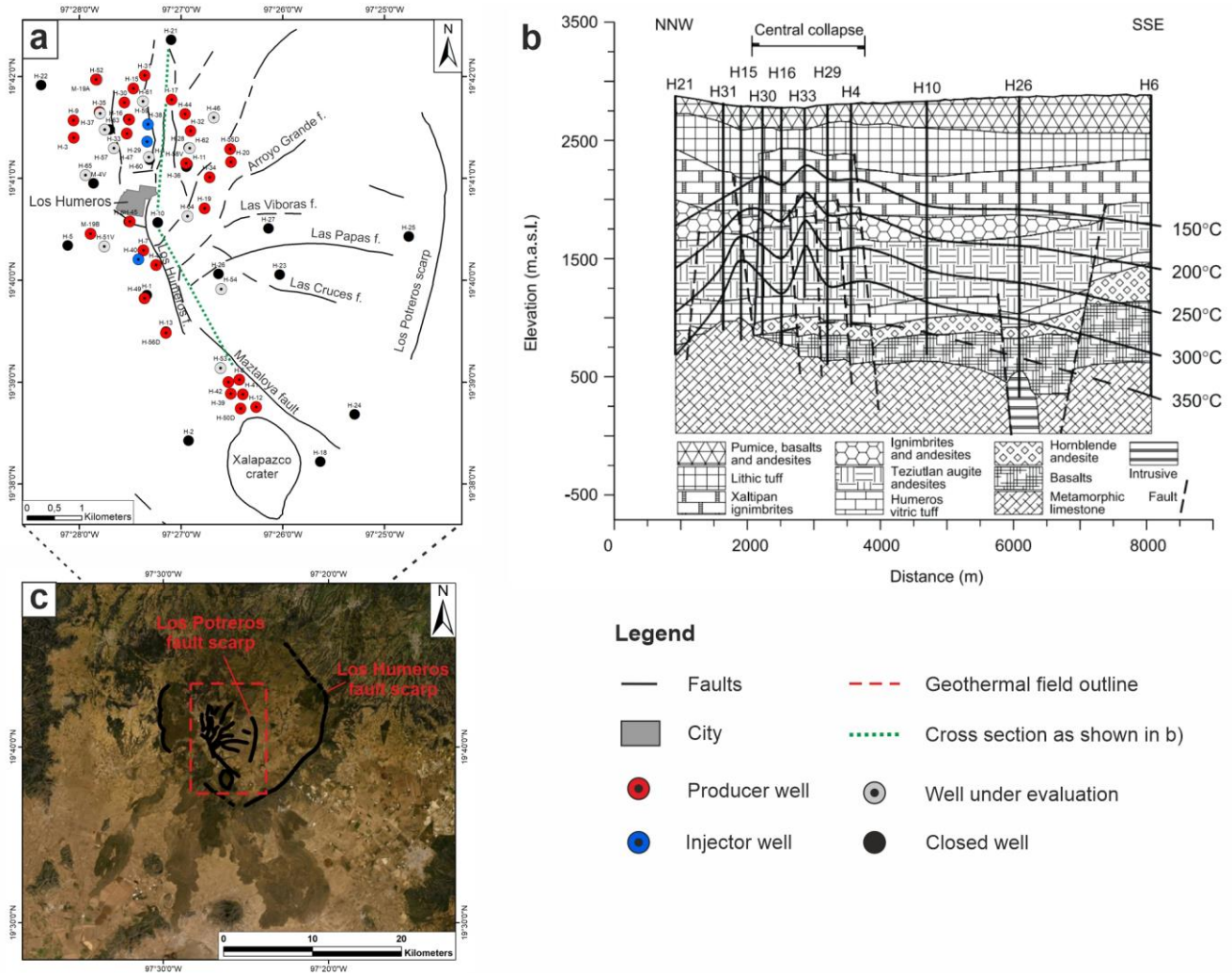
Figure 6: Landsat image of the caldera complex (c) and close-up view of the geothermal field (a). (b) shows the conceptual geological model of the Los Humeros geothermal field after Arellano et al. (2003) used at the beginning of the GEMex project.

The geothermal field contains low-saline NaCl to H_2CO_3-SO_4 fluids, which are oversaturated with quartz and calcite and locally contain high boron, ammonia, and arsenic concentrations (Izquíerdo et al., 2009). Furthermore, acidic fluids with low pH (2.5–4) were identified in some deep and very hot wells in the central collapse zone, which led to heavy corrosion and silica scaling. Attempts to neutralize the acidic fluids with 47% NaOH were carried out (Flores-Armenta et al., 2010), but most of the deeper production zones were plugged with cement and drilling into these super-hot and acidic zones has been avoided since then (Gutiérrez-Negrín and Izquíerdo-Montalvo, 2010).

Only a fraction (~ 16%) of the produced fluids is currently reinjected into the reservoir with an average temperature of 90 °C (González-García et al., 2021). The exploitation of fluids over the past 30 years caused boiling with steam condensation, production of returns from injection, interaction with deep fluids, and a decrease in liquid saturation due to insufficient recharge (Arellano et al., 2015).
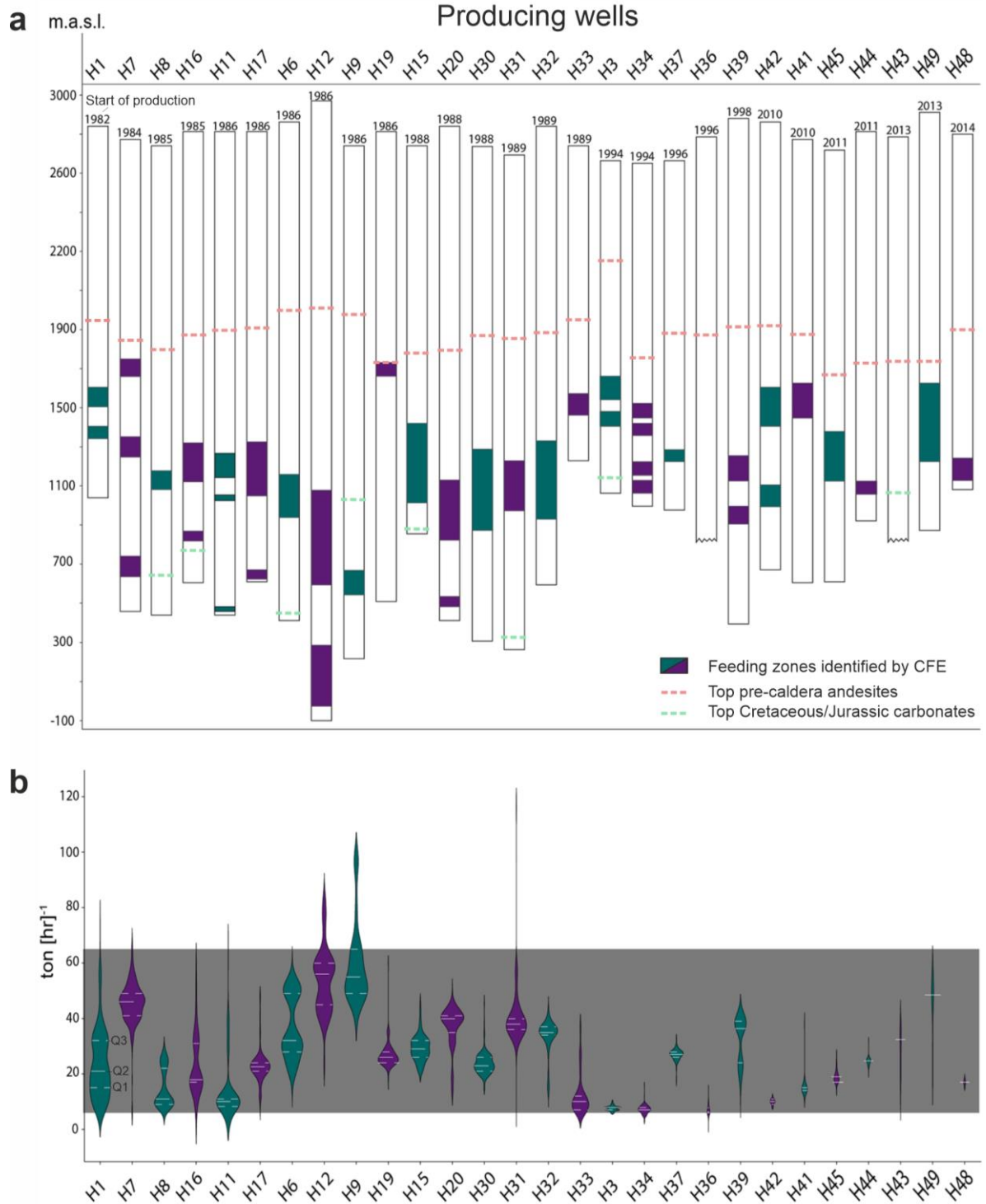
Figure 7: (a) Well depths and feeding zones of the producing wells in Los Humeros (modified from González-García et al., 2021). (b) Violin charts showing the distribution of the production rates (the width is proportional to the number of data points for the respective flow rate; the white lines represent the median (Q2), 25-quartiles (Q1), and 75-quartiles (Q3)). The grey box represents the range of the production of the geothermal field. The bottom of the box is defined by the Q1 of the less productive well and the top by the Q3 of the most productive well.

1.4. GEMex Project

To utilize super-hot resources sustainably and economically in the future, comprehensive and detailed exploration is needed to improve reservoir understanding and enable better reservoir modeling. Therefore, the GEMex project (EU-H2020, GA Nr. 727550) focused on the development of (hot) EGS and SHGS on two sites in the northeastern part of the Trans-Mexican Volcanic Belt (TMVB), the Acoculco and Los Humeros caldera complexes (Puebla).

Although already exploited for over 30 years, the super-hot zones of the Los Humeros geothermal field are untapped yet (chapter 1.3). To increase the productivity of the geothermal field and to tackle the encountered problems caused by the challenging reservoir conditions, the Los Humeros geothermal field was selected as a potential site for the development of an SHGS.

The Acoculco caldera complex is still under exploration and only two exploration wells have been drilled so far. Although promising temperatures of approximately 300 °C at about 2 km depth were encountered and a well-developed fracture network was identified in the field, both wells were found dry. Therefore, reservoir stimulation was planned to connect existing fractures and to develop an EGS.
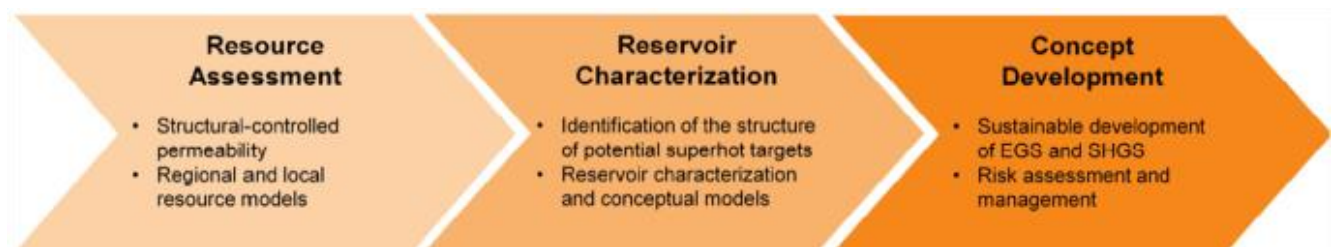
Figure 8: Simplified workflow of the GEMex project comprising three milestones (GEMex, 2022; www.gemex-h2020.eu).

The GEMex project included an international consortium of eight Mexican and 24 European institutions as well as CFE who granted access to the sites and operational data. A multidisciplinary approach (Fig. 8) was applied to find new transferable exploration approaches and technologies based on three milestones which are (1) resource assessment, (2) reservoir characterization, and (3) concepts for site development (Jolie et al., 2018). Between 2016 and 2020 extensive geological, geochemical, geophysical, and technical investigations were performed within eight work packages. The project comprised a complex workflow for the compilation and integration of extensive data sets from different scientific disciplines (e.g., geophysical surveys, field data, and laboratory analyses). The resulting data and models of all work groups were combined in integrated reservoir models at a local, regional and super-regional scale (Fig. 9; Calcagno et al., 2022).
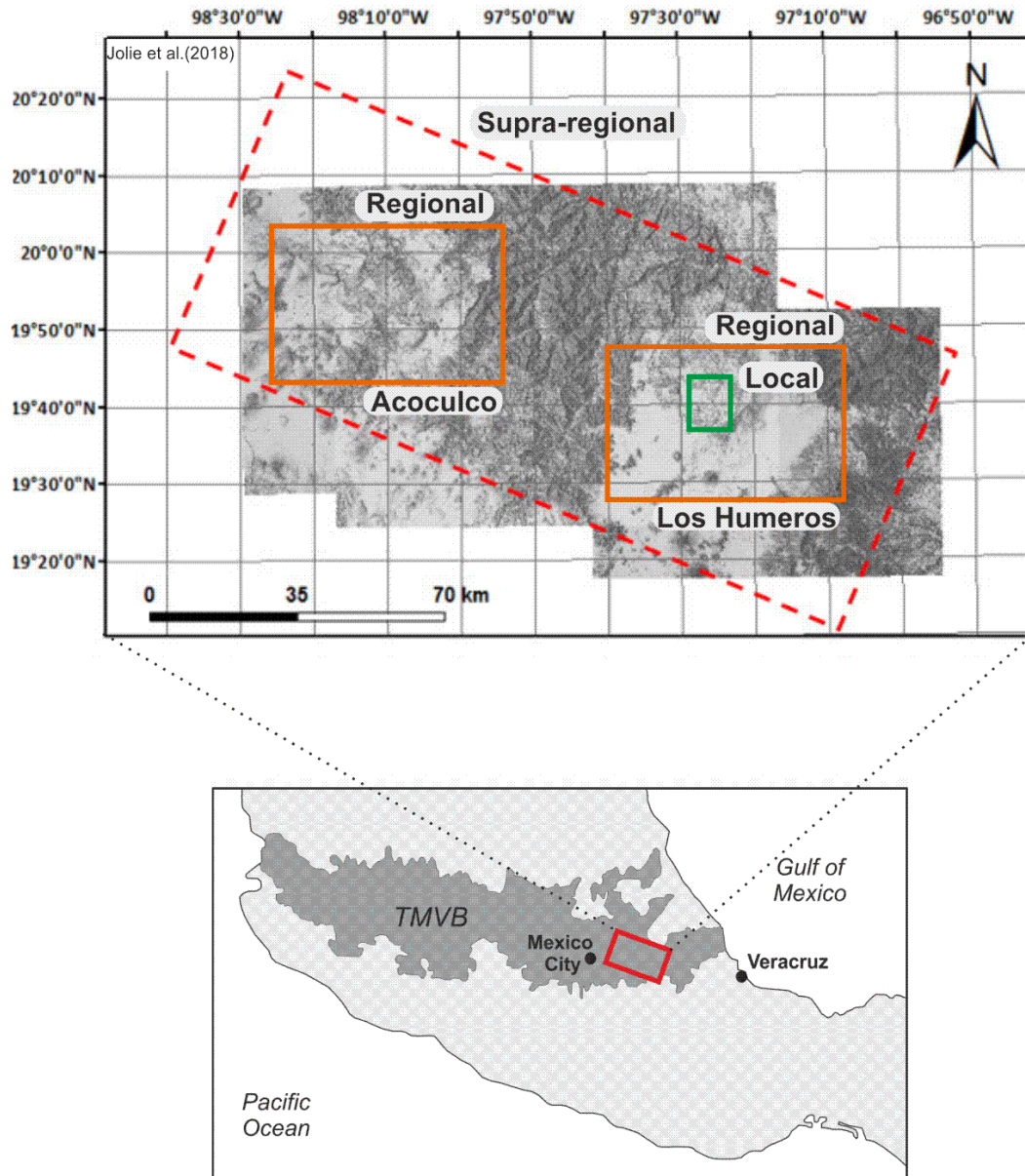
Figure 9: Location of the study area within the TMVB and outline of the supra-regional, regional, and local reservoir models created within the GEMex project (upper figure modified from Jolie et al., 2018).

For this purpose, preliminary 3D geological models were created already at the beginning of the project and constantly updated. Figure 10 shows the preliminary regional (56 km × 36 km × 12 km) and local model (9.5 km × 12.5 km × 12 km) of the Los Humeros geothermal field provided by Calcagno et al. (2018, 2020, 2022). The regional model comprises four units, which are (1) post-caldera group, (2) caldera group, (3) pre-caldera group, and (4) pre-volcanic basement. The local model subdivides the first three regional units and consists of nine units in total. The classification of the model units was based on existing conceptual models (Cedillo, 2000; Arellano et al., 2003), information on the stratigraphy, and preliminary cross-sections (Carrasco-Núñez et al., 2017a; Norini et al., 2015). These models served as the starting point for the research presented in this thesis.
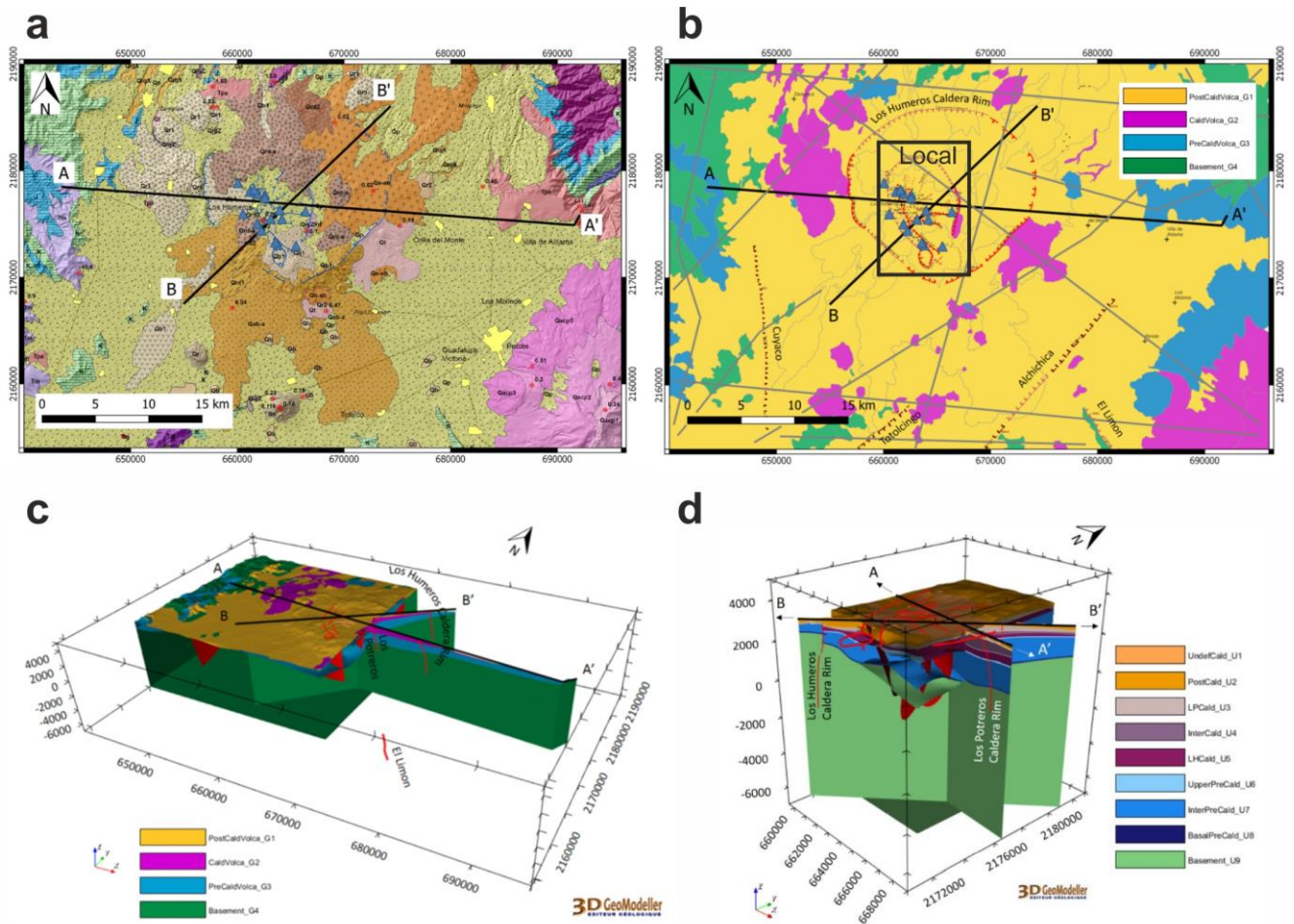
Figure 10: Preliminary 3D reservoir models of the Los Humeros geothermal field (Calcagno et al., 2018). (a) represents the first version of the new geological map of the Los Humeros Volcanic Complex provided by Carrasco-Núñez et al. (2017a) and (b) represents the reinterpreted geological map used for creating the regional 3D model (c). AA' and BB' represent cross-sections presented in Carrasco-Núñez et al. (2017a) and Norini et al. (2015), respectively. The blue triangles represent the lithostratigraphic profiles provided by CFE used to create the local 3D model presented in (d).

1.5. Objectives

Although the Los Humeros geothermal field has been under exploration for more than 40 years, many questions remain unsolved. The previous conceptual models (e.g., Cedillo, 2000; Arellano et al., 2003, and Verma, 1985) which assume rather homogenous and horizontally layered reservoirs fed by one uniform heat source, are not suitable to explain:

- temperature anomalies (> 300 °C) at comparatively shallow depths (< 1500 m bgl) as observed in downhole temperature profiles of some wells (Urbani et al., 2020 and 2021; Deb et al., 2021),
- fluid temperatures of up to 33 °C in shallow groundwater wells in the Perote plain southeast of the caldera (at about 2400 m a.s.l.; Lelli et al., 2020),
- the variable production rates within one subsurface unit (< 6–56 tons of steam per hour; González-García et al., 2021) and problems with the recharge of the geothermal reservoir (Arellano et al., 2015), although the majority of the producer wells target the assumed andesitic reservoirs (which are supposed to have sufficient permeability),
- the hydrogeology of the study area, and the locally high B, HCl, and HF contents as well as acidic reservoir fluids (< 4 pH) within the geothermal field (Flores-Armenta et al., 2010),
- the variety of alteration facies within the geothermal reservoir with occasionally low-temperature (< 250 °C) and high-temperature alteration minerals (> 350 °C) at the same depth (Martínez-Serrano, 2002) as well as local pervasive silicification observed in some borehole core samples (Izquíerdo et al., 2011),
- the variety of rock formations in the post-caldera group, which features very heterogenous basaltic to rhyolitic lavas (Lucci et al., 2020),
- inconsistencies in the original lithostratigraphic profiles of the boreholes regarding lithology, model units and their thickness.

The problems encountered during drilling and reservoir operation (Flores-Armenta et al., 2010; Arellano et al., 2015) demonstrate that the internal geological structures and the controlling processes of the geothermal system are not yet fully understood. To ensure successful reservoir development in the future, the way high-temperature resources are targeted needs to be re-evaluated, particularly for the development of super-hot to supercritical reservoirs.

Thus, this thesis focuses on the reservoir characterization of super-hot unconventional systems using the Los Humeros and Acoculco caldera complexes as natural laboratories. Since information on the reservoir properties of the target units were scarce or not available in the study area, this work aims to:

- characterize all relevant key units from the cap rock to the basement regarding their mineralogy, chemistry, petrophysical, and mechanical rock properties
- provide high-quality input data for a wide range of applications, which is able to depict the geological heterogeneity at different scales
- systematically investigate the hydraulic rock properties of the target units for better quantification and possible identification of potential reservoirs and fluid pathways in the subsurface
- identify and quantify processes that affect reservoir quality, and thus, geothermal production.

This information is crucial for the development of conceptual geological models, economic assessments, the interpretation of geophysical surveys, and the parametrization of numerical THMC reservoir models.

Due to time and budget constraints, the determination of rock properties commonly takes up only a small part during reservoir exploration or is completely discarded, and literature values are used for the estimation of reservoir properties. This leads to a high degree of uncertainty and is only suitable for preliminary assessments. Literature data and small sample sets are not able to depict the geological

heterogeneity of the study area as well as site-specific impacts on the reservoir properties caused by diagenetic, tectonic, metamorphic, and hydrothermal processes.

Challenges for a detailed rock characterization arise from the large study area (GEMex: ~ 100 × 160 km), the number of target units to be studied, their accessibility in the field, and geological heterogeneity. In contrast to sedimentary basins, magmatic settings commonly feature a large number of units with variable thickness and extension (no uniform horizontal layers), which makes the estimation of potential geothermal reservoirs, their thickness, extension, and rock characteristics extremely difficult. The majority of previous studies focused on a single unit, rock type, and/or a small set of parameters only (Bär et al., 2020; Weydt and Bär et al., 2021), and thus, the application of the results for the GEMex project was not suitable. Providing data sets that meet the requirements of various modeling approaches and geophysical surveys within a large research project leads to a high number of samples as well as considerable organizational and technical efforts. To make the results comparable with each other, laboratory methods and their measurement workflows need to be standardized. Furthermore, meta data such as outcrop coordinates or sample descriptions as well as data retrieved from different project partners need to be homogenized. Finally, the results need to be made available in a comprehensive but easy-to-use database.

To overcome these challenges, an innovative multi-scale and multi-method approach was developed and applied within the GEMex project. This approach includes (Fig. 11):

1) coordinated field work – scientists from different disciplines join forces and work together in the same outcrops to combine e.g., structural analyses with petrographic and rock property analyses

2) coordination of the sampling campaign and sample distribution for various laboratory analyses between the project partners – ensuring that all project partners work on the same sample set in the laboratory to validate measurement results (benchmark analyses) and that they are able to link their results with data from other disciplines

3) multi-method approach – whenever possible all rock parameters were analyzed on each sample, which allows the identification of relationships between different rock parameters and helps to link different investigation scales (from outcrop investigation to SEM analyses)

4) coordinated data collection – creation of an extensive ready-to-use database

5) application-specific processing and provision of data – statistical evaluation and pre-processing of the data for various geological, geophysical and modeling approaches within the project.

Based on this, the data and results from different disciplines can be integrated and interpreted to update the preliminary static 3D model.
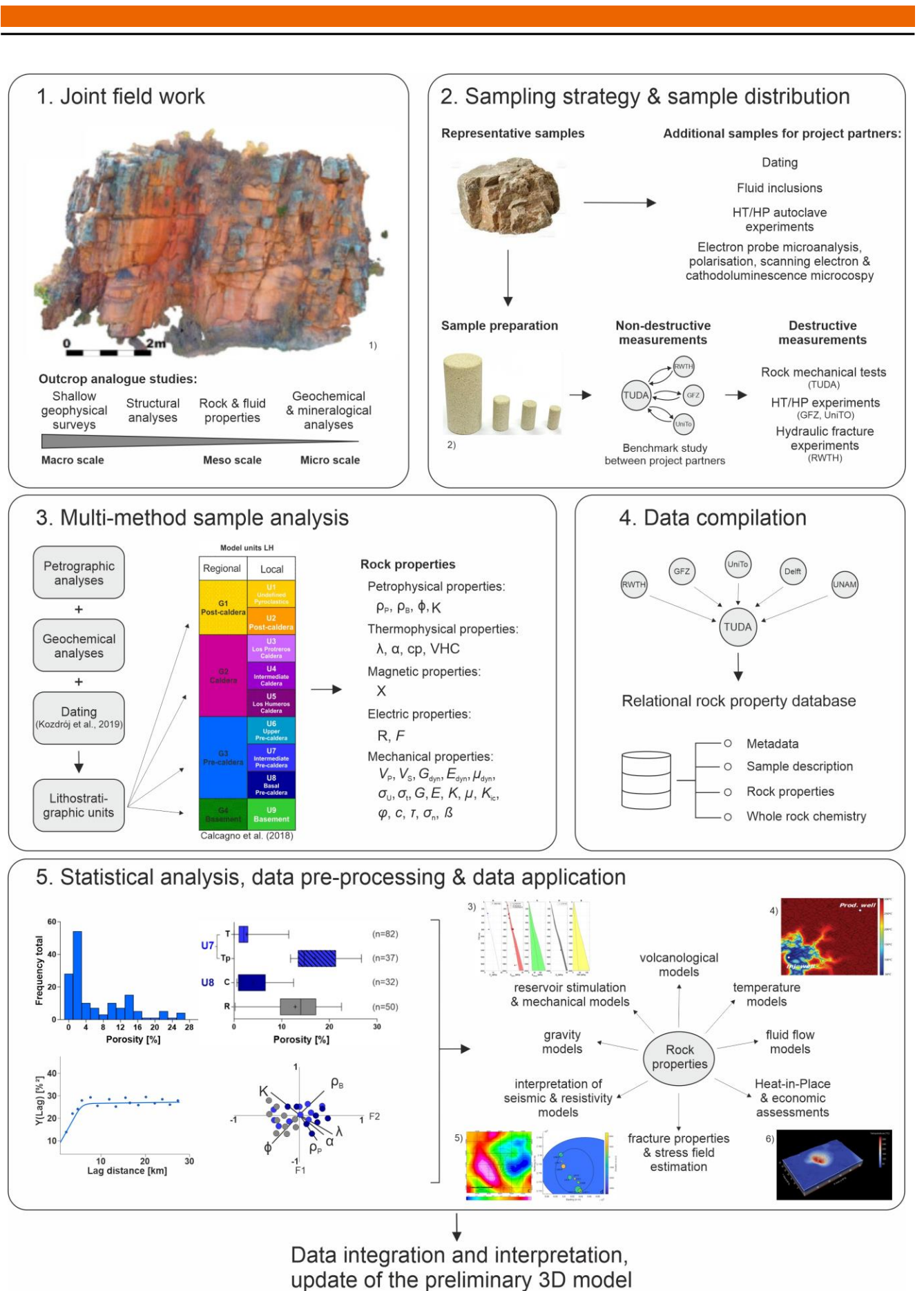
Figure 11: Work flow for reservoir characterization applied in the GEMex project (figures taken from 1 = Villarreal et al., 2020; 2 = Riabokon et al., 2021; 3 = Kruszewski et al., 2020; 4 = Lepillier et al., 2019; 5 = Deb et al., 2021; 6 = Deb, 2018).

2. Geological Setting

This chapter briefly describes the geological units of the basement underlying the caldera complexes, its deformation and structural setting as well as the evolution of the Trans-Mexican Volcanic Belt. Furthermore, the geological setting of the exhumed system of Las Minas will be addressed. A detailed geological description of the Los Humeros and Acoculco calderas is presented in chapters 3 to 5, and thus, will not be presented here.

2.1. Pre-Volcanic Basement and Structural Setting

The regional basement in the study area includes a Paleozoic to Mesozoic complex, also referred to as Teziutlán Massif, which comprises metamorphic and intrusive rocks and is partly covered by up to 3 km thick and highly deformed Mesozoic sediments (Yáñez and García, 1982; a simplified geologic map is shown in Fig. 12). The sedimentary succession contains Jurassic sandstones, shales, limestones and dolostones as well as Cretaceous limestones, shales, and marls and is part of the Sierra Madre Oriental NW-SE thrusts and fold province (Fitz-Díaz et al., 2017).
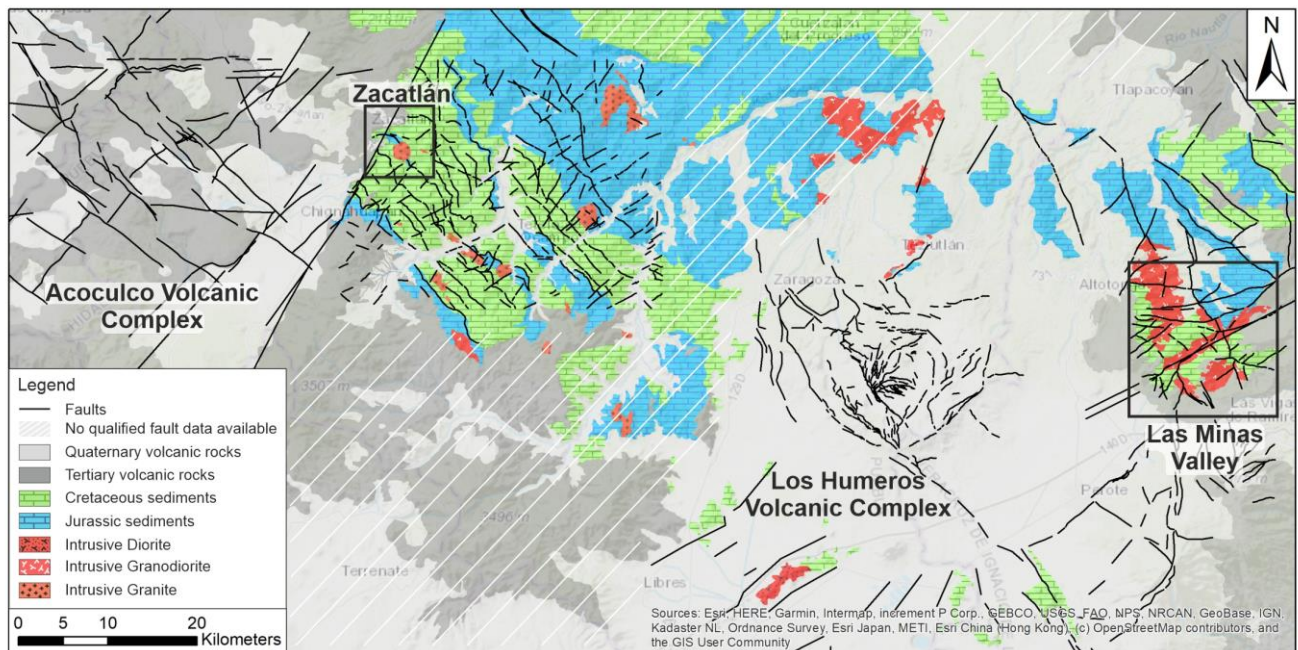
Figure 12: Outcropping sedimentary units and intrusive bodies in the study area (based on Lepillier, 2020; geological map modified from SGM 2002a, 2000b). Illustrations of the faults are retrieved from Liotta et al. (2019, for Acoculco only), Piccardi (2020) and Lepillier et al. (2019). The dataset from Piccardi (2020) is derived from Insar data and morpho-structural analyses. The regional faults presented in Lepillier et al. (2019) are retrieved from geological maps provided by the Servicio Geológico Mexicano (SGM 2002a, 2000b). The white shaded sections represent areas where qualifiable information on the faults supported by field measurements is currently not available.

The Jurassic sequences in the study area correspond to the Cahuasas, Tepéxic, Tamán, Santiago, and Pimienta Formations (sorted old to younger) and the Cretaceous outcrops predominantly exhume the Orizaba, San Felipe, Agua Nueva, Tamaulipas Inferior, and Superior Formations.

The Cahuasas Formation (Early to Middle Jurassic) represents volcaniclastic continental sandstones, conglomerates, and to a lesser extent siltstones and mudstones with a distinct red to purple and sometimes greenish-grey color (Yáñez and García, 1982; Ochoa-Camarillo, 1999). They are commonly referred to as 'redbeds' and contain no fossils. In the state Hidalgo, which borders Puebla to the northeast,

the Cahuasas Formation has an average thickness of ~ 300 m and can reach a maximum thickness of up to 1000 m (Ochoa-Camarillo, 1999). A sea-level rise caused a marine transgression in the Late Jurassic and resulted in the deposition of calcarenites, calcareous shales and limestones (Fitz-Díaz et al., 2012). Reactivation of normal faults resulted in horst and graben structures and the deposition of deep- and shallow water facies (Fitz-Díaz et al., 2012). The Tepéxic (~ 15–25 m thick), Tamán (~150–200 m thick in Hildago) and Santiago Formations (about 100 m thick in Puebla; SGM, 2022) overly the Cahuasas Formation and predominantly comprise blackish and fossil-rich calcarenites, calcareous shales, marls and some limestones intercalated with siltstones (Tamán Fm.; Ochoa-Camarillo, 1999). The overlying Pimienta Formation contains blackish argillaceous limestones and black to grey dolostones (Yáñez and García, 1982).

The Cretaceous marked the beginning of mainly carbonate sedimentation on platforms or in basins with various extensions (Fitz-Díaz et al., 2017). The Tamaulipas Inferior constitutes of stratified, fine-grained, grey limestones (mudstones – wackestones) with abundant irregular blackish to white chert lenses. The formation has a thickness of 60–400 m (SGM, 2022). Likewise, the Tamaulipas Superior comprises light grey to cream-coloured limestones (mudstones – wackestones) with stylolites and irregular chert nodules with a thickness of 0.1–0.3 m that are parallel to the stratification. The fossil-rich limestones (ammonites) are constituted in thick layers to banks and reach a thickness of about 200–400 m (SGM, 2022). The Orizaba Formation is known for its abundance of fossils and even contains fragments of mega fossils that can be identified in outcrops (Yáñez and García, 1982). This unit is characterized by dark grey, massive limestones (occasionally with chert) presented in banks with a thickness of 2–4 m that can be related to the reef facies and thinner layers (0.2–1.0 m) of mudstone to wackestones representing the off-reef facies. The reef facies often contain boundstones of rudists, gastropods, sponges and corals (Viniegra-Osario, 1965). Thickness data vary greatly and thicknesses between 300 m and 1300 m were reported in literature (SGM, 2022). The Agua Nueva Formation contains grey argillaceous limestones (wackestone to packstone), which is presented in layers of about 0.4 m with abundant chert bands and nodules (Yáñez and García, 1982). Occasionally the limestones are intercalated with thin grey-greenish bentonitic clays. In outcrops, the thickness was estimated as ~ 30 m in the Sierra Madre Oriental (SGM, 2022).

According to Gutiérrez-Negrín and Izquíerdo-Montalvo (2010) and references therein, fossiliferous limestones were identified in the subsurface of the Los Humeros geothermal field (well H2, 1140–2280 m), which were correlated to the Early Cretaceous (Tamaulipas Fm.) and Late Jurassic (Pimienta and possibly also Tamán and Santiago Fm.).

Two main tectonic events affected the pre-volcanic basement. The Late-Cretaceous to Eocene orogenic phase formed the Mexican fold and thrust belt, while an Eocene to Pliocene extensional tectonic deformation resulted in the formation of scattered NE-striking normal faults (Fitz-Díaz et al., 2017). The latter were interpreted as preferential pathways for Eocene-Oligocene intrusions preceding the onset of the Miocene volcanism of the TMVB as well as the Pliocene to Quaternary volcanism of the caldera complexes (López-Hernández, 1995; Norini et al., 2019).

The sedimentary basement has been intensively folded and thrust faults developed during the Oligocene-Miocene (Norini et al., 2019, Fig. 13). This structural setting can be observed in outcrops showing outcrop-scale folds interpreted as detached above km-scale thrusts with a dominant NE-directed transport. The carbonate units predominantly display a SW-dipping attitude, while almost cylindrical folding at different wavelengths with NW–SE trending fold axes have been recognized (Norini et al., 2019). Intra-formational thrust faults show a NE vergence and kinematic indicators suggest that the area deformed under a compressive stress field with dominant NE–SW trending maximum horizontal stress.

After the collisional stage, the area underwent extension due to the back arc evolution of the volcanic arc. In this new geodynamic setting, new structures developed, favoring flow of magmatic fluids along

pre-existing and forming fractures. Miocene dikes intruded into the basement rocks, which predominantly strike NE–SW and are parallel to the NE-striking normal faults and the maximum horizontal stress. In contrast, subvertical sills were mostly emplaced parallel to the SW-dipping bedding of the carbonatic rocks (along the weak bedding interfaces of the carbonates).
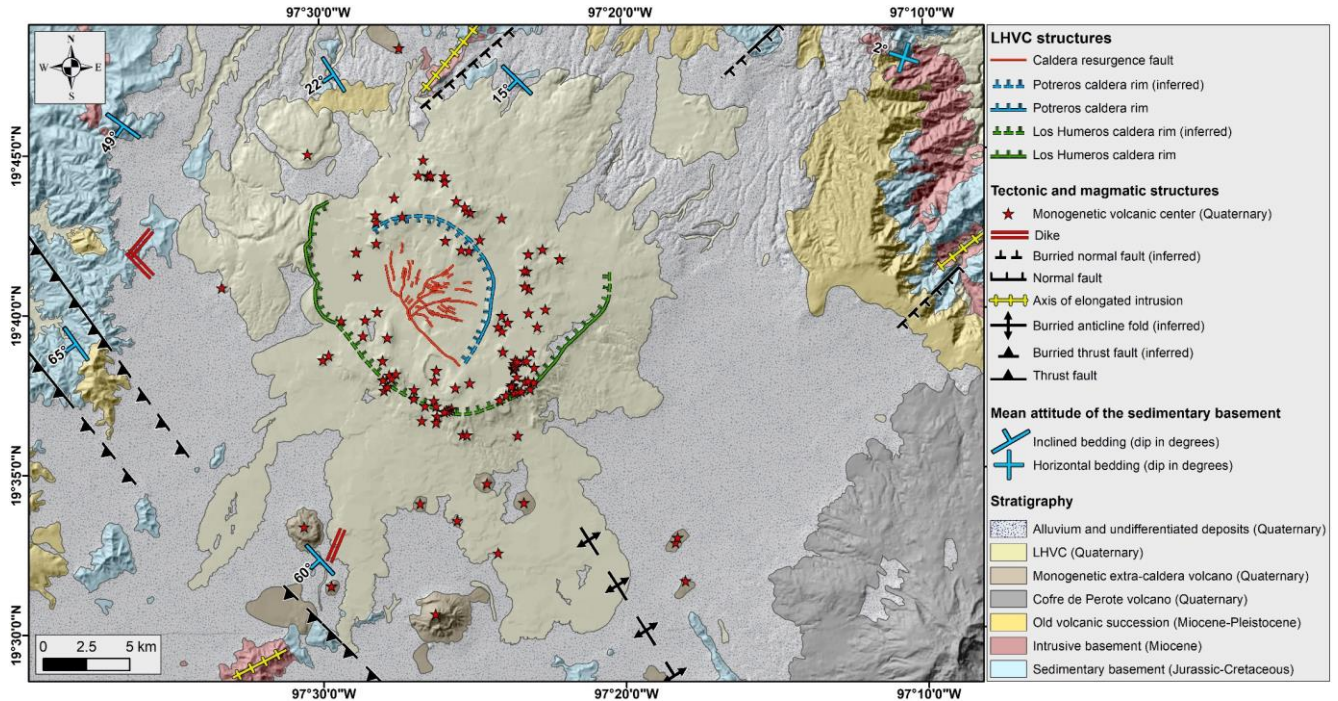
Figure 13: Tectonic and magmatic structures of the Los Humeros Volcanic Complex (Norini et al., 2019).

According to Bastesen et al. (2019) the NE–SW structures, which exhibit the major control on the intrusions in the study area, seem to be the oldest ones. Thereby, the E–W to ENE–WSW oriented structures appear to control the emplacement of the magma at depth in the Los Humeros Volcanic Complex. At present, these structures appear to be the most prominent lineament affecting the volcanic complex and they seemed to serve as a conduit for lava flows that occurred up until ~ 3 ka ago (Carrasco-Núñez et al., 2017a). The N–S oriented structures, which were observed within the Los Humeros caldera and that control the main caldera rims, appear to be the most recent ones, being limited in extension within the volcanic edifice and representing the main conduits for the fluids circulating in the Los Humeros geothermal field.

2.2. Evolution of the Trans-Mexican Volcanic Belt

The Trans-Mexican Volcanic Belt (TMVB) is an active, E–W trending ~ 1000 km long mostly calk-alkaline arc which encompasses an area of 160,000 km² with a varying width of 90–230 km (Ferrari et al., 2012). The arc reaches from the Pacific Ocean to the Gulf of Mexico in Southern Mexico (Fig. 14) and includes more than 8000 volcanic structures (Mora-Klepeis, 2021).
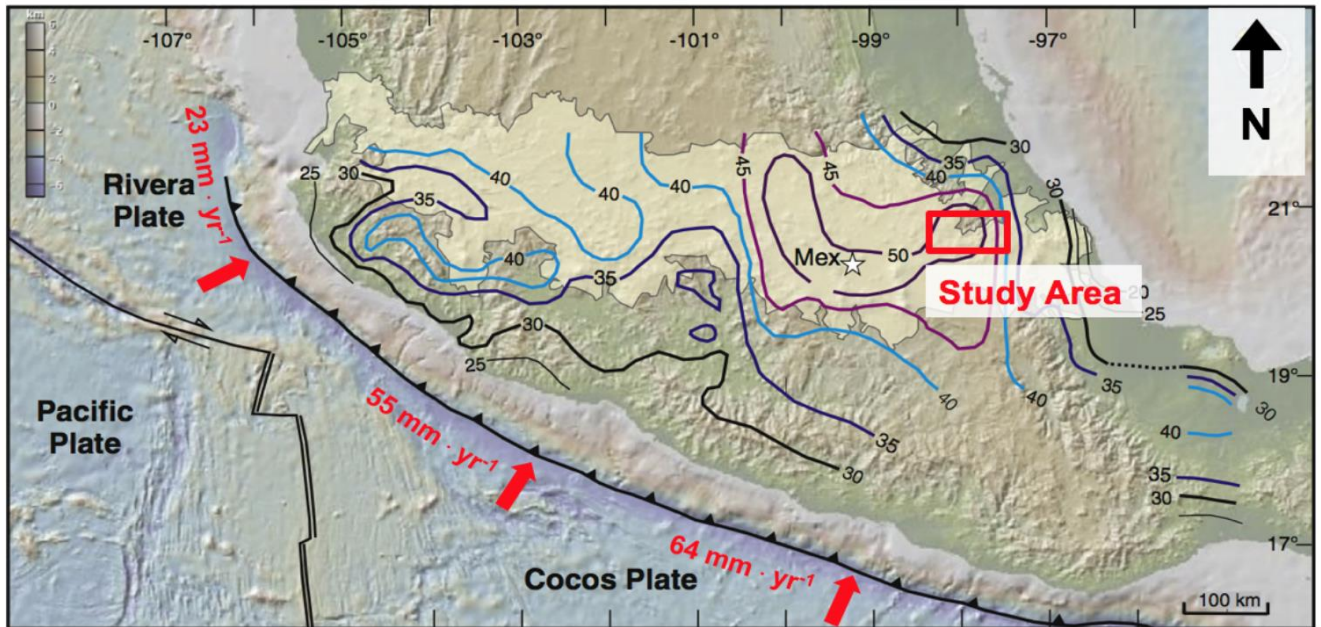
Figure 14: Map of the Trans-Mexican Volcanic Belt showing the thickness of the crust, plate boundaries and the subduction rates (Bech, 2018; modified from Ferrari et al., 2012).

The TMVB is built upon Cretaceous and Cenozoic magmatic provinces and tectonostratigraphic units of different lithology and age (Mesozoic to Precambrian). The formation of the TMVB is directly linked to the subduction of the Rivera and Cocos plates beneath the North American plate along the Middle-American Trench (López-Hernández et al., 2009). Thereby, the Rivera and Cocos plates are separated by a trench-orthogonal tear. The subduction started around 19 Ma with a propagation of the volcanic arc from E to W (Ferrari et al., 2012). The volcanic arc is oriented oblique to the subduction trench, caused by the difference in subduction rates of 23 mm a^{-1} in the NW to 64 mm a^{-1} in the SE. Thus, the age of subduction is older in the SE (17 Ma) than in the NW (10 Ma). The time differences in the volcanic processes are the reasons for the distinct crustal thickness of up to 50 km in the eastern part in contrast to the western part of the TMVB with 30 km thickness (Ferrari et al., 2012). During the prograde subduction, the volcanism underwent compositional changes over time and shows significant differences in direction and extension (Fig. 15) which can be grouped into four evolutionary stages.

The first stage (A and E in Figure 15) started about 19 Ma ago with the initial volcanism of intermediate lavas and intrusive bodies propagating from E towards W. The first activity was located in the eastern and central areas of the TMVB and is characterized by the emplacement of intrusive bodies with a tonalitic composition into the basement. The intrusive bodies and their metamorphic by-products can be observed in the exhumed systems of Las Minas and Zacatlán in the study area. Furthermore, calc-alkaline andesitic to dacitic lavas were emplaced during this period. One example is the Cerro Grande Volcanic Complex close to the Los Humeros Volcanic complex dating back to 10.5 Ma (Carrasco-Núñez et al., 2017a).
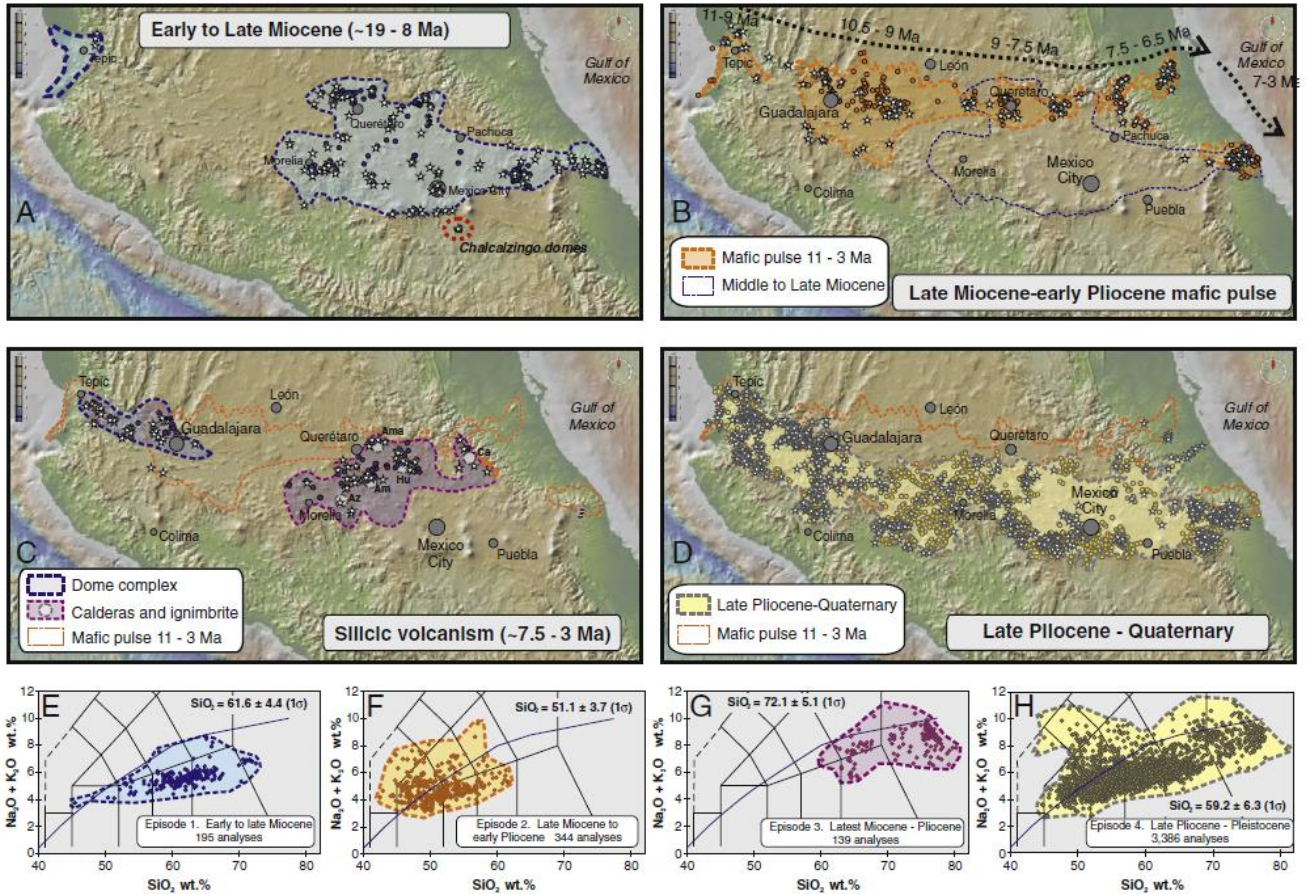
Figure 15: Evolution of the Trans-Mexican Volcanic Belt after Ferrari et al. (2012) showing four distinct stages (A-D) and respective chemical compositions (E-H).

The end of the first stage is indicated by a mafic pulse beginning in the late Miocene with an E to W oriented movement (Gómez-Tueña et al., 2007). The second stage includes tholeiitic to calc-alkaline mafic lavas with an eastward migrating volcanism along with a volume decrease of effusive material from W to E (Fig. 15B and 15F). Changes in the chemical composition are caused by differences in the crustal thickness and composition of the basement rocks. Between 7 and 4 Ma, mafic lavas became more sporadic and migrated to the east. During this period (stage 3) large volumes of silicic magma were produced resulting in the eruption of rhyolitic and dacitic ignimbrites in the eastern and central areas of the TMVB and effusive bimodal volcanism in the western parts. During the Early Pliocene voluminous monogenetic volcanism was widespread and large stratovolcanoes and cinder cones formed (Mora-Klepeis, 2021). The volcanism became bimodal with mafic to silicic composition.

The fourth stage (Fig. 15D and 15F) started in the Late Pliocene and represents a divers and compositionally variable volcanism with the volcanic front moving westwards reaching the recent configuration in the Late Pleistocene (Ferrari et al., 2012). During this stage stratovolcanoes like the Cofre de Perote, Pico de Orizaba, Colima and Popocatépetl were formed. The volcanic activity of the Acoculco and Los Humeros volcanic complexes are associated with the stages three and four.

2.3. The Exhumed System of Las Minas

The Las Minas valley is considered to represent the analogue of the currently exploited geothermal reservoir in Los Humeros (Olvera-García et al., 2020). It is located about 25 km east of the Los Humeros geothermal field at the edge of the Los Humeros plateau and descends from ~ 2400 to ~ 1100 m a.s.l., thereby exposing all rock units from the Paleozoic to Holocene age (Kozdrój et al., 2020) in road cuts, quarries, and mines. Within the framework of the GEMex project a new stratigraphic profile and geological map were created (Fig. 16) along with dating of the rock units, mineralogical, and structural analyses (Kozdrój et al., 2020). Further investigations on intrusive bodies and their associated skarn deposits are presented in Fuentes-Guzmán et al. (2020). The Tatatila-Las Minas mining district is well-known for its ore and gold deposits found in the highly mineralized skarn bodies. Magnetite and sulphides that contain gold, copper or silver were explored and exploited over the past decades.

The deepest parts of the valley expose Miocene granodioritic intrusive bodies that intruded into the carbonatic basement (mainly Cretaceous limestones in our outcrops) causing the formation of skarns, marble and hornfels due to hydrothermalism. Four stages of magmatic activity have been identified with ages between 24.6 Ma and ~ 19 Ma, whereby Pliocene intrusions and extrusive rocks could be correlated with the volcanic evolution of the Los Humeros caldera (Fuentes-Guzmán et al., 2020). Paleozoic granitoids (~ 240 Ma) are exposed further eastward and often cannot be separated in the field from the younger intrusions.

Skarn bodies are typically located within fault damage zones at the contact between intrusive bodies and carbonates reaching a thickness of up to 100 m. The skarns exhibit variable appearances and chemical compositions depending on the protolith and due to complex prograde and retrograde alteration. They can be grouped into mainly pyroxene- and garnet-dominated skarns (exoskarns vs. endoskarns; Olvera-García et al., 2020). Likewise, marbles were formed due to contact metamorphism caused by the intrusion of the granodioritic bodies. In Las Minas their composition varies from calcic to dolomitic marble with grain sizes ranging from fine to coarse with a granoblastic texture. In some outcrops they attain a width of up to 400 m (Fuentes-Guzmán et al., 2020).

Several effusive lavas, lacustrine sediments, and pyroclastic deposits overlay the pre-volcanic basement in the Las Minas area. Thereby, the andesite 1 and andesite 2 as shown in Fig. (16) correspond to the andesitic lavas within the Los Humeros geothermal field. Several mafic to felsic dykes were observed in outcrops in the basement and andesitic lavas. According to Fuentes-Guzmán et al. (2020) the mafic dykes are about 4 Ma old. Numerous mafic dykes have also been observed in outcrops of Cretaceous limestones in the surrounding area of the Los Humeros Volcanic Complex (Bär and Weydt, 2019).

Particular emphasis was given to the relationship between structures and the skarn deposits since they represent former fluid circulation in the fossil geothermal system (Liotta and Bastesen et al., 2021; Fig. 17). The structural measurements showed SW–NE and NNW–SSE striking faults. Thereby, the SW–NE faults mainly represent normal movements and the NNW–SSE faults are defined by right-lateral movements. Due to their coeval activities, the NNW–SSE fault system were interpreted as a transfer fault system, which has been active together with the SW–NE faults in the context of the regional NNW–SSE striking extension in the study area. Dominant lateral kinematics in the NNW–SSE structures indicate preferential vertical to close-to-vertical structural fluid pathways that channeled deep hypersaline fluids with magmatic origin.
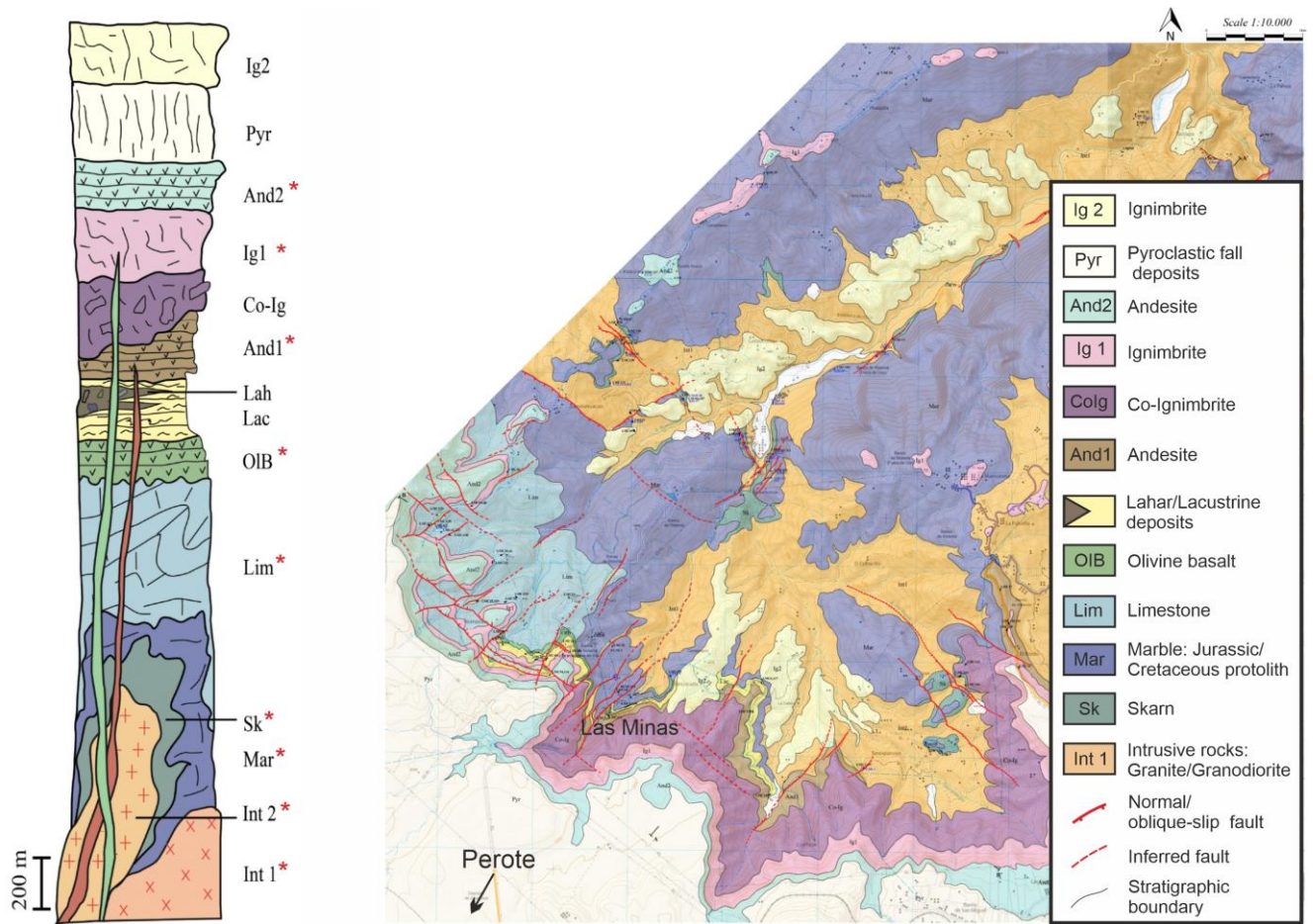
Figure 16: Schematic stratigraphic log and new geological map of the Las Minas area (modified from Olvera-García et al., 2020). The red stars mark units where outcrop samples were taken for petrophysical measurements.
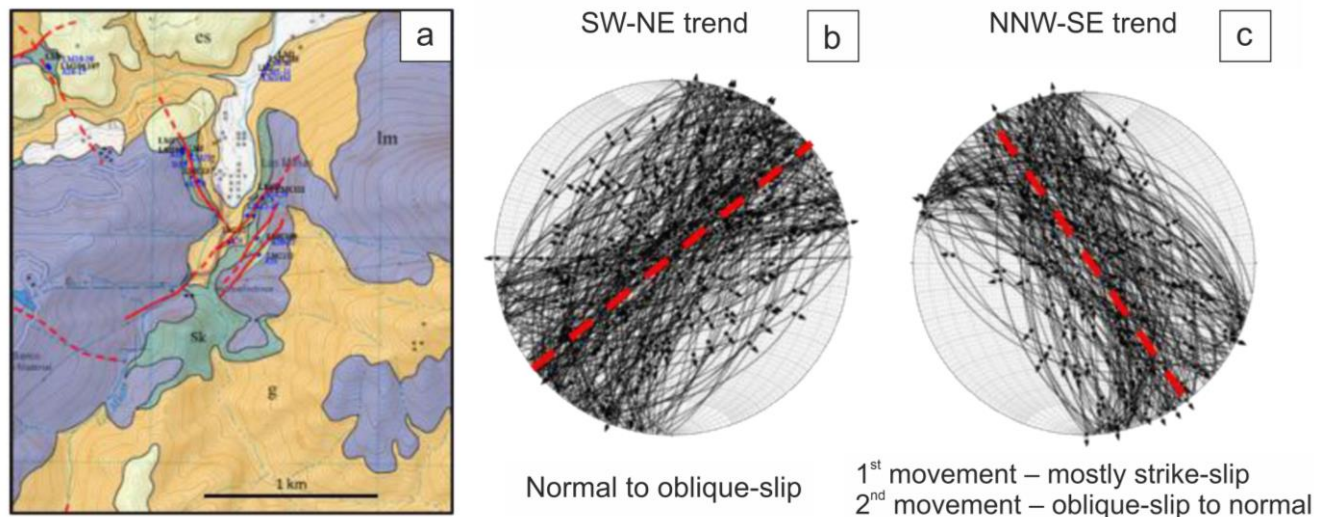
Figure 17: (a) Geological map of the area around the Las Minas village showing the two main fault trends (symbols: g = granitoids, lm = limestone and marble, sk = skarn, es = eolian sands). (b) and (c) showing the two main orientations of the meso-faults and kinematic indicators (modified from Liotta and Bastesen et al., 2021).

3. Petrophysical and Mechanical Rock Property Database

This chapter is based on the article "Weydt, L. M., Ramírez-Guzmán, Á. A., Pola, A., Lepillier, B., Kummerow, J., Mandrone, G., Comina, C., Deb, P., Norini, G., González-Partida, E., Avellán, D. R., Macías, J. L., Bär, K., and Sass, I.: Petrophysical and mechanical rock property database of the Los Humeros and Acoculco geothermal fields (Mexico), Earth Syst. Sci. Data, 13, 571–598, https://doi.org/10.5194/essd-13-571-2021, 2021." The abstract is not included and the alphanumeric order of figures and tables may differ from the original article. If necessary, the alphabetical order of quotations has been adapted to the content of the dissertation. Likewise, the formatting was adjusted to fit the layout of this work.

3.1. Introduction

The knowledge of petrophysical and mechanical rock properties of the deep subsurface is essential for reservoir exploration and assessment of the reservoir potential for a variety of industrial applications such as petroleum reservoir engineering, geothermal heat extraction, mining or nuclear waste disposal. The data are most commonly used for interpreting geophysical data, creating conceptual geological models or populating numerical models (Lévy et al., 2018; Scott et al., 2019; Deb et al., 2019a, 2019b; Árnason, 2020). Depending on the scale of investigation (e.g., local, regional or continental scale), highly accurate spatial predictions of relevant rock properties are required to increase the success and accuracy of reservoir operations and to reduce economic risks.

Rock formations are usually characterized by a heterogeneous internal structure, mineral composition, and pore and fracture distribution resulting in great variability in petrophysical and mechanical properties (Schön, 2015). Thereby, tectonic events, diagenetic or metamorphic processes, and hydrothermal alteration significantly affect the rock properties (Pola et al., 2012; Aretz et al., 2015; Weydt et al., 2018a; Mordensky et al., 2019a; Durán et al., 2019, Heap et al., 2020a), leading to a high geological heterogeneity often observed within hundreds-of-meter to sub-meter scales (e.g., Canet et al., 2010). Although most exploration methods or geological models are aligned to the reservoir scale, the controlling factors within the reservoir need to be understood and quantified at different scales to estimate the heterogeneity of each relevant formation and to assess the uncertainty in the input parameters for different modeling approaches. However, on the one hand, detailed information about rock properties for the relevant target formations is often not available, is inconsistent or is distributed over the literature. On the other hand, important metadata such as petrographic descriptions, details on sample locations and applied methods for data acquisition are missing (Bär et al., 2020). Without sufficient information, it is often not possible to evaluate and profit from existing laboratory data from specific locations or reservoir formations for future modeling approaches or studies related to similar geological settings. Consequently, most reservoir models are based on assumed or generalized data sets and local geological heterogeneities are often not considered (Mielke et al., 2015). While most studies focus on a single parameter (Clauser and Huenges, 1995) or a small set of samples, extensive data sets are required, which contain data of numerous different analyses performed on each sample in order to constrain statistical and causal relationships between the parameters (Linsel et al., 2020).

Addressing these challenges, the GEMex project (Horizon 2020, grant agreement no. 727550) embedded the petrophysical and mechanical rock characterization of the target formations in a comprehensive workflow providing the basis for different modeling approaches, geophysical surveys, ongoing and future volcanological studies. The GEMex project is a European–Mexican collaboration which aims to develop new transferable exploration and exploitation approaches for enhanced geothermal systems (EGSs) and super-hot unconventional geothermal systems (SHGSs). For this purpose, the Acoculco and Los Humeros geothermal fields have been selected as demonstration sites. Both fields are linked

to caldera complexes located in the northeastern part of the Trans-Mexican Volcanic Belt (TMVB). Extensive geological, geochemical, geophysical and technical investigations were performed to improve the reservoir understanding and to facilitate future drilling operations.

Up until the beginning of the project in 2016, information on rock properties of the different geological units in the study area was scarce or not available. Previous studies focused on the investigation of reservoir core samples of both geothermal fields (Contreras et al., 1990; García-Gutiérrez and Contreras, 2007; Canet et al., 2015). However, the existing data were not sufficient for the definition and parameterization of model units within the reservoir due to the limited core material available (six pieces for Acoculco; Canet et al., 2015) or the lack of petrographic descriptions and chemical data for individual samples (Contreras et al., 1990).

Therefore, outcrop analog studies and reservoir core studies were performed in order to characterize all relevant key units from the basement to the cap rock (Weydt et al., 2018b; Bär and Weydt, 2019). Geological heterogeneities were investigated on different scales: (1) macroscale (outcrops), (2) mesoscale (rock samples) and (3) microscale (thin-section and chemical analysis). Analog studies of the geological units exposed in outcrops around the investigated geothermal fields offer a cost-effective opportunity to investigate and correlate facies, diagenetic and metamorphic processes, and lithofacies-related rock properties from outcrops down to the subsurface (Howell et al., 2014). The definition of thermo-facies units (Sass and Götz, 2012) and the quantification of uncertainties for each parameter enable a reliable prediction of rock properties in the subsurface.

A comprehensive database was developed including petrophysical, thermophysical, magnetic, electric, dynamic and static mechanical properties combined with chemical and mineralogical data. In total 34 parameters were determined on more than 2160 plugs retrieved from 306 outcrop samples from both caldera complexes and 66 reservoir core samples of the Los Humeros geothermal field as well as 8 core samples of the Acoculco geothermal field covering volcanic, sedimentary, metamorphic and igneous rocks from Jurassic to Holocene age. Here, we present the workflow and current status of the GEMex rock property database (Weydt et al., 2020; https://doi.org/10.25534/tudatalib-201.10). These data not only provide the basis for ongoing research in the study area but also facilitate a wide field of applications in different disciplines, for example, a first assessment of the subsurface properties at early exploration stages (Bär et al., 2020), different modeling approaches, geostatistical and stochastic analyses, or the validation of different measurement methods.

3.2. GEMex Project Framework and Sampling

The geothermal system in Los Humeros is steam dominated and has been under production since 1990, operated by the Comisión Federal de Electricidad (CFE). With a production of 94.8 MWe in 2018 it is the third-largest geothermal field in Mexico (Romo-Jones et al., 2019) with 65 wells drilled so far, of which 28 are productive and 5 are used as injection wells. With temperatures above 380 °C encountered below 2 km depth in the northern part of the field, the Los Humeros caldera complex was characterized as a suitable target for the development of a SHGS within GEMex. In Acoculco two exploration wells have been drilled so far, which have encountered temperatures of approximately 300 °C at a depth of about 2 km (Canet et al., 2015). Although a well-developed fracture network exists within the area, both wells were dry (López-Hernández et al., 2009). Thus, the GEMex project aims to develop a deep EGS in Acoculco in order to connect the existing wells to proximal fluid-bearing fracture zones.

The project comprises a multidisciplinary approach based on three milestones which are (1) resource assessment, (2) reservoir characterization and (3) concepts for site development (Jolie et al., 2018). The first milestone focused on a comprehensive understanding of structurally controlled permeability and the fluid flow in the reservoir including extensive fieldwork regarding stratigraphy and structural geology, fracture distribution, hydrological and geochemical studies of natural springs, comprehensive

soil–gas studies (e.g., CO_2 flux; Jentsch et al., 2020), and airborne thermal imaging. The second milestone includes several geophysical surveys (e.g., passive and active seismic, gravity and magnetotelluric surveys) to characterize active faults and to identify deep structures. In addition, extensive sampling campaigns were conducted for petrophysical, rock mechanical, chemical and mineralogical investigations of the key lithologies in the study area. Resulting data and models of all work groups are being combined in integrated reservoir models at a local, regional and superregional scale. The third milestone includes the investigation of transferable concepts for developing EGSs and the utilization of SGHSs; the identification of suitable materials and well designs, which can resist high temperatures and corrosive fluids in the reservoir; and the determination of possible drill pathways along with a comprehensive risk assessment and management.
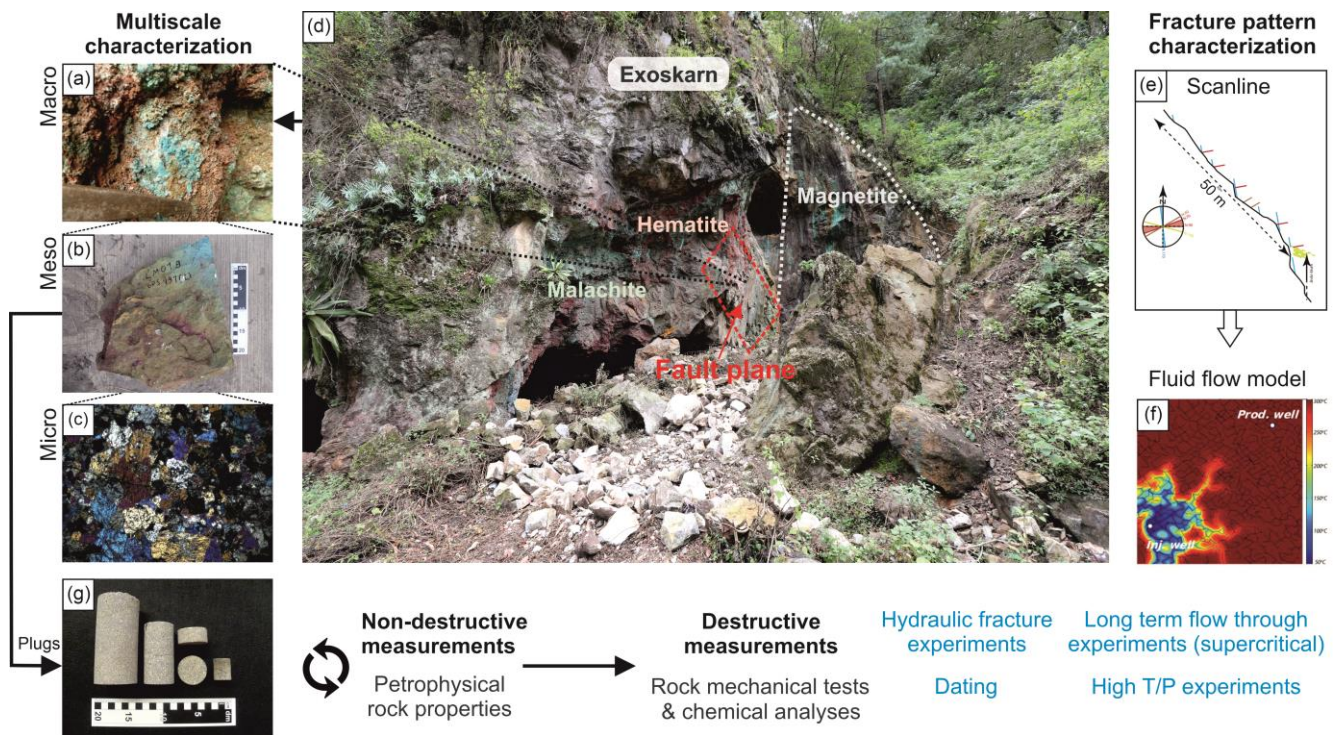
Figure 18: Schematic workflow of the GEMex project using the example of the El Dorado mine in Las Minas (d) with view on the footwall of the present fault (photo from Maximilian Bech). The quarry exposes exoskarn in many variations. Outcrop analysis included detailed investigation of kinematic indicators, mineralogy (a) and the main fracture pattern (e) to create numerical fluid flow models (f) as presented in Lepillier et al. (2019). Rock samples were taken for lab investigation (b), geochemical and thin section analysis (c) (photo from Caterina Bianco). Cylindrical plugs were drilled from the outcrop samples (g) and distributed between the partners in order to determine rock properties, dating or highT/P experiments (the experiments marked in blue are not included in this study).

The work presented in this study is part of milestone 2 (reservoir characterization) and focuses on the mineralogical, petrophysical and mechanical rock characterization of both geothermal systems. Several joint field campaigns with Mexican and European partners were conducted in order to cover and sample all relevant geological key units from the basement to the cap rock. In this context, work groups with different areas of expertise worked together in a joint approach (Fig. 18). Thus, structural geologists worked together with volcanologists, petrologists and petrophysicists on the same outcrops to, e.g., combine results of fracture pattern characterization and rock property analysis obtained from the same outcrops in a numerical fluid flow model (Lepillier et al., 2019). Likewise, samples for detailed mineralogical investigations were collected together with samples for petrophysical experiments. Over 300 representative samples were collected from more than 140 outcrops inside the caldera complexes

and in the surrounding area (Fig. 19). In addition to outcrop analysis in the Acoculco and Los Humeros areas, particular attention was paid to the exhumed systems Zacatlán (east of Acoculco) and Las Minas (east of Los Humeros), where all units from the cap rock to the basement are exposed. These so-called "fossil systems" serve as proxies for the active geothermal fields and help in the understanding of the fluid flow and mineralization processes in the "active" geothermal reservoirs under discussion. Whenever possible, each geological unit was sampled several times at different outcrop locations to cover the unit's heterogeneity, and only samples with an overall fresh appearance unaffected by weathering were considered. Hydrothermal alteration of different intensities was observed in some outcrops in close proximity to fault zones and dikes. In these cases, hydrothermally altered samples were deliberately collected to analyze the effect of these processes on the rock properties. Besides analyzing outcrops and outcrop samples, the CFE granted extensive sampling of wellbore core material of both geothermal fields at the CFE camp in Los Humeros. In total 66 samples drilled from 37 core sections covering 16 wells drilled in Los Humeros and 8 core samples drilled from 6 core sections from well EAC1 of the Acoculco geothermal field were obtained. All samples were directly drilled within the field or sent as boulders to Europe or the Mexican institutes and subsequently distributed between the partners. This approach ensures that further work on the project, such as long-term flow experiments (Kummerow et al., 2020), high-T/P experiments, hydraulic fracture experiments (Deb et al., 2019c), detailed mineralogical analyses (thin-section and scattered electron microscope; Lacinska et al., 2020), isotope analyses or dating (Kozdrój et al., 2019), can be directly correlated with the results presented in this study. Furthermore, some parameters of the same sample set were analyzed by multiple institutes to compare and validate different analytical approaches.
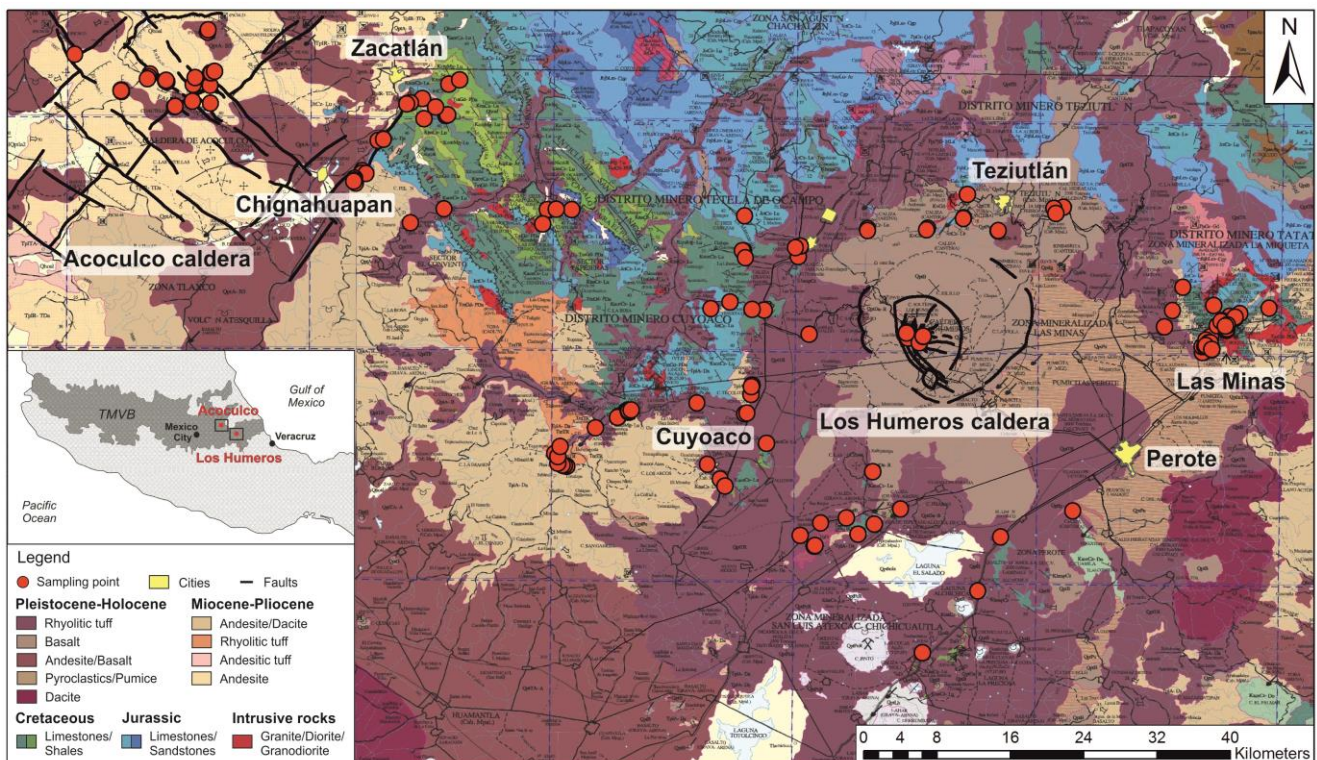
Figure 19: Geological map of the Acoculco and Los Humeros region including the sampling points of the outcrop samples (SGM, 2002a and b). The faults were recently mapped and characterized by Liotta et al. (2019) and Norini et al. (2019).

3.3. Geological Setting

The Acoculco and Los Humeros caldera complexes are located in the northeastern part of the Trans-Mexican Volcanic Belt (TMVB), 125 and 180 km east of Mexico City, respectively. The E–W trending TMVB is a ∼ 1000 km long calc-alkaline arc which is directly linked to the subduction of the Rivera and Cocos plates beneath the North American Plate along the Middle America Trench (Ferrari et al., 2012; Macías et al., 2012; Avellán et al., 2018). The volcanic complexes are located over a ∼ 50 km thick continental crust (Pérez-Campos et al., 2008) and are situated ∼ 100 km north of the Popocatépetl and Pico de Orizaba volcanoes, which define the most active front of the TMVB in central eastern Mexico (Ferrari et al., 2012; Macías et al., 2012; Avellán et al., 2020).

Both volcanic complexes are emplaced on intensively folded Mesozoic sedimentary rocks (Mexican fold-and-thrust belt; Fitz-Díaz et al., 2017) belonging to the Sierra Madre Oriental comprising Jurassic sandstones, shales, hydrocarbon-rich limestones and dolomites overlain by Cretaceous limestones and shales (López-Hernández et al., 2009; Fitz-Díaz et al., 2017). The regional tectonic setting is characterized by Late Cretaceous–Eocene NW–SE striking thrusts and folds and subordinate NE-striking normal faults that are associated with an Eocene–Pliocene extensional deformation phase (Norini et al., 2019). Oligocene to Miocene granitic and syenitic plutons as well as andesitic and basaltic dikes intruded into the sedimentary sequences, leading to local metamorphism of marble, hornfels and skarn (Ferriz and Mahood, 1984; Fuentes-Guzmán et al., 2020). The sedimentary basement is exposed east and southeast of the Acoculco caldera close to Chignahuapan and Zacatlán as well as in the surroundings of the Los Humeros caldera. Furthermore, it was also cut at different depth levels in drill cores in both geothermal fields (López-Hernández, et al., 2009; Carrasco-Núñez et al., 2017a). The granitic plutons are spread over the study area, and new aeromagnetic data of the Acoculco caldera constrain the occurrence of at least four intrusive bodies hosted in the Cretaceous limestones at > 1 km depth. Those were interpreted as a series of horizontal mafic intrusions providing the energy to maintain the geothermal field (Avellán et al., 2020).

The Acoculco caldera complex has an 18 km×16 km semi-circular shape (Avellán et al., 2018) and predominantly comprises Pliocene to Pleistocene basaltic to rhyolitic lavas, domes, cinder cones and ignimbrites. The caldera complex sits on an intersecting NE–SW and NW–SE fault system creating an orthogonal arrangement of grabens, half grabens and horsts (García-Palomo et al., 2002, 2018). Thereby the regional tectonic regime strongly affected the local tectonic behavior and structural deformation of the caldera (Sosa-Ceballos et al., 2018). The Acoculco caldera is located on the NE–SW Rosario-Acoculco horst and was built on top of Cretaceous limestones and the Zacatlán basaltic plateau (so far undated) as well as Miocene and Pliocene lavas and domes related to the regional volcanism of the TMVB (Avellán et al., 2018, 2020). Thereby the pre-caldera lavas and scoria cones exposed north and northeast of the Acoculco caldera complex were related to the Apan-Tezontepec Volcanic Field (Miocene and Pliocene), whereas Miocene andesitic and dacitic lavas are exposed west of the Acoculco caldera complex. Magmatic activity of the Acoculco caldera can be divided into five different eruptive phases, including recent deposits and hydrothermal altered areas inside the caldera (Avellán et al., 2018). It began with the emplacement of the Acoculco ignimbrite (∼ 2.7 Ma; ^{40}Ar/^{39}Ar), followed by several early (∼ 2.6–2.1 Ma) and late (∼ 2.0–< 0.016 Ma) post-caldera volcanic events producing basaltic to trachyandesitic and rhyolitic lava flows restricted within the caldera and rhyolitic lava domes, scoria cones and two ignimbrites that predominantly migrated to the caldera rim and periphery, respectively. The extra-caldera volcanism (2.4–0.19 Ma) comprises several basaltic trachyandesitic to basaltic andesitic lavas and scoria cones, related to the volcanism of the Apan-Tezontepec Volcanic Field. Products of the extra-caldera volcanism are interbedded with the lavas of the Acoculco caldera complex. It has to be emphasized that recent studies (Avellán et al., 2018, 2020) are not in line with previous volcanological studies performed by López-Hernández et al. (2009). In the study conducted by López-

Hernández et al. (2009), the authors concluded that the Acoculco caldera (1.7–0.24 Ma) is nested within the older and larger Tulancingo caldera (~ 3.0–2.7 Ma) forming the so-called Tulancingo–Acoculco caldera complex and that a third volcanic episode (1.8–0.2 Ma) occurred, which was related to monogenetic volcanism without a caldera collapse.

The younger Los Humeros caldera is the largest active caldera of the TMVB with a 21 km × 15 km irregular shape and comprises predominantly Pleistocene to Holocene basaltic andesitic to rhyolitic volcanic rocks (Carrasco-Núñez et al., 2018; Norini et al., 2019). The oldest volcanic activity in this area is represented by a thick sequence of Miocene andesites, dacites and basaltic lava flows of the Cuyoaco and Alseseca andesite unit (~ 10.5 Ma; Yáñez and García, 1982) and Pliocene to Pleistocene basaltic to andesitic lavas belonging to the Teziutlán andesite unit (dated between 1.44 ± 0.31–2.65 ± 0.43 Ma, $^{40}Ar/^{39}Ar$; Carrasco-Núñez et al., 2017a). Miocene lavas have a cumulative thickness of up to 900 m and can be related to the Cerro Grande Volcanic Complex dated between 8.9–11 Ma (Carrasco-Núñez et al., 1997; Gómez-Tuena and Carrasco-Núñez, 2000), and Teziutlán andesite lavas have a reported thickness of up to 1500 m (López-Hernández, 1995). Both units are classified as "andesitic and basaltic volcanic basement" and form the currently exploited reservoir in the subsurface of the Los Humeros geothermal field (Carrasco-Núñez et al., 2018). The beginning of the magmatic activity of the Los Humeros volcanic complex is represented by rhyolitic lavas and abundant rhyolitic domes, mainly located at the western side of the volcanic complex (270 ± 17 and 693 ± 1.9 ka; Carrasco-Núñez et al., 2018). However, the caldera collapse itself is associated with the emplacement of the high-silica rhyolite Xáltipan ignimbrite at ~160 ka with an estimated volume of 291 km^3 and a thickness of up to 880 m (Carrasco-Núñez et al., 2018; Cavazos and Carrasco-Núñez, 2020). After the emplacement of the Xáltipan ignimbrite, which caused the characteristic trapdoor structure of the caldera, further explosive events led to the deposition of thick rhyodacitic Plinian deposits called Faby Tuff (Norini et al., 2015; Carrasco-Núñez et al., 2017a). Afterwards, a second caldera-forming eruption occurred at ~ 69 ka and is related to the Zaragoza ignimbrite emplacement forming the Los Potreros caldera within the Los Humeros caldera. The post-caldera stage is represented by rhyolitic and dacitic domes within the center of the caldera (44.8 ± 1.7 ka) and basaltic to trachyandesitic lava flows (8.9 ± 0.03 ka), volcaniclastic breccias and fallout deposits (7.3 ± 0.1 ka) with a highly variable lateral and vertical distribution (Carrasco-Núñez et al., 2017a, 2018).

3.4. Workflow

After the samples were distributed between the partners, cylindrical cores with diameters ranging from 25 to 65 mm were drilled and subsequently cut according to standards (ASTM D4543-19, 2019) for the required sample length, and the irregular and rough core ends were cut to be parallel. The laboratory tests were divided into three stages: (1) general petrophysical characterization including all non-destructive measurements, (2) mechanical rock characterization, and (3) chemical and mineralogical characterization. Non-destructive tests included particle density, bulk density, porosity, intrinsic matrix permeability, thermal conductivity in dry and saturated conditions, thermal diffusivity in dry and saturated conditions, P-wave velocity and S-wave velocity in dry and saturated conditions, specific heat capacity, magnetic susceptibility, and electric resistivity in dry and saturated conditions. Afterwards the destructive rock mechanical tests such as the Brazilian disc test, the chevron bend test, the point load test, and uniaxial and triaxial tests were performed to determine uniaxial compressive strength, Young's modulus, the Poisson ratio, tensile strength, fracture toughness, the friction angle and cohesion. Samples that were identified as suitable for destructive tests such as uniaxial or triaxial tests were ground plane-parallel prior to analysis. Quantitative and qualitative chemical analyses like X-ray fluorescence (XRF) and X-ray diffraction (XRD) as well as thin-section analyses were performed for the petrological and geochemical characterization. Figure 20 shows the schematic laboratory workflow of TU Darmstadt.
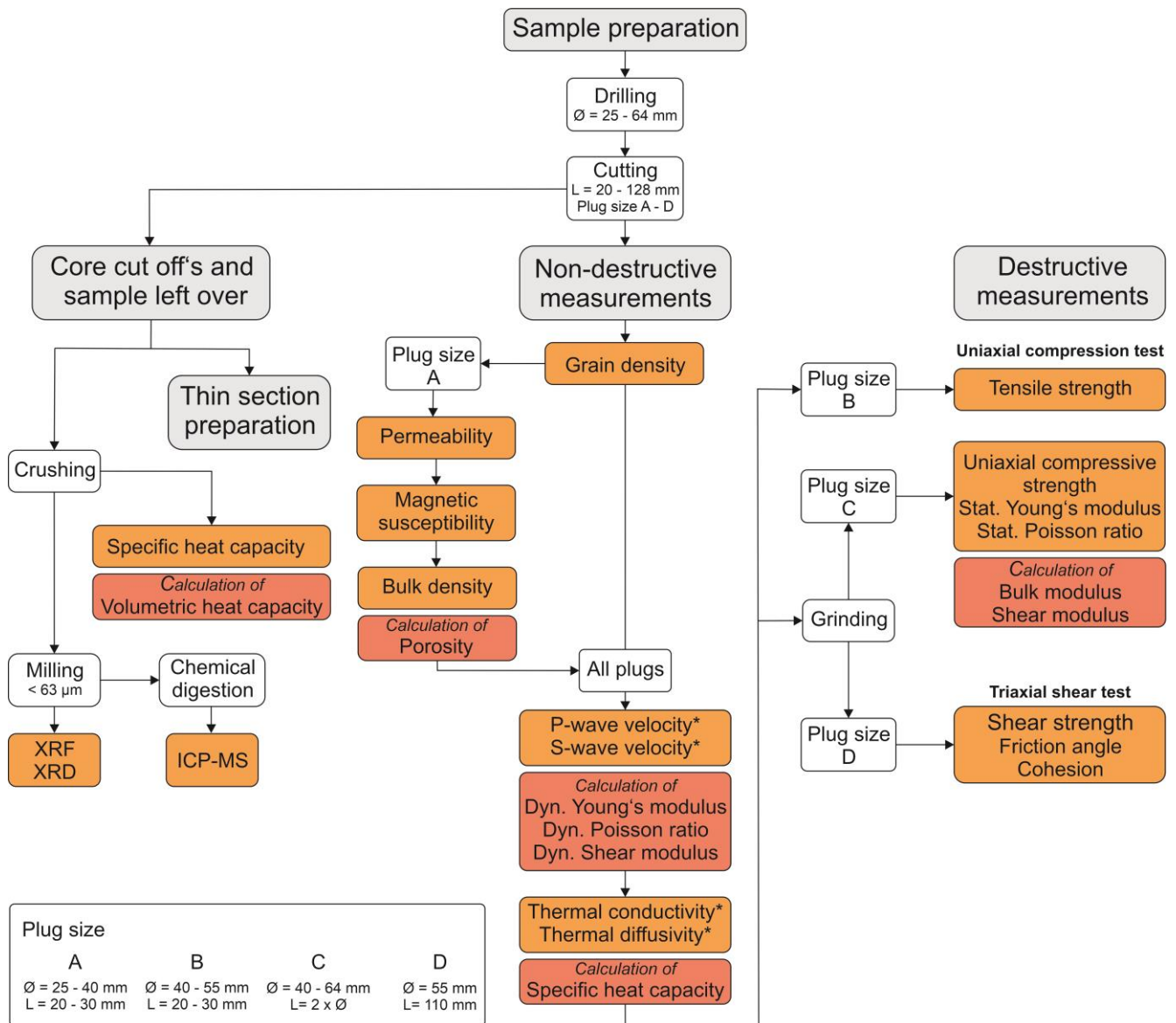
Figure 20: Schematic work flow representing the measurement procedure at TU Darmstadt. The properties displayed in orange were determined on sample material and used to calculate those shown in red. Parameters marked with * were analyzed at dry and saturated conditions.

3.5. Structure of the Database and Sample Classification

The database is publicly available under https://doi.org/10.25534/tudatalib-201.10 (Weydt et al., 2020) and contains petrophysical and rock mechanical properties as well as chemical data obtained by laboratory experiments within the scope of the GEMex project. This database is provided in a flat file Excel format and in CSV format to keep the handling as simple as possible. Its internal structure is based on the PetroPhysical Property Database – P3 – previously developed during the IMAGE project (Bär et al., 2020) with some project-specific modifications. The P3 database's internal design comprises multiple tables for petrography, stratigraphy, quality controls, chemical analyses and petrophysical properties and follows the concept of relational database management (Codd, 1970). As the database presented in this study is restricted to one study area, the P3 structure was simplified, and the sample's information has been compiled in two data sheets so far. The main objective was to provide the data in a user-friendly and well-structured form, allowing easy filtering and a transfer of data into other database

formats like SQL (structural query language) to easily visualize it or to implement it for modeling approaches.

The first and main data sheet comprises all analyzed petrophysical parameters and sample information (metadata) compiled during this project. Each analyzed plug was provided with a sample ID, which acts as the primary key for all records. Sample information provided in the database is explained in the following sub-sections.

The second data sheet includes all chemical data, retrieved from composite sample material, and does not directly correspond to measurements on single plugs. The data are provided separately to increase handling and readability. Here, the sample name represents the primary key which links the data to the petrophysical measurements provided in the first table.

3.5.1. Metadata

The metadata include all additional sample information from sample ID to sample dimensions and can be used for rapid filtering and the precise categorizing of parameters.

Each analyzed plug or sample received a unique sample ID, which is derived from the sample name given in the field, the geothermal reservoir (LH or AC), the field trip (e.g., M17 for May 2017) and an abbreviation for the rock type (e.g., GD for granodiorite). This classification was developed within the project due to the high number of samples collected during different field trips. Furthermore, the sample ID provides information about the sample preparation. In hierarchical order the sample name, core name and plug name are provided. For each drilled core the sample name was complemented with C1 (i.e., core number 1), C2, C3 and so on. Whenever the core did not meet the requirements for destructive measurements (length-to-diameter ratio of 2:1 or too fragile), the core was cut into plugs. The core name was then complemented with capital letters A, B, C, etc. representing the way the core was cut (Fig. 21). The implementation of this hierarchical order allows for quick access of the parameters per plug, per core or per sample. Whenever a core was not cut into several plugs, the core and plug name are identical to avoid gaps in the database. For practical reasons the term "plug" was used for all cylindrical samples after sample preparation (cutting and grinding) ready to be analyzed. For the reservoir core samples, the existing core names were adopted. The ID begins with the well name (e.g., H23), followed by the core number (e.g., number 2), the core section (e.g., 14, or x for undefined) and the number of the drilled subcore (C1 or C2).
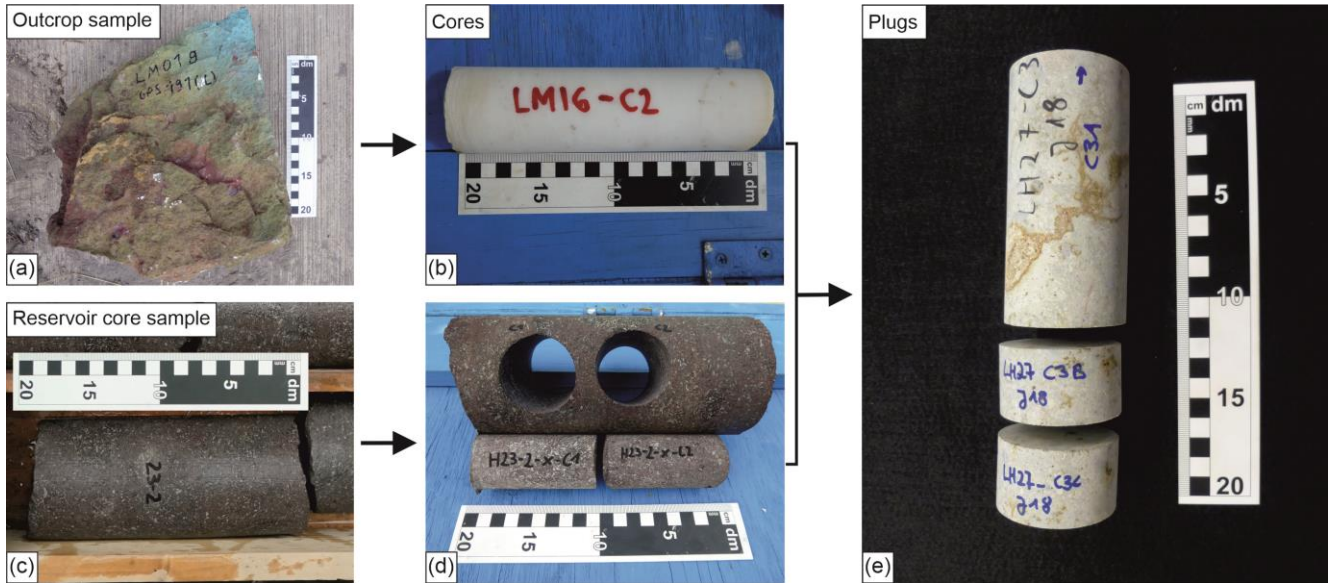
Figure 21: Overview of the different preparation steps and sample labelling. Cores (b = various diameters, d = 40 mm in diameter) were drilled from outcrop samples (a) and reservoir core samples (c) and subsequently cut into plugs (e) to meet the individual requirements of the measurement devices. The plugs were labelled with capital letters.

The samples were classified regarding their rock type and stratigraphic unit based on the recently published geological maps and volcanological studies conducted in Acoculco and Los Humeros (Avellán et al., 2018, 2020; Carrasco-Núñez et al., 2017a, b, 2018). Rock types were predominantly determined using macroscopic analyses complemented by thin-section analyses (whenever available). Additionally, bulk chemical analyses (XRF) were used to better characterize the volcanic rocks using the TAS classification (Le Maitre and Streckeisen, 2003). However, this classification is only applicable for unaltered sample material. The classification of the stratigraphic unit is based on the international chronostratigraphic chart of the IUGS (Cohen et al., 2013) according to international standardization. Whenever possible the local stratigraphic unit is given. The volcanological studies are still ongoing, and the ages of some units or areas are not yet well constrained.

Coordinates of the sampling locations are provided as latitude and longitude in decimal degrees (WGS84) and x and y coordinates (UTM WGS84). For the reservoir core samples, the coordinates of the well heads are included. All this information is given in meters above sea level (m a.s.l.) and represents the surface evaluation of the outcrops or the evaluation at reservoir depth for the reservoir core samples. The latter was provided in measured depth (MD) by the CFE, and the core sample material was obtained from vertically drilled wellbores.

Furthermore, the outcrop names and field trips are documented as project internal information and enable the placing of this work in relation to other work conducted within the study area. Samples from six field trips are provided in the database as shown in Table 3.

Table 3: Overview of the field campaigns and related work

No.	Field campaign	Related work
1	January 2017	Mapping, structural and mineralogical analyses in Las Minas and Acoculco (Liotta et al., 2019; Lepillier et al., 2019)
2	March 2017	Hydraulic fracture experiments on large blocks (Deb et al., 2019c)
3	May 2017	Structural analyses in Los Humeros and Las Minas (Norini et al., 2019), samples for high temperature triaxial tests (Vagnon et al., 2021; Bär and Weydt, 2019), samples for long-term flow through experiments at supercritical conditions (Kummerow et al., 2020), samples for scanning electron microscopy, electron probe microanalysis, cathodoluminescence microscopy and high temperature fluid-rock reaction experiments (Lacinska et al., 2020; Bär and Weydt, 2019)
4	June 2017	Petrophysical characterization and mechanical evolution of hydrothermal altered rocks
5	January 2018	Mapping, structural and mineralogical analyses in Acoculco and Las Minas (Liotta et al., 2019, Lepillier et al., 2019), dating (Kozdrój et al., 2019), samples for high temperature triaxial tests (Vagnon et al, 2021; Bär and Weydt, 2019), samples for scanning electron microscopy, electron probe microanalysis, cathodoluminescence microscopy and high temperature fluid-rock reaction experiments (Lacinska et al., 2020; Bär and Weydt, 2019), samples for fluid inclusions (Ruggeri et al., 2020)
6	March 2018	Shallow geophysical surveys, determination of mechanical properties at field scale, electrical resistivity tomography (Mandrone et al., 2020)

The "location" was inserted in addition to the outcrop name and sample coordinates to classify the samples according to their sampling area, distinguishing between Acoculco, Los Humeros, and the exhumed systems Las Minas and Zacatlán–San Miguel Tenango (SMT). The column "institution" refers to the institution and authors that generated the data and indirectly links this to the applied methods described in Sect. 3.5.

Based on the rock type and stratigraphic classification, the samples were related to the model units of the regional and local geological models created within the GEMex project (Calcagno et al., 2018, 2020). The regional and local model units were defined to consider the most representative geological formations in the study area, the scale of the model and the objective of the project (Calcagno et al., 2018). For Los Humeros four regional and nine local model units were defined (Fig. 22). The classification is mostly based on recent work of Carrasco-Núñez et al. (2017a, b, 2018) and Norini et al. (2015, 2019) and information about formation depth, thickness and distribution provided by the CFE stratigraphic drilling profiles. Samples collected from basaltic and andesitic dikes as well as from intrusive bodies in Los Humeros and Las Minas were related to the basement (G4 and U9). The classification of the local units of the reservoir core samples represents the classification used for the latest update of the local model of Los Humeros (Calcagno et al., 2020).

Regional model	Local model	Rock type	Age (Ma)
G1 Post-caldera	U1 Undefined pyroclastic	Tuff, pumice and some alluvium	< 0.003
	U2 Post-caldera	Rhyodacite, andesite, basaltic andesite and olivine basalt lava flows with intercalated pyroclastic deposits	0.003-0.050
G2 Caldera	U3 Los Potreros caldera	Rhyodacitic flows and Zaragoza ignimbrite	0.069
	U4 Intermediate caldera	Faby tuff with andesitic-dacitic flows, rhyolitic and obsidian domes	0.07-0.074
	U5 Los Humeros caldera	Mainly composed of Xaltipán ignimbrite with minor andesitic and rhyolitic lava	0.165
G3 Pre-caldera	U6 Upper pre- caldera	Pyroxene andesites (Teziutlán andesite unit) with mafic andesites in the basal part and/or dacites and rhyolites	1.46-2.61
	U7 Intermediate pre-caldera	Undifferentiated Rocks: Intercalation of rocks highly altered whose origin has not been defined so far	2.62-8.8
	U8 Basal pre-caldera	Hornblende andesites (Alseseca andesites and Cerro Grande volcanism) and dacites	8.9-10.5
G4 Basement	U9 Basement	Middle Miocene granite	15.12
		Cretacic limestones, shale and minor flint	~140
		Jurassic limestone and shale	~190
		Paleozoic granite and schist (Teziutlán Massif)	> 251

Figure 22: Regional and local model units of the 3D geological model of Los Humeros (slightly modified from Calcagno et al., 2018, 2020).

For the regional model of Acoculco, five units were defined (Fig. 23). All volcanic deposits were merged into one unit called AC5-Volcanites, whereas the basement rocks were split into four separate units: AC4-Limestones, AC3-Skarns, AC2-Granite and AC1-Basement. The description and stratigraphic classification is based on López-Hernández et al. (2009), Lorenzo-Púlido et al. (2010), Sosa-Ceballos et al. (2018) and Avellán et al. (2018).

Regional model	Rock type	Age
AC5 Volcanites	Ignimbrites, dacites, rhyodacites, andesite (pre to post caldera volcanites plus extra caldera and alluvial units)	< 12.7 Ma
AC4 Limestones	Limestone, marbles, hornfels	Cretaceous
AC3 Skarns	Limestone skarns	Cretaceous
AC2 Granite	Hornblende granite and microgranitic dikes	Mid-Miocene
AC1 Basement	Phyllites	Paleozoic

Figure 23: Regional model units of the 3D geological model of Acoculco (slightly modified from Calcagno et al., 2018).

As the last entities belonging to the metadata, sample descriptions and dimensions for each plug are provided. The sample description includes a brief macroscopic description and gives information about the occurrence of fractures, joints and fissures or other remarks (e.g., chert nodules or stylolites). Furthermore, the information is given as to whether thin sections were prepared or not. The section "sample dimensions" includes the length, diameter (exact and drilled diameter), weight (dry and saturated) and shape of the plug. Plug shapes were inserted for quality control and were distinguished between "ideal cylindrical plug", "cylindrical plug with a broken edge", "irregular shape" and "cuboid". This information

needs to be considered when the bulk density or volume is calculated by using the sample's dimensions. The exact sample dimensions provide the opportunity to analyze scale-dependent effects (Enge et al., 2007). Therefore, plugs with varying diameters and lengths were drilled and analyzed. Thus, small-scale samples (25 mm in diameter) for which the bulk volume reaches the minimal representative elementary volume (REV; e.g., Ringrose and Bentley, 2015) are included.

3.5.2. Rock Properties

Rock properties provided are grouped into (1) classical petrophysical parameters such as density, porosity and permeability; (2) ultrasonic wave velocities; (3) thermal properties; (4) magnetic susceptibility; (5) electric resistivity; and (6) rock mechanical parameters. The results are provided as mean values with standard deviation (whenever possible) for each plug. For thermal conductivity and thermal diffusivity the maximum and minimum values were added. In total 34 different parameters were obtained following the recommendations of international standardization institutions and committees (e.g., ISRM, ASTM or DIN). Columns for specific remarks were included to provide further details whenever needed. Detailed information on methods and procedures is given in Sect. 3.6.

3.5.3. Chemical Analyses

The results of chemical analyses (XRF and XRD) are provided in the second data sheet of the database. These data are retrieved from composite sample material, and a total of 131 samples (reservoir core samples and outcrop samples) were analyzed. The sample name acts as the primary key and allows for linking of chemical data with petrophysical data. Results of the XRF analyses are presented in weight percent for the major elements and in parts per million for the trace elements. For both analyses (XRF and XRD) the responsible institution is added to relate the data to the applied method.

3.6. Material and Methods

The following sections briefly describe the applied methods conducted by the different partners. A more extensive description for the non-destructive measurements and the field trips can be found in project reports on the GEMex web page (Bär and Weydt, 2019; http://www.gemex-h2020.eu, last access: 21 October 2020). Sample material from TU Delft (field trip January 2017) and TU Darmstadt (field trip May 2017) were distributed to GFZ, RWTH Aachen and UniTO for non-destructive petrophysical measurements.

3.6.1. Sample Preparation

Drill cores with diameters ranging from 25 to 65 mm were drilled from the outcrop samples and cut into plugs as described above. More than 2100 plugs and cores with an axial length ranging from ~30 to 128 mm were prepared according to international standard ASTM D4543-19 (2019). The short plugs (diameter 25 to 40 mm, length 25 to ~30 mm) were predominantly used for the non-destructive petrophysical measurements like bulk density, porosity and permeability due to the specific sample size requirements of the measurement devices. Remaining plugs were prepared to meet the requirements for the different destructive rock mechanical tests, which were conducted after the petrophysical characterization. For most of the rock mechanical tests a length-to-diameter ratio of 2:1 (uniaxial and triaxial tests) or 1:2 (Brazilian test) is required. Furthermore, the plane surfaces of the plugs had to be plane-parallel with a maximum angular misalignment of 0.05°.

To ensure reproducibility of the results, the plugs were measured in oven-dry conditions (105 °C for more than 24 h or 64 °C for more than 48 h) and cooled down to room temperature in a desiccator (20 °C). Microcracking or significant mass losses caused by mineralogical changes or the collapse of clay minerals during heating in the oven were not observed since a majority of the outcrop samples

contain no clays and samples affected by hydrothermal or metamorphic processes contain mineral assemblages developed at higher temperatures.

In order to perform measurements in saturated conditions, the samples were evacuated in a desiccator and subsequently saturated with (de-ionized) water (TU Darmstadt and GFZ) or the samples were fully immersed in water for up to 4 weeks (RWTH Aachen and UniTO).

3.6.2. Non-destructive Tests

At TU Darmstadt, density measurements were performed in a multi-step procedure using an AccuPyc helium pycnometer (ASTM D5550-14, 2014) and a GeoPyc powder pycnometer (Micromeritics, 1997, 1998, 2014), analyzing particle and bulk volume five times for each plug, respectively. Bulk density was then automatically calculated by dividing the dry weight of the plug by its measured volume. Afterwards porosities were calculated from the resulting differences in volume and represent the gas-effective porosity, also known as connected porosity. The accuracy of the method is 1.1% (Micromeritics, 1998). Porosity measurements at TU Delft and UNAM were also performed using a helium gas pycnometer (Ultrapyc 1000 Version 2.12 and Ultrapyc 1200e gas pycnometers, respectively, both Quantachrome Corporation, USA) to determine the grain density (ASTM D5550-14, 2014), while bulk density was determined using caliper techniques according to ASTM D7263-16 (2016). Every plug was measured up to 20 times.

At GFZ and RWTH Aachen, particle density, bulk density and porosity were determined using the triple weighing method (ISRM, 1981). This method is based on the Archimedes principle, which uses the masses of the dry and fluid-saturated samples as well as that of the sample totally immersed in the fluid to calculate the pore volume and the porosity. The mass was determined with an accuracy of ± 0.2 g. Usually, the accuracy is 1.5% or better, but this especially depends on the surface condition for low-porosity samples. Thus, the measurements were performed up to three times per plug. A similar approach was used at UniTO by applying caliper techniques and the dry and saturated mass of each sample for the calculation of density and porosity (ISRM, 1979). Variations in particle and bulk density between the different methods applied on the same samples in this study range between 0.3%–3% (coefficient of variation) for limestones with porosities smaller than 3% and 0.5%–3.5% for pyroclastic rocks with porosities between 11% and 15%, verifying the different methods and sample saturation procedures as sufficient to obtain data with the accuracy needed.

Matrix permeability was determined on cylindrical plugs (diameter and length ranging from 25 to 40 mm and $\sim$ 20 to 80 mm, respectively) with column gas permeameters constructed according to ASTM D4525-13e2 (2013) and ASTM D6539-13 (2013) standards at TU Darmstadt, GFZ and UNAM. The plugs were analyzed in a confined cell at constant differential pressure under a steady-state gas flow using at least five pore fluid pressure levels (Tanikawa and Shimamoto, 2008). Corresponding gas flow rates were measured with different flowmeters that allow for the detection of flow rates in the range between 10 and 10 000 cm min^{-1}. This applied method is based on Darcy's law enhanced by factors for the compressibility and viscosity of gases in order to calculate the gas permeability (Scheidegger, 1974; Jaritz, 1999). The water equivalent permeability was derived from the gas permeability after the Klinkenberg correction (Klinkenberg, 1941). At TU Darmstadt the samples were analyzed with dried compressed air at five pressure levels ranging from 1 to 3 bar and 1 MPa confining pressure (Hornung and Aigner, 2004; Filomena et al., 2014). At GFZ a confining pressure of 8.5 MPa and five pressure levels ranging between 7.5 and 35 bar were applied (operated with argon), while at UNAM the permeability was determined using a confining pressure of 2.8 MPa and also five pressure levels up to 1 MPa (operated with nitrogen). Measurement accuracy of the TU Darmstadt permeameter varies from 5% for highly permeable rocks (K > 10^{-14} m^2) to 400% for impermeable rocks (K < 10^{-16} m^2) (Bär, 2012). The recorded flow rates were tested for turbulent fluid flow according to Kushnir et al. (2018) prior to the

Klinkenberg correction to ensure a laminar fluid flow. A correction after Forchheimer (1901) was not required, since the corrected values were within the error range of the measurement device.

At TU Darmstadt, thermal conductivity and thermal diffusivity were measured simultaneously on oven-dried and saturated plugs using a thermal conductivity scanner (Lippmann and Rauen, Germany) after Popov et al. (1999, 2016). The device consists of a sample platform and an optical scanning system that moves along the sample surfaces, including a heat emitter and three infrared sensors facilitating a continuous profile. Samples are heated up by a defined heat flow, and the subsequent cooling rate is measured by the temperature sensors. Bulk thermal conductivity and thermal diffusivity were then calculated after Bär (2012) by using two reference standards. Both parameters were measured four to six times on each plug for saturated and dry conditions, respectively (two to three times on every planar surface including slight turning after every measurement to account for sample anisotropy). At RWTH Aachen, the same optical scanning method was used to determine thermal conductivity along the core axis of large cylindrical cores with diameters of 60 and 64 mm. To ensure uniform reflection conditions, the samples were painted with black acrylic paint on the planar surface (TU Darmstadt) and along the core axis (RWTH Aachen). According to Lippman and Rauen (2009), the measurement accuracy for thermal conductivity and thermal diffusivity is 3% and 5%, respectively.

Specific heat capacity was determined at TU Darmstadt using a heat-flux differential scanning calorimeter (C80; Setaram Instrumentation, 2009); crushed sample material was heated at a steady rate from 20 up to 200 °C within a period of 24 h. Specific heat capacities were derived from the resulting temperature curves through heat flow differences. The accuracy is 1% (Setaram Instrumentation, 2009). Volumetric heat capacity was calculated by multiplying the specific heat capacity with the associated bulk density of each sample. For direct comparison, specific heat capacity was calculated for each plug by dividing thermal conductivity by the product of bulk density and thermal diffusivity (Buntebarth, 1980).

Ultrasonic wave velocity was measured along the sample axis with pulse generators (TU Darmstadt – UKS-D including a USG-40 pulse generator and a digital PicoScope oscilloscope from Geotron-Elektronik, 2011; UniTO – Pundit Lab, Proceq, Switzerland according to ASTM D2845-08, 2008; GFZ – Panametrics HV pulser–receiver model 5058PR in combination with digital oscilloscope model DSO6012A from Agilent Technologies, USA) comprising point-source transmitter–receiver transducers. Thereby, the transducers were pressed against the parallel surfaces of the samples using a contact pressure of about 1 bar. Polarized pulses at high voltage in a frequency range from 20 kHz to 1 MHz for the USG-40 and Panametrics as well as from 54 to 250 kHz for the Pundit Lab were generated. The transmitted signals were recorded using digital oscilloscopes, and the arrival times of the P- and S-waves were picked manually and corrected for the dead time, which arises from the recording device (transducer, function generator, oscilloscope).

Bulk density and P- and S-wave velocities were used to determine dynamic elastic mechanical parameters, such as the dynamic shear modulus, G_{dyn}; dynamic Young's modulus, E_{dyn}; and dynamic Poisson ratio, μ_{dyn}, after Zoback (2011):

$$G_{dyn} = \frac{v_s^2}{\rho} \tag{1}$$

$$E_{dyn} = \frac{\rho v_s^2 (3v_p^2 - 4v_s^2)}{v_p^2 - v_s^2} \tag{2}$$

$$\mu_{dyn} = \frac{v_p^2 - v_s^2}{2(v_p^2 - v_s^2)} \tag{3}$$

where ρ is the bulk density [kg m^{-3}], v_p is the compressional wave velocity [m s^{-1}] and v_s is the shear wave velocity [m s^{-1}].

Additional field measurements of P-wave velocities were performed by UniTO on irregularly shaped outcrop samples by using the same Pundit Lab Proceq device along different directions on the sample surfaces in order to identify anisotropy and the effect of fractures. Measurements were conducted

following ASTM D2845-08 (2008) standard requirements. At TU Darmstadt both velocities were measured four to six times on each plug in both saturated and dry conditions. For analyzing the samples in saturated conditions, the samples were stored in degassed and de-ionized water to avoid desaturation. After preparing the device and measurement setup, the samples were immediately installed between the transducers and the transmitted signals were recorded until the sample started to desaturate. The data provided by GFZ represent average values from at least 4 to 10 individual measurements per plug (dry and saturated conditions), and at UniTO each sample was analyzed up to 20 times in order to depict the matrix heterogeneity of the larger cores and outcrop samples. The error in P-wave velocities is 3% on average, whereas for S-wave velocities the average error is 8% or higher, due to the higher attenuation and distortion of the S-wave signals.

Electric resistivity measurements were carried out on selected cylindric plugs at GFZ and UniTO and on outcrop samples in the field. At UniTO electric resistivity measurements were performed with a purpose-built square quadrupole (Syscal-Pro from Iris Instruments, France) after Clement et al. (2011). This consists of a rubber jacket with four steel electrodes (2 mm diameter and 40 mm length), arranged at the edges of two perpendicular diameters of the core sample at half of its longitudinal length. Electrical resistivity measurements were performed with a current injection between two subsequent electrodes and detection of the resulting electric potential between the remaining pair of electrodes. Current and potential electrodes were progressively reversed and rotated around the sample for a total of eight different potential measurements. The sequence was repeated three times, and each sample was tested in both dry and saturated (wet) conditions. Saturated conditions were reached by immersing the sample in a saline solution (with electrical conductivity equal to 1000 μS cm^{-1}) for 24 h. A detailed description of the measurement procedure is also included in Vagnon et al. (2019).

Electric resistivity measurements at GFZ were executed with a four-electrode layout as well using an impedance spectrometer (Zahner Zennium electrochemical work station; Zahner Scientific Instruments, 2008), which supplied an AC voltage with an amplitude of 200 mV via disc-shaped current electrodes to the plane-parallel faces of the sample cylinders. The sample resistance was determined via detection of the impedance and the phase angle at distinct frequencies. Subsequently, the bulk resistivity was calculated from the sample resistance at 1 kHz, the cross-sectional area of the sample, and the distance between the potential electrodes that were pinned to the cylinder surface of the sample plugs. The measurements were performed on dry and on saturated samples. Oven-dry sample cores were saturated under vacuum with a NaCl solution with electrical conductivity equal to 1080 μS cm^{-1} and equilibrated for about 24 h. Prior to the measurements the samples were jacketed with a tight-fitting silicon sleeve to reduce the risk of desaturation. The accuracy of measurements in dry conditions is better than 3.5%. In contrast, in saturated conditions for porous samples, the error increases to a maximum of 16% if fluid evaporates or leaks from the pore space during the measurement interval.

The formation factor, F, of the samples was determined after Flovenz et al. (2005) from linear plots of bulk conductivities versus fluid conductivities at different brine concentrations, where F is the reciprocal of the linear fitting lines of the data points measured at fluid salinities varying between 0.56–10.42 S m^{-1}.

Magnetic susceptibility was analyzed using the magnetic susceptibility meter SM30 (ZH Instruments, 2008), which consists of an oscillator with a pickup coil. An interpolating mode was applied including two air reference measurements and one measurement directly on the sample surface. The frequency change in the oscillator is proportional to the magnetic susceptibility of the rock sample. To ensure optimal contact of the sensor on the sample surface and to reduce the impact of air while measuring, only the plane surfaces of the plugs were analyzed.

Furthermore, a multi-sensor core logger (MSCL) from Geotek (2000) was used for measurements of gamma density, P-wave velocity, magnetic susceptibility and electrical resistivity at RWTH Aachen on whole cores with a diameter of 60–64 mm. Matrix density was calculated based on attenuation of gamma rays emitted from cesium-137, while porosity was calculated from the density measurements.

P-wave velocity was measured using P-wave transducers (receiver and transmitter) mounted on opposite faces on the center sensor stand. A short pulse is produced at the transmitter, which propagates perpendicularly to the axis of the core and is detected by the receiver on the other side. The outer diameter of the core is measured with an accuracy of 0.1 mm. An absolute accuracy of ± 3 m s^{-1} is achievable while computing the P-wave velocity. Magnetic susceptibility was determined using a Bartington loop sensor with a 5% calibration accuracy. The sensor includes an oscillator circuit that generates a low-intensity alternating magnetic field at 0.565 kHz.

3.6.3. Destructive Tests

Simple (non-cyclic) and cyclic uniaxial tests were performed to determine the rock's unconfined compressive strength and elastic rock mechanical properties, such as the static Young's modulus, Poisson's ratio, *G* modulus (also known as shear modulus) and bulk modulus. For the determination of the unconfined compressive strength (UCS) at TU Darmstadt, cylindrical plugs with a diameter of 40 mm and a length of 80 mm were introduced into a hydraulic uniaxial press (FORM+TEST Prüfsysteme, Germany) with a capacity of 1000 kN and a maximum loading rate of 0.5 kN s^{-1} until sample failure. The stress at this particular point represents the UCS, which was calculated according to ASTM D7012-14 (2014) and DIN 18141-1:2014-05:

$$UCS = \frac{F}{A},$$
(4)

where *F* is the load at failure [N] and *A* is the cross-sectional area of the sample [mm^2]. Whenever the plugs were shorter than 80 mm and did not fulfill the required 2:1 length / diameter ratio, a correction function was applied as proposed by DIN 18141-1:2014-05:

$$\sigma_{U(2)} = \frac{8 \cdot \sigma_U}{7 + 2\frac{d}{l}},$$
(5)

where $\sigma_{U(2)}$ is the corrected UCS [MPa] and σ_U the measured UCS [MPa], respectively, and *d* is the sample diameter [mm], while *l* denotes its length [mm]. At TU Darmstadt the destructive tests using the hydraulic uniaxial press were performed "force controlled" with a maximum loading rate of 0.5 kN s^{-1}. The exceptions form very soft or fragile samples, such as ignimbrites, pumice or intensively fractured limestones. For these samples, the loading rate was individually reduced to 0.25 or 0.1 kN s^{-1} to meet the test requirements and to ensure the minimal test duration (e.g., 3 min for UCS and tensile strength). For the determination of the static Young's modulus and Poisson's ratio, cyclic uniaxial tests were performed on three plugs (same dimension as described above) for each sample according to DIN 18141-1:2014-05 and Mutschler (2004). In order to record the axial displacement and lateral extension of the plug, three vertical and three lateral displacement transducers (LVDTs) were installed at an angle of 120° around the plug. The measurement was conducted in two cycles with the first cycle reaching 40% and the second cycle reaching 60% of the previously determined UCS from the same sample set. For intensively fractured limestones, the maximum load of the cycles was individually reduced to 30% and 50% of the previously determined UCS, respectively, to avoid an early rock failure and possible damage of the sensors. According to Mutschler (2004) a holding time of 5 min was set at the maximum value of each cycle. After the end of the holding time of the second cycle, the sensors were removed and the sample was loaded until failure to obtain the UCS. Using the results of the first unloading cycle, the static Young's modulus (average modulus) of each plug was calculated as the difference in stress divided by the difference in the vertical deformation according to ASTM D3148-02 (2002). Likewise, the static Poisson ratio was calculated as the ratio of lateral deformation and original diameter divided by the ratio of vertical deformation and original plug length. Subsequently, the *G* modulus, *G*, and bulk modulus, *K*, were calculated after ASTM D7012-14 (2014):

$$G = \frac{E}{2(1+\mu)}, \tag{6}$$

$$K = \frac{E}{3(1-2\mu)}, \tag{7}$$

where E is the Young's modulus [N mm^{-2} or MPa] and μ is the Poisson ratio [–].

Furthermore, simple uniaxial tests were performed at TU Delft and UNAM to determine UCS, the static Young's modulus and the static Poisson ratio using a uniaxial stress–strain device with a capacity of 500 and 250 kN, respectively (GDSVIS load frame, GDS instruments, UK). Plugs with a dimension of 30 mm in diameter and a length of 75 mm drilled from marble, skarn, granodiorite and limestone samples from Las Minas were tested with a loading rate of 0.15 kN s^{-1} at TU Delft, while plugs with a dimension of 53 mm in diameter and a length of ~110 mm drilled from volcanic rocks from Acoculco were analyzed at UNAM (displacement controlled with 0.05 mm min^{-1}). Local axial and radial strains at UNAM were measured by the GDS LVDT local strain transducers, while at TU Delft axial displacement was recorded using two LVDTs and radial displacement was recorded using a radial chain with an LVDT sensor around the plugs. UCS, the static Poisson ratio and the static Young's modulus (TU Delft – tangent modulus; UNAM – secant modulus at 50% of UCS) were calculated as described above following the ASTM guidelines (ASTM D3148-02; 2002).

Tensile strength of the sample material was determined at TU Darmstadt and TU Delft performing the indirect tensile test, also called the Brazilian test, according to ASTM D3967-16 (2016) and Lepique (2008). Cylindrical plugs with diameters of 55 and 40 mm (TU Darmstadt) and 30 mm (TU Delft) and a diameter / length ratio of 2:1 were loaded in a hydraulic uniaxial press by a linear distributed load until failure (diametrical compression). Afterwards the tensile strength of the plug was calculated using the following equation:

$$\sigma_t = \frac{2 \cdot F}{\pi \cdot d \cdot l}, \tag{8}$$

where σ_t is the tensile strength [N mm^{-2} or MPa], F the load at failure [N], d the diameter [mm] and l the sample length [mm].

Fracture toughness was then calculated for granite, limestone, marble and skarn samples analyzed at TU Delft after Guo et al. (1993). In order to obtain more precise values, further chevron bend tests were performed on the same sample material at TU Delft. The tests were performed on cylindrical plugs with a length of 15 mm and a diameter of 30 mm using the uniaxial device following the methods proposed by ISRM (1988). Fracture toughness (K_{Ic}) of the sample material was determined first using a direct loading to failure (equal to K_{Ic} at Level I) and secondly using cyclic loading to calculate the correction of fracture toughness for non-linearity (equal to K_{cIc} at Level II).

Additionally, point load tests were performed at UNAM in order to correlate the results to the tensile and uniaxial strength as proposed by ASTM D731-18 (2018). The tests were performed following the ISRM 325-89 (1984) and ASTM D5731-08 (2008) guidelines using a point load device from Controls (model 0550) with a maximum capacity of 100 kN. Therefore, cylindrical plugs with diameters of 25 mm and lengths ranging between 25 and 55 mm were jacked in a neoprene membrane during the test to confine the specimen and to avoid the fragmentation due to impacts with the ground.

Triaxial compression tests were performed on oven-dry samples at TU Darmstadt using a hydraulic triaxial press (Wille Geotechnik, Germany) with a capacity of 500 kN in order to determine the friction angle (φ), cohesion (c), shear (τ) and normal stress (σ_n) of the sample material. Depending on the availability, three plugs (diameter of 55 mm, length of 110 mm) for each sample were tested using different confining pressures (σ_3) of 10, 20 and 30 MPa, respectively. According to ASTM D2664-04 (2004) the confining pressures and resulting vertical stresses (σ_1) were transferred into a shear stress diagram to construct the Mohr–Coulomb criterion of failure to derive cohesion (intersection with the vertical axis)

and the friction angle (the angle between the line and the horizontal axis). Whenever needed, the vertical stresses from UCS tests (with $\sigma_3 = 0$) were considered to construct an additional circle in the shear stress diagram, thus enhancing the data evaluation.

3.6.4. Chemical Analyses

In order to perform quantitative and qualitative chemical analyses, representative composite sample material from selected outcrop samples and the reservoir core samples was milled with a disc swing mill (Siebtechnik, Germany) for 2.5 min at 1000 rpm at TU Darmstadt and with a colloid mill (Mixer Mill MM301, Retsch GmbH, Germany) for about 1 min at TU Delft to obtain a grain size smaller than 63 µm. XRD analyses at TU Delft and GFZ were performed using a Bruker D8 Advance diffractometer (Bruker, Karlsruhe, Germany) and the software DIFFRAC.EVA (TU Delft) and Match! (GFZ) for data evaluation. For XRF measurements at TU Delft, a Panalytical Axios Max WDXRF spectrometer was used and data evaluation was performed with SuperQ5.0i/Omnian software. In addition to the Omnian standards, many NIST SRM samples and pure compounds were used for calibration. At GFZ the XRF measurements were performed with a Panalytical Axios Advanced spectrometer in combination with the software SuperQ. For the analysis three reference standards (basalt ZGI-BM, granite ZGI-GM and shale ZGI-TB) were used. At TU Darmstadt, major and trace elements were analyzed with a Bruker S8 TIGER 4 WDXRF spectrometer using the Quant Express method. Accuracy is < 5% for the major elements and < 10% for the trace elements. The proposed limit of detection ranges between 400 ppm (Na) and 10 ppm (e.g., Rb, Sr, Nb). Further XRD analyses were performed at UniTO using a Siemens D5000 automatic X-ray diffractometer. The qualitative interpretation of the data has been realized with the software DIFFRACplus EVA Application 7.0.0.1 (2001), by comparing the positions and intensity of the data with suitable databases (ICDD, previously JCPDS; ICSD; PCPDFWIN).

3.7. Status of the Database

The database presented here comprises petrophysical and mechanical rock properties of outcrop samples and reservoir core samples of two caldera complexes located in the northeastern part of the TMVB. So far, the database comprises 31982 data entries (Table 4) as a result of 34 properties determined for 2169 plugs and rock samples (2138 cylindrical plugs and 31 uncored samples). Destructive tests were conducted on more than 970 plugs. In addition, 133 XRF and 113 XRD analyses were performed.

In total 380 samples were analyzed covering volcanic rocks (950 plugs), sedimentary rocks (716 plugs), igneous rocks (147 plugs) and metamorphic rocks (356 plugs). Thereof, 80 outcrop samples were collected for Acoculco and 226 outcrop samples were collected for Los Humeros, resulting in 563 and 1606 analyzed plugs and samples including the reservoir core samples, respectively. The difference between the number of collected samples for Los Humeros and Acoculco is biased due to the purposes of the different field trips and the targets of the project. The main targets for the development of a deep EGS in Acoculco and SHGS in Los Humeros are marbles and skarns (AC3 and AC2) and the pre-caldera andesites and Cretaceous limestones and marbles (G3 and G4), respectively. As the basement rocks (AC1 to AC3) are not exposed in Acoculco, the exhumed systems were used as analogs. Therefore, the main attention was paid to Las Minas where 101 samples were collected (here associated with Los Humeros). In Las Minas it is possible to investigate the igneous bodies and their metamorphic products like skarn, hornfels or marble (Fuentes-Guzmán et al., 2020) as well as some outcrops belonging to the metamorphic basement below the Cretaceous and Jurassic units.

(a)

Regional model	Local model	No. of samples
G1 Post-caldera	U1	1
	U2	9
G2 Caldera	U3	4
	U4	-
	U5	15
G3 Pre-caldera	U6	35
	U7	8
	U8	14
G4 Basement	U9	169

(b)

Regional model	No. of samples
AC5 Volcanites	46
AC4 Limestones	40
AC3 Skarns	1
AC2 Granite	1
AC1 Basement	-

Figure 24: Number of collected samples (outcrop and reservoir core samples) per model unit for the regional and local models of the Los Humeros (a) and Acoculco (b) geothermal systems.

The samples were classified regarding their model units as shown in Fig. 24. Following this approach almost all local model units for Los Humeros were covered. For some samples a classification is not possible at this stage of the project. Ongoing volcanological studies are underway and further dating is planned to overcome these knowledge gaps. The outcrop samples belonging to the pre-caldera group predominantly represent the Teziutlán andesite unit (U6) and the Cuyoaco andesite unit (U8). U5 comprises ignimbrites and pumice layers from the Xáltipan ignimbrite unit, while very recent basaltic lavas, ashfall deposits and ignimbrites collected within the Los Humeros caldera are associated with the post-caldera group (G1). The basement comprises a wide range of different rock types. G4 includes Jurassic sandstones and limestones; Cretaceous limestones, marls and shales; and Miocene granitic and granodioritic intrusive bodies and their metamorphic products marble and skarn. Regarding the regional model of Acoculco, outcrop samples from the two upper units AC5 and AC4 were collected. The uppermost unit comprises all volcanic deposits from the pre-caldera volcanics to the extra-caldera volcanism. Among others, samples from the Acoculco ignimbrite, Terrerillos andesite lava, Manzanito andesite and Perdernal rhyolitic lava were collected. The unit AC4 includes Jurassic limestones and sandstones and Cretaceous limestones. The reservoir core samples from well EAC1 cover ignimbrite (core 1), dacitic to rhyolitic lavas (core 2 and 3), skarn (core 4), marble (core 5) and granodiorite (core 6).

The number of measurements for each parameter resulted from the availability of measurement devices at the different institutes, required sample size, sample preparation and test duration as well as test setup. While most of the non-destructive parameters were analyzed on each plug, more time-intensive tests, such as specific heat capacity measurements or XRF and XRD analyses, were performed for each sample only (composite sample material). Likewise, rock mechanical tests are significantly more time-consuming as they require a specific sample size and sample preparation or in the case of triaxial tests a minimum number of samples to evaluate the test results. Although the total number of measurements significantly differs between some parameters, all parameters were analyzed on sample sets covering all relevant lithologies in the study area.

Table 4: Number of measurements for each parameter

Parameter	No. of measurements
Particle density	1,878
Bulk density	1,379
Porosity	1,352
Permeability	1,052
Thermal conductivity (dry)	1,669
Thermal conductivity (sat)	1,465
Thermal diffusivity (dry)	1,617
Thermal diffusivity (sat)	1,396
Specific heat capacity	210
Specific heat capacity (calculated)	1,093
Volumetric heat capacity	210
P-wave velocity (dry)	1,819
S-wave velocity (dry)	1,753
P-wave velocity (sat)	1,416
S-wave velocity (sat)	1,375
Dynamic Young's modulus (dry)	1,752
Dynamic Young's modulus (sat)	1,375
Dynamic Poisson ratio (dry)	1,736
Dynamic Poisson ratio (sat)	1,375
Dynamic Shear modulus (dry)	1,743
Dynamic Shear modulus (sat)	1,375
Magnetic susceptibility	921
Electric resistivity (dry)	31
Electric resistivity (sat)	50
Formation factor	39
UCS	465
Static Young's modulus	242
Static Poisson ratio	243
Shear modulus	209
Bulk modulus	209
Tensile strength	407
Fracture toughness	86
Friction angle	20
Cohesion	20
Total	**31,982**

3.8. Discussion

3.8.1. Data Availability and Data Application

Rock properties are commonly used for reservoir exploration, assessment and modeling. While petrophysical, dynamic and static mechanical properties are the primarily used parameters for reservoir exploration, production and stimulation scenarios (Saller and Henderson, 1998; Rybacki et al., 2016; Gan and Elsworth, 2016; Ghassemi, 2017; Qu et al., 2019; Scott et al., 2019; Bohnsack et al., 2020), thermal properties are of great importance to assessing the subsurface temperature, the geothermal gradient, heat transport and heat storage (Weides et al., 2013; Weides and Majorowicz, 2014; Ebigbo et al., 2016; Franco and Donatini, 2017; Nurhandoko et al., 2019; Békési et al., 2020). Especially in active high-enthalpy hydrothermal systems, electric resistivity and magnetic susceptibility data are very useful to identify or map the cap rock and different lithologies or hydrothermally altered zones within the reservoir (Oliva-Urcia, 2011; Lévy et al., 2018, 2019), whereas high-T/P and detailed mineralogical studies help to estimate rock properties in reservoir conditions (Nono et al., 2020; Kummerow et al., 2020; Lacinska et al., 2020).

Within the scope of the GEMex project, petrophysical and rock mechanical data were used for various purposes. Deb et al. (2019a) used petrophysical and thermophysical properties to parameterize the structural model of Los Humeros and Acoculco (Calcagno et al., 2018) for simulating the initial state of the super-hot geothermal system. Several stimulation scenarios were investigated to evaluate the potential of the basement rocks in Acoculco for the development of an EGS (Deb et al., 2019b). Based on the fracture network characterization of outcrop analogs in Las Minas and petrophysical and rock mechanical data, Lepillier et al. (2019) created FEM models to calculate the fluid flow and heat exchange of fracture-controlled reservoirs in marble, skarn and limestone as an equivalent to the deep subsurface of Acoculco. Kruszewski et al. (2021) used rock mechanical parameters together with well parameters and geophysical logs to estimate the local stress field of the Acoculco geothermal field. Current studies focus on fracture propagation models and hydraulic fracture stimulation scenarios to estimate fracture geometries. The results of the petrophysical properties and volcanological studies are being used to interpret results of electric resistivity surveys (Benediktsdóttir et al., 2020), local earthquake tomography (Toledo et al., 2020a), or gravity and magnetotelluric surveys (Cornejo, 2020).

Compared to siliciclastic or carbonate basins used for oil and gas exploitation, the number of petrophysical and mechanical rock property data for volcanic settings in the context of high-enthalpy geothermal systems is less documented.

So far, geothermal exploration studies in volcanic settings have provided rock properties analyzed on outcrop (e.g., Lenhardt and Götz, 2011; Pola et al., 2014; Mielke et al., 2016; Heap and Kennedy, 2016; Navelot et al., 2018; Mordensky et al., 2019a; Eggertson et al., 2020) or reservoir core (Stimac et al., 2004; Siratovich et al., 2014; Ólavsdóttir et al., 2015; Mielke et al., 2015; Cant et al., 2018) samples. However, this study highlights the importance of the analysis of both outcrop and reservoir core samples. The comparison of reservoir samples, exhumed systems and outcrops in the surrounding area enables the identification of the processes that occurred within the reservoir and quantifying the impact on the properties correctly.

The need for valuable input data for reservoir modeling and assessment has recently led to an increased number of studies and publications (Bär et al., 2020). While several extensive national or global databases have already been developed and published for geothermal well data (National Geothermal data system NGDS, 2014; BritGeothermal, 2017; DOE Data Explorer, 2018); rock chemistry; geochronology; petrology; petrophysical data such as porosity, density or magnetic susceptibility derived from geophysical borehole data (Petlab, 2020; Sciencebase Minnesota, 2010; Georoc Mainz, 2020; Rock Properties Database British Columbia Canada, 2018; global whole-rock geochemical database compilation in Gard et al., 2019; National Geochemical Database USGS, 2014; the North American Volcanic

and Intrusive Rock Database NAVDAT data base, 2020); lithology (the new global lithological map database GLiM in Hartmann and Moosdorf, 2012); mineralogy (BRITROCKS project, 2020); and petrography (RockViewer, 2020), a comprehensive and quality-proofed collection of laboratory rock properties has just recently been released by Bär et al. (2020; not considering fee-based and non-open-access databases that exist for oil and gas data like the AccuMap or geoSCOUT databases; IHS Markit, 2020; GeoScout, 2020). The PetroPhysical Property Database (P^3) presented in Bär et al. (2020) collected rock property data from 316 research articles and comprises 75 573 data points of 28 different rock properties analyzed on a wide variety of lithologies worldwide. While the P^3 database significantly increases the availability of standardized rock properties, it still contains a limited number of data points or parameters for each investigated area or formation. To increase the level of detail for the GEMex study area to the required spatial and stratigraphic coverage, the database presented in this paper contains more than 31000 data points and 34 different parameters covering all important lithologies from the basement to the cap rock. The high number of analyzed plugs and samples enables detailed statistical and spatial geostatistical analyses on different scales (plug, sample, outcrop, formation or model unit), spatial evaluation of the results in 2D or 3D, and the validation of different analytical methods. Whenever possible, all parameters were analyzed on each plug. This approach allows the identification of statistical and causal relationships between the parameters and, thus, improves the accuracy of geostatistical predictions, which are crucial for upscaling or downscaling (see next section; Linsel et al., 2020). The usage of plugs with different dimensions (drilled diameter ranges from 25 to 65 mm with a length from ~12 mm to 30 cm) enables the identification of scale effects, which need to be considered for the evaluation of dynamic mechanical properties (Bayuk and Tikhotsky, 2018). The level of detail presented in this study has not only significantly improved the geological understanding of both geothermal systems and super-hot geothermal systems in general but also helped in the better understanding of the relationship between different parameters and how they are affected by different processes (e.g., fracturing or hydrothermal alteration). The database not only provides the basis for ongoing research in the study area but also facilitates various applications in comparable geological settings within the TMVB or similar volcanic geothermal play types worldwide. Combined with other data sets (P^3 in Bär et al., 2020, or Weinert et al., 2021), these data could be used to train machine learning algorithms to develop rock property prediction tools to improve and speed up parametrization of 3D geological models in the future.

3.8.2. Data Processing and Upscaling

The database presented in this study includes laboratory data analyzed on core and outcrop samples (centimeter to decimeter scale defined here as mesoscale), thus representing rock matrix properties only (with small-scale or single fractures in few samples). Oven-dried samples were analyzed under ambient laboratory conditions (room temperature of ~21 °C and atmospheric pressure of 0.1 MPa) to standardize the test procedure and to ensure the comparability of the results for the different samples and rock types. Consequently, the data do not reflect in situ conditions such as high reservoir temperatures, overburden pressure, confining pressure and fluid properties at reservoir depth. Depending on the aim and scale of future applications, the data need to be corrected for reservoir conditions and transferred to the reservoir scale (macroscale). Hydraulic properties such as porosity and permeability tend to decrease with increasing stress and pressure at reservoir depth by closing fractures and compaction of the rock mass (rock compressibility; Zimmermann et al., 1986; Moosavi et al., 2014; Hatakeda et al., 2017; You et al., 2020), often also resulting in increased bulk density, heat conduction, electric resistivity and wave velocities (Horai and Susaki, 1989; Clauser and Huenges, 1995; Schön, 2015). However, the relationships between different properties related to temperature and pressure changes are complex. At higher temperatures thermal expansion of minerals can cause microfracturing, which again negatively affects thermal conductivity, ultrasonic wave velocities and rock strength (Heap

et al., 2014a; Vinciguerra et al., 2005) but increases hydraulic properties. Several analytical and empirical relationships and correction functions have been identified and developed in the past to transfer hydraulic (Zimmermann et al., 1986; Li et al., 2004; Zheng et al., 2015; Heap and Kennedy, 2016), thermal (Sass et al., 1971; Zoth and Hänel, 1988; Somerton, 1992; Vosteen and Schellschmidt, 2003; Hartmann et al., 2005; Whittington et al., 2009; Rühaak et al., 2015; Zhao et al., 2016; Merriman et al., 2018; Norden et al., 2020; Clauser, 2020), magnetic (Ohnaka, 1969; Ali and Potter, 2012; Zhang et al., 2020), electric (Shankland et al., 1997; Hatakeda et al., 2017; Kummerow and Raab, 2015; Kummerow et al., 2020; Nono et al., 2020) and mechanical (Mobarak and Somerton, 1971; Vinciguerra et al., 2005; Siratovich et al., 2011; Heap et al., 2014a; Hassanzadegan et al., 2013; Vagnon et al., 2021) properties from laboratory to reservoir conditions. Transferring rock properties from core sample to the reservoir scale is challenging and has been the focus of numerous studies in the past (Christie, 1996; Farmer, 2002; Qi and Hesketh, 2005; Khajeh, 2013). Even though computer processing capacities have drastically increased over the past decades, the resolution (number of grids) and complexity of static geological models often tend to be too high to run numerical reservoir simulations, which solve complex, e.g., fluid or heat flow, equations. Thus, upgridding and upscaling techniques are required that retain as much of the original structure, geometry, petrophysical characteristics and facies heterogeneity as possible to deliver the vital information needed for reservoir assessment and operation (Walia and Leahy, 2014). Existing upscaling approaches can be grouped into direct or two-step and local or global upscaling methods (Wen and Gomez-Hernandez, 1996; Farmer, 2002). The most common upscaling techniques are simple cross correlations, (power-law) averaging (arithmetic, geometric or harmonic averaging often in combination with Monte Carlo techniques), renormalization, pressure-solver or tensor methods, and pseudofunctions (Qi and Hesketh, 2005). However, particularly the first-mentioned techniques tend to spatially smear out extremes within the reservoir, such as flow barriers or open fractures, and thus are not very useful for complex and heterogenous reservoirs (Ding et al., 1992; Qi and Hesketh, 2005). Geostatistical analyses and modeling using estimation algorithms (e.g., variogram analyses and kriging techniques) or sequential simulations (e.g., Gaussian simulation) have been applied to populate numerical models in geologically complex and/or fractured reservoirs (Hartanato, 2004; Bourbiaux et al., 2005; Ebong et al., 2019). However, integrating geological information regarding the geometry, distribution and connectivity of faults and fractures as well as linking fracture and matrix properties and fluid flow remains challenging (multiphase and dual-porosity modeling; Bourbiaux, 2010). Since hydrothermal alteration significantly influences the matrix properties (Heap et al., 2020a), estimating the size and spatial distribution of hydrothermal aureoles along fractures in active volcanic settings becomes important to improving the accuracy of the reservoir model. While upscaling of hydraulic properties with application to oil and gas reservoirs has been intensively analyzed in the past (Wen and Gomez-Hernandez, 1996; Farmer, 2002; Sánchez-Vila et al., 2006), relatively little work has been done for thermal properties (Scheibe and Yabusaki, 1998; Hartmann et al., 2005; Rühaak et al., 2015). According to Rühaak et al. (2015) upscaling thermal conductivity can be fundamentally different from upscaling hydraulic or other transport parameters in porous media and rocks. The authors found that harmonic- and geometric-mean upscaled values most accurately reflect local values. Rühaak et al. (2014) and Gu et al. (2017) recommend kriging with external drift (KED) to interpolate subsurface temperature and thermal conductivity, respectively.

3.8.3. Limitations with Respect to Modeling the Los Humeros and Acoculco Geothermal Systems

Besides the many advantages described above, a number of limiting factors have to be considered prior to using this data set for modeling the Los Humeros and Acoculco geothermal systems. The field-work and the results of the petrophysical measurements revealed the complexity of both geothermal systems. Composition, lateral extension and distribution of the volcanic sequences are very variable within the study area. Furthermore, the basement rocks showed a high geological heterogeneity comprising several different rock types including shales, limestones, sandstones, intrusive bodies, marble and skarn. The definition of the preliminary model units is predominantly based on the local stratigraphy of the study area (Calcagno et al., 2018), and some model units comprise multiple different rock types. The results of the petro- and thermophysical properties however reveal high variability and a wide parameter range for individual units leading to high uncertainties during modeling. For this reason, the results for each lithostratigraphic unit were weighted with respect to their relative contribution in the study area for the population of the geological model of Los Humeros (Deb et al., 2019a), which was mainly based on lithostratigraphic well descriptions provided by the CFE. As this is not known in detail for every model unit, the relative contribution of each rock type was based on field observations.

The number of samples per unit strongly depended on the quality, availability and accessibility of representative outcrops in the field or reservoir core samples in the core storage. Thus, it was not possible to cover all local model units for Los Humeros.

Likewise, the number of measurements for each parameter was strongly affected by the availability of measurement devices, sample preparation and test duration. Although the data for each parameter cover all key lithologies in the study area, future work should focus on additional electric resistivity and rock mechanical tests (fracture toughness and triaxial tests) to better support the interpretation of MT, TEM and DC surveys or 3D geomechanical models. Furthermore, further research is needed on HT–HP experiments reaching supercritical conditions to better evaluate the processes within the reservoir and to transfer rock properties from laboratory to reservoir conditions of super-hot geothermal systems. The core samples of the Los Humeros geothermal field were predominantly retrieved from the reservoir pre-caldera andesite units. They show high matrix variability due to hydrothermal alteration of different intensities, which caused significant differences regarding petrophysical and thermophysical properties compared to the equivalent outcrop samples. For about one-quarter of the samples, intensive hydrothermal alteration prevents a clear identification of the original rock type and correlation to equivalent units in the outcrops. This suggests that a comprehensive identification and characterization of the hydrothermal alteration aureoles in the geothermal fields is also required for the accurate assessment and modeling of these systems (e.g., by MT sounding or other direct or indirect analyses). Current studies on the reservoir core samples including detailed petrographic analyses and ICP-MS measurements aim to provide a better sample description and classification (Weydt et al., 2020, 2022). Only a few reservoir core samples were available representing the overlaying cap rock (Xáltipan ignimbrite) or the basement below. While the Xáltipan ignimbrite unit can be investigated in several outcrops around the Los Humeros caldera, the deeper part of the basement remains mostly unknown. The high number of collected samples in the exhumed systems and in the surrounding area of the caldera complexes greatly depicts the heterogeneity of the basement. However, the analyses of outcrops and the few reservoir core samples only cover the upper limited parts of the basement (approximately tens to hundreds of meters). Thus, in the field it is not possible to investigate the spatial extension of the intrusive bodies within the (meta)sedimentary basement. However, Urbani et al. (2020) concluded that the recent uplift within the Los Proteros caldera was caused by multiple intrusive bodies at a very shallow depth (425 ± 170 to < 1000 m). Likewise, in Acoculco several intrusive bodies had already been identified at 1000 m depth (below ground level; Avellán et al., 2020).

Regarding the regional model of Acoculco, only rocks of the two upper units are exposed in the field. For the parameterization of the remaining units, the project emphasizes using the exhumed system in Las Minas as an analog. Regarding the results of the petrophysical measurements, this concept can be applied for almost all units. However, the sedimentary sequences reveal the highest variability compared to other units comprising argillaceous mudstones to dolomitic marbles. The properties of the limestones and marbles resemble the different facies and diagenetic or metamorphic overprint. In Las Minas the limestones and marbles comprise dolomite, while the reservoir core samples from Los Humeros and most of the limestones collected from the outcrops in the surrounding area of both systems represent undolomitized, marine, fine-grained mudstones to wackestones. In addition, the reservoir core samples from the upper part of the carbonatic basement show intensive fracturing and recrystallization as a result of the complex tectonic activity caused by caldera collapses, uplift and ascending lavas. Furthermore, the term "skarn" has been widely used in the literature (related to the study area) without a precise description. The skarns in Las Minas commonly resemble Fe-rich ore deposits in close proximity to intrusive bodies. In contrast the units classified as skarn within the upper parts of the geothermal reservoirs (López-Hernández et al., 2009) formed instead due to intensive metasomatic processes caused by Ca-rich fluids migrating into the overlaying lavas. Once more, the physical properties reflect the different mineralogical composition of both skarn types.

3.9. Conclusions

Within the scope of the GEMex project, an extensive rock property database was created comprising more than 31000 data entries covering a great variety of different rock types and lithologies of Jurassic to Holocene age. The database includes petrophysical, thermophysical, magnetic, electric, and dynamic and static mechanical properties complemented by the results of XRF and XRD analyses. In total 34 properties were determined on 2169 plugs retrieved from more than 300 outcrop samples collected from the Acoculco and Los Humeros caldera complexes, 66 reservoir core samples drilled from 37 core sections from 16 wells of the Los Humeros geothermal field, and 8 core samples drilled from 6 core sections obtained from well EAC1 of the Acoculco geothermal field. The database was created in a simple and transparent format including comprehensive metainformation to facilitate application in various geoscientific disciplines worldwide.

The compiled data set allows for the
- prediction of rock properties of target formations in the subsurface at early exploration stages or in the case of low data density,
- assessment of the reservoir potential and estimation of economic risks and uncertainties,
- population of 3D geological models (numeric thermo-hydraulic–mechanical–chemical (THMC) models),
- statistical evaluation to identify relationships between the properties and trends required for upscaling approaches, and
- validation of different analytical methods.

The data and workflow presented here will improve the planning and execution of future research projects. Outcrop analyses and the characterization of petrophysical and mechanical properties of outcrop and reservoir core samples are paramount for profound reservoir characterization and should in general be considered in future geoscientific studies to a greater extent to enable a more precise prediction of reservoir properties. Hereby, an integration of shallow geophysical and classical (e.g., scan-line) or state-of-the-art (lidar) fracture network characterization methods has great potential to further enhance 3D reservoir characterization.

The current structure of the database allows for easy modification and extension. It is planned to create an outcrop catalogue of all field campaigns conducted within GEMex and to improve it by adding the results of ongoing ICP-MS and detailed petrographic analyses.

3.10. Acknowledgements

4. Petrophysical Characterization of the Los Humeros Geothermal Field – From Outcrop to Parametrization of a 3D Geological Model

This chapter is based on the article "Weydt, L. M., Bär, K., and Sass, I.: Petrophysical characterization of the Los Humeros geothermal field (Mexico): From outcrop to parametrization of a 3D geological model, Geothermal Energy, 10, 5(2022), 48 pp., 2022." The abstract is not included and the alphanumeric order of figures and tables may differ from the original article. If necessary, the alphabetical order of quotations has been adapted to the content of the dissertation. Likewise, the formatting was adjusted to fit the layout of this work.

4.1. Introduction

Super-hot geothermal systems (> 350 °C, SHGS) are important targets for electric power production and have recently been of high interest in the industry and scientific community (Reinsch et al., 2017). An important threshold is achieved when reservoir fluids reach supercritical conditions and recent studies have proven that the extraction of supercritical fluids increases the productivity by a factor of ten compared to conventional wells, including fossil fuels (Cladouhos et al., 2018; Friðleifsson et al., 2014a, b). However, the majority of previous deep and high-temperature drilling projects encountered several problems like corrosion and scaling due to aggressive reservoir fluids, unsuccessful cementing operations as well as damage of the casing material or surface equipment, which often led to well failure and abandonment (Reinsch et al., 2017). To exploit these super-hot reservoirs and to be able to handle the challenging conditions in the reservoir, comprehensive and detailed exploration is needed to enhance the reservoir understanding and modeling (Reinsch et al., 2017; Jolie et al., 2018).

The majority of high-temperature geothermal resources at comparatively shallow depths (< 4 km) are linked to volcanic settings, which often exhibit a complex structural architecture and geological evolution, resulting in various rock types with highly variable mineralogical and hydromechanical characteristics (Pola et al., 2012; Heap and Violay, 2021). Furthermore, hydrothermal alteration, diagenetic and metamorphic processes significantly change the properties of the rocks (Frolova et al., 2014; Aretz et al., 2016; Mielke et al., 2015; Villeneuve et al., 2019). The prediction of the thermo-hydro-mechanical behavior of the target formations in the reservoir is challenging, which in turn is crucial to build conceptual geological models, to interpret geophysical data and to parameterize 3D numerical reservoir models. Comprehensive datasets are often scarce or focus on a limited number of parameters only and thus, subsurface models are commonly populated with generalized or assumed values resulting in high uncertainties (Bär et al., 2020). Since diagenetic, hydrothermal or metamorphic processes can enhance or decrease hydraulic, mechanical or thermal properties (Mielke et al., 2015; Wyering et al., 2014; Weydt et al., 2018a, 2021a; Durán et al., 2019; Heap et al., 2020a, 2021), the controlling factors need to be understood and considered during reservoir assessment also from an economical perspective.

The GEMex project (Horizon 2020; GA Nr. 727550) aims to develop new transferable exploration and exploitation approaches for enhanced (EGS) and super-hot unconventional geothermal systems (SHGS). For this purpose, the Los Humeros Volcanic Complex (LHVC) has been selected as demonstration site, which is the third largest active caldera in the Trans-Mexican Volcanic Belt (TMVB) hosting a hydrothermal system that reaches temperatures above 380 °C below 2 km depth (Pinti et al., 2017). The conventional hydrothermal reservoir of Los Humeros has been exploited and operated by the Comisíon Federal Electricidad (CFE) since 1990 (Romo-Jones et al., 2020) and 65 wells have been drilled so far. However, a sustainable utilization of these super-hot sections in the reservoir has not yet been realized. Various geological, geochemical, geophysical, as well as hydrological studies have been performed in the past and conceptual geological models were built and regularly updated (Cedillo, 1999, 2000; Arellano et al., 2003). Nevertheless, recent studies revealed a much higher complexity of the

reservoir than previously expected (Lucci et al., 2020; Carrasco-Núñez et al., 2021) and the understanding of the internal structure of the reservoir is still limited.

Within the framework of the GEMex project, which aims to build integrated reservoir models at a local, regional and supra-regional scale, preliminary 3D geological models were created (Calcagno et al., 2020) that served as the basis for the evaluation and incorporation of results from combined geological, geophysical and technical investigations (Jolie et al., 2018). Besides the latest update of the geological map (Carrasco-Núñez et al., 2017a), this was the first time that the regional geological formations were considered during exploration. However, until the beginning of the project, information on the different geological units and their physicochemical properties were not available. To overcome the lack of suitable data that meet the spatial coverage and resolution required within the project, a comprehensive outcrop analogue study was performed (Weydt et al., 2018b, 2021a). Therefore, all relevant key units from the cap rock to the basement were characterized regarding their mineralogy, geochemistry, petrophysical and mechanical properties on different scales: (1) macroscale (outcrops), (2) mesoscale (rock samples), and (3) microscale (thin section and chemical analyses). The investigation of outcrop analogues represents a cost-effective opportunity to investigate and correlate, e.g., facies, geologic heterogeneities, hydrothermal processes and petrophysical properties from outcrops to the subsurface and to create a representative dataset sufficient for various modeling approaches (Sass and Götz, 2012).

In total, 226 outcrop samples were collected from more than 200 outcrops in the inside of the caldera, the surrounding area and in the exhumed fossil system in Las Minas, which is located east of the LHVC. The samples were analyzed for particle and bulk density, porosity, permeability, thermal conductivity, thermal diffusivity, P-wave and S-wave velocity as well as magnetic susceptibility. Whenever possible, each parameter was analyzed on each plug allowing for the identification of statistical and causal relationships between the parameters. This approach improves the accuracy of geostatistical predictions that are needed for upscaling or downscaling techniques or stochastic approaches. Complementary X-ray fluorescence measurements were conducted to obtain information on the bulk chemistry and to classify the samples into lithological units. New geochronological information obtained during the project were used to assign the samples to different stratigraphic units. Thin section and X-ray diffraction measurements were used to quantify the mineralogical composition as well as possible hydrothermal, metamorphic or diagenetic processes and their impact on the rock properties. Afterwards, the rock properties were statistically analyzed to define lithostratigraphic units with similar petrophysical characteristics and to investigate their variability and probability.

Here, we present a comprehensive dataset of laboratory-measured rock properties and a stepwise workflow for the prediction of in situ reservoir properties that provides the basis for a more precise resource and risk assessment of the Los Humeros geothermal field and geologically similar super-hot geothermal systems related to volcanic settings worldwide.

4.2. Geological Setting

The LHVC is located about 185 km east of Mexico City and predominantly comprises Pleistocene to Holocene basaltic to rhyolitic volcanic rocks (Norini et al., 2019; Carrasco-Núñez et al., 2018). With a 21 × 15 km irregular shape, it is the largest and easternmost active caldera of the Trans-Mexican Volcanic Belt (TMVB), which is a E–W trending about 1000 km long and up to 300 km wide Neogene calc-alkaline volcanic arc (López-Hernández et al., 2009; Fig. 25). The TMVB is commonly associated to the subduction of the Rivera and Cocos plates beneath the North American plate along the Middle-American Trench (Ferrari et al., 2012). The caldera structure developed in the Serdán-Oriental basin, which is a closed basin at the Mexican high plateau characterized by bimodal, mainly monogenetic volcanic structures of basaltic to rhyolitic composition (e.g., rhyolitic domes, scoria cones, lava fields, maars and tuff-rings) and older felsic domes (Yáñez and García, 1982; Carrasco-Núñez et al., 2021).

The basin is filled with Quaternary sediments, pyroclastic and volcanoclastic deposits and is limited to the east by large andesitic stratovolcanoes and dome complexes of the Cofre de Perote-Citlaltépetl volcanic chain and to the west by Miocene andesitic lavas of the Tlaxco-Cerro Grande range (Carrasco-Núñez et al., 2017a).
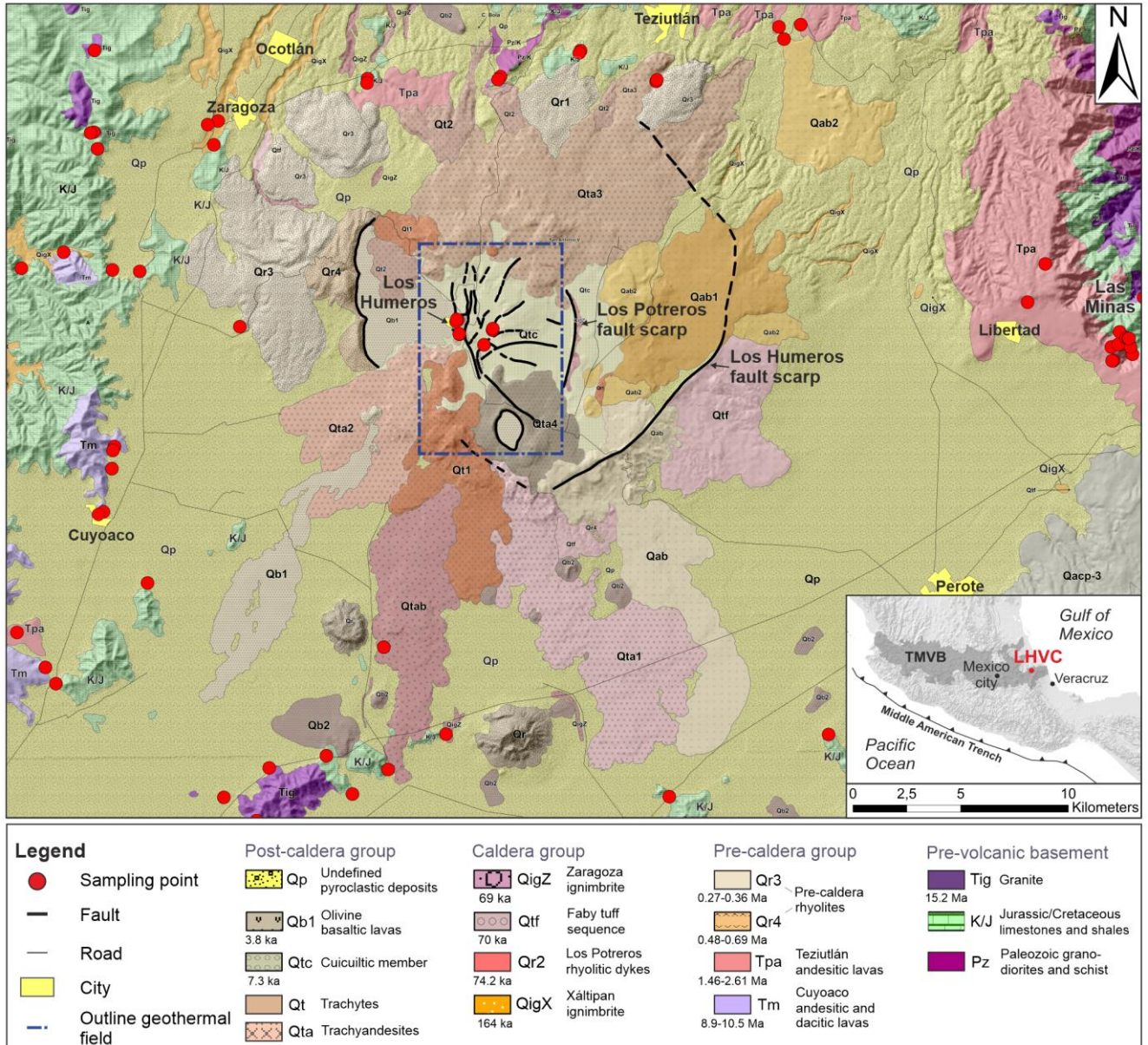
Figure 25: Geological map of the LHVC slightly modified from Carrasco-Núñez et al. (2017a). The red points mark the sampling locations of the outcrop samples. Inset map showing the location of the LHVC and extension of the TMVB in Mexico.

Based on new stratigraphic and geochronological data, the different geological units in the study area can be classified into: (1) post-caldera volcanism; (2) caldera volcanism; (3) pre-caldera volcanism and the (4) pre-volcanic basement (Carrasco-Núñez et al., 2017a and 2018; Figs. 25, 26).

Group	Stratigraphic units of the LHVC area	Age [a]
Post-caldera group	Pyroclastics (undifferentiated)	-
	Basaltic, trachyandesitc and trachytic lava flows	2.86 ka – 7.3 ka
	Cuicuiltic Member	7.3 ka
	San Antonio/Las Chapas trachyandesitic lava flows	8.9 ka
	Llano tuff	28.27 ka
	Maztaloya rhyodacite	<50 ka
	Xoxoctic Member	<50 ka [a,b]
	Rhyolitic domes	44.8 – 50.7 ka
Caldera group	Zaragoza ignimbrite	69 ka
	Faby tuff	70 ka
	Los Potreros rhyolitic lavas	74.2 ka
	Xáltipan ignimbrite	164 ka
Pre-caldera group	Rhyolitic lavas and domes	155.7 – 693 ka
	Teziutlán andesitic lavas	1.46 – 2.61 Ma
	Cuyoaco/Alseseca andesitic and dacitic lavas	8.9 – 10.5 Ma
Basement	Granites	15.2 Ma
	Skarn, Marble	12.18 – 17.8 Ma [c]
	Basaltic and andesitic dykes	11.2 – 16.5 Ma [d]
	Limestone, shale and sandstone	Cretaceous/Jurassic
	Igneous and metamorphic basement	131 – 246 Ma

References: a = Carrasco-Núñez et al. (2018), b = Willcox (2011), c = Fuentes-Guzmán et al. (2020) and d = Kozdrój et al. (2020) with c and d representing the Las Minas area only.

Figure 26: Stratigraphy of the Los Humeros Volcanic Complex in (a) and a simplified stratigraphic profile in (b) based on Willcox (2011), Carrasco-Núñez et al. (2012, 2017a, 2017b, 2018), Olvera-García et al. (2020), and Calcagno et al. (2020). The color scheme is based on Carrasco-Núñez et al. (2017a). The estimated thickness or occurrence of the individual units might vary throughout the study area (not all units of the LHVC have been dated or described in detail yet and geological studies are ongoing).

The pre-volcanic basement group comprises the Paleozoic crystalline basement in the eastern TMVB, which is exposed in the Teziutlán Massif and partially covered by up to 3000 m thick, intensively folded and thrusted Mesozoic sedimentary rocks belonging to the Sierra Madre Oriental (López-Hernández et al., 2009). The Teziutlán Massif consists of green schists, granites and granodiorites dated at 246–131 Ma representing the stratigraphically oldest units exposed in the study area (Carrasco-Núñez et al., 2018). The Mesozoic sedimentary successions include sandstones, shales, hydrocarbon-rich limestones and dolomites of Jurassic age, which are overlain by Cretaceous limestones, marls and shales. The basement was deformed by the Late Cretaceous–Eocene compressive Laramide Orogeny resulting in NW–SE striking thrusts and folds and subordinate NE-striking normal faults that are associated to an Eocene–Pliocene extensional tectonic deformation phase (Norini et al., 2019; Fítz-Díaz et al., 2017; López-Hernández et al., 1995). Oligocene to Miocene granitic and syenitic plutons as well as basaltic to andesitic dykes intruded into the sedimentary basement causing local metamorphism of marble, hornfels and skarn (Ferriz and Mahood, 1984). Thereby, Eocene–Pliocene extensional structures acted as preferential pathways for Eocene–Oligocene magmatic intrusions preceding the onset of the subsequent volcanism in the study area (Norini et al., 2019; López-Hernández et al., 1995). Metamorphic rocks are exposed in the exhumed system of Las Minas east of the LHVC, which is considered as an analogue to the deeper reservoir rocks of the Los Humeros geothermal field (Olvera-García et al., 2020).

The pre-caldera volcanism in the study area is represented by Late Miocene (~ 10.5 ± 0.7 Ma K/Ar; Yáñez and García, 1982) and Pliocene to Pleistocene lavas (1.44 ± 0.31 and 2.65 ± 0.43 Ma, Ar/Ar; Carrasco-Núñez et al., 2017a) of the Cuyoaco and Alseseca as well as Teziutlán andesite units, respectively. The Cuyoaco and Alseseca lavas mainly comprise andesitic and dacitic lava flows with a cumulative thickness of 800–900 m, which can be correlated to the Cerro Grande volcanic complex

dated between 8.9 and 11 Ma (K/Ar; Carrasco-Núñez et al., 1997; Gómez-Tuena and Carrasco-Núñez, 2000). The fractured pre-caldera andesites form the currently exploited geothermal reservoir in the subsurface of the Los Humeros geothermal field. Thereby, the Teziutlán andesites have a reported thickness of up to 1500 m according to lithostratigraphic profiles the geothermal wells (Carrasco-Núñez et al., 2017b; López-Hernández et al., 1995; Fig. 26).

The beginning of the magmatic activity of the LHVC is represented by the emplacement of rhyolitic lavas and rhyolitic domes, which are mainly located at the western side of the LHVC (Carrasco-Núñez et al., 2017a). Radiometric ages of the domes range between 270 ± 17 and 693 ± 1.9 ka with occurrences at 486.5 ± 2.2 and > 350 ka (Ar/Ar and U/Th; Carrasco-Núñez et al., 2018; Ferriz and Mahood, 1984).

The LHVC is associated with two main caldera-forming eruptions separated by large plinian and subplinian eruptive phases (Norini et al., 2019; Carrasco-Núñez et al., 2021) resulting in the outer Los Humeros caldera and the smaller inner Los Potreros caldera (8 × 10 km in diameter). The Los Humeros caldera collapse is associated with the emplacement of the high-silica rhyolite Xáltipan ignimbrite (164.0 ± 4.2 ka, Ar/Ar and U/Th; Carrasco-Núñez et al., 2018) with an estimated thickness of up to 880 m and a volume of 291 km^3 (dense rock equivalent, Cavazos and Carrasco-Núñez, 2020). After the emplacement of the Xáltipan ignimbrite eruption, a sequence of explosive events (70.0 ± 23 ka, Ar/Ar, Carrasco-Núñez et al., 2018) lead to the deposition of thick rhyodacitic Plinian deposits called Faby Tuff (9–16 m thick in Ferriz and Mahood, 1984). The second caldera-forming eruption is related to the deposition of the rhyodacitic to andesitic Zaragoza ignimbrite (69 ± 16 ka, Ar/Ar, Carrasco-Núñez et al., 2018; 2–60 m thick, Carrasco-Núñez et al., 2012, 2017b).

The most recent volcanic activity in the study area is represented by the post-caldera stage, which mainly consist of lava flows, scoria deposits as well as pumice fall out deposits with a highly lateral and vertical distribution, as well as a variable chemical composition. The unit can be divided into a Late Pleistocene resurgence phase and a Holocene reactivation phase (Carrasco-Núñez et al., 2021). The Late Pleistocene phase is characterized by rhyolitic and dacitic domes within the Los Humeros caldera center (44.8 ± 1.7 ka, U/Th; Carrasco-Núñez et al., 2018) and north of the Los Humeros caldera (55.7 ± 4.4 ka, Ar/Ar; Carrasco-Núñez et al., 2018) followed by a sequence of explosive eruptions producing dacitic pumice fall units (Xoxoctic Tuff; Ferriz and Mahood, 1984), volcaniclastic breccias and pyroclastic flow deposits (Llano Tuff, ~ 10 m thick in Ferriz and Mahood, 1984; Willcox, 2011). During the Holocene alternated episodes of effusive and explosive eruptions occurred producing basaltic to trachyandesitic lava flows (8.9 ± 0.03 ka, C14; Carrasco-Núñez et al., 2017a; > 30 m thick in Ferriz and Mahood, 1984) and basaltic and trachyandesitic fall out deposits (Cuicuiltic Member, 7.3 ± 0.1 ka, C14, ~ 1.5–8 m thickness; Dávila-Harris and Carrasco-Núñez, 2014). The thickness of the post-caldera group ranges between 100 and 300 m in the wells (Carrasco-Núñez et al., 2017b; Fig. 26).

4.3. Materials and Methods

4.3.1. Sampling Campaign and Sample Preparation

In order to provide a reliable and sufficiently large data set for each target unit, a high sampling rate is required allowing the determination of statistical parameters and probability distributions for numerical simulations (Hartmann et al., 2008). During the field campaigns 226 representative samples with a dimension of ~ 30 × 30 × 20 cm were collected from more than 200 outcrops inside of the caldera, in the surrounding area as well as in the exhumed system of Las Minas. Whenever possible, each geological unit was sampled several times at different outcrop locations to cover the unit's heterogeneity. Only samples with an overall fresh appearance unaffected by weathering were considered. Hydrothermal alteration was observed in some outcrops in close proximity to fault zones and dykes. In these cases, hydrothermally altered samples were deliberately collected to analyze the effect of these processes on

the rock properties. The samples were directly drilled in the field or shipped as boulders to Germany. Cylindrical cores with diameters ranging from 25 to 64 mm were drilled from the outcrop samples and subsequently cut into plugs according to the international standard ASTM D4543 (2019) for the required sample length whereby the irregular and rough core ends were cut to be parallel to one another. In total 1507 plugs with an axial length ranging between ~ 25 and 128 mm were prepared from the outcrop samples. Thereby, short plugs (diameter: 25–40 mm, length: 25 to ~ 30 mm) were predominantly used for the non-destructive petrophysical measurements like bulk density, porosity and permeability due to the specific sample size requirements of the measurement devices. Remaining plugs were prepared to meet the requirements for different destructive rock mechanical tests, which were performed within the GEMex project (Weydt et al., 2021a). To ensure reproducibility of the results, the plugs were analyzed under oven-dried conditions (105 °C for more than 24 h or 64 °C for 48 h) and stored in a desiccator at room temperature (20 °C). To perform measurements under saturated conditions, a vacuum desiccator (approx. − 1 bar) filled with de-ionized water was used.

4.3.2. Laboratory Measurements

Material and methods of the petrophysical and geochemical measurements are described in detail in Weydt et al. (2021a), which also includes the raw data used in the figures and tables presented in this study. Thus, the measurement procedures are only mentioned briefly in the following sections. All measurements described below were performed under ambient laboratory temperature (~ 20 °C) and pressure (~ 0.1 MPa).

Grain and bulk densities were determined in a multi-step procedure using a helium pycnometer (AccuPyc 1330) and a powder pycnometer (GeoPyc 1360), thereby measuring the particle and bulk volume five times for each plug, respectively. Subsequently, porosity was calculated from the resulting differences in volume and represents the gas-effective porosity. The accuracy is given as 1.1% by the manufacturer (Micromeritics, 1997, 1998).

The intrinsic matrix permeability was determined after Filomena et al. (2014) based on the principle of Klinkenberg (1941) using a column gas permeameter constructed according to ASTM D4525 (2013). The plugs were analyzed in a confined cell (1 MPa) with dried compressed air at five air pressure levels ranging from 1 to 3 bar. Measurement accuracy varies from 5% for high permeable rocks ($K > 10^{-14}$ m²) to 400% for low-permeability rocks ($K < 10^{-16}$ m²) (Bär, 2012).

In order to determine bulk thermal conductivity and thermal diffusivity a thermal conductivity scanner (Lippmann and Rauen TCS) was used applying the optical scanning method after Popov et al. (2016). Both parameters were measured four to six times on each plug for saturated and dry conditions, respectively. Measurement accuracy is 3% for thermal conductivity and 5% for thermal diffusivity (Lippman and Rauen, 2009).

Specific heat capacity was determined using a heat-flux differential scanning calorimeter from Setaram Instrumentation (2009). Crushed sample material was heated at a steady rate from 20 up to 200 °C within a period of 24 h, thereby monitoring the heat flux in the sample chamber and an empty reference chamber. Specific heat capacities were derived from the resulting temperature curves through heat flow differences. The measurement accuracy is 1% (Setaram Instrumentation, 2009). Subsequently, volumetric heat capacity was calculated by multiplying the specific heat capacity with the associated bulk density of each sample.

Compressional and shear wave velocities were measured using the Geotron USG40 (UKS-D) ultrasound generator from Geotron-Elektronik (2011) including a digital PicoScope oscilloscope and mounted point-source transmitter–receiver transducers. Continuous measurements were performed with a frequency of 80 kHz to 250 kHz and a constant contact pressure of 0.1 MPa. The arrival times

of the P- and S-waves were picked manually. Both velocities were measured four to six times on each plug under saturated and dry conditions, respectively.

Magnetic susceptibility was analyzed with a magnetic susceptibility meter SM30 from ZH Instruments (2008). An interpolating mode was applied including two air reference measurements and one measurement directly on the sample surface. Each plane surface of a plug was measured five times to account for mineralogical heterogeneities.

Geochemical analyses included powder X-ray diffractometry (XRD) and X-ray fluorescence spectroscopy (XRF), which were performed at three different institutes (GFZ Potsdam, TU Delft and TU Darmstadt). XRD measurements were performed using a Bruker D8 Advance diffractometer and the software Diffrac.EVA (TU Delft) as well as the software Match! (GFZ). XRF measurements were conducted to analyze the bulk composition of the rock samples using a Panalytical Axios Max WD-XRF spectrometer and the SuperQ5.0i/Omnian software 15 (TU Delft) and a PANalytical AXIOS Advanced spectrometer in combination with the software Super Q (GFZ) as well as a Bruker S8Tiger 4 WD-XRF spectrometer using the Quant Express method (TU Darmstadt). Measurement accuracy is < 5% for the major elements and < 10% for the trace elements. The proposed limit of detection ranges between 400 ppm (Na) and < 10 ppm (e.g., Rb, Sr, Nb).

Furthermore, the samples were studied by optical microscope using thin sections and acetate peels, which were prepared from small 20 × 40 mm blocks cut from selected outcrop samples.

4.3.3. Data Evaluation

Based on the results of the chemical and petrographic analyses the samples were classified into lithological units. New geochronological information provided by the project partners (Carrasco-Núñez et al., 2018; Kozdrój et al., 2019; Fuentes-Guzmán et al., 2020) was used to assign the samples to stratigraphic units, which allowed the definition of lithostratigraphic units as well as the correlation with the different regional and local model units of the preliminary 3D model of Los Humeros presented in Calcagno et al. (2020). The results are displayed in "Petrophysical properties — Data distribution and Parameter Correlations" section. Thereby, the color code is based on Carrasco-Núñez et al. (2017a) and SGM (2002b).

To investigate the variability and distribution of the petrophysical properties, univariate descriptive statistical parameters such as mean, standard deviation, median, the 25% and the 75% quartiles and the coefficient of variance were determined, which are often used as a direct input in design calculations or numerical models (Hartmann et al., 2008). Scatter plots and histograms were created to allow for a quick investigation of the relationships between parameters and their probability distribution. Whenever required, lithostratigraphic units were divided into subunits that are petrophysically similar to increase the accuracy of predicting the unit's properties. A more complex statistical approach is the principal component analysis (PCA; Jolliffle, 2005), which was used to visualize the whole data set and the relations between the properties as well as the lithostratigraphic units and subunits. The classification of Bär (2012) was used to evaluate the unit's properties regarding their geothermal potential. Descriptive statistics, scatter plots, normality and lognormality tests were performed using the software GraphPad Prism Version 8.0.2, while the PCA was performed using XLSTAT-biomat-2019.3.1 (Addinsoft, Boston, Massachusetts, USA).

4.4. Results

4.4.1. Sample Classification and Descriptions

Post-caldera group

Samples belonging to the post-caldera volcanism were predominantly collected inside of the Los Humeros caldera and comprise hydrothermally altered basaltic lavas, pyroclastic and ash fall deposits. The pyroclastic deposits represent the geologically youngest unit in the study area with an estimated age of < 2.8 ka (Carrasco-Núñez et al., 2018). They consist of soft, fine-grained beige to brownish, porous tuff with small phenocrysts of up to 3 × 5 mm in size (Fig. 27a). Outcrops are widely distributed around the caldera complex; however, the source of these pyroclastic deposits has not been identified yet (Carrasco-Núñez et al., 2017a) and thus, are referred to as "pyroclastics, undifferentiated" in this study.

Pyroclastics

Post-caldera group

Holocene
(not dated, < 2.8 ka, undifferentiated)

5 mm
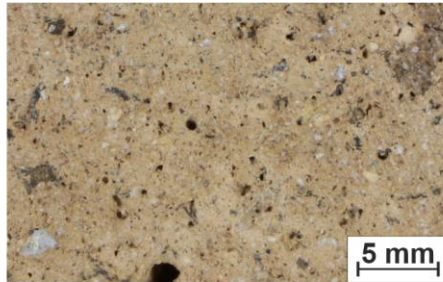
Ash fall deposits

Post-caldera group

Pleistocene

Xoxoctic member
(< 50 ka)

5 mm
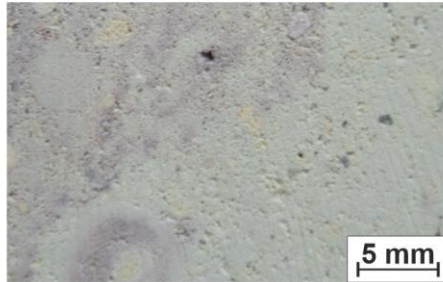
Zaragoza ignimbrite

Caldera group

Pleistocene
(69 ± 16 ka)

1 cm

Xáltipan ignimbrite

Caldera group

Pleistocene
(164 ± 4.2 ka)

1 cm
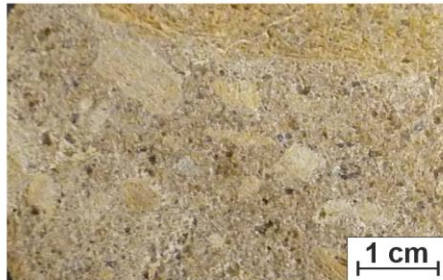
Scoria

Pre-caldera group

Pleistocene
(not dated)

1 cm
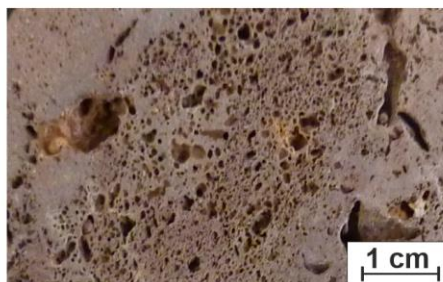
Basaltic lava

Post-caldera group

Holocene
(not dated, < 7.3 ka)
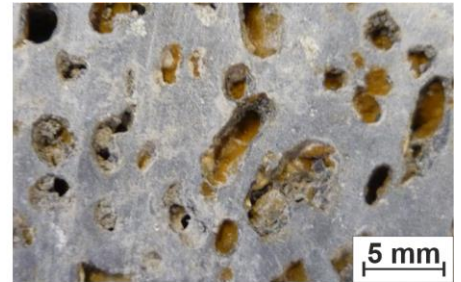
5 mm

Basaltic lava

Post-caldera group

Pleistocene

Xoxoctic member
(< 50 ka)

1 cm

Xáltipan ignimbrite

Caldera group

Pleistocene
(164 ± 4.2 ka)

1 cm
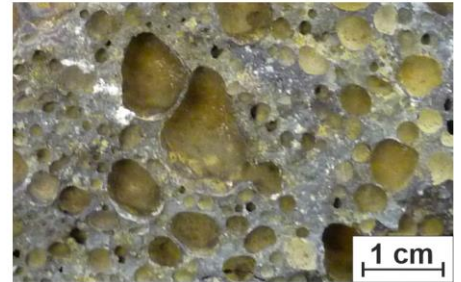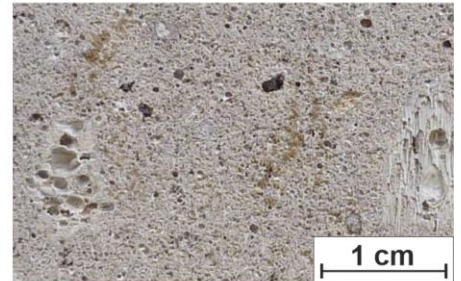
Xáltipan ign. pumice

Caldera group

Pleistocene
(164 ± 4.2 ka)

1 cm

Fallout deposits

Pre-caldera group

Pleistocene
(not dated)

1 cm
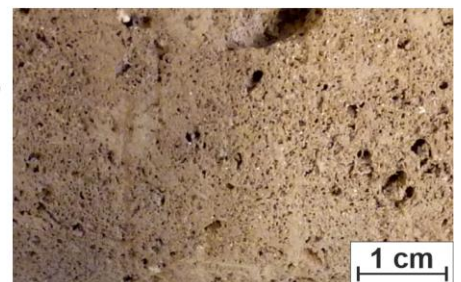
Figure 27a: Photographs of the volcanic outcrop samples representing the post-caldera, caldera and pre-caldera group in the study area. Stratigraphic ages are retrieved from section 4.2.

Teziutlán andesite
Pre-caldera group
Pleistocene/ Pliocene
(1.46 ± 0.31 Ma – 2.61 ± 0.43 Ma)

1 cm
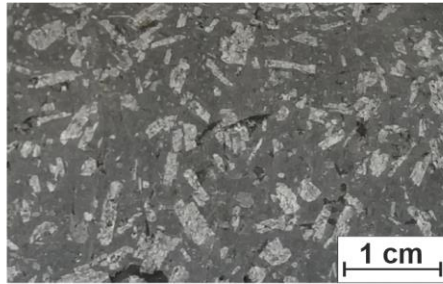
Cuyoaco andesite
Pre-caldera group
Miocene
(8.9 ± 0.4 Ma – 10.5 ± 0.7 Ma)

1 cm
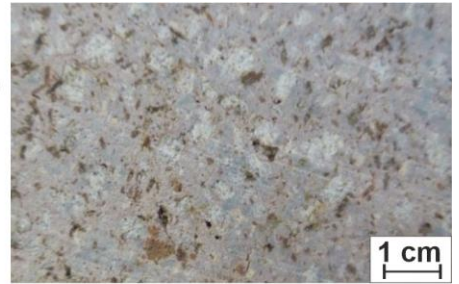
Limestone with chert
Basement
Cretaceous

1 cm
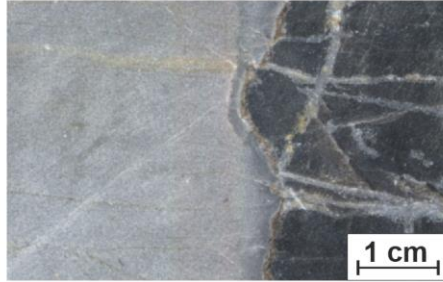
Shales
Basement
Cretaceous

10 cm

Sandstone
Basement
Jurassic
Cahuasas Fm.

1 cm
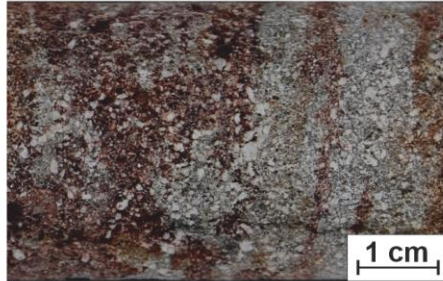
Marble
Basement
Miocene

1 cm
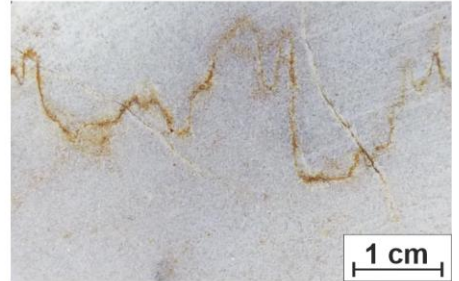
Skarn (Magnetite)
Basement
Miocene

1 cm
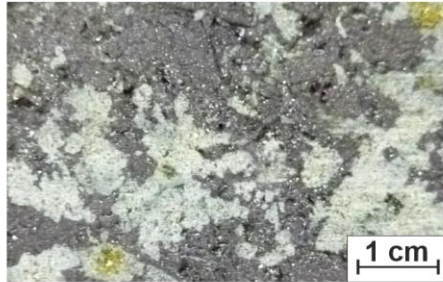
Skarn (Garnet)
Basement
Miocene

1 cm
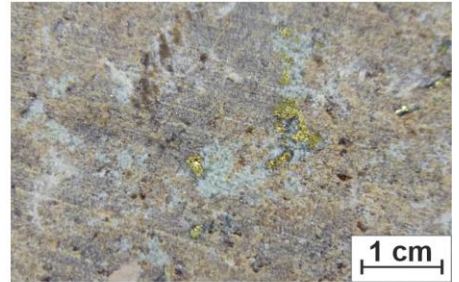
Quartz veins
Basement
Miocene

1 cm

Granodiorite
Basement
Miocene
(15.12 ± 0.64 Ma)

1 cm
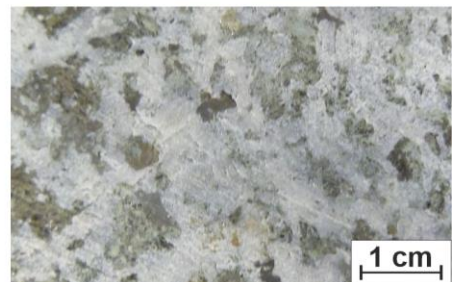
Figure 27b: Photographs of outcrop samples representing the pre-caldera group and basement of the LHVC. Stratigraphic ages are retrieved from section 4.2.

Two different basaltic lava flows were sampled within the caldera complex. The first one represents a fractured Holocene pahoehoe lava flow north of the Los Humeros town building a rectilinear topographic scarp in the field (Norini et al., 2019). The lavas contain a dark grey to blackish, vesicular groundmass with a porphyritic texture (Fig. 27a) and the irregular vesicles (< 1 mm in diameter, up to 5 × 10 mm) are often rimmed or partially filled with secondary clays and alteration minerals. This particular lava flow has not been dated yet, but according to Carrasco-Núñez et al. (2017a) the age of these young olivine-

bearing basaltic lava flows in the study area is about 3.87 ± 0.13 ka (unit Qb1 in Fig. 25) representing one of the last volcanic stages related to the caldera activity. Furthermore, it overlies the Cuicuiltic Member, which has been dated at 7.3 ± 0.1 ka (Carrasco-Núñez et al., 2017a). The second basaltic lava related to the post-caldera volcanism was retrieved from an outcrop located east of the Los Humeros town representing the Xoxoctic member as described in Willcox (2011). The collected samples consist of a blackish, vesicular and fractured groundmass with a porphyritic texture. The samples show a weak-to-moderate hydrothermal overprint, especially along fractures, and the pores are often partially filled with secondary clays. Further sample material collected from the Xoxoctic member contains soft, fine-grained and well-sorted, highly porous beige to reddish ash fall deposits.

Caldera group

Outcrop samples representing the caldera group of the LHVC include the Zaragoza and Xáltipan ignimbrites (Fig. 27a). Samples of the Zaragoza ignimbrite were collected inside of the caldera east of the town of Los Humeros and comprise beige, poorly sorted, lithic-rich, fine-grained, partially welded lapilli tuff with a dacitic composition (Fig. 28a). The samples contain numerous angular white to black lava clasts and pumice that are highly variable in size and occasionally fiamme structures.
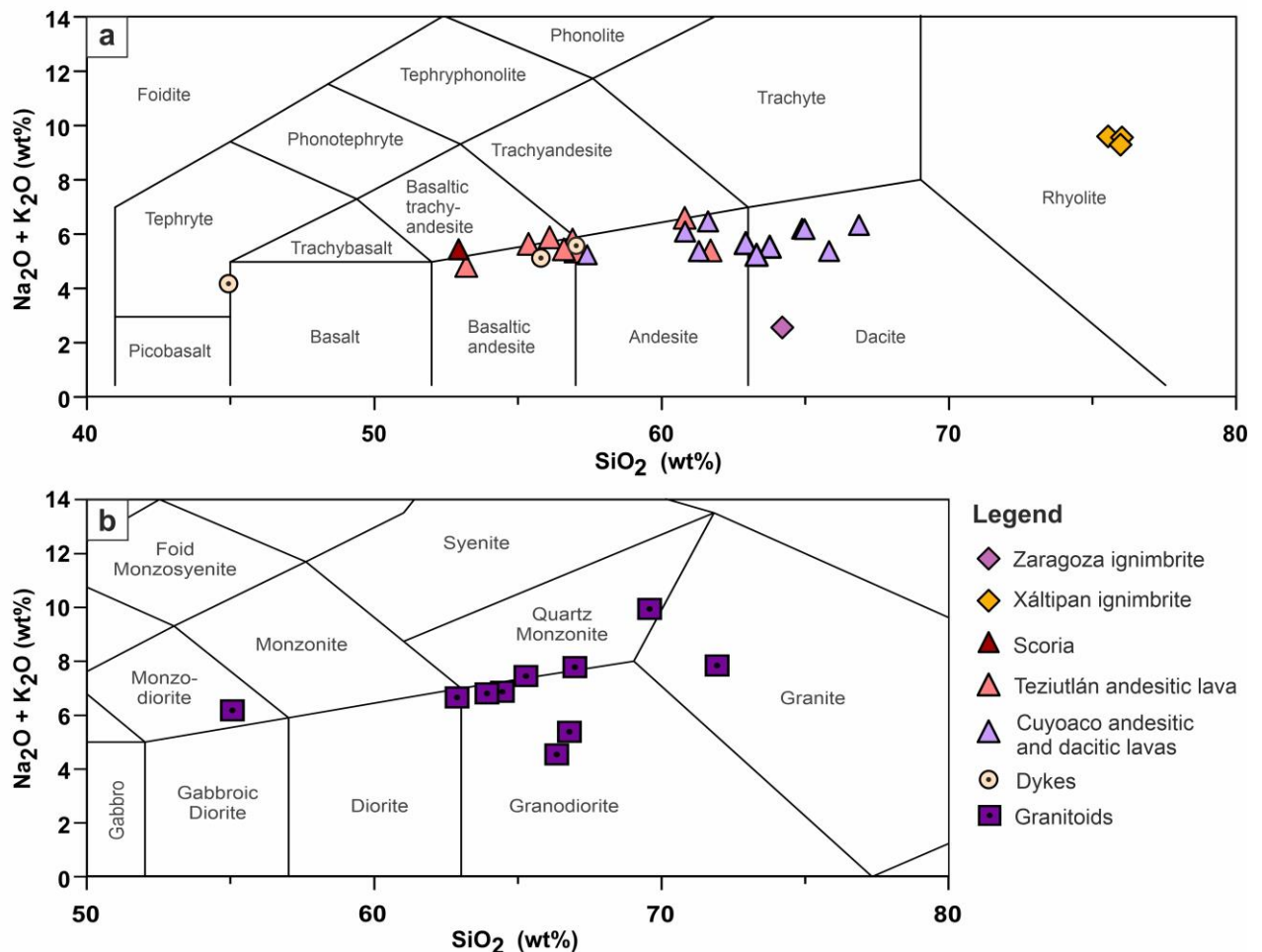
Figure 28: Total alkali versus silica (TAS) diagram for the (a) volcanic (Le Maitre et al., 2002) and (b) plutonic outcrop samples (Middlemost, 1994).

Samples of the Xáltipan ignimbrite were collected from several outcrops, quarries and road cuts in the surrounding area of the caldera complex. The samples represent a heterogenous collection of

predominantly non-welded to slightly welded, matrix-supported, massive lapilli tuff and pumice fallout deposits. XRF measurements of selected samples reveal a rhyolitic composition (Fig. 28a). The color is highly variable and ranges from rosé over reddish to ochre–brown–grey. Likewise, the clast load ranges from a few pumice clasts to abundant lithic fragments (volcanic rock fragments, but also intrusive and sedimentary fragments from the pre-volcanic basement). Vesicles in the pumice fallouts vary widely in both size and shape, but are commonly elongated. In addition, one sample of beige, massive, welded tuff was collected west of the town Cuyoaco, which has been affected by hydrothermal alteration (argillization in form of secondary clays, occasionally microcrystalline quartz in fractures; further details are presented in Cavazos-Álvarez et al., 2020).

Pre-caldera group

Samples related to the pre-caldera group include the Teziutlán and Cuyoaco andesite units (Fig. 27b) as well as scoria and fallout deposits. The latter was collected from a scoria cinder cone located approximately 5 km west of the Los Humeros caldera, which can be related to a sequence of basaltic and basaltic andesitic scoria cones dated at 190 ± 20 ka (Carrasco-Núñez et al., 2017a). Results of the XRF measurements of the scoriaceous lava revealed a basaltic trachyandesitic composition (Fig. 28a). The samples consist of a reddish-brown color, aphanitic texture and abundant ellipsoidal vesicles (< 1 mm up to 2 cm in length). The fallout deposits represent soft ashes to ash tuff, which are reddish-brown in color, fine-grained, well-sorted and occasionally contain small blackish to grey lava fragments (< 1 cm in length). Since this unit has not been investigated in greater detail yet, we refer to it as scoria and fallout deposits in this study.

The Teziutlán andesite unit comprises dark grey to medium grey, basaltic andesitic to andesitic lavas with a porphyric to glomeophyric texture. The lavas are often fractured and predominantly massive without macroscopically visible pores. Several outcrops located northeast of the Los Humeros caldera (east of the town Teziutlán) comprise vesicular basaltic andesitic lavas. Phenocrysts commonly consist of plagioclase, pyroxene and minor olivine, while the groundmass predominantly comprises microcrystalline plagioclase.

Outcrops of the Miocene Cuyoaco andesite unit occur west of the Los Humeros caldera close to the town Cuyoaco as well as southwest of the caldera complex. The collected samples comprise grey to slightly reddish, fractured and massive andesitic to dacitic lavas with a porphyritic to glomeophyric texture and a microcrystalline groundmass that mainly comprises plagioclase. The phenocrysts predominantly consist of plagioclase, pyroxene and minor olivine. In contrast to previous studies (Ferriz and Mahood, 1984, Carrasco-Núñez et al., 2017a), hornblende was not identified. However, both andesite units have not been investigated in greater detail yet and further volcanological studies are needed to fully understand their temporal evolution and extension.

Pre-volcanic basement

Outcrops of the pre-volcanic basement are widely distributed in proximal distance around the Los Humeros caldera. However, metamorphic rocks like marble and skarns are only exposed in the exhumed system of Las Minas. The Cretaceous is mainly represented by light to dark grey, fine-grained, medium to thick bedded and intensively folded limestones (Figs. 27b, A1) often with black chert nodules (~ 5 to 20 cm thick, cm- to dm-scale in length) or interbedded ochre-brownish marl and chert layers with a thickness of ~ 5 to 25 cm. Referred from thin section analyses, the collected samples represent nonporous, open marine mudstones to wackestones. However, joints and fractures (< 1 mm to a few cm wide) are very common and often filled with calcite. Similarly, the chert layers and nodules contain numerous fractures that are usually filled with calcite. Furthermore, grey to greenish, fine-grained and finely laminated shales were collected from outcrops west of the town Cuyoaco. Due to their fragile nature, only

a few plugs were suitable for petrophysical measurements. In addition, it was not possible to obtain samples from the friable marl layers. The Cretaceous outcrops in the study area predominantly correspond to the Tamaulipas Inferior and Tamaulipas Superior Formations and to a lesser extent to the Agua Nueva, San Felipe (Viniegra-Osario, 1965; SGM, 2011, 2012) and Orizaba Formation (predominantly in the Las Minas area; SGM, 2007). Samples representing the Jurassic units comprise light to dark grey, thin to medium bedded, fine-grained limestones to argillaceous limestones (Pimienta, Taman and Santiago Formations; SGM, 2011, 2012) and reddish-beige, medium to coarse, grain-supported sandstones of the Cahuasas Formation or so-called red beds (Ochoa-Camarillo et al., 1999). The limestones comprise nonporous mudstones to wackestones, which commonly contain fine, calcite-filled veins (< 1 mm wide). The samples of the Cahuasas Formation are made of rather fairly sorted angular grains of quartz and feldspar, occasionally granophyric grains and trace amounts of clay minerals coated by iron oxides that cause the reddish color of the samples. Pores are generally smaller than 1 mm and fractures are unfilled.

Outcrops of intrusive rocks are spread over the study area, but are best accessible in the exhumed system of Las Minas (Figs. 27b, A1). The collected samples predominantly represent granodiorites, but also have monzodioritic, dioritic to granitic compositions (Fig. 28b). For the following evaluation, the samples are referred to as 'granitoids' in this study. The samples usually contain quartz, plagioclase, K-feldspar, hornblende, biotite and pyroxenes. The majority of the collected granitoids showed a weak-to-moderate hydrothermal overprint (greenish-greyish color and minerals such as epidote, chlorite or sericite). Strongly altered and fractured samples often containing macroscopically visible fracture porosity were grouped separately as 'granitoids strongly altered'.

The intrusive bodies led to the generation of variable skarn assemblages with prograde mineralization caused by contact metamorphism followed by retrograde mineralization due to hydrothermal alteration along fractures and fault zones (Fuentes-Guzmán et al., 2020). According to Fuentes-Guzmán et al. (2020) the skarns can be classified into endoskarns with grossular-andradite, clinopyroxenes, and quartz in prograde associations, and magnetite, chalcopyrite, bornite, and native gold in retrograde associations as well as exoskarns, which comprise wollastonite, clinopyroxenes, potassium feldspar, quartz, epidote, and chromian muscovite. The collected samples show a high mineralogical variability and span from brownish garnet-dominated, greenish-grey magnetite-dominated to reddish hematite-dominated skarn associations. Quartz veins range from centimeter to meter scale and occur associated with skarn bodies. They are most likely the product of cooled down silica- and iron-rich fluids sealing existing fractures. Furthermore, they consist of several generations of quartz and are intensively fractured indicating a repeated reactivation and sealing of these fractures.

The formation of marble is caused by the contact metamorphism during Miocene as described above (Fig. A1l). The collected samples have a calcic to dolomitic composition, vary from white to grey in color and contain a fine to coarse grain size with a granoblastic texture. Since the marbles are predominantly associated to skarn deposits and intrusions along large fractures and fault zones, they often contain numerous veins and fractures, and hydrothermal minerals such as wollastonite, diopside, garnet, serpentine and talc were identified (Rochelle et al., 2021). Several mafic dykes crosscutting the Cretaceous formations and intrusive bodies (Fig. A1o) were observed in the outcrops. They commonly contain a basaltic to andesitic composition (Fig. 28a), blackish to dark grey color and predominantly have an aphanitic as well as occasionally a porphyric texture.

4.4.2. Petrophysical Properties — Data Distribution and Parameter Correlations

The results of the petrophysical analyses are displayed in the cross-plots, histograms and boxplots of Figs. 29, 30, 31, and 32, respectively.
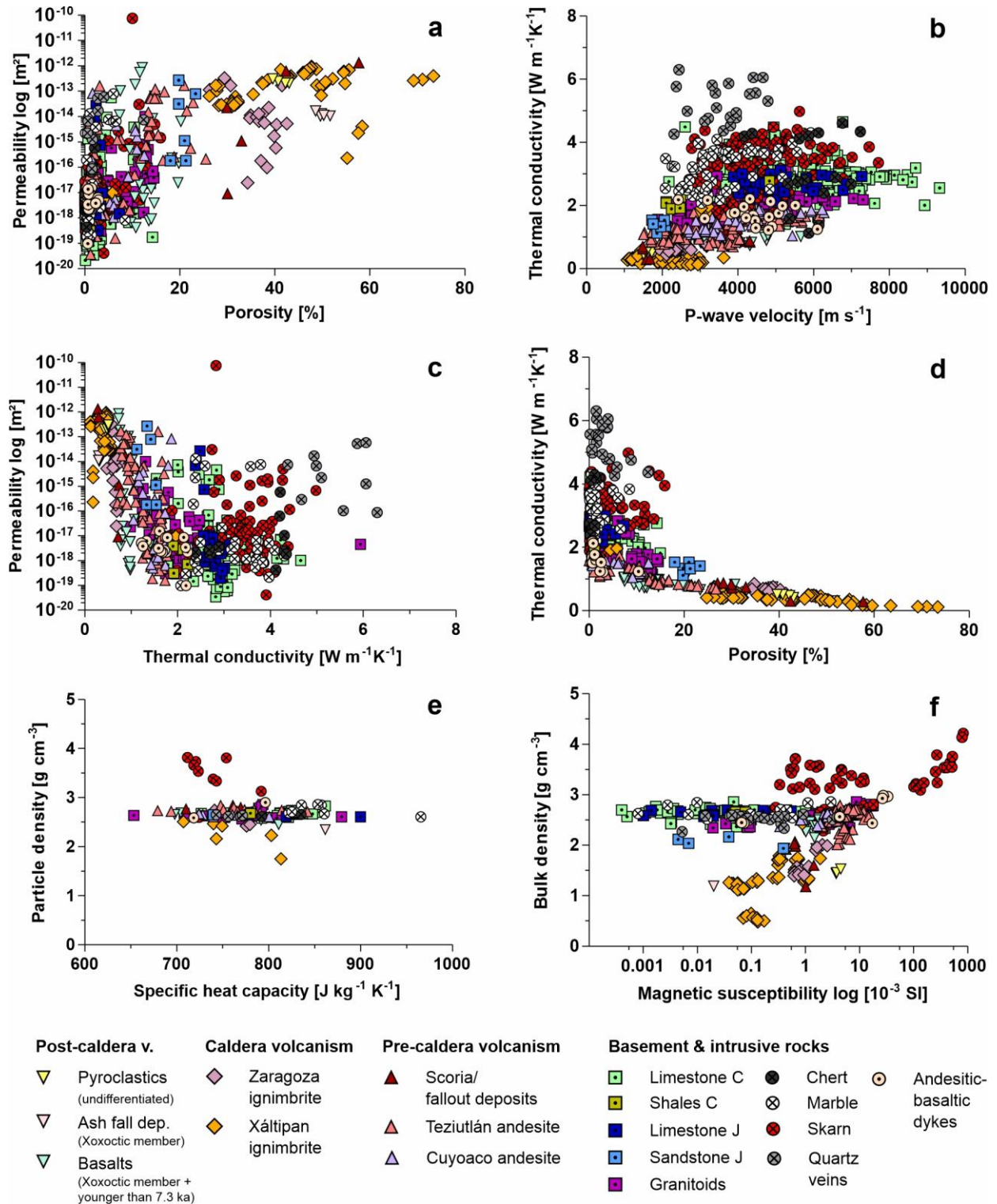
Figure 29: Scatter plots of selected rock properties analyzed under dry conditions of the outcrop samples with respect to their lithostratigraphic units.
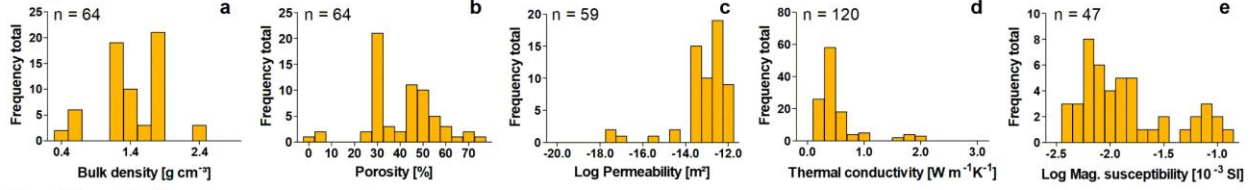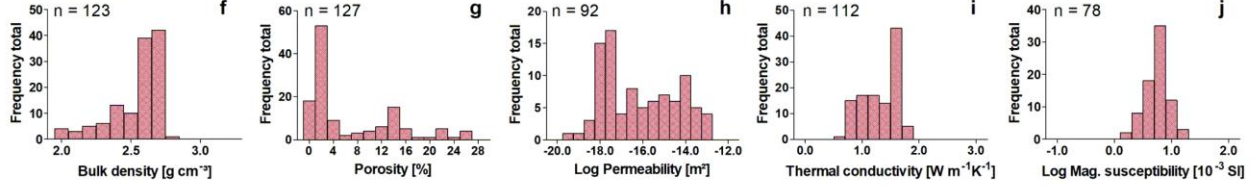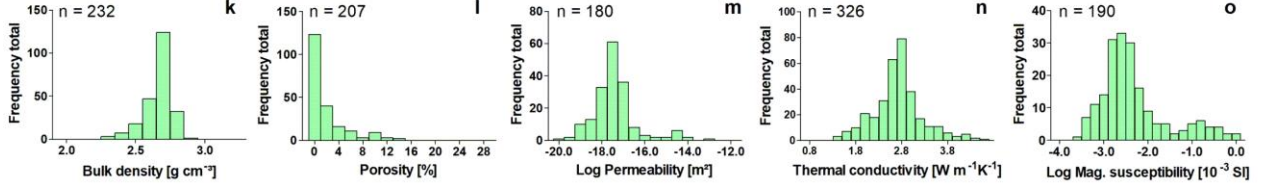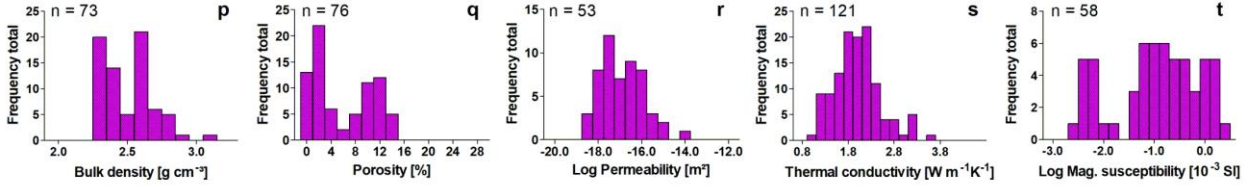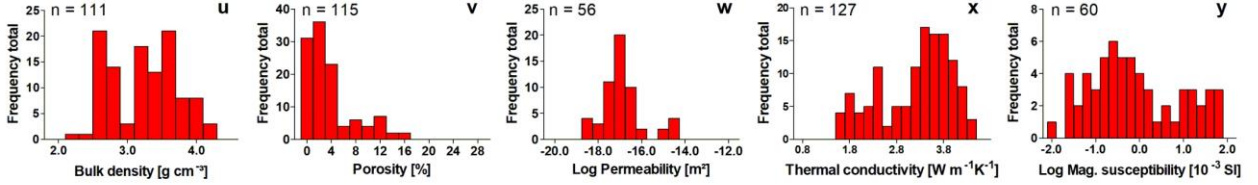
Figure 30: Histograms of selected units for bulk density, porosity, permeability, thermal conductivity and magnetic susceptibility. N = number of analyzed plugs. (a–e) Xáltipan ignimbrite, (f–j) Teziutlán andesite unit, (k–o) Cretaceous limestone, (p–t) granitoids, and (u–y) skarns.
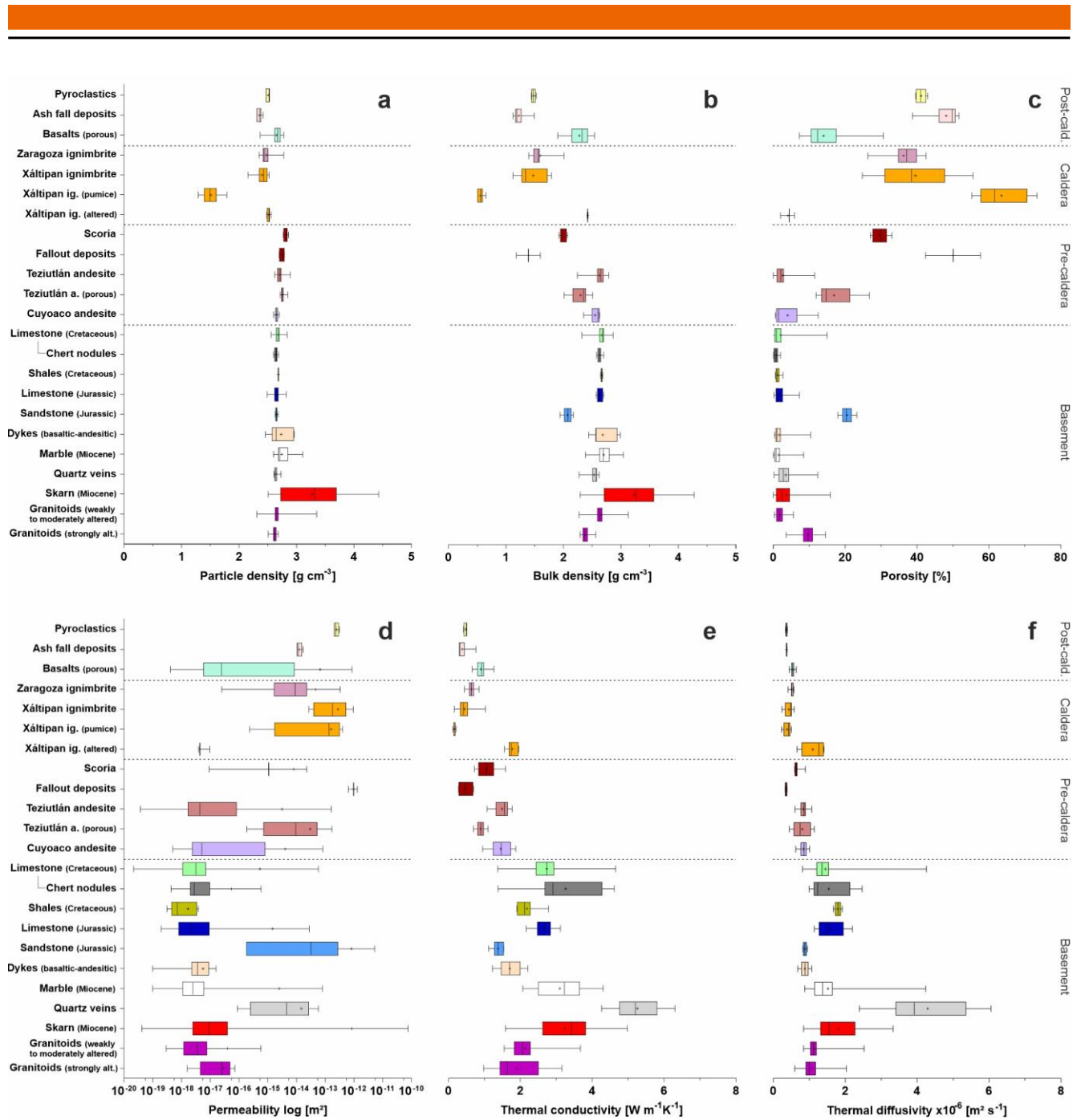
Figure 31: Box plots of petrophysical (a and b), hydraulic (c and d) and thermal properties (e and f) of the outcrop samples analyzed under dry conditions.
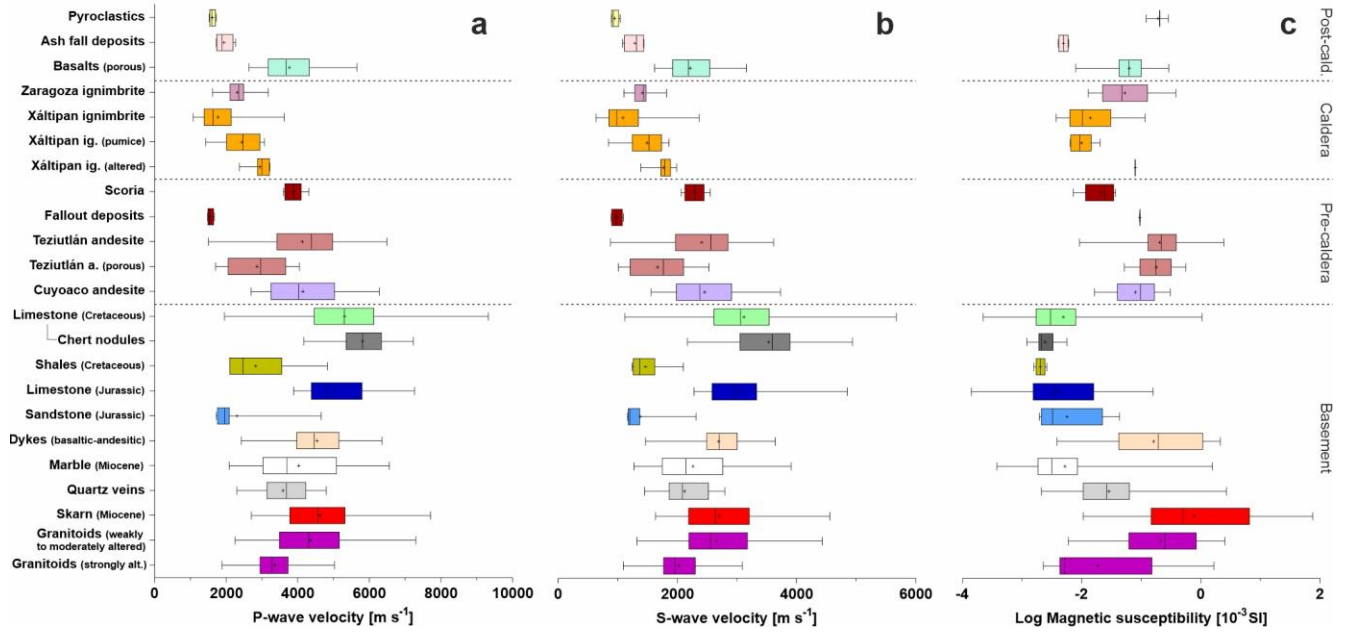
Figure 32: Ultrasonic wave velocities (a and b) and magnetic susceptibility (c) of the outcrop samples analyzed under dry conditions.

Except for the pumice fallout deposits and skarns, particle density is relatively constant throughout the data set and ranges between 2.64 and 2.80 g cm^{-3} (Figs. 29e, 31a). Bulk density, porosity and permeability are highly variable ranging from 0.48 to 4.27 g cm^{-3}, from < 1 to 73% and from 10^{-20} to 10^{-10} m^2 (Figs. 29, 30, 31), respectively. Matrix porosity and bulk density are negatively correlated, while porosity and permeability show only a weak correlation (Fig. 29a). Matrix porosity of the units related to the pre-volcanic basement is generally lower than 5%, while only the Jurassic sandstones exhibit porosities of about 21%. Higher porosities observed on the limestones and metamorphic rocks are mainly caused by fractures and microfractures and their associated mineralization products (e.g., quartz and calcite fillings), which leads to a right skewed distribution, as is the case for the Cretaceous limestones (Fig. 30l) and skarns (Fig. 30v). Likewise, fractures increase the in general low matrix permeabilities (median: 10^{-17} to 10^{-18} m^2) about several orders of magnitudes (up to 10^{-10} m^2 for skarns). With respect to matrix porosity and permeability, the volcanic rocks can be grouped into: (1) low-porous samples (< 5%) with predominantly fracture controlled permeabilities (e.g., Cuyoaco andesite); (2) samples with intermediate porosity (~ 10–16%) and low to high permeability due to vesicular pores and occasionally fractures (e.g., Teziutlán andesite porous); and (3) samples with high porosities (> 20%) and permeabilities that are predominantly pore controlled (> 10^{-15} m^2; ignimbrites, ash fall and pumice fallout deposits). Some units reveal distinct bimodal or multimodal distributions for bulk density, porosity or permeability (Fig. 30). In order to provide representative average values for each unit with respect to the scale of the 3D model, further subunits were defined (Figs. 31 and 32). For example, the properties of the Xáltipan ignimbrite were subdivided into Xáltipan ignimbrite (unwelded–partially welded), Xáltipan ignimbrite (pumice) and Xáltipan ignimbrite (altered and welded).

Thermal conductivity and thermal diffusivity vary from 0.17 ± 0.03 (Xáltipan ignimbrite pumice) to 5.25 ± 0.61 W m^{-1} K^{-1} (quartz veins) and from 0.37 ± 0.02 (pyroclastics) to 4.30 ± 1.08·10^{-6} m^2 s^{-1} (quartz veins), respectively. Thermal conductivity and thermal diffusivity of the volcanic rocks show a strong positive correlation with matrix porosity (Fig. 29d) and to a lesser extend with P-wave (Fig. 29b) and S-wave velocity. Furthermore, both parameters decrease with decreasing bulk density and increasing permeability (Fig. 29c). In contrast, the units belonging to the pre-volcanic basement show a higher scattering while correlating thermal conductivity and diffusivity with porosity, permeability or P-wave

velocity. However, rock type-specific clusters are identifiable. Furthermore, Figs. 30 and 31 imply that besides porosity, mineral composition and to a lesser extent microfractures play an important role. Thermal conductivity analyzed under saturated conditions increased for all rock types; up to 0.75 W m^{-1} K^{-1} for porous samples like the Xáltipan ignimbrite (Table A2). Thermal diffusivity, however, changes for each unit differently under saturated conditions. For marbles, saturated thermal diffusivity is almost twice as high compared to dry conditions, while it shows reduced values for the intensively fractured quartz veins (Table A2).

The average specific heat capacity shows only a small variation within the data set ranging from 707 J kg^{-1} K^{-1} (Xáltipan ignimbrite altered) to 833 J kg^{-1} K^{-1} (pyroclastics, Table A4). Thus, volumetric heat capacity follows the same trends as described for bulk density.

The results of the ultrasonic wave measurements reveal a wide parameter range for individual units. Thereby, the units with high porosities like ash fall deposits or samples with foliation like shales comprise lower P-wave velocities and S-wave velocities in the range of ~ 1500 to 3000 m s^{-1} and ~ 1000 to 1800 m s^{-1}, respectively (Figs. 29 and 32). The basaltic to andesitic lavas, intrusive and metamorphic rocks show intermediate values (P-wave: 2000–6000 m s^{-1}; S-wave: 1000–5500 m s^{-1}), while the Cretaceous limestones exhibit the highest variability with values of up to 9300 m s^{-1} for P-wave velocity (Fig. 32). The correlation of the sonic wave velocities with porosity and thermal conductivity shows rock type-specific clusters, but overall, only a weak correlation (Fig. 29). Furthermore, the correlation with permeability shows no trend at all. P-wave and S-wave velocity analyzed under saturated conditions is significantly higher and increase up to 45% (pyroclastics, Table A3).

Magnetic susceptibility ranges from −0.12·10^{-3} SI (Cretaceous limestones) to 818.5·10^{-3} SI (skarns, Figs. 29, 30, 32) throughout the data set. Contrary to the parameters described above, magnetic susceptibility is not affected by matrix porosity and strongly depends on the mineralogical composition of the samples and their magnetic behavior. The correlation with bulk density reveals an almost linear trend for the sedimentary and metamorphic rocks, while the volcanic units show an exponential trend (Fig. 29f, negative values are not presented in this graph). As common for sedimentary rocks, the limestones, shales, marbles, but also the Jurassic sandstones are characterized by a diamagnetic to paramagnetic behavior, thus, showing slightly negative to slightly positive magnetic susceptibilities (10^{-5} to 10^{-4} SI). The slightly higher values and the resulting bimodal distribution observed on the Cretaceous limestones can be attributed to fracture fillings in samples collected in close proximity to dykes (Fig. 30o). The basaltic to andesitic lavas exhibit magnetic susceptibilities of about one to two orders of magnitudes higher compared to the sedimentary rocks, while the pyroclastic rocks show a very variable magnetic behavior featuring slightly negative magnetic susceptibilities to positive values in the order of magnitude of 10^{-3} SI. Hydrothermal alteration observed on the intrusive rocks significantly reduces the magnetic susceptibility from ~ 5.2 to 0.036 10^{-3} SI resulting in a bimodal distribution (Fig. 30t). Magnetic susceptibility of the skarn samples ranges about four orders of magnitude. Thereby, the skarns that are rich in calcite or garnet show slightly positive magnetic susceptibilities (10^{-4} SI), while skarns with magnetite reveal the highest values (10^{-1} SI, Figs. 30y and 32).

A principal component analysis (PCA) was applied to assess the differences between each unit and subunit regarding their petrophysical characteristics (Fig. 33). Thereby, PCA in total covered 65.66% of the overall variation in the dataset, while factor F1 contributed with 52.34% to the separation of the units and subunits, whereas factor F2 accounted for 13.32%. Overall, ~ 4/5 of the displayed variation among the units and subunits can be attributed to factor F1, whereas the remaining ~ 1/5 can be attributed to factor F2 (Fig. 33). The variables (in this case the rock parameters) porosity, specific heat capacity, and thermal conductivity predominantly contributed towards factor F1. In contrast, permeability, magnetic susceptibility, and particle density mostly contributed towards factor F2. The impact of the variable's bulk density, thermal diffusivity, and the sonic wave velocities is in large parts observable on axis F1, but to a lesser extent also noticeable on axis F2. The distance of the variables from the origin of the

plot indicates their impact on the overall variance. Thus, particle density, magnetic susceptibility, permeability had the highest variances, whereas specific heat capacity clearly had the lowest variance (Fig. 33a). On one hand, the parameters magnetic susceptibility and particle density, P-wave and S-wave velocity as well as porosity and specific heat capacity each showed a strong correlation. On the other hand, porosity and specific heat capacity are negatively correlated with thermal conductivity, thermal diffusivity, and the sonic wave velocities as was previously observed in the cross-plots (cf. Figure 29). In addition, it is important to note, that permeability, magnetic susceptibility, and particle density were mostly indifferent to the remaining seven parameters.
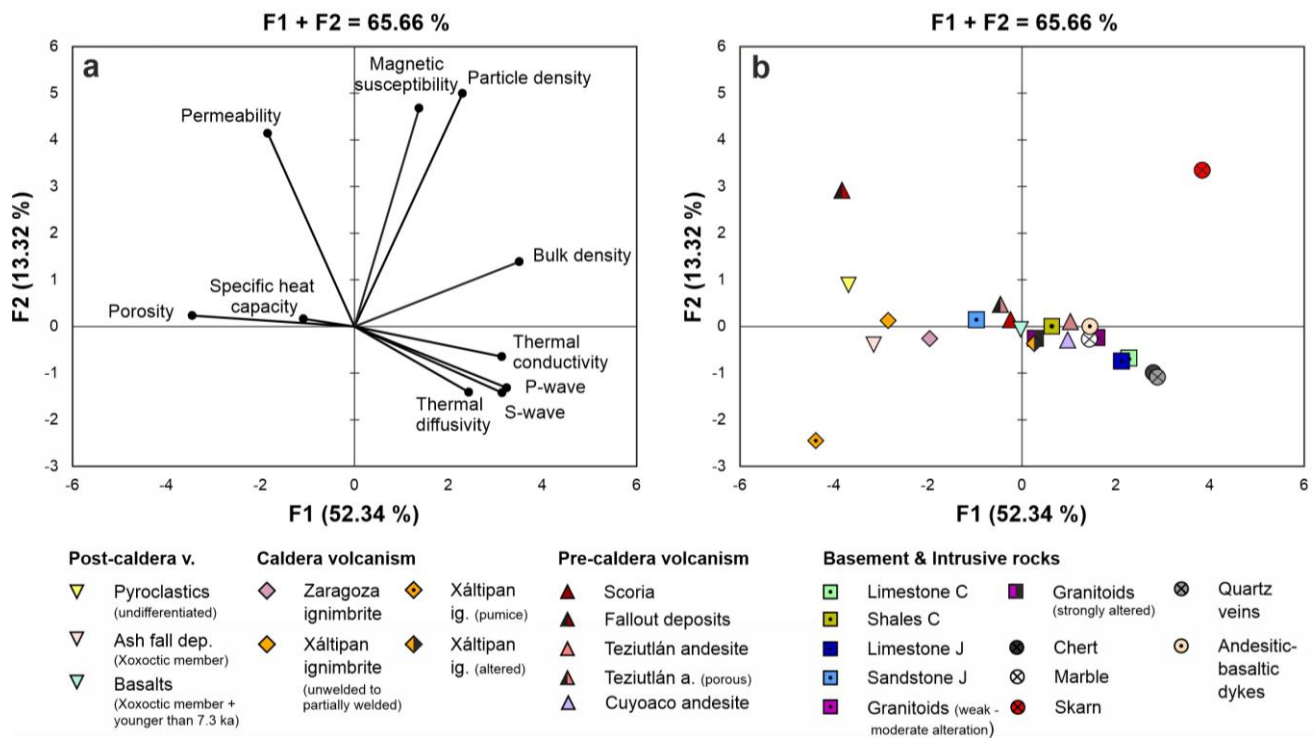
Figure 33: Principal component analysis applied to the magnetic susceptibility, sonic wave velocities as well as petrophysical, and thermophysical properties of the investigated lithostratigraphic units and subunits of the LHVC. (a) Represents the contribution of each parameter to the overall separation between the units and subunits as shown by factors F1 and F2. Each data point in (b) represents arithmetic means of all analyzed plugs for the respective unit or subunits.

Based on the PCA, the units and subunits can be separated into three groups, namely the highly porous pyroclastic rocks like the Xáltipan and Zaragoza ignimbrites, the major cluster of rocks comprising, e.g., the Jurassic sandstones and granitoids (F1: − 2 to 2 with decreasing porosity and increasing thermal conductivity and sonic wave velocities), and metamorphic rocks like quartz and skarn (Fig. 33b), which exhibit high thermal conductivities or magnetic susceptibilities. Figure 33b shows that differences within a lithostratigraphic unit are in some cases higher than those between different units, as is the case for the Xáltipan ignimbrite or Teziutlán andesite.

4.5. Discussion

4.5.1. Petrophysical Characterization of the Los Humeros Geothermal Field

The investigation of outcrop analogues revealed the complexity and high geological variability of the key formations in the study area that are relevant for modeling the Los Humeros geothermal field. The composition, lateral extension and distribution of the volcanic sequences are very variable, particularly of the cap rock and post-caldera group, but also the pre-volcanic basement showed a high geological heterogeneity consisting of several different rock types like limestones, shales, sandstones, mafic dykes as well as marble, quartz and skarn that are associated with intrusive bodies.

The high geological variability of the different units is also depicted in the results of the petrophysical measurements. The youngest volcanic sequences and the upper sections of the cap rock consist of alternating pyroclastic deposits and basaltic to rhyodacitic lavas showing contrasting physiochemical characteristics. Thereby, the ash fall deposits and ignimbrites can be characterized as highly porous ($> 35\%$) and permeable with a very low thermal conductivity (dry conditions: ≤ 0.5 W m^{-1} K^{-1}) and diffusivity ($\leq 1 \cdot 10^{-6}$ m^2 s^{-1}), but high heat capacity (> 760–880 J kg^{-1} K^{-1}). Due to their weak mechanical strength and high compressibility (Table A4), they are very sensitive to pressure changes with increasing depth.

The post-caldera lavas, however, feature very low to intermediate porosities (< 5–15%) and matrix permeabilities ($< 10^{-16}$–10^{-14} m^2). Thermal conductivity and diffusivity are also very low to low (< 1.5 W m^{-1} K^{-1} and $\leq 1 \cdot 10^{-6}$ m^2 s^{-1}, respectively), but bulk density and sonic wave velocities are significantly higher compared to the pyroclastic rocks.

The Xáltipan ignimbrite represents the thickest section of the cap rock and in contrast to the aforementioned units has a much larger lateral extension (~ 50 km in both directions from the Los Humeros caldera). From a petrophysical perspective, this unit shows the highest variability and widest parameter range and can be grouped into a non-welded to partially welded facies, a highly welded facies and pumice fall outs. The samples collected in this study predominantly represent the non-welded to partially welded facies and pumice fall outs that show high to very high porosities (> 35–$> 60\%$) and high permeabilities (10^{-13} m^2). With only one sample location, the welded facies are somehow underrepresented, due to the limited number of outcrops in the sampling area. Furthermore, a revised petrographic description and map of the Xáltipan ignimbrite was just recently published (Cavazos-Álavarez et al., 2019, 2020) and the extension of this unit was significantly smaller in previous studies (Ferriz and Mahood, 1984; Willcox, 2011; both do not include the welded facies). The welded and hydrothermally altered samples collected in this study are characterized by a very low matrix porosity ($\sim 4\%$) and permeability ($6 \cdot 10^{-18}$ m^2) as well as intermediate thermal properties (1.8 W m^{-1} K^{-1} and $1.4 \cdot 10^{-6}$ m^2 s^{-1}). According to Cavazos-Álavarez et al. (2020) the transition from non-welded over partially welded to highly welded is gradual from top to base and matrix porosity and permeability range from 52 to 4% and $2 \cdot 10^{-12}$ to $2 \cdot 10^{-18}$ m^2 (n = 9), respectively, which is well in line with the results presented here. In previous conceptual geothermal models, the Xáltipan ignimbrite was described as a texturally homogenous and low permeable unit with a uniform lateral extension that act as an aquitard in the geothermal system (Cedillo, 1999, 2000). However, the recent petrographic and petrophysical investigations identified distinct lateral and vertical heterogeneities (this study and Cavazos-Álavarez et al., 2020).

The lavas belonging to the pre-caldera group feature properties in a similar range than the lavas of the post-caldera group. Thereby, the laterally and vertically most extensive and thus most important unit is the Teziutlán andesite, which hosts the currently exploited geothermal reservoir in the Los Humeros geothermal field. Regarding its spatial extension, the Teziutlán andesites predominantly consist of fractured and massive low porous and low permeable lavas and to a lesser extent of vesicular lavas. Thereby, the ratio of massive versus porous lavas is similar than observed in the geothermal reservoir

(Lorenzo-Pulido et al., 2008; Deb et al., 2019d) suggesting that fluid flow in the pre-caldera group is predominantly fracture controlled.

Except for the Jurassic sandstones, the investigated units belonging to the basement are characterized by a very low matrix porosity (< 4%) and permeability (10^{-18} m^2). Fractures are abundant and higher porosities observed for example in limestones are associated with fractures and fracture filling minerals. The weak correlation between matrix porosity and permeability indicates that fluid flow is predominantly fault controlled in the study area, which has been confirmed by Lelli et al. (2020). Likewise, hydrothermal alteration observed in outcrops is predominantly restricted to fractures and fault zones (Weydt et al., 2021a). Alteration observed in granitic samples increased matrix porosity and permeability, but reduced the thermal properties, sonic wave velocities and magnetic susceptibility. Thermal conductivity and thermal diffusivity of the basement rocks can be classified as intermediate to high and are significantly higher than observed for the overlying volcanic sequences, while the results for specific heat capacity show a similar range. However, limestones and marbles make up the largest proportion of the basement and revealed significantly higher specific heat capacities compared to the magmatic and metamorphic rocks. Likewise, the limestones show the highest sonic wave velocities. The wide parameter range observed on the sonic wave velocities might be the result of mineralogical differences between the outcrops, the abundance of microfractures and the sample size. In general, small samples (30 mm length) contain less microfractures and thus, tend to have higher sonic velocities than larger ones (125 mm length). However, more detailed investigations would be required to provide a final conclusion. Figures 31, 32, 33 show that the low-porous andesites, carbonates and intrusive rocks feature bulk densities, porosities, permeabilities and P-wave velocities in a similar range, making the interpretation of geophysical surveys at greater depth increasingly difficult. However, the results of the magnetic susceptibility measurements are highly variable throughout the dataset showing formation-related trends, which might be helpful to identify skarn bodies and intrusions in the basement as well as alteration zones or highly porous layers in the volcanic successions. Magnetic susceptibility measurements are very sensitive to mineralogical changes even on a cm-scale and thus, have been frequently used in mapping, mineral exploration (Hrouda et al., 2009; Baroomand et al., 2015), to solve geotechnical problems (von Dobeneck et al., 2021) or to investigate hydrothermal alteration in geothermal reservoirs (Oliva-Urcia et al., 2011).

The comparison with literature data (Table 5) underlines the importance of a detailed petrophysical characterization for each case study in order to avoid under- or overestimation of thermal, storage and fluid flow properties or mechanical behavior.

Table 5: Petrophysical data retrieved from literature - 1 = Mielke et al. (2015), 2 = Lenhardt and Götz (2015), 3 = Pola et al. (2016), 4 = Mielke et al. (2017), 5 = Navelot et al. (2018), 6 = Eshagi et al. (2019), 7 = Heap et al. (2020b), 8 = Weinert et al. (2021)

Rock type	ρ_B [g cm^{-3}]	ϕ [%]	K [m^2]	λ dry [W m^{-1} K^{-1}]	α dry [10^{-6} m^2 s^{-1}]	Ref.
Ash tuff	1.57 (125)	40.56 (125)	3E-14 (125)	0.79 (125)		1
Scoria, pumice and ashes	1.52 (20)	34.24 (16)	8E-13 (10)	0.54 (25)		5
Tuff, non-welded		> 36	5.1E-15 (6)	0.5 (6)		2
Tuff, incipiently welded		30-36	6.4E-14 (17)	0.6 (17)		2
Tuff, partially welded		2-30	2.2E-14 (33)	0.9 (33)		2
Tuff, densely welded		< 2	3.8E-16 (13)	1.7 (13)		2
Ignimbirte, welded (lithic and pumice lithofacies)	1.59 ± 0.046	34				3
Ignimbirte, welded (lithic and pumice stratified lithofacies)	1.44 ± 0.056	31				3
Volcaniclastic rocks	2.86 ± 0.15 (668)					6
Andesite	2.64 (210)	4 (31)	6E-18 (46)	1.68 (50)		5
Andesite	2.37 (24)	9.52 (24)	4E-17 (24)	1.32 (24)		1
Andesite	2.27 ± 0.37 (57)	17.3 ± 12.7 (57)		1.08 ± 0.30 (57)	0.61 ± 0.10 (57)	7
Basalt		11.8 ± 9.6 (15)		1.7 ± 0.47 (75)		4
Intermediate extrusive rocks	2.78 ± 0.10 (280)					6
Mafic intrusive rocks	2.89 ± 0.12 (1384)					6
Rhyolite				2.84 ± 0.16 (63)		4
Sedimentary rocks	2.75 ± 0.10 (1384)					6
Medium sandstone		15 ± 4.5 (219)		2.5 ± 0.37 (349)		4
Limestone		3 ± 1.3 (45)		2.45 ± 0.22 (108)		4
Dolomite		2.4 ± 1.6 (22)		2.68 ± 0.1 (24)		4
Marble				2.84 ± 0.17 (38)		4
Metamorphic rocks	2.78 ± 0.13 (1825)					6
Granite	2.62 ± 0.08 (238)	1.93 ± 1.59 (233)		2.74 ± 0.42 (293)	1.44 ± 0.28 (292)	8
Granite	2.66 ± 0.07 (666)					6
Granodiorite	2.69 ± 0.07 (296)	1.82 ± 1.88 (262)		2.48 ± 0.36 (394)	1.22 ± 0.19 (386)	8

arithmetic mean values in normal font, ± = standard deviation, () = number of analyzed samples, ρ_B = bulk density, ϕ = porosity, K = permeability, λ = thermal conductivity, α = thermal diffusivity

Table 5 continuation: Petrophysical data retrieved from literature - 1 = Mielke et al. (2015), 2 = Lenhardt and Götz (2015), 3 = Pola et al. (2016), 4 = Mielke et al. (2017), 5 = Navelot et al. (2018), 6 = Eshagi et al. (2019), 7 = Heap et al. (2020b), 8 = Weinert et al. (2021)

Rock type	cp [J kg^{-1} K^{-1}]	V$_P$ dry [m s^{-1}]	V$_S$ dry [m s^{-1}]	X [10^{-3} SI]	Ref.
Ash tuff	630 (125)				1
Scoria, pumice and ashes	880 (15)	1642 (17)		8.84 (14)	5
Tuff, non-welded					2
Tuff, incipiently welded					2
Tuff, partially welded					2
Tuff, densely welded					2
Ignimbirte, welded (lithic and pumice lithofacies)		1490 ± 70	790 ± 60		3
Ignimbirte, welded (lithic and pumice stratified lithofacies)		2150 ± 130	1250 ± 150		3
Volcaniclastic rocks				0.34 ± 0.10 (16)	6
Andesite	750 (28)	4589 (34)		13.92 (41)	5
Andesite	740 (24)				1
Andesite	783 ± 79 (57)				7
Basalt		4730 ± 1160 (75)			4
Intermediate extrusive rocks				1.74 ± 7.13 (1351)	6
Mafic intrusive rocks				8.51 ± 25.7 (2747)	6
Rhyolite		4220 ± 470 (63)			4
Sedimentary rocks				1.59 ± 7.52 (1408)	6
Medium sandstone		2930 ± 570 (349)			4
Limestone		5030 ± 730 (108)			4
Dolomite		5140 ± 1120 (24)			4
Marble		3180 ± 0.99 (38)			4
Metamorphic rocks				3.44 ± 13.48 (1111)	6
Granite		4711 ± 1116 (225)	2623 ± 679 (225)		8
Granite				1.91 ± 3.52 (344)	6
Granodiorite		4489 ± 975 (284)	2541 ± 561 (284)		8

arithmetic mean values in normal font, ± = standard deviation, () = number of analyzed samples, V$_P$ = P-wave velocity, V$_S$ = S-wave velocity, cp = specific heat capacity, X = magnetic susceptibility

Particularly, the petrophysical properties of volcanic rocks are highly variable and are mostly controlled by matrix porosity and secondly by the occurrence of microfractures (Mielke et al., 2015; Navelot et al., 2018; Heap et al., 2020b). Notable are also the drastic decrease of matrix porosity with increased welding observed in ignimbrites from Central Mexico (Lenhardt and Götz, 2015). However, the decrease of matrix permeability with increasing welding observed on samples of the Xáltipan ignimbrite is even two orders of magnitude higher. Similar to observations presented in Heap and Kennedy (2016), the porosity–permeability relationships of the volcanic rocks cannot be described with one linear trend. This becomes important when upscaling the parameters to reservoir scale. For example, Farquharson et al.

(2015) defined a critical porosity threshold beneath which the fluid flow is predominantly restricted to small microcracks. With higher vesicular porosity (> 14–16%) the fluid flow is mainly pore controlled. In general, the investigated rock types of the pre-volcanic basement exhibit data for most parameters in a similar range compared with literature (Table 5). However, especially mineralogical differences can impact bulk density and thermal conductivity (Weinert et al., 2021; Weydt et al., 2018a). For example, thermal conductivity of marble, limestone and dolomite presented in Mielke et al. (2017) are significantly lower compared to the results in this study or Weydt et al. (2018a). While the assumption of rock properties based on literature data might be sufficient for preliminary assessments and numerical models, it cannot account for site-specific depositional environments in sedimentary rocks (Sass and Götz, 2012; Aretz et al., 2016), diagenesis (Homuth et al., 2015; Weydt et al., 2018a), hydrothermal and metamorphic overprints (Mielke et al., 2016; Heap et al., 2020a) and their impact on the rock properties.

The here presented rock properties are well in line with data obtained on the few available wellbore core samples of the Los Humeros geothermal field (Weydt et al., 2021a). For example, particle density, bulk density, matrix porosity as well as magnetic susceptibility of the marble wellbore core samples (n = 3) representing the upper section of the carbonatic basement in the geothermal reservoir are in the same range compared to the marbles retrieved from outcrops in Las Minas. However, the wellbore core samples exhibit increased matrix permeabilities (10^{-14} m^2) and reduced sonic wave velocities (P-wave velocity = ~ 2600 m s^{-1}, S-wave velocity = ~ 1500 m s^{-1}) due to numerous fractures. Likewise, wellbore core samples retrieved from the andesitic units were affected by fracturing, brecciation and hydrothermal alteration of different intensities resulting in increased hydraulic properties, but reduced bulk densities and sonic wave velocities. Thereby, hydrothermal alteration is commonly restricted to fractures and the alteration intensity often varies on the cm-scale.

The majority of the wellbore core samples were retrieved in close proximity to fault zones. Depending on the scale, accuracy and future application, the observed differences in the physiochemical behavior of the reservoir formations need to be considered during parametrization of a reservoir model. For local, small-scaled reservoir models (e.g., drill path or fault zones) with a high resolution (grid size) the usage of the wellbore core data would be favorable, whereas for large-scaled regional models with a large grid size the usage of this data would significantly overestimate, e.g., matrix porosity and permeability and probably lead to false interpretations and numerical calculations.

4.5.2. Variability and Probability Density

Deterministic approaches in numerical 3D models are not suitable to capture the intrinsic variability of a rock mass since they commonly assign a single mean value only (Heidarzadeh, 2021). In order to deal with the heterogenous nature of rock formations, probability methods are common tools to express and address their variability and uncertainty. Probability density functions (pdfs) are commonly used in stochastic assessments and determined using the mean value and standard deviation of a parameter. Thereby, pdfs represent the likeliness of each parameter value in the unit and provide a quantitative description of the state of knowledge and uncertainty of our data (the higher and narrower the peaks, the higher the probability; Takahashi, 2000). With the help of the previously determined relationships between rock properties pdfs are often used to model other properties and to quantify their uncertainty (Scott et al., 2019).

In order to directly compare the variability and probability distribution of the different lithostratigraphic units, pdfs were calculated (Fig. 34). Since it was not possible to investigate each unit to the same extent due to the complex geological setting and the resulting sample availability, Monte Carlo simulations of the parameters with 1000 random iterations were run using Microsoft Excel 2019. Pdfs were calculated by fitting a normal or beta distribution depending on the outcome of normality and lognormality tests. The majority of the investigated parameters can be depicted with a normal distribution. In

a few cases, the data showed a non-normal distribution, e.g., for matrix porosity of the Cretaceous limestones, skarns or granitoids. In these cases, a beta distribution represented the best fit. Figure 34 shows that the probability not only differs between the different units, but also between the parameters within a unit. For example, the pdfs of bulk density and porosity of the Cretaceous limestones show a high and narrow peak (Fig. 34a and b) and thus, high probability. However, the pdfs of the same unit for thermal conductivity and P-wave velocity show a much broader shape compared to the remaining units suggesting a much higher uncertainty. Likewise, a high variability and uncertainty needs to be considered for the porosity and bulk density of the Xáltipan ignimbrite in future modeling applications. In some cases, the pdfs of different units overlap, e.g., the pdfs of bulk density or P-wave velocity of the Teziutlán andesites and granitoids.
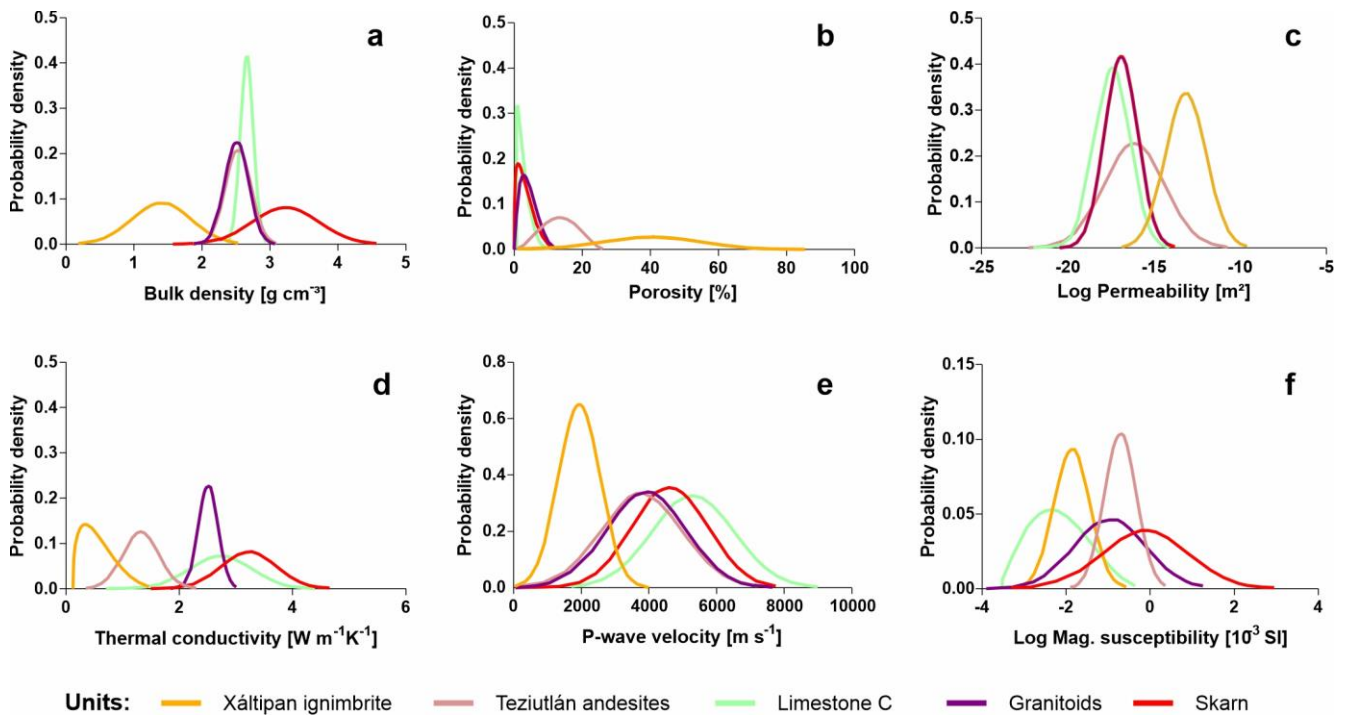
Figure 34: Probability density functions of selected units (cf. Figure 30) for bulk density (a), porosity (b), permeability (c), thermal conductivity (d), P-wave velocity (e) and magnetic susceptibility (f).

The normal distribution is commonly chosen for simplification reasons or in cases with limited information (Adams, 2005; Takahashi, 2000). However, the results indicate that the data distribution cannot be generalized for a parameter or a reservoir unit and should be tested prior modeling whenever frequency distributions of input parameters are available to avoid parameter overestimations or underestimations. Likewise, uncertainty should be addressed for each unit and parameter. Stochastic approaches are commonly used for geotechnical assessments (Sari, 2009; Contreras et al., 2018; Heidarzadeh et al., 2021), processing of geophysical data and modeling (Scott et al., 2019) to address the natural variability of the reservoir formations and geological features as well as to overcome the problem with limited available in situ data. However, it has to be emphasized that the pdfs are biased by the quality of input data. Although more advanced techniques like the Markov Chain Monte Carlo method or Bayesian approach (Contreras et al., 2018) try to overcome lacking information in the input data, the lithological heterogeneities need to be addressed properly during field work and laboratory analyses before modeling.

4.5.3. Prediction of Reservoir Properties

The petrophysical data presented in this study were determined under standardized laboratory conditions to ensure the reproducibility of the measurements and the comparability between the samples and different rock types. Consequently, the data do not reflect in situ conditions such as high fluid and reservoir temperatures, high overburden stress or fluid composition at reservoir depth. Hydraulic properties such as porosity and permeability are sensitive to pressure changes, particularly for soft volcanic rocks. They tend to decrease with increasing pressure at reservoir depth due to consolidation of the rock mass and by closing of fractures (Zimmermann et al., 1986; Jiang et al., 2010; Ashena et al., 2020). The decrease in porosity and the closure of fractures often results in increased bulk density, thermal conductivity, electric resistivity and sonic wave velocities (Clauser and Huenges, 1995; Schön, 2015). However, with increasing temperature thermal expansion of minerals can cause micro-fracturing, which increases matrix porosity and permeability, but might in turn reduce thermal conductivity, sonic wave velocities or rock strength (Heap et al., 2014a; Vinciguerra et al., 2005). Several physical models, empiric or semi-empiric equations have been developed in the past to predict reservoir conditions (Weydt et al., 2021a). To account for temperature- and pressure-dependent changes on the properties, the measured data were transferred to reservoir conditions using the temperature data of well H8 as an example of the central part of the Los Humeros geothermal field with temperatures of ~ 300 °C at 2 km depth. The thickness of the reservoir units was estimated based on lithostratigraphic well logs and their interpretation used in the preliminary 3D geological model of the Los Humeros geothermal field presented in Calcagno et al. (2020). In this paper, the authors defined four units for the regional 3D model and nine units for the local 3D model of the Los Humeros geothermal field (Table 6). Changes in porosity with reservoir depth were determined after Ashena et al. (2020) based on Athy's law (Athy, 1930) by calculating the rock compressibility for each individual unit:

$$\Phi = \Phi_0 e^{-cf \cdot z} \, , \tag{9}$$

where Φ_0 is the initial porosity at zero overburden pressure, cf is the formation compaction or compressibility calculated for each individual unit and z is the reservoir depth. Subsequently, changes in matrix permeability were calculated based on the changes in porosity after Wang et al. (2016) using the Carman–Kozeny equation as shown in Eq. 10:

$$K = K_{m0} \cdot \left(\frac{1-\Phi_0}{1-\Phi}\right)^3 \cdot \left(\frac{\Phi}{\Phi_0}\right)^3, \tag{10}$$

where K_{m0} is the initial matrix permeability at ambient pressure and temperature. To account for mineralogical changes with temperature, thermal expansion coefficients for the different rock types and their change with temperature were retrieved from Heard and Page (1982) and Konietzky and Wang (2019) and integrated into the porosity equation after Wang et al. (2016).

Available chemical data of reservoir fluids from previous studies (e.g., Tello, 2005; Bernard et al., 2011) indicated that total dissolved solid (TDS) contents are low at around 1 g kg^{-1} of solution on average and at about 4 g kg^{-1} at maximum. Given the low TDS contents of the majority of the reservoir fluids, it can be implied that their liquid phase properties will closely match those of pure water properties at given pressure and temperature conditions (IAPWS R15-11, 2011; IAPWS R6-95, 2016; Zarrouk and Watson, 2010; assuming that the fluid state is subcritical), which were used to account for saturated conditions at depth by applying the arithmetic-mean model. For example, bulk density of the reservoir formations was calculated as follows:

$$\rho B = \Phi \cdot \rho F + (1 - \Phi) \cdot \rho P \, , \tag{11}$$

with ρB = bulk density at reservoir depth, ρF = fluid density for the respective temperature and pressure conditions, ρP = particle density of the rock matrix, and Φ = porosity at reservoir depth. Then, the overburden pressure was obtained by simple gravitational modeling using the previously calculated in situ

bulk density and formation thickness multiplied by gravity acceleration. The effect of temperature on specific heat capacity was determined according to Vosteen and Schellschmidt (2003) who provide empirical temperature-correction functions for magmatic, metamorphic and sedimentary rocks. Likewise, thermal conductivity of the majority of rock types was corrected for reservoir temperature after Vosteen and Schellschmidt (2003). The exception forms the highly porous volcanic rocks, such as ignimbrites with very low thermal conductivities, which were corrected on the basis of laboratory experiments presented in Chen et al. (2021). Pressure corrections of the resulting thermal conductivities were applied after Abdulagatov et al. (2006) and Abdulagatova et al. (2009). To adapt thermal diffusivity to reservoir conditions, temperature-correction functions after Durham et al. (1987) for volcanic rocks and Vosteen and Schellschmidt (2003) for the remaining rock types were applied. Pressure has only a minor effect on thermal diffusivity of rocks (≤ 0.05–$0.1 \cdot 10^{-6}$ mm s^{-1} for a pressure change of 50 MPa in gabbros, granites and basalts; Durham et al., 1987) and laboratory experiments are scarce. Therefore, the influence of pressure on thermal diffusivity was neglected in this study. Temperature and pressure dependencies of P-wave and S-wave velocities were calculated after experimental data from Qi et al. (2020; carbonates), Vinciguerra et al. (2005, tuff), Hughes and Maurette (1957) and Birch (1961; magmatic and intrusive rocks). Additional information is presented in Appendix B.

Table 6: Rock properties transferred to reservoir conditions of the Los Humeros geothermal field

Lithology	Model unit*	M [m]	P [MPa]	T [°C]	φ [%]	K [m²]	ρB sat [g cm⁻³]	λ sat [W m⁻¹ K⁻¹]
Undefined pyroclastic deposits	U1	50	≤ 0.93	15 - 67	41.1 - 40.5	2.4E-13 - 2.2E-13	1.89	0.52 - 0.57
Rhyodacite, andesite, basalts	U2	200	0.93 - 5.56	67 - 179	15.9 - 15.6	1.2E-15 - 8.2E-16	2.37 - 2.36	0.93 - 0.97
Rhyodacite and Zaragoza ignimbrite	U3	150	5.56 - 8.85	179 - 210	21.0 - 20.7	2.8E-15 - 2.6E-15	2.24	0.99
Faby tuff and andesites	U4	100	8.85 - 11.04	210 - 240	20.7 - 20.5	2.6E-15 - 2.5E-15	2.24 - 2.23	0.99 - 0.97
Xáltipan ignimbrite	U5	450	11.04 - 20.48	240 - 255	36.4 - 15.5	4.2E-14 - 9.9E-15	1.75 - 2.14	0.60 - 1.27
Teziutlán andesites (30% porous and 70% nonporous lava)	U6	1150	20.48 - 49.63	255 - 310	6.81 - 6.68	7.1E-17 - 7.0E-17	2.58	1.37 - 1.33
Basement (until 3 km depth, 80% marble, 10% granites and 10% skarn)	U9	1000	49.63 - 73.58	310 - 340	1.80 - 1.81	6.41E-18 - 6.42E-18	2.72 - 2.71	2.36 - 2.38

* = classification after Calcagno et al. (2020), (weighted) arithmetic mean values in normal font, ρB = bulk density, φ = porosity, K = permeability, λ = thermal conductivity, sat = saturated, T = reservoir temperature range, P = calculated overburden pressure range, M = estimated average thickness of the unit

Table 6 continuation: Rock properties transferred to reservoir conditions of the Los Humeros geothermal field

Lithology	Model unit*	M [m]	P [MPa]	T [°C]	α sat [10^{-6} m² s^{-1}]	Cp sat [J kg^{-1} K^{-1}]	VHC sat [J m^3 K^{-1}]	V_P sat [m s^{-1}]	V_S sat [m s^{-1}]
Undefined pyroclastic deposits	U1	50	≤ 0.93	15 - 67	0.27 - 0.28	2245 - 2268	3028 - 3100	2667 - 2703	1070 - 1106
Rhyodacite, andesite, basalts	U2	200	0.93 - 5.56	67 - 179	0.50 - 0.42	1379 - 1471	2530 - 2674	5184 - 5649	3156 - 3621
Rhyodacite and Zaragoza ignimbrite	U3	150	5.56 - 8.85	179 - 210	0.59 - 0.57	1658 - 1689	2726 - 2742	4489 - 4528	2783 - 2822
Faby tuff and andesites	U4	100	8.85 - 11.04	210 - 240	0.57 - 0.55	1689 - 1736	2742 - 2764	4528 - 4512	2822 - 2806
Xáltipan ignimbrite	U5	450	11.04 - 20.48	240 - 255	0.41 - 0.72	2339 - 1569	2787 - 2387	2355 - 3330	1352 - 1966
Teziutlán andesites (30% porous and 70% nonporous lava)	U6	1150	20.48 - 49.63	255 - 310	0.56 - 0.52	1227 - 1318	2668 - 2758	6179 - 6406	4022 - 4248
Basement (until 3 km depth, 80% marble, 10% granites and 10% skarn)	U9	1000	49.63 - 73.58	310 - 340	1.03	1170 - 1214	2994 - 3038	7832 - 7948	4998 - 5114

* = classification after Calcagno et al. (2020), (weighted) arithmetic mean values in normal font, α = thermal diffusivity, V_P = P-wave velocity, V_S = S-wave velocity, cp = specific heat capacity, VHC = volumetric heat capacity, sat = saturated, T = reservoir temperature range, P = calculated overburden pressure range, M = estimated average thickness of the unit

The effect of pressure or temperature on selected hydraulic, thermal and dynamic mechanical properties is shown in Fig. 35. Matrix porosity decreases exponentially with increasing depth for the highly porous ignimbrites and fall out deposits, which also contain the highest calculated rock matrix compressibility (~ 10^{-4} PSI). Already at about 1000 m depth, the porosity of the Xáltipan ignimbrite pumice layers would be halved, while the porosity of the Zaragoza ignimbrite would be reduced by about 5% (Fig. 35a). The large changes in porosity of the ignimbrites and ash fall deposits is commonly the result of inelastic compaction due to cataclastic pore collapse, which can occur at very low threshold pressures (Heap et al., 2014b; Vinciguerra et al., 2006), and thus, affect the rock properties already at relatively shallow reservoir depth. Reported UCS values for the Xáltipan ignimbrite range between 2 and 6 MPa for pumice fallouts and ~ 10–45 MPa for the non-welded to partially welded facies (Weydt et al., 2021a). The porous Teziutlán andesite lavas, basalts and Jurassic sandstones show a steady, but small decrease in porosity with depth. In contrast, the porosity of the low-porous sedimentary, intrusive and metamorphic rocks remains almost constant. The comparatively small porosity reductions in the units with very low-to-intermediate porosity are predominantly caused by the closure of microfractures (elastic compaction; Zimmermann et al., 1986). As previously described, detailed investigations of the different lithofacies in the field in combination with laboratory experiments are necessary to accurately estimate matrix porosity and fluid properties at reservoir depth.
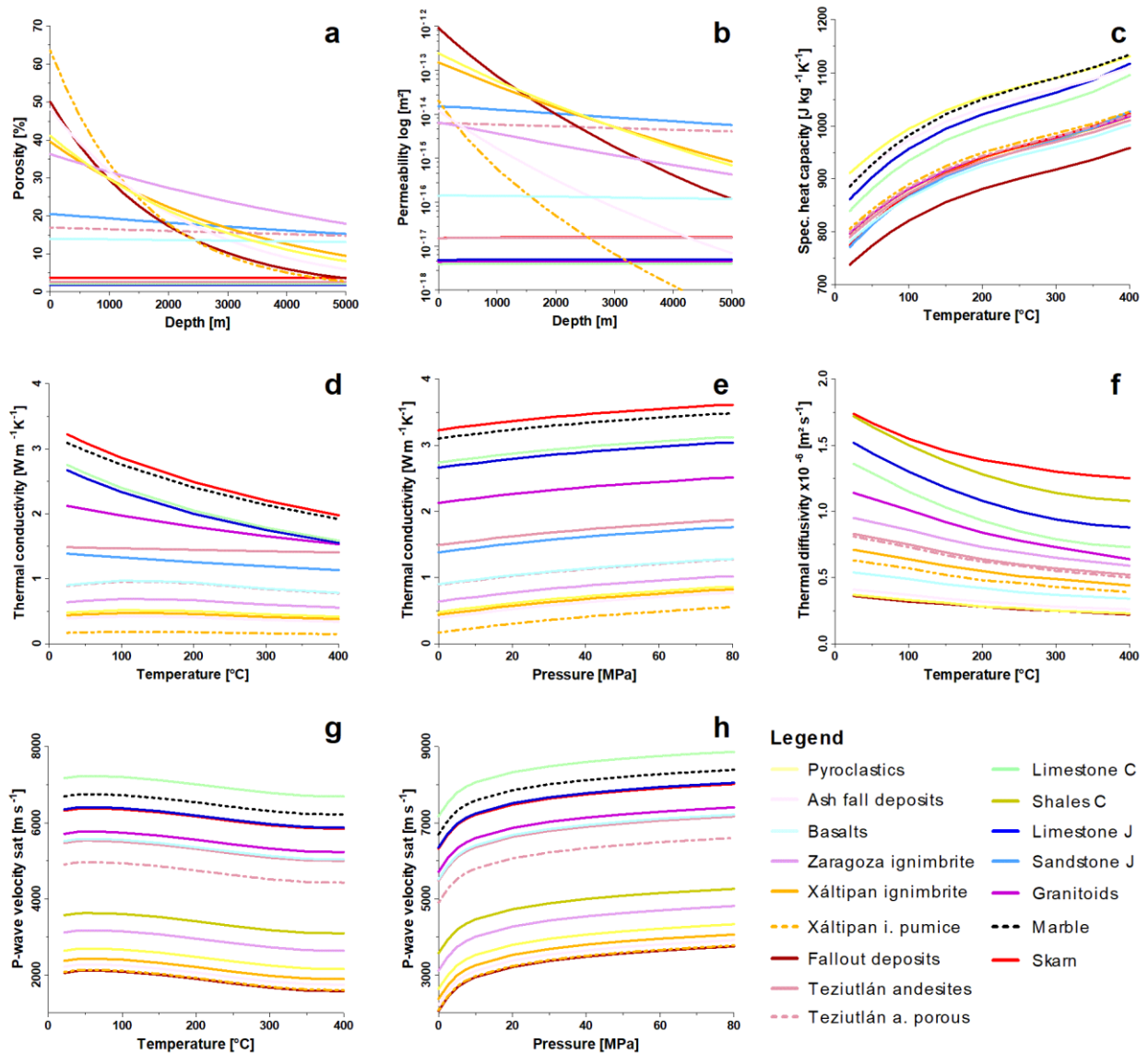
Figure 35: Depth correction of porosity (a) and matrix permeability (b), temperature correction of specific heat capacity, thermal conductivity, thermal diffusivity and P-wave velocity (c, d, f, g) as well as pressure correction of thermal conductivity and P-wave velocity in e and h.

Since the change in matrix permeability was calculated after Wang et al. (2016) using the results of the matrix porosity, the same trends can be observed (Fig. 35b). The influence of thermal expansion on matrix porosity and permeability is very small (predominantly < 1% until 350 °C) and thus, might be neglectable for the selected temperature and depth range.

Specific heat capacity significantly increases by about ~ 25–30% (Fig. 35c) with reservoir temperature based on the empirical equations presented in Vosteen and Schellschmidt (2003). Thermal conductivity and thermal diffusivity of the metamorphic, intrusive and carbonatic rocks decrease up to 45% (skarns, marble and limestones) until 400 °C. However, the increase in pressure, and thus the closure of fractures and the reduction in matrix porosity have the opposite effect on thermal conductivity. Pressure and temperature changes of the P-wave velocities determined after Qi et al. (2020) and Hughes and Maurette (1957) are presented in Fig. 35g and h. Thereby, the increasing effect of pressure on the sonic wave velocities predominates the decreasing effect of temperature and thus, the effect of thermal expansion and microcracking.

Table 6 comprises the rock properties at saturated conditions transferred to reservoir pressure and temperature (here ≤ 3 km depth) for the individual lithostratigraphic units which were classified into local model units after Calcagno et al. (2020). The determined overburden pressure reaches ~ 74 MPa at 3 km depth. The formation thickness represents the average thickness of the individual units within the geothermal reservoir based on lithostratigraphic well logs and their interpretation presented in Calcagno et al. (2020). However, the well logs do not always provide detailed thickness estimations for each lithology and rather provide classifications of lithostratigraphic groups that are composed of different rock types. Therefore, the assigned properties for the model units in part represent weighted averages reflecting the estimated contributions of the different rock types within each unit. For example, the alternating lavas and pyroclastic deposits of unit 2 (Table 6) were estimated containing 60% basaltic to andesitic lavas, 20% dacites to rhyolitic lavas and 20% tuff. Furthermore, the units 3 and 4 were estimated containing about 50% pyroclastic deposits and 50% lavas each and the pre-caldera andesitic lavas were estimated containing about 30% porous and 70% massive lavas based on the results of the only available sonic log (Lorenzo-Pulido et al., 2008; Deb et al., 2019d). For the parametrization of the Xáltipan ignimbrite, a gradual transition with reservoir depth from unwelded over partially welded to welded was assumed based on petrographic descriptions presented in Cavazos-Álavarez et al. (2020). The carbonatic basement predominantly consists of recrystallized limestones within the Los Humeros geothermal field and a percentage of 10% intrusive rocks and 10% skarns were assumed based on the outcrop investigations and preliminary results of the geophysical surveys. The results presented in Table 6 reveal a highly variable change of the average rock properties with increasing reservoir depth. Especially the thermal properties are very sensitive to changes in porosity, due to the different thermal properties of water compared to the rock matrix (Zarrouk and Watson, 2010) as well as the decreasing volume of fluid with decreasing porosity.

The effects of reservoir temperature and pressure are often only partially considered (Deb et al., 2019d) or completely neglected (Cornejo et al., 2020; Kruszewski et al., 2020; González-García et al., 2020) during reservoir modeling leading to oversimplified predictions of the reservoir behavior (Norden et al., 2020). For example, the application of correction functions for thermal conductivity without applying a pressure correction leads to significantly underestimated thermal conductivities (Norden et al., 2020). Commonly, the thermomechanical behavior of the reservoir formations and their complex interplay with fluid properties, stress, overburden pressure and reservoir temperature are commonly solved numerically. The usage of empirical and analytical equations already provides a good prediction of the rock properties at reservoir depth, particularly in cases without geophysical well log data. However, since they are commonly based on laboratory experiments performed on sample sets collected from different study areas, they are not able to represent the site-specific fracture pattern, microstructural variability, mineralogy, as well as hydrothermal, diagenetic or metamorphic overprints. Additionally, the majority of high T/P experiments presented in the literature focus on rock types with low to intermediate porosity (e.g., granites, limestones or sandstones). The response to pressure changes of high-porosity rocks can be however fundamentally different compared to low-porous rocks (inelastic vs. elastic compaction; Vinciguerra et al., 2006; Heap et al., 2014b). Up to now, high T/P laboratory tests considering pyroclastic rocks are scarce, particularly for thermal properties, and therefore their behavior under high T/P is not fully understood yet. Thus, for a more precise reservoir property prediction further high T/P experiments would be required for each target unit.

4.5.4. Data Application and Limitations with Respect to Modeling the Los Humeros Geothermal Field

In a previous attempt, a preliminary structural-geological model of Los Humeros was created (Calcagno et al., 2020) and used for simulating the initial state of the super-hot geothermal system (Deb et al., 2019d). Due to lack of data at this stage of the project, the classification of the model units was based on the local stratigraphy as presented in Fig. 26 and the parametrization was performed mainly using assumed average values for each unit. However, some of these model units comprise multiple different rock types, which leads to a wide parameter range and high uncertainty during modeling. Based on the presented findings, the following updates are suggested.

The pre-volcanic basement revealed the highest geological heterogeneity and thus, the highest parameter range, e.g., for thermal conductivity. The recharge and fluid flow of the Los Humeros geothermal field are controlled by fault zones and fractures in the carbonatic basement and subsequently in the andesitic reservoir (Lelli et al., 2020). Furthermore, the heat flow is controlled by shallow intrusions that are nested in the carbonates (Lucci et al., 2020) and potentially even in the upper section of the andesitic unit (Urbani et al., 2020). The intrusions in the carbonates led to the formation of skarn and marble bodies, which attain up to 100 m in width for skarns (Olvera-García et al., 2020) and between 300 and 400 m in width for marble (Fuentes-Guzmán et al., 2020) in the exhumed system of Las Minas. With their high thermal conductivities and abundant fractures, they act as heat conduits in the subsurface. To improve the accuracy of a 3D geothermal model, these rather 'vertical features' should be implemented as additional model units in the pre-volcanic basement unit.

While in previous studies the Cuyoaco andesite unit has been assumed to have a thickness of several hundreds of meters in the reservoir (Cedillo, 1999; Calcagno et al., 2020), recent petrographic investigations concluded that this unit might have a very limited extension in the subsurface of the Los Humeros geothermal field (Carrasco-Núñez et al., 2017a). However, due to the hydrothermal overprint observed on the wellbore core samples, a clear correlation with the outcropping units or between wells remains challenging. Since the Cuyoaco and Teziutlán andesites exhibit very similar physiochemical characteristics, it seems plausible to merge both pre-caldera andesites in one model unit instead of using stratigraphic ages to define differences.

The Xáltipan ignimbrite represents the cap rock of the Los Humeros geothermal field and resembles the most heterogenous lithostratigraphic unit considering its variable thickness (70–880 m) and petrophysical properties (Figs. 32, 33, 34, 35). Furthermore, especially the basal section of the Xáltipan ignimbrite within the Los Humeros geothermal field were affected by fracturing, brecciation and occasionally by hydrothermal alteration due to the caldera collapse events and volcanic activities during the post-caldera phase (Cavazos-Álavarez et al., 2020; Urbani et al., 2020; Weydt et al., 2021b). In previous studies, the Xáltipan ignimbrite was described as a nonpermeable, rather homogeneous layer (Cedillo, 1999), however, the results of the petrographic (Cavazos-Álavarez et al., 2020) and petrophysical characterization have shown that a much higher heterogeneity and thus, uncertainty need to be considered. The remaining units of the caldera and post-caldera group have a thickness of a few meters to tens of meters only. Up to now accurate information about their thickness and lateral distribution are not available for the Los Humeros geothermal field and thus, it is not possible to define further units that exhibit petrophysically similar properties. The interpretation of geophysical data is still ongoing and might provide new insights for an updated 3D geological model of Los Humeros.

The investigation of outcrop analogues and their petrophysical characterization significantly improved the geological understanding of the LHVC and forms the basis for the interpretation of geophysical surveys (e.g., electric resistivity, gravimetric and magnetotelluric surveys; Benediktsdóttir et al., 2020; Cornejo et al., 2020), economical assessments (e.g., productivity index and Heat-in-Place calculations; González-García et al., 2020), the estimation of the local stress field (Kruzewski et al., 2020), an accurate assessment of the heat transport and heat storage in the reservoir as well as a precise

parametrization of numerical reservoir models to simulate, e.g., reservoir temperature (Deb et al., 2019d) or production and stimulation scenarios (Hofmann et al., 2021).

However, despite the high number of analyzed samples, it was not possible to cover all units to the same extent in the study area. The number of samples per unit strongly depended on the availability and accessibility of representative outcrops in the field that allowed to gain a representative overview of the unit's heterogeneity and to collect large boulders for the petrophysical characterization. In addition, the number of samples per unit was influenced by the project goals, which targeted the currently exploited hydrothermal reservoir (pre-caldera units) and the potential supercritical reservoir (pre-volcanic basement). Thus, a further criterion was the importance of a unit with respect to a 3D geological model considering the thickness and extension in the study area.

Furthermore, the here presented data set comprises matrix properties only and does not account for fracture properties, which can vary over several orders of magnitude for different scales. For example, matrix permeabilities commonly underestimate the equivalent permeability at reservoir scale since they do not depict fracture networks and their permeabilities (Heap and Kennedy, 2016; Farquharson and Wadsworth, 2018). Depending on the aim and scale of future applications, the data need to be individually processed, which is also called upscaling. Various different approaches have been developed in the past to tackle the problem of retaining as much information of the original structure, facies heterogeneities, geometry, petrophysical and hydraulic properties on reservoir scale (Farmer, 2002; Qi and Hesketh, 2005; Rühaak et al., 2015; Chen et al., 2018; Ringrose and Bentley, 2021). The simplest and fastest techniques are cross-correlations or (power law) averaging (calculating the arithmetic, harmonic or geometric mean value of a respective volume; weighted sum of an independent property), which is often applied in combination with stochastic techniques, e.g., the Monte Carlo method (Qi and Hesketh, 2005). More advanced approaches such as variogram analysis, Kriging or Gaussian simulations are often used to populate numerical models of geologically complex and/or fractured reservoirs (Bourbiaux et al., 2005; Ebong et al., 2019). Furthermore, Discrete Fracture Networks or dual porosity/permeability models allow to explicitly represent fractures and their geometries in reservoir simulations (Ringrose and Bentley, 2021). In conclusion, numerous upscaling techniques exist, which need to be chosen carefully for each parameter considering the geological setting, rock type and application.

4.6. Conclusions

This study provides an assessment of petrophysical, thermophysical, dynamic mechanical as well as magnetic rock properties for the Los Humeros Volcanic Complex which hosts a currently exploited high-temperature (> 350 °C) geothermal reservoir. For a reliable reservoir characterization, 226 samples were collected from more than 200 outcrops in the inside of the Los Humeros caldera, the surrounding area of the volcanic complex and the nearby exhumed system of Las Minas to investigate and cover the heterogeneity of all key formations from the basement to the cap rock that are relevant for regional and local 3D numerical geothermal models of the Los Humeros geothermal field. Based on chemical and petrographic analyses as well as new information on dating, the samples were assigned to lithostratigraphic units. About 1500 plugs were petrophysically analyzed resulting in an extensive rock property database covering sedimentary, magmatic and metamorphic rocks from Jurassic to Holocene age. The distribution and variability of the petrophysical properties as well as the relationship between the parameters were statistically investigated and displayed for each lithostratigraphic unit. For a more reliable reservoir characterization, the rock properties were transferred to reservoir conditions of the Los Humeros geothermal field of up to 3 km depth using empiric and analytical correction functions.

The study highlights the geological complexity of the study area which is also depicted in the petrophysical properties:

- More than 20 lithostratigraphic units and subunits were defined that exhibit distinct properties. The basement and andesitic reservoir predominantly comprise low-to-very low matrix porosities and permeabilities as well as intermediate-to-high densities, thermal properties and sonic wave velocities.
- The weak correlation between matrix porosity and permeability suggests that fluid flow in the study area is predominantly controlled by faults.
- The high variability of thermal conductivity and diffusivity observed on the basement rocks should be considered in future thermal models, whereby intrusions and their associated metamorphic rocks might act as heat conduits.
- The cap rock and the overlying younger volcanic sequences show the highest variability with respect to matrix porosity and bulk density, but feature overall low-to-intermediate thermal conductivities and sonic wave velocities.
- Specific heat capacity shows comparatively small variations throughout the dataset. In contrast, magnetic susceptibility varies over more than four orders of magnitude showing formation-related trends that could be helpful for the interpretation of geophysical surveys.
- Rock properties are sensitive to pressure and temperature changes with increasing reservoir depth. Particularly, matrix porosity and permeability of the pyroclastic rocks significantly decrease with reservoir depth due to their high rock compressibility. The effects of pressure and temperature on the thermal and mechanical properties are complex and often counteract each other. Thus, correction functions for both parameters should be considered in numerical simulations to depict the rock properties at reservoir depth as accurate as possible.
- Furthermore, the probability density distribution should be assessed for each parameter and unit individually during stochastic modeling.

The dataset provided in this study improves the understanding of the Los Humeros Volcanic Complex and super-hot geothermal systems in general, and underlines the importance of outcrop analogue studies and the assessment of petrophysical properties during reservoir exploration for the development of conceptual geological models, the interpretation of geophysical data or the parametrization of 3D numerical geothermal models. Beyond the scope of the GEMex project, the level of detail presented in this study facilitates various applications in comparable geological settings within the TMVB or similar volcanic geothermal play types worldwide. Since extensive field campaigns and laboratory measurements are time consuming and often exceed project budgets, our study improves the prediction of rock properties in the subsurface at early exploration stages or in case of low data densities and thus, could be used to improve and speed-up reservoir simulation of future projects.

4.7. Acknowledgements

5. The Impact of Hydrothermal Alteration on the Physiochemical Characteristics of Reservoir Rocks – the case of the Los Humeros Geothermal Field

This chapter is based on the article "Weydt, L. M., Lucci, F., Lacinska, A., Scheuvens, D., Carrasco-Núñez, G., Giordano, G., Rochelle, C. A., Schmidt, S., Bär, K., and Sass, I.: The impact of hydrothermal alteration on the physiochemical characteristics of reservoir rocks: the case of the Los Humeros geothermal field (Mexico), Geothermal Energy, 10, 20(2022), 49 pp., 2022." The abstract is not included and the alphanumeric order of figures and tables may differ from the original article. If necessary, the alphabetical order of quotations has been adapted to the content of the dissertation. Likewise, the formatting was adjusted to fit the layout of this work.

5.1. Introduction

Unconventional geothermal systems such as high-temperature or so called super-hot geothermal systems (SHGS, > 350°C) are important targets for the generation of electric power (Reinsch et al., 2017). The majority of the currently exploited high temperature geothermal resources are related to magmatic settings, predominantly to active volcanic systems (Heřmanská et al., 2019). The petrophysical characterization of volcanic systems is often challenging due to their complex structural and geological evolution resulting in various rock types that exhibit complex characteristics regarding mineralogy, petrophysical and rock mechanical behaviour (Pola et al., 2012). Additionally, hydrothermal alteration is a widely observed process in volcanic settings, which significantly changes the intrinsic physiochemical properties of pristine rocks (Pola et al., 2016; Mordensky et al., 2019a, 2019b; Durán et al., 2019; Pandarinath et al., 2020; Heap et al., 2019, 2022). The circulation of hydrothermal fluids leads to mineral dissolution, replacement or precipitation (Browne, 1978) causing partial to complete modification in the mineralogical composition and subsequent physical behaviour of the affected rocks (Wyering et al., 2014). Thereby, the impact of hydrothermal alteration on the rock properties strongly depends on the original rock types and their mineralogical and petrophysical characteristics, pressure and temperature conditions within the reservoir, chemical composition of the reservoir fluid as well as the duration of the fluid-rock interaction (e.g., Sillitoe, 2010; Frolova et al., 2014; Rabiee et al., 2019; Sillitoe and Brogi, 2021).

The influence of hydrothermal alteration on rock properties of volcanic rocks has been investigated in the past to assess the longevity of geothermal reservoirs (Villeneuve et al., 2019), but also regarding slope instability (Sánchez-Núñez et al., 2021), heat flux, volcanic activity and the possible impact on phreatic eruptions (Mayer et al., 2016; Heap et al., 2019, 2022). Previous studies aimed to identify general trends in altered rocks, e.g., increased porosity and permeability along with reduced rock strength (Pola et al., 2014; Wyering et al., 2014), reduced permeability due to mineral precipitation (Mordensky et al., 2018), reduced porosity and permeability due to silicification (Dobson et al., 2003) or reduced porosity and increased thermal conductivity associated with an increased degree of hydrothermal alteration (Mielke et al., 2015), respectively. However, such changes are highly variable, even within a single reservoir, and are not fully understood yet. Comprehensive data sets are rarely available and most reservoir assessment studies or models are based on assumed or generalized data and thus, effects of fluid-rock interactions on rock properties and their spatial extent are commonly neglected for simplification reasons. Since hydrothermal alteration can both increase or decrease key reservoir properties, e. g., matrix porosity, permeability, rock strength, it also impacts the economic potential of the geothermal reservoir, and the controlling factors need to be understood and considered during reservoir assessment.

To investigate the influence of hydrothermal alteration on the physiochemical properties of rocks, we investigated borehole core samples retrieved from an active hydrothermal geothermal reservoir and

compared the results with outcrop samples that are stratigraphically equivalent to the reservoir units. For this purpose, the Los Humeros Volcanic Complex (LHVC) hosting one of the largest active silicic calderas located in the north-eastern part of the Trans-Mexican Volcanic Belt (TMVB), was selected as case-study. The LHVC hosts a steam-dominated hydrothermal system in predominantly andesitic sequences with temperatures above 380 °C below 2 km in the northern part of the caldera (Pinti et al., 2017; Deb et al, 2021). The geothermal reservoir has been operated by the Comisión Federal Electricidad (CFE) since 1990 (Romo-Jones et al., 2020) and 65 boreholes have been drilled so far. However, a sustainable utilization of these so called 'super-hot' regions for power production has not yet been possible due to aggressive reservoir fluids causing corrosion and scaling problems (Flores-Armenta et al., 2010). Various geological (Ferriz and Mahood, 1984; Carrasco-Núñez et al., 2017a, 2017b), geochemical (Prol-Ledesma and Browne, 1989; Martínez-Serrano, 1993, 2002; Izquíerdo et al., 2011, 2015), geophysical (Lermo et al., 2008; Arzate et al., 2018) and hydrological studies (Tello, 2005) have been performed in the past and most recently within the framework of the GEMex project (EU-H2020, GA Nr. 727550; Jolie et al., 2018; Weydt et al., 2018b, 2021b; Lucci et al., 2020; Urbani et al., 2020, 2021) to improve reservoir understanding and to create conceptual (Cedillo, 2000; Arellano et al., 2003) and 3D geological models (Calcagno et al., 2020; Deb et al., 2019d). However, even after more than 40 years of exploration, information on rock properties of the different geological units in the study area were scarce or not available. To overcome the lack of suitable data for economic assessments, numerical reservoir simulations and the interpretation of geophysical surveys, an extensive outcrop analogue study has been performed to characterize all relevant key units regarding their geochemistry, mineralogy, petrophysical and mechanical rock properties (Weydt et al., 2021a, 2022a).

This study focuses on the geochemical and petrophysical characterization of mainly andesitic lavas collected from outcrops and borehole core samples (from here on defined as reservoir samples) that are considered to represent the reservoir units hosting the hydrothermal system in the Los Humeros geothermal field. Therefore, 66 reservoir samples were drilled from 37 core sections covering 16 boreholes (H7 until H40). Additionally, 24 samples of Miocene to Pleistocene lavas of the Teziutlán and Cuyoaco andesite units representing the stratigraphically equivalent analogues to the reservoir formations in the deep subsurface, were collected from 14 outcrops located in the surrounding area of the LHVC. The samples were analyzed for bulk and particle density, porosity, permeability, thermal conductivity, thermal diffusivity, specific heat capacity as well as ultra-sonic wave velocities and magnetic susceptibility. Polarized light and scanning electron microscopes (PLM and SEM, respectively) investigations were performed to evaluate the intensity of hydrothermal alteration and to define alteration facies. Furthermore, whole rock compositions were determined and chemical weathering indices (CWI) were applied to quantify elemental concentration changes and thus, the impact of fluid-rock interactions (Pola et al., 2012; Pandarinath et al., 2020) and the post-alteration physiochemical properties. Correlation of reservoir samples to outcropping analogues were done following the approach proposed by Carrasco-Núñez et al. (2017b) and using selected elements considered to be unaffected by hydrothermalism and capable to act as geochemical indices (Winchester and Floyd, 1977; MacLean and Barrett, 1993).

The data set presented in this study aims to provide new insights on the impact of hydrothermal alteration on reservoir rocks in high-temperature hydrothermal systems. It will help future reservoir assessments define more accurate estimations of petrophysical properties at reservoir depths – both at the Los Humeros geothermal field and also geologically similar super-hot geothermal systems elsewhere in the world.

5.2. Geological Setting

The LHVC is located in the eastern sector of the Trans-Mexican Volcanic Belt (TMVB; Fig. 36, inset box). The TMVB is an E–W trending Miocene-Holocene continental volcanic arc some 1000 km long, which is linked to the subduction of the Rivera and Cocos plates beneath the North American plate along the Middle-American Trench (López-Hernández et al., 2009; Ferrari et al., 2012). The LHVC occupies an area approximately 21 × 15 km (Ferriz and Mahood, 1984) and is the largest active caldera of the TMVB, predominantly comprising Pleistocene to Holocene basaltic to rhyolitic volcanic rocks (Carrasco-Núñez et al., 2017a, 2017b, 2018; Cavazos-Álvarez et al., 2020; Lucci et al., 2020). The geology in the study area (Fig. 36) is characterized by: (1) pre-volcanic basement units, (2) pre-caldera volcanism units, (3) caldera stage units, and (4) post-caldera stage units (Carrasco-Núñez et al., 2017a; Carrasco-Núñez et al., 2018).
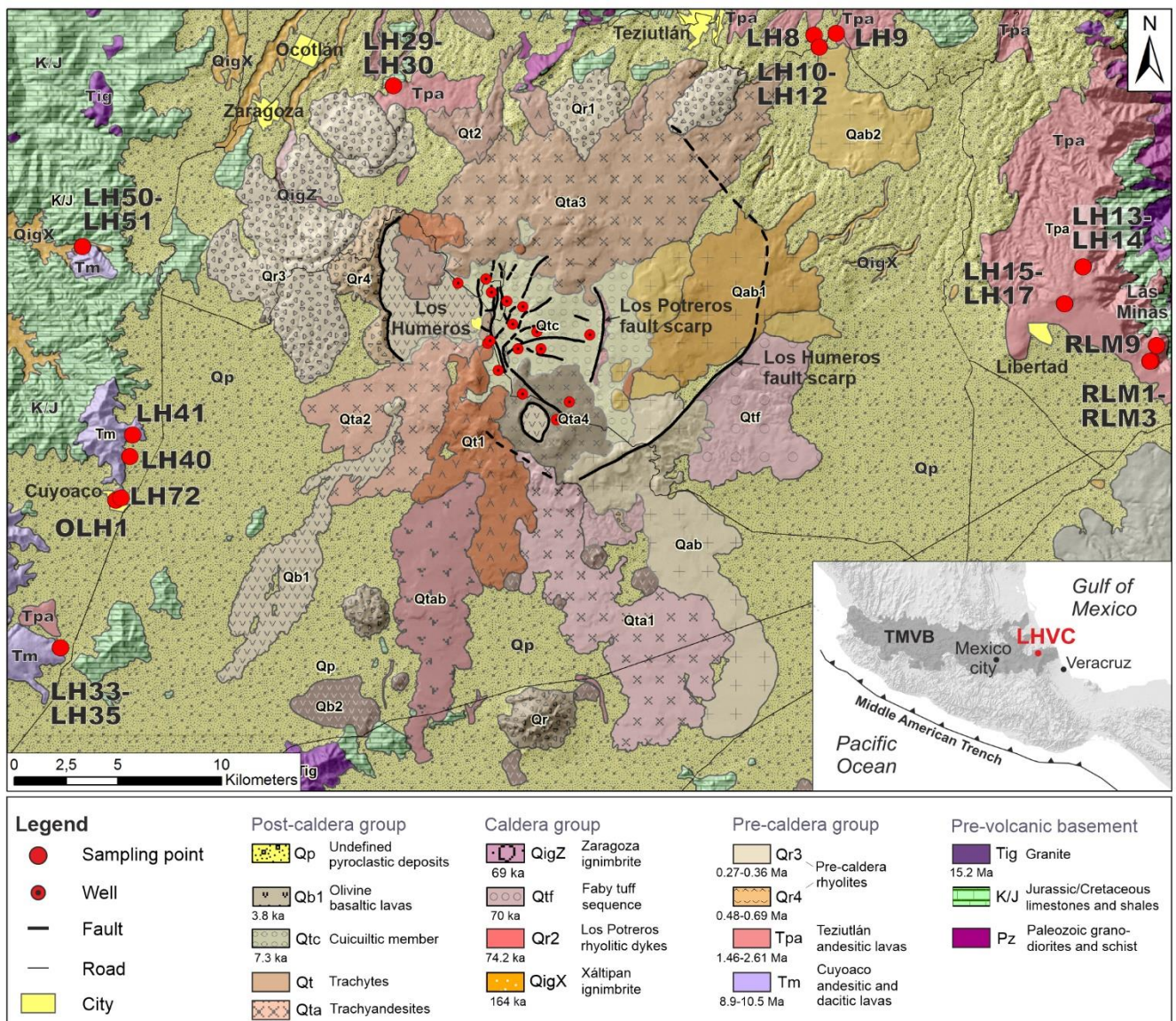
Figure 36: Geological map of the Los Humeros Volcanic Complex (LHVC) modified from Carrasco-Núñez et al. (2017a). The red points mark the sampling locations of the outcrop samples collected from the Cuyoaco andesites (Tm, with purple color) and the Teziutlán andesites (Tpa, pink color). Inset map showing the location of the LHVC and extension of the TMVB.

The pre-volcanic basement is represented by metamorphic (greenschists) and intrusive (granites and granodiorites) rocks dated at 246–131 Ma mainly exposed in the Teziutlán Massif and partially covered by up to 3 km thick Mesozoic sedimentary rocks belonging to the Sierra Madre Oriental (Yáñez and García,1982). The Mesozoic sedimentary successions comprise Jurassic and Cretaceous limestones, dolomites, shales, marls and sandstones. This pre-volcanic basement was deformed by the Late Cretaceous–Eocene compressive Laramide Orogeny resulting in NW–SE striking thrusts and folds and subordinate NE-striking normal faults that are associated to an Eocene-Pliocene extensional tectonic deformation phase (Fitz-Díaz et al., 2017; López-Hernández, et al., 1995). Oligocene to Miocene granitic and syenitic plutons as well as andesitic and basaltic dykes intruded into the sedimentary sequences and led to local thermal metamorphism producing marble, hornfels and skarn (Ferriz and Mahood, 1984).

The pre-caldera volcanism in the study area started in the Late Miocene at ~ 10.5 ± 0.7 Ma (Yáñez and García, 1982) with the emplacement of the Cuyoaco and Alseseca lavas comprising mainly fractured andesitic and dacitic lava flows with a cumulative thickness of 800–900 m. These lava flows can be related to the activity of the Cerro Grande volcanic complex dated between 8.9–11 Ma (Carrasco-Núñez et al., 1997; Gómez-Tuena and Carrasco-Núñez, 2000). The Pliocene to Pleistocene pre-caldera volcanism is instead represented by the Teziutlán andesites dated between 1.44 ± 0.31 and 2.65 ± 0.43 Ma (Carrasco-Núñez et al., 2017a), mainly comprising fractured dark grey massive, porphyritic andesitic lavas composed of plagioclase and two-pyroxene phenocrysts as well as olivine-bearing basaltic lavas (Carrasco-Núñez et al., 2017a). These late Miocene to Pleistocene fractured pre-caldera andesites show a thickness of up to 1500 m as reported in the lithostratigraphic profiles of the geothermal wells (Fig. 37; Carrasco-Núñez et al., 2017b; López-Hernández et al., 1995) and constitute the currently exploited reservoir of the Los Humeros geothermal field. In previous studies, the pre-caldera reservoir samples were described as augite andesites, tuff, hornblende andesites and basalts (from top to base; Cedillo, 2000). Despite the variability in chemical composition, the Cuyoaco and Teziutlán lavas are commonly referred to as pre-caldera andesites or Teziutlán and Cuyoaco andesites for simplicity (e.g., Arellano et al., 2003; Calcagno et al., 2020). In this article, we will also use these terms for simplification reasons.

The onset of magmatic activity of the LHVC caldera stage is represented by partially buried rhyolitic lavas and abundant rhyolitic domes mainly located at the western side of the LHVC. Radiometric ages of the domes range between 270 ± 17 and 693 ± 1.9 ka (Carrasco-Núñez et al., 2018).

The LHVC caldera stage activity is characterized by two main caldera-forming eruptive events separated by a sequence of several large plinian and sub-plinian eruptive phases (Carrasco-Núñez et al., 2021). The Los Humeros caldera collapse is associated with the emplacement of the Xáltipan ignimbrite (164 ± 4.2 ka; Carrasco-Núñez et al., 2018), which is well-exposed in the surrounding area of the LHVC, but has a highly variable thickness (90–780 m) within the reservoir (Cavazos-Alvarez Álvarez et al., 2020). Afterwards, a sequence of explosive episodes occurred at 70 ± 23 ka (Carrasco-Núñez et al., 2018) depositing thick rhyodacitic Plinian deposits named as the Faby Tuff (Ferriz and Mahood, 1984; Willcox, 2011). The second caldera forming event occurred shortly after the Faby Tuff emplacement and is related to the rhyodacitic to andesitic Zaragoza ignimbrite at 69 ± 16 ka (Carrasco-Núñez et al., 2018) forming the smaller Los Potreros nested caldera (8 to 10 km in diameter).

The LHVC post-caldera stage represents the most recent volcanic activity in the study area and can be divided into two eruptive phases, which are a Late Pleistocene resurgence phase followed by a Holocene reactivation phase (Carrasco-Núñez et al., 2021). The Late Pleistocene phase is characterized by rhyolitic and dacitic domes within the centre of the Los Humeros caldera center (44.8 ± 1.7 ka, Carrasco-Núñez et al., 2018) and north of the Los Humeros caldera (55.7 ± 4.4 ka, Carrasco-Núñez et al., 2018) followed by a sequence of explosive eruptions producing dacitic pumice fall units (Xoxoctic Tuff, Ferriz and Mahood, 1984), volcaniclastic breccias and pyroclastic flow deposits (Llano Tuff, Ferriz

and Mahood, 1984; Willcox, 2011). During the Holocene alternating episodes of effusive and explosive eruptions occurred producing basaltic to trachyandesitic lava flows (8.9 ± 0.03 ka, Carrasco-Núñez et al., 2017a), followed by a rhythmic alternation of contemporaneous basaltic and trachyandesitic fall out deposits constituting the Cuicuiltic Member (7.3 ± 0.1 ka, Dávila-Harris and Carrasco-Núñez, 2014), a ring-fracture episode erupting trachyandesite and olivine-basalt lava flows (3.9 ± 0.13 ka, Carrasco-Núñez et al., 2017a) and trachytic lava flow at 2.8 ± 0.03 ka (Carrasco-Núñez et al., 2017a).

In particular, the Holocene LHVC post-caldera volcanic activity is associated with a complex magma plumbing system vertically distributed within the whole crust (Lucci et al., 2020) and shallow intrusions in the Los Potreros caldera within the Los Humeros geothermal field (< 1 km depth; Urbani et al., 2020, 2021; Deb et al., 2021), which causes several very localized temperature anomalies mainly along the NNW–SSE trending Maxtaloya and Los Humeros lineament (Jentsch et al., 2020; Deb et al., 2021). Except for the water-producing well H1, the produced fluids are predominantly steam with an enthalpy of more than 2000 kJ kg^{-1} (Romo-Jones et al., 2020). The geothermal field contains low-saline NaCl to H_2CO_3-SO_4 fluids, which are oversaturated in quartz and calcite and locally contain high boron, ammonia, and arsenic concentrations (Izquíerdo et al., 2009). Most of the geothermal fluids show a near neutral pH between 7 and 8 (Tello, 2005), while a few wells in the central to northern part of the geothermal field feature very low pH brines (< 5; Flores-Armenta et al., 2010). The Los Humeros geothermal field is characterized by a trap-door collapse structure (Bonini et al., 2021) and the topographic top of the sedimentary basement shows a high displacement between the northern-central part of the geothermal field (~ 1720 m bgl [below ground level] in H43; north of Los Humeros in Fig. 37) and the southern sector close to the Xalapazco crater (deeper than 3300 m bgl in H24).

Up to now, hydrothermal alteration was predominantly investigated on cuttings retrieved from boreholes (Prol-Ledesma and Browne, 1989; Prol-Ledesma, 1990; Martínez-Serrano, 2002; González-Partida et al., 2022). Prol-Ledesma and Browne (1989) defined four laterally distributed areas through the identification of secondary mineral assemblages and defining temperatures ranging from 250 to > 300 °C in the northern-central part of the geothermal field and lower temperatures of ~ 120 °C moving to the caldera rim. Martínez-Serrano (2002) defined three main alteration zones from top to base based on cutting analyses of five boreholes in the central collapse zone: (1) a shallow argillic zone which is present in the upper levels of the volcanic sequences and characterized by kaolinite-montmorillonite, chlorite and zeolites as well as calcite; (2) a propylitic zone between 500 and 1800 m depth mainly comprising epidote, quartz, amphibole, calcite, chlorite, montmorillonite-illite, sulfides and iron oxides and (3) a skarn zone at depths of greater than 1800 m composed of garnet, wollastonite, clinopyroxene and biotite. González-Partida et al. (2022) redefined these units and proposed a high-temperature high-silica advanced argillic alteration zone in the deeper sections of the pre-caldera andesites associated with subcritical brines.
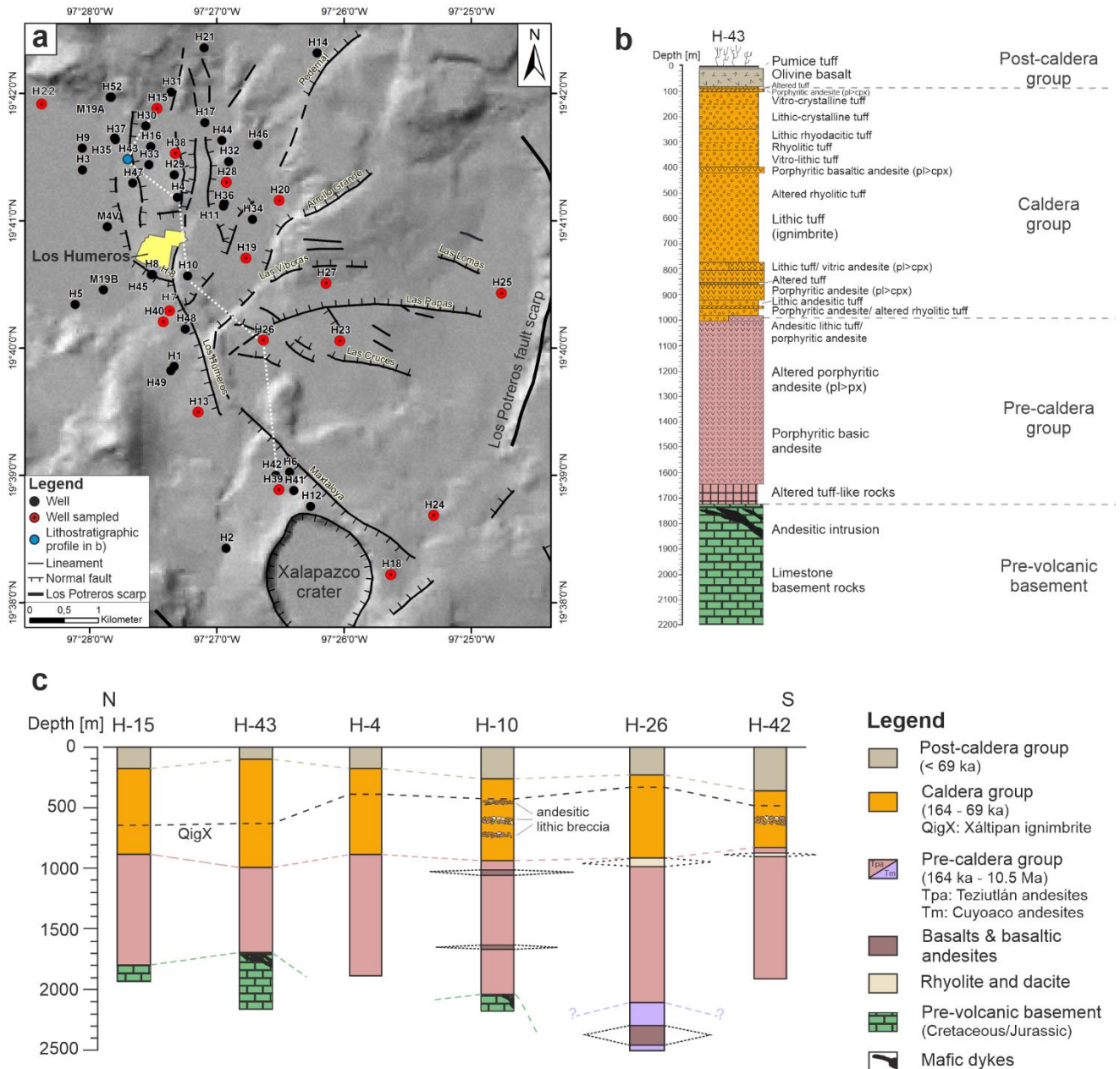
Figure 37: (a) Location of the geothermal wells drilled within the Los Humeros caldera and (b) the lithostratigraphic profile of well H43 (modified from Carrasco-Núñez et al., 2017b). (c) Lithostratigraphic profiles and in-depth correlation of the main stratigraphic groups modified from Urbani et al. (2020) and Carrasco-Núñez et al. (2017b) with new data from Cavazos-Álvarez et al. (2020).

5.3. Material and Methods

During the field campaigns 24 samples with a dimension of ~ 30 × 30 × 20 cm were collected from 14 outcrops (Table C1) representing the Teziutlán and Cuyoaco andesite units (Fig. 36). Cylindrical sub-samples with diameters ranging from 25 to 64 mm were drilled from the outcrop samples. In addition, 66 sub-samples with a diameter of 40 mm and an approximately length of 75 mm were drilled from 37 wellbore cores of the Los Humeros geothermal field (Fig. 37, Table C2). Following the international standard ASTM D4543 (2019), 207 and 99 plugs were prepared from the outcrop and reservoir core samples (length: ~ 25–128 mm), respectively. Given the sample size used in this study, the petrophysical measurements presented here provide matrix properties of the rocks, eventually including small-scale or single fractures.

The methodology of the petrophysical and geochemical measurements are described in detail in Weydt et al. (2021a) and thus, are only mentioned briefly in the following sections. All petrophysical measurements were performed under ambient laboratory conditions (0.1 MPa and ~ 20 °C). To ensure reproducibility of the results, the plugs were oven-dried and cooled down to room temperature in a desiccator (20 °C). In order to perform measurements under saturated conditions, a vacuum desiccator (approx. -1 bar) filled with de-ionized water was used.

For the determination of particle and bulk density a multi-step procedure using a helium pycnometer (AccuPyc 1330) and a powder pycnometer (GeoPyc 1360) was applied. Thereby the particle and bulk volume were measured five times, respectively. Matrix porosity was then calculated from the resulting differences in volume and represents the gas-effective or so-called connected porosity. According to Micromeritics (1997, 1998) the measurement reproducibility is given as 1.1%.

Intrinsic permeability was determined with a column permeameter constructed according to ASTM D4525 (2013) standard using dried compressed air at five air pressures (1–3 bar) in order to calculate gas permeability. The intrinsic permeability was derived from the apparent gas permeability after the Klinkenberg correction (Klinkenberg, 1941). Measurement error varies from 5% for high permeable rocks (K > 10^{-14} m²) to 400% for impermeable rocks (K < 10^{-16} m²) (Bär, 2012).

Thermal conductivity and diffusivity were measured after Popov et al. (2016) using a thermal conductivity scanner (Lippmann and Rauen GbR). Both parameters were measured four to six times on each plug under saturated and dry conditions, respectively. The measurement error is given as 3% for thermal conductivity and 5% for thermal diffusivity according to Lippman and Rauen (2009).

A heat-flux differential scanning calorimeter was used to determine specific heat capacity (Setaram Instrumentation, 2009). Crushed sample material was heated at a steady rate from 20 up to 200 °C within a period of 24 h. The measurement error is 1% (Setaram Instrumentation, 2009). Volumetric heat capacity was calculated by multiplying the specific heat capacity with the associated bulk density of each sample.

An ultrasound generator (UKS-D) from Geotron-Elektronik (2011) was used to determine compressional and shear wave velocities. Continuous measurements were performed with a contact pressure of 0.1 MPa and a frequency of 80 kHz to 250 kHz. Both velocities were measured four to six times on each plug under saturated and dry conditions, respectively, whereby the arrival times of the P- and S-waves were picked manually.

A magnetic susceptibility meter SM30 from ZH Instruments (2008) was used to determine magnetic susceptibility directly on the plane surface of each plug. To account for mineralogical heterogeneities each plane surface of a plug was measured five times.

The classification of Bär (2012) was used to evaluate the rock properties regarding their geothermal potential (ranging from very low to very high).

To analyze the bulk chemical composition of the samples whole-rock X-ray fluorescence spectroscopy (XRF) analyses were performed using Panalytical Axios spectrometers (Max WD-XRF at TU Delft and Advanced at GFZ) in combination with the software SuperQ for data evaluation as well as a Bruker S8Tiger 4 WD-XRF spectrometer using the Quant Express method (at TU Darmstadt). Measurement error is < 5% for the major elements and < 10% for the trace elements. The proposed limit of detection ranges between 400 ppm (Na) and < 10 ppm (e.g., Rb, Sr, Nb). Rare earth elements (REE) of the reservoir samples and selected outcrop samples were analyzed at TU Darmstadt using an Analytik Jena Plasma Quant MS Elite® ICP-MS based on an application note by Analytik Jena and Yu et al. (2001). Method validation and recovery experiments were carried out using two certified reference standards (Basalt, Columbia River [BCR-2] and Andesite, Guano Valley [AGV-2] -Fluxana Bedburg-Hau, Germany) as well as sample material (cuttings) from Carrasco-Núñez et al. (2017b). Geochemical data were analyzed using a nonparametric statistical approach (Kruskal-Wallis test with $p = 0.05$; Vargha and Delaney, 1998; XLSTAT Premium V2020.5.1). A detailed analysis of clay minerals or

aluminosilicates and their distribution using X-ray Diffraction methods has already been performed in previous studies (e. g., Prol-Ledesma, 1990; Martínez-Serrano, 2002; González-Partida et al., 2022), and thus, was not repeated in this study.

Furthermore, the collected samples were prepared as polished thin sections and studied by polarized light microscope (PLM). Selected reservoir samples were then analyzed with a scanning electron microscope (SEM; further details are included in the supplementary material) to gain information on the primary assemblages, intensity of alteration, mineralogy and alteration facies, texture, porosity, (micro-) fractures, grain size and shape. Mineral abbreviations used in this study follow Whitney and Evans (2010). Samples were classified into three groups based on the intensity of alteration and macroscopic features (e.g., change of structure, color, intensity of mineral replacement or neoformed minerals; Pola et al., 2012; Navelot et al., 2018), including "none-to-weak alteration" (pristine mineralogy to first signs of alteration), "moderate alteration" (hydrothermal alteration impacts the groundmass or phenocrysts to a variable extent) and "strong alteration" (alteration is pervasive and strongly affects the groundmass and phenocrysts).

Several chemical weathering indices (CWI) were tested, such as chemical index of weathering (CIW; Harnois, 1988), chemical index of alteration (CIA; Nesbitt and Young, 1982), plagioclase index of alteration (PIA; Fedo et al., 1995), Ishikawa alteration index (AI; Mathieu, 2018) and chlorite-carbonate-pyrite index (CCPI; Mathieu, 2018) to investigate the relationship between chemical changes and alteration intensity as described in Pola et al. (2012) or Lee et al. (2021). These indices have been developed to better characterize the alteration intensity using weight percentage of major elements and assume that the (re-) distribution of these elements is controlled by the alteration intensity.

Furthermore, variations of the major, trace and rare earth elemental concentrations of the reservoir samples were calculated according to Pandarinath et al. (2020) using the outcrop analogues as preserved protoliths.

5.4. Results

5.4.1. Petrographic Analyses

5.4.1.1 Outcrop Samples

The Teziutlán andesite unit comprise different massive to porous, predominantly porphyritic lavas with a dark grey to medium grey as well as brownish-grey color (Fig. 38a-h; Table 7). The primary assemblage is dominated by plagioclase with pyroxene (clinopyroxene and orthopyroxene), olivine and subordinate (Ti-)magnetite and ilmenite. The groundmass is made up of a comparable microcrystal assemblage. The samples LH13-LH17, RLM1, RLM2, and RLM9 show no macroscopically visible pores. The samples LH8-LH12 contain a vesicular matrix with abundant circular to elongated pores (1–5 mm in diameter), while LH29, LH30 and RLM3 contain only a few pores with an irregular distribution. Occasionally microfractures occur. RLM3 shows alteration rims along fine cracks and fissures and contains some secondary alteration minerals (most likely clay-minerals).

The lavas related to the late Miocene Cuyoaco andesite unit show a variable grey to beige and reddish color with a porphyritic to glomerophyric texture comprising plagioclase, clinopyroxene (augite), olivine, and ilmenite (Fig. 38i-n, Table 7). The nonporous lavas often show small-scaled fractures. LH40, LH41, LH72 as well as OLH1 samples show a weak alteration characterized by overprints at outer rims of pyroxenes and appearance of secondary oxides such as hematite (Fig. 38i and j). LH50 and LH51 are significantly different with a beige, nonporous microcrystalline matrix containing plagioclase, quartz, pyroxene, hornblende, and biotite (Fig. 38o and p). These samples were interpreted as subvolcanic/hypabyssal rocks.
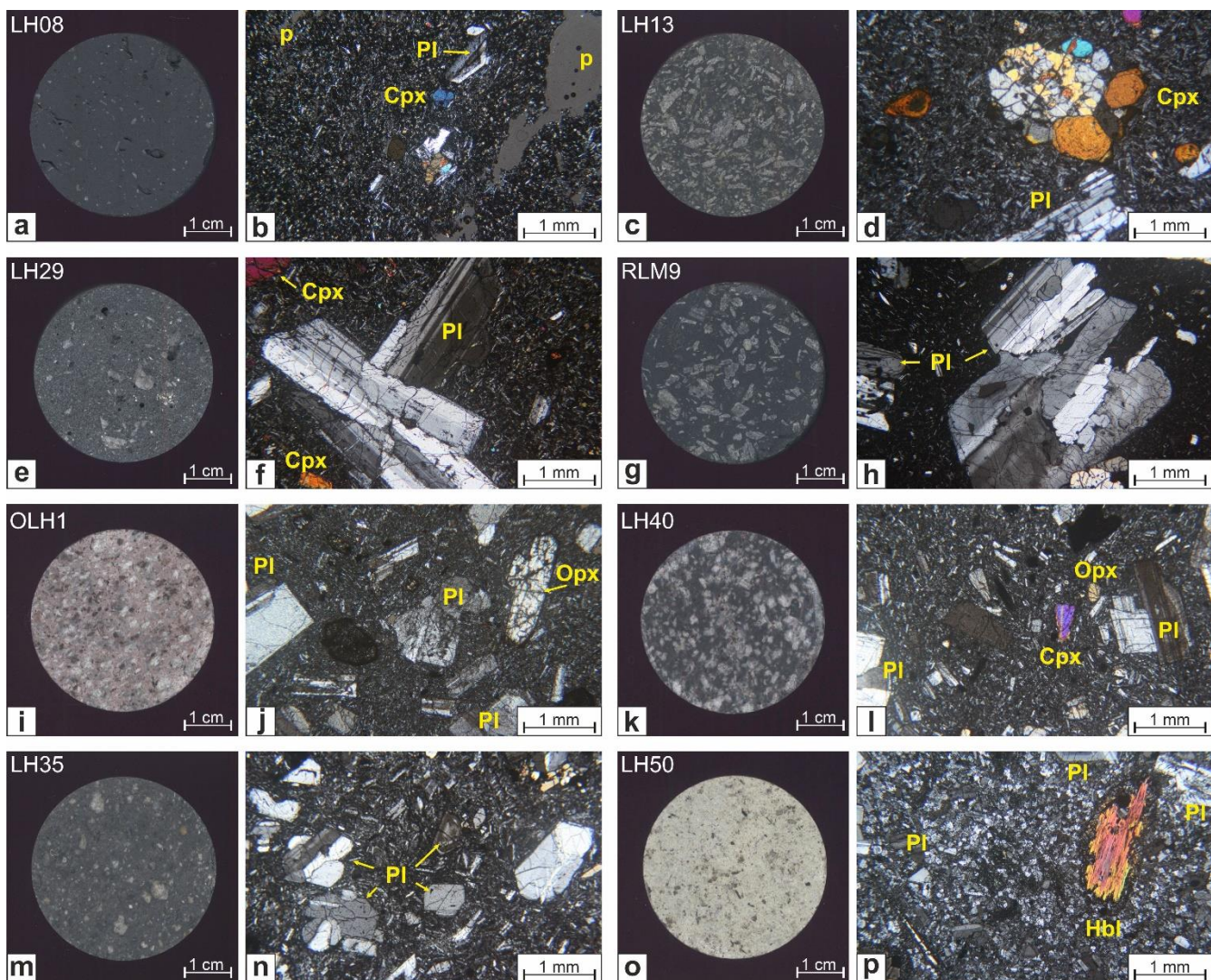
Figure 38: Scans of polished plugs and corresponding thin section images (XPL) from selected outcrop samples. (a) to (h) represent the Teziutlán andesite unit and (i) to (p) represent the Miocene Cuyoaco andesite unit. Abbreviations: Cpx = Clinopyroxene, Hbl = hornblende, p = pores, Pl = plagioclase, Opx = Orthopyroxene.

Table 7: Summary of petrographic features for the outcrop samples

Stratigraphic unit	Sample ID	Petrographic description
Teziutlán andesite unit (1.44–2.65 Ma)	LH8 - LH12	dark grey; vesicular matrix, pores with 1–5 mm in diameter, relatively few phenocrysts ~ 0.5 × 1 mm in size; plagioclase, pyroxene, olivine, magnetite, ilmenite
	LH13 - LH17	medium grey; nonporous, occasionally fractured, porphyritic to glomerophyric texture with abundant, irregularly distributed subhedral to euhedral plagioclase phenocrysts (up to 10 mm long); plagioclase, pyroxene, magnetite, occasionally olivine
	LH29 - LH30	medium grey; few pores 1 to 3 mm in diameter, porphyritic to glomerophyric texture with comparatively few, unequally distributed phenocrysts with a size ranging between < 1 mm and 10 mm; plagioclase, pyroxene, olivine, some altered olivine in LH29
	RLM1 - RLM3	brownish - grey; RLM1 and RLM2: nonporous, RLM3: few pores with a diameter of < 1 mm to 2 mm partially plugged with secondary alteration minerals, fine cracks and fissures with alteration rims along these cracks, porphyritic with large phenocrysts (up to 2–5 mm long); plagioclase, pyroxene (augite), olivine, magnetite
	RLM9	dark grey; nonporous, fractured, porphyritic texture comprising relatively large plagioclase phenocrysts that are up to 10 mm long; plagioclase, pyroxene, magnetite
Cuyoaco andesite unit (8.9–10.5 Ma)	LH33 - LH35	medium grey; nonporous, porphyritic to glomerophyric texture with comparatively few and irregularly distributed subhedral to euhedral plagioclase phenocrysts (up to 10 mm long) as well as augite and olivine
	LH40	medium grey; nonporous, occasionally fractures, porphyritic to glomerophyric texture with abundant phenocrysts up to ~ 1 × 2 mm in size, some alteration rims
	LH41	light grey to beige; slightly reddish; nonporous, occasionally fractures, porphyritic to glomerophyric texture with abundant phenocrysts up to ~ 1 × 2 mm in size, weak alteration
	LH50 - LH51	beige; nonporous, microcrystalline matrix with plagioclase, quartz, pyroxene, hornblende and biotite; interpreted as subvolcanic/hypabyssal rocks
	LH72 - OLH1	light grey to reddish; nonporous, abundant fractures, porphyritic texture with phenocrysts ~ 1 × 2 mm in size, weak alteration; plagioclase, pyroxene (augite), olivine, ilmenite

5.4.1.2 Reservoir Samples

The investigated reservoir core samples include a highly variable suite of magmatic and metamorphic rocks from aphanitic to porphyritic basaltic-andesitic to rhyolitic lavas and ignimbrites as well as skarns and marbles collected from 37 core sections drilled at 353 m to 2900 m bgl (Table 8, Figs. 39 to 41, Figs. C1 and C2). The core sections cover 16 boreholes, thus providing good spatial coverage of the inner part of the caldera. Most of the samples were affected by hydrothermal alteration of different intensities, brecciation, and fracturing, thus, resulting in high matrix heterogeneity (Fig. C1). Hydrothermal alteration varies from weak to strong, and predominantly occurs along fractures and cracks with a limited lateral extension, often of a few centimetres only. For example, H39-2-C2 shows intense hydrothermal alteration and bleaching along a fracture (Fig. 41a), while the second plug (H39-2-C1), which was drilled only a few centimetres away, shows only a weak to moderate hydrothermal overprint. In some cases, the rock matrix was completely replaced by secondary minerals, thus preventing a clear identification of the original protolith.

The shallowest sample H26-1 retrieved from 353 m bgl comprises a beige to light grey vitroclastic tuff that most likely represents the upper part of the Xáltipan ignimbrite unit (Fig. 39a and b). The sample shows only a weak hydrothermal overprint.

The samples retrieved from 633 to 1400 m bgl were identified as mafic, andesitic, trachyandesitic, and rhyolitic lavas as well as andesite-ignimbrite breccias (at 633–673 m bgl, Fig. 39c and d). The samples have a highly variable appearance and texture, again characterized by strongly variable alteration

intensities, varying from weak to strong. While some samples represent relatively fresh lavas showing unaltered plagioclase, olivine, and clinopyroxene (H27-1 at 1110 m bgl, Fig. 39e and f), other lavas retrieved from a similar depth level are strongly altered (H18-1 at 796 m bgl). This section of the reservoir is dominated by argillic alteration as well as the beginning of propylitic alteration with the main alteration assemblages made up of calcite, quartz, chlorite, hematite, and clay-minerals such as kaolinite and mixed layers smectite-illite. Calcite is very abundant and occurs in pores, fractures, and pervasively in the matrix replacing also both plagioclase and K-feldspar phenocrysts. Allotriomorphic to idiomorphic quartz crystals predominantly grow at the outer rim of pores and fractures. Chlorite appears as light green, very fine-grained patches or very fine radial aggregates in pores and fractures, especially in the upper depth levels together with other clay-minerals. Epidote occurs locally as small subhedral to euhedral crystals overgrowth on plagioclase. Pores are usually smaller than 0.5 mm in diameter. However, one sample of strongly altered andesitic lava (H20-4, 1400 m bgl, Fig. 40a and d) contains largely elongated, partially filled pores of up to 10 × 30 mm in size, leading to a tuffaceous appearance.
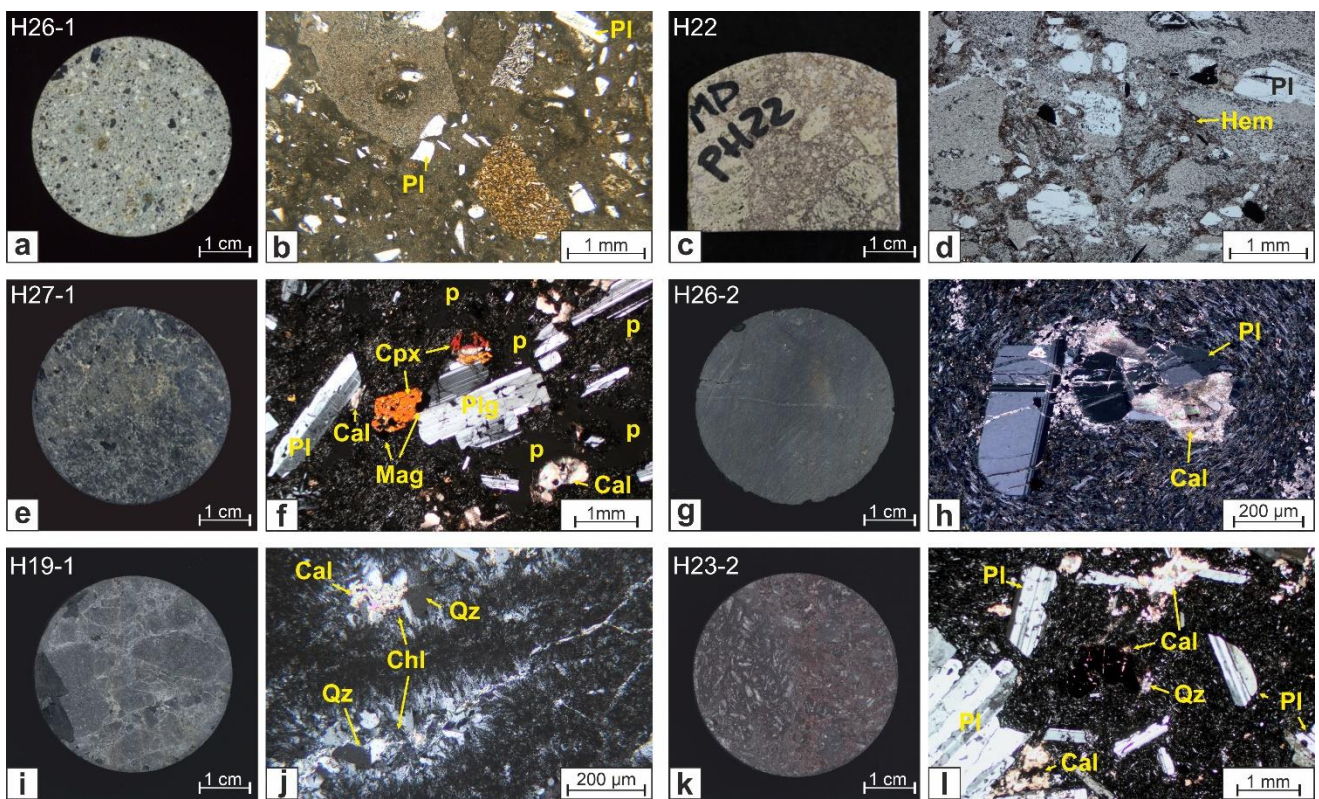
Figure 39: Scans and photographs of selected reservoir samples and corresponding thin sections with PPL = (b) and (d) and XPL = (f), (h), (j), and (l). (a) to (d) represent the upper Xáltipan ignimbrite and andesite/ignimbrite breccias of the caldera group, (e) to (l) represent mafic to rhyolitic lavas of the upper part of the pre-caldera group predominantly affected by argillic alteration. Abbreviations: Cal = calcite, Chl = chlorite, Cpx = Clinopyroxene, Hem = hematite, Mag = magnetite, p = pores, Pl = plagioclase, Qz = quartz.
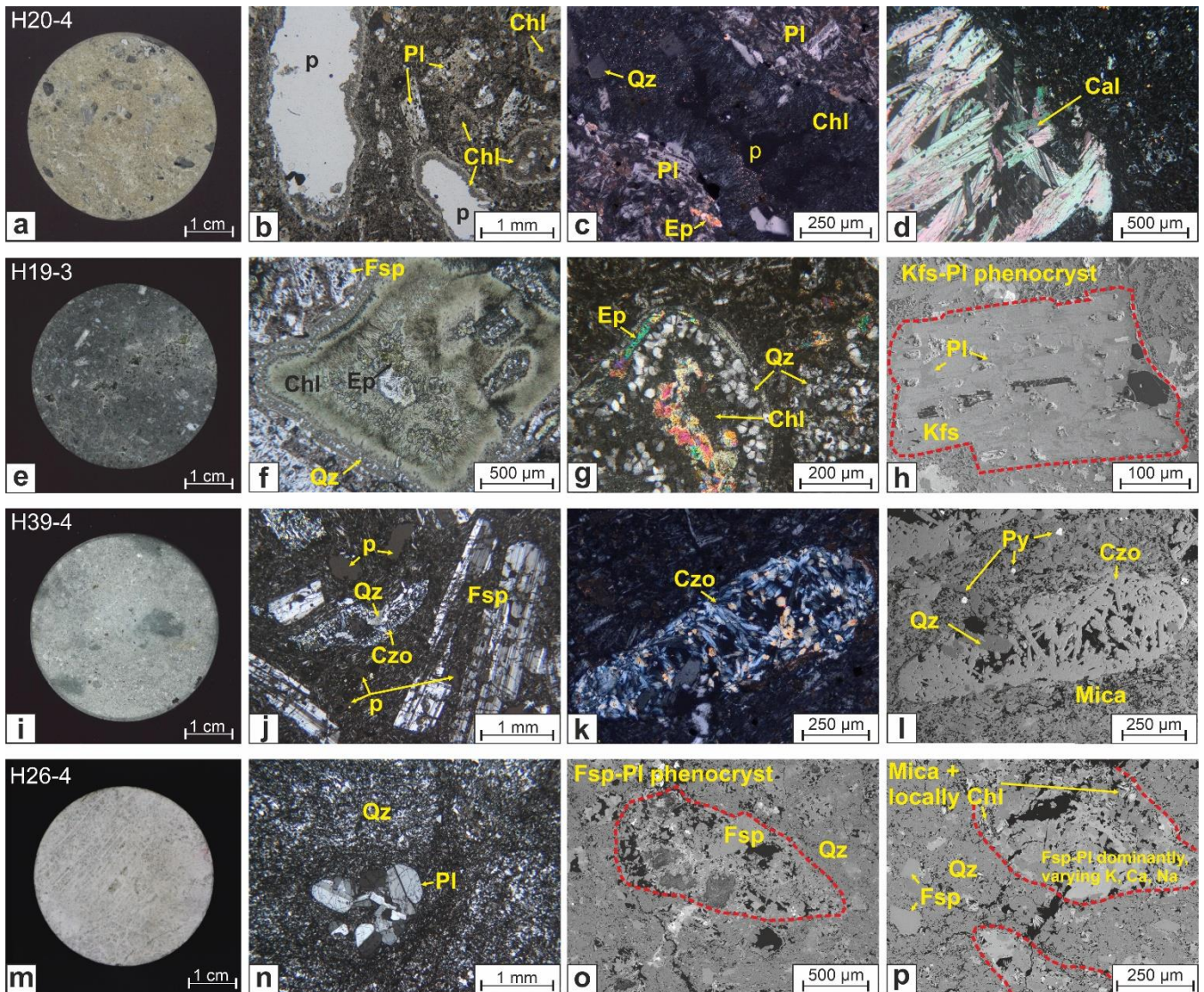
Figure 40: Low-temperature (a to d), moderate-temperature (e to h) to high-temperature propylitic alteration (i to l) as well as advanced silicification (m to p) with relics of original phenocrysts and secondary porosity (black patches) observed in thin sections with PPL = (b) and (f) and XPL = (c), (d), (g), (k), and (n) as well as SEM images of selected altered andesitic lavas displayed as (h), (l), (o), and (p). Abbreviations: Cal = calcite, Chl = chlorite, Ep = epidote, Czo = clinozoisite, Fsp = feldspar, Kfs = K-feldspar, p = pores, Pl = plagioclase, Py = pyrite, Qz = quartz.

Samples retrieved from ≥ 1500 m bgl predominantly comprise basaltic to andesitic lavas (Table 8) and are dominated by propylitic alteration with an alteration assemblage composed of epidote, chlorite, albite, K-feldspar, quartz, calcite, pyrite, hematite, titanite, Ti-Fe-oxides as well as occasionally clinozoisite. The abundance of chlorite and epidote led to the typical greenish-yellow color and patchy appearance of the rock matrix (Fig. 40, Fig. C1). The primary plagioclase is completely transformed in albite, calcite and epidote with also the appearance of secondary K-feldspar, chlorite and subordinate apatite and Ti-bearing minerals such as titanite and Ti-oxides. Likewise, clino- and orthopyroxene phenocrysts are completely altered. Amygdales are filled with chlorite, epidote, and calcite rimmed with quartz (H19-3, Fig. 40f, Fig. C2). However, in several samples some pores remained unfilled (Fig. 40). Fractures, cracks and brecciated sections are abundant and are also typically filled with an assemblage made up of chlorite, epidote, calcite, quartz, subordinate pyrite, and Fe-oxides (Fig. 40, Fig. C1). Magnetite occurs in some samples in the most preserved portions (H39-2, Fig. 41b), but is commonly substituted by secondary titanite, hematite, and other Fe-oxides. Clinozoisite locally occurs associated with epidote s.s. and chlorite. In samples with reduced Fe_2O_3 concentrations, clinozoisite occurs as nests of

euhedral radiating crystals growing in vugs or on plagioclase (Fig. 40i to 40l). The H38-4 sample, which originated from 1950 m bgl represents an exceptional case comprising ≤ 5 mm euhedral to subhedral crystals of andradite garnet intergrown with elongate and blocky calcite crystals in fractures and in the matrix along with notable secondary porosity (Lacinska et al., 2020). The garnets are rich in mineral inclusions, predominantly clinopyroxene (diopside-augite) with a lesser amount of calcite, pyrite, and wollastonite. The latter was also observed as acicular crystals on the garnet-calcite intergrowths. Furthermore, rare amphibole phenocrysts altered to chlorite-epidote assemblage were observed (Fig. 41d to 41g).

Two skarn samples were retrieved from the deepest section of the reservoir, close to the Xalapazco crater (2844–2900 m bgl). The samples are composed of quartz, calcite, apatite and possibly acicular wollastonite with very small garnet crystals growing on the crystal surfaces as well as actinolite and clays. The significant leaching of elements and replacement of the matrix with quartz and other secondary minerals led to a white to greyish colour of the samples (also called bleaching, Fig. 41h). However, pervasive silicification was also observed at shallower depth levels (~ 2000 m bgl, H26-4 (Fig. C1) and H28-2). SEM investigations and Xray mapping revealed that the samples underwent intensive chemical changes including the dissolution of the original phenocrysts (Fig. 40o and p, Fig. C2), the development of secondary porosity and extensive silicification of the groundmass with locally mica, chlorite as well as some radial nests of pore-filling biotite.

Intensively fractured marble samples were retrieved from cores in the central part of the caldera (1970–2414 m bgl), which represent the upper section of the pre-volcanic basement (Fig. 41j to 41k, Fig. C2). They predominantly consist of a mosaic of interlocking coarsely crystalline calcite cross-cut by numerous calcite-filled fractures and veins that occasionally include wollastonite, garnet and subordinate diopside, apatite, pyrite, epidote and sulphides. Due to the dense array of calcite fractures and veins, the marbles are very friable.

Table 8: Summary of petrographic features for the reservoir core samples

Unit	Sample depth [m bgl]	Petrographic description	Alteration intensity	Alteration facies
Caldera group	353 m	**Xáltipan ignimbrite** (H26-1; Fig. 39a-b): beige to light grey vitroclastic lapilli tuff with white to blackish phenocrysts, pumice, marble and lava fragments with a size of up to 5 × 15 mm; unaltered feldspars, lithic clasts, biotite; elongated glass fibers indicate a low grade of welding, some oxides were observed in altered clasts that most likely originated from greater depth	weak	none – argillic
	633–673 m	**Ignimbrite/andesite breccia**: H23-1: beige to grey vitrolithic lapilli tuff to tuffaceous breccia with grey to blackish lava and marble clasts as well as grey, vesicular, porphyritic andesitic lava; overall fresh appearance, H22-1 (Fig. 39c-d): vitric tuff clasts and reddish-grey lava with large phenocrysts; fractured, moderate alteration, abundant hematite, calcite, quartz	weak - moderate	argillic
Pre-caldera group	796–1400 m	M**afic, andesitic, trachyandesitic and rhyolitic lavas**: highly variable appearance, texture, alteration intensity and facies; predominantly argillic alteration, abundant calcite, quartz, chlorite, occasionally epidote; rhyolites (H19-1, 981 m; Fig. 40i-j): moderate alteration along fractures, xenomorphic to idiomorphic quartz, chlorite, and calcite are filling the fractures, while the remaining matrix consists of very fine-crystalline felsic assemblage of quartz + feldspars; trachyandesites (H24-1, 1008 m; H26-2, 1200 m; Fig. 40g-h): moderate alteration, groundmass preserved, calcite, quartz, phenocrysts partially altered	weak - strong	argillic - propylitic
	1500–2495 m	**Basaltic to andesitic lavas**: grey, greenish, yellow color; epidote, chlorite, albite, K-feldspar, quartz, calcite, pyrite, occasionally magnetite, hematite, titanite, Ti-Fe-oxides and in some samples clinozoisite, groundmass: plagioclase and K-feldspar often pervasively replaced by chlorite and epidote; some samples contain altered lava fragments that most likely originated from greater depth; H38-4 (1950 m; Fig. 41d-g): andradite garnet, acicular wollastonite and blocky calcite in fractures, relicts of amphibole, mineral inclusions in garnet contain diopside-augite, calcite, pyrite, and wollastonite	strong	propylitic
	~ 2000 m	**Silicified lavas** (H26-4, H28-2): white-grey color, fractured, brecciated; H26-4 (Fig. 40m-p): microcrystalline groundmass (quartz) with remains of phenocrysts, plagioclase, locally mica, chlorite and radial biotite filling secondary pores; H28-2: mixture of clay minerals (illite-smectite) and quartz, some scattered apatite and relicts of feldspars rich in Na; partial "bleaching" also observed in H39-2 (1650 m; Fig. 41a-c) and H24-3 (2300 m)	strong	silicification
	2844–2900 m	**Skarn** (H24-4, H18-4): white-grey color, H18-4 (Fig. 41h-i): calcite, quartz, apatite, possibly acicular wollastonite, very small garnet crystals; H24-4: calcite, quartz, clays and actinolite, in some parts protolith still identifiable	strong	skarn
Pre-volcanic basement	1970–2414 m	**Marble** (H13-3, H15-4, H7-x): light to medium grey, coarse crystalline calcite matrix; very fragile due to numerous calcite-filled fractures and veins (< 200 µm to a few cm wide) composed of coarse interlocking calcite crystals (up to 1 mm); thinner veins in H13-3 (Fig. 41j-k) and H15-4 contain wollastonite, grossular and subordinate diopside, apatite, and pyrite in the central parts and interstitially intergrown with coarse calcite, occasionally interstitial wollastonite and grossular within the calcite matrix; H15-4: andradite garnets, epidote, and polymetallic sulphides in metasomatic veins; foraminifera-rich limestone identifiable, no complete alteration to marble	strong	marble
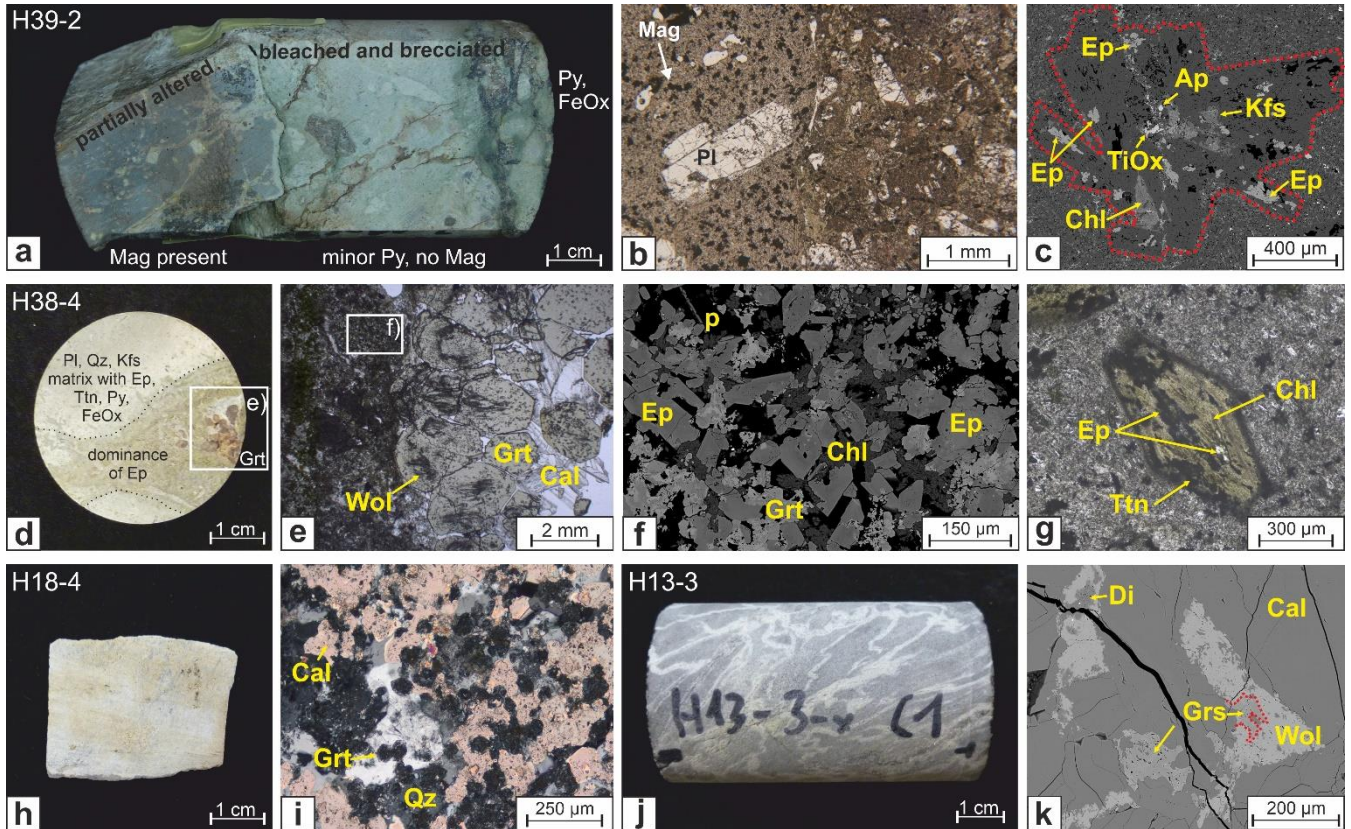
Figure 41: Scans and photographs of selected samples and corresponding thin sections (PPL = b, e, g, and XPL = i) and SEM images (c, f, k) representing (a to c) andesitic lava affected by propylitic alteration and silicification, (d to g) high-temperature propylitic alteration in a fracture of an andesitic lava, (h to i) skarn, and (j to k) marble. Abbreviations: Ap = apatite, Cal = calcite, Chl = chlorite, Di = diopside, Ep = epidote, FeOX = iron oxides, Grt = garnet, Grs = grossular garnet, Kfs = K-feldspar, Mag = magnetite, p = pores, Pl = plagioclase, Qz = quartz, Ttn=titanite, TiOx= titanium oxide, Wol = wollastonite.

5.4.2. Whole Rock Chemistry

The major, trace and rare earth elemental chemistry of studied samples is presented in Figs. 42, 43 and 44 as well as in Table D1. The outcrop samples show basaltic andesitic to dacitic composition (Fig. 42a) with a general calc-alkaline character (Rickwood, 1989). The SiO_2 content of the Teziutlán and Cuyoaco andesite units ranges from 53 to 62 wt% and from 61 to 65 wt%, respectively with Na_2O + K_2O ranging from 4.8 to 6.6 wt% and from 5.4 to 6.1 wt%, respectively. Likewise, the reservoir samples consist of varying SiO_2 concentrations ranging between ~ 52 wt% and ~ 77 wt% (basaltic to rhyolitic composition). Harker variation diagrams of selected major elements using SiO_2 wt% as differentiation index are shown in Fig.42b-i. Increasing SiO_2 concentrations are typically correlated with decreasing concentrations of CaO, MgO, Fe_2O_3, Al_2O_3, P_2O_5 and TiO_2 as well as increasing K_2O concentrations. In contrast, Na_2O vs. SiO_2 shows no distinct trend. Samples affected by advanced silicification and skarns show increased SiO_2 concentrations and plot in the same range as the rhyolitic lavas and Xáltipan ignimbrite (samples H19-1 and H26-1, respectively). Furthermore, they are characterized by lower Fe_2O_3, P_2O_5 and TiO_2 contents as well as highly variable CaO, MgO and Na_2O values. Similar compositional changes were observed for trace elements and REE (Figs. 43 and 44). Trace elements such as Nb, Sr and Zr and related ratios (e.g., Zr/Al_2O_3, Ti/1000, Sr/Nb and Nb/La) usually believed to be immobile and constant, respectively, during hydrothermal alteration (Winchester and Floyd, 1977; Floyd and Winchester, 1978; MacLean and Barrett, 1993; Carrasco-Núñez et al., 2017b; Pandarinath et al., 2020), show instead great variability and scattering.

Chondrite normalized (Sun and McDonough, 1989) spider diagrams for the REE are presented in Fig. 44. The studied andesitic lavas are characterized by fractionated patterns with LREE (light rare earth elements) enrichment and gently sloping profiles moving to HREE (heavy rare earth elements) with no evidence of Eu anomaly (Fig. 44a). Most of the analyzed Teziutlán andesites are characterized by higher REE concentrations compared to the Cuyoaco andesites. To note, a relevant number of samples from both Teziutlán and Cuyoaco andesites show a positive Sm anomaly. The reservoir samples are characterized by REE patterns overlapping with those of Teziutlán lavas. The rhyolite sample H19-1 and the shallow-depth cuttings from H20 and H43 boreholes show fractionated REE patterns with a well-developed Eu negative anomaly (Fig. 44b). A slight Ce positive anomaly is instead reported in samples H13-1, H18-1 and H39-1 characterized by a strong alteration overprint dominated by calcite-forming and collected between ~ 800 and 1200 m bgl from boreholes located in the southern sector of the geothermal field close to the Los Humeros-Maxtaloya lineament. Skarns and silicified samples are characterized by fractionated REE-patterns (Fig. 44c) showing LREE-enriched gently dipping profiles generally overlapping with both reservoir samples and outcropping Teziutlán and Cuyoaco andesites.
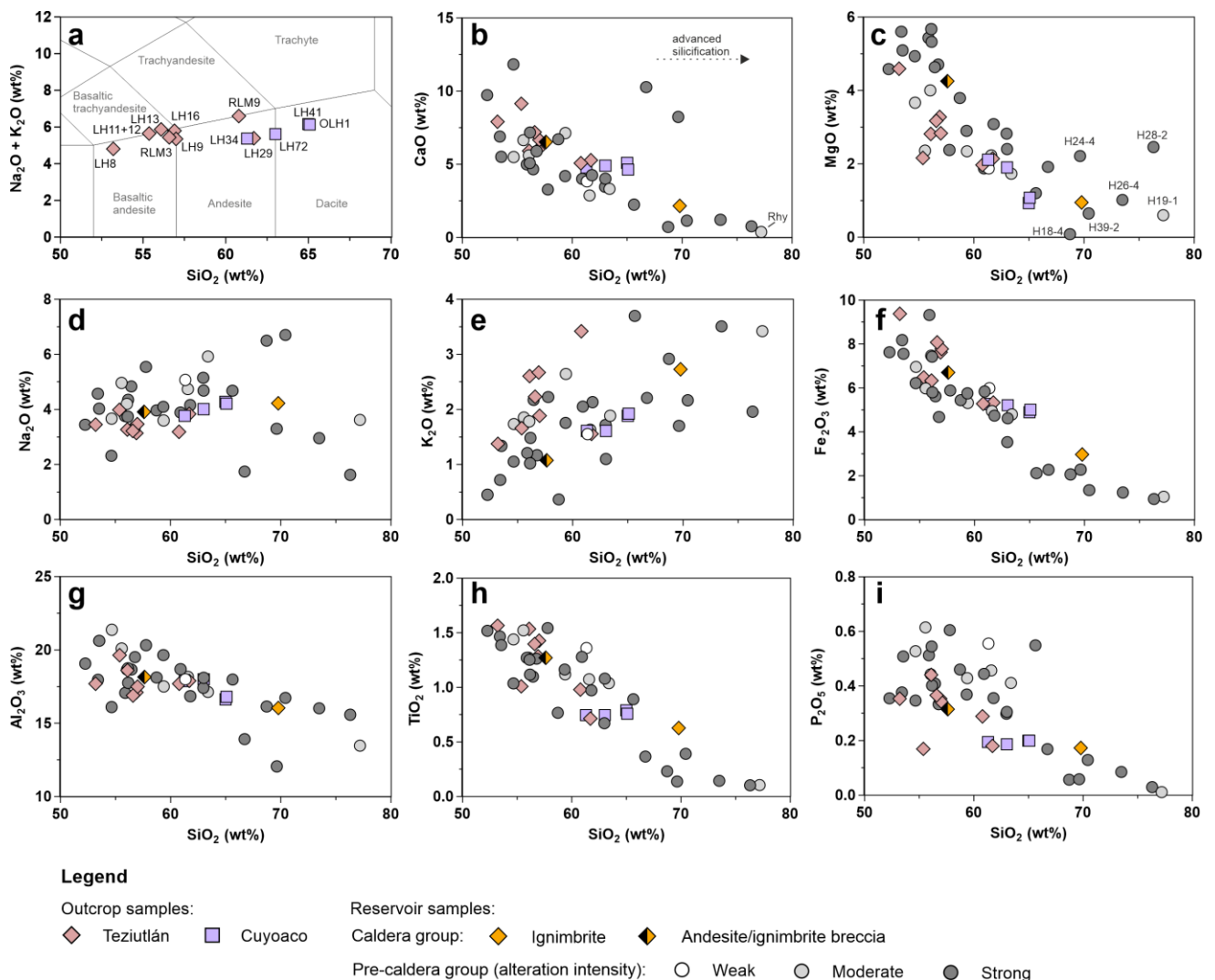
Figure 42: (a) Total alkali versus silica (TAS) diagram (Le Maitre et al., 2002) of the pre-caldera andesite outcrop samples. Selected major-element Harker diagrams of the outcrop and reservoir samples in (b) to (i). The pre-caldera reservoir samples were classified regarding their degree of hydrothermal alteration observed during petrographic analyses (weak, moderate, and strong).
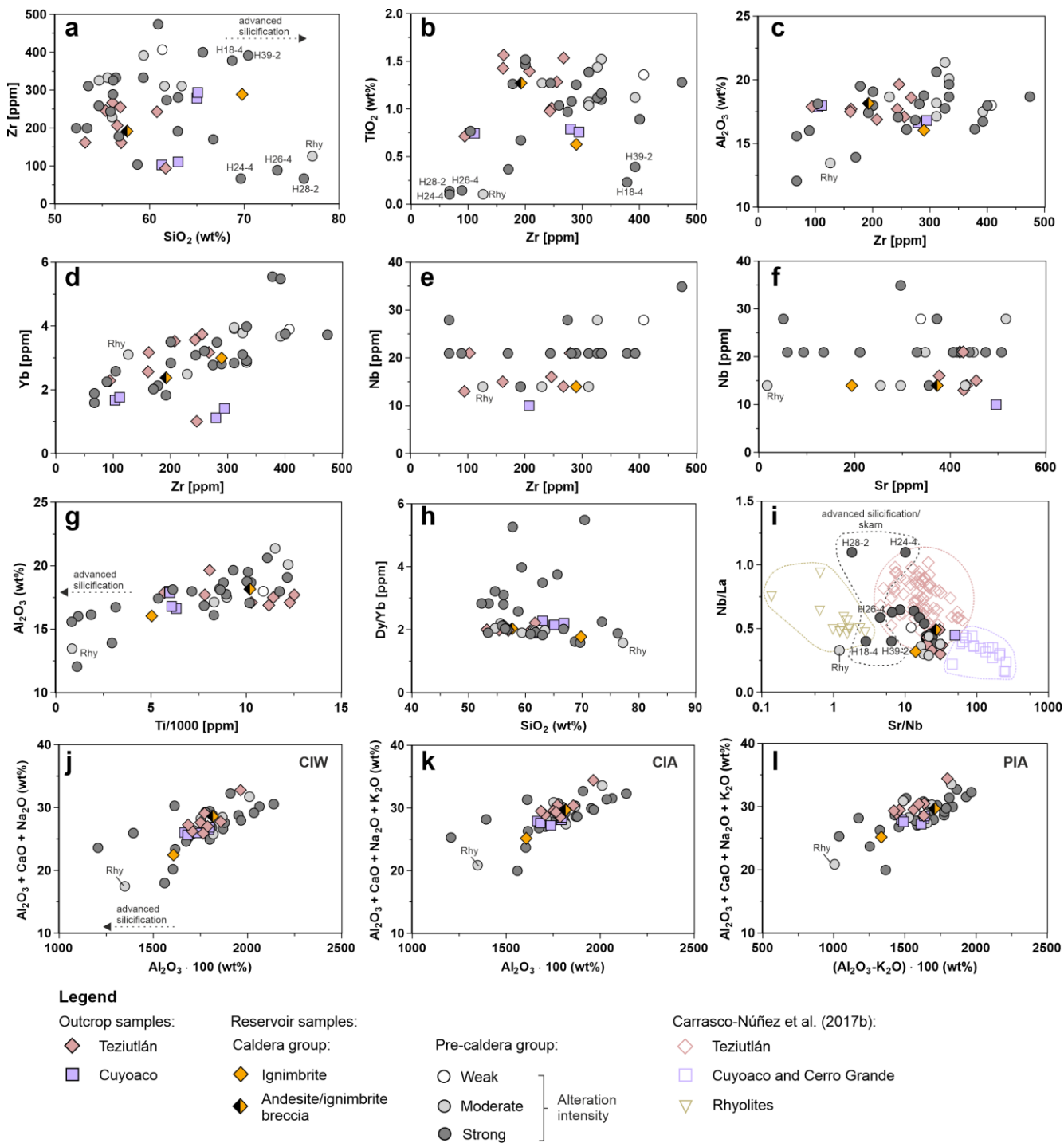
Figure 43: Selected REE and trace element concentrations of the reservoir and outcrop samples in (a) to (h). (i) Nb/La vs. Sr/Nb plot after Carrasco-Núñez et al. (2017b). Chemical indices such as (j) CIW, (k) CIA and (l) PIA were applied to investigate the relationship between the intensity of alteration and the physiochemical changes of the rocks.
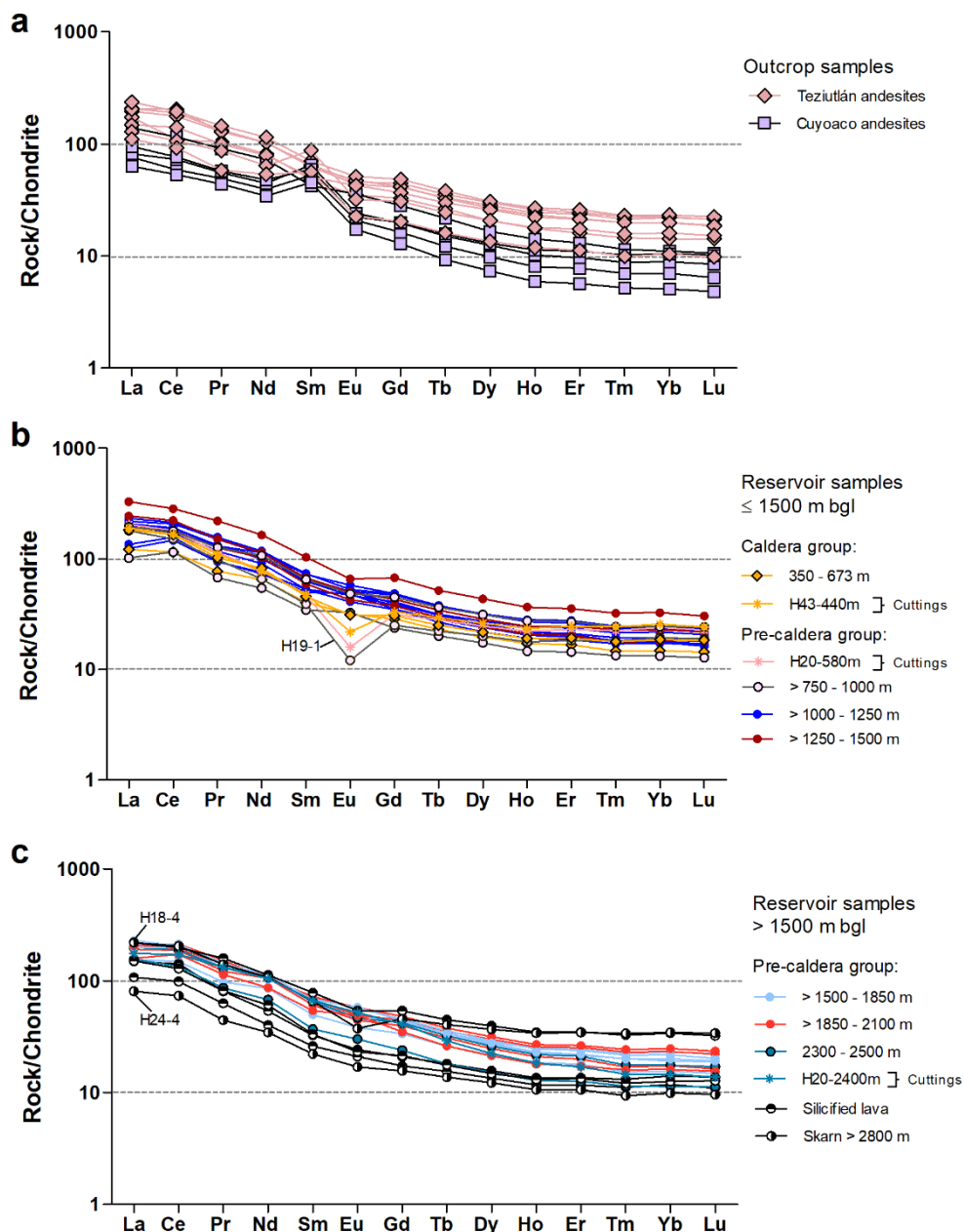
Figure 44: REE/Chondrite normalized values of (a) the outcrop and (b and c) reservoir samples after Sun and Mc Donough (1989).

The results of the chemical indices are presented in Table 9 and Table D2. In Table 9, the results of the reservoir core samples are classified with respect to their alteration facies and alteration intensity, respectively. Samples affected by strong silicification show increasing CIW, CIA, PIA and AI values, whereas skarns are again characterized by strongly variable CIW, CIA and PIA indices values. Both silicified andesites and skarns are characterized by decreasing CCPI values with respect to non-altered and analogue outcropping samples (Fig. 43).

Table 9: Chemical indices calculated for the outcrop and reservoir samples with respect to alteration facies and intensity

Group	CIW	CIA	PIA	CCPI	AI
Outcrop samples:					
Teziutlán andesites	64.0	59.3	61.0	47.4	33.5
Cuyoaco andesites	66.0	61.8	63.5	40.5	26.8
Alteration intensity (reservoir samples):					
Weak	65.2	62.2	63.4	47.3	30.8
Moderate	67.6	62.2	64.7	42.6	34.9
Strong	66.3	61.9	63.9	43.4	36.3
Alteration facies (reservoir samples):					
Argillic alteration	66.4	61.9	64.0	43.4	34.0
Propylitic alteration	66.0	62.7	64.1	49.0	35.6
Advanced silicification	71.9	64.4	68.6	34.0	42.2
Skarn	60.1	54.5	56.0	24.1	27.4

5.4.3. Petrophysical Properties

The results of the petrophysical measurements are presented in Figs. 45 to 46 and in Table 10. Particle densities of the outcrop and reservoir samples are within the same range and vary between 2.59 and 2.88 g cm^{-3} (Fig. 45e and f). Exceptions form the highly porous ignimbrites (2.43 g cm^{-3}) and sample H38-4 (2.99 g cm^{-3}), which comprises a high amount of calcite and large garnet crystals. Bulk densities of the outcrop samples range between 2.00 and 2.78 g cm^{-3} and bulk densities of the reservoir samples range between 1.63 and 2.78 g cm^{-3}, in ignimbrites and skarn, respectively. Thereby, bulk density is negatively correlated with porosity, and thus, is positively correlated with (i) thermal conductivity, (ii) thermal diffusivity and (iii) to a lesser extent with P-wave and S-wave velocities. While particle and bulk densities of the outcrop samples show location specific clusters (Fig. 45a and f), the reservoir samples show a higher degree of scattering without any clear lithological trends.

The Teziutlán and Cuyoaco andesites predominantly exhibit low matrix porosity (< 5%) and matrix permeability (< 10^{-17} m²), with these two parameters showing a very weak correlation trend (Fig. 46a). Thereby, fractures observed in some plugs result in increased permeability values of up to 10^{-13} m². The vesicular Teziutlán andesite lavas form the exception and show an increased matrix porosity ranging between 10 and 30%, along with permeability values ranging between 10^{-16} and 10^{-13} m². Compared to the outcrop samples, the reservoir samples show an increased average matrix porosity and permeability (~ 10^{-16} m², Fig. 46b). Matrix porosities of the basaltic andesitic to rhyolitic lavas vary between 5 and 25%. The ignimbrite samples show the highest porosity (~ 33%), but a comparably low matrix permeability (5·10^{-18} m²). The marbles show the opposite trend, exhibiting the highest matrix permeability (10^{-14} to 10^{-15} m²), but a very low matrix porosity of approximately 1%.

Thermal conductivity and thermal diffusivity of the outcrop samples varies between 0.69 and 1.87 W m^{-1} K^{-1} and 0.45 and 1.1·10^{-6} m² s^{-1}, respectively (Figs. 45a, C3). Both parameters are positively correlated (Fig. C3) and decrease with matrix porosity (Fig. 46e). Although the reservoir core samples exhibit a higher matrix porosity and permeability as well as lower bulk density, they show a significantly increased average thermal conductivity and diffusivity compared to the outcrop samples (Fig. 46d and f, Table 10). With 0.67 W m^{-1} K^{-1} the ignimbrites show the lowest thermal conductivity, while some skarns and silicified lavas exhibit increased thermal conductivities of up to 3.27 W m^{-1} K^{-1} (sample H28-2).

Under saturated conditions, thermal conductivity and thermal diffusivity of the reservoir samples increase by about 20% and 50% in average, respectively (Table 10, Fig. C3). For samples with low porosity (< 5%), saturated thermal conductivity and thermal diffusivity are consistent with measurements performed under dry conditions, while both parameters increase for samples with an intermediate to high porosity (10 to 33%) and/or permeability (e.g., brecciated or fractured lavas and ignimbrites). Likewise, saturated thermal conductivity and thermal diffusivity of the outcrop samples is on average ~ 13 and ~ 30% higher compared to the dry measurements showing a similar trend. However, the correlation of both parameters under saturated conditions shows significant degree of scatter (Fig. C3).

Specific heat capacity shows comparatively small variations throughout the dataset and ranges between 752 and 807 J kg^{-1} K^{-1}, whereby the ignimbrites, andesitic lavas and marbles from the reservoir cores show the highest values. The volumetric heat capacity is controlled by the respective bulk density of the samples. Therefore, the porous ignimbrite and ignimbrite-andesite breccias feature the lowest volumetric heat capacity and the marbles feature the highest volumetric heat capacity.

P-wave and S-wave velocity of the outcrop samples range between 1510 and 6276 m s^{-1} as well as 880 and 3730 m s^{-1}, respectively (Fig. 45c) and are positively correlated (Fig. C3). Thereby, samples that contain abundant fractures (e.g., RLM9, LH40-LH72), plot in the same range as the porous lavas (LH8-12). The sonic wave velocities are positively correlated with thermal conductivity, thermal diffusivity and density, but decrease with increasing porosity. Similar to the observations made for thermal conductivity, both parameters show no correlation with matrix permeability. Compared to the outcrop samples, the reservoir samples show slightly lower average P-wave and S-wave velocities (Table 10). It is notable that marbles and ignimbrites, which are usually plotting opposing to each other (Fig. 45b, Fig. 46b and f), feature sonic wave velocities in the same order of magnitude (Fig. 45d). This phenomenon is most likely caused due to the high porosity of these ignimbrite samples and the abundance of fractures observed on the marbles, which both reduce propagation of sound waves. Saturated P-wave and S-wave velocities increased by a factor of up to 1.35 and 1.1, respectively, compared to the measurements under dry conditions. Contrary to the thermal properties, they maintain a positive linear trend (Fig. C3).

Most of the outcrop samples feature magnetic susceptibilities between 2 and 16·10^{-3} SI. Only few lavas show reduced values of about 0.3 to 0.9·10^{-3} SI indicating weathering/alteration (Fig. 38j, Fig. 45e). Furthermore, the results indicate mineralogical differences between the sampling locations and units. On average, the Teziutlán andesites feature higher magnetic susceptibilities (3–16·10^{-3} SI) compared to the Cuyoaco andesites (2–4·10^{-3} SI, Table 10). Opposite, the reservoir samples show a wider range and a high variation. As shown in Fig. 45f, the samples can be grouped in two clusters. The first one comprises ignimbrite, breccias and lavas affected by argillic as well as propylitic alteration with a weak to strong alteration intensity. These samples exhibit magnetic susceptibilities from 1.5 up to 18.05·10^{-3} SI, whereby the ignimbrites and rhyolitic lavas contain lower values than the remaining lavas. The second population contains magnetic susceptibilities below 0.45 to 0.1·10^{-3} SI (below 0 in Fig. 45f) and comprises lavas and breccias with a predominantly strong hydrothermal overprint as well as marbles, skarns and silicified lavas. In general, limestones and quartz-rich rocks are known to show a diamagnetic behaviour (Hrouda et al., 2009). However, while the marbles from core H13-3 show negative values (diamagnetic), the other marbles show low, but positive values of about 0.01 to 0.63·10^{-3} SI (paramagnetic).
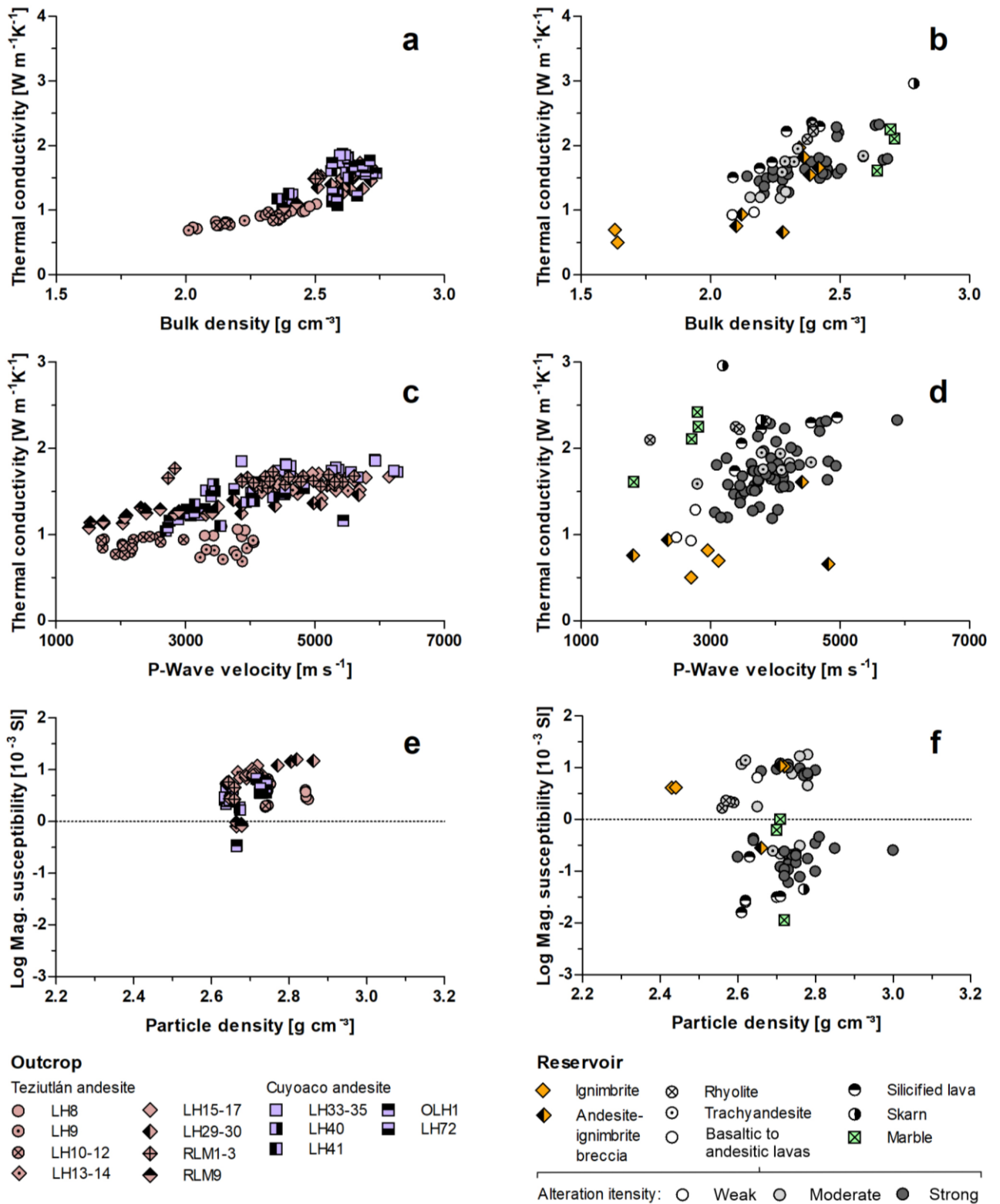
Figure 45: Correlation of density, P-wave velocity, magnetic susceptibility and thermal conductivity analyzed under dry conditions (for the number of analyzed plugs see Table 10).
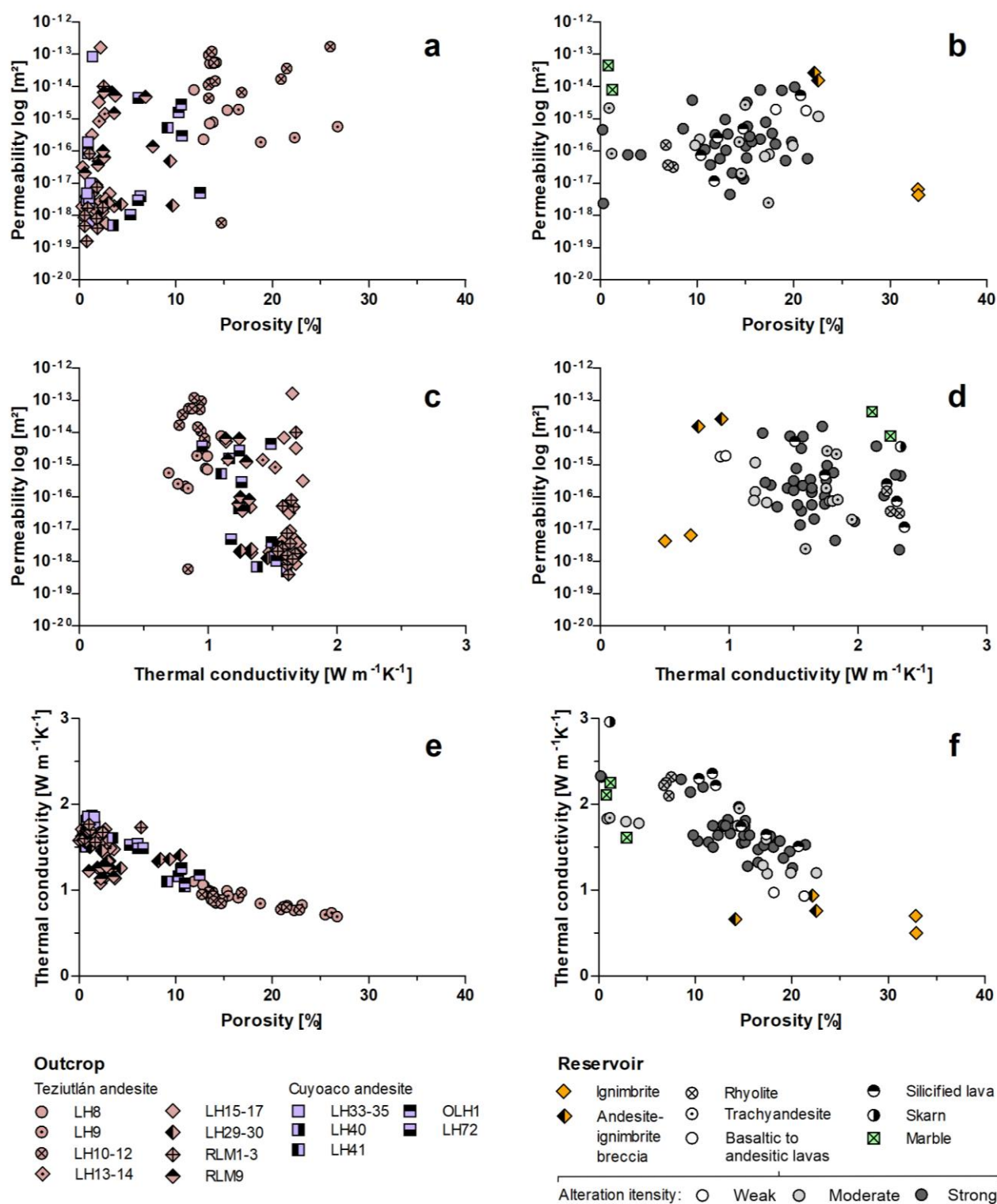
Figure 46: Correlation of permeability, porosity and thermal conductivity analyzed under dry conditions (for number of analyzed plugs see Table 10).

Table 10: Petrophysical rock properties of the outcropping andesite units and reservoir core samples of the Los Humeros geothermal field

Lithology	ρ_P [g cm^{-3}]	ρ_B [g cm^{-3}]	ϕ [%]	K [m²]	λ (dry) [W m^{-1} K^{-1}]	λ (sat) [W m^{-1} K^{-1}]	α (dry) [10^{-6} m² s^{-1}]	α (sat) [10^{-6} m² s^{-1}]
Outcrop samples								
Teziutlán andesites total	2.72/**2.72** (142) ± 0.06	2.53/**2.60** (131) ± 0.19	6.9/**2.7** (126) ± 7.3	1.0E-14/ **4.6E-17** (92) ± 3.1E-14	1.32/**1.35** (112) ± 0.32	1.50/**1.52** (112) ± 0.12	0.82/**0.86** (110) ± 0.15	1.10/**1.09** (110) ± 0.16
Teziutlán a. porous	2.76/**2.75** (37) ± 0.04	2.30/**2.35** (37) ± 0.15	16.9/**14.7** (37) ± 4.6	3.0E-14/**9.5E-15** (24) ± 4.4E-14	0.89/**0.90** (32) ± 0.10	1.47/**1.48** (32) ± 0.08	0.81/**0.74** (30) ± 0.24	1.00/**1.00** (32) ± 0.06
Teziutlán a. massive	2.71/**2.71** (105) ± 0.05	2.63/**2.65** (94) ± 0.10	2.7/**2.1** (89) ± 2.5	3.1E-15/**4.3E-18** (68) ± 2.0E-14	1.49/**1.56** (80) ± 0.18	1.52/**1.54** (80) ± 0.13	0.83/**0.86** (80) ± 0.10	1.14/**1.14** (78) ± 0.17
Cuyoaco andesites	2.64/**2.65** (50) ± 0.02	2.55/**2.61** (32) ± 0.10	4.0/**1.4** (32) ± 4.1	4.0E-15/ **5.1E-18** (26) ± 1.6E-14	1.46/**1.47** (47) ± 0.26	1.67/**1.63** (38) ± 0.21	0.84/**0.86** (48) ± 0.10	1.38/**1.38** (38) ± 0.18
Reservoir samples								
Ignimbrite	2.36/**2.43** (3) ± 0.14	1.64 (2) ± 0.01	32.9 (2) ± 0.01	5.3E-18 (2) ± 1.5E-18	0.67/**0.70** (3) ± 0.16	1.31/**1.37** (3) ± 0.22	0.48/**0.47** (3) ± 0.08	0.87/**0.86** (3) ± 0.13
Ignimbrite/andesite breccia	2.66/**2.69** (4) ± 0.08	2.17/**2.12** (3) ± 0.10	19.6/**22.1** (3) ± 4.7	1.4E-14/ **1.5E-14** (3) ± 1.3E-14	0.99/**0.85** (4) ± 0.43	1.41/**1.41** (4) ± 0.22	0.59/**0.63** (4) ± 0.19	0.91/**1.41** (38) ± 0.62
Rhyolite	2.58/**2.58** (4) ± 0.01	2.39/**2.40** (4) ± 0.01	7.1/**7.1** (4) ± 0.3	7.3E-17/ **3.6E-17** (3) ± 6.8E-17	2.22/**2.24** (4) ± 0.09	2.39/**2.45** (4) ± 0.16	1.23/**1.22** (4) ± 0.04	1.63/**1.66** (4) ± 0.12
Trachyandesite	2.69/**2.71** (9) ± 0.07	2.34/**2.31** (8) ± 0.16	13.22/**14.7** (8) ± 8.0	8.1E-16/ **1.7E-16** (8) ± 1.1E-15	1.67/**1.76** (9) ± 0.28	1.82/**1.86** (9) ± 0.11	0.93/**0.98** (9) ± 0.11	1.41/**1.48** (9) ± 0.29
Basaltic–andesitic lava	2.69/**2.72** (62) ± 0.11	2.36/**2.36** (39) ± 0.14	13.99/**15.1** (39) ± 4.9	1.4E-15/ **1.9E-16** (40) ± 3.2E-15	1.68/**1.68** (61) ± 0.32	1.97/**2.01** (61) ± 0.24	0.91/**0.91** (61) ± 0.15	1.40/**1.43** (61) ± 0.29
Silicified lava	2.64/**2.63** (9) ± 0.05	2.27/**2.27** (6) ± 0.12	14.5/**13.4** (6) ± 3.9	1.2E-15/ **2.5E-16** (5) ± 2.3E-15	2.08/**2.06** (9) ± 0.55	2.39/**2.48** (9) ± 0.53	1.15/**1.17** (9) ± 0.11	2.39/**2.48** (9) ± 0.53
Skarn	2.82 (2) ± 0.03	2.78 (1)	1.2 (1)	3.6E-15 (1)	2.65 (2) ± 0.45	2.87 (2) ± 0.51	2.36 (2) ± 1.48	1.78 (2) ± 0.31
Marble	2.72/**2.73** (6) ± 0.01	2.67/**2.67** (4) ± 0.04	1.9/**1.9** (4) ± 0.9	2.6E-14 (2) ± 2.6E-14	2.10/**2.18** (4) ± 0.35	2.80/**2.86** (4) ± 0.38	1.10/**1.11** (4) ± 0.13	1.88/**1.90** (4) ± 0.37

arithmetic mean values in normal font, the numbers in bold represent the median, ± = standard deviation, () = number of analyzed plugs, ρ_P = particle density, ρ_B = bulk density, ϕ = porosity, K = permeability, λ = thermal conductivity, α = thermal diffusivity, (dry) or (sat) = analyzed at dry or saturated conditions; for sample classifications refer to tables C1 and C2.

Table 10 continuation: Petrophysical rock properties of the outcropping andesite units and reservoir core samples of the Los Humeros geothermal field

Lithology	cp [J kg^{-1} K^{-1}]	VHC [J m³ K^{-1}]	V_P (dry) [m s^{-1}]	V_P (sat) [m s^{-1}]	V_S (dry) [m s^{-1}]	V_S (sat) [m s^{-1}]	X [10^{-3} SI]
Outcrop samples							
Teziutlán andesites total	765/**766** (14) ± 40	1963/**2044** (15) ± 148	3787/**3879** (138) ± 1204	5341/**5425** (117) ± 1022	2200/**2286** (132) ± 683	3168/**3213** (114) ± 619	6.10/**5.70** (80) ± 2.85
Teziutlán a. porous	772/**774** (5) ± 27	1767/**1761** (4) ± 59	2863/**2972** (37) ± 826	4908/**5196** (28) ± 799	1667/**1762** (37) ± 474	2889/**3009** (28) ± 523	4.11/**4.11** (25) ± 1.55
Teziutlán a. massive	762/**765** (10) ± 46	2035/**2044** (11) ± 92	4125/**4384** (101) ± 1145	5476/**5556** (89) ± 1050	2407/**2561** (95) ± 639	3259/**3285** (86) ± 622	7.00/**6.52** (55) ± 2.86
Cuyoaco andesites	752/**744** (7) ± 26	1941/**1924** (7) ± 127	4142/**4029** (48) ± 1039	5280/**4893** (37) ± 1314	2457/**2377** (48) ± 602	3083/**2972** (37) ± 775	2.37/**2.47** (23) ± 1.27
Reservoir samples							
Ignimbrite	795 (1)	1272 (1)	2925/**2955** (3) ± 214	2875/**2842** (3) ± 119	1642/**1727** (3) ± 185	1665/**1691** (3) ± 87	4.15 (2) ± 0.03
Ignimbrite/andesite breccia	769 (2) ± 17	1685 (2) ± 136	3345/**3379** (4) ± 1495	4140/**3575** (3) ± 1102	2007/**1982** (4) ± 1026	2122/**1934** (3) ± 540	7.31/**10.68** (3) ± 6.08
Rhyolite	-	-	3188/**3418** (4) ± 775	4821/**4856** (4) ± 811	1723/**1865** (4) ± 337	2549/**2473** (4) ± 514	2.09/**2.18** (4) ± 0.29
Trachyandesite	755/**745** (3) ± 23	1758/**1726** (3) ± 67	3750/**3812** (9) ± 570	4173/**3876** (9) ± 923	2061/**2053** (9) ± 261	2405/**2239** (9) ± 483	4.46/**0.23** (6) ± 6.61
Basaltic–andesitic lava	791/**783** (21) ± 39	1867/**1856** (21) ± 198	3854/**3836** (60) ± 571	4126/**4017** (61) ± 700	2148/**2145** (60) ± 312	2304/**2200** (61) ± 416	3.40/**0.27** (40) ± 4.69
Silicified lava	776/**776** (4) ± 5.4	1823/**1824** (4) ± 93	3933/**3777** (7) ± 605	4128/**4251** (7) ± 545	2060/**2029** (7) ± 313	2331/**2360** (7) ± 339	0.29/**0.03** (7) ± 0.66
Skarn	762 (2) ± 9.8	1966 (2) ± 242	3483 (2) ± 416	3022 (2) ± 1427	1677 (2) ± 16	1659 (2) ± 827	0.045 (1)
Marble	807/**808** (3) ± 3.3	2146/**2134** (3) ± 35	2616/**2797** (5) ± 459	4189/**4555** (5) ± 1005	1490/**1549** (5) ± 206	2265/**2634** (5) ± 634	0.12/**0.008** (5) ± 0.28

arithmetic mean values in normal font, the numbers in bold represent the median, ± = standard deviation, () = number of analyzed plugs, V_P = P-wave velocity, V_S = S-wave velocity, cp = specific heat capacity, VHC = volumetric heat capacity, X = magnetic susceptibility, (dry) or (sat) = analyzed at dry or saturated conditions; for sample classifications refer to tables C1 and C2.
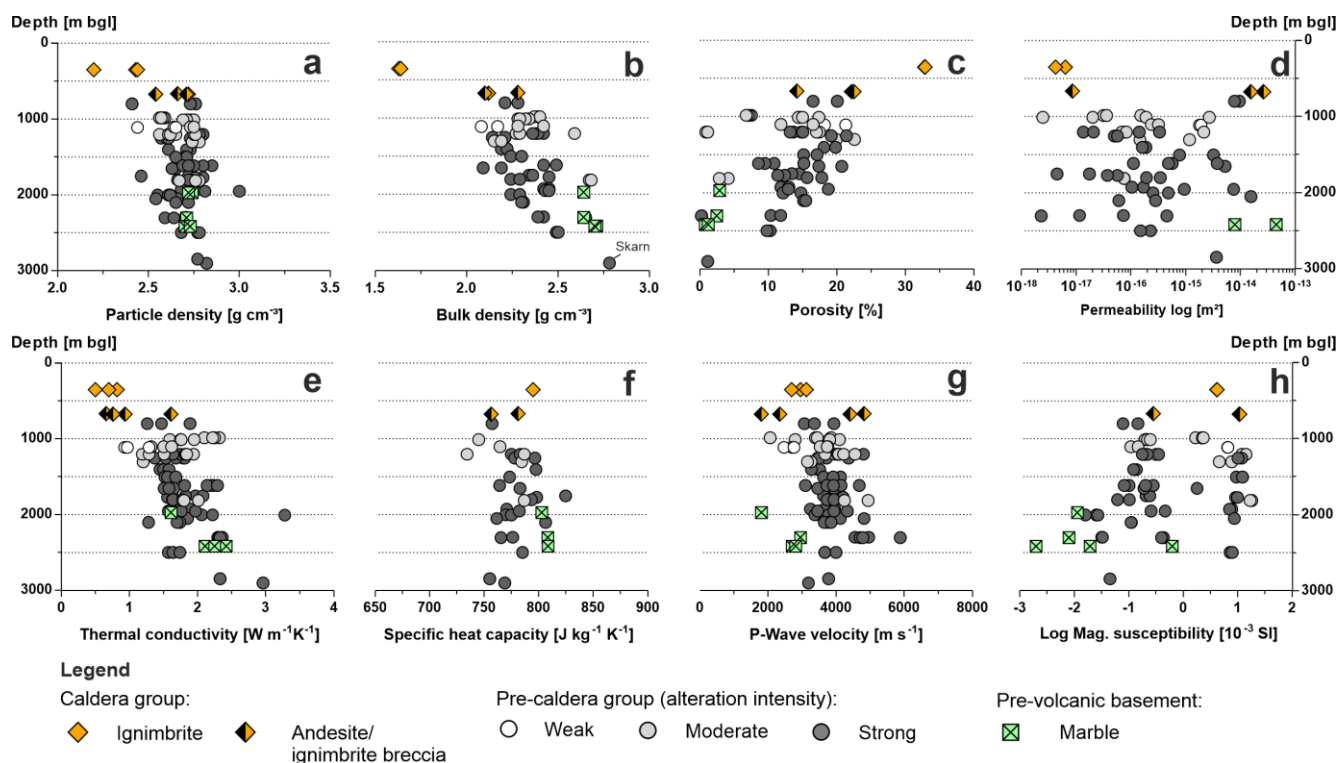
Figure 47: Selected rock properties of the reservoir samples plotted against reservoir depth. The pre-caldera lavas were classified with respect to their degree of hydrothermal alteration (weak, moderate and strong).

Particle and bulk density, thermal conductivity and diffusivity as well as volumetric heat capacity gradually increase with reservoir depth (Fig. 47; from top to base particle density: 2.2 to 2.82 g cm^{-3}, bulk density: 1.62 to 2.78 g cm^{-3}, thermal conductivity: 0.5 to 2.96 W m^{-1} K^{-1}, and VHC: 1272 to 2146 J m^3 K^{-1}). Likewise, sonic wave velocity increases with reservoir depth, but shows a higher variation in the shallow and deep reservoir sections. Since porosity is negatively correlated with the aforementioned parameters, it gradually decreases with reservoir depth from > 30% to ~ 1% (Fig. 47c). However, low porosity lavas (< 5%) occur at several depth levels. Matrix permeability, specific heat capacity, and magnetic susceptibility indicate no correlation with reservoir depth. Particularly, matrix permeability and magnetic susceptibility show a high variability at all depth levels.

A classification with respect to alteration facies or chemical indices does not reveal any clear relationships between the different investigated parameters (Fig. 48). In general, propylitic alteration seems to cause more homogeneous rock petrophysical properties than argillic alteration (Fig. 48a to d) when compared to outcrop samples (Figs. 45 and 46). The chemical indices again show no relevant correlation with the investigated parameters (Fig. 48e and f).
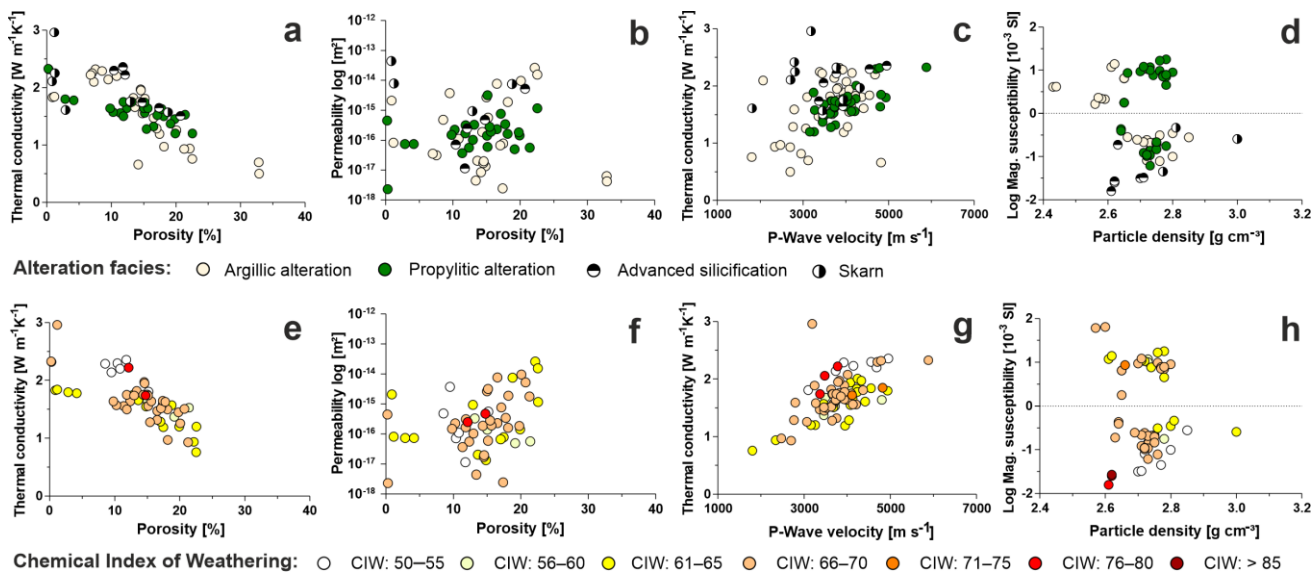
Figure 48: Cross plots of matrix permeability, porosity, P-wave velocity, magnetic susceptibility and thermal conductivity analyzed on the reservoir samples with respect to their alteration facies in (a) to (d) and the chemical index of weathering (CIW, here excluding marbles and ignimbrites) in (e) to (h).

5.5. Discussion

5.5.1. Petrography and Hydrothermal Alteration

The investigated Teziutlán andesite unit comprises a suite of different basaltic andesitic to andesitic, porphyritic, massive and minor porous lavas with a dark grey to medium grey colour. The Cuyoaco andesite unit comprises grey to slightly reddish-violet, porphyritic, massive and often fractured lavas with andesitic to dacitic composition, in agreement with the description of the Alseseca/Cuyoaco andesites presented in Yáñez and García (1982) and Carrasco-Núñez et al. (1997). However, the Cuyoaco andesite unit is generally classified as the 'Hornblende-andesite' in literature (Viggiano and Robles, 1988a, 1988b; Cedillo, 1997, 2000; Arellano et al., 2003). Except for sample LH51 (Fig. 38), hornblende was not identified in the studied samples.

Hydrothermal alteration observed on the reservoir samples is often restricted to fractures and varies on the cm-scale, which leads to high heterogeneity in terms of sample appearance, chemical composition and rock properties. Consequently, each collected sample has unique features and it is challenging to correlate between individual boreholes.

In previous studies, the reservoir samples retrieved from the shallower reservoir were classified as (Teziutlán) augite andesites (Cedillo, 2000; Arellano et al., 2003). The reservoir samples retrieved from shallow to intermediate depth levels (~ 350–1400 m bgl) consist of different, very heterogenous and often fractured mafic, trachyandesitic, andesitic and rhyolitic lavas as well as andesite/ignimbrite breccias and ignimbrites. The samples are mainly affected by argillic to propylitic alteration with alteration intensities varying from weak to strong. These ignimbrites and ignimbrite/andesite breccias belong to the caldera group and are commonly interpreted as the cap rock of the geothermal reservoir (Cedillo, 2000; Arellano et al., 2003).

Samples retrieved between 1500 and ~ 2500 m bgl consist of strongly altered often fractured or brecciated basaltic to andesitic lavas. Propylitic alteration with epidote, chlorite, K-feldspar, calcite and quartz is dominant in these samples. According to González-Partida et al. (2022) deeper samples with predominantly clinozoisite, epidote, chlorite, along with smectite/illite, magnetite, biotite, sericite, pyrite, chalcopyrite, quartz and calcite represent high-temperature propylitic alteration (~ 250–> 350°C). The deepest samples collected in this study comprise skarns (> 2800 m bgl). Both, skarns and marbles,

contain numerous fractures mainly filled with calcite and often contain high-temperature minerals such as garnet, diopside, apatite and/or wollastonite. However, high-temperature alteration minerals such as garnet, diopside, and wollastonite were also observed at shallower depth levels as shown in fracture fillings of sample H38-4 (1950 m) in the central to northern zones of the geothermal field (also referred to as the central collapse area). This observation is well in line with findings from (i) Martínez-Serrano (2002), who defined the beginning of a skarn zone at about 1800 m depth in the central collapse area, (ii) Jentsch et al. (2020), who reported the highest temperature anomalies at Loma Blanca within the central collapse area, as well as (iii) Urbani et al., (2021), who discussed existing borehole-temperature profiles in the same area. However, our findings show that high-temperature secondary mineral assemblages are not limited to the central collapse area as previously described in Prol-Ledesma and Browne (1989).

Advanced silicification along with a significant transformation of the phenocrysts and groundmass was observed at different depth levels and boreholes in the reservoir. González-Partida et al. (2022) defined a deep-seated silicic or high-temperature argillic alteration zone that occurs below ~ 2500 m depth (> 350 °C) with mainly quartz, but also anhydrite, pyrophyllite, dickite and white mica. However, partial or complete silicification might also occur at shallower depth levels as observed in sample H39-2 (1650 m bgl, Fig. 40). Silicification and the generally elevated amounts of quartz at all depths could be related to deep acidic supercritical fluids with high HCL, HF and B concentrations with pH < 4 (Prol-Ledesma, 1998; Flores-Armenta et al., 2010; Izquíerdo et al., 2011). Further sources of acidic fluids might be shallow intrusions (degassing of supercritical fluids), temperature/pressure changes, boiling or reactivation of fractures (González-Partida et al., 2022). We interpret silicification at shallower depth levels within the propylitic alteration zone as well as the local occurrence of high-temperature minerals at different depth levels as possible evidence of shallow intrusions, in agreement with the shallowest geometry of the Los Humeros post-caldera stage magmatic plumbing system (Lucci et al., 2020) and with the results from field-constrained analogue modelling proposed by Urbani et al., (2020, 2021). Shallow cryptodomes (e.g., Urbani et al., 2020) and/or magma pockets (Lucci et al., 2020) could be also responsible for thermal metamorphism in limestones and lavas that locally underwent transformation to marble, hornfels and skarn, respectively. Furthermore, the occurrence of low and high-temperature alteration minerals at the same depth or even within one sample (Martínez-Serrano, 2002; Prol-Ledesma, 1998), plus the high variability of alteration facies and intensity in the upper section of the pre-caldera group, points to the possibility of several heterogenous heat sources. This observation is well in line with temperature profiles and modeling of shallow magma pockets as presented in Deb et al. (2021), Lucci et al. (2020), Urbani et al. (2020, 2021), and Bonini et al. (2021). For example, Deb et al. (2021) predicts the occurrence of a mafic magma pocket in the central collapse area (close to well H3) at approximately 1.5 km depth and larger mafic to trachyandesitic magma pockets close to the Xalapazco crater and well H18 at about 2.5–3 km depth. Thereby, associated mineral assemblages dominated by quartz form in close vicinity of the intrusions (Heřmanská et al., 2019) often causing a sealing effect (Martínez-Serrano, 2002; González-Partida et al., 2022).

The temporal evolution of the different hydrothermal processes was not investigated in this study but is described for selected samples in Rochelle et al. (2021) and is discussed in González-Partida et al. (2022). Martínez-Serrano (2002) and Prol-Ledesma (1998) proposed at least two different stages of hydrothermal activity due to the coexistence of high- and low-temperature minerals at shallow depths (high-temperature hydrothermal activity followed by a low-temperature stage), which was most likely caused by permeability changes in the reservoir and reactivation of faults and fracturing over time. González-Partida et al. (2022) described preferential fluid pathways with different fluid sources which might have significantly shifted over time in some areas of the reservoir. However, fragments of altered lavas, marble and skarn found in some andesitic lavas and in the Xáltipan ignimbrite suggest that hydrothermal alteration of the deeper reservoir, skarn-metasomatism as well as marble-contact

metamorphism already existed prior to the collapse of the Los Humeros caldera and has been influenced since then by the volcanic activity of the caldera and post-caldera group. Multiple temporal and spatial alteration events could explain the high variability in terms of sample appearance, alteration intensity, alteration facies and changes in chemical composition in our sample set.

Contrary to previous studies (Cedillo, 2000; Arellano et al., 2003), a thick tuff layer, which separates the pre-caldera andesites within the reservoir into an upper and lower andesite unit was not identified. In these previous works, the deeper andesite sections were interpreted as equivalent to the Cuyoaco andesites and described as 'Hornblende andesites'. Besides a few remnants of possibly amphibole in two samples, we could not identify hornblende in the reservoir samples. However, despite a few studies and short reports from the early exploration phase of the Los Humeros geothermal field in the late 70's and early 80's (e.g., Yáñez and García, 1982; Ferriz, 1982; Ferriz and Mahood, 1984), not much attention was paid to the pre-caldera andesites in the study area. Further detailed petrological investigations and dating are needed to better understand their temporal and spatial evolution.

5.5.2. Bulk Geochemistry

The reservoir samples are characterized by significant compositional variations compared to the outcropping Teziutlán andesites (Table D4). Calculated compositional variations for the different facies of hydrothermal alteration are shown in Fig. 49a. The SiO_2 content shows variations of (i) ± 5% in samples affected by argillic and propylitic alteration and (ii) up to + 33% in samples that underwent advanced silicification. All the studied reservoir samples are characterized by a strong enrichment in Fe_2O_3. In general, the reservoir samples are characterized by highly variable trends, from enrichment to depletion, of the other major and trace element contents (Table D4).

Different widely used chemical indices were then tested (Table 9, Figs. 40, 41 and 48) to search possible relationships between bulk compositional changes and petrophysical properties. In contrast with the existing literature (e.g., Pola et al., 2012; Lee et al., 2021) the applied chemical indices seem to not correlate with the observed degree of hydrothermal alteration. With respect to studied reservoir rocks: (i) the CIW, CIA, PIA and AI indices are not discriminant between argillic and propylitic alteration facies, (ii) the CCPI index is lowered for argillic alteration while increased for propylitic alteration, (iii) pervasive silicification is characterized by higher CIW, CIA, PIA and AI and lower CCPI values, and (iv) skarns are characterized by lower values for all the applied indices.

When the REE budget is investigated it is possible to observe that the outcropping Teziutlán and Cuyoaco andesite units show comparable fractionated REE patterns with LREE-enrichment and gently sloping profiles with Teziutlán andesites generally slightly higher in REE contents than those of Cuyoaco andesites. To note, many samples from both Teziutlán and Cuyoaco andesite units are characterized by a significative Sm_N positive anomaly (chondrite-normalized) that can be interpreted as the response of localized interactions with carbonatic groundwaters (Johannesson and Xiaoping, 1997) or with carbonatic weathering materials (Savichev and Vodyanitskii, 2011) such as the underlying Mesozoic limestones.

The studied reservoir samples show comparable fractionated REE profiles to those of the Teziutlán andesites except for some samples characterized by argillic and propylitic alterations and showing a Ce_N positive anomaly (Fig. 44, Table C1). Existing literature (e.g., Braun et al., 1993; Jayananda et al., 2016) have widely demonstrated that Ce anomalies are the consequence of oxidation processes of Ce+3 to Ce+4 and following precipitation of the latter one in CeO_2, with negative anomalies related to removal of Ce by fluids and positive anomalies related to (i) Ce precipitation from the fluid phase in oxidizing conditions (Jayananda et al., 2016) or (ii) formation of Ce-bearing secondary minerals (Fodor et al., 1994).

Few reservoir samples such as the rhyolite H19-1 and the shallow-depth cutting from H20 and H43 wells show a well-developed Eu negative anomaly (Fig. 44b, 49b), that is typical of differentiated felsic magmas (e.g., Lucci et al., 2018). Similar to the observation from Carrasco-Núñez et al. (2017b), the Eu anomaly combined with Ti/SiO_2 ratio allows to discriminate the rhyolites from the andesites and from skarns and silicified lavas (Fig. 49d).

A cross-correlation analysis of the REE budget (Table D3) revealed linear trends for the HREE (r = 0.90–0.99) and to a lesser extent for the LREE (r = 0.77–0.99) suggesting a general immobile behaviour of the HREE and a possible minor mobility of LREE during hydrothermal alteration, in agreement with the work of Whitford et al. (1988) and Morgan and Wandless (1980).

Studies on compositional changes during hydrothermal processes indicate that elemental mobility could change under different alteration conditions and are strongly dependent by reservoir conditions and original unaltered protolith (Yongliang and Yusheng, 1991). In Los Azufres geothermal field (Mexico), Torres-Alvarado et al. (2010) documented basaltic material at depth of ca. 2700 m affected by propylitic alteration and silicification and characterized by relevant loss of all major elements, and also of Nb, Zr, Hf, P, Th and REE. Opposite, Pandarinath et al. (2008), working on shallower (< 450 m depth) rhyolites from the same geothermal field documented a general immobile REE-behavior. Moreover, Pandarinath et al. (2020) again documented inert behaviour of REE in intensively and hydrothermally altered (i.e., argillic and silicic alteration) outcropping dacitic lavas from the Acoculco geothermal field (Mexico). During the last half century, it was proposed that (i) REE behave highly selective in different alteration facies (e.g., Paraspoor et al., 2009), that (ii) epidote s.l. could play a relevant role in reallocating and controlling REE concentrations (e.g., Palacios et al., 1986; Torres-Alvarado et al., 2010), (iii) and important REE-loss during alteration dominated by a single SiO_2 phase such as opaline silica and quartz (e.g., Hopf, 1993), and REE-mobility controlled by REE-concentration in reservoir fluids and the concomitant availability of complexing ions such as CO_3^{2-}, F^-, PO_4^{3-} and in acidic conditions Cl^-, SO_4^{2-} (Hikov, 2011, Yongliang and Yusheng, 1991).

However, the here-developed statistical analysis showed no significant differences between the reservoir samples and the Teziutlán andesites (see Kruskal-Wallis tests in Table D5), confirming the main accepted immobile behaviour of REE and their capability to maintain the signature of the unaltered/unmetamorphosed magmatic precursor (e.g., Buchs et al., 2013; Rossetti et al., 2017). In this view, the REE-budget variations in the reservoir samples can therefore be interpreted as compositional heterogeneities of the volcanic material. Further detailed investigations integrating the quantification of REE contents in the reservoir fluids and in primary and secondary mineral phases are therefore required to fully understand the elemental mobility during hydrothermal alteration in active geothermal settings.

To conclude, a general elemental mobility was identified for the reservoir samples making unlikely the application of classic discrimination methods (e.g., Graf, 1977; MacGeehan et al., 1980; Winchester and Floyd, 1977; Floyd and Winchester, 1978; Cullers and Graf, 1984; Rollinson, 1993; McLean and Barrett, 1993). Furthermore, also the Nb/La vs. Sr/Nb method proposed by Carrasco-Núñez et al. (2017b) appears unrealistic plotting silicified lavas and skarns in the field of rhyolites. However, a statistical analysis shows significative differences in REE contents between the reservoir samples and the Cuyoaco andesites (Fig. 49c; see Kruskal-Wallis tests in Table D5). Furthermore, integrating the sample depth and considering that shallow samples generally show ∑HREE ~ 15, the majority of the investigated reservoir core samples can be assigned to the Teziutlán andesites.
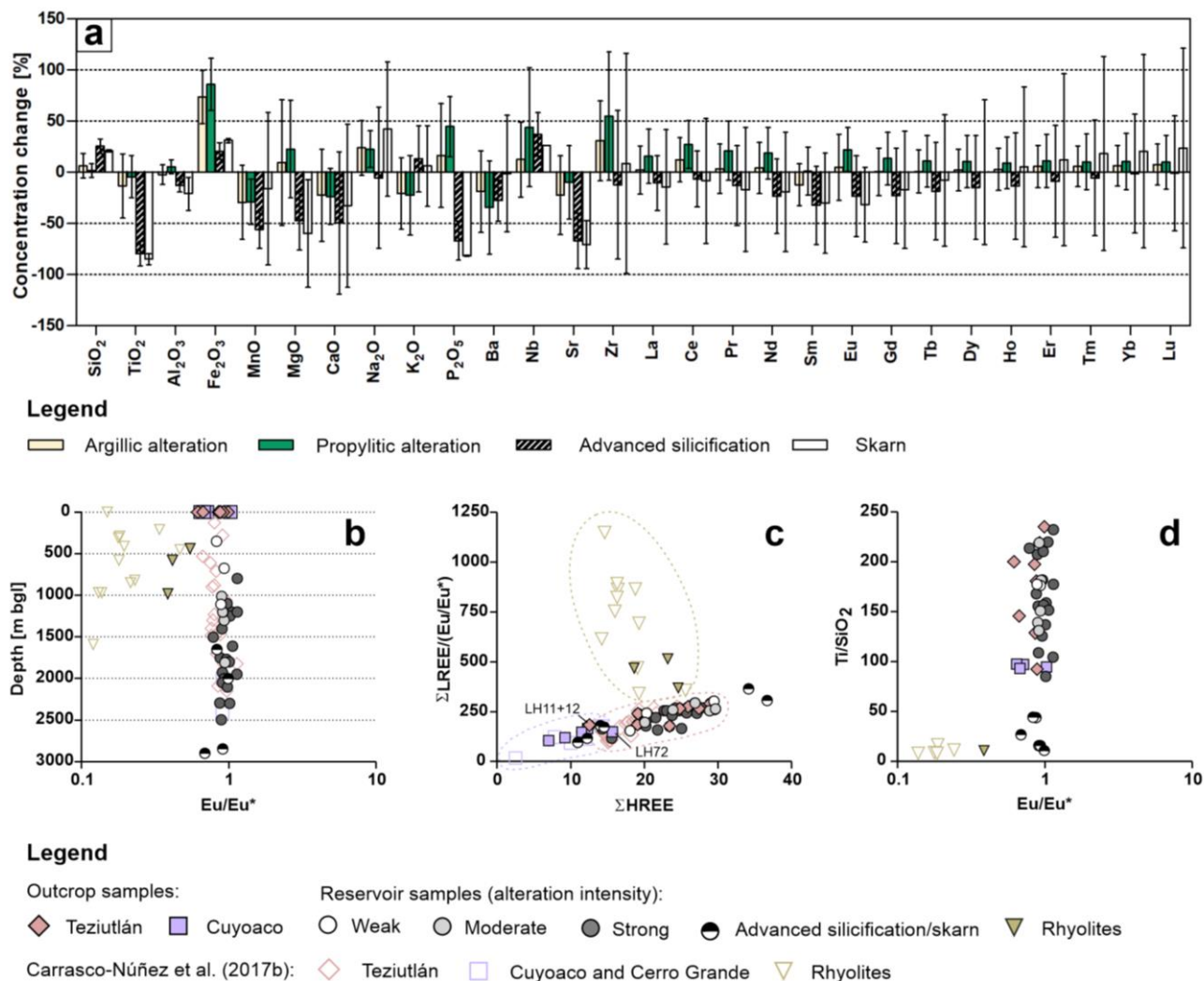
Figure 49: (a) Calculated concentration changes and standard deviation for major, trace, and rare earth elements with respect to the different alteration facies. The concentration changes were calculated using the average chemical composition of the Teziutlán andesite unit. (b) Plot depth vs. Eu/Eu* after Carrasco-Núñez et al. (2017b) and plot ∑LREE/(Eu/Eu*) vs. ∑HREE showing clearly lower Eu/Eu* ratios for the rhyolitic lavas. (d) Plot Ti/SiO₂ vs. Eu/Eu* showing different groups for rhyolites, silicified samples and the remaining lavas of the pre-caldera group.

5.5.3. Petrophysical Properties – Outcrop vs. Reservoir Samples

The petrophysical data reflect the geological heterogeneity and the impact of hydrothermal alteration observed on the reservoir samples, but also minor mineralogical differences between the outcrop samples as well as the influence of fractures. Comparison of both reservoir and outcrop samples reveals significant changes in the petrophysical characteristics.

Most of the lavas collected in the outcrops are characterized by an overall low average matrix porosity (< 4%) and matrix permeability (< 10^{-18} m² to 10^{-16} m²) as well as an intermediate thermal conductivity (~ 1.48 W m^{-1} K^{-1}), thermal diffusivity (~ 0.84 10^{-6} m² s^{-1}), and sonic wave velocities (V_P: ~ 5400 m s^{-1}, V_S: ~ 2450 m s^{-1}). The weak correlation between matrix porosity and permeability implies that fluid flow is predominantly fracture-controlled, which has been confirmed by Lelli et al. (2021). The vesicular lavas of the Teziutlán andesite unit collected north and northeast of the Los Humeros caldera feature higher matrix porosities (~ 15%) and permeabilities (10^{-16} m² to 10^{-14} m²), but overall lower bulk densities, thermal conductivities and sonic wave velocities. Specific heat capacity shows no distinct differences,

while magnetic susceptibility shows a high variability and reveals mineralogical differences between the sampling locations.

In contrast to the outcrop samples, the reservoir samples show a higher parameter range and scattering (e.g., porosity: < 2% to > 30%, permeability: 10^{-18} m² to 10^{-14} m², and thermal conductivity: 0.7 W m^{-1} K^{-1} to 2.7 W m^{-1} K^{-1}). Results of the marbles and ignimbrites are well in line with measurements performed on outcrop samples collected from the Xáltipan ignimbrite and marbles from Las Minas (Weydt et al., 2022a). However, the ignimbrite core samples investigated in this study only represent the unwelded to partially welded upper section of the Xáltipan ignimbrite. According to Cavazos-Álvarez et al. (2020), the Xáltipan ignimbrite shows an increased degree of welding with reservoir depth alongside a porosity reduction. Therefore, porosity of the highly welded basal sections can be smaller than < 5% (Weydt et al., 2022a; Cavazos-Álvarez et al., 2020).

Taking only the lavas of the pre-caldera group into account, the reservoir samples show an increased average matrix porosity, permeability, thermal conductivity, thermal diffusivity, heat capacity and thus enhanced reservoir quality, but reduced average sonic wave velocities and magnetic susceptibility (Table 10, Fig. 50). However, both datasets reveal a bi- to multimodal distribution for the majority of parameters investigated (Fig. 50). A distinct shift in the density functions can be observed for bulk density, porosity, permeability, magnetic susceptibility and to a lesser extent for thermal diffusivity and thermal conductivity.
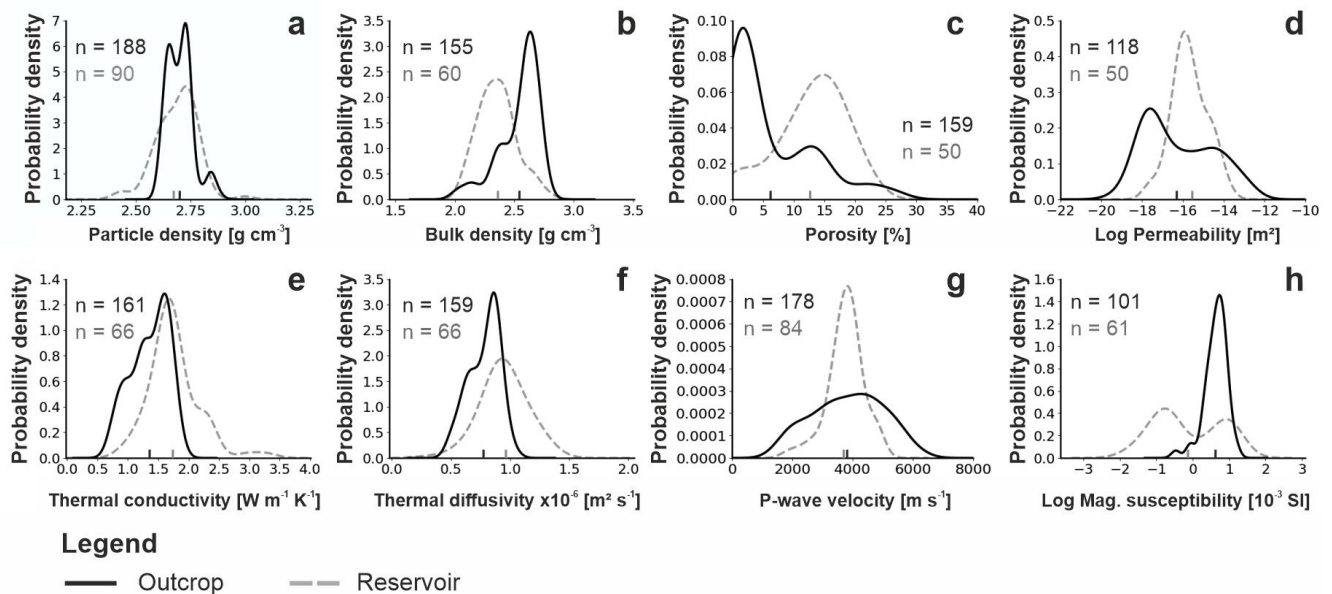
Figure 50: Kernel probability density functions of selected properties of the pre-caldera outcrop samples (black line) and reservoir samples (grey dashed line; excluding marbles and ignimbrites). N = number of analyzed plugs, vertical lines = mean value.

Results from sonic well logging (well H42) conducted within the Los Humeros geothermal field show a similar porosity distribution for the andesitic lavas than the outcrop samples (Deb et al., 2019d) with two distinctive groups: massive lavas with porosities < 5% and porous/fractured lavas with porosities ranging from ~ 10 to 30%. Thereby, the average porosity of the logged interval is 9 ± 6% and the 'high porosity sections' were interpreted as fracture zones that occur at different depth levels (Lorenzo-Pulido, 2008; Deb et al., 2019d). Deb et al. (2019d) concludes that about 30% of the andesitic lavas might contain these highly porous/fractured sections, while the remaining sections are massive andesites with a porosity of 3% to 4%. In our sample set, the observed increased matrix porosity is caused by mineral dissolution and precipitation predominantly along fractures modifying the initial pore network (Figs. 39 to 41, Figs. C1 and C2). Results of X-ray microCT analyses performed on seven andesitic samples

retrieved from well H20 show the importance of microporosity as a result of hydrothermal alteration (Cid et al., 2021). Thereby, macropores account for an average total rock volume fraction of 3.7 ± 0.9%, whereas microporosity (< 1 μm in diameter) is higher with a rock volume fraction of 6.2 ± 0.6%. The round to elongated macropores in the samples are often isolated, suggesting that micropores, which often form a network near larger grains/structures, provide an important link between larger pores. According to Cid et al. (2021) microporosity enhances the matrix permeability by approximately 80%. With simulated porosities of 6.6% up to 14.5% and permeabilities of 10^{-17} m² up to 10^{-15} m², the calculations are in good agreement with our results. The enhanced matrix porosity and permeability (Fig. 50, Figs. 39 to 41, Fig. C2) and the change in the porosity-permeability relationship in the majority of the hydrothermally altered reservoir samples becomes important when upscaling hydraulic permeameters to reservoir scale in numerical models. Comparable to the work of Heap and Kennedy (2016), the porosity–permeability relationships of the andesitic lavas cannot be described with one linear trend (Fig. 46a and b). Farquharson et al. (2015) identified a critical porosity threshold where fluid flow changes from crack- to pore dominated at about 14% in andesitic lavas. Likewise, Kushnir et al. (2016) identified a changepoint at 10.5% in basaltic andesitic lavas. For future reservoir simulations of the Los Humeros geothermal field, these changepoints in the parameter relationships need to be considered. Additionally, the reservoir samples were predominantly retrieved from the hydrothermally altered and fractured damage zones of larger faults within the geothermal field (Fig. 37). For a more precise simulation of fluid flow in a local reservoir model, it would be essential to correctly estimate the lateral extension of the fault damage zone and the hydrothermal aureoles and to distinguish between unaltered, low-porous and hydrothermally altered and high-porous reservoir sections.

The outcrop samples show a negative correlation of thermal conductivity with porosity. Thus, an increased porosity would expect a reduced matrix thermal conductivity. Although thermal conductivity of the reservoir samples is also negatively correlated with matrix porosity, thermal conductivity is significantly increased contrary to expectations. One plausible explanation is the enrichment of calcite and quartz in the system, which can be observed most clearly in the skarns showing the highest thermal conductivities and lavas that underwent pervasive silicification. After Clauser and Huenges (1995; and references herein), calcite (~ 3.6 W m^{-1} K^{-1}) and quartz (~ 7.7 W m^{-1} K^{-1}), together with less abundant alteration minerals like pyrite (~ 19.2 W m^{-1} K^{-1}), magnetite (~ 5.1 W m^{-1} K^{-1}), hematite (~ 11.3 W m^{-1} K^{-1}) and garnet (~ 5.5 W m^{-1} K^{-1}, grossular), have higher thermal conductivities compared to feldspars (~ 2.0–2.7 W m^{-1} K^{-1}). Likewise, the presence of alteration minerals like epidote (~ 2.5–3.1 W m^{-1} K^{-1}) and chlorite (~ 3.1–5.3 W m^{-1} K^{1}) led to an increased bulk thermal conductivity of the rock matrix.

According to Hrouda et al. (2009) volcanic rocks are often strongly magnetic and the variation in their magnetic susceptibility can be used as a geological indicator, e.g., for mapping mineralogical heterogeneities, metamorphic zones, or to differentiate between units. Furthermore, magnetic susceptibility is a very sensitive indicator of hydrothermal alteration (Hrouda et al., 2009). The oxidation of (titano)magnetite to iron oxides like hematite can reduce the magnetic susceptibility by several orders of magnitude, thereby the smaller the grains the faster the alteration. Magnetic susceptibility decreases in the following order: Ms-magnetite (~ $3,000 \cdot 10^{-3}$ SI) > Ms-maghemite (< $3,000–2,000 \cdot 10^{-3}$ SI) > Ms-hematite (1.3–$7 \cdot 10^{-3}$ SI; Dunlop and Özdemir, 2015; Hrouda et al., 2009). The outcrop samples indicate local variations of magnetic susceptibility in the study area. The older Cuyoaco andesites contain magnetic susceptibilities of ~ 2 to $4 \cdot 10^{-3}$ SI, whereas the Teziutlán andesites show a much wider range with magnetic susceptibilities of ~ 2 up to $16 \cdot 10^{-3}$ SI. Thereby, weathering/alteration observed on some samples of the Cuyoaco andesites decreases the susceptibility by about one order of magnitude. The reservoir samples can be grouped into: (1) altered samples that still contain ferromagnetic minerals (10^{-3}–10^{-2} SI); (2) altered samples exhibiting magnetic susceptibilities reduced by about one to two orders of magnitude compared to group 1 (10^{-3}–10^{-4} SI); and (3) marbles, silicified lavas and skarns showing a diamagnetic to paramagnetic behaviour with magnetic susceptibilities that are up to three orders of magnitude

smaller compared to group 1 (10^{-4}–10^{-6} SI). The loss of magnetic signals in the hydrothermally altered rocks could be used to identify and map the hydrothermal aureoles and thus, prospective fluid pathways in the reservoir using geophysics (e.g., borehole logs, airborne magnetic surveys; Kanakiya et al., 2021).

The results of the petrophysical measurements performed on the reservoir samples are in good agreement with previous studies (Contreras et al., 1990; García-Gutiérrez and Contreras, 2007). For example, matrix porosity and permeability data of mainly andesitic lavas and tuff of the Los Humeros geothermal field presented in Contreras et al. (1990) range between 2.5% and 23.3 % (mean = 11.6%) and 10^{-15} m² and 10^{-17} m² (mean = $3.3 \cdot 10^{-16}$ m²), respectively. These data also show a high degree of scatter, similar to our observations. In general, both particle and bulk density increase with reservoir depth, and porosity decreases with reservoir depth, while matrix permeabilities show a high variability at all depths. Thus, a uniform non-permeable layer within the pre-caldera group as described in Cedillo (2000) and Arellano et al. (2003) cannot be confirmed.

Martínez-Serrano (2002) and Prol-Ledesma (1998) reported self-sealing processes and the reduction of permeability due to hydrothermal alteration in the deeper part of the reservoir, while Izquíerdo et al. (2011) described the generation of millimeter-sized vugs caused by intensive leaching in silicified lavas (sample H26-4). A definitive conclusion about this is not possible at this stage, especially because of the high geological heterogeneity observed in our samples. In general terms, the precipitation of secondary phases (e.g., clay minerals, calcite, quartz or epidote) in pores and along fractures reduces matrix porosity and permeability. However, fracturing or reactivation of fractures (thus facilitating further fluid-rock interactions) counteracts this effect. Self-sealing processes can be observed most clearly in the deepest part of the reservoir in the marble and skarn samples (porosities < 2%), which contain numerous fractures and fissures of different generations that are predominantly filled with calcite. Uniform positive density anomalies occur at about 1000 m above sea level in the central area of the Los Humeros geothermal field in density models (Cornejo, 2020), which correlate with the skarn zone described in Martínez-Serrano (2002) confirming self-sealing processes as observed on the skarns and carbonates.

The comparison with literature data underlines the high geological variability of volcanic rocks (Table C3), which are predominantly controlled by matrix porosity and the occurrence of fractures (Mielke et al., 2015; Navelot et al., 2018). In general, hydrothermally altered andesitic lavas feature higher matrix porosities and permeabilities. Hence alteration type, the intensity of alteration, matrix porosity and density of fracturing control the rock parameters. The impact of hydrothermal alteration on the rock properties strongly depends on the protolith and its initial pore network (Villeneuve et al., 2019). Thus, hydrothermal alteration affects each rock unit in a different way leading to a high geological heterogeneity on the centimetre to tens-of-meter scale.

Villeneuve et al. (2019) reported that deeply-buried lavas affected by propylitic alteration from different geothermal fields in New Zealand tend to have low porosity, low permeability and deform through microcracking and dilation resulting in hydraulic active zones localized in fractured intervals. Although similar alteration types and intensities to those described in this study were observed in deep geothermal reservoirs in New Zealand (Siratovich et al., 2014; Weyering et al., 2014; Table C3), the andesitic reservoir rocks in Los Humeros show significantly higher matrix porosities and permeabilities (Table 10). Mordensky et al. (2019a, 2019b) and Frolova et al. (2014) reported increased porosities and permeabilities in reservoir samples for argillic as well as propylitic alteration. According to Frolova et al. (2014) porosity decreases from low-temperature alteration (argillic, zeolitic; ~ 24–40%) to high-temperature alteration (propylitic, 5.6%) and increase again in secondary quartzites (12%; usually form during 300–550 °C, pH: 1–4) and quartz-feldspar metasomatites (20%). In contrast to the findings of the aforementioned studies, Heap and Kennedy (2016) reported significant smaller porosities and permeabilities in altered andesitic lavas compared to unaltered lavas collected from outcrops.

While changes in matrix porosity and permeability have been widely discussed (Frolova et al., 2014; Heap and Kennedy, 2016; Mielke et al., 2016, Kushnir et al., 2016), only a few studies provide information on changes in thermal properties and the results seem to differ from study to study. Navelot et al. (2018) reported consistent thermal conductivities with increasing intensity of hydrothermal alteration, while Mielke et al. (2015) and Heap et al. (2020b) reported decreasing values. Furthermore, Heap et al. (2020b) concluded that specifically acid-sulphate alteration increases specific heat capacity and reduces thermal conductivity and diffusivity.

Navelot et al. (2018) reported higher median magnetic susceptibility values for slightly to moderately altered lavas ($11.97 \cdot 10^{-3}$ SI) than for fresh andesitic lavas ($11.6 \cdot 10^{-3}$ SI) due to increased concentrations of iron oxides during the first phase of alteration of pyroxenes and plagioclase. However, a complete transformation of the initial minerals removes the magnetic minerals and reduces magnetic susceptibility about two orders of magnitude ($0.09 \cdot 10^{-3}$ SI for advanced altered andesitic lavas). Likewise, Kanakiya et al. (2021) reported high remnant magnetization in altered lavas of the Whakaari geothermal field. This phenomenon can also be observed to some extent in our data (Fig. 50, Table 10), where some reservoir samples affected by propylitic and argillic alteration show slightly higher magnetic susceptibilities than the outcrop samples. However, more detailed investigations are required, which determine and quantify the magnetic minerals and their alteration products in our sample set in order to draw a final conclusion.

In contrast to previous studies (Pola et al., 2012; Frolova et al., 2014), the correlations between alteration intensity, chemical indices and alteration facies, show no clear trends (Figs. 43 and 48, Table 9) and thus, the indices prove not to be useful for predicting the petrophysical characteristics of the reservoir rocks. Propylitic alteration seems to cause less scattering of the parameters and deviations from the parameter trends as observed on the outcrop samples.

5.5.4. Data Processing and Implications for Modeling the Los Humeros Geothermal Field

Rock property measurements of the outcrop and reservoir core samples provide matrix properties and thus, represent the centimetre to decimetre scale only (eventually with small-scale or single fractures). Analysis under standardized laboratory conditions is necessary to ensure the comparability of the results. Consequently, the data generated do not reflect in-situ conditions such as high reservoir temperatures, overburden pressures, confining pressures and fluid properties at reservoir depths. Therefore, the data need to be corrected for reservoir conditions (Weydt et al., 2022a) and (depending on the aim and scale of future applications) corrected to reservoir scale (up-scaling). Several analytical and empirical relationships and correction functions have been identified in the past to convert the parameters to reservoir conditions (Farmer, 2002; Rühaak et al., 2015; Ringrose and Bentley, 2021). However, the majority of recent studies do not consider reservoir temperatures above 350 °C. Future research is needed to better estimate the in-situ rock characteristics in super-hot geothermal reservoirs (including up to super-critical conditions, e.g., Kummerow et al., 2020; Heap et al., 2020a).

Since the beginning of the exploration of the Los Humeros geothermal field several conceptual geological models have been developed (Viggiano and Robles, 1988a, 1988b; Martínez-Serrano and Alibert, 1994; Cedillo, 1997, 2000; Arellano et al., 2003). Viggiano and Robles (1988a, 1988b) classified the reservoir rocks according to the four main stratigraphic units, whereby the pre-caldera andesites were divided into augite andesites in the upper part (equivalent to the Teziutlán andesites) and hornblende andesites in the basal part (equivalent to the Alseseca and Cuyoaco andesites). Later on, Cedillo (2000) subdivided the reservoir rocks into ten units, which form mainly continuous layers in the subsurface. The incorporation of ignimbrites and tuffs forming an impermeable continuous layer between the augite and hornblende andesites led several authors to discuss whether the Los Humeros geothermal field hosts two different geothermal reservoirs or not (Izquíerdo et al., 2003, 2015; Gutiérrez-Negrín and

Izquíerdo, 2010). However, the revision of nine lithostratigraphic profiles (Carrasco-Núñez et al., 2017b) as well as the petrographic and petrophysical analyses presented in this study cannot confirm a sufficiently-thick tuff layer, which would act as an aquitard within the andesitic reservoir. Furthermore, the hornblende andesites unit covers several hundred meters in the preliminary 3D model (Calcagno et al., 2020). Based on our findings, the reservoir samples can most likely be related to the Teziutlán andesites unit in the outcrops, which supports the findings of Carrasco-Núñez et al. (2017b) who concluded that the Cuyoaco andesites have a very limited extension and have only been identified in the bottom of a few boreholes. However, since both andesite units feature similar rock properties, it is not necessary to define separate units within a 3D numerical model.

According to Carrasco-Núñez et al. (2017b, 2018) the mafic to rhyolitic lavas identified between ~ 900 m to 1400 m bgl can be linked to the pre-caldera rhyolites (~ 270–693 ka), which has also been defined as the pre-caldera stage. However, considering the new findings presented in Lucci et al. (2020), Urbani et al. (2020, 2021) and Deb et al. (2021) some of these lavas could also possibly be related to the post-caldera stage magmatic activity. A distinct feature is their variable thickness along with no lateral continuity (Carrasco-Núñez et al., 2017b; Urbani et al., 2020, 2021; Cavazos-Álvarez et al., 2020). Based on our findings, together with additional borehole data provided by CFE, these lavas occur more frequently in the upper section of the pre-caldera group and thus, this unit might have a much larger lateral extent as previously described (Cedillo, 2000; Arellano et al., 2003; Carrasco-Núñez et al., 2017b, 2018). Due to the highly variable lateral extension, thickness, alteration intensity, hydraulic properties and most likely fracture pattern of these lavas, it would be useful to define a separate model unit in local reservoir models with a high resolution (small grid size).

For the parametrization of reservoir models of the Los Humeros geothermal field, it has to be emphasized that the majority of the reservoir samples mainly represent the fractured and hydrothermally altered sections in close proximity to larger fractures and fault zones within the geothermal field. Data from the outcrop samples could be used to depict the unaltered and low-porous sections in the reservoir. For a large-scale regional model (with a large grid size), we suggest using data from outcrop samples in order to avoid an overestimation of matrix porosity and permeability.

5.6. Conclusions

This study presents a new dataset of petrophysical rock properties of mainly andesitic lavas from the Los Humeros geothermal field (Mexico), combined with petrographic and geochemical (XRF and ICP-MS) analyses. Hydrothermally altered borehole core samples were compared with stratigraphically equivalent outcrop samples to quantify the impact of hydrothermal alteration on the physiochemical characteristics of reservoir rocks in geothermal systems linked to active volcanic systems. The PLM and SEM observations were used to discriminate primary and secondary assemblages, alteration intensity and facies. The bulk elemental modifications as well as selected chemical indices were discussed with the aim to highlight the possible relationship between chemical changes, alteration intensity and rock properties.

In summary, the results showed:

- The investigated Cuyoaco and Teziutlán andesites comprise a variable suite of mainly unaltered, occasionally fractured, pyroxene-bearing andesitic to dacitic as well as basaltic andesitic to andesitic lavas with a porphyritic to glomerophyric texture, respectively.
- From top to base, the reservoir samples represent shallow ignimbrites and ignimbrite/andesite breccias (~ 350–670 m bgl), followed by a variable suite of mafic to rhyolitic lavas between ~ 800–1400 m depth, basaltic to andesitic lavas between ~ 1500 and 2500 m as well as skarns (~ 2900 m) and marble (pre-volcanic basement). The samples show a high geological variability prohibiting a clear correlation between the boreholes.

- Hydrothermal alteration observed on the reservoir samples predominantly occurs along cracks and fractures and is highly variable on a cm scale. Argillic alteration was mainly observed at shallow to intermediate depths (to ~ 1400 m) followed by propylitic alteration and skarn. However, advanced silicification and high-temperature minerals were observed in samples at different depths, which could have resulted from separate, shallow intrusions.
- Significative bulk chemistry changes were identified in the reservoir samples, mainly in those affected by advanced silicification. Thus, standard discrimination methods are not applicable for our dataset. The Teziutlán and Cuyoaco andesites both show fractionated REE-patterns with LREE enrichment and gently slope towards HREEs. The reservoir samples show REE-budget and fractionated patterns strongly overlapping with those of Teziutlán andesites, while differences are identified with respect to the Cuyoaco andesites. The negative Eu anomaly observed in rhyolites and in shallow-depth cuttings, together with the TiO_2/SiO_2 ratio allows to discriminate felsic material in the reservoir. The general inert REE-behaviour during hydrothermal processes is highlighted.
- The Teziutlán and Cuyoaco andesites are predominantly characterized by low matrix porosities (< 4%) and permeabilities (< 10^{-17} m²) as well as intermediate thermal conductivities, thermal diffusivities and sonic wave velocities. Additionally, the Teziutlán andesites comprises a few porous basaltic andesitic lavas with intermediate to high matrix permeabilities. Bulk density, thermal conductivity and sonic wave velocities are mainly controlled by matrix porosity. However, fractures significantly increase matrix permeabilities (up to 10^{-13} m³) and reduce wave velocities. Specific heat capacity shows comparatively small variations, while magnetic susceptibility shows location specific trends.
- In contrast, the reservoir samples show enhanced hydraulic and thermal properties, but reduced bulk densities, sonic wave velocities and magnetic susceptibility. In general, matrix porosity decreases with reservoir depth, while thermal conductivity and bulk density increase. Other parameters, such as matrix permeability and magnetic susceptibility show a high degree of scatter at all depths. The significant loss of magnetic susceptibility in the reservoir samples could be helpful to identify hydrothermal aureoles as an indicator for possible fluid pathways during geophysical surveys. The correlation with alteration intensity, alteration facies or chemical indices reveals no clear trends, which might be the result of multiple hydrothermal processes/stages.

5.7. Acknowledgements

6. Discussion

6.1. Petrophysical Characterization of the Los Humeros and Acoculco Geothermal Fields

6.1.1. Data Application and Limitations

In the past, numerous extensive national or global databases have been developed for e.g., geothermal well data (National Geothermal data system NGDS, 2014; BritGeothermal, 2017; DOE Data Explorer, 2018), geochemistry (Gard et al., 2019), or mineralogy (BRITROCKS project, 2020). However, comprehensive datasets including multiple rock parameters analyzed on the same sample set are still scarce. A first comprehensive and quality-proofed collection of laboratory rock properties has been developed by Bär et al. (2020) containing data from 316 research articles and more than 75 000 data points. However, this database only contains a limited number of data points or parameters for each investigated study area or rock unit.

The work flow and applied methods presented in this thesis allow to overcome these problems and to systematically analyze target areas with the required level of detail and spatial coverage. The database presented here provides the basis for ongoing and future research in the study area, e.g., for reservoir exploration, assessment, and modeling studies, but also facilitates various applications (e.g., in the petroleum or mining industry) in comparable geological settings within the TMVB or similar volcanic settings worldwide. The level of detail presented in this work has not only significantly improved the geological understanding of both geothermal systems and super-hot geothermal systems in general, but also helped to better understand the relationship between various parameters and how they are affected by different processes (e.g., fracturing or hydrothermal alteration). Thereby, the high number of analyzed plugs and the usage of different sample sizes as well as the performance of interlaboratory tests allows for statistical analyses on different scales (plug, sample, outcrop, formation or model unit), the identification of scale effects, and the validation of different analytical methods. Combined with similar datasets for which all parameters were determined on each sample, the data could be used to train machine learning algorithms to develop rock property prediction tools and to improve and speed up parametrization of 3D geological models in the future.

However, a number of limiting factors have to be considered prior to using this dataset for reservoir modeling or geothermal assessment studies (chapter 3). As is typical for volcanic complexes and such large study areas, some units exhibit high geologic variability (Fig. 51). This is reflected in the results of petrophysical measurements with some geologic units showing a wide range for most of the parameters. The number of samples per unit highly depended on the quality, availability and accessibility of representative outcrops in the field or reservoir core samples in the core storage facility. In the case of the Los Humeros geothermal field, no outcrops were identified for model unit U4 in the field and no reservoir core samples were available. Furthermore, only a few reservoir core samples were available that comprised the cap rock or upper limit of the carbonatic basement. Thus, it was not possible to cover each unit to the same extent and a possible sampling bias should also be considered. Despite the high number of samples, spatial analyses such as variogram analyses were only possible for a few units with a large number of sampling points.

Although detailed characterization was not possible for each individual unit, the identified parameter trends and parameter relationships (Fig. 52) significantly reduce the uncertainty during reservoir property estimation and could increase the accuracy of stochastic modeling approaches (which are often used when dealing with small sample numbers). Thereby, the identified strong relationships between thermal conductivity, sonic wave velocities, and porosity observed in most rock units could be used as a tool for reservoir characterization (Mielke et al., 2017). Additional information on the parameter relationships is provided in Appendix E.

6.1.2. Outcrop Analogue versus Borehole Core Samples

Previous geothermal exploration studies in volcanic settings have provided rock properties analyzed on outcrop (e.g., Lenhardt and Götz, 2011; Pola et al., 2014; Mielke et al., 2016; Heap and Kennedy, 2016; Navelot et al., 2018; Mordensky et al., 2019a; Eggertson et al., 2020) or on borehole core samples (Stimac et al., 2004; Siratovich et al., 2014; Ólavsdóttir et al., 2015; Mielke et al., 2015; Cant et al., 2018). To date, there are only a small number of studies available that investigated both, outcrop and borehole core samples (Homuth et al., 2015; Mielke et al., 2015; Aretz et al., 2016; Weydt and Heldmann et al., 2018).

In this study, for the first time, all units of a geothermal field were systematically analyzed, taking into account samples from the reservoir, exhumed system, and surrounding area of the caldera complex. This approach allows to identify the processes at reservoir depth and to quantify the impact of e.g., hydrothermal, diagenetic, or metamorphic processes on the reservoir properties.

In the case of Los Humeros, the comparison between outcrop and borehole core sample has provided important insights. In general, the findings and data of the outcrop analogue study were well in line with data from the subsurface. For example, the outcrops of the Xáltipan ignimbrite were well suited to study and predict the rock properties in the reservoir (Fig. 51a-b and Fig. 52a; Cavazos-Álvarez et al., 2020). Since mainly drill cuttings were available for this unit, the examination of outcrops helped to characterize the different facies and to better understand their behavior as potential cap rock. Not only did the unit exhibit strong spatial heterogeneity, but it also showed an increasing change with reservoir depth and associated degree of welding (Cavazos-Álvarez et al., 2020*)*.

As described in the previous chapter, the rock properties of the pre-caldera lavas retrieved from wellbore cores showed significant differences in the physiochemical properties compared to their stratigraphically equivalent outcropping units (Fig. 51c-d, Fig. 52b). Fluid-rock interactions causing the dissolution and precipitation of minerals as well as fracturing altered the reservoir rocks. The resulting secondary microporosity exerted important influence on the hydraulic properties (chapter 5). Again, the study of outcrop analogues helped to better describe the spatial heterogeneity of the unit and to better estimate the hydraulic properties in the subsurface. The investigation of borehole core samples provided important insights on fluid-rock interactions and alteration facies, which in turn provided information on the (past and present) temperature regime, fluid chemistry and possible fluid pathways.

In the past, the term skarn has been widely used in the study area and was applied to describe very different metamorphic rocks (e.g., marble by local geologists), which caused confusion when parametrizing model units (GEMex WP7 and WP8 internal discussions). The investigation of outcrops in the exhumed system and borehole cores from Acoculco and Los Humeros has shown that it is very important to distinguish between the different skarn types in the study area as they feature significantly different rock properties (Fig. 51e-g, Fig. 52d). Thus, the ore-bearing skarn deposits from Las Minas (carbonate-intrusion contact) are no suitable analogue for the shallower skarn deposits within the pre-caldera units of the Los Humeros and Acoculco geothermal fields (lava-carbonate/lava-intrusion contact or interaction with Ca-rich fluids; Rochelle et al., 2021). However, they allowed to study the processes and fluid pathways within the deeper carbonatic basement (or potential super-hot/supercritical reservoir), which was not reached by the existing boreholes.

Likewise, the formation of marble differed within the reservoirs. It has to be emphasized that within Los Humeros the upper section of the carbonatic basement did not undergo a full transformation to marble (Gutiérrez-Negrín and Izquíerdo-Montalvo, 2010). In several boreholes, Jurassic to Cretaceous limestones were identified. With numerous healed fractures and veins, the investigated limestone/marble borehole cores in chapter 5 resembled fractured limestones collected in the vicinity of dykes (Fig. 51h-j, Fig. 52c).
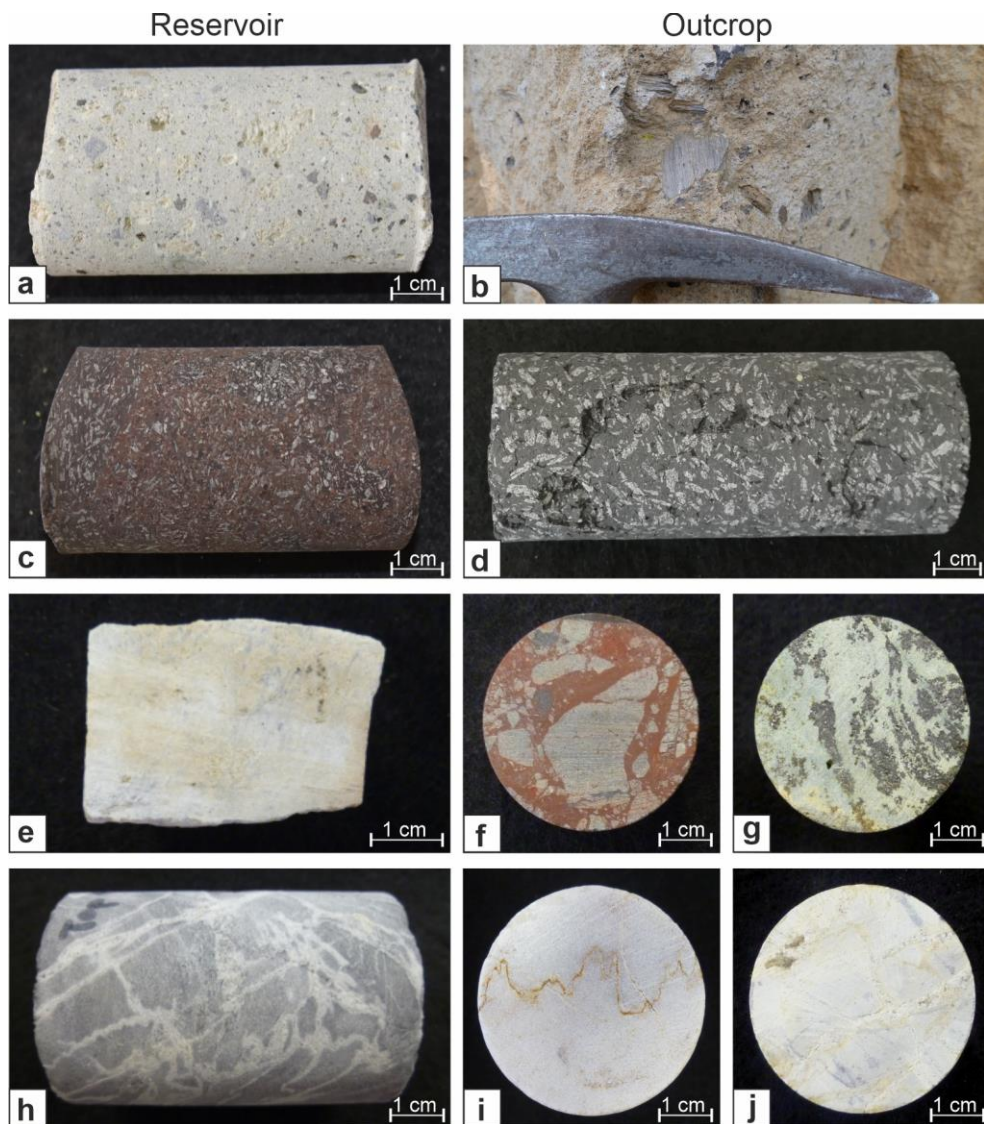
Figure 51: Comparison of borehole core samples of the Los Humeros geothermal field (a, c, e, h) with rocks collected from outcrops (b, d, f, g, I, and j): (a and b) Xáltipan ignimbrite, (c and d) pre-caldera lavas, (e, f and g) skarn, (h and i) marble and (j) limestone collected in close vicinity of a dyke.
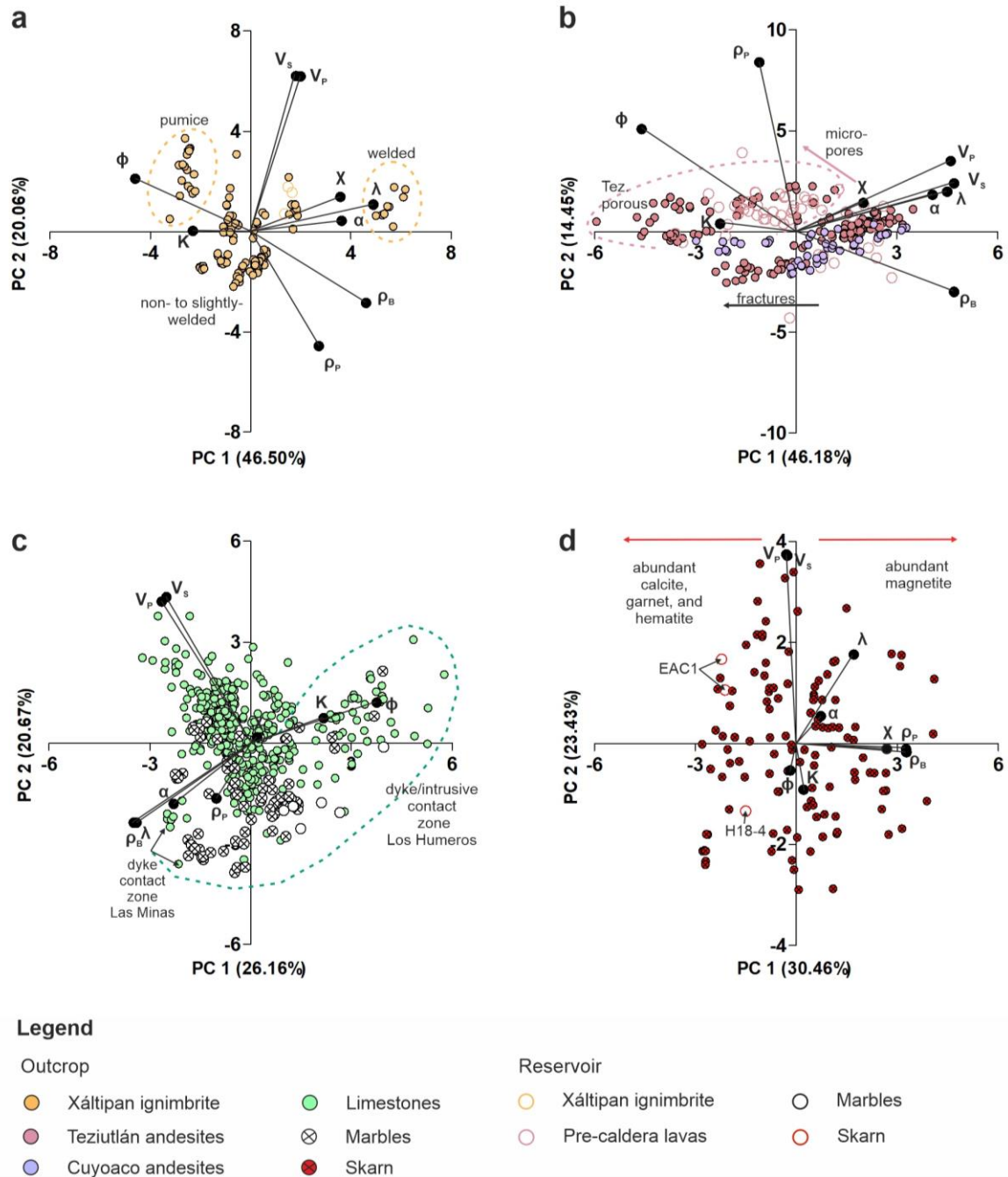
Figure 52: Selected PCAs plotting outcrop and reservoir sample data of the Xáltipan ignimbrite (a), the pre-caldera lavas (b), limestones and marbles (c), as well as skarns (d).

6.1.3. Los Humeros versus Acoculco

The methods described in detail for Los Humeros in chapters 4 and 5 were also applied to Acoculco. Within the GEMex project 80 outcrop samples as well as 8 borehole core samples were collected and analyzed (chapter 3).

With respect to the given model units presented in Calcagno et al. (2022), the outcrop samples were classified into 15 lithostratigraphic units. The results show similar parameter relationships and parameter ranges for the different rock types as identified for Los Humeros (Fig. 53).

Matrix permeability and porosity of the carbonatic basement are generally below 10^{-17} m² and < 5%, respectively. However, small-scaled fractures and joints led to matrix permeabilities of up to 10^{-15} m². The volcanic rocks collected in the study area represent rocks from Miocene to Pleistocene age as described in Avellán et al. (2018) and cover various rock types. The post-caldera and caldera units exhibit a higher matrix porosity (up to 40%) and permeability (up to 10^{-13} m²). Thereby, hydrothermal alteration observed in some outcrops significantly increased matrix porosity and permeability (up to 50% and 10^{-12} m², Perdernal rhyolitic lavas).

Thermal conductivity of the volcanic units is rather low (< 0.4–1.7 W m^{-1} K^{-1}), while thermal conductivity of limestones varies greatly but is generally higher, and increases with decreasing clay content and increasing dolomitization and metamorphic overprint.

Similar to Los Humeros, the subsurface rocks have been affected by numerous fracturing events and fluid-rock interaction (Bär and Weydt, 2019). Six drill cores have been drilled for well EAC-1, which can be classified as ignimbrite (core 1, 100 m MD), rhyolite/dacite (core 2, 300 m MD and core 3, 600 m MD), skarn (core 4, 852 m MD), marble (core 5, 1500 m MD), and granite (core 6, 1815 m MD). The samples are moderately to strongly altered, thus, a clear classification is difficult. López-Hernández et al. (2009) referred to core 1 as Acoculco ignimbrite, to core 2 as Cruz Colorada dacite, and to core 3 as Las Minas rhyodacite. Calcite precipitation and argillic alteration is dominant in the upper three cores. Core 4 represents a metasomatized ash tuff and contains garnet, wollastonite, and diopside as well as abundant calcite and pyrite in veins and to a lesser extent also chlorite, apatite, and sphene. The observed alteration was most likely the product of fluids rich in Ca, CO_2 and Fe. The samples of core 4 show clear signs of retrograde alteration. Core 5 was previously described as skarn (López-Hernández et al., 2009). However, the sample was identified as intensively fractured marble. Almost all cores show healed cracks and fractures (predominantly filled with calcite), especially core 4 and 5 indicate numerous fracturing events.

In contrast to the findings of Los Humeros, the hydraulic properties of the volcanic rocks in the subsurface are rather low (Table 11). Matrix porosity and permeability range from 3 to 7.4% and from 10^{-15} to 10^{-17} m², respectively, and are within the range of the skarns, marbles, and granites (< 5% and 10^{-17} m²). As a consequence, thermal conductivity and P-wave velocity are significantly higher than in the bore hole core samples of the Los Humeros geothermal field. The diamagnetic behavior of the samples indicates pervasive alteration and complete loss of the pristine magnetic minerals (e.g., plagioclase, magnetite). Results of the Acoculco ignimbrite (core 1) are in the range of the basal and welded facies of the Xáltipan ignimbrite and thus, the sample shows rather contrasting properties compared to the outcrop analogue samples. Measurements on core 6 samples are well in line with results from granitoids collected at Las Minas. Likewise, the measurements performed on core 5 are consistent with the results obtained on the marbles of the Los Humeros geothermal field. Both samples feature reduced mechanical properties. Tensile strength of the marbles from the Los Humeros geothermal field is only 1.1 MPa. Thus, these observations confirm the modeling results of Lepillier et al. (2019), who identified the fractured marbles in Acoculco as potential candidates for EGS development.

In summary, the measurement results from the Acoculco outcrop samples are in good agreement with the findings from Los Humeros. For future exploration projects it seems feasible to use the Los Humeros data for preliminary assessments in areas with a similar geological setting. However, the impact of hydrothermal alteration or metamorphic processes should be investigated for each field individually.
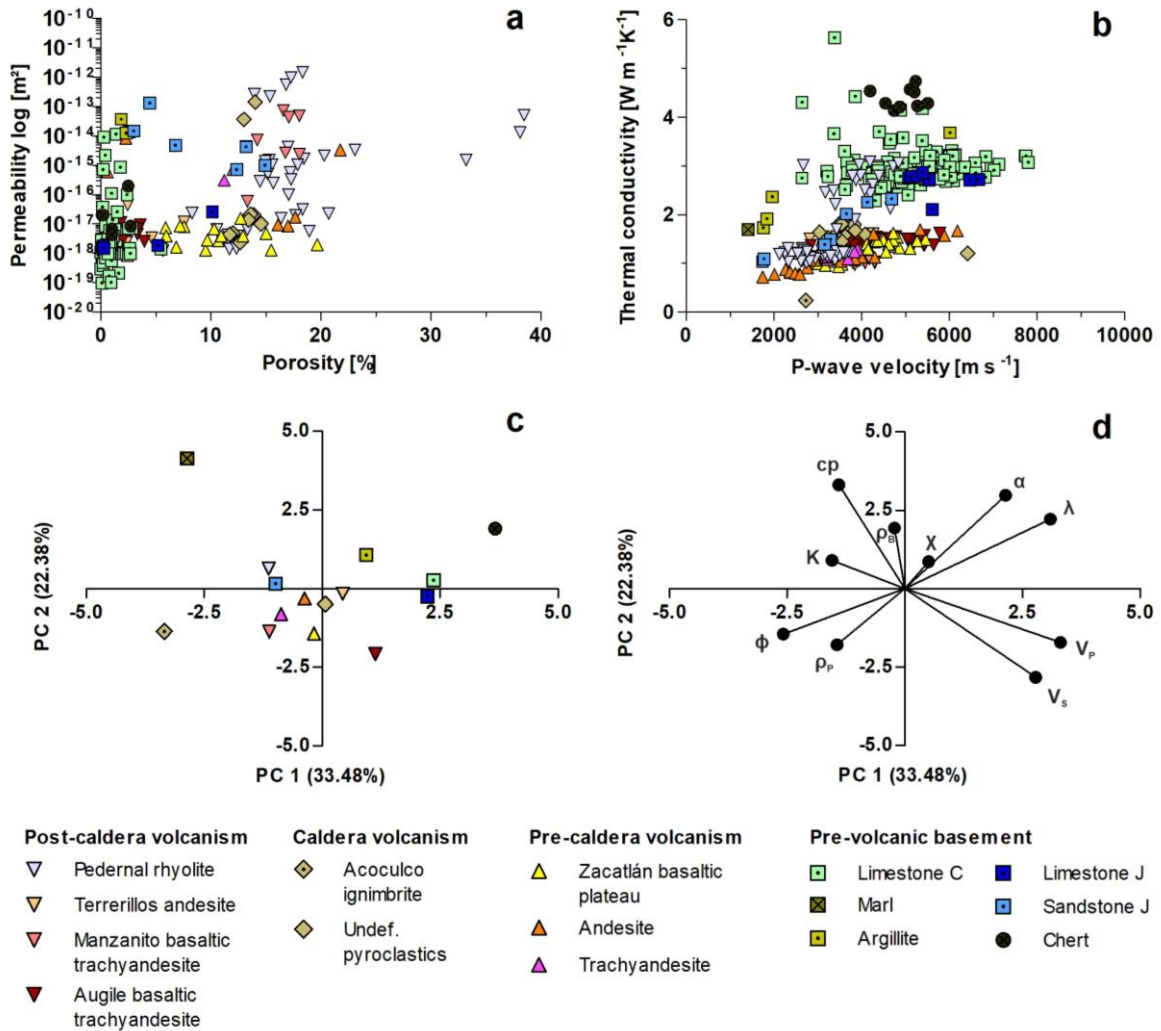
Figure 53: Cross-plots of matrix porosity vs. matrix permeability in (a), and thermal conductivity vs. P-wave velocity in (b) analyzed under dry conditions on outcrop samples collected in the Acoculco volcanic complex (modified from Weydt and Bär et al., 2021). PCA calculated from the arithmetic means of all analyzed plugs for the respective unit (c and d).

Table 11: Selected rock properties of the Acoculco wellbore core samples

Unit	ρ_P [g cm^{-3}]	ρ_B [g cm^{-3}]	ϕ [%]	K [m²]	λ dry [W m^{-1} K^{-1}]	V_P dry [m s^{-1}]	X [10^{-3} SI]
Ignimbrite (core 1)	2.71 (2) ± 0.02	2.40 (2) ± 0.003	6.53 (2) ± 0.9	2.2E-17 (2) ± 3.6E-18	1.99 (2) ± 0.11	6530 (2) ± 214	0.629 (2) ± 0.007
Dacite (core 2)	2.53 (3) ± 0.06	2.37 (2) ± 0.02	7.43 (2) ± 0.9	1.2E-17 (2) ± 9.6E-18	2.39 (2) ± 0.04	5234 (3) ± 471	-0.036 (2) ± 0.003
Rhyodacite (core 3)	2.59 (3) ± 0.02	2.53 (2) ± 0.02	2.95 (2) ± 0.9	1.1E-15 (2) ± 7.5E-16	2.23 (2) ± 0.24	4983 (3) ± 651	-0.012 (2) ± 0.019
Skarn (core 4)	2.69 (2) ± 0.05	2.64 (2) ± 0.04	1.86 (2) ± 0.44	4.3E-17 (1)	3.51 (2) ± 0.11	5581 (2) ± 337	-0.012 (2) ± 0.015
Marble (core 5)	2.73 (1)	2.69 (1)	1.35 (1)	3.7E-17 (1)	2.29 (1) ± 0.05	2006 (1) ± 6	0.250 (1) ± 0.147
Granite (core 6)	2.60 (1)	2.48 (1)	4.40 (1)	-	2.02 (1) ± 0.07	2821 (1) ± 15	5.777 (1) ± 1.716

arithmetic mean values, ± = standard deviation () = number of analyzed plugs

6.2. Results in the Context of Recent Findings from the GEMex Project

6.2.1. Deep Structures and Heat Sources of the Los Humeros Geothermal Field

Based on a 1D shear velocity model, Löer et al. (2020) estimated the bottom depth of the sedimentary sequences (Sierra Madre Oriental Basin) below the LHVC at ~ 5 km, and the thickness of the Teziutlán Massif to be about 5.5 km. The investigation of zircons in intrusive samples from the Las Minas area revealed a complex and protracted magma crystallization in multi-level chambers and a possible presence of the Grenvillian orogen (936–1244 Ma) in the upper/middle crust (Kozdrój et al., 2020).

The abundance and variety of intrusive bodies and dykes observed during the field campaigns in the study area and their possible connection to the current state of the LHGF was already presented and discussed during the early stage of the GEMex project (Bär et al., 2017; Weydt and Bär, 2019). However, a change in view – from a single large magma chamber and heat source (Verma, 1985) to the possible existence of multiple smaller magma pockets at different depths – only began after the introduction of a new magmatic plumbing system model (Lucci et al., 2020; Fig. 54a). Based on mineralogical and geochemical analyses performed on lavas of the post-caldera group, a vertically extensive plumbing system was proposed with (1) a deep mafic reservoir at ~ 30 km depth, (2) an intermediate magma storage system in the middle to upper crust (6−4 kbar, ~ 14 km depth), and (3) a shallow storage zone (0.5 kbar, < 3 km depth) where rapidly ascending basalts stall before eruption and at times smaller portions of mafic magmas differentiate to trachyandesites and trachytes. Thereby, shallow intrusions and cryptodomes might even occur below 1 km depth in the pre-caldera and caldera group of the LHVC (Urbani et al., 2020, 2021; Fig. 54b), which most likely resulted in the resurgent behaviour/movements observed inside of the Los Potreros caldera (Urbani et al., 2021; Bonini et al., 2021) and created small sub-anomalies within the geothermal field (Deb et al., 2021).

The proposed plumbing system model explains the variety of lavas observed in the post-caldera group and their temporal evolution. Seismic imaging (Granados-Chavarría et al., 2022) recently identified three low-velocity bodies that match with the proposed magma pockets in Lucci et al. (2020): (1) a deep storage region at ~ 11 km depth, (2) a second storage region from 3 to 8 km depth which can possibly be related to the collapse of the Los Humeros caldera, and which feeds (3) shallow low-velocity bodies between 1.3 and 2.2 km depth (Fig. 54c).
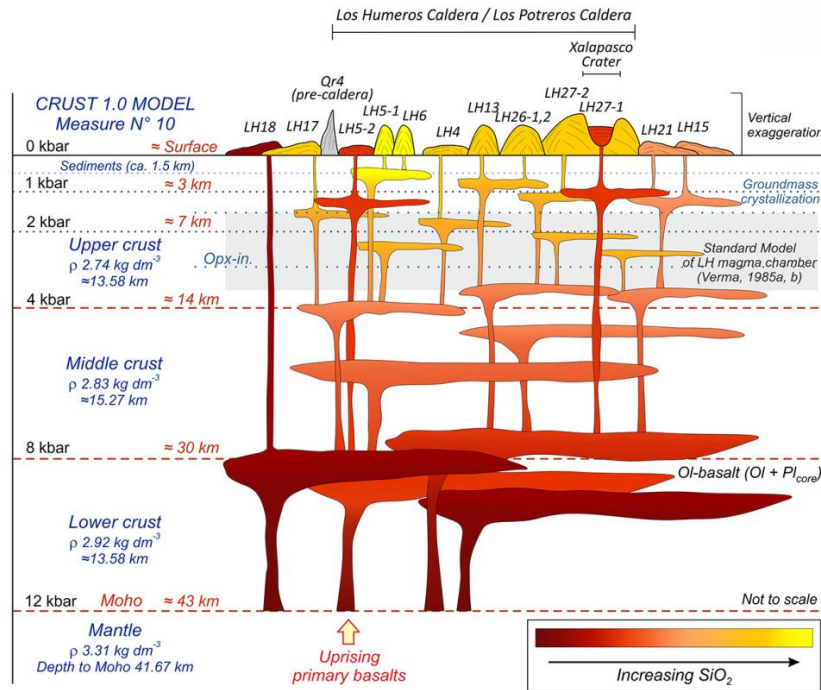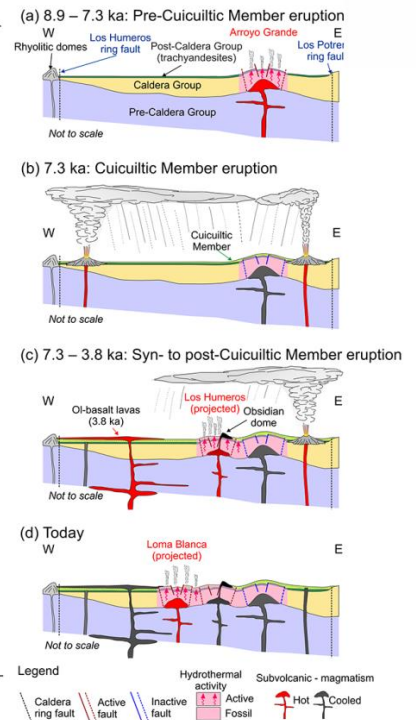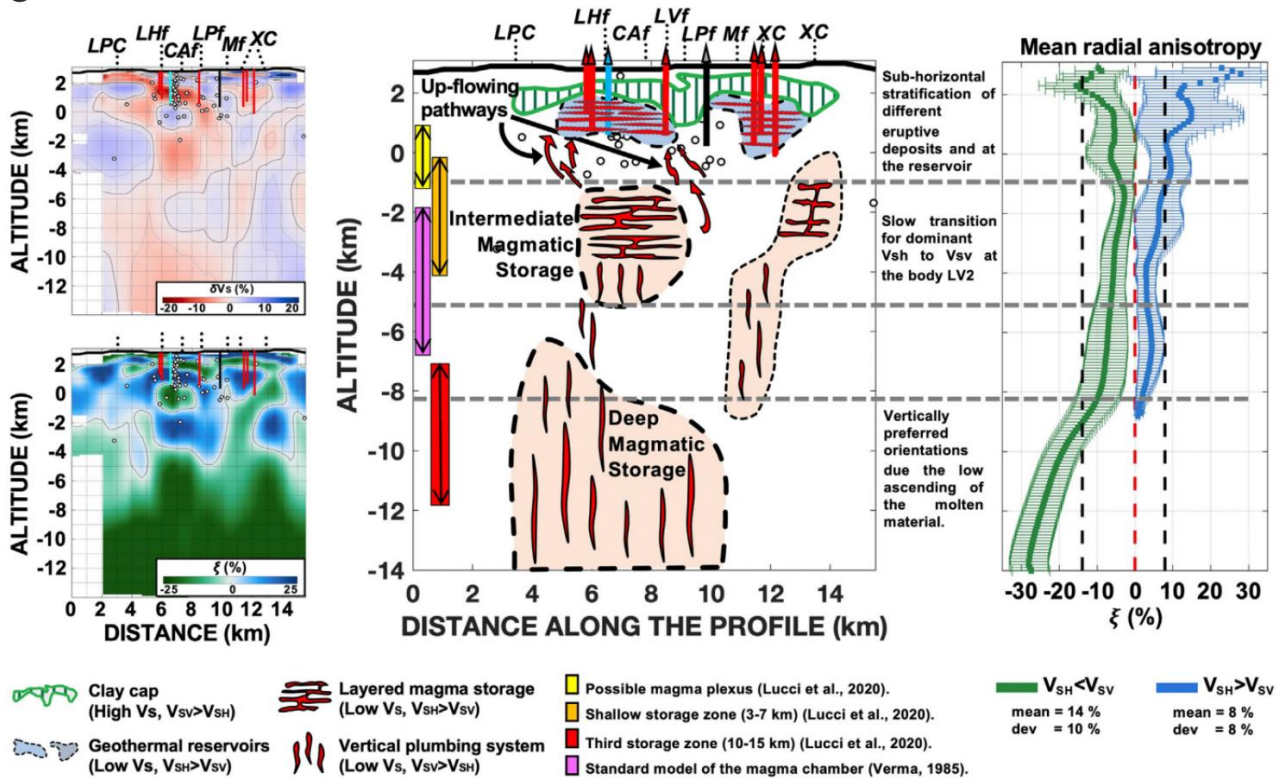
Figure 54: (a) Magmatic plumbing system of the LHVC derived by pressure-temperature estimates obtained from mineral-liquid thermobarometry models (Lucci et al., 2020), (b) conceptual model of shallow intrusions and crypto-domes in the upper part of the caldera (Urbani et al., 2020 and 2021), and (c) shear wave and anisotropy model of the LHVC (Granados-Chavarría et al., 2022) displaying the different magma pockets feeding the geothermal field.

The existence of small-scaled and shallow intrusions and possibly cryptodomes between < 1 and 3 km depth (Urbani et al. 2020) explains the occurrence of basaltic to rhyolitic lavas with a limited lateral extension in the upper section of the pre-caldera group (Carrasco-Núñez et al., 2017b, Weydt and Lucci et al., 2022) and the high variability regarding alteration facies and alteration intensity observed within the geothermal field (González-Partida et al., 2022; Weydt and Lucci et al., 2022).

Based on geological, petrological, and geochemical data from the GEMex project as well as thermo-barometric analyses, Deb et al. (2021) simulated the temporal evolution of shallow magma pockets inside of the Los Humeros caldera (Fig. 55). Several smaller intrusions with a volume between 0.01 km³ and 1.3 km³ of Holocene age were estimated at depths between 0.5 and < 3 km. The results indicate that almost 80% of the present-day heat flow results from the deeper and larger magma pockets related to the caldera-forming events of the Los Potreros and Los Humeros calderas (Deb et al., 2021). The smaller, but frequent magma eruptions during the post-caldera period only led to a local temperature increase and thus, creating localized hotspots and potential super-hot resources at shallow depth.

These findings match with temperature anomalies in downhole temperature profiles below 2 km depth (Urbani et al., 2021) and temperature anomalies along the Los Humeros-Maztaloya fault observed during temperature and heat flux measurements at the surface (Jentsch et al., 2020; Fig. 56). Furthermore, smaller magma pockets explain the local occurrence of acidic fluids within the geothermal reservoir (Izquíerdo et al., 2009; Flores-Armenta et al., 2010; González-Partida et al., 2022).

While geophysical surveys performed within the GEMex project were able to possibly depict larger magma pockets at greater depth (Cornejo, 2020; Toledo et al., 2020b; Granados-Chavarría et al., 2022), the geometry, depth, and location of smaller and shallow magma pockets remains speculative. Granodioritic intrusions with hornblende and biotite were reported in several wells (H5, H8, H9, H11, H12, H21, H26, H28, H37) in the carbonatic basement and occasionally in the pre-caldera andesites. They were often reported together with basaltic to andesitic dykes. However, the observed inaccuracies and inconsistencies in the original lithological well profiles (Carrasco-Núñez et al., 2017b) and the lack of geophysical well logs prevent more precise assumptions about their size and extension.

Nevertheless, the investigation of outcrops in the exhumed systems and in the surrounding area of the LHVC allowed for an estimation of the size of the intrusions and their impact on the host rock (~ 100 m in width for skarns and between 300 and 400 m in width for marble; Olvera-García et al., 2020). The investigation of dykes and intrusions in the surrounding area of the LHVC showed rather sharp contacts between host rock and intrusion as well as restricted alteration zones (~ 5 to 50 m depending on the size of the intrusion/dyke or fault zone; Bär and Weydt, 2019).
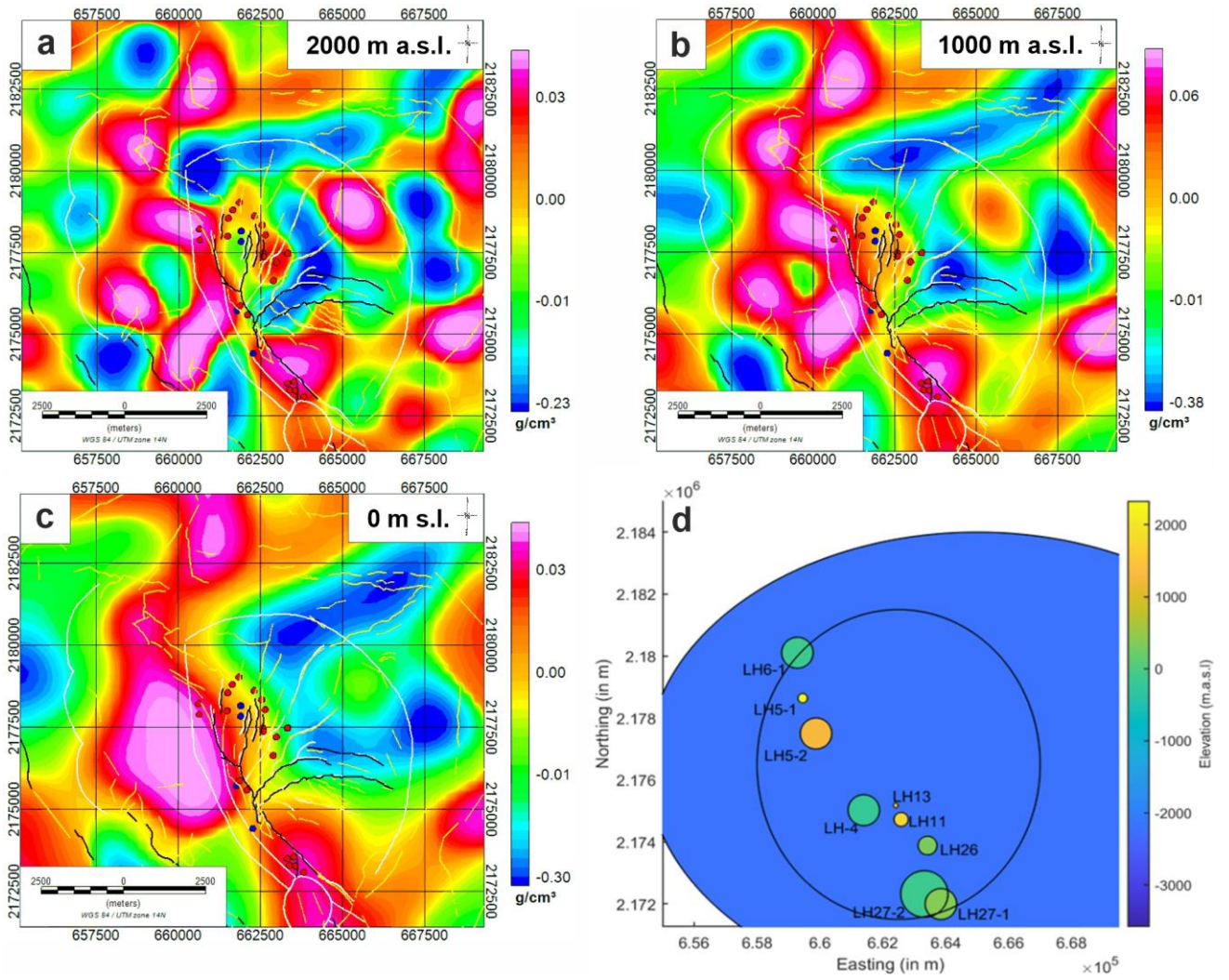
Figure 55: Density maps at (a) 2000 m a.s.l., (b) at 1000 m a.s.l., and (c) at sea level of the LHVC obtained from 3D inversion of gravity data (Cornejo, 2020). Densities are provided as Δρ (g cm⁻³) with respect to the Bouguer density (2.67 g cm⁻³). (d) represents the approximate locations and depths of the shallow magma pockets modeled in Deb et al. (2021).
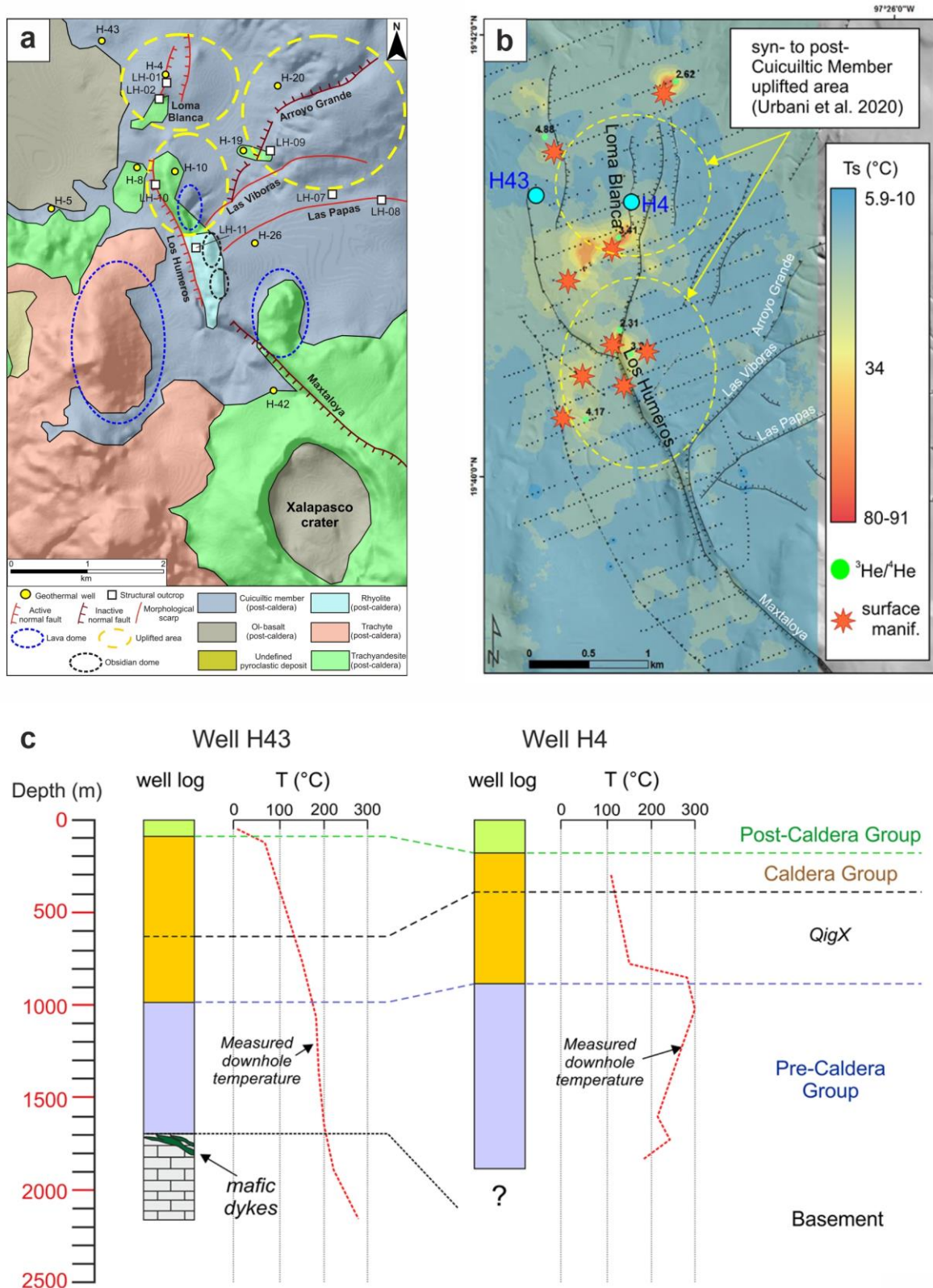
Figure 56: Small-scale deformations and uplifted areas (a) correlate with temperature anomalies observed during soil gas measurements (Jentsch et al., 2020) and downhole temperatures (c; figures from Urbani et al., 2021).

6.2.2. Structural Setting, Fluid Flow and Hydrothermal Alteration of Los Humeros

Fluid flow in the study area is predominantly fracture controlled. As presented in chapters 4 and 5, the laboratory measurements revealed mainly low to very low matrix permeabilities (classification after Bär, 2012) for the rock units of the pre-volcanic basement and pre-caldera group. Thus, homogeneous and extensive aquifers could not be inferred. The Jurassic sandstones (red beds, Cahuasas Fm.) and the vesicular lavas of the Teziutlán andesite unit form an exception. The Cahuasas Fm. is several 100 m thick in the neighbouring states (Ochoa-Camarillo, 1999). While the occurrence of permeable sandstones cannot be excluded at greater depth, the boreholes encountered predominantly Early Cretaceous (Tamaulipas Fm.) and Late Jurassic limestones/marbles (Pimienta and possibly Tamán and Santiago Fm.; Gutiérrez-Negrín and Izquíerdo-Montalvo, 2010). As discussed in chapter 5, the proportion of porous andesites (~ 10 to 30%) within the geothermal field is estimated at 30% and is mainly associated with fault zones (Lorenzo-Pulido, 2008; Deb et al., 2019d). Fractures can increase the matrix permeability by several orders of magnitude. This is clearly reflected by the increased matrix permeability values of otherwise low permeable skarns, marbles, limestones, and granitoids in the vicinity of fault zones and dykes (chapter 4).

In contrast to previous beliefs assuming the fluid flow to be limited to the Los Humeros caldera (Cedillo, 1999; Portugal et al., 2002), recharge of the geothermal field takes place via major fault zones in the sedimentary sequences of the Sierra Madre Oriental west of the LHVC (Lelli et al., 2020). While Cedillo (1999) assumed that the intrusive bodies observed in the surrounding area of the LHVC act as a fluid barrier and isolate the caldera from the regional recharge, the field investigations in the exhumed systems tended to suggest the opposite. Particularly, the fractured marbles and skarns associated with the intrusive bodies not only represent fluid pathways, but are also the result of continuous fluid flow as shown by mineralogical investigations (Olvera-García et al., 2020; Fuentes-Guzmán et al., 2020; Rochelle et al., 2021). According to Arzate et al. (2018) this is also the case in the basement below the LHVC, where pressured thermal fluids most likely travel along altered and weakened contact zones of intrusions to shallow depths. Additional recharge of the geothermal field occurs in the northern sector of the caldera complex via rapid infiltration of meteoric water, and via deep-seated magmatic and possibly fossil fluids (Pinti et al., 2021; Bernard et al., 2011).

The study area is controlled by mainly NE–SW and NW–SE-oriented structures (Cornejo-Triviño et al., 2022; Fig. 57). Thereby, major fault zones appear to be independent from the volcanic activity of the LHVC and are considered to be of tectonic origin. These structures not only control the fluid flow in the regional study area, but most likely also controlled the development and geometry of the Los Humeros caldera (Cornejo-Triviño et al., 2022) and represent preferred pathways for dykes and intrusions (Norini et al., 2019; chapter 2). Dykes cutting intrusive bodies as observed in Las Minas and as reported in some lithologic well logs of the geothermal field indicate that these fault zones have been reactivated over time. Gravimetric and morphological studies have shown that the NE–SW-oriented major faults control the southeast (Hidalgo fault) and the northwestern side of the Los Humeros caldera, as well as

the southern section of the Los Potreros caldera (Cornejo-Triviño et al., 2022; Fig. 57). Structures with similar orientation can also be found inside and outside of the caldera. Elevated fluid temperatures (~ 25 to 33 °C) encountered in shallow groundwater wells that reach into the pre-caldera lavas southeast of the Los Humeros caldera rim (Lelli et al., 2020) suggest that the geothermal reservoir is not restricted to the caldera itself (Fig. 57).
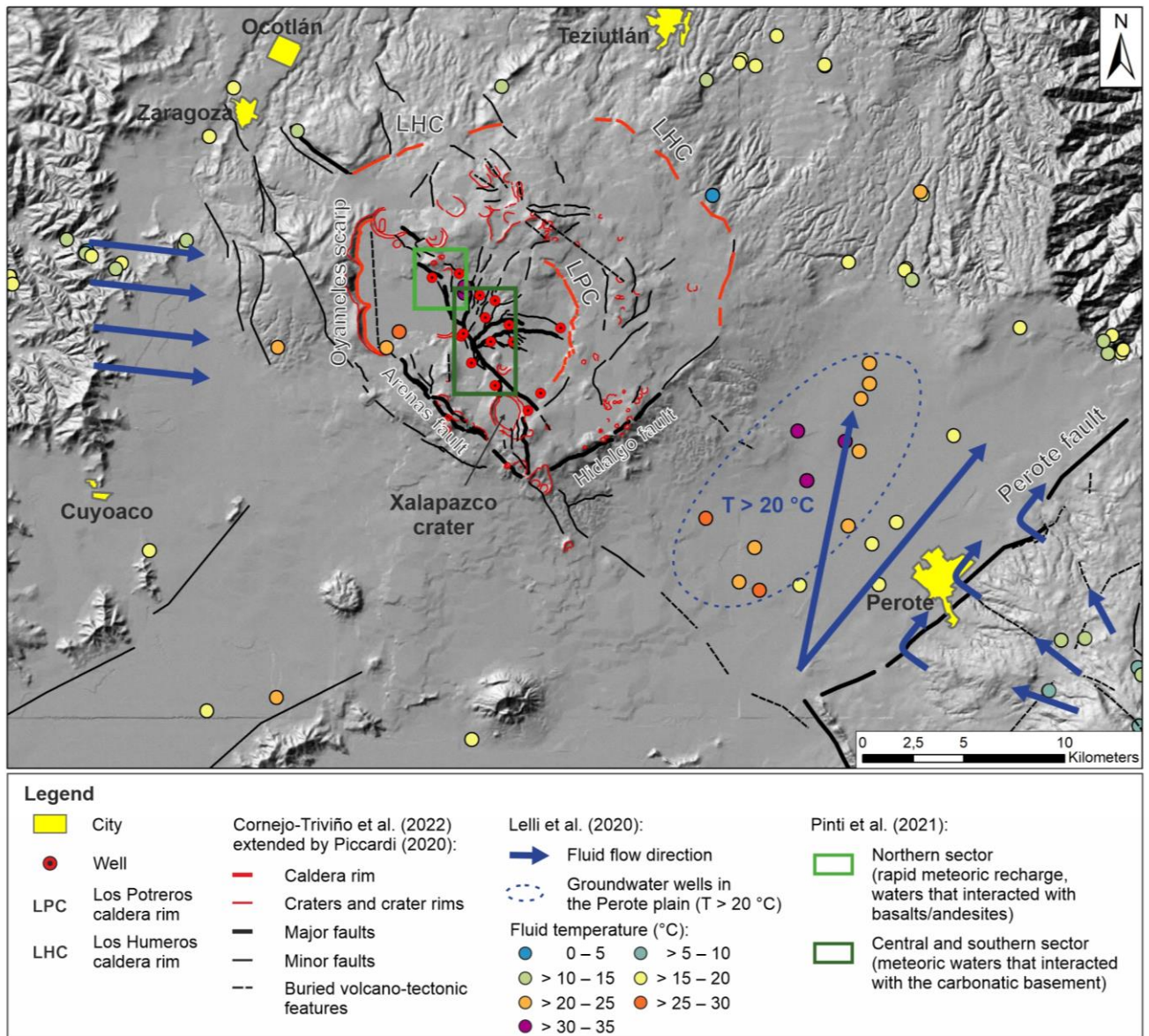
Figure 57: Regional structures of the study area based on morpho-structural analyses performed within the GEMex project (Luigi Piccardi in Cornejo-Triviño et al., 2022) and results from fluid and gas analyses collected from outcrops (colored circles and arrows, modified from Lelli et al. 2020) and geothermal wells (Pinti et al., 2021; green boxes).

While fluid flow in the deeper sections (carbonates and possibly basal pre-caldera group) of the geothermal field is most likely controlled by the NE–SW and NW–SE-oriented fault zones, the occurrence and orientation of faults in the upper pre-caldera group to post-caldera group inside of the caldera might differ. Based on MT resistivity models, Arzate et al. (2018) and Corbo-Camargo et al. (2020) identified

numerous shallow faults within the geothermal field that don't reach the pre-volcanic basement (some without surface expression), and which were formed during the caldera resurgence or possibly due to ground subsidence as a result of the geothermal production. Analogue modeling (Bonini et al., 2021) revealed that intrusions at shallow depth most likely caused the sub-angular intra-caldera fault pattern (active normal faults and subordinately reverse faults; Norini et al., 2019), doming, and uplift inside of the Los Potreros caldera. The complex fault pattern includes two main orientations, which are (1) the NNW to NS-striking Los Humeros and Maztaloya faults representing the main structure of the system, and (2) smaller E–W to NE–SW striking faults like the Las Papas or Arroyo Grande faults that branch-off from the Los Humeros and Maztaloya faults. Additionally, the small shallow magmatic intrusions (< 1 km depth) as described above led to small-scale deformations (a few tens of meters to ~ 1 km²) showing normal faulting at their top, and discontinuous uplift within the Los Potreros caldera (Urbani et al., 2020). According to the authors the uplift moved progressively northwards from the south and north-eastern sector of the caldera towards the north (Los Humeros fault scarp and Loma Blanca).

The reservoir rocks within the geothermal field were affected by the volcanic-tectonic activities over time starting with the emplacement of the pre-caldera rhyolites followed by two caldera forming events and multiple smaller explosive events as well as the resurgence phase during the Holocene. The resulting faults and their associated damage zones represent preferential pathways for geothermal fluids creating hydrothermal systems within the volcanic deposits. The fluids interact with the host rock and thereby change its physiochemical properties (chapter 5). While geophysical surveys are able to depict large-scaled alteration pattern (Arzate et al., 2018; Corbo-Camargo et al., 2020; Benediktsdóttir et al., 2020), results of petrological investigations performed on cutting material and borehole cores indicate a more complex evolution. To better understand the weak correlation between bulk chemical data, chemical indices, and rock properties as presented in chapter 5, the temporal and spatial evolution of the geothermal field need to be taken into account. However, due to lack of data, only general assumptions can be made at this point. Prol-Ledesma (1990) and Martínez-Serrano (2002) proposed two alteration events in order to explain the occurrence of high-temperature and low-temperature minerals within one sample at comparatively shallow depth. González-Partida et al. (2022) concluded that several different preferential fluid pathways existed over time, which possibly shifted spatially. This concept is coinciding with the findings of Urbani et al. (2021), who observed a spatial shift in the post-caldera activity.
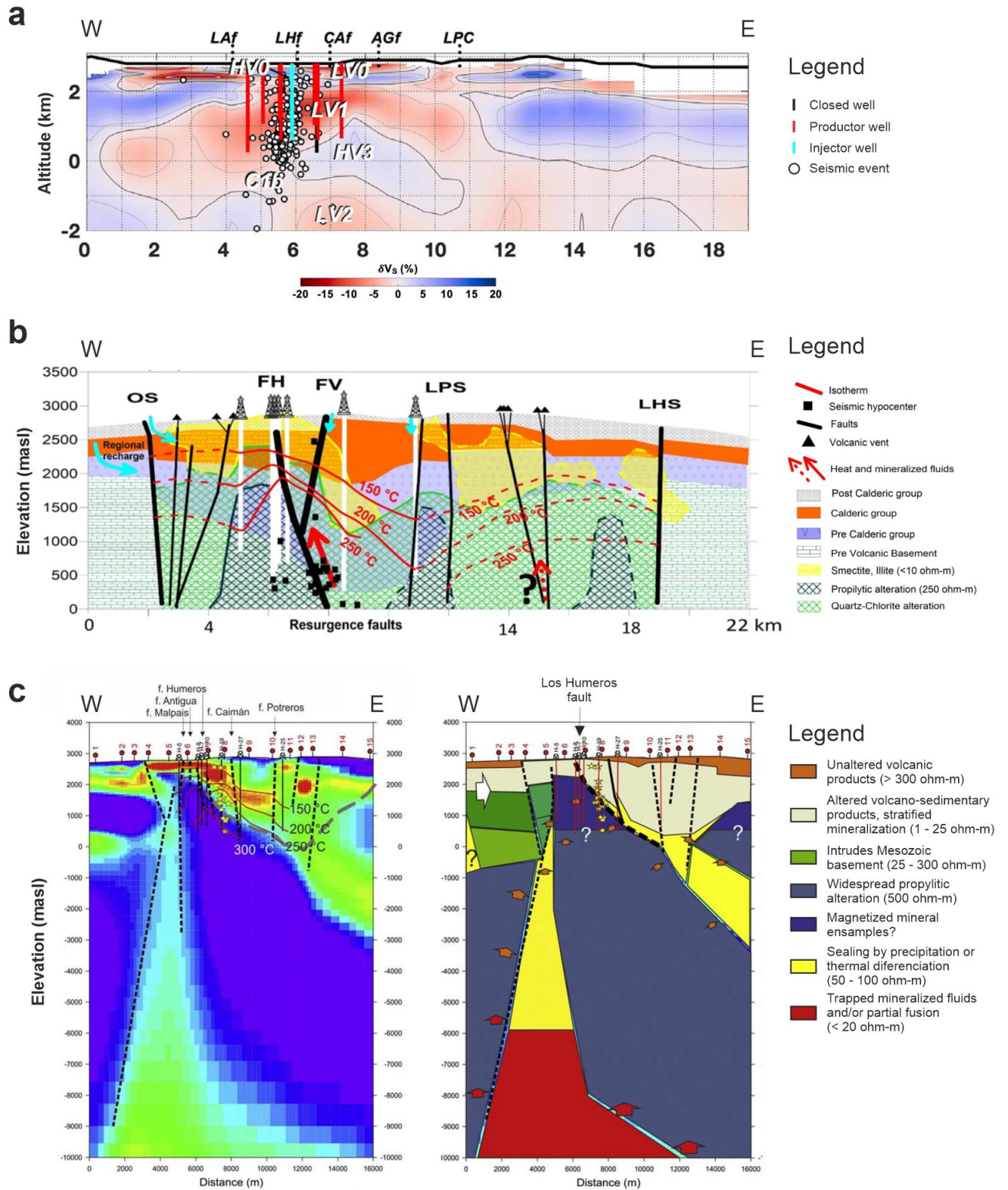
Figure 58: W–E corss-sections derived from geophysical surveys representing the central collapse area of the Los Humeros geothermal field. (a) Shear velocity model (modified from Granados-Chavarría et al., 2022), and mapped alteration facies based on MT resistivity models (b = modified from Corbo-Camargo et al., 2020; c= modified from Arzate et al., 2018).

Similar to the findings from Las Minas (Fuentes-Guzmán et al., 2020; Rochelle et al., 2021), the current state of the geothermal field is possibly the result of multiple spatially and temporally limited alteration events, which caused the overlap of prograde and most likely retrograde alteration assemblages due to the reactivation and the sealing of fractures. Different altered lava, skarn, and marble fragments observed in hydrothermal andesite breccias (pre-caldera) as well as in the Xáltipan ignimbrite suggest that hydrothermal alteration started before the post-caldera volcanic activity already. One possible hypothesis is that the large magma chambers responsible for the Los Humeros and Los Potreros collapses created the large-scale alteration facies (e.g., propylitic and argillic alteration as inferred from geophysical surveys) and that the smaller eruptions and shallow intrusions of the post-caldera stage only caused local alteration aureoles.

According to numerical simulations (Deb et al., 2021) most of the smaller intrusions cooled relatively quickly (a few thousand years). Depending on their volume (0.01–1.3 km²), they possibly caused a localized temperature increase of between 10 K and ~ 380 K. Additionally, the petrographic analyses of the borehole core samples showed that silicification occurred after the propylitic alteration. While some authors assume that the silicification is artificially caused due to geothermal production (Portugal et al., 2002), other authors refer to deep-seated super-critical fluids of magmatic origin (Bienkowski et al., 2005; González-Partida et al., 2022). The fluid analyses performed in the GEMex project showed that the deep fluids which infiltrated the reservoir via the carbonatic basement reacted with the overlying andesitic lavas and were neutralized quickly (Sanjuan et al., 2020; Lelli et al., 2020). In fact, most of the fluids have a pH between 7 and 8 (Tello, 2005), which is well in line with the observed propylitic and argillic alteration facies. Thus, a deep magmatic source (~ 4–5 km depth) alone does not explain the scattered occurrence of silicification or the advanced argillization (González-Partida et al., 2022) at shallow depths.

The results of the geophysical surveys (Fig. 58) indicate a sub-horizontal stratification in the upper part of the caldera complex and to a lesser extent in pre-caldera andesites (Arzate et al., 2018; Corbo-Camargo et al., 2020; Benediktsdóttir et al., 2020; Toledo et al., 2020b; Granados-Chavarría et al., 2022). This observation matches the alternating pyroclastic deposits and lavas of the caldera and post-caldera group (until ~ 900 m bgl). The Cuyoaco and Teziutlán andesites are usually described in the literature as voluminous lava flows. However, the outcrop analogue study has shown that both units consist of a heterogenous suite of different lavas. According to Carrasco-Núñez et al. (2017b), the pre-caldera lavas and occasional lava domes were emplaced on a highly irregular topography and formed multiple overlapping lava flows. Furthermore, highly altered zones with a tuffaceous appearance were identified at different depths which show no lateral continuity. These were interpreted as local boundaries between units or sites affected by fractures that facilitate a more advanced hydrothermal alteration (Carrasco-Núñez et al., 2017b). Thus, although vertical fluid flow dominates along fault zones and fractures, Los Humeros represents a mixture of lateral geothermal reservoirs and purely fault-controlled geothermal reservoirs as defined in Liotta et al. (2021, Fig. 59).
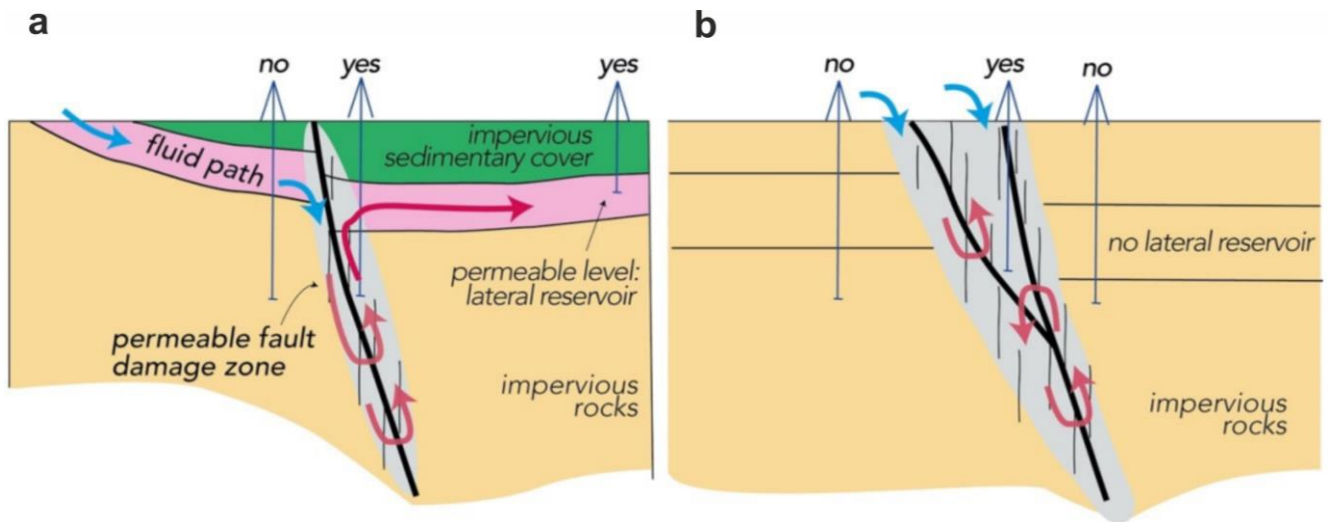
Figure 59: Schematic sketches of lateral (a) and fault-controlled (b) geothermal systems (Liotta et al., 2021). On the right the fluid flow is limited to the fault damage zone, while in lateral reservoirs the fluids follow lateral permeable levels.

6.3. Recommendations for the Update of the Los Humeros Geological Model

In previous conceptual models the subsurface rocks of the Los Humeros geothermal field (Fig. 60) were classified into eight (Cedillo, 1997, 2000) to ten units (Arellano et al., 2003), which form rather homogenous horizontal layers. So far, it has been assumed that the geothermal field hosts two andesitic reservoirs separated by a low permeable tuff layer and that the fluid flow is confined to the caldera (Cedillo, 2000; Portugal et al., 2002). Based on these assumptions, a preliminary 3D geological model was created to incorporate the results from the numerous geophysical, geological, geochemical, and technical investigations performed within the GEMex project (Calcagno et al., 2018, 2022).
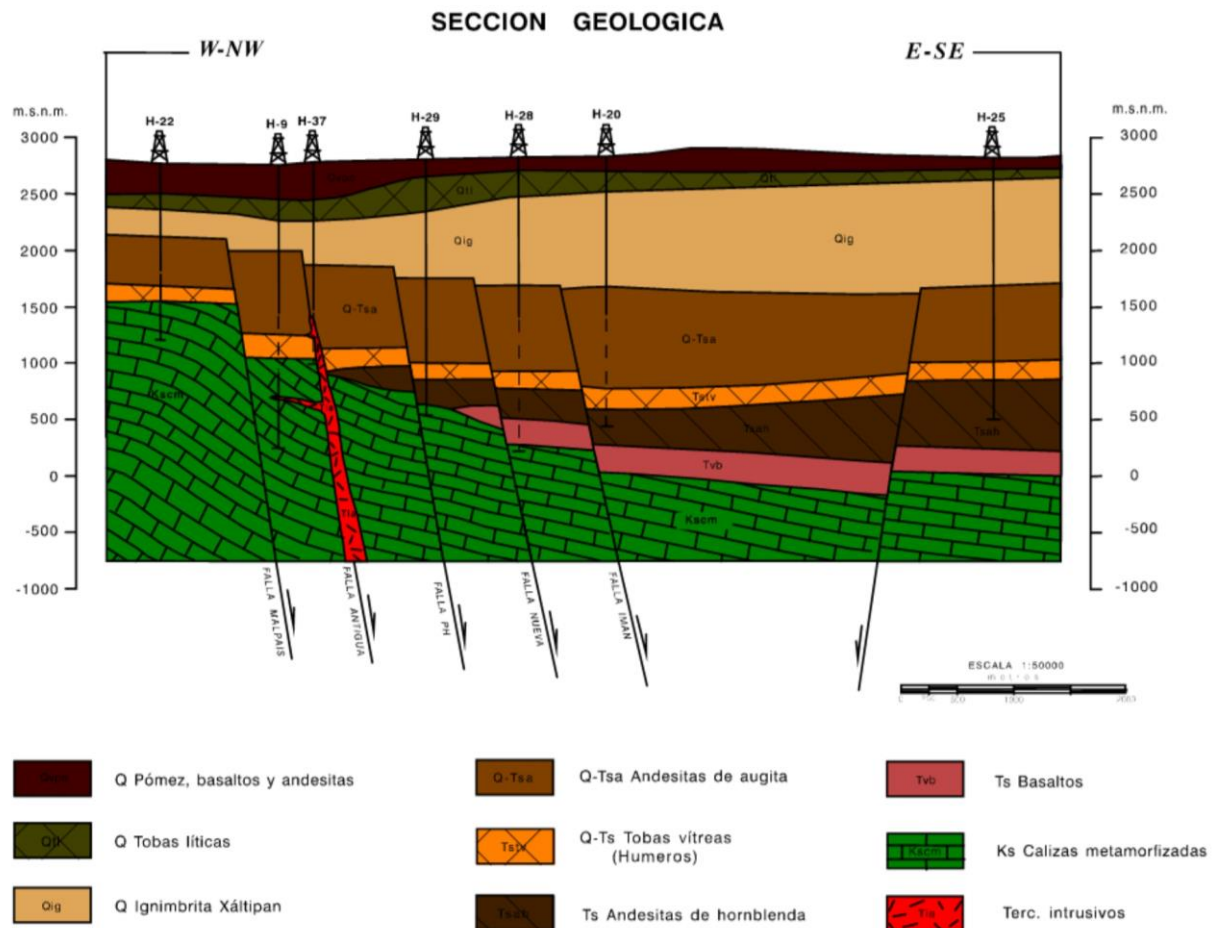
Figure 60: Geological cross-section of the Los Humeros geothermal field modified from Cedillo (1997).

However, the 'horizontal layer approach' used in the preliminary 3D model was not able to depict the subsurface temperature distribution and heat flow in the geothermal field (Deb et al., 2019d; Deb et al., 2021), and to reproduce the observed temperature sub-anomalies as presented in Jentsch et al. (2020) or Urbani et al. (2021).

Based on the results presented in chapters 4 and 5 as well as other findings from the GEMex project (section 6.2), the geological model can be improved.

6.3.1. Cap Rock

Prior to the GEMex project, the Xáltipan ignimbrite was described as homogenous and thick layer of poorly-sorted, matrix supported, massive (lapilli) tuff (Ferriz and Mahood, 1984; Willcox, 2011) with an overall low permeability (Cedillo, 1997), and was considered the cap rock of the geothermal field. The

results of the outcrop analogue study and petrophysical measurements have shown that the Xáltipan ignimbrite mainly consists of heterogenous, predominantly non-welded to slightly-welded, matrix-supported, massive lapilli tuff and pumice fallout deposits with high matrix porosities (up to 70%) and permeabilities (up to 10^{-13} m²). Only the basal welded facies exhibit low matrix porosities (5%) and permeabilities (10^{-18} m²), and may behave as a cap rock for the geothermal field. Within the geothermal field, the Xáltipan ignimbrite shows a substantial variation in thickness ranging from 90 to 770 m (Carrasco-Núñez et al., 2017b; Cavazos-Álvarez et al., 2020). Petrological investigations of cutting material from eleven boreholes revealed a steady increase of welding with increasing depth along with a continuous reduction of porosity and permeability (Cavazos-Álvarez et al., 2020). Only in areas where the thickness of the Xáltipan ignimbrite is greater than 400 m, the basal facies was formed. In addition, the unit has been influenced by volcanic activity of the caldera and post-caldera groups (section 6.2), and evidence of argillic and propylitic alteration indicates that the unit is locally part of the geothermal reservoir (Cavazos-Álvarez et al., 2020).

Whenever possible, future modelling approaches should consider the revised thickness and facies classifications of Cavazos-Álvarez et al. (2020), or use a trimodal probability density function for parametrization, which would consider the rock property changes with depth.

6.3.2. Pre-Caldera Group

The rocks of the pre-caldera group predominantly comprise basaltic to andesitic lavas and can be associated with the Teziutlán andesite unit in the outcrops (chapter 5). However, the occurrence and extension of the deeper Hornblende andesites in the subsurface is questionable. In contrast to previous studies, hornblende was neither found in the andesitic lavas in the outcrops nor in the borehole core samples. The only sample containing hornblende was identified as subvolcanic rock (Fig. 38; thereby the outcrop was marked as Cuyoaco andesite in the geological map). Numerous granodioritic intrusions with hornblende and biotite were reported in the original lithological well profiles, which intrude into the pre-caldera andesites (well H8, H11, H12, H26, H28, H37). Considering the strong alteration intensity observed in the deeper section of the pre-caldera group, those rocks might have been misinterpreted as altered andesitic lavas. Since the andesites have not yet been studied in greater detail (there is no literature available except for the preliminary studies and maps created by CFE; e.g., Ferriz and Mahood, 1984), further geological investigations and dating are required to better understand their geological evolution and extension in the study area. However, distinctly different rock properties between the two andesite units as described in Calcagno et al. (2022) were not observed. Therefore, it seems reasonable to depict the two andesite units as part of a single model unit.

Additionally, basaltic to rhyolitic lavas with a variable thickness and limited extension were identified in the shallow section of the pre-caldera group (between ~ 700–1400 m bgl; chapter 5; Carrasco-Núñez et al., 2017b; Cavazos-Álvarez et al., 2020). The exact age of these lavas is not yet known, but they most likely can be related to the pre-caldera rhyolitic lavas and domes (Carrasco-Núñez et al., 2017b), or to the volcanic activity of the post-caldera group (Urbani et al., 2020, 2021). Due to the high geological heterogeneity regarding rock type, thickness, extension, and degree of hydrothermal alteration, it could be favourable to define an additional model unit in small-scaled models with a high resolution (small grid size). In addition, the structural setting and fluid flow might differ at this depth from those in the deeper sections of the pre-caldera group or pre-volcanic basement.

A thick tuff layer (the Humeros vitric tuff; Cedillo et al., 2000) within the pre-caldera group was not identified in the subsurface of the geothermal field. All samples that were originally classified as Humeros tuff were identified as hydrothermally altered andesitic lavas. Our petrographic results confirmed the findings of Carrasco-Núñez et al. (2017b), who revised the lithological well profiles from nine boreholes. The lithological well profiles provided by CFE are mainly based on the macroscopic analysis of

cuttings. Hydrothermal alteration led to discolouring (beige-brownish to greenish colour) and a rather tuffaceous appearance in some cores, which can be easily misinterpreted during the analysis of cutting material (chip size of a few mm).

Prior to the GEMex project, the outcropping units in the roadcuts of the Las Minas area were considered analogues to the subsurface of the LHGF (personal discussions with the Mexican partners in the field). These roadcuts reveal an upper andesitic lava flow, followed by a brownish ignimbrite and a lower andesitic lava flow showing distinct petrographic characteristics compared to the upper andesitic lava flow (Fig. 16). It was assumed that this sequence represents the Teziutlán andesite, Humeros tuff and Cuyoaco andesite from top to base. This led to the conclusion that both the Humeros tuff and the Miocene Cuyoaco andesite unit form extensive layers within the geothermal field. However, dating and detailed petrographic analyses (Kozdrój et al., 2020) revealed that both andesite flows (And2 and And1 in Fig. 16) observed in the roadcuts can be related to the Teziutlán andesite unit and that the ignimbrite (Ig1) and co-ignimbrite described in Olvera-García et al. (2020) might not be related to the volcanic activity of the LHVC.

The Humeros tuff has a variable thickness (30–300 m) and depth range in the original lithological well profiles and was not observed in some of the boreholes (e.g., H44, H45, H55). Although this unit has been questioned within the GEMex project, the local model unit U7 was implemented in the updated version of the local Los Humeros model (Calcagno et al., 2019, 2022). However, petrographic (Carrasco-Núñez et al., 2017b; Cavazos-Álvarez et al., 2020; chapter 5) and fluid analyses (Bienkowski, 2005; Gutiérrez-Negrín and Izquíerdo-Montalvo, 2010; Lelli et al., 2020) as well as results from geophysical surveys (Granados-Chavarría et al., 2022) point to a single (fracture-controlled) reservoir and did not identify an extensive and homogenous fluid barrier within the geothermal field. Based on these findings, we recommend to discard this unit in future modeling approaches.

6.3.3. Pre-Volcanic Basement

Cedillo (1997) described the pre-volcanic basement as a low-permeable aquifer consisting of Cretaceous and Jurassic limestones, marbles, and hornfels as well as some intrusions. The fluid flow in the carbonates is restricted to faults with secondary porosity. The intrusive bodies ascended along large fault zones. Due to their low permeability, they were interpreted as fluid barriers in the subsurface that impede the regional lateral fluid flow and recharge of the geothermal field. However, recent studies have shown that the recharge of the geothermal field indeed takes place via fault zones and thrust faults in the carbonatic basement (Lelli et al., 2020; Pinti et al., 2021). Furthermore, the fractured metamorphic zones that developed around the intrusions represent preferred fluid pathways (observed due to hydrothermalism in fractures and fault zones; Rochelle et al., 2021; González-Partida et al., 2022) and are possible targets for the development of EGS (Lepillier, 2020).

In the preliminary 3D model (Calcagno et al., 2019), the basement unit U9 extends from ~ 2 km to 12 km depth. The bottom depth of the sedimentary sequences below the LHGF was estimated at 5 km depth (Löer et al., 2020). For future modeling approaches, the metamorphic basement (Teziutlán Massif) should be included as a separate model unit as it accounts for more than 50% of the model volume. For the temperature models (Deb et al., 2019d), the units were parametrized using weighted mean values for each parameter (for unit U9: limestones 95%, and chert/marble/skarn 5%) assuming conductive heat transport. Vertical features representing intrusive bodies and their metamorphic by-products could be implemented to better depict the heat flow in the subsurface. Furthermore, convective heat transport along major fault zones should be considered.

6.4. Gravity Survey and Parametrization of a Local 3D Model of Los Humeros

The following section represents the last step of the workflow "data integration and joint interpretation" as shown in Figure 11, and has been performed in collaboration with Natalia Cornejo from Karlsruhe Institute of Technology, Germany (KIT, WP5 in GEMex). Parts of this section are included in the publication Cornejo-Triviño and Weydt et al. (2022, in preparation).

In order to get a better understanding of the shallow units of the caldera complex, a local gravity survey was carried out in the central collapse zone within the Los Potreros caldera (Schill and Cornejo, 2019; GEMex Deliverable WP5.6). The findings of chapters 3 to 5 were used to parametrize a slightly modified version of the local 3D model of the Los Humeros geothermal field and to perform forward modeling and gravity inversion.

6.4.1. Data Acquisition and Processing

About 260 gravity stations were measured along ten E–W profiles (5.5 km length) with inter-station and inter-profile distances of 200 m and 500 m, respectively. For the measurements a CG-5 Autograv Gravity Meter (Scintrex Ltd., instrumental accuracy of 0.001 mgal) and differential GPS (DPGS; two Trimble 5700 receivers and two Trimble antennas TRM39105 and TRM41249 with an instrumental accuracy of 5 mm vertical) were used. During the surveys, the gravity measurements (single measurement duration of 120 s) were repeated three times and the measurement with the lowest standard deviation was selected for further investigation. Standard deviation of the raw gravity measurements ranges between 0.008 and 0.119 mGal, and the DGPS measurements ranges between 0.0012 and 0.3893 m.

After pre-processing of the data (instrumental drift, earth tide, latitude and elevation corrections using GravProcess), a terrain correction was performed using Oasis Montaj™ (Geosoft). To obtain a regional complete Bouguer anomaly a Bouguer density of 2,670 kg m^{-3} was used by applying a Gaussian filter (Schill and Cornejo, 2019). Likewise, the processing of the local gravity data was carried out using a Bouguer density of 2,670 kg m^{-3}. Afterwards, the regional trend was subtracted from the local complete Bouguer anomaly to obtain the residual anomaly.

To investigate the correlation between the obtained gravity values and the 3D geological model provided by Calcagno et al. (2019), forward modeling was performed with the software GeoModeller using the corresponding model section of the local model covered by the gravity stations (~ 5.5 × ~ 4 km; Fig. 61) and rock densities retrieved from chapters 3 to 5. Afterwards, inverse modeling was performed using a Markov Chain Monte Carlo Stochastic Inversion method in GeoModeller.
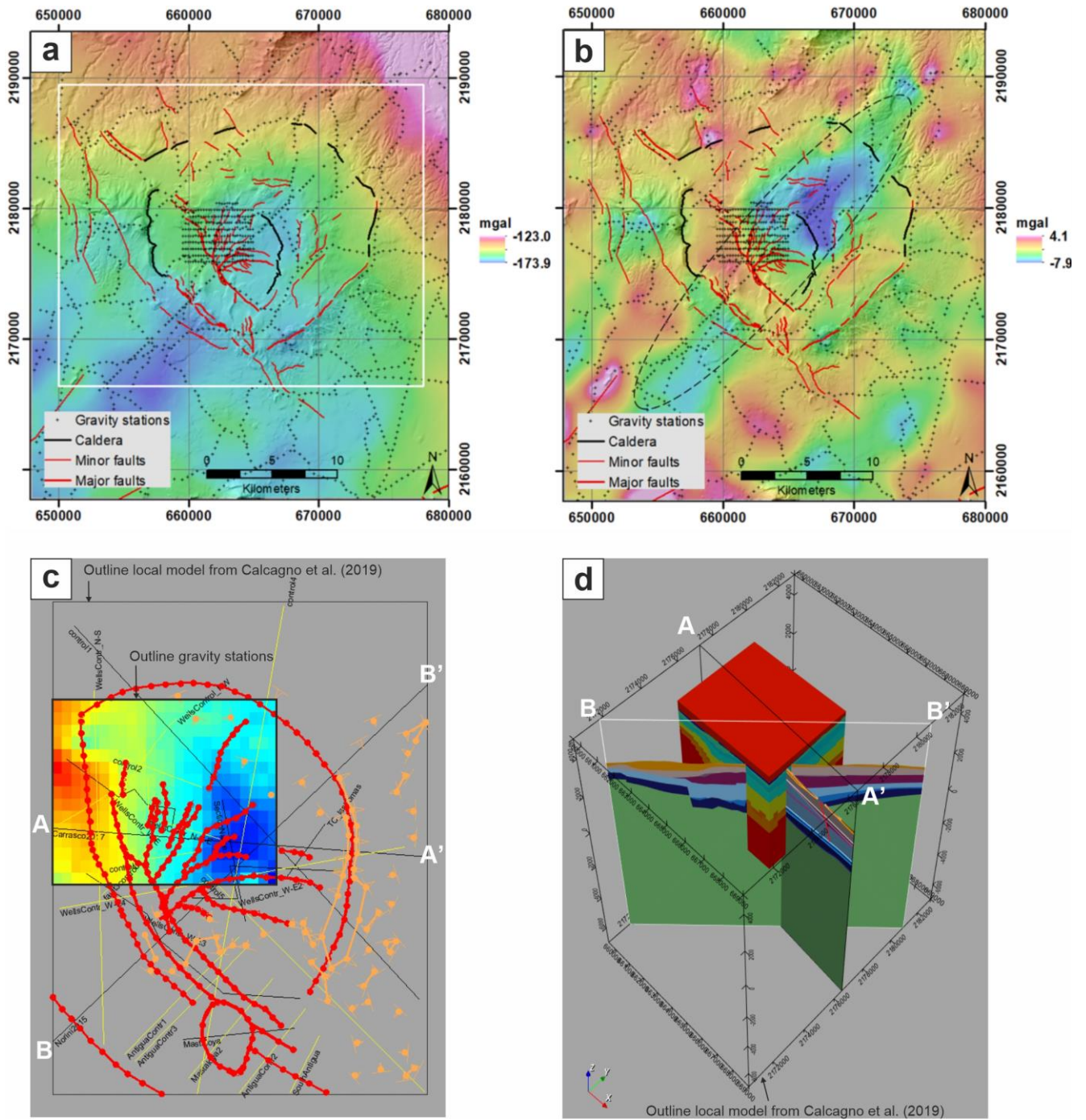
Figure 61: (a) Complete Bouguer anomaly and (b) residual anomalies of the LHGF and surroundings displayed on a digital elevation model (15 m resolution DEM) from Cornejo-Triviño et al. (2022). The black crosses in the central part of the Los Potreros caldera represent the gravity stations used in this study. The black oval in (b) shows a prominent NE–SW low gravity anomaly, which is interrupted by a high anomaly. (c) outline of the gravity stations and (d) local model used for the forward modeling and gravity inversion in this study. A-A' and B-B' represent the orientation of geological cross-sections presented in Carrasco-Núñez et al. (2017b), and Norini et al. (2015), respectively.

6.4.2. Model Parametrization

Unfortunately, at this point, no data from well logs are available that could provide more accurate information on the thickness of the expected lithologies and their rock density. Therefore, for the parametrization of the model units in this particular part of the caldera, the depth and volume of the different lithostratigraphic units were estimated based on Calcagno et al. (2019), revised lithological borehole profiles presented in Carrasco-Núñez et al. (2017b) and Cavazos-Álvarez et al. (2020) as well as field data (Weydt et al., 2022a). As the investigated borehole core samples (chapter 5) do not cover all model units, data from both the outcrop samples and the borehole core samples were used. The rock densities were transferred to reservoir conditions using the workflow presented in chapter 4 (Table 12).

Table 12: Rock densities from Weydt et al. (2021a) transferred to reservoir conditions for the different model units

Model unit	Lithologies	Density sat [g cm^{-3}]	Volume estimation for each lithology per unit in [%]
U1 Undefined pyroclastic	Undefined pyroclastic deposits	1.89	100
U2 Post-caldera	Rhyodacite (4%), tuff (4%), and pumice (17%); weighted mean value	1.50	25
	Andesitic lava	2.60	25
	Basaltic lava	2.42	50
U3 Los Potreros caldera	Andesitic lava	2.60	36
	Tuff	1.93	60
	Pumice	1.20	4
U4 Intermediate caldera*	Tuff	1.93	50
	Andesitic lava	2.59	50
U5 Los Humeros caldera	Upper Xáltipan ignimbrite (non to slightly welded)	1.88	35
	Middle Xáltipan ignimbrite (slightly to moderately welded)	2.31	50
	Basal Xáltipan ignimbrite (highly welded)	2.45	15
U6 Upper pre-caldera	Rhyolitic lavas	2.45	20
	Basaltic to andesitic lavas	2.40	80
U7 Intermediate pre-caldera	Basaltic to andesitic lavas	2.44	40
	Basaltic to andesitic lavas (low porous)	2.66	60
U8 Basal pre-caldera	Basaltic to andesitic lavas	2.44	70
	Skarn	2.80	30
U9 Basement (here 2200 m to ~ 3000 m depth)	Marble	2.68	85
	Granite	2.62	10
	Skarn	3.10	5

sat = saturated conditions, * = no outcrops or wellbore core data available, estimations based on data from U3

Different approaches were tested for the forward modeling using GeoModeller: (1) populating the model units with assumed density values, (2) the multi-modal density distribution, and (3) the optimization density approach. In a first test-run, the model units were parametrized with assumed density values (Table 13) based on the rock property database (chapter 3). These values represent average rock densities per unit and are neither corrected for reservoir conditions, nor do they take into account the probability of the different lithologies per unit. It has to be emphasized that for unit U4 no data exists and that the input parameters were estimated based on the data from units 3 and 5. For the other two approaches, the density values presented in Table 12 (corrected for reservoir conditions) were used. The multi-modal density approach allows to insert up to three density values for one model unit, while the density optimization approach calculates weighted average densities for each unit. The results of the forward modeling are presented in Fig. (62) and show a reduced misfit between the observed and computed gravity values when using the multi-modal distribution or density optimization. Likewise, the number of iterations needed to perform the forward model significantly decreases.

Table 13: Assumed density values per unit

GEMex local model unit	Bulk density [g cm^{-3}]
U1	1.48
U2	2.09
U3	1.60
U4*	1.53
U5	1.45
U6	2.49
U7	2.32
U8	2.50
U9	2.75

* = no outcrops or wellbore core data available, average value was calculated from U3 and U5
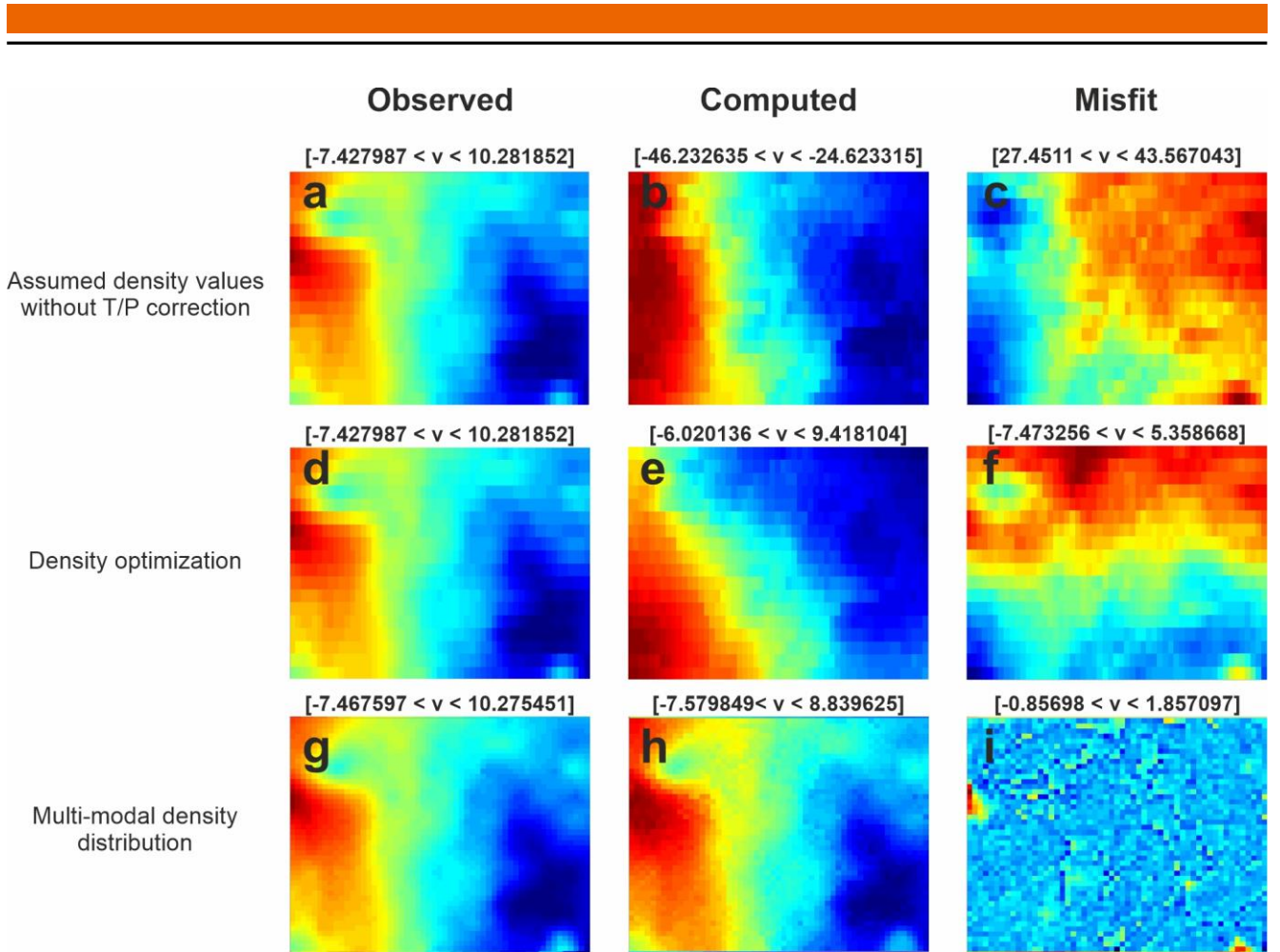
Figure 62: Forward modeling testing different approaches: (a) to (c) assumed average density values, (d) to (f) density optimization approach using weighted densities, and (g) to (i) multi-modal density distribution (horizontal cell size: 100 m). Values are presented in mgal.

Afterwards, an inversion of the gravity data was performed using the forward models (optimized density values = model convergence with a standard deviation of 0.2 g cm⁻³, and the multi-modal density distribution using 0.1 g cm⁻³ for the standard deviation). For reasons of simplification, the model unit boundaries were not modified at this point. The results are presented in Fig. 63.
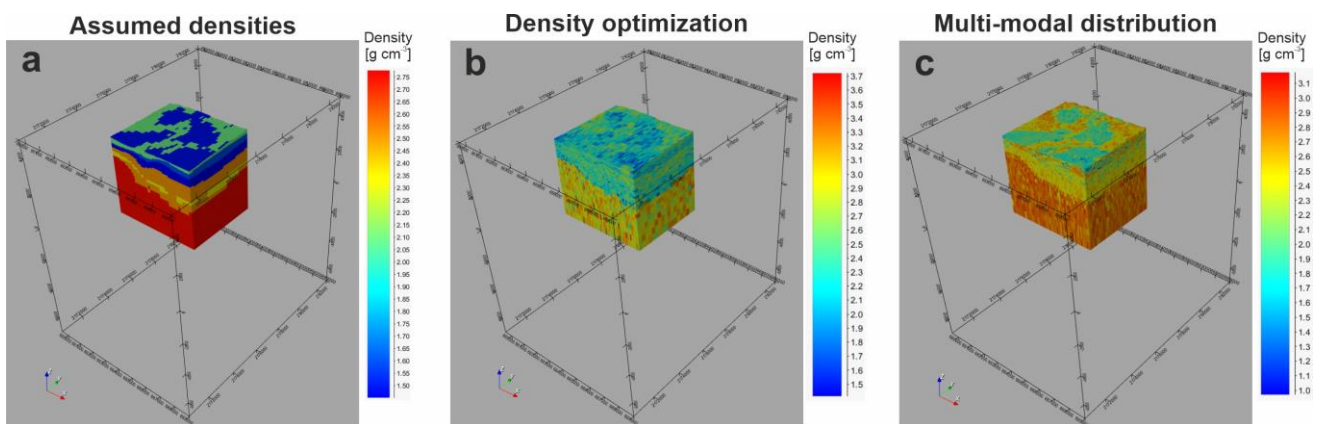
Figure 63: Output models after gravity inversion using (a) assumed densities without T/P-correction, (b) the density optimization approach, and (c) the multi-modal density distribution approach.

The multi-modal density approach resulted in the smallest misfit and improved the visualization of the density differences. Fig. 64a represents the top-view of the model which shows young lava flows (yellow to orange) as well as ash fall deposits and pyroclastic rocks (blue) of the post-caldera group. Several volcanic vents are located in the central collapse zone (Carrasco-Núñez et al., 2017a; Lucci et al., 2020). For example, Fig. 64c shows a young (< 7 ka) basaltic lava flow north of the town Los Humeros with an approximate thickness of 4 to 10 m in the outcrop. The lava flows are surrounded and/or covered by highly porous ashfall deposits and pyroclastic deposits, resulting in significant density contrasts.
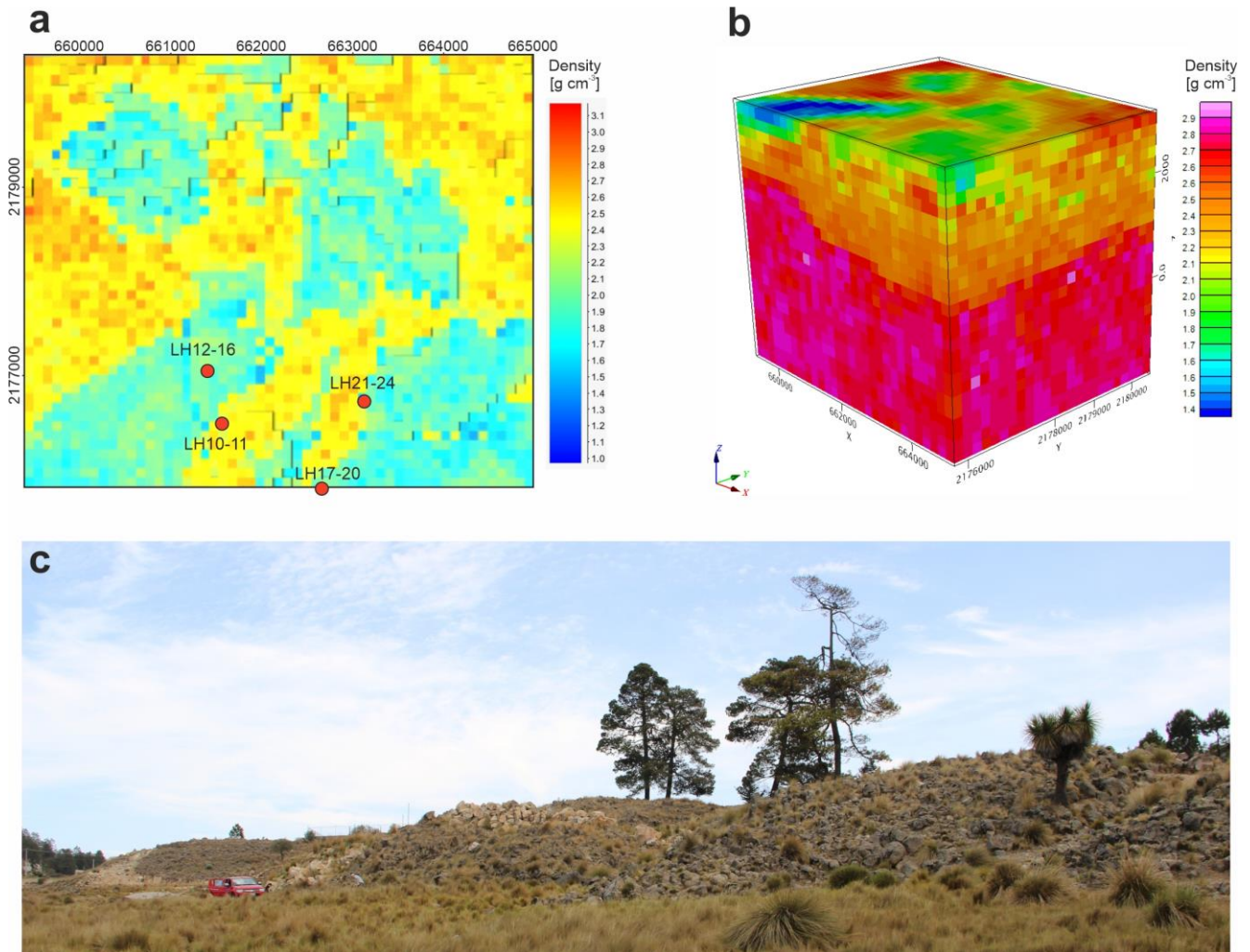
Figure 64: Top view of the output model of the gravity inversion using a multi-modal density distribution (a) and the 3D density model displayed in the Oasis Montaj software after smoothing (b). The red circles in (a) represent the sampling locations of the outcrop analogue study (chapter 3) and the respective sample numbers are displayed. (c) Young basaltic lavas (< 7 ka) inside of the caldera with an approximate thickness of 4–10 m (outcrop north of Los Humeros; samples LH12-16).

For the interpretation of the results, the 3D density model was imported into the Oasis Montaj software (linear density distribution and data smoothing was applied, Fig. 64b). Density maps for different depth levels were created and are presented in Fig. 65. For a better comparison, the rock types as described in the lithologic drill profiles are displayed for the respective depth level. The ground surface elevation inside of the caldera ranges from 2750 to 3000 m above sea level.

The results indicate various lavas (red to pink) with flow directions south and southwest, and possibly lava domes with a diameter of up to 400 m (e.g., lower right corner in Fig. 65a-d). North and north-west of the central collapse zone, voluminous layers occur consisting of multiple mafic to intermediate lavas (possibly a buried crater rim). In the south-west to south-east, the lavas seem to be thinner and are covered by pyroclastic deposits (yellow/orange to blue). At greater depth pyroclastic deposits of the Xáltipan ignimbrite predominate (Fig. 65e) and some andesitic to rhyolitic lavas are present. At about 2550 m a.s.l. the Xáltipan ignimbrite is moderately to highly welded (Cavazos-Álvarez et al., 2020). Thus, the density contrast to the andesitic and rhyolitic lavas is rather small.

In general, the density contrasts are in good agreement with the lithologies reported in the lithostratigraphic well profiles. However, it has to be emphasized that only a small number of the well profiles were revised (Carrasco-Núñez et al., 2017b; Cavazos-Álvarez et al., 2020), and that detailed rock descriptions or information on the e.g., matrix porosity, degree of welding or hydrothermal alteration are not available.

The low-density anomaly observed north-east of the central collapse zone coincides with the area marked as "northern sector" in Pinti et al. (2021), where rapid meteoric recharge was identified (Fig. 57; section 6.2.2). One possible explanation is that rainwater infiltrates the highly porous volcaniclastic rocks in this area and quickly travels along the smaller faults as mapped in Piccardi (2020).

The model units U7 and U8 (intermediate and lower pre-caldera group) feature higher average rock densities than estimated (Table 12). A higher proportion of skarn as well as reservoir sealing due to mineral precipitation in the deeper reservoir sections could be a possible explanation.

A thick homogeneous layer separating the andesites, as described in section 6.3.2, cannot be derived from the density model.
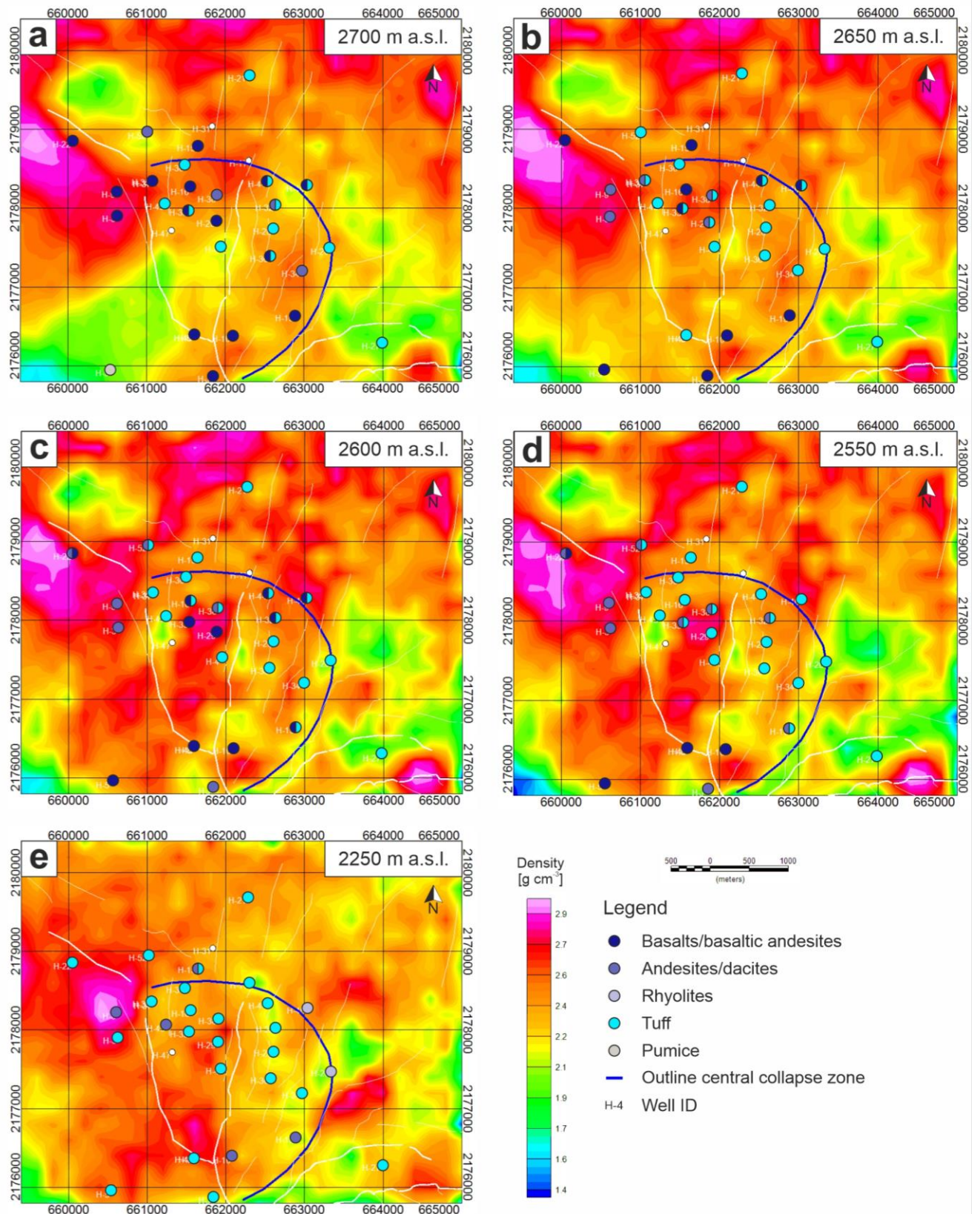
Figure 65: Density maps of the central collapse area at (a) 2700 m a.s.l., (b) 2650 m a.s.l., (c) 2600 m a.s.l., and (d) 2250 m a.s.l. showing the distribution of lavas and volcaniclastic deposits of the post-caldera and caldera group. The grey to blue circles represent the identified rock types as described in the lithological well profiles provided by CFE and Carrasco-Núñez et al. (2017b) and Cavazos-Álvarez et al. (2020).

6.4.3. Sensitivity Analysis

After identifying the best parametrization approach, a sensitivity analysis was performed with GeoModeller, allowing the software not only to vary the density values, but also to vary the layer boundaries of the geologic model (Table 14). Thereby, the contours of the formations at the ground surface (~ 2750–3000 m a.s.l.) were kept constant as they were confirmed by mapping (Carrasco-Núñez et al., 2017a).

Table 14: Results of the sensitivity analysis showing the misfit between observed and computed gravity data of the respective output models

| Probability of property change [%] | | Misfit [mgal] | | |
Rock density	3D model units	Minimum	Maximum	Range
100	0	-1.036842	2.313116	3.349958
80	20	-1.218982	2.022533	3.241515
60	40	-1.436149	2.146333	3.582482
40	60	-1.221409	2.164976	3.386385
50	50	-1.395746	1.932958	3.328704
20	80	-1.590811	2.074753	3.665564
0	100	-2.83167	2.313116	5.144786

The resulting models show a similar density distribution (Fig. 66) as well as a similar misfit (Table 14). According to this approach, the 80/20-output model shows the smallest misfit range. The small differences between the models indicate that the original 3D geological model (Calcagno et al., 2022) and the estimated rock densities (Table 12, multi-modal density distribution approach) already represent a good estimation of the reservoir. However, in contrast to the 100/0-scenario, the output models with a higher variability with respect to the model units (80/20- to 50/50-scenarios) show increased high-density values in the pre-caldera and post-caldera group (particularly the units U6 and U5).
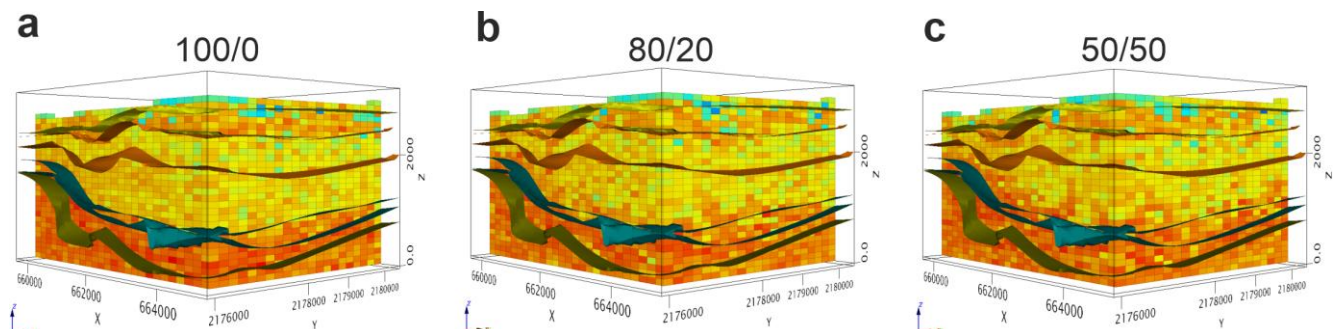
Figure 66: Output models (here horizontal cell size: 200 m) representing (a) the 100/0-scenario (rock density is 100% variable and the model boundaries are fixed), (b) the 80/20-scenario, and (c) the 50/50-scenario.

The 80/20-scenario density model displayed in Oasis Montaj (Fig. 67) indicates lateral lava flow in the pre-caldera group between ~ 2000 and 2700 m a.s.l. As shown in Fig. 67c these lavas have a very irregular distribution, which results in a very uneven and irregular relief that has been filled with volcaniclastic deposits. The high-density anomalies at this depth level could be interpreted as lava sills and dikes (Fig. 67a and d).
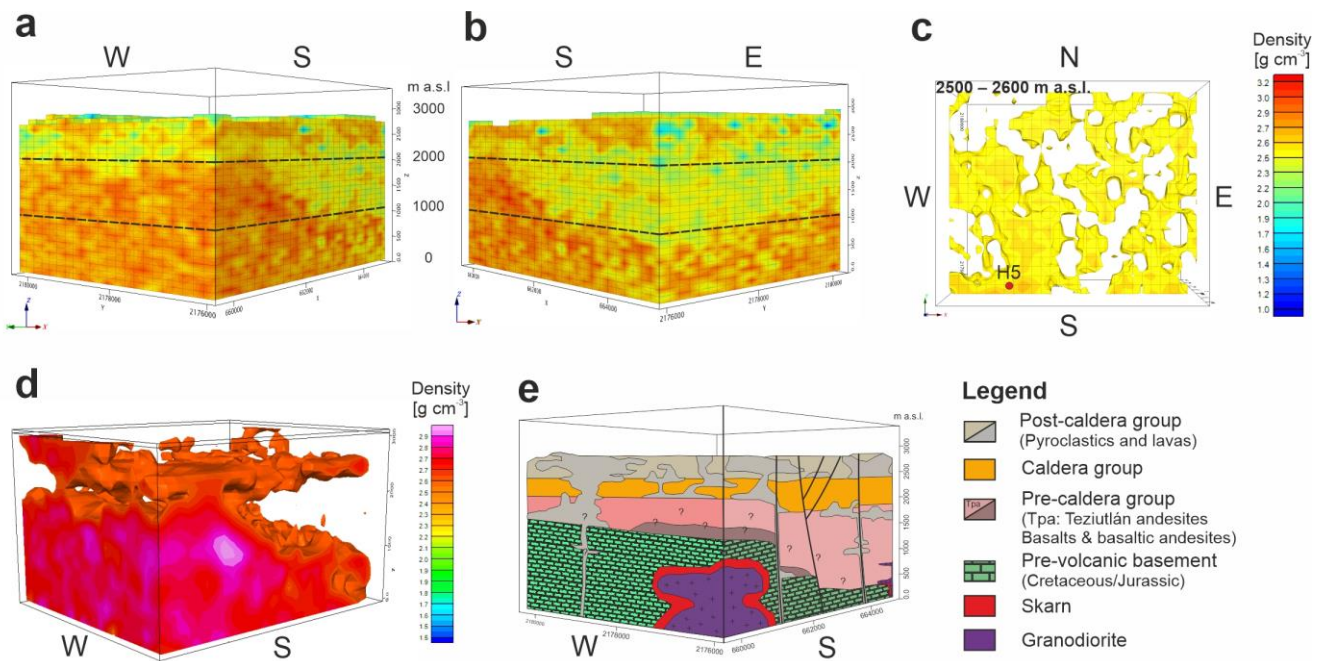
Figure 67: W–S view (a) and S–E view (b) of the density model displayed in Oasis Montaj (80/20-scenario, smoothing and linear density distribution were applied). (c) Top-view showing the rock units with densities > 2.57 g cm^{-3} between 2500 and 2600 m a.s.l. (d) W–S view of high-density areas (here a different visualization-option was used in Oasis Montaj) indicating lateral lava flow between ~ 2000 and ~2700 m a.s.l. (e) preliminary geological interpretation of (a) also using information retrieved from well logs (CFE data; Carrasco-Núñez et al., 2017b; Cavazos-Álvarez et al., 2020). Faults (black lines) were retrieved from Calcagno et al. (2019).

Likewise, high-density anomalies with a rather lateral extension are observed at ~ 1500 m a.s.l. in the upper pre-caldera group. These anomalies correlate with trachyandesitic and basaltic lavas identified in H26 and H27, respectively. This observation matches the findings from Arzate et al. (2017), Corbo-Camargo et al. (2020), and Granados-Chavarría et al. (2022) who identified stratified volcanic deposits and alteration at this depth level.

Further density anomalies can be observed in the intermediate to basal pre-caldera group (> 1000 m a.s.l., Fig. 67a and b). However, at this point it can not be determined whether they result from fluid-rock interactions along fault zones or represent intrusions. For example, the high-density values in the W–S corner (Fig. 67a and d) resemble a laccolith-like structure. However, Carrasco-Núñez et al. (2017b) reported about 200 m thick basalts and basaltic andesites belonging to the pre-caldera group on top of the carbonatic basement in this area (well H5), which are overlain by strongly altered rocks and Teziutlán andesites.

At the bottom of H5 (W–S corner), granodiorite was reported in the lithological well profile (~ 900 m a.s.l.). In Fig. 60, the granodiorites in the reservoir were interpreted as dyke-like structures. However, the size and shape of the high-density anomalies (with > 3.1 g cm^{-3}) in this section suggest a larger structure as well as skarn deposits (~ 3.2 g cm^{-3}, Table A1). The size and shape of this intrusion remains speculative, however, the results from Corbo-Camargo et al. (2020) point out to a tabular shape. Granodiorite was reported in eight other wells between 1500 and 3100 m bgl in the central collapse zone.

While the interpretation of deeper reservoir units is subject to high uncertainties (also considering the decreasing resolution with reservoir depth), the approach presented here allowed a better quantification of the thickness and extension of the shallow lavas and volcaniclastic deposits, which is important to better characterize the cap rock and meteoric fluid recharge of the geothermal field.

7. Conclusions

Untapping the geothermal potential of unconventional high-temperature geothermal resources could represent a turning point in the geothermal energy sector and provide environmentally friendly, safe and scalable energy that is economically competitive with fossil fuels. There is still much more research and exploration needed before this technology is technically and economically feasible. First, the control mechanism must be understood in order to fully adapt conventional exploration and exploitation technologies to high temperatures and challenging reservoir conditions. Thus, this thesis focused on reservoir characterization of super-hot unconventional geothermal systems related to volcanic systems in Mexico. Two caldera systems, the Los Humeros and Acoculco caldera complexes, were used as natural laboratories to (1) study the physiochemical and mechanical behavior of reservoir rocks, (2) investigate hydraulic rock properties to identify potential reservoirs and fluid pathways, and (3) quantify processes that could affect the reservoir quality of super-hot unconventional geothermal systems. Geothermal exploration is the most important phase during a geothermal project. Detailed reservoir characterization based on multi-disciplinary datasets is crucial for the understanding of complex processes within the geothermal reservoir. Particularly for hydrothermal systems, accurate identification of geological heterogeneities and petrophysical anisotropies that could affect fluid flow in the subsurface can determine the success or failure of a geothermal project.

The multi-method approach presented in this work makes it possible to efficiently provide qualitative input data which covers the geological heterogeneity of the subsurface rocks at different scales for a wide range of applications and different disciplines. The resulting relational database is unique as it comprises metadata, petrographic descriptions, bulk geochemical data and up to 34 rock parameters determined for each sample. More than 31000 data entries were generated covering a great variety of different rock types and lithologies of Jurassic to Holocene age. This approach allows to accurately determine the relationships between the parameters and to better depict the reservoir properties. The applied sampling strategy and sample distribution not only reduce costs in the field, but also ensure that all data obtained in the laboratories are comparable and can be linked to different disciplines (e.g., structural investigations, shallow geophysical surveys, and high-T/P experiments). Furthermore, all project partners are able to use the same dataset for the parametrization of reservoir models, interpretation of geophysical surveys, and economic assessments. In a nutshell, the implementation of rock characterization as a fundamental element in geothermal projects reduces the uncertainty during reservoir characterization and data integration.

The fieldwork and the results of the rock property measurements revealed the complexity of both geothermal systems. Composition, lateral extension, and distribution of the volcanic sequences are very variable within the study area. Furthermore, the pre-volcanic basement showed a high geological heterogeneity comprising several different rock types including shales, limestones, sandstones, granitoids, marbles and skarns. Thus, the petrophysical and mechanical rock properties show a high variability and a wide range for most of the parameters. Based on statistical analysis it was possible to define lithostratigraphic units with distinct parameter ranges. In general, the rocks of the pre-volcanic basement and Miocene to Pleistocene lavas, which have been considered as geothermal reservoirs, feature low to very low matrix porosities (< 5%) and permeabilities (< 10^{-16} m²), as well as intermediate-to-high densities, thermal properties, and sonic wave velocities. The overall low matrix permeability and the weak correlation between matrix porosity and permeability suggests that fluid flow in the study area is predominantly controlled by faults and fractures. The pyroclastic rocks, which were considered the cap rock of the geothermal field, and the overlying younger volcanic sequences show the highest variability with respect to matrix porosity and bulk density, but feature overall low-to-intermediate thermal conductivities and sonic wave velocities. In the case of the Los Humeros caldera, only the low-permeable welded facies of the Xáltipan ignimbrite might act as the cap rock of the geothermal field. Specific heat

capacity shows comparatively small variations throughout the dataset. In contrast, magnetic suscepti-bility varies over more than four orders of magnitude showing formation-related trends that could be helpful for the interpretation of geophysical surveys.

The detailed investigation of borehole core samples and the comparison with data from stratigraphically equivalent outcrop samples allows the identification of processes that occurred in the reservoir and their effect on the reservoir properties. Within the Los Humeros geothermal field, the reservoir rocks were affected by hydrothermal alteration of different intensities, brecciation, and fracturing. Thus, the sam-ples showed a high geological variability prohibiting a clear correlation between the boreholes or the outcropping units. Different alteration facies were identified comprising argillic alteration observed at shallow to intermediate depths (to ~ 1400 m bgl) followed by propylitic alteration (> 1400 m bgl) and the formation of skarns (> 2800 m bgl). In addition, advanced silicification caused by acidic fluids as well as high-temperature minerals were observed in samples at different depths, which may indicate (small-scaled) shallow intrusions in the reservoir. In comparison to the outcrop data, the borehole core samples showed significant changes in bulk chemical and petrophysical properties. Hydrothermal alteration is mainly fracture-controlled and varies on a cm-scale. The samples showed enhanced hydraulic proper-ties due to microfractures, mineral dissolution and precipitation creating additional secondary mi-croporosity. As a consequence, the samples featured reduced bulk densities and sonic wave velocities. The observed increased thermal conductivities can be explained by the replacement of the pristine rock matrix with minerals like calcite, quartz, epidote, and chlorite, which feature higher thermal conductivi-ties than the original feldspars. Significant losses of magnetic susceptibility could be used to estimate the extent of hydrothermal aureoles as an indicator for possible fluid pathways during geophysical sur-veys. Results of the petrographic analyses and the weak correlation between alteration indices and the rock properties imply that the reservoir rocks were affected by multiple alteration events over time. New discrimination methods based on rare earth element concentrations were proposed to relate the bore-hole core samples to the outcropping units and to distinguish between rhyolitic and silicified lavas.

The rock properties presented in this work were obtained under laboratory conditions. However, the majority is sensitive to pressure and temperature changes with increasing reservoir depth. Particularly, matrix porosity and permeability of the pyroclastic rocks significantly decrease with reservoir depth due to high rock compressibility. Likewise, the effects of pressure and temperature on the thermal and me-chanical properties are complex and often counteract each other. A step-by-step work flow was pro-posed, which allows for an estimation of the reservoir properties under in-situ conditions using semi-empirical and analytical correction functions.

Previous conceptual geological models of the Los Humeros geothermal field used at the beginning of the GEMex project were not able to explain the volcanological evolution of the caldera complex, or to accurately depict the hydrogeology, heat source, and temperature distribution in the subsurface. Thus, it was not possible to simulate shallow temperature anomalies as observed in downhole temperature profiles, heat flow or recharge of the geothermal system in numeric reservoir models. The integrated field-based approach proposed in this work helped to unravel the complexity of geothermal reservoir rocks in active volcanic settings and, together with findings from different disciplines, contributed to update the conceptual geological model of the Los Humeros geothermal field. In contrast to previous beliefs, the geothermal field is fed by multiple heat sources, and super-hot to supercritical resources might occur already at relatively shallow depths of < 2 km. Fluid flow is not restricted to the caldera complex and recharge is mainly controlled by major regional fault zones in the carbonatic basement and subsequently in the overlying Miocene to Pleistocene lavas. The faults and damage zones inside the caldera are the result of the regional tectonic events as well as the volcanic activity of the Los Humeros volcanic complex, which allowed a mixture of meteoric and magmatic fluids to interact with the host rocks and constantly alter its physiochemical behaviour over time.

The new knowledge gained from the outcrop and reservoir core studies was applied to a local 3D model of the Los Humeros geothermal field to perform forward modeling and gravity inversion of data obtained during a local gravity survey within the main collapse zone of the caldera complex. Thereby, the usage of multi-modal density distributions (corrected for reservoir conditions) significantly reduced the misfit between observed and computed gravity data. The results demonstrate the importance of a detailed assessment of the rock formations and their characteristics, as it significantly improves the interpretation of geophysical surveys and allows for mapping different lithologies in the subsurface.

To conclude, the combination of outcrop analogue and reservoir core studies represents a cost-effective and powerful tool to characterize the subsurface units and their geological heterogeneity at different scales. A detailed assessment of geochemical, petrophysical, and mechanical rock properties is paramount for e.g., the development of conceptual geological models, the interpretation of geophysical data or the parametrization of 3D numerical models. The findings presented in this work improved the understanding of the caldera complexes and super-hot geothermal systems related to volcanic systems in general. The high amount of data and level of detail presented in this study facilitate various applications in comparable geological settings within the Trans-Mexican Volcanic Belt or similar volcanic geothermal play types worldwide.

8. Outlook

To complement the existing database, future work should focus on additional electric resistivity and rock mechanical tests (fracture toughness and triaxial tests) to better support the interpretation of magnetotelluric, transient electromagnetic, or electric resistivity surveys and the parametrization of 3D geomechanical models. Micro-CT analyses would be helpful to better understand the internal pore and fracture network of the reservoir rocks, which is important for upscaling the hydraulic properties to reservoir scale.

Since this thesis focused on the assessment of petrophysical and mechanical rock properties performed under laboratory conditions, semi-empirical and analytical correction functions were used to transfer the rock parameters from laboratory to reservoir conditions. While these correction functions already provide a good prediction of the rock properties at reservoir depth, they are not able to represent the site-specific fracture pattern and microstructural variability, mineralogy, as well as hydrothermal, diagenetic, or metamorphic processes affecting the reservoir rocks. Thus, for a more precise reservoir property prediction of the Los Humeros and Acoculco geothermal fields further high-temperature and high-pressure experiments would be required for each target unit.

Up to now, high-temperature and high-pressure experiments performed to estimate the rock parameters under in-situ conditions are scarce or, particularly for volcanic rocks, not available yet. Existing literature mainly focuses on the temperature- or pressure-dependence of single parameters for moderate- to low-porous rocks, such as limestones, granites, or sandstones. However, the response of high-porosity rocks to pressure changes can be fundamentally different. To correctly estimate the reservoir properties under in-situ conditions, future research should focus on laboratory experiments which are capable of determining multiple parameters simultaneously (e.g., permeability, thermal conductivity, and P-wave velocity) under super-critical conditions (high-T and high-P) also considering the fluid chemistry at reservoir depth. With the current state of technology, such experiments are not yet feasible. To take a decisive step towards this goal, the first true-triaxial press is currently under development at GFZ Potsdam (funded by ILB, Brandenburg; personal comment from Dr. Blöcher), which allows the investigation of coupled processes at laboratory scale (e.g., thermal, hydraulic, and mechanical properties as well as elastic and plastic rock deformation). Here, samples can be tested under true triaxial pressure conditions with the possibility of controlling all three principal stress directions ($\sigma 1 \neq \sigma 2 \neq \sigma 3$) as well as applying fluid flow in all three main directions (using high-pressure injection pumps at up to 600 bar). Furthermore, integrated Acoustic Emission Systems allow to simultaneously monitor the response of the sample to the pressure and temperature (up to 200 °C) changes.

For future modeling approaches, the results of the GEMex project should be taken into account and the current 3D geological models (Calcagno et al., 2022) should be updated accordingly. However, some questions remain unsolved. While the geophysical surveys performed within the GEMex project allowed for an identification of deep structures on a large scale (Arzate et al., 2018; Corbo-Camargo et al., 2020; Löer et al., 2020; Toledo et al., 2020b; Granados-Chavarría et al., 2022), the knowledge of the different pre-caldera lavas in the subsurface is still scarce. Further petrological analyses combined with dating could shed light on their extension and temporal evolution. Up to now, only two geophysical well logs were performed in the Los Humeros geothermal field. Additional well logs would be beneficial to better estimate the fracture network, density, and porosity distribution as well as the hydrothermal overprint in the reservoir. This work should be complemented by detailed petrographic and bulk chemical analyses (XRF and ICP-MS) of the cutting material to avoid misinterpretations in the lithological descriptions as pointed out in previous studies (Carrasco-Núñez et al., 2017b; Cavazos-Álvarez et al., 2020; Weydt et al., 2022b). With a better understanding of the internal architecture of the geothermal field, resource risks could be reduced. The majority of the wells in the Los Humeros geothermal field were drilled vertically and targeted the pre-caldera andesites or the underlying carbonatic basement. However,

future drilling operations should specifically target the major faults and their damage zones and/or consider the development of EGS in the fractured andesites and marbles.

Recent investigations highlighted comparatively high CO_2-emissions of the Los Humeros geothermal field (González-García et al., 2022). Currently, only a fraction (~ 16%) of the produced fluids is reinjected into the reservoir. The natural CO_2-emissions of the geothermal field were estimated at 84 t per day (Jentsch et al., 2020). However, the geothermal production increases this amount by a factor of 10 (González-García et al., 2022). For a more environmentally friendly energy production, new exploitation strategies as well as CO_2 capture and storage technologies should be evaluated and considered in the future. According to recent calculations (González-García et al., 2022), the usage of closed systems, such as binary power plants, could reduce the CO_{2eq} footprint of the geothermal field by 82%. In addition, targeting the super-hot resources in the pre-caldera units would increase the electric yield per well and thus, reduce the CO_{2eq} footprint per kW_{el}. Recent fluid analyses revealed that the reservoir fluids do not release C from the carbonatic basement and the majority of C is of mantle origin or originates from other sources (Pinit et al., 2021). Thus, developing future supercritical resources in the carbonates would most likely not cause artificially increased emission levels. Further options could be CO_2-sequestration for industrial use, as it is done for the Kizildere geothermal field in Turkey, or the reinjection of CO_2 into the subsurface as demonstrated in the Hellisheidi geothermal field (Iceland) within the framework of the carbfix (www.carbfix.com) and geco projects (https://geco-h2020.eu). The latter is based on the concept that basaltic reservoirs react quickly with CO_2 saturated fluids and convert it into solid minerals. However, the reservoir fluids in Los Humeros are already oversaturated in quartz and calcite (Izquíerdo et al., 2009) and further research would be required.

About 15 volcanic complexes such as Acoculco, Las Derrumbadas, Cerro Pinto, and Cuitzeo Lake are currently under exploration for geothermal utilization within the Trans-Mexican Volcanic Belt (Prol-Ledesma and Morán-Zeteno, 2019). The TMVB is characterized by a high average heat flow of 180 mW m^{-2}, and a geothermal gradient above 80 °C km^{-1} can be expected in most areas. Thus, the TMVB represents the most promising province for geothermal utilization in Mexico. For example, the comparatively new geothermal field Domo de San Pedro (production start in 2015; Romo-Jones et al., 2019) already produces ~ 25 MWe with four production wells. In addition, the potential for heat generation has not been exploited so far. According to CFE the calculated geothermal reserves of Mexico are about 10000 MWe (Prol-Ledesma and Morán-Zeteno, 2019), which could triple taking unconventional resources such as EGS into account (ThinkGeoenergy, 2019). Although numerous sites are currently under exploration and several geothermal projects have been authorized, the high investment costs and the competition with natural gas and solar energy hinder a fast and widespread installation of geothermal applications (ThinkGeoenergy, 2019). The comparison between Los Humeros and Acoculco has shown that the data obtained in this work could be applied to new fields (at least for preliminary resource assessments) and thus, reduce exploration costs and speed up future geothermal projects. However, the effects of hydrothermal alteration or metamorphic processes on the reservoir rocks should be evaluated on a field-by-field basis.

9. References

Abdulagatov, I. M, Emirov, S. N., Abdulagatova, Z. Z., Askerov, S. Y.: Effect of Pressure and Temperature on the Thermal Conductivity of Rocks, J Chem Eng Data, 51(1), 22–33, https://doi.org/10.1021/je050016a, 2006.

Abdulagatova, Z., Abdulagatov, I. M., and Emirov, V. N.: Effect of temperature and pressure on the thermal conductivity of sandstone, International Journal of Rock Mechanics and Mining Sciences, 46(6), 1055–1071, https://doi.org/10.1016/j.ijrmms.2009.04.011, 2009.

Adams, S. J.: Quantifying Petrophysical Uncertainties, SPE 93125, SPE International conference proceeding, the 2005 Asia Pacific Oil and Gas Conference and Exhibition, 5–7 April, Jakarta, Indonesia, 6 pp., 2005.

Ali, A., and Potter, D. K.: Temperature dependence of the magnetic properties of reservoir rocks and minerals and implications for in situ borehole predictions of petrophysical parameters, Geophysics, 77, WA211–WA221, https://doi.org/10.1190/GEO2011-0282.1, 2012.

AltaRock: Super Hot EGS – Reducing the Cost of Geothermal Through Technology Breakthrough, http://altarockenergy.com/, last access 21 March 2022, 2022.

Aminzadeh, F., and Dasgupta, S. N.: Reservoir characterization, in: Developments in Petroleum Science, Elsevier, Amsterdam, the Netherlands, 151–189, https://doi.org/10.1016/B978-0-444-50662-7.00006-8, 2013.

Arellano, V. M., Barragán, R. M., Ramírez, M., López, S., Paredes, A., Aragón, A., and Tovar, R.: The response to exploitation of the Los Humeros (México) geothermal reservoir, Proceedings World Geothermal Congress 2015, Melbourne, Australia, 19–25 April, 7 pp., 2015.

Arellano, V. M., García, A., Barragán, R. M., Izquíerdo, G., Aragón, A., and Nieva, D.: An updated conceptual model of the Los Humeros geothermal reservoir (Mexico), Journal of Volcanology and Geothermal Research, 124(1-2), 67–88, https://doi.org/10.1016/S0377-0273(03)00045-3, 2003.

Aretz, A., Bär, K., Götz, A. E., and Sass, I.: Outcrop analogue study of Permocarboniferous geothermal sandstone reservoir formations (northern Upper Rhine Graben, Germany): Impact of mineral content, depositional environment and diagenesis on petrophysical properties, Int. J. Earth Sci., 135, 1431–1452, https://doi.org/10.1007/s00531-015-1263-2, 2015.

Árnason, K.: New Conceptual Model for the Magma-Hydrothermal-Tectonic System of Krafla, NE Iceland, Geosciences, 10, 27 pp., https://doi.org/10.3390/geosciences10010034, 2020.

Arzate, J., Corbo, F., Norini, G., Carrasco-Núñez, G., Hernández, J., and Yustis, V.: The Los Humeros (Mexico) geothermal field model deduced from new geophysical and geological data, Geothermics, 71, 200–211, http://dx.doi.org/10.1016/j.geothermics.2017.09.009, 2018.

Ashena, R., Behrenbruch, P., and Ghalambor, A.: Log-based rock compressibility estimation for Asmari carbonate formation, Journal of Petroleum Exploration and Production Technology, 10, 2771–2783, https://doi.org/10.1007/s13202-020-00934-0, 2020.

ASTM D2664-04: Standard Test Method for Triaxial Compressive Strength of Undrained Rock Core Specimens Without Pore Pressure Measurements (Withdrawn 2005), ASTM International, West Conshohocken, PA, USA, 4 pp., https://doi.org/10.1520/D2664-04, 2004.

ASTM D2845-08: Standard Test Method for Laboratory Determination of Pulse Velocities and Ultrasonic Elastic Constants of Rock, ASTM International, West Conshohocken, PA, USA, 7 pp., https://doi.org/10.1520/D2845-08, 2008.

ASTM D3148-02: Standard Test Method for Elastic Moduli of Intact Rock Core Specimens in Uniaxial Compression, ASTM International, West Conshohocken, PA, USA, 6 pp., https://doi.org/10.1520/D3148-02, 2002.

ASTM D3967-16: Standard Test Method for Splitting Tensile Strength of Intact Rock Core Specimens, ASTM International, West Conshohocken, PA, USA, 5 pp., https://doi.org/10.1520/D3967-16, 2016.

ASTM D4525-13e2: Standard Test Method for Permeability of Rocks by Flowing Air, ASTM International, West Conshohocken, PA, USA, 5 pp., https://doi.org/10.1520/D4525-13E02, 2013.

ASTM D4543-19: Standard Practices for Preparing Rock Core Specimens and Determining Dimensional and Shape Tolerances, ASTM International, West Conshohocken, PA, USA, 13 pp., https://doi.org/10.1520/D4543-19, 2019.

ASTM D5550-14: Standard Test Method for Specific Gravity of Soil Solids by Gas Pycnometer, ASTM International, West Conshohocken, PA, USA, 5 pp., https://doi.org/10.1520/D5550-14, 2014.

ASTM D5731-08: Standard Test Method for Determination of the Point Load Strength Index of Rock and Application to Rock Strength Classifications, ASTM International, West Conshohocken, PA, USA, 12 pp., https://doi.org/10.1520/D5731-08, 2008.

ASTM D6539-13: Standard Test Method for Measurement of the Permeability of Unsaturated Porous Materials by Flowing Air, ASTM International, West Conshohocken, PA, USA, 10 pp., https://doi.org/10.1520/D6539-13, 2013.

ASTM D7012-14: Test methods for compressive strength and elastic moduli of intact rock corespecimens under varying states of stress and temperatures, ASTM International, West Conshohocken, PA, USA, 9 pp., https://doi.org/10.1520/D7012-14, 2014.

ASTM D7263-16: Standard Test Methods for Laboratory Determination of Density (Unit Weight) of Soil Specimens, ASTM International, West Conshohocken, PA, USA, 7 pp., https://doi.org/10.1520 /D7263-09R18E02, 2016.

ASTM D731-18: Standard Test Method for Molding Index of Thermosetting Molding Powder, ASTM International, West Conshohocken, PA, USA, 4 pp., https://doi.org/10.1520/D0731-18, 2018.

Athy, L. F.: Density, porosity and compaction of sedimentary rocks, AAPG Bull., 14(1), 1–24, https://doi.org/10.1306/3D93289E-16B1-11D7-8645000102C1865D, 1930.

Avellán, D. R., Macías, J. L., Layer, P. W., Sosa-Ceballos, G., Cisneros, G., Sanchez, J. M., Martha Gómez-Vasconcelos, G., López-Loera, H., Reyes Agustín, G., Marti, J., Osorio, S., García-Sánchez, L., Pola-Villaseñor, A., García-Tenorio, F., and Benowitz, J.: Geology of the Pleistocene Acoculco Caldera Complex, eastern Trans-Mexican Volcanic Belt (México), J. Maps, 15, 8–18, https://doi.org/10.1080/17445647.2018.1531075, 2018.

Avellán, D. R., Macías, J. L., Layer, P. W., Sosa-Ceballos, G., Gómez-Vasconcelos, M. G., Cisneros-Máximo, G., and Benowitz, J.: Eruptive chronology of the Acoculco caldera complex – A resurgent caldera in the eastern Trans-Mexican Volcanic Belt (México), J. S. Am. Earth Sci., 98, 102412, https://doi.org/10.1016/j.jsames.2019.102412, 2020.

Bär, K.: Untersuchung der tiefengeothermischen Potenziale von Hessen, PhD thesis, Technische Universität Darmstadt, Germany, 265 pp., https://tuprints.ulb.tu-darmstadt.de/3067/, 2012.

Bär, K., Rochelle, C., and Weydt, L.: Report on the WP6 Sampling Campaign May 2017, WP6, Task 6.1, June 2017, V1, 33 pp., 2017.

Bär, K., and Weydt, L. M.: Comprehensive report on the rock and fluid samples and their physical properties in the Acoculco and Los Humeros regions, Deliverable D6.1, WP6, GEMex H2020 project, European Comission, 304 pp., available at: http://www.gemex-h2020.eu (last access: 25 May 2020), 2019.

Bär, K., Reinsch, T., and Bott, J.: The PetroPhysical Property Database (P3) – a global compilation of lab-measured rock properties, Earth Syst. Sci. Data, 12, 2485–2515, https://doi.org/10.5194/essd-12-2485-2020, 2020.

Baroomand, M., Safari, A., and Bahroudi, A.: Magnetic susceptibility as a tool for mineral exploration (Case study: Southern of Zagros Mountians), Int. J. Min. and Geo-Eng., 49, 57–66, https://doi.org/10.22059/IJMGE.2015.54364, 2015.

Bastesen, E., Torabi, A., Wheeler, W. H., Garcia, O., and Lepillier, B.: Fracture systems from outcrop analogs for use in Los Humeros reservoir E&P models, in: Deliverable 4.1, WP4, GEMex H2020 project, European Commission, 1, available at: http://www.gemex-h2020.eu (last access: 28 March 2020), 78–94, 2019.

Bayuk, I., and Tikhotskiy, S.: Upscaling and downscaling of reservoir elastic properties – Rock Physics approach, in: SEG International Exposition and 88th Annual Meeting, 14–19 October 2018, Anaheim, CA, USA, 3653–3657, https://doi.org/10.1190/segam2018-2985365.1, 2018.

Bech, M.: Petrophysical and hydraulical properties of andesitic geothermal reservoir rocks of Los Humeros and Acoculco, Mexico, unpublished Master thesis, Institut für Angewandte Geowissenschaften, Technische Universität Darmstadt, Darmstadt, 73 pp. + XXXIII Appendix, 70 Figures, 2018.

Békési, E., Struijk, M., Bonté, D., Veldkamp, H., Limberger, J., Fokker, P. A., Vrijlandt, M., and van Wees, J.-D.: An updated geothermal model of the Dutch subsurface based on inversion of temperature data, Geothermics, 88, 101880, https://doi.org/10.1016/j.geothermics.2020.101880, 2020.

Benediktsdóttir, A., Arango-Galván, C., Páll Hersir, G., Held, S., Romo-Jones, J. M., Luis-Salas, J., Avils, T., Ruiz-Aguilar, D., and Már Vilhjálmsson, A.: The Los Humeros superhot geothermal resource in Mexico: Results from an extensive resistivity survey, GEMex Final Conference, Potsdam, Germany, 18–19 February 2020, S6.1, 2020.

Bernard, R., Taran, Y., Pennisi, M., Tello, E., and Ramirez, A.: Chloride and Boron behavior in fluids of Los Humeros geothermal field (Mexico): A model based on the existence of deep acid brine, Applied Geochemistry, 26, 2064–2073, https://doi.org/10.1016/j.apgeochem.2011.07.004, 2011.

Bienkowski, R.: Genese hochsaurer Fluide im Geothermalfeld von Los Humeros, Zentral-Mexiko, Diplomarbeit, Institut für Angewandte Geowissenschaften, Technische Universität Darmstadt, 2003.

Bienkowski, R., Torres-Alvarado, I. S., and Hinderer, M.: Geochemical Modeling of Acid Fluids in Los Humeros Geothermal Field, Mexico, Proceedings World Geothermal Congress 2005, Antalya, Turkey, 24–29 April, 2005.

Birch, F.: The Velocity of Compressional Waves in Rocks to 10 Kilobars, Part 2, Journal of Geophysical Research, 66, 2199–2224, https://doi.org/10.1029/JZ066i007p02199, 1961.

Bohnsack, D., Potten, M., Pfrang, D., Wolpert, P., and Zosseder, K.: Porosity-permeability relationship derived from Upper Jurassic carbonate rock cores to assess the regional hydraulic matrix properties of the Malm reservoir in the South German Molasse Basin, Geotherm. Energy, 12, 1–47, https://doi.org/10.1186/s40517-020-00166-9, 2020.

Bonini, M., Maestrelli, D., Corti, G., Del Ventisette, C., Moratti, G., Carrasco-Nunez, G., Giordano, G., Lucci, F., Norini, G., Piccardi, L., Urbani, S., and Montanari, D.: Modeling Intra-caldera Resurgence Settings: Laboratory Experiments with Application to the Los Humeros Volcanic Complex (Mexico), Journal of Geophysical Research: Solid Earth, 126, e2020JB020438, https://doi.org/10.1029/2020JB020438, 2021.

Bourbiaux, B.: Fractured Reservoir Simulation: a Challenging and Rewarding Issue, Oil Gas Sci. Technol., 65, 227–238, https://doi.org/10.2516/ogst/2009063, 2010.

Bourbiaux, B., Basquet, R., Daniel, J. M., Hu, L. Y., Jenni, S., Lange, G., and Rasolofosaon, P.: Fractured reservoirs modelling a review of the challenges and some recent solutions, First Break, 23, 33–40, https://doi.org/10.3997/1365-2397.2005018, 2005.

Braun, J.-J., Pagel, M., Herbilln, A., and Rosin, C.: Mobilization and redistribution of REEs and thorium in a syenitic lateritic profile: A mass balance study, Geochimica et Cosmochimica Acta, 57(18), 4419–4434, https://doi.org/10.1016/0016-7037(93)90492-F, 1993.

BritGeothermal: Deep geothermal energy research in the UK, available at: http://www.britgeothermal. org/ (last access: 21 October 2020), 2017.

BRITROCKS project: BRITROCKS Rock collections: BGS Mineralogy and petrology collection database, available at: https://www.bgs.ac.uk/technologies/databases/bgs-rock-collections/ (last access: 21 October 2020), 2020.

Bromley, C., Axelsson, G., Asanuma, H., Manzella, A., Dobson, P.: Supercritical Fluids – Learning about the Deep Roots of Geothermal Systems from OEA Geothermal Collaboration, Proceedings World Geothermal Congress 2020+1 Reykjavik, Iceland, April–October 2021, 9 pp., 2021.

Browne, P. R. L.: Hydrothermal alteration in active geothermal fields, Annu. Rev. Earth Planet. Sci., 6 (1), 229–248, https://doi.org/10.1146/annurev.ea.06.050178.001305, 1978.

Buchs, D. M., Bagheri, S., Martin, L., Hermann, J., and Arculus, R.: Palaeozoic to Triassic ocean opening and closure preserved in Central Iran: constraints from the geochemistry of meta-igneous rocks of the Anarak area, Tectonophysics, 172–173, 267–287, https://doi.org/10.1016/j.lithos.2013.02.009, 2013.

Buntebarth, G.: Geothermie, Springer, Berlin -Heidelberg, Germany, https://doi.org/10.1007/978-3-662-00910-9, 1980.

Calcagno, P., Evanno, G., Trumpy, E., Gutiérrez-Negrín, L. C., Macías, J. L., Carrasco-Núñez, G., and Liotta, D.: Preliminary 3-D geological models of Los Humeros and Acoculco geothermal fields (Mexico) – H2020 GEMex Project, Adv. Geosci., 45, 321–333, https://doi.org/10.5194/adgeo-45-321-2018, 2018.

Calcagno, P., Trumpy, E., Gutiérrez-Negrín, L. C., Norini, G., Macías, J. L., Carrasco-Núñez, G., and Liotta, D.: Updating the 3D Geomodels of Los Humeros and Acoculco Geothermal Systems (Mexico), H2020 GEMex Project, Internal report, 2019.

Calcagno, P., Trumpy, E., Gutiérrez-Negrín, L. C., Liotta, D., Carrasco-Núñez, G., Norini, G., Brogi, A., Garduño-Monroy, V. H., Benediktsdóttir, A., Gaucher, E., Toledo, T., Páll Hersir, G., Manzella, A., Santilano, A., Gola, G., Macías, J. L., Vaessen, L., Evanno, G., and Arango-Galván, C.: 3D Geomodels of Los Humeros and Acoculco geothermal systems (Mexico) – H2020 GEMex Project: Methodology, products and feedback, GEMex Final Conference, Potsdam, Germany, 18–19 February 2020, S1.2, 2020.

Calcagno, P., Trumpy, E., Gutiérrez-Negrín, L. C., and Liotta, D.: A collection of 3D geomodels of the Los Humeros and Acoculco geothermal systems (Mexico), scientific data, 9:280, 22 pp., https://doi.org/10.1038/s41597-022-01327-0, 2022.

Canet, C., Arana, L., González-Pertida, E., Pi, T., Prol-Ledesma, R. M., Franco, S. I., Villanueva-Estrada, R. E., Camprubí, A., Ramírez-Silva, G., and López-Hernández, A.: A statistics-based method for the short-wave infrared spectral analysis of altered rocks: An example from the Acoculco Caldera, Eastern Trans-Mexican Volcanic Belt, J. Geochem. Explor., 105, 1–10, https://doi.org/10.1016/j.gexplo.2010.01.010, 2010.

Canet, C., Trillaud, F., Prol-Ledesma, R., González-Hernández, G., Peláez, B., Hernández-Cruz, B., and Sánchez-Córdova, M. M.: Thermal history of the Acoculco geothermal system, eastern Mexico: Insights from numerical modeling and radiocarbon dating, J. Volcanol. Geoth. Res., 305, 56–62, https://doi.org/10.1016/j.jvolgeores.2015.09.019, 2015.

Cant, J. L., Siratovich, P. A., Cole, J. W., Villeneuve, M. C., and Kennedy, B. M.: Matrix permeability of reservoir rocks, Ngatamariki geothermal field, Taupo Volcanic Zone, New Zealand, Geotherm. Energy, 2, 1–28, https://doi.org/10.1186/s40517-017-0088-6, 2018.

Carrasco-Núñez, G., Gómez-Tuena, A., and Lozano, V. L.: Geologic map of Cerro Grande volcano and surrounding area, Central Mexico, Geol. Soc. Am. Map Chart Ser. MCH 081, 10 pp., available under https://www.worldcat.org/title/geologic-map-of-cerro-grande-volcano-and-surrounding-area-central-mexico/oclc/37949323&referer=brief_results (last access 28 Sep 2021), 1997.

Carrasco-Núñez, G., McCurry, M., Branney, M. J., Norry, M., and Willcox, C.: Complex magma mixing, mingling, and withdrawal associated with an intraplinian ignimbrite eruption at a large silicic caldera volcano: Los Humeros of central Mexico. Geological Society of America Bull 124(11-12), 1793–1809, https://doi.org/10.1130/B30501.1, 2012.

Carrasco-Núñez, G., Hernández, J., De Léon, L., Dávilla, P., Norini, G., Bernal, J. P., Jicha, B., Jicha, B., Navarro, M., and López-Quiroz, P.: Geologic Map of Los Humeros volcanic complex and geothermal field eastern Trans-Mexican Volcanic Belt, terra digitalis, 1, 1–11, https://doi.org/10.22201/igg.terradigitalis.2017.2.24.78, 2017a.

Carrasco-Núñez, G., López-Martínez, M., Hernández, J., and Vargas, V.: Subsurface stratigraphy and its correlation with the surficial geology at Los Humeros geothermal field, eastern Trans-Mexican Volcanic Belt, Geothermics, 67, 1–17, https://doi.org/10.1016/j.geothermics.2017.01.001, 2017b.

Carrasco-Núñez, G., Bernal, J. P., Dávilla, P., Jicha, B., Giordano, G., and Hernández, J.: Reappraisal of Los Humeros Volcanic Complex by New U/Th Zircon and 40Ar/39Ar Dating: Implications for Greater Geothermal Potential, Geochem. Geophy. Geosy., 19, 132–149, https://doi.org/10.1002/2017GC007044, 2018.

Carrasco-Núñez, G., Norini, G., Giordano, G., Lucci, F., Hernández, J., Cavazos, J., Cid-Luna, H., Dávila, P., Peña, D., Barrios, S., and Fernández, F.: Towards a Comprehensive Volcanologic, Magmatic and Structural Model for Superhot Geothermal Systems: Case Study of Los Humeros Caldera Complex, Mexico, Proceedings, World Geothermal Congress 2020+1, Reykjavik, Iceland, April–October 2021, 15 pp., 2021.

Cavazos-Álvarez, J. A., and Carrasco-Núñez, G.: Effective mapping of large ignimbrites by using a GIS-based methodology; case of the Xáltipan ignimbrite from Los Humeros Volcanic Complex, Terra Digit 3(2), 78–97, https://doi.org/10.22201/ igg.25940694.2019.2.65.142, 2019.

Cavazos, J., and Carrasco-Núñez, G.: Anatomy of the Xáltipan ignimbrite at Los Humeros Volcanic Complex; the largest eruption of the Trans-Mexican Volcanic Belt, J. Volcanol. Geoth. Res., 392, 106755, https://doi.org/10.1016/j.jvolgeores.2019.106755, 2020.

Cavazos-Álvarez, J. A., Carrasco-Núñez, G., Dávila-Harris, P., Peña, D., Jáquez, A., and Artega, D.: Facies variations and permeability of ignimbrites in active geothermal systems; case study of the Xáltipan ignimbrite at Los Humeros Volcanic Complex, Journal of South American Earth Sciences, 104, 102810, https://doi.org/10.1016/j.jsames.2020.102810, 2020.

Cedillo, F.: Geología del subsuelo del campo geotérmico de Los Humeros, Pue. Internal Report HU/RE/03/97, Comisión Federal de Electricidad, Gerencia de Proyectos Geotermoeléctricos, Residencia Los Humeros, Puebla, 30 pp., 1997.

Cedillo, F.: Modelo hidrogeológico de los yacimientos geotérmicos de Los Humeros, Pue., Mexico, Geotermia, Revista Mexicana de Geoenergía, 15(3), 159–170, 1999.

Cedillo, F.: Hydrogeologic model of the geothermal reservoirs from Los Humeros, Puebla, Mexico, Proceedings World Geothermal Congress 2000, Kyushu-Tohoku, Japan, May 28–June 10, 2000.

Chen, C., Zhu, C., Zhang, B., Tang, B., Li, K., Li, W., and Fu, X.: Effect of Temperature on the Thermal Conductivity of Rocks and Its Implication for In Situ Correction, Geofluids, 2021-6630236, 12 pp., https://doi.org/10.1155/2021/6630236, 2021.

Chen, T., Clauser, C., Marquat, G., Willbrand, K., and Hiller, T.: Upscaling permeability for three-dimensional fractured porous rocks with multiple boundary method, Hydrogeol Journal, 26, 1903–1916, https://doi.org/10.1007/s10040-018-1744-z, 2018.

Christie, M.: Upscaling for reservoir simulation, J. Pet. Technol., 48, 1004–1010, https://doi.org/10.2118/37324-JPT, 1996.

Cid, H. E., Carrasco-Núñez, G., Manea, V. C., Vega, S., and Castaño, V.: The role of microporosity on the permeability of volcanic-hosted geothermal reservoirs: A case study from Los Humeros, Mexico. Geothermics, 90, 102020, https://doi.org/10.1016/j.geothermics.2020.102020, 2021.

Cladouhos, T., Petty, S., Bonneville, A. H., Schultz, A., and Sorlie, F.: Super-Hot EGS and the Newberry Deep Drilling project, Proceedings, 43nd Workshop on Geothermal Reservoir Engineering, Standford University, Stanford, California, 13 pp., 2018.

Clauser, C.: Thermal Storage and Transport Properties of Rocks, II: Thermal Conductivity and Diffusivity, in: Encyclopedia of Solid Earth Geophysics. Encyclopedia of Earth Sciences Series, edited by: Gupta, H. K., Springer, Cham, Switzerland, 1–20, https://doi.org/10.1007/978-3-030-10475-7_67-1, 2020.

Clauser, C., and Huenges, E.: Thermal conductivity of rocks and minerals. Rock Physics & Phase Relations, in: Rock Physics and Phase relations: A Handbook of Physical Constants, edited by: Ahrens, T. J., American Geophysical Union, Washington, USA, 3, 105–126, https://doi.org/10.1029/rf003p0105, 1995.

Clement, R., Bergeron, M., and Moreau, S.: COMSOL Multiphysics modelling for measurement device of electrical resistivity in laboratory test cell, in: Proceedings of the 2011 COMSOL Conference, 26–28 October 2011, Stuttgart, 6 pp., 2011.

Codd, E. F.: A Relational Model of Data for Large Shared Data Banks, Communications of the ACM, 13, 377–387, https://doi.org/10.1145/362384.362685, 1970.

Cohen, K. M., Finney, S. C., Gibbard, P. L., and Fan, J.-X.: The ICS International Chronostratigraphic Chart, Episodes 36, 199–204, available at: http://www.stratigraphy.org/ICSchart/ChronostratChart2020-01.pdf (last access: 09 Decmeber 2020), 2013.

Contreras, L. E., Domínguez, A. B., and Rivera, M. O.: Mediciones petrofisicas en nucleos de perforacion del campo geotermico Los Humeros, Geotermia, 6, 9–42, 1990.

Contreras, L. F., Brown, E. T., and Ruest, M.: Bayesian data analysis to quantify the uncertainty of intact rock strength, Journal of Rock Mechanics and Geotechnical Engineering, 10, 11–31, https://doi.org/10.1016/j.jrmge.2017.07.008, 2018.

Corbo-Camargo, F., Arzate, J., Fregoso, E., Norini, G., Carrasco-Núñez, G., Yutsis, V., Herrera, J., and Hernández, J.: Shallow structure of Los Humeros (LH) caldera and geothermal reservoir from magnetotellurics and potential field data, Geophysical Journal International, 223(1), 666–675, https://doi.org/10.1093/gji/ggaa338, 2020.

Cornejo, N.: Towards visualization ofthe reservoir settings in the Los Humeros and Acoculco geothermal fields using gravity, GEMex Final Conference, Potsdam, Germany, 18–19 February 2020, S1.6, 2020.

Cornejo-Triviño, N., Liotta, D., Piccardi, L., Brogi, A., Perez, M., Carrillo-Lopez, J., Calcagno, P., Sass, I., and Schill, E.: Gravimetric and Morpho-structural Analyses in the Superhot Geothermal System Los Humeros: An Example from Central Mexico, Geothermal Energy, in review, 2022.

Cullers, R. L., and Graf, J. L.: Chapter 8 - Rare earth elements in igneous rocks of the continental crust: intermediate and silicic rocks–ore petrogenesis, in Henderson, P. (Ed.): Developments in Geochemistry, Vol. 2, Elsevier, Amsterdam, The Netherlands, 275–316, 1984.

Dávila-Harris, P., and Carrasco-Núñez, G.: An unusual syn-eruptive bimodal eruption: the Holocene Cuicuiltic Member at Los Humeros caldera, Mexico, Journal of Volcanology and Geothermal Research, 271, 24–42, https://doi.org/10.1016/j.jvolgeores.2013.11.020, 2014.

Deb, P.: WP6 Reservoir Characterization and Conceptual models – Status update, GEMex conference, October 2018, Morelia, Mexico, 2018.

Deb, P., Knapp, D., Clauser, C., and Montegrossi, G.: Modeling Natural Steady-State of Super-Hot Geothermal Reservoir at Los Humeros, Mexico, in: Proceedings of the European Geothermal Congress 2019, Den Haag, the Netherlands, 11–14 June 2019, 6 pp., 2019a.

Deb, P., Knapp, D., Marquart, G., and Clauser, C.: Report on the numerical reservoir model used for the simulation of the Acoculco reservoir in Mexico, Deliverable 6.2, WP6, GEMex H2020 project, European Commission, 1.2, available at: http://www.gemex-h2020.eu (last access: 26 May 2020), 2019b.

Deb, P., Salimzadeh, S., Dübner, S., and Clauser, C.: Laboratory experiments and numerical simulations of hydraulic fracturing for enhanced geothermal systems, in: Proceedings of the European Geothermal Congress 2019, Den Haag, the Netherlands, 11–14 June 2019, 4 pp., 2019c.

Deb, P., Knapp, D., Marquart, G., and Clauser, C.: Report on the numerical reservoir model used for the simulation of the Los Humeros super-hot reservoir in Mexico, Deliverable 6.3(1), WP6, GEMex H2020 project, European Commission, 50 pp., available at: http://www.gemex-h2020.eu (last access: 28 Sep 2021), 2019d.

Deb, P., Giordano, G., Shi, X., Lucci, F., and Clauser, C.: An approach to reconstruct the thermal history in active magmatic systems: Implications for the Los Humeros volcanic complex, Mexico, Geothermics, 96, 102162, https://doi.org/10.1016/j.geothermics.2021.102162, 2021.

Delayre, C., Mas, P. P., Sardini, P., Cosenza, P., and Thomas, A.: Quantitative evolution of the petrophysical properties of andesites affected by argillic alteration in the hydrothermal system of Petite Anse-Diamant, Martinique, Journal of Volcanology and Geothermal Research, 401, 106927, https://doi.org/10.1016/j.jvolgeores.2020.106927, 2020.

DIN 18141-1: 2014-05: Baugrund-Untersuchung von Gesteinsproben – Teil 1: Bestimmung der einaxialen Druckfestigkeit, Beuth, https://doi.org/10.31030/2100323, 2014.

Ding, L. Y., Mehra, R. K., and Donnelly, J. K.: Stochastic Modeling in Reservoir Simulation, SPE Reservoir Engineering, 7, 98–106, https://doi.org/10.2118/18431-PA, 1992.

Dobson, P. F., Kneafsey, T. J., Hulen, J., and Simmons, A.: Porosity, permeability, and fluid flow in the Yellowstone geothermal system, Wyoming, Journal of Volcanology and Geothermal Research, 123, 313–324, https://doi.org/10.1016/S0377-0273(03)00039-8, 2003.

Dobson, P., Asanuma, H., Huenges, E., Poletto, F., Reinsch, T., and Sanjuan, B.: Supercritical geothermal systems—review of past studies and ongoing research activities. Proceedings, 42nd Workshop on Geothermal Reservoir Engineering, Stanford University, Stanford, 13 pp., 2017.

DOE Data Explorer: U.S. Department of Energy Office of Scientific and Technical Information, DOE Data Explorer Utah Forge, available at: https://www.osti.gov/dataexplorer/biblio/dataset/1452765 (last access: 21 October 2020), 2018.

Dunlop, D. J., and Özdemir, Ö.: Chapter 5.08.3.4 -Magnetizations in Rocks and Minerals, in Schubert, G. (Ed.): Treatise on Geophysics, Volume 5 Geomagnetism: An Introduction and Overview, second edition, Elsevier, United Kingdom, 255–308, 2015.

Durán, E. L., Adam, L., Wallis, I. C., and Barnhoorn, A.: Mineral Alteration and Fracture Influence on the Elastic Properties of Volcaniclastic Rocks, J. Geophys. Res.-Sol. Ea., 124, 4576–4600, https://doi.org/10.1029/2018JB016617, 2019.

Durham, W. B., Mirkovich, V. V., and Heard, H. C.: Thermal Diffusivity of Igneous Rocks at Elevated Pressure and Temperature, Journal of Geophysical Research, 92, 11615–11634, 1987.

Ebigbo, A., Niederau, J., Marquart, G., Dini, I., Thorwart, M., Rabbel, W., Peching, R., Bertani, R., and Clauser, C.: Influence of depth, temperature, and structure of a crustal heat source on the geothermal reservoirs of Tuscany: numerical modelling and sensitivity study, Geotherm. Energy, 5, 1–29, https://doi.org/10.1186/s40517-016-0047-7, 2016.

Ebong, E. D., Akpan, A. E., and Ekwok, S. E.: Stochastic modelling of spatial variability of petrophysical properties in parts of the Niger Delta Basin, southern Nigeria, Journal of Petroleum Exploration and Production Technology, 10, 569–585, https://doi.org/10.1007/s13202-019-00787-2, 2019.

Eggertsson, G. H., Lavallée, Y., Kendrick, J. E., and Markússon, S. H.: Improving fluid flow in geothermal reservoirs by thermal and mechanical stimulation: The case of Krafla volcano, Iceland, J. Volcanol. Geoth. Res., 391, 106351, https://doi.org/10.1016/j.jvolgeores.2018.04.008, 2020.

Elders, W. A., Friðleifsson, G., and Albertsson, A.: Drilling into magma and the implications of the Iceland Deep Drilling project (IDDP) for high-temperature geothermal systems worldwide, Geothermics, 49, 111–8, doi:10.1016/j.geothermics.2013.05.001, 2014.

Enge, H. D., Buckley, S. J., Rotevatn, A., and Howell, J. A.: From outcrop to reservoir simulation model: workflow and procedures, Geosphere, 3, 469–490, https://doi.org/10.1130/GES00099.1, 2007.

Eshagi, E., Smith, S., and Ayer, J.: Petrophysical characterisation (i.e. density and magnetic susceptibility) of major rock units within the Abitibi Greenstone Belt, Laurentian University Mineral Exploration Research Centre, MERC-ME-2019-144, 88 pp., 2019.

Farmer, C. L.: Upscaling: a review, Int. J. Numer. Meth. Fl., 40, 63–78, https://doi.org/10.1002/fld.267, 2002.

Farquharson, J. I., Heap, M. J., Varley, N. R., Baud, P., and Reuschlé, T.: Permeability and porosity relationships of edifice-forming andesites: A combined field and laboratory study, J. Volcanol. Geotherm. Res., 297, 52–68, https://doi.org/10.1016/j.jvolgeores.2015.03.016, 2015.

Farquharson, J. I., and Wadsworth, F. B.: Upscaling permeability in anisotropic volcanic systems, J. Volcanol. Geotherm. Res., 364, 35–47, https://doi.org/10.1016/j.jvolgeores.2018.09.002, 2018.

Fedo, C. M., Nesbitt, H. W., and Young, G. M.: Unravelling the effects of potassium metasomatism in sedimentary rocks and paleosols, with implications for paleo-weathering conditions and provenance, Geology, 23(10), 921–924, https://doi.org/10.1130/0091-7613(1995)023<0921: UTEOPM >2.3.CO;2, 1955.

Feng, G., Wanf, Y., Xu, T., Wang, F., and Shi, Y.: Multiphase flow modeling and energy extraction performance for supercritical geothermal systems, Renewable Energy, 173, 442–454, https://doi.org/10.1016/j.renene.2021.03.107, 2021.

Ferrari, L., Orozco-Esquivel, T., Manea, V., and Manea, M.: The dynamic history of the Trans-Mexican Volcanic Belt and the Mexico subduction zone, Tectonophysics, 522/523, 122–149, https://doi.org/10.1016/j.tecto.2011.09.018, 2012.

Ferriz, H.: Geologic and preliminary reservoir data on the Los Humeros geothermal system, Puebla, Mexico, Proceedings Eight Workshop Geothermal Reservoir Engineering, Stanford University, Stanford, California, USA, December 1982, SGP-TR-60, 19-24, 1982.

Ferriz, H., and Mahood, G.: Eruptive rates and compositional trends at Los Humeros volcanic center, Puebla, Mexico, J. Geophys. Res., 89, 8511–8524, https://doi.org/10.1029/JB089iB10p08511, 1984.

Filomena, C. M., Hornung, J., and Stollhofen, H.: Assessing accuracy of gas-driven permeability measurements: a comparative study of diverse Hassler-cell and probe permeameter devices, Solid Earth, 5, 1–11, https://doi.org/10.5194/se-5-1-2014, 2014.

Fitz-Díaz, E., Tolson, G., Hudleston, P., Bolaños-Rodríguez, D., Ortega-Flores, B., and Vásquez-Serrano, A.: The role of folding in the development of the Mexican fold- and-thrust belt, Geosphere, 8(4), 931–949, https://doi.org/10.1130/GES00759.1, 2012.

Fitz-Díaz, E., Lawton, T. F., Juárez-Arriaga, E., and Chávez-Cabello, G.: The Cretaceous-Paleogene Mexican orogen: structure, basin development, magmatism and tectonics, Earth-Sci. Rev., 183, 56–84, https://doi.org/10.1016/j.earscirev.2017.03.002, 2017.

Flores-Armenta, M. R., Miguel, R. M., Rigoberto, T. A., and Fernando, S. M.: The Neutralization of acid fluids: an alternative of commercial exploitation wells on Los Humeros geothermal field, Proceedings World Geothermal Congress, Bali, Indonesia, April 25–29, 2010, 5 pp., 2010.

Flovenz, O. G., Spangenberg, E., Kuhlenkampff, J., Arnason, K., Karlsdottir, R., and Huenges, E.: The role of electrical interface conduction in geothermal exploration, in: Proceedings of the World Geothermal Congress 2005, Antalya, Turkey, 24–29 April 2005, 9 pp., 2005.

Floyd, P. A., and Winchester, J. A.: Identification and discrimination of altered and metamorphosed volcanic rocks using immobile elements, Chemical Geology, 21(3-4), 291–306, https://doi.org/10.1016/0009-2541(78)90050-5, 1978.

Fodor, R. V., Jacobs, R. S., and Bauer, G. R.: Hollandite in Hawaiian basalt; a relocation site for weathering-mobilized elements, Mineralogical Magazine, 58(4), 589–596, 1994.

Forchheimer, P.: Wasserbewegung durch Boden, Z. Ver. Dtsch. Ing., 45, 1782–1788, 1901.

Franco, A., and Donatini, F.: Methods for the estimation of the energy stored in geothermal reservoirs, J. Phys., 796, 012025, https://doi.org/10.1088/1742-6596/796/1/012025, 2017.

Friðleifsson, G. Ó., Armannsson, H., Gudmundsson, A., Arnason, K., Mortensen, A. K., Palsson, B., Einarsson, G. M.: Site selection for the well IDDP-1 at Krafla, Geothermics, 49, 9–15, https://doi.org/10.1016/j.geothermics.2013.06.001, 2014a.

Friðleifsson, G. Ó., Elders, W. A., Albertsson, A.: The concept of the Iceland Deep Drilling Project, Geothermics, 49, 2–8, https://doi.org/10.1016/j.geothermics.2013.03.004, 2014b.

Frolova, J., Vladimir, L., Sergey, R., and David, Z.: Effects of hydrothermal alterations on physical and mechanical properties of rocks in the Kuril-Kamchatka Island arc, Engineering Geology, 183, 80–95, https://doi.org/10.1016/j.enggeo.2014.10.011, 2014.

Fuentes-Guzmán, E., González-Partida, E., Camprubí, A., Hernández-Avilés, G., Gabites, J., Ruggieri, G., Iriondo, A., and López-Martínez, M.: The Miocene Tatatila-Las Minas IOCG skarn deposits (Veracruz) as a result of adakitic magmatism in the Trans-Mexican Volcanic Belt Short running title: Miocene IOCG deposits and adakitic magmas in the Trans-Mexican Volcanic Belt, Boletín de la Sociedad Geológica Mexicana, 73, A1105020, https://doi.org/10.18268/BSGM2020v72n 3a110520, 2020.

Gan, Q., and Elsworth, D.: Production optimization in fractured geothermal reservoirs by coupled discrete fracture network modelling, Geothermics, 62, 131–142, https://doi.org/10.1016/ j.geothermics.2016.04.009, 2016.

García-Gutiérrez, A., and Contreras, E.: Measurement of Thermal Conductivity and Diffusivity of Drill Core Samples from the Los Humeros Geothermal Field, Mexico, by a Line-Source Technique, GRC Transactions, 31, 555–559, 2007.

García-Palomo, A., Macías, J. L., Tolson, G., Valdez, G., and Mora, J. C.: Volcanic stratigraphy and geological evolution of the Apan región, east-central sector of the Trans-Mexica Volcanic Belt, Geofís. Int., 41, 133–150, 2002.

García-Palomo, A., Macías, J. L., Jiménez, A., Tolson, G., Mena, M., Sánchez-Núñez, J. M., Arce, J. L, Layer, P. W., Santoyo, M. A., and Lermo-Samaniego, J.: NW-SE Pliocene-Quaternary extension in the Apan-Acoculco region, eastern Trans-Mexican Volcanic Belt, J. Volcanol. Geoth. Res., 349, 240–255, https://doi.org/10.1016/j.jvolgeores.2017.11.005, 2018.

Gard, M., Hasterok, D., and Halpin, J. A.: Global whole-rock geochemical database compilation, Earth Syst. Sci. Data, 11, 1553–1566, https://doi.org/10.5194/essd-11-1553-2019, 2019.

GEMex: The GEMex project – Cooperation in Geothermal energy research Europe-Mexico for development of Enhanced Geothermal Systems and Superhot Geothermal Systems, available at: http://www.gemex-h2020.eu/; https://goo.gl/DuS5qW (last access 28 July 2022), 2022.

Georoc Mainz: GEOROC database, Geochemistry of Rocks of the Oceans and Continents, available at: http://georoc.mpch-mainz.gwdg.de/georoc/ (last access: 21 October 2020), 2020.

GeoScout database: geoLogicSystems, geoScout database, available at: https://www.geologic.com/products/geoscout/ (last access: 11 November 2020), 2020.

Geotek: Multi-Sensor Core Logger, Manual, Geotek, Nene House, Drayton Fields, Daventry, Northants, UK, 2000.

Geotron-Elektronik: LightHouse UMPC V1.02, Installations- und Bedienungshandbuch, 1.6, Pirna: Geotron-Elektronik, 47 pp., 2011.

Ghassemi, A.: Application of rock failure simulation in design optimization of the hydraulic fracturing, in: Porous Rock Fracture Mechanics with Application to Hydraulic Fracturing, Drilling and Structural Engineering, edited by: Shojaei, A. K. and Shao, J., Elsevier, Duxford, UK, 3–23, https://doi.org/10.1016/B978-0-08-100781-5.00001-4, 2017.

Gómez-Tuena, A., and Carrasco-Núñez, G.: Cerro Grande volcano: the evolution of a Miocene stratocone in the early Trans-Mexican Volcanic Belt. Tectonophysics, 318, 249–280, https://doi.org/10.1016/S0040-1951(99)00314-5, 2000.

Gómez-Tuena, A., Orozco-Esquivel, T., Ferrari, L.: Igneous petrogenesis of the Trans-Mexican Volcanic Belt, In: Alaniz-Álvarez, S.A., Nieto-Samaniego, Á.F. (Eds.), Geology of México: celebrating the Centenary of the Geological Society of México: Geological Society of America Special Paper, 422, pp. 1–53, https://doi.org/10.1130/ 2007.2422(05), 2007.

González-García, H., Francke, H., and Huenges, E.: Estimation of depression cones of Los Humeros, GEMex Final Conference, Potsdam, Germany, 18–19 February 2020, 2020.

González-García, H., Francke, H., Sass, I., and Huenges, E.: Production forecast and estimation of the recovery factor of the Los Humeros geothermal field, Mexico, Geothermal Energy, 9:13, https://doi.org/10.1186/s40517-021-00194-z, 2021.

González-García, H., Francke, H., Göllner-Völker, L., Welsch, B., Kranz, S., Huenges, E., Schebeck, L., and Sass, I.: CO2 emission assessment of the geothermal power station Los Humeros, Mexico, Geothermics, 104, 102471, 12 pp., https://doi.org/10.1016/j.geothermics.2022.102471, 2022.

González-Partida, E., Camprubí, A., López-Hernández, A., Santoyo, E., Izquíerdo-Montalvo, G., Pandarinath, K., Yáñez-Dávila, D., González-Ruiz, L. E., González-Ruiz, D., Díaz-Carreño, E., and Juárez-Hilarios, E.: Distribution of hypogene alteration and fluid evolution in the Los Humeros Geothermal Field (Puebla, Mexico): Multiple sourced fluids, interrelations, and processes in a superhot system, Applied Geochemistry, 136, 105159, 19 pp., https://doi.org/10.1016/j.apgeochem.2021.105159, 2022.

Graf, J. L.: REE as hydrothermal tracers during the formation of massive sulfide deposits in volcanic rocks. Econ. Geol., 72, 527–548, https://doi.org/10.2113/gsecongeo.72.4.527, 1977.

Granados-Chavarría, I., Calò, M., Figueroa-Soto, A., and Philippe, J.: Seismic imaging of the magmatic plumbing system and geothermal reservoir of the Los Humeros caldera (Mexico) using anisotropic shear wave models, Journal of Volcanology and Geothermal Research, 421, 107441, 15 pp.https://doi.org/10.1016/j.jvolgeores.2021.107441, 2022.

Gu, Y., Rühaak, W., Bär, K., and Sass, I.: Using seismic data to estimate the spatial distribution of rock thermal conductivity at reservoir scale, Geothermics, 66, 61–72, https://doi.org/10.1016/j.geothermics.2016.11.007, 2017.

Guo, H., Aziz, N. I., and Schmidt, L. C.: Rock fracture-toughness determination by the Brazilian test, Eng. Geol., 33, 177–188, https://doi.org/10.1016/0013-7952(93)90056-I, 1993.

Gutiérrez-Negrín, L. C. A., and Izquíerdo-Montalvo, G.: Review and update of the main features of the Los Humeros geothermal field, Mexico, Proceedings World Geothermal Congress 2010, Bali, Indonesia, 25–29 April 2010, 7 pp., 2010.

Harnois, I.: The CIW index, Sedimentary Geology, 55, 319–322, https://doi.org/10.1016/0037-0738(88)90137-6, *1*988.

Hartanato, L.: Different Scales and Integration of data in Reservoir Simulation, PhD thesis, Curtin University of Technology, Perth, Australia, 135 pp., 2004.

Hartmann, A., Rath, V., and Clauser, C.: Thermal conductivity from core and well log data, Int. J. Rock Mech. Min. Sci., 42, 1042–1055, https://doi.org/10.1016/j.ijrmms.2005.05.015, 2005.

Hartmann, A., Peching, R., and Clauser, C.: Petrophysical analysis of regional-scale thermal properties for improved simulations of geothermal installations and basin-scale heat and fluid flow, International Journal of Earth Sciences, 97, 421–433, https://doi.org/10.1007/s00531-007-0283-y, 2008.

Hartmann, J., and Moosdorf, N.: The new global lithological map database GLiM: A representation of rock properties at the Earth surface, Geochem. Geophys. Geosyst., 13, Q12004, https://doi.org/10.1029/2012GC004370, 2012.

Hassanzadegan, A., Blöcher, G., Milsch, H., Urpi, L., and Zimmermann, G.: The Effects of Temperature and Pressure on the Porosity Evolution of Flechtinger Sandstone, Rock Mech. Rock Eng., 47, 421–434, https://doi.org/10.1007/s00603-013-0401-z, 2013.

Hatakeda, K., Lin, W., Hirose, T., Tanikawa, W., Hamada, Y., and Tadai, O.: Electrical resistivity measurements of rocks under confining pressure condition, JAMSTEC Report of Research and Development, 24, 1–9, https://doi.org/10.5918/jamstecr.24.1, 2017.

Heap, M. J., and Kennedy, B. M.: Exploring the scale-dependent permeability of fractured andesite, Earth Planet. Sci. Lett., 447, 139–150, https://doi.org/10.1016/j.epsl.2016.05.004, 2016.

Heap, M. J., and Violay, M. E.: The mechanical behaviour and failure modes of volcanic rocks: a review, Bulletin of Volcanology, 83(5):33, 1–47, https://doi.org/10.1007/s00445-021-01447-2, 2021.

Heap, M. J., Lavallée, Y., Petrakova, L., Baud, P., Reuschlé, T., Varley, N. R., and Dingwell, D. B.: Microstructural controls on the physical and mechanical properties of edifice-forming andesites at Volcán de Colima, Mexico, J. Geophys. Res.-Sol. Ea., 119, 2925–2963, https://doi.org/10.1002/2013JB010521, 2014a.

Heap, M. J., Baud, P., Meredith, P. G., Vinciguerra, S., and Reuschlé, T.: The permeability and elastic moduli of tuff from Campi Flegrei, Italy: implications for ground deformation modelling, Solid Earth, 5(1), 25–44, https://doi.org/10.5194/se-5-25-2014., 2014b.

Heap, M. J., Troll, V. R., Kushnir, A. R. L., Gilg, A., Collinson, A. S. D., Deegan, F. M., Darmawan, H., Seraphine, N., Neuberg, J., and Walter, T. R.: Hydrothermal alteration of andesitic lava domes can lead to explosive volcanic behaviour, Nature Communications, 10:5063, 11 pp., https://doi.org/10.1038/s41467-019-13102-8, 2019.

Heap, M. J., Gravley, D. M., Kennedy, B. M., Gilg, H. A., Bertolett, E., and Barker, S. L.: Quantifying the role of hydrothermal alteration in creating geothermal and epithermal mineral resources: The Ohakuri ignimbrite (Taupo Volcanic Zone, New Zealand), J. Volcanol. Geoth. Res., 390, 106703, https://doi.org/10.1016/j.jvolgeores.2019.106703, 2020a.

Heap, M. J., Kushnir, A. R. L., Vasseur, J., Wadsworth, F. B., Harlé, P., Baud, P., Kennedy, B. M., Troll, V. R., and Deegan, F. M.: The thermal properties of porous andesite, Journal of Volcanology and Geothermal Research, 398, 106901, 13 pp., https://doi.org/10.1016/j.jvolgeores.2020.106901, 2020b.

Heap, M. J., Baumann, T. S., Rosas-Carbajal, M., Komorowski, J. C., Gilg, H. A., Villeneuve, M., Moretti, R., Baud, P., Carbillet, L., Harnett, C., and Reuschlé, T.: Alteration-Induced Volcano Instability at La Soufrière de Guadeloupe (Eastern Caribbean), Journal of Geophysical Research: Solid Earth, 126(8), e2021JB022514, https://doi.org/10.1029/2021JB022514, 2021.

Heap, M. J., Jessop, D. J., Wadsworth, F. B., Rosas-Carbajal, M., Komorowski, J.-C., Gilg, H. A., Aron, N., Buscetti, M., Gential, L., Goupil, M., Masson, M., Hervieu, L., Kushnir, A. R. L., Baud, P., Carbillet, L., Ryan, A. G., and Moretti, R.: The thermal properties of hydrothermally altered andesites from La Soufrère de Guadeloupe (Eastern Caribbean), Journal of Volcanology and Geothermal Research, 421, 10744, 17 pp., https://doi.org/10.1016/j.jvolgeores.2021.107444, 2022.

Heard, H. C., and Page, L.: Elastic Moduli, Thermal Expansion, and Inferred Permability of Two Granites to 350°C and 55 Megapascals, Journal of Geophysical Research, 87, 9340-9348, 1982.

Heidarzadeh, S., Saeidi, A., Lavoie, C., and Rouleau, A.: Geochemical characterization of a heterogenous rock mass using geological and laboratory test results: a case study of the Niobec Mine, Quebec (Canada), SN Applied Sciences, 3:640, 20 pp., https://doi.org/10.1007/s42452-021-04617-1, 2021.

Heřmanská, M., Kleine, B. I., and Stefánsson, A.: Supercritical Fluid Geochemistry in Geothermal Systems, Geofluids, 6023534, 14 pp., https://doi.org/10.1155/2019/6023534, 2019.

Hikov, A.: Rare Earth Element Mobility during Hydrothermal Alteration in Asarel Porphyry Copper Deposit, Central Srednogorie, Geologie, 64 (8), 1163–1170, 2011.

Hofmann, H., Peters, E., Hernández-Ochoa, A. F., Parisio, F., and Lepillier, B.: Hydraulic stimulation scenarios for a potential Enhanced Geothermal System (EGS) in Acoculco, Mexico, Proceedings World Geothermal Congress 2020+1, Reykjavik, Iceland, April–October 2021, 6 pp., 2021.

Homuth, S., Götz, A. E., and Sass, I.: Reservoir characterization of the Upper Jurassic geothermal target formations (Molasse Basin, Germany): role of thermofacies as exploration tool, Geoth. Energ. Sci, 3, 41–49, https://doi.org/10.5194/gtes-3-41-2015, 2015.

Hopf, S.: Behaviour of rare earth elements in geothermal systems of New Zealand, Journal of Geochemical Exploration, 3(47), 333–357, https://doi.org/10.1016/0375-6742(93)90075-W, 1993.

Horai, K.-I., and Susaki, J.-I.: The effect of pressure on the thermal conductivity of silicate rocks up to 12 kbar, Phys. Earth. Planet. Inter., 55, 292–305, https://doi.org/10.1016/0031-9201(89)90077-0, 1989.

Hornung, J., and Aigner, T.: Sedimentäre Architektur und Poroperm-Analyse fluviatiler Sandsteine: Fallbeispiel Coburger Sandstein, Franken, Hallesches Jahrb. Geowiss., 18, 121–138, 2004.

Howell, J. A., Allard, W. M., and Good, T. R.: The application of outcrop analogues in geological modeling: a review, present status and future outlook, Geol. Soc. Lond. Spec. Publ., 387, 1–25, https://doi.org/10.1144/SP387.12, 2014.

Hrouda, F., Chlupáčová, M., and Chadima, M.: The Use of Magnetic Susceptibility of Rocks in Geological Exploration, Terraplus, Brno 2009, 25 pp., available at: https://www.geomatrix.co.uk/cms/resources/downloads/the-use-of-magnetic-susceptibility-of-rocks-in-geological-exploration-v1-1.pdf (last access 20 September 2021), 2009.

Huenges, E.: Geothermische Stromerzeugung – Grundstrom für den erneuerbaren Energiemix 2050, FVEE Themen 2010, 73– 76, 2010, in: Tagungsband 2010: Forschung für das Zeitalter der erneuerbaren Energien, Forschungs Verbund Erneuerbare Energien, Renewable Energy Research Association, Berlin, Germany, 148 pp., 2010.

Hughes, D. S., and Maurette, C.: Variation of Elastic Wave Velocities in Basic Igneous Rocks with Pressure and Temperature, Geophysics, 22(1), 23–31, https://doi.org/10.1190/1.1438332, 1957.

Huttrer, G. W.: Geothermal Power Generation in the World 2015-2020 Update Report, Proceedings World Geothermal Congress 2020+1, Reykjavik, Iceland, April–October 2021, 17 pp., 2021.

IAPWS R15-11: International Association for the Properties of Water and Steam, Release on the IAPWS Formulation 2011for the Thermal Conductivity of Ordinary Water Substance, 2011.

IAPWS R6-95: International Association for the Properties of Water and Steam, Revised Release on the IAPWS Formulation 1995 for the Thermodynamic Properties of Ordinary Water Substance for General and Scientific Use, 2016.

IEA: International Energy Agency, Paris, Mexico country report 2020, available at: https://www.iea.org/countries/mexico (last access: 25.08.2022), 2020.

IEA: International Energy Agency, Paris, Geothermal Power – report 2021, available at: https://www.iea.org/reports/geothermal-power (last access: 25.08.2022), 2021.

Iglesias, E. R., Torres, R. J., Martínez-Estrella, J. I., and Reyes-Picasso, N.: Summary of the 2014 Assessment of Medium- to Low-Temperature Mexican Geothermal Resources, Proceedings World Geothermal Congress 2015, Melbourne, Australia, 19–25 April 2015, 7 pp., 2015.

IHS Markit: The AccuMap database, available at: https://ihsmarkit.com/products/oil-gas-tools-accumap.html (last access: 11 November 2020), 2020.

ISRM: Suggested methods for determining the uniaxial compressive strength and deformability of rock materials, in: The Complete ISRM Suggested Methods for Rock Characterization, Testing and Monitoring: 1974–2006, edited by: Ulusay, R. and Hudson, J. A., Ankara, Turkey, Pergamon Press, 137–138, 1979.

ISRM: Suggested Methods – Rock characterization testing and monitoring, edited by: Brown, E. T., Pergamon Press, Oxford, UK, 211 pp., 1981.

ISRM: Suggested methods for determining point load test, RTH 325-89, in: The Complete ISRM Suggested Methods for Rock Characterization, Testing and Monitoring: 1974–2006, edited by: Ulusay, R. and Hudson, J. A., Pergamon Press, Ankara, Turkey, 53–60, 1984.

ISRM: Suggested methods for determining the fracture toughness of rock, Int. J. Rock Mech. Min. Sci. Geomech., 25, 71–96, https://doi.org/10.1016/0148-9062(88)91871-2, 1988.

Izquíerdo, G., Portugal, E., and Arellano, V. M.: Mineralogy and Geochemistry of the Two Hydrothermal Reservoirs in the Los Humeros Geothermal System, GRC Transactions, 27, October 12–15 2003, 5 pp., 2003.

Izquíerdo, G., Gutierrez-Negrín, L. C. A., Aragon, A.: Considerations on the origin of acid fluids in Los Humeros geothermal field, Pue., Mexico, GRC Trans, 33, 59–62, 2009.

Izquíerdo, G., Aragón, A., and Díaz M., D.: Evidence of deep acid fluids in the Los Humeros Geothermal System, Mexico, GRC Transactions, 35, 625–630, 2011.

Izquíerdo, G., Aragón, A., Gómez, F. R., and Flores, M.: Reaction of Hydrothermally Altered Volcanic Rocks in Acid Solutions, Fundamentals of Renewable Energy and Applications, 5, 183, 1–5, https://doi.org/10.4172/20904541.1000183, 2015.

Jaritz, R.: Quantifizierung der Heterogenität einer Sandsteinmatrix am Beispiel des Stubensandstein (Mittlerer Keuper, Württemberg), Tübinger Geol. Abhandlungen, 48, 104 pp., 1999.

Jayananda, M., Duraiswami, R. A., Aadhiseshan, K. R., Gireesh, R. V., Prabhakar, B. C., Tushipokla, K., and Namratha, R.: Physical volcanology and geochemistry of Palaeoarchaean komatiite lava flows from western Dharwar craton, southern India: implications for Archaean mantle evolution and crustal growth, International Geology Review, 58(13), 1569–1595, https://doi.org/10.1080/00206814.2016.1172350, 2016.

Jentsch, A., Jolie, E., Jones, D. G., Taylor-Curran, H., Peiffer, L., Zimmer, M., and Lister, B.: Magmatic volatiles to assess permeable volcano-tectonic structures in the Los Humeros geothermal field, Mexico, J. Volcanol. Geoth. Res., 394,106820, https://doi.org/10.1016/j.jvolgeores.2020.106820, 2020.

Jiang, X.-W., Wang, X.-S., and Wan, Li: Semi-empirical equations for the systematic decrease in permeability with depth in porous and fractured media, Hydrogeology Journal, 18, 839–850, https://doi.org/10.1007/s10040-010-0575-3, 2010.

Johannesson, K. H., and Xiapoping, Z.: Geochemistry of the Rare Earth Elements in Natural Terrestrial Waters: A Review of What is Currently Known, Chines Journal of Geochemistry, 16(1), 20–42, https://doi.org/10.1007/BF02843369, 1977.

Jolie, E., Bruhn, D., López Hernández, A., Liotta, D., Garduño-Monroy, V. H., Lelli, M., Páll Hersir, G., Arango-Galván, C., Bonté, D., Calcagno, P., Deb, P., Clauser, C., Peters, E., Hernández Ochoa, A. F., Huenges, E., González Acevedo, Z. I., Kieling, K., Trumpy, E., Vargas, J., Gutiérrez-Negrín, L. C., Aragón-Aguilar, A., Halldórsdóttir, S., González Partida, E., van Wees, J.-D., Ramírez Montes, M. A., Diez León, H. D., and the GEMex team: GEMex – A Mexican-European Research Cooperation on Development of Superhot and Engineered Geothermal Systems, in: Proceedings of the 43rd Workshop on Geothermal Reservoir Engineering, Stanford, CA, USA, 12–14 February 2018, 10 pp., 2018.

Jolliffle, I.: Principal Component Analysis, Encyclopedia of statistics in behavioral science, 3, 1580–1584, https://doi.org/10.1002/0470013192.bsa501, 2005.

Kanakiya, S., Turner, G. M., Rowe, M. C., Adam, L., and Lindsay, J. M.: High remanent magnetization measured in hydrothermally altered lavas, Geophysical Research Letters, 48, e2021GL095732, https://doi.org/10.1029/2021GL095732, 2021.

Khajeh, M. M.: Heterogeneity Consideration and Upscaling of Elastic Properties in Coupled Geomechanical Flow Simulation of SAGD, PhD thesis, University of Alberta, Edmonton, Canada, 131 pp., 2013.

Klinkenberg, L. J.: The permeability of porous media to liquids and gases, Drilling Production Practice, API, 200–213, available under https://www.onepetro.org/conference-paper/API-41-200, last access 20 September 2021, 1941.

Konietzky, H., and Wang, F.: Thermal behaviour of rocks, Institut für Geotechnik, TU Bergakademie Freiberg, 20 pp., available at: https://tu-freiberg.de/sites/default/files/media/professur-felsmechanik-32204/E-book/30_thermal_behaviour_of_rocks_0.pdf (last access: 15 September 2021), 2019.

Kozdrój, W., Nawrocki, J., Pańczyk-Nawrocka, M., ZiółkowskaKozdrój, M., Wójcik, K., Kumek, J., and González-Partida, E.: Stratigraphic, petrological features and datings of Los Humeros rocks from outcrops and boreholes, in: Final report on active systems: Los Humeros and Acoculco, Deliverable 4.1, WP4, GEMex H2020 project, European Comission, available at: http://www.gemex-h2020.eu (last access: 26 May 2020), 2019.

Kozdrój, W., Pańczyk-Nawrocka, M., Nawrocki, J., Ziółkowska-Kozdrój, M., and Wójcik, K.: Geochronological and paleomagnetic constraints on evolution of Palaeozoic plutonic basement and Miocene-Pleistocene volcanic succession of the Las Minas area (E-part of the Trans-Mexican Volcanic Belt), GEMex Final Conference, Potsdam, Germany, 18–19 February 2020, available at: http://www.gemex-h2020.eu (last access: 28 Sep 2021), 2020.

Kruszewski, M., and Wittig, V.: Review of failure modes in supercritical geothermal drilling projects, Geothermal Energy, 6, https://doi.org/10.1186/s40517-018-0113-4, 29 pp., 2018.

Kruszewski, M., Hofmann, H., Alvarez, F. G., Bianco, C., Haro, A. J., Garduno, V. H., Liotta, D., Trumpy, E., Brogi, A., Wheeler, W., Basteesen, E., Parisio, F., and Saenger, E. H.: Integrated Stress Field Estimation and Implications for Enhanced Geothermal System Development in Acoculco, Mexico, GEMex Final Conference, Potsdam, Germany, 18–19 February 2020, S3.5, 2020.

Kruszewski, M., Hofmann, H., Gomez-Alvarez, F., Bianco, C., Jimenez-Haro, A., Garduno, V. H., Liotta, D., Trumpy, E., Brogi, A., Wheeler, W., Bastesen, E., Parisio, F., and Saenger, E. H.: Integrated Stress Field Estimation and Implications for Enhanced Geothermal System Development in Acoculco, Mexico, Geothermics, 89, 101931, https://doi.org/10.1016/j.geothermics.2020.101931, 2021.

Kummerow, J., and Raab, S.: Temperature dependence of electrical resistivity – Part II: A new experimental set-up to study fluid-saturated rocks, Energy Proced., 76, 247–255, https://doi.org/10.1016/j.egypro.2015.07.855, 2015.

Kummerow, J., Raab, S., and Spangenberg, E.: The impact of reactive flow on electrical and hydraulic rock properties in supercritical geothermal settings, GEMex Final Conference, Potsdam, Germany, 18–19 February 2020, 32, 2020.

Kushnir, A. R. L., Martel, C., Bourdier, J. L., Heap, M. J., Reuschlé, T., Erdmann, S., Komorowski, J. C., and Cholik, N.: Probing permeability and microstructure: Unravelling the role of a low-permeability dome on the explosivity of Merapi (Indonesia), Journal of Volcanology and Geothermal Research, 316, 56–71, https://doi.org/10.1016/j.jvolgeores.2016.02.012, 2016.

Kushnir, A. R. L., Heap, M. J., and Baud, P.: Assessing the role of fractures on the permeability of the Permo-Triassic sandstones at the Soultz-sous-Forêts (France) geothermal site, Geothermics, 74, 181–189, https://doi.org/10.1016/j.geothermics.2018.03.009, 2018.

Lacinska, A. M., Rochelle, C., Kilpatrick, A., Rushton, J., Weydt, L. M., Bär, K., and Sass, I.: Evidence for fracture-hosted fluid-rock reactions within geothermal reservoirs of the eastern Trans-Mexican Volcanic Belt, GEMex Final Conference, Potsdam, Germany, 18–19 February 2020, 33, 2020.

Le Maitre R. W., Streckeisen, A., Zanettin, B., Le Bas, M. J., Bonin, B., Bateman, P., Bellieni, G., Dudek, A., Efremova, S., Keller, J., Lameyre, J., Sabine, P. A., Schmid, R., Sorensen, H., and Woolley, A. R.: Igneous rocks: a classification and glossary of terms—recommendations of the International Union of Geological Sciences Subcommission on the systematics of igneous rocks, 2nd edition, Cambridge University Press, Cambridge, UK, 237 pp., https://doi.org/10.1017/CBO 9780511535581, 2002.

Le Maitre, R. W., and Streckeisen, A. (Eds.): Igneous rocks: a classification and glossary of terms – recommendations of the International Union of Geological Sciences Subcommission on the Systematics of Igneous Rocks, Cambridge University Press, Cambridge, UK, 252 pp., https://doi.org/10.1017/CBO9780511535581, 2003.

Lee, E. Y., Tejada, M. L. G., Song, I., Chun, S. S., Gier, S., Riquier, L., White, L. T., Schnetger, B., Brumsack, H.-J., Jones, M. M., and Martinez, M.: Petrophysical Property Modifications by Alteration in a Volcanic Sequence at IODP Site U1513, Naturaliste Plateau, Journal of Geophysical Research: Solid Earth, 126, e2020JB021061, 27 pp., https://doi.org/10.1029/2020JB021061, 2021.

Lelli, M., Kretzschmar, T. G., Cabassi, J., Doveri, M., Sanchez-Avila, J. I., Gherardi, F., Magro, G., and Norelli, F.: Fluid geochemistry of the Los Humeros geothermal field (LHGF – Puebla, Mexico): New constraints for the conceptual model, Geothermics, 90, 101983, https://doi.org/10.1016/ jgeothermics.2020.101983, 2020.

Lenhardt, N., and Götz, A. E.: Volcanic settings and their reservoir potential: an outcrop analog study on the Miocene Tepoztlán Formation, Central Mexico, J. Volcanol. Geoth. Res., 204, 66–75, https://doi.org/10.1016/j.jvolgeores.2011.03.007, 2011.

Lenhardt, N., and Götz, A. E.: Geothermal reservoir potential of volcaniclastic settings: the Valley of Mexico, Central Mexico, Renew. Energy, 77, 423–429, https://doi.org/10.1016/j.renene. 2014.12.034, 2015.

Lepillier, B. P.: Characterization of a Fracture-Controlled Enhanced Geothermal System (EGS) in the Trans-Mexican-Volcanic-Belt (TMVB): Predictive Mechanical Model for Fracture Stimulation in an Enhanced Geothermal System Context (EGS), PhD Thesis, Delft University of Technology, The Netherlands, https://doi.org/10.4233/uuid:8c8e04ec-b697-4ebd-aee4-46a01434021c, 2020.

Lepillier, B., Daniilidis, A., Doonechaly Gholizadeh, N., Bruna, P.-O., Kummerow, J., and Bruhn, D.: A fracture flow permeability and stress dependency simulation applied to multi-reservoirs, multi-production scenarios analysis, Geotherm. Energy, 24, 1–16, https://doi.org/10.1186/s40517-019-0141-8, 2019.

Lepique, M.: Empfehlung Nr. 10 des Arbeitskreises 3.3 "Versuchstechnik Fels" der Deutschen Gesellschaft für Geotechnik e. V.: Indirekter Zugversuch an Gesteinsproben – Spaltzugversuch, Bautechnik, 85, 623–627, https://doi.org/10.1002/bate.200810048, 2008.

Lermo, J., Antayhua, Y., Quintanar, L., and Lorenzo, C.: Estudio sismológico del campo geotérmico de Los Humeros, Parte I, Sismicidad, mecanismos de fuente y distribución de esfuerzos, Geotermia 21, 25–41, 2008.

Lévy, L., Gibert, B., Sigmundsson, F., Flóvenz, Ó. G., Hersir, G. P., Briole, P., and Pezard, P. A.: The role of smectites in the electrical conductivity of active hydrothermal systems: electrical properties of core samples from Krafla volcano, Iceland, Geophys. J. Int., 215, 1558–1582, https://doi.org/10.1093/gji/ggy342, 2018.

Lévy, L., Maurya, P. K., Byrdina, S., Vandemeulebrouck, J., Sigmundsson, F., Árnson, K., Ricci, T., Deldicque, D., Roger, M., Gibert, B., and Labazuy, P.: Electrical resistivity tomography and time-domain induced polarization field investigations of geothermal areas at Krafla, Iceland: comparison to borehole and laboratory frequency-domain electrical observations, Geophys. J. Int., 218, 1469–1489, https://doi.org/10.1093/gji/ggz240, 2019.

Li, C., Chen, X., and Du, Z.: A New Relationship of Rock Compressibility with Porosity, SPE 88464-MS, in: SPE Asia Pacific Oil and Gas Conference and Exhibition, Perth, Australia, 18–20 October 2004, 2004.

Linsel, A., Wiesler, S., Hornung, J., and Hinderer, M.: High-resolution analysis of the physicochemical characteristics of sandstone media at the lithofacies scale, Solid Earth, 11, 1511–1526, https://doi.org/10.5194/se-11-1511-2020, 2020.

Liotta, D., Brogi, A., Garduño-Monroy, V. H., Gomez, F., Wheeler, W. H., Bastesen, E., Torabi, A., Bianco, C., Jimenez-Haro, A., Olvera-García, E., and Zucchi, E.: Regional Geological Structures, in: Final report on active systems: Los Humeros and Acoculco, Deliverable 4.1, WP4, GEMex H2020 project, European Comission, available at: http://www.gemex-h2020.eu (last access: 26 May 2020), 2019.

Liotta, D., Bastesen, E., Bianco, C., Brogi, A., Caggianelli, A., Garduño-Monroy, V.-H., González-Partida, E., Jimenez-Haro, A., Kozdrój, W., Lacinska, A., Lepillier, B., Morelli, G., Nawrocki, J., Olvera-García, E., Pańczyk-Nawrocka, M., Rochelle, C., Ruggieri, G., Torabi, A., Ventruti, G., Wheeler, H. W., Wójcik, K., Ziólkowska-Kozdrój, M., and Zucchi, M.: Analogue Geothermal Systems In Mexico: Insights Into The Deep Part Of Los Humeros Geothermal Field From The Las Minas Mining Area (Eastern Mexico), Proceedings World Geothermal Congress 2020+1, Reykjavik, Iceland, April–October 2021, 9 pp., 2021.

Liotta, D., Brogi, A., Ruggieri, G., and Zucchi, M.: Fossil vs. Active Geothermal Systems: A Field and Laboratory Method to Disclose the Relationships between Geothermal Fluid Flow and Geological Structures at Depth, Energies, 14, 933, 27 pp., https://doi.org/10.3390/en14040933, 2021.

Lippmann, E., and Rauen, A.: Measurements of Thermal Conductivity (TC) and Thermal Diffusivity (TD) by the Optical Scanning Technology, Lippmann and Rauen GbR, Schaufling, Germany, 2009.

Löer, K., Toledo, T., Norini, G., Zhang, X., Curtis, A., and Saenger, E. H.: Imaging the Deep Structures of Los Humeros Geothermal Field, Mexico, Using Three-Component Seismic Noise Beamforming, Seismol. Res. Lett. XX, 1–9, https://doi.org/10.1785/0220200022, 2020.

López-Hernández, A.: Estudio Regional Volcánico y Estructural del Campo Geotérmico de Los Humeros, Puebla., México, Geotermia Revista Mexicana de Geoenergía, 11, 17–36, 1995.

López-Hernández, A., García-Estrada, G., Aguirre-Díaz, G., González-Partida, E., Palma-Guzmán, H., and Quijano-Léon, J.: Hydrothermal activity in the Tulancingo-Acoculco Caldera Complex, central Mexico: Exploratory studies, Geothermics, 38, 279–293, https://doi.org/10.1016/j.geothermics.2009.05.001, 2009.

Lorenzo-Pulido, C. D.: Borehole Geophysics and Geology of Well H-43, Los Humeros Geothermal Field, Puebla, México, Comisíon Federal de Electricidad, Report 23, 40 pp., 2008.

Lorenzo-Púlido, C., Armenta-Flores, M., and Ramírez-Silva, G.: Characterization of the Acoculco Geothermal Zone as a HDR System, GRC Transactions, 34, 369–372, 2010.

Lu, S.-M.: A global review of enhanced geothermal system (EGS), Renewable and Sustainable Energy Reviews, 81, https://doi.org/10.1016/j.rser.2017.06.097, 2902–2921, 2018.

Lucci, F., Rossetti, F., Becchio, R., Theye, T., Gerdes, A., Opitz, J., Baez, W., Bardelli, L., De Astis, G., Viramonte, J., and Giordano, G.: Magmatic Mn-rich garnets in volcanic settings: Age and longevity of the magmatic plumbing system of the Miocene Ramadas volcanism (NW Argentina), Lithos, 322, 238-249, https://doi.org/10.1016/j.lithos.2018.10.016, 2018.

Lucci, F., Carrasco-Núñez, G., Rossetti, F., Theye, T., White, J. C., Urbani, S., Azizi, H., Asahara, Y., and Giordano, G.: Anatomy of the magmatic plumbing system of Los Humeros Caldera (Mexico): implications for geothermal systems, Solid Earth, 11, 125–159, https://doi.org/10.5194/se-11-125-2020, 2020.

Macías, J. L., Arce, J. L., García-Tenorio, F., Layer, P. W., Rueda, H., Reyes-Agustin, G., and Avellán, D.: Geology and geochronology of Tlaloc, Telapón, Iztaccíhuatl, and Popocatépetl volcanoes, Sierra Nevada, central México, Field Guides 25, 163–193, https://doi.org/10.1130/2012.0025 (08), 2012.

MacGeehan, P. J., and MacLean, W. H.: Tholeiitic basalt-rhyolite magmatism and massive sulfide deposits at Matagami, Quebec, Nature, 283, 153–157, https://doi.org/10.1038/283153a0, 1980.

MacLean, W. H., and Barrett, T. J.: Lithogeochemical techniques using immobile elements, Journal of Geochemical Exploration, 48, 109–133, https://doi.org/10.1016/0375-6742(93)90002-4, 1993.

Malek, A. E., Adams, B. M., Rossi, E., Schiegg, H., and Saar, M. O.: Electric Power Generation, Specific Capital Cost, and Specific Power for Advanced Geothermal Systems (AGS), Proceedings, 46th Workshop on Geothermal Reservoir Engineering Stanford University, Stanford, California, February 15–17, 2021, SGP-TR-218, 12 pp., 2021.

Mandrone, G., Comina, C., and Vacha, D.: Faults characterization aimed at geothermal fluid path identification and quantification, GEMex Final Conference, Potsdam, Germany, 18–19 February 2020, 41, 2020.

Martínez-Serrano, R. G.: Caractérisation minéralogique, géochimique et isotopique du champ géothermique de Los Humeros, Mexique: interactions fluide-roche dans un système à fluide mixte (eau-vapeur), Université de Nancy, Nancy, France, unpublished PhD thesis, 1993.

Martínez-Serrano, R. G., and Alibert, C.: Características geoquímicas de las rocas volcánicas del sistema geotérmico Los Humeros, Puebla, y su relacíon con la mineralogía de alteración, Geofisica Internacional, 33(4), 585–605, 1994.

Martínez-Serrano, R.G.: Chemical variations in hydrothermal minerals of the Los Humeros geothermal system, Mexico, Geothermics, 31(5), 579–612, https://doi.org/10.1016/S0375-6505(02)00015-9, 2002.

Mathieu, L.: Quantifying Hydrothermal Alteration: A Review of Methods, Geosciences, 8, 245, 27 pp., https://doi.org/10.3390/geosciences8070245, 2018.

Mayer, K., Scheu, B., Montanaro, C., Yilmaz, T. I., Isaia, R., Aßbichler, D., and Dingwell, D. B.: Hydrothermal alteration of surficial rocks at Solfatara (Campi Flegrei): Petrophysical properties and imlications for phreatic eruption processes, Journal of Volcanology and Geothermal Research, 320, 128–143, https://doi.org/10.1016/j.jvolgeores.2016.04.020, 2016.

Merriman, D., Hofmeister, A. M., Roy, D. J., and Whittington, A. G.: Temperature-dependent thermal transport properties of carbonate minerals and rocks, Geosphere, 14, 1961-1987, https://doi.org/10.1130/GES01581.1, 2018.

Micromeritics: AccuPyc 1330 Pycnometer, V2.02, Part No. 133-42808-01, Micromeritics GmbH, Munich, Germany, 1997.

Micromeritics: AccuPyc II 1340, Product Broschure, Micromeritics Instrument Corporation, Norcross, available at: http://www.micromeritics.com/Product-Showcase/AccuPyc-II-1340.aspx (last access: 9 December 2020), 2014.

Micromeritics: GeoPyc 1360, V3., Part 136-42801-01, Micromeritics GmbH, Munich, Germany, 1998.

Middlemost, E. A. K.: Naming materials in the magma/igneous rock system, Earth-Science Reviews, 37(3-4), 215–224, https://doi:10.1016/0012-8252(94)90029-9, 1994.

Mielke, P., Nehler, M., Bignall, G., and Sass, I.: Thermo-physical rock properties and the impact of advancing hydrothermal alteration – a case study from the Tauhara geothermal field, New Zealand, J. Volcanol. Geoth. Res., 301, 14–28, https://doi.org/10.1016/j.jvolgeores.2015.04.007, 2015.

Mielke, P., Weinert, S., Bignall, G., and Sass, I.: Thermo-physical rock properties of greywacke basement rock and intrusive lavas from the Taupo Volcanic Zone, New Zealand, J. Volcanol. Geoth. Res., 324, 179–189, https://doi.org/10.1016/j.jvolgeores.2016.06.002, 2016.

Mielke, P., Bär, K., and Sass, I.: Determining the relationship of thermal conductivity and compressional wave velocity of common rock types as a basis for reservoir characterization, J. Appl. Geophys., 140, 135–144, https://doi.org/10.1016/j.jappgeo.2017.04.002, 2017.

Mobarak, S. A., and Somerton, W. H.: The Effect Of Temperature And Pressure On Wave Velocities In Porous Rocks, in: Proceedings of the Fall Meeting of the Society of Petroleum Engineers of AIME, New Orleans, Louisiana, 18 pp., https://doi.org/10.2118/3571-MS, 1971.

Moeck, I.: Catalog of geothermal play types based on geologic controls, Renewable and Sustainable Energy Reviews, 37, 867–882, https://doi.org/10.1016/j.rser.2014.05.032, 2014.

Moosavi, S. A., Goshtasbi, K., Kazemzadeh, E., Bakhtiari, H. A., Esfahani, M. R., and Vali, J.: Relationship between porosity and permeability with stress using pore volume compressibility characteristic of reservoir rocks, Arab. J. Geosci., 7, 231–239, https://doi.org/10.1007/s12517-012-0760-x, 2014.

Mora-Klepeis, G.: Mexico and the Gulf of Mexico, in: Alderton, D., and Elias, S. A. (Eds.): Encyclopedia of Geology, Second Edition, Academic Press, Volume 4, 68–79, https://doi.org/10.1016/B978-0-08-102908-4.00138-7, 2021.

Mordensky, S. P., Villeneuve, M. C., Farquharson, J. I., Kennedy, B. M., Heap, M. J., and Gravley, D. M.: Rock mass properties and edifice strength data from Pinnacle Ridge, Mt. Ruapehu, New Zealand, Journal of Volcanology and Geothermal Research, 367, 46–62, https://doi.org/10.1016/j.jvolgeores.2018.09.012, 2018.

Mordensky, S. P., Heap, M. J., Kennedy, B. M., Gilg, H. A., Villeneuve, M. C., Farquharson, J.I., and Gravley, D.M.: Influence of alteration on the mechanical behaviour and failure mode of andesite: implications for shallow seismicity and volcano monitoring, Bulletin of Volcanology, 81:44, 12 pp., https://doi.org/10.1007/s00445-019-1306-9, 2019a.

Mordensky, S. P., Kennedy, B. M., Villeneuve, M. C., Lavallée, Y., Reichow, M. K., Wallace, P. A., Siratovich, P. A., And Gravley, D. M.: Increasing the permeability of hydrothermally altered andesite by transitory heating, Geochemistry Geophysics Geosystems, 20(11), 5251–5269, https://doi.org/10.1029/2019GC008409, 2019b.

Morgan, J. W., and Wandless, G. A.: Rare earth element distribution in some hydrothermal minerals: evidence for crystallographic control, Geochimica et Cosmochimica Acta, 44(7), 973–980, https://doi.org/10.1016/0016-7037(80)90286-0, 1980.

Mutschler, T.: Neufassung der Empfehlung Nr. 1 des Arbeitskreises "Versuchstechnik Fels" der Deutschen Gesellschaft für Geotechnik e. V.: Einaxiale Druckversuche an zylindrischen Gesteinsprüfkörpern, Bautechnik, 81, 825–834, https://doi.org/10.1002/bate.200490194, 2004.

National Geochemical Database USGS: Geochemical database of the US Geological Survey, USA, available at: https://www.usgs.gov/energy-and-minerals/mineral-resources-program/science/national-geochemical-database?qt-science_center_objects (last access: 21 October 2020), 2014.

National Geothermal data system NGDS: Database of various reports and data sets related to geothermal and geological projects in the USA, available at: https://data.geothermaldata.org/ (last access: 11 November 2020), 2014.

NAVDAT data base: The North American Volcanic and Intrusive Rock Database (NAVDAT), available in the EarthChem Portal, available at: http://portal.earthchem.org/ (last access: 21 October 2020), 2020.

Navelot, V., Géraud, Y., Favier, A., Diraison, M., Corsini, M., Lardeaux, J.-M., Verati, C., de Lépinary, J. M., Legendre, L., and Beauchamps, G.: Petrophysical properties of volcanic rocks and impacts of hydrothermal alteration in the Guadeloupe Archipelago (West Indies), J. Volcanol. Geoth. Res., 360, 1–21, https://doi.org/10.1016/j.jvolgeores.2018.07.004, 2018.

Nesbitt, H. W., and Young, G. M.: Early Proterozoic climates and plate motions inferred from major element chemistry of lutites, Nature, 199, 715–717, https://doi.org/10.1038/299715a0, 1982.

Nono, F., Gibert, B., Parat, F., Loggia, D., Cichy, S. B., and Violay, M.: Electrical conductivity of Icelandic deep geothermal reservoirs up to supercritical conditions: Insight from laboratory experiments, JVGR, 391, 106364, https://doi.org/10.1016/j.jvolgeores.2018.04.021, 2020.

Norden, B., Förster, A., Förster, H.-J., and Fuchs, S.: Temperature and pressure corrections applied to rock thermal conductivity: impact on subsurface temperature prognosis and heat-flow determination in geothermal exploration, Geothermal Energy, 1, 1–19, https://doi.org/10.1186/s40517-020-0157-0, 2020.

Norini, G., Gropelli, G., Sulpizio, R., Carrasco-Núñez, G., Dávila-Harris, P., Pellicioli, C., Zucca, F., and De Franco, R.: Structural analysis and thermal remote sensing of the Los Humeros Volcanic Complex: Implications for volcano structure and geothermal exploration, J. Volcanol. Geoth. Res., 301, 221–237, https://doi.org/10.1016/j.jvolgeores.2015.05.014, 2015.

Norini, G., Carrasco-Núñez, G., Corbo, F., Lermo, J., Hernández, J., Castro, C., Bonini, M., Montanari, D., Corti, G., Moratti, G., Piccardi, L., Chavez, G., Zuluaga, M. C., Ramírez, M., and Cedillo, F.: The structural architecture of the Los Humeros volcanic complex and geothermal field, J. Volcanol. Geoth. Res., 381, 312–329, https://doi.org/10.1016/j.jvolgeores.2019.06.010, 2019.

Nurhandoko, B. E. B., Kurniadi, R., Susilowati, Tryoso, K., Widowati, S., Hadi, M. R. A., Abda, M. R., Martha, R. K., Fatiah, E., and Komara, R.: Integrated Subsurface Temperature Modeling beneath Mt. Lawu and Mt. Muriah in The Northeast Java Basin, Indonesia, Open Geosci., 11, 341–351, https://doi.org/10.1515/geo-2019-0027, 2019.

Ochoa-Camarillo, H., Buitrón-Sánchez, B. E., and Silva-Pineda, A.: Redbeds of the Huayacocotla anticlinorium, state of Hidalgo, east-central Mexico, Special Paper 340: Mesozoic Sedimentary and Tectonic History of North-Central Mexico, 59–68, https://doi.org/10.1130/0-8137-2340-x.59, 1999.

Ohnaka, M.: Stability of Remanent Magnetization of Rocks under Compression – Its Relation to the Grain Size of Rock-forming Ferromagnetic Minerals, J. Geomagn. Geoelectr., 21, 495–505, https://doi.org/10.5636/jgg.21.495, 1969.

Ólavsdóttir, J., Andersen, M. S., and Boldreel, L. O.: Reservoir quality of intrabasalt volcaniclastic units onshore Faroe Islands, North Atlantic Igneous Province, northeast Atlantic, AAPG Bull., 99, 467–497, https://doi.org/10.1306/08061412084, 2015.

Oliva-Urcia, B., Kontny, A., Vahle, C., and Schleicher, A. M.: Modification of the magnetic mineralogy in basalts due to fluid-rock interactions in a high-temperature geothermal system (Krafla, Iceland), Geophys. J. Int., 186, 155–174, https://doi.org/10.1111/j.1365-246X.2011.05029.x, 2011.

Olvera-García, E., Bianco, C., Garduño-Monroy, V. H., Brogi, A., Liotta, D., Wheeler, W., Gómez-Alvarez, S. N.-B., Jiménez-Haro, A., Guevara-Alday, J. A., Bastesen, E., Lepillier, B., Zucchi, M., Caggianelli, A., and Ruggieri, G.: Geology of Las Minas: an example of an exhumed geothermal system (Eastern Trans-Mexican Volcanic Belt), Journal of Maps, 16:2, 918–926, https://doi.org/10.1080/17445647.2020.1842815, 2020.

Palacios, C. M., Hein, U. F., and Dulski, P.: Behavior of rare earth elements during hydrothermal alteration at the Buena Esperanza copper–silver deposit, northern Chile, Earth Planet. Sci. Lett., 80, 208–216, https://doi.org/10.1016/0012-821X(86)90105-6 ,1986.

Pandarinath, K., Dulski, P., Torres-Alvarado, I. S., and Verma, S. P.: Element mobility during the hydrothermal alteration of rhyolitic rocks of the los Azufres geothermal field, Mexico, Geothermics, 37, 53–72, https://doi.org/10.1016/j.geothermics.2007.10.002, 2008.

Pandainath, K., García-Soto, A. Y., Santoyo, E., Guevara, M., and González-Partida, E.: Mineralogical and geochemical changes due to hydrothermal alteration of the volcanic rocks at Acoculco geothermal system, Mexico, Geological Journal, 55, 9, 6508–6526, https://doi.org/10.1002/gj.3817, 2020.

Parisio, F., Vilarrasa, V., Wang, W., Kolditz, O., and Nagel, T.: The risk of long-term re-injection in supercritical geothermal systems, Nature Communications, 10, 11 pp., https://doi.org/10.1038/s41467-019-12146-0, 2019.

Parsapoor, A., Khalili, M., and Mackizadeh, M. A.: The behaviour of trace and rare earth elements (REE) during hydrothermal alteration in the Rangan area (Central Iran), Journal of Asian Earth Sciences, 34(2), 123–134, https://doi.org/10.1016/j.jseaes.2008.04.005, 2009.

Pérez-Campos, X., Kim, Y., Husker, A., Davis, P. M., Clayton, R. W., Iglesias, A., Pacheco, J., Singh, S., Constantin, M. V., and Gurnis, M.: Horizontal subduction and truncation of the Cocos plate beneath central Mexico, Geophys. Res. Lett. 35, 1–6, https://doi.org/10.1029/2008GL035127, 2008.

Petlab database: GNS Science, Petlab database, available at: http://pet.gns.cri.nz/ (last access: 21 October 2020), 2020.

Petty, S., Cladouhos, T., Watz, J., and Garrison, G.: Technology Needs for SuperHot EGS Development, PROCEEDINGS, 45th Workshop on Geothermal Reservoir Engineering Stanford University, Stanford, California, February 10–12, 2020, SGP-TR-216, 8 pp., 2020.

Piccardi, L.: Dataset on recent and active faults inferred from remote sensing of the Acoculco and Los Humeros geothermal fields, published online on 16 June 2020, available at: https://gemex.igg.cnr.it/layers/repoigg:geonode:faglie_piccardi (last access: 29 July 2022), 2020.

Pinti, D. L., Castro, M. C., López-Hernández, A., Han, G., Shouakar-Stash, O., Hall, C. M., and Ramírez-Montes, M.: Fluid circulation and reservoir conditions of the Los Humeros Geothermal Field (LHGF), Mexico, as revealed by a noble gas survey, J. Volcanol. Geoth. Res., 333–334, 104–115, https://doi.org/10.1016/j.jvolgeores.2017.01.015, 2017.

Pinti, D. L., Castro, M. C., López-Hernández, A., Hernández-Hernández, M. A., Shouakar-Stash, O., Hall, C. M., Bahena-Romero, J., Ramírez-Montes, M.: Origin of volatile species and aqueous fluids in the Los Humeros Geothermal Field, Mexico, Chemical Geology, 584, 120539, 15 pp., https://doi.org/10.1016/j.chemgeo.2021.120539, 2021.

Pioro, I.: Application of Supercritical Pressure in Power Engineering, Supercritical Fluid Technology for Energy and Environmental Applications, 201–233, https://doi.org/10.1016/b978-0-444-62696-7.00011-3, 2014.

Pola, A., Crosta, G., Fusi, N., Barberini, V., and Norini, G.: Influence of alteration on physical properties of volcanic rocks, Tectonophysics, 566/567, 67–86, https://doi.org/10.1016/j.tecto.2012.07.017, 2012.

Pola, A., Crosta, G. B., Fusi, N., and Castellanza, R.: General characterization of the mechanical behaviour of different volcanic rocks with respect to alteration, Eng. Geol., 169, 1–13, https://doi.org/10.1016/j.enggeo.2013.11.011, 2014.

Pola, A., Martínez-Martínez, J., Macías, J. L., Fusi, N., Crosta, G., Garduño-Monroy, V. H., and Núñez-Hurtado, J. A.: Geomechanical characterization of the Miocene Cuitzeo ignimbrites, Michoacán, Central Mexico, Engineering Geology, 214, 79–93, https://doi.org/10.1016/j.enggeo.2016.10.003, 2016.

Popov, Y. A., Sass, P. D., Williams, C. F., and Burkhardt, H.: Characterization of rock thermal conductivity by high resolution optical scanning, Geothermics, 28, 253–276, https://doi.org/10.1016/S0375-6505(99)00007-3, 1999.

Popov, Y., Beardsmore, G., Clauser, C., and Roy, S.: ISRM Suggested Methods for Determining Thermal Properties of Rocks from Laboratory Tests at Atmospheric Pressure, Rock Mech. Rock Eng., 49, 4179–4207, https://doi.org/10.1007/s00603-016-1070-5, 2016.

Portugal, E., Izquíerdo, G., Barragán, R. M., and Romero, B. I.: Hydrodynamic model of Los Humeros geothermal field, Mexico, based on geochemical, mineralogical and isotopic data, Geofísica International, 41(4), 415–420, https://www.redalyc.org/articulo.oa?id=56841409, 2002.

Prol-Ledesma, R. M.: Recent cooling in Los Humeros geothermal field México, inferred from clay minerals distribution, Geotherm. Resour. Council Trans., 14, 959–964, 1990.

Prol-Ledesma, R. M.: Pre-and post-exploitation variations in hydrothermal activity in Los Humeros geothermal field, Mexico, Journal of Volcanology and Geothermal Research, 83(3-4), 313–333, https://doi.org/10.1016/S0377-0273(98)00024-9, 1998.

Prol-Ledesma, R. M., and Browne, P. R. L.: Hydrothermal alteration and fluid inclusion geothermometry of Los Humeros geothermal field, México, Geothermics, 18(5-6), 677–690, https://doi.org/10.1016/0375-6505(89)90100-4, 1989.

Prol-Ledesma, R. M., and Morán-Zenteno, D. J.: Heat flow and geothermal provinces in Mexico, Geothermics, 78, 183–200, https://doi.org/10.1016/j.geothermics.2018.12.009, 2019.

Qi, D., and Hesketh, T.: An Analysis of Upscaling Techniques for Reservoir Simulation, Pet. Sci. Technol., 23, 827–842, https://doi.org/10.1081/LFT-200033132, 2005.

Qi, H., Ba, J., and Müller, T. M.: Temperature effect on the velocity-porosity relationship in rocks, JGR Solid Earth, 126, e2019JB019317, 23 pp., https://doi.org/10.1029/2019JB019317, 2020.

Qu, H., Yang, B., Tian, X., Liu, X., Yang, H., Dong, W., and Chen, Y.: The primary controlling parameters of porosity, permeability, and seepage capability of tight gas reservoirs: a case study on Upper Paleozoic Formation in the eastern Ordos Basin, Northern China, Pet. Sci., 16, 1270–1284, https://doi.org/10.1007/s12182-019-00373-5, 2019.

Rabiee, A., Rossetti, F., Tecce, F., Asahara, Y., Azizi, H., Glodny, J., Lucci, F., Nozaem, R., Opitz, J., and Selby, D.: Multiphase magma intrusion, ore-enhancement and hydrothermal carbonatisation in the Siah-Kamar porphyry Mo deposit, Urumieh-Dokhtar magmatic zone, NW Iran, Ore Geology Reviews, 110, 102930, https://doi.org/10.1016/j.oregeorev.2019.05.016, 2019.

Reinsch, T., Dobson, P., Asanuma, H., Huenges, E., Poletto, F., and Sanjuan, B.: Utilizing supercritical geothermal systems: a review of past ventures and ongoing research activities, Geoth. Energy, 5, 16(2017), 25 pp., https://doi.org/10.1186/s40517-017-0075-y, 2017.

Riabokon, E., Poplygin, V., Turbakov, M., Kozhevnikov, E., Kobiakov, D., Guzev, M, and Wiercigroch, M.: Nonlinear Young's Modulus of New Red Sandstone: Experimental Studies, Acta Mech. Solida Sin, 34, 989–999, https://doi.org/10.1007/s10338-021-00298-w, 2021.

Rickwood, P. C.: Boundary lines within petrologic diagrams which use oxides of major and minor elements, Lithos, 22(4), 247–263, https://doi.org/10.1016/0024-4937(89)90028-5, 1989.

Ringrose, P., and Bentley, M.: Reservoir Model Design, Springer, Dordrecht, the Netherlands, https://doi.org/10.1007/978-94-007-5497-3, 2015.

Ringrose, P., and Bentley, M.: Reservoir Model Design – A Practitioner's Guide. Springer, Switzerland, 249 pp., https://doi.org/10.1007/978-3-030-70163-5, 2021.

Rochelle, C. A., Lacinska, A., Kilpatrick, A., Rushton, J., Weydt, L. M., Bär, K., and Sass, I.: Evidence for fracture-hosted fluid-rock reactions within geothermal reservoirs of the eastern Trans-Mexico volcanic belt, Proceedings World Geothermal Congress 2020+1, Reykjavik, Iceland, April–October 2021, 11 pp., 2021.

Rock Properties Database British Columbia Canada: Rock Properties Database, a collaborative Geoscience BC project among Mira Geoscience, the Geological Survey of Canada and CAMIRO, Open file resource, available at: https://catalogue.data.gov.bc.ca/datas et/2dc8a4f1-c8f8-4603-813e-855af99b7ba5/resource/51f0620a-42cf-458f-821c-bdd895f24fdc/download/of2008-4rpd.xls (last access: 21 October 2020), 2018.

RockViewer: Software for Organization of Petrographic Photomicrographs, available at: https://www.endeeper.com/product/rockviewer (last access: 21 October 2020), 2020.

Rollinson, H.: Using geochemical data: Evaluation, presentation, interpretation, Pearson Education Limited, Longman Group UK Limited, Edinburgh, United Kingdom, xxvi + 352 pp., 1993.

Romo-Jones, J. M., Gutiérrez-Negrín, L. C., and Canchaela-Félix, I.: 2018 México Country Report, IEA Geothermal, available at: https://drive.google.com/file/d/1G2mYo4rKScLyHe_zpUHr50RvtxdmvVKo/view (last access: 28 May 2020), 2019.

Romo-Jones, J. M., Gutiérrez-Negrín, L. C., and Canchola-Félix, I.: 2019 México Country Report, IEA Geothermal, available at: https://drive.google.com/file/d/1Nq9gPbgzto7bMvv5hktjhi5JBxwJXV49/view (last access: 28 Sep 2021), 2020.

Romo-Jones, J. M., Gutiérrez-Negrín, L. C., and Canchaela-Félix, I.: 2020 México Country Report, IEA Geothermal, available at: https://drive.google.com/file/d/1GJjsv9n--iNUibYq8pSW_rCZwEORpukO/view (last access: 10 March 2022), 11 pp., 2021.

Rossetti, F., Monié, P., Nasrabady, M., Theye, T., Lucci, F., Saadat, M.: Journal of the Geological Society, 174, 741-758, https://doi.org/10.6084/m9.figshare.c.3706852, 2017.

Ruggeri, G., Morelli, G., Zucchi, M., Braschi, E., Agostini, S., Ventruti, G., Brogi, A., Liotta, D., Boschi, C., and González-Partida, E.: Insight into the fluids occurring in the super-hot reservoir of the Los Humeros geothermal system from fluid inclusions and isotopic data of the Las Minas exhumed system (Mexico), GEMex Final Conference, Potsdam, Germany, 18–19 February 2020, 53, 2020.

Rühaak, W., Bär, K., and Sass, I.: Combining numerical modeling with geostatistical analysis for an improved reservoir exploration, Energy Proced., 59, 315–322, https://doi.org/10.1016/j.egypro.2014.10.383, 2014.

Rühaak, W., Guadagnini, A., Geiger, S., Bär, K., Gu, Y., Aretz, A., Hohmuth, S., and Sass, I.: Upscaling thermal conductivities of sedimentary formations for geothermal exploration, Geothermics, 58, 49–61, https://doi.org/10.1016/j.geothermics.2015.08.004, 2015.

Rybacki, E., Meier, T., and Dresen, G.: What controls the mechanical properties of shale rocks? – Part II: Brittleness, J. Petrol. Sci. Eng., 144, 39–58, https://doi.org/10.1016/j.petrol.2016.02.022, 2016.

Saller, A. H., and Henderson, N.: Distribution of Porosity and Permeability in Platform Dolomites: Insight from the Permian of West Texas, AAPG Bull., 82, 1528–1550, https://doi.org/10.1306/1D9BCB01-172D-11D7-8645000102C1865D, 1998.

Sánchez-Núñez, J. M., Pola, A., Cisneros, G., Sereno, H. I., Serrano-Flores, M. E., Jiménez, L. A., and Rodríguez, P.: Physical-mechanical behavior of fresh and completely altered rocks as an important factor of slope instability in the El Rosario Monarch Butterfly Sanctuary, Michoacán, Mexico, Revista Mexicana de Ciencias Geológicas, 38(3), 272–282, https://doi.org/10.22201/cgeo.20072902e.2021.3.1674, 2021.

Sánchez-Vila, X., Guadagnini, A., and Carrera, J.: Representative hydraulic conductivities in saturated groundwater flow, Rev. Geophys., 44, RG3002, https://doi.org/10.1029/2005RG000169, 2006.

Sanjuan, B., Gal, F., and Alfaro, R.: Developments of auxiliary chemical geothermometers applied to the Los Humeros and Acoculco geothermal fields (Mexico), GEMex Final Conference, Potsdam, Germany, 18–19 February 2020, 2020.

Sari, M.: The stochastic assessment of strength and deformability characteristics for a pyroclastic rock mass, International Journal of Rock Mechanics and Mining Sciences, 46, 613–626, https://doi.org/10.1016/j.ijrmms.2008.07.007, 2009.

Sass, I., and Götz, A. E.: Geothermal reservoir characterization: a thermofacies concept, Terra Nova, 24, 142–147, https://doi.org/10.1111/j.1365-3121.2011.01048.x, 2012.

Sass, J. H., Lachenbruch, A. H., Munroe, R. J., Greene, G. W., and Moses Jr., T. H.: Heat flow in the Western United States, J. Geophys. Res., 76, 6376–6413, https://doi.org/10.1029/JB076i026p06376, 1971.

Savichev, A. T., and Vodyanitskii, Y. N.: X-ray radiometric determination of lanthanides (Praseodymium, neodymium, and samarium) in soils, Eurasian Soil Science, 44, 386–393, https://doi.org/10.1134/S1064229311040089, 2011.

Scheibe, T., and Yabusaki, S.: Scaling of flow and transport behavior in heterogeneous groundwater systems, Adv. Water Resour., 22, 223–238, https://doi.org/10.1016/S0309-1708(98)00014-1, 1998.

Scheidegger, A. E.: The Physics of Flow Through Porous Media, 3rd ed., 372 pp., University of Toronto Press, Toronto, Canada, available at: https://www.jstor.org/stable/10.3138/j.ctvfrxmtw (last access: 25 May 2020), 1974.

Schill, E., and Cornejo, N.: Gravity modelling, Deliverable 5.6, WP5, GEMex H2020 project, European Commission, 40 pp., available at: http://www.gemex-h2020.eu (last access: 25 May 2022), 2019.

Schön, J. H.: Physical properties of rocks: Fundamentals and principles of petrophysics, Developments in petroleum science, Elsevier, Amsterdam, the Netherlands, 512 pp., 2015.

Sciencebase Minnesota: US Geological Survey (USGS) – Collection of rock properties database from Minnesota USA, available at: https://www.sciencebase.gov/catalog/item/4f4e49d8e4b07f02db5df226 (last access: 21 October 2020), 2010.

Scott, S., Driesner, T., and Weis, P.: Boiling and condensation of saline geothermal fluids above magmatic intrusions, Geophysical Research Letters, 44, 10 pp., https://doi.org/10.1002/2016GL071891, 2017.

Scott, S. W., Covell, C., Júlíusson, E., Valfells, Á., Newson, J., Hrafnkelsson, B., Pállson, H., and Gudjónsdóttir, M.: A probalistic geological model of the Krafla geothermal system constrained by gravimetric data, Geotherm. Energy, 29, 1–30, https://doi.org/10.1186/s40517-019-0143-6, 2019.

Setaram Instrumentation: K/C80-1A C80 Commissioning, Setaram Instrumentation KEP Technologies, Caluire, France, 52 pp., 2009.

SGM: CARTA GEOLÓGICO – MINERA, E14-2, Servicio Geológico Mexicano, Ciudad de Mexico, Mexico, first edition, 2002a.

SGM: CARTA GEOLÓGICO – MINERA, E14-3, Servicio Geológico Mexicano, Veracruz, Mexico, first edition, 2002b.

SGM: CARTA GEOLÓGICO – MINERA, Perote, E14-B26, Veracruz y Puebla, Servicio Geológico Mexicano, first edition, 2007.

SGM: CARTA GEOLÓGICO – MINERA, Xonactlán, E14-B25, Veracruz y Puebla, Servicio Geológico Mexicano, first edition, 2011.

SGM: CARTA GEOLÓGICO – MINERA, Mexcaltepec, E14-B24, Veracruz y Puebla, Servicio Geológico Mexicano, first edition, 2012.

SGM: Servico Geológico Mexicano – Léxico Estratigráfico de México, Léxico_Estratigráfico_de_México, available at: sgm.gob.mx (last access: 21 March 2022), 2022.

Shankland, T. J., Duba, A. G., Mathez, E. A., and Peach, C. L.: Increase of electrical conductivity with pressure as an indicator of conduction through a solid phase in midcrustal rocks, J. Geophys. Res., 102, 14741–14750, https://doi.org/10.1029/96JB03389, 1997.

Sillitoe, R. H.: Porphyry copper systems, Econ. Geol., 105(1), 3–41, https://doi.org/10.2113/gsecongeo.105.1.3, 2010.

Sillitoe, R. H., and Brogi, A.: GEOTHERMAL SYSTEMS IN THE NORTHERN APENNINES, ITALY: MODERN ANALOGUES OF CARLIN-STYLE GOLD DEPOSITS, Econ. Geol., 116(7), 1491–1501, https://doi.org/10.5382/econgeo.4883, 2021.

Siratovich, P. A., Sass, I., Homuth, S., and Bjornsson, A.: Thermal Stimultaion of Geothermal Reservoirs and Laboratory Investigation of Thermally Induced Fractures, GRC Transactions, 35, 1529–1536, 2011.

Siratovich, P., Heap, M. J., Villeneuve, M., Cole, J., and Reuschlé, T.: Physical property relationships of the Rotokawa Andesite, a significant geothermal reservoir rock in the Taupo Volcanic Zone, New Zealand, Geotherm. Energy, 10, 1–31, https://doi.org/10.1186/s40517-014-0010-4, 2014.

Siratovich, P. A., Heap, M. J., Villeneuve, M. C., Cole, J. W., Kennedy, B. M., Davidson, J., and Reuschlé, T.: Mechanical behaviour of the Rotokawa Andesites (New Zealand): Insight into permeability evolution and stress-induced behaviour on an actively utilised geothermal reservoir, Geothermics, 64, 163 – 179, https://doi.org/10.1016/j.geothermics.2016.05.005, 2016.

Somerton, W. H.: Thermal properties and temperature-related behavior of rock-fluid systems, Dev. Pet. Sci., 37, Elsevier, Amsterdam, the Netherlands, 257 pp., 1992.

Sosa-Ceballos, G., Macías, J. L., Avellán, D. R., Salazar-Hermenegildo, N., Boijseauneau-López, M. E., and Pérez-Orozco, J. D.: The Acoculco Caldera Complex magmas: genesis, evolution and relation with the Acoculco geothermal system, J. Volcanol. Geoth. Res., 358, 288–306, https://doi.org/10.1016/j.jvolgeores.2018.06.002, 2018.

Stimac, J. A., Powell, T. S., and Golla, G. U.: Porosity and permeability of the Tiwi geothermal field, Philippines, based on continuous and spot core measurements, Geothermics, 33, 87–107, https://doi.org/10.1016/j.geothermics.2003.03.002, 2004.

Stober, I., and Bucher, K.: Geothermal Energy – From Theoretical Models to Exploration and Development, Second Edition, Springer, Cham, Switzerland, 390 pp., 2021.

Suárez-Arriaga, M.-C.:Thermodynamics of Deep Supercritical Geothernal Systems, IOP. Conf. Series: Earth and Enviromental Sciences, 249, 14 pp., https://doi.org/10.1088/1755-1315/249/1/012019, 2019.

Sun, S.-S., and McDonough, W. F.: Chemical and isotopic systematics of oceanic basalts: Implications for mantle compositions and processes, in Saunders, A. D. and Norry, M. J. (Eds.): Magmatism in the ocean basins, Geological Society, London, Special Publications, 42, 313–345, 1989.

Takahashi, I.: Quantifying Information and Uncertainty of Rock Property Estimation from Seismic Data, Dissertation, Geophysics, Stanford University, California, USA, 200 pp., 2000.

Tanikawa, W., and Shimamoto, T.: Comparison of Klinkenberg corrected gas permeability and water permeability in sedimentary rocks, Int. J. Rock Mech. Min. Sci., 46, 229–238, https://doi.org/10.1016/j.ijrmms.2008.03.004, 2008.

Tello, H. E.: Estado de equilibrio soluto-mineral y saturación de minerales de alteración en fluidos geotérmicos de alta temperatura, Facultad de Ingeniería, UNAM, Mexico, PhD Thesis, xvii + 271 pp., 2005.

ThinkGeoenergy: The sad state of affairs for geothermal energy development in Mexico, article by Alexander Richter, 2 September 2019, available at: https://www.thinkgeoenergy.com/the-sad-state-of-affairs-for-geothermal-energy-development-in-mexico/#:~:text=According%20to%20data%20from%20the%20Energy%20Regulatory%20Commission,24%2C700%20MW%20for%20maximum%20depth%20of%203%2C000%20meters (last access: 10 August 2022), 2019.

Toledo, T., Gaucher, E., Jousset, P., Maurer, H., Krawczyk, C., Calò, M., and Figueroa, Á.: Local earthquake tomography at the Los Humeros geothermal field, GEMex Final Conference, Potsdam, Germany, 18–19 February 2020, 6.3, 2020a.

Toledo T., Gaucher, E., Jousset, P., Jentsch, A., Haberland, C., Maurer, H., Krawczyk, C., Calò, M., and Figueroa, A.: Local earthquake tomography at Los Humeros geothermal field (Mexico), Journal of Geophysical Research: Solid Earth, 125, e2020JB020390, https://doi.org/10.1029/2020JB020390, 2020b.

Torres-Alvarado, I. S., Pandarinath, K., Verma, S. P., and Dulski, P.: Element Mobility Due to Hydrothermal Alteration in Los Azufres Geothermal Field, Mexico, Proceedings World Geothermal Congress 2010, 25–29 April, Bali Indonesia, 5 pp., 2010.

Urbani, S., Giordano, G., Lucci, F., Rossetti, F., Acocella, V., and Carrasco-Núñez, G.: Estimating the depth and evolution of intrusions at resurgent calderas: Los Humeros (Mexico), Solid Earth, 11, 527–545, https://doi.org/10.5194/se-11-527-2020, 2020.

Urbani, S., Giordano, G., Lucci, F., Rossetti, F., and Carrasco-Núñez, G.: Reply to Norini and Groppelli's comment on "Estimating the depth and evolution of intrusions at resurgent calderas: Los Humeros (Mexico)" by Urbani et al. (2020), Solid Earth, 12(5), 1111–1124, https://doi.org/10.5194/se-11-2549-2020, 2021.

Vagnon, F., Colombero, C., Colombo, F., Comina, C., Ferrero, A. M., Mandrone, G., and Vinciguerra, S. C.: Effects of thermal treatment on physical and mechanical properties of Valdieri Marble, NW Italy, Int. J. Rock Mech. Min. Sci., 116, 75–86, https://doi.org/10.1016/j.ijrmms.2019.03.006, 2019.

Vagnon, F., Colombero, C., Comina, C., Ferrero, A. M., Mandrone, G., Missagia, R., and Vinciguerra, S. C.: Relating physical properties to temperature induced damage in carbonate rocks, Geotechnique Letters, 11(2), 147–157, https://doi.org/10.1680/jgele.20.00122, 2021.

Vargha, A., and Delaney, H. D.: The Kruskal-Wallis test and stochastic homogeneity, Journal of Educational and behavioral Statistics, 23, 2, 170–192, https://doi.org/10.2307/1165320, 1998.

Verma, S. P.: Heat source in Los Humeros geothermal area, Puebla, Mexico, Geoth. Res. T, 9, 521–525, 1985.

Verma, S. P., Gómez-Arias, E., and Andaverde, J.: Thermal sensitivity analysis of emplacement of the magma chamber in Los Humeros caldera, Puebla, Mexico, Search Result Int. Geol. Rev., 53 (8), 905-925, https://doi.org/10.1080/00206810903234296, 2011.

Viggiano, J. C., and Robles, C.: Mineralogía hidrotermal en el campo geotérmico de Los Humeros, Pue., I: Su uso como indicadora de temperatura y del estado hidrológico, Geotermia Rev. Mex. Geoen., 4, 15–28, 1988a.

Viggiano, J. C., and Robles, C.: Mineralogía hidrotermal in el campo geotérmico de Los Humeros, Pue., II: Geometría del yacimiento, Geotermia Rev. Mex. Geoen., 4, 1, 29–40, 1988b.

Villarreal, C. A., Rojas, J. D., and Ríos, C. A.: 3D digital outcrop modelling of the Lower Cretaceous Los Santos formation sandstones, Mesa de Los Santos region (Colombia): Imlications for structural analysis, Journal of Structural Geology, 141, 10214, https://doi.org/10.1016/j.jsg.2020.104214, 2020.

Villeneuve, M., Kennedy, B., Gravley, D., and Mordensky, S.: Characteristics of altered volcanic rocks in geothermal reservoirs, in Fontoura, S.A.B., Rocca, R. J., and Mendoza, J. P. (Eds.): Rock Mechanics for Natural Resources and Infrastructure Development, Proceedings of the 14th International Congress on Rock Mechanics and Rock Engineering (ISRM 2019), September 13-18, 2019, Foz do Iguassu, Brazil, Volume 6, CRC Press Taylor and Francis Group, United Kingdom, SG3120-3127, 2019.

Vinciguerra, S., Trovato, C., Meredith, P. G., Benson, P. M.: Relating seismic velocities, thermal cracking and permeability in Mt. Etna and Iceland basalts, Int. J. Rock Mech. Min. Sci., 42, 7–8, 900–910, https://doi.org/10.1016/j.ijrmms.2005.05.022, 2005.

Vinciguerra, S., Trovato, C., Meredith, P. G., Benson, P. M., Troise, C., De Natale, G.: Understanding the seismic velocity structure of Campi Flegrei caldera (Italy): from the laboratory to the field scale, Pure and Applied Geophysics, 163(10), 2205–2221, https://doi.org/10.1007/s00024-006-0118-y, 2006.

Viniegra-Osario, F.: Geología del Macizo de Teziutlán y la Cuenca Cenozoica deVeracruz, Asociación Mexicana de Geólogos Petroleros, Boletín 17, 101–163, 1965.

von Dobeneck, T., Müller, M., Bosbach, B., and Klügel, A.: Ground Magnetic Surveying and Susceptibility Mapping Across Weathered Basalt Dikes Reveal Soil Creep and Pedoturbation, Front. Earth. Sci., 8, 592986, https://doi.org/10.3389/feart.2020.592986, 2021.

Vosteen, H.-D., and Schellschmidt, R.: Influence of temperature on thermal conductivity, thermal capacity and thermal diffusivity for different types of rock, Phys. Chem. Earth, 28, 499–509, https://doi.org/10.1016/S1474-7065(03)00069-X, 2003.

Walia, S., and Leahy, G.: Addressing challenges in petrophysical modelling, HARTENERGY, available at: https://www.hartenergy.com/exclusives/addressing-challenges-petrophysical-modeling-20246 (last access: 6 November 2020), 2014.

Wang, S., Huang, Z., Wu, Y.-S., Winterfeld, P. H., and Zerpa, L. E.: A semi-analytical correlation of thermal-hydraulic-mechanichal behaviour of fractures and its application to modeling reservoir scale cold water injection problems in enhanced geothermal reservoirs, 64, 81–95, http://dx.doi.org/10.1016/j.geothermics.2016.04.005, 2016.

Watanabe, N., Numakura, T., Sakaguchi, K., Saishu, H., Okamoto, A., Ingebritsen, S. E., and Tsuchiya, N.: Potentially exploitable supercritical geothermal resources in the ductile crust, Nature Geoscience, 10, 140–144, https://doi.org/10.1038/NGEO2879, 2017.

Weides, S., and Majorowicz, J.: Implications of Spatial Vari-ability in Heat Flow for Geothermal Resource Evalua-tion in Large Foreland Basins: The Case of the West-ern Canada Sedimentary Basin, Energies, 7, 2573–2594, https://doi.org/10.3390/en7042573, 2014.

Weides, S., Moeck, I., Majorowicz, J., Palombi, D., and Grobe, M.: Geothermal exploration of Paleozoic forma-tions in Central Alberta, Can. J. Earth Sci., 50, 519–534, https://doi.org/10.1139/cjes-2012-0137, 2013.

Weinert, S., Bär, K., and Sass, I.: Database of Petrophysical Properties of the Mid-German Crystalline High, Earth Syst. Sci. Data, 13, 1441–1459, https://doi.org/10.5194/essd-13-1441-2021, 2021.

Wen, X.-H. and Gomez-Hernandez, J.: Upscaling hydraulic conductivities in heterogeneous media: an overview, J. Hydrol., 183, ix–xxxii, https://doi.org/10.1016/S0022-1694(96)80030-8, 1996.

Weydt, L. M., Heldmann, C.-D. J., Machel, H. G., and Sass, I.: From oil field to geothermal reservoir: assessment for geothermal utilization of two regionally extensive Devonian carbonate aquifers in Alberta, Canada, Solid Earth, 9, 953–983, https://doi.org/10.5194/se-9-953-2018, 2018a.

Weydt, L. M., Bär, K., Colombero, C., Comina, C., Deb, P., Lepillier, B., Mandrone, G., Milsch, H., Rochelle, C. A., Vagnon, F., and Sass, I.: Outcrop analogue study to determine reservoir properties of the Los Humeros and Acoculco geothermal fields, Mexico, Adv. Geosci., 45, 281–287, https://doi.org/10.5194/adgeo-45-281-2018, 2018b.

Weydt, L. M., Ramírez-Guzmán, Á. A., Pola, A., Lepillier, B., Kummerow, J., Mandrone, G., Comina, C., Deb, P., Norini, G., González-Partida, E., Avellán, D. R., Macías, J. L., Bär, K., and Sass, I.: Petrophysical and mechanical rock property database of the Los Humeros and Acoculco geothermal fields (Mexico), TU Darmstadt datalib, https://doi.org/10.25534/tudatalib-201.10, 2020.

Weydt, L. M., Ramírez-Guzmán, Á. A., Pola, A., Lepillier, B., Kummerow, J., Mandrone, G., Comina, C., Deb, P., Norini, G., González-Partida, E., Avellán, D. R., Macías, J. L., Bär, K., and Sass, I.: Petrophysical and mechanical rock property database of the Los Humeros and Acoculco geothermal fields (Mexico), Earth Syst. Sci. Data, 13, 571–598, https://doi.org/10.5194/essd-13-571-2021, 2021a.

Weydt, L. M., Bär, K., and Sass, I.: Petrophysical Reservoir Characterization of the Los Humeros and Acoculco Geothermal Fields, Mexico, Proceedings World Geothermal Congress 2020+1, Reykjavik, Iceland, April–October 2021, 11 pp., 2021b.

Weydt, L. M., Bär, K., and Sass, I.: Petrophysical characterization of the Los Humeros geothermal field (Mexico): From outcrop to parametrization of a 3D geological model, Geothermal Energy, 10, 5(2022), 48 pp., https://doi.org/10.1186/s40517-022-00212-8, 2022a.

Weydt, L. M., Lucci, F., Lacinska, A., Scheuvens, D., Carrasco-Núñez, G., Giordano, G., Rochelle, C. A., Schmidt, S., Bär, K., and Sass, I.: The impact of hydrothermal alteration on the physiochemical characteristics of reservoir rocks: the case of the Los Humeros geothermal field (Mexico), Geothermal Energy, 10, 20(2022), 49 pp., https://doi.org/10.1186/s40517-022-00231-5, 2022b.

Whitford, D. J., Korsch, M. J., Porritt, P. M., and Craven, S. J.: Rare-earth element mobility around the volcanogenic polymentallic massive sulfide deposit at Que River, Tasmania, Australia, Chemical Geology, 68(1-2), 105–119, https://doi.org/10.1016/0009-2541(88)90090-3, 1988.

Whitney, D. L., and Evans, B. W.: Abbreviations for names of rock-forming minerals, American Mineralogist, 95, 185–187, https://doi.org/10.2138/am.2010.3371, 2010.

Whittington, A. G., Hofmeister, A. M., and Nabelek, P. I.: Temperature-dependent thermal diffusivity of the Earth's crust and implications for magmatism, Nature, 458, 319–321, https://doi.org/10.1038/nature07818, 2009.

Willcox, C.: Eruptive, magmatic and structural evolution of a large explosive caldera volcano: Los Humeros México, PhD thesis, University of Leicester, United Kingdom, available at: https://leicester.figshare.com/articles/thesis/Eruptive_Magmatic_and_Structural_Evolution_of_a_Large_Explosive_Caldera_Volcano_Los_Humeros_Central_Mexico/10104785/1 (last access: 21 March 2022), x + 326 pp., 1 Appendix, 2011.

Winchester, J. A., and Floyd, P. A.: Geochemical discrimination of different magma series and their differentiation products using immobile elements, Chemical geology, 20, 325–343, https://doi.org/10.1016/0009-2541(77)90057-2, 1977.

Wyering, L. D., Villeneuve, M. C., Wallis, I. C., Siratovitch, P. A., Kennedy, B. M., Gravley, D. M., and Cant, J. L.: Mechanical and physical properties of hydrothermally altered rock, Taupo Volcanic Zone, New Zealand, Journal of Volcanology and Geothermal Research, 288, 76–93, https://doi.org/10.1016/j.jvolgeores.2014.10.008, 2014.

Yáñez, C., and García, S.: Exploración de la región geotérmica Los Humeros-Las Derrumbadas, Estados de Puebla y Veracruz (Internal report), Comisión Federal de Electricidad, Mexico City, Mexico, 96 pp., 1982.

Yongliang, X., and Yusheng, Z.: The mobility of rare-earth elements during hydrothermal activity: a review, Chinese journal of geochemistry, 10(4), 295–306, https://doi.org/10.1007/BF02841090, 1991.

You, B., Xu, J., Shi, S., Liu, H., and Li, H.: Effect of Stress and Water Pressure on Permeability of Fractured Sandstone Based on Response Surface Method, Front. Earth. Sci., 11, 1–8, https://doi.org/10.3389/feart.2020.00011, 2020.

Yu, Z., Robinson, P., and McGoldrick, P.: An Evaluation of Methods for the Chemical Decomposition of Geological Materials for Trace Element Determination using ICP-MS, Geostandards Newsletter: the Journal of Geostandards and Geoanalysis, 25, 199–217, 2001.

Zahner Scientific Instruments: Zahner-Zennium Electrochemical Workstation, User's manual, 212 pp., Zahner Scientific Instruments, Kronach, Germany, 2008.

Zarrouk, S., and Watson, A.: Thermodynamic and transport properties of saturated steam and water, Geothermal Program, the University of Auckland, Faculty of Engineering, 23 pp., 2010.

ZH Instruments: ZH Instruments Magnetic suceptibility meter SM30, User's manual, Brno, Czech Republic, 2008.

Zhang, H., Sun, Q., and Ge, Z.: Analysis of the characteristics of magnetic properties change in the rock failure process, Acta Geophys., 68 289–302, https://doi.org/10.1007/s11600-020-00406-3, 2020.

Zhao, X. G., Wang, J., Chen, F., Li, P. F., Ma, L. K., Xie, J. L., and Liu, Y.: Experimental investigation on the thermal conductivity characteristics of Beishan granitic rocks for China's HLW disposal, Tectonophysics, 683, 124–137, https://doi.org/10.1016/j.tecto.2016.06.021, 2016.

Zheng, J., Zheng, L., Liu, H.-H., and Ju, Y.: Relationships between permeability, porosity and effective stress for low-permeability sedimentary rock, Int. J. Rock Mech. Min., 78, 304–318, https://doi.org/10.1016/j.ijrmms.2015.04.025, 2015.

Zimmermann, R. W., Somerton, W. H., and King, M. S.: Compressibility of porous rocks, J. Geophys. Res., 91, 765–777, https://doi.org/10.1029/JB091iB12p12765, 1986.

Zoback, M. D.: Reservoir geomechanics, Cambridge University Press, Cambridge, UK, 2011.

Zoth, G., and Hänel, R.: Thermal conductivity, in: Handbook of terrestrial heat flow density determination, edited by: Hanel, R., Rybach, L., and Stegena, L., Kluwer, Dordrecht, the Netherlands, 449–453, 1988.

Appendix A – Additional Data to Chapter 4 (Outcrop Analogue Samples)
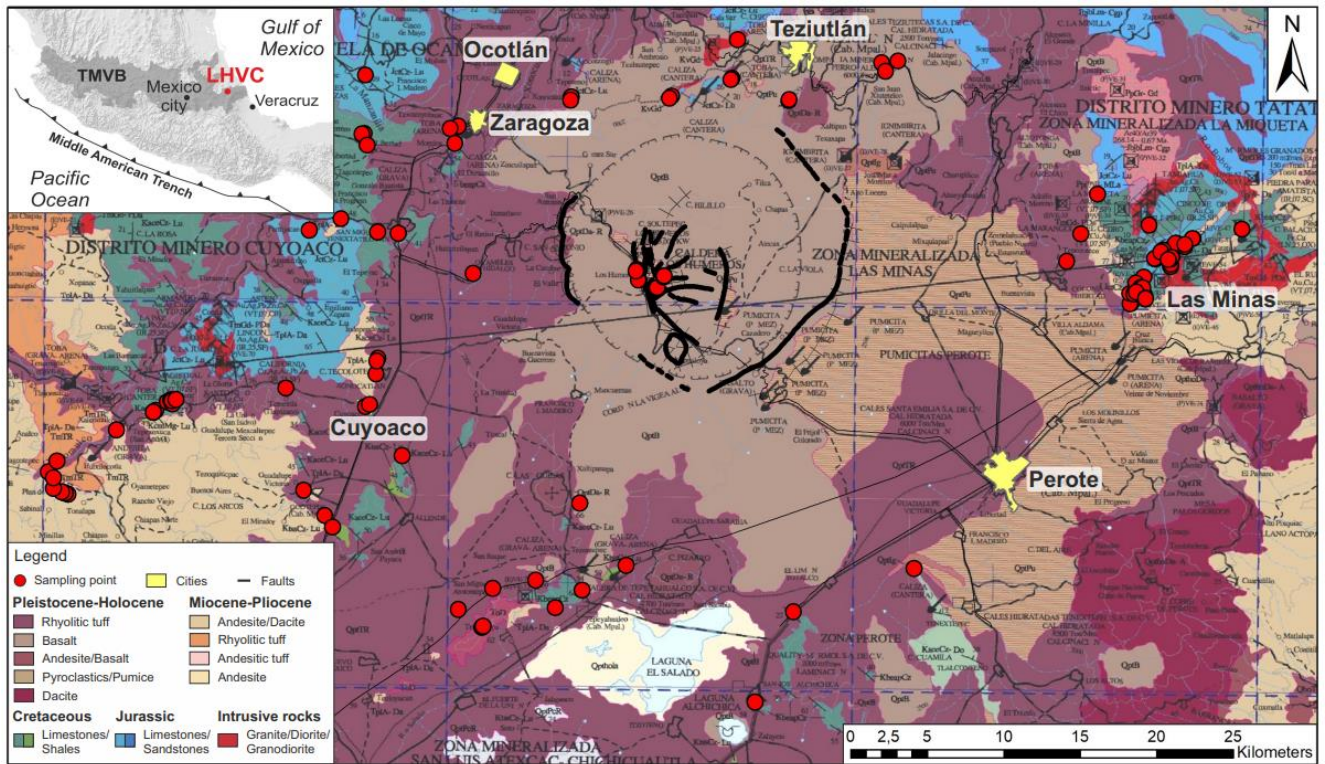
Figure A1: Regional geological setting with the Los Humeros Volcanic Complex in the center (SGM, 2002b). The red circles represent the sampling points of the outcrop samples investigated in this study.

Figure A2: Photographs of selected outcrops representing (a) Holocene basaltic lava flows and (b) ash deposits of the Xoxoctic member inside of the Los Humeros caldera, (c) unwelded Xáltipan ignimbrite located northwest of the LHVC close to the town Temextla, (d) the Teziutlán andesite unit located east of the LHVC, (e) the Cuyoaco andesite unit located west of the LHVC, (f) andesitic dykes intruding into Cretaceous limestones located southwest of the LHVC (road cut), (g) Cretaceous shales, (h) Jurassic sandstone deposits, (i–k) Cretaceous limestones, marl and chert layers as well as chert nodules, (l) Miocene marbles, (m) skarn deposits of the Eldorado mine, (n) quartz veins associated with skarn deposits and (o) a granitic intrusion cut by a mafic dyke in a riverbed (l–o represent outcrops in Las Minas).

Table A1: Petrophysical and hydraulic properties of the LHVC

Unit	ρP [g cm⁻³]	ρB [g cm⁻³]	φ [%]	K [m²]
Post-caldera group				
Pyroclastics, undifferentiated	2.51/**2.52** (6) ± 0.03 Q1: 2.47, Q3: 2.53 CV: 1.15%	1.48/**1.48** (6) ± 0.03 Q1: 1.45, Q3: 1.51 CV: 2.32%	41.1/**41.0** (6) ± 1.3 Q1: 39.8, Q3: 42.4 CV: 3.24%	2.4E-13/**2.3E-13** (4) ± 4.7E-14 Q1: 2.1E-13, Q3: 2.9E-13 CV: 19.03%
Basalts	2.65/**2.67** (40) ± 0.10 Q1: 2.62, Q3: 2.72 CV: 3.9%	2.28/**2.33** (28) ± 0.18 Q1: 2.14, Q3: 2.42 CV: 8.01%	14.0/**12.3** (28) ± 5.4 Q1: 10.5, Q3: 17.5 CV: 38.65%	6.7E-14/**2.5E-17** (27) ± 1.9E-13 Q1: 5.8E-18, Q3: 8.4E-15 CV: 291.46%
Ash fall deposits	2.36/**2.36** (6) ± 0.04 Q1: 2.31 Q3: 2.38 CV: 1.78%	1.23/**1.19** (6) ± 0.13 Q1: 1.17, Q3: 1.27 CV: 10.81%	48.1/**49.8** (6) ± 4.7 Q1: 46.1, Q3: 50.6 CV: 9.82%	1.3E-14/**1.1E-14** (5) ± 2.7E-15 Q1: 1.1E-14, Q3: 1.5E-14 CV: 21.80%
Caldera group				
Zaragoza ignimbrite	2.48/**2.44** (34) ± 0.11 Q1: 2.42, Q3: 2.50 CV: 4.33%	1.60/**1.56** (23) ± 0.18 Q1: 1.48, Q3: 1.58 CV: 11.40%	36.3/**37.1** (23) ± 4.5 Q1: 34.8, Q3: 39.8 CV: 12.32%	4.7E-14/**8.8E-15** (19) ± 8.8E-14 Q1: 1.7E-15, Q3: 2.3E-14 CV: 188.13%
Xáltipan ignimbrite total	2.28/**2.41** (120) ± 0.34 Q1: 2.25, Q3: 2.49 CV: 15.02%	1.40/**1.33** (64) ± 0.44 Q1: 1.24, Q3: 1.72 CV: 31.01%	40.9/**42.9** (64) ± 14.5 Q1: 31.0, Q3: 50.1 CV: 35.46%	2.5E-13/**1.7E-13** (59) ± 2.6E-13 Q1: 3.3E-14, Q3: 4.1E-13 CV: 103.68%
Xáltipan ig. (unaltered)	2.40/**2.43** (93) ± 0.10 Q1: 2.36, Q3: 2.49 CV: 4.25%	1.47/**1.34** (53) ± 0.23 Q1:1.28, Q3: 1.72 CV: 15.71%	39.5/**38.4** (53) ± 9.5 Q1: 31.0, Q3: 47.7 CV: 23.92%	2.8E-13/**1.7E-13** (50) ± 2.7E-13 Q1: 3.9E-14, Q3: 5.2E-13 CV: 96.38%
Xáltipan ig. (pumice)	1.51/**1.50** (18) ± 0.15 Q1: 1.40, Q3: 1.61 CV: 9.86%	0.56/**0.56** (8) ± 0.06 Q1: 0.51, Q3: 0.59 CV: 9.92%	63.5/**61.6** (8) ± 6.9 Q1: 57.8, Q3: 70.6 CV: 10.87%	1.6E-13/**1.3E-13** (6) ± 1.8E-13 Q1: 1.7E-15, Q3: 3.1E-13 CV: 111.85%
Xáltipan ig. (altered, welded)	2.52/**2.52** (9) ± 0.03 Q1: 2.49, Q3: 2.53 CV: 1.03%	2.42/**2.42** (3) ± 0.01 Q1: 2.41, Q3: 2.43	4.1/**4.5** (3) ± 1.9 Q1: 2.1, Q3: 5.9	6.0E-18/**4.3E-18** (3) ± 3.2E-18
Pre-caldera group				
Cinder cones total	2.80/**2.81** (15) ± 0.05 Q1: 2.77, Q3: 2.83 CV: 1.64%	1.82/**1.98** (7) ± 0.32 Q1: 1.60, Q3: 2.03 CV: 17.72%	35.5/**30.1** (7) ± 11.0 Q1: 28.3, Q3: 42.4 CV: 31.1%	3.9E-13/**2.3E-14** (5) ± 5.8E-13 Q1: 5.5E-16, Q3: 9.7E-13 CV: 147.54%
Scoria	2.82/**2.83** (11) ± 0.03 Q1: 2.78, Q3: 2.84 CV: 1.11%	2.00/**1.98** (5) ± 0.06 Q1: 1.95, Q3: 2.05 CV: 2.85%	29.7/**29.9** (5) ± 2.2 Q1: 27.7%, Q3: 31.5 CV: 7.54%	7.9E-15/**1.1E-15** (3) ± 1.3E-14
Fallout deposits	2.75/**2.75** (4) ± 0.04 Q1: 2.71, Q3: 2.79	1.39 (2) ± 0.30	50.0 (2) ± 10.8	9.7E-13 (2) ± 4.8E-13
Teziutlán andesite unit total	2.72/**2.72** (142) ± 0.06 Q1: 2.69, Q3: 2.74 CV: 2.07%	2.53/**2.60** (131) ± 0.19 Q1: 2.39, Q3: 2.68 CV: 7.44%	6.9/**2.7** (126) ± 7.3 Q1: 1.5, Q3: 13.4 CV: 106.26%	1.0E-14/**4.6E-17** (92) ± 3.0E-14 Q1: 2E-18, Q3: 2.5E-15 CV: 299.72%
Teziutlán and. (nonporous)	2.71/**2.71** (105) ± 0.05 Q1: 2.67, Q3: 2.73 CV: 1.96%	2.63/**2.65** (94) ± 0.10 Q1: 2.59, Q3: 2.69 CV: 3.89%	2.7/**2.1** (89) ± 2.5 Q1: 1.1, Q3: 2.9 CV: 92.58%	3.1E-15/**4.3E-18** (68) ± 2.0E-14 Q1:1.7E-18, Q3: 8.2E-17 CV: 627.69%
Teziutlán and. (porous)	2.76/**2.75** (37) ± 0.04 Q1: 2.74, Q3: 2.77 CV: 1.53%	2.30/**2.35** (37) ± 0.15 Q1: 2.17, Q3: 2.39 CV: 6.31%	16.9/**14.7** (37) ± 4.6 Q1: 13.4, Q3: 21.3 CV: 27.21%	3.0E-14/**9.5E-15** (24) ± 4.4E-14 Q1: 7.2E-16, Q3: 5.2E-14 CV: 147.99%
Cuyoaco andesite unit	2.64/**2.65** (50) ± 0.02 Q1: 2.64, Q3: 2.67 CV: 0.87%	2.55/**2.61** (32) ± 0.10 Q1: 2.50, Q3: 2.62 CV: 3.75%	4.0/**1.4** (32) ± 4.1 Q1: 0.9, Q3: 6.6 CV: 100.81%	4.0E-15/**5.1E-18** (26) ± 1.6E-14 Q1: 2.4E-18, Q3: 7.9E-16 CV: 407.02%
Basement				
Limestone Cretaceous	2.67/**2.68** (352) ± 0.05 Q1: 2.65, Q3: 2.70 CV: 1.78%	2.66/**2.68** (232) ± 0.10 Q1: 2.63, Q3: 2.70 CV: 3.61%	2.1/**0.8** (201) ± 3.0 Q1: 0.5, Q3: 2.6 CV: 141.52%	5.3E-16/**3.2E-18** (179) ± 4.4E-15 Q1: 1.1E-18, Q3: 6.9E-18 CV: 825.21%
Chert nodules	2.63/**2.65** (19) ± 0.03 Q1: 2.62, Q3: 2.66 CV: 1.02%	2.63/**2.63** (15) ± 0.04 Q1: 2.60, Q3: 2.65 CV: 1.42%	0.8/**0.8** (14) ± 0.6 Q1: 0.2, Q3: 1.2 CV: 74.50%	5.4E-17/**2.8E-18** (13) ± 1.6E-16 Q1: 2E-18, Q3: 9.5E-18 CV: 303.80%
Shales Cretaceous	2.68/**2.68** (7) ± 0.01 Q1: 2.68, Q3: 2.69 CV: 0.20%	2.66/**2.66** (6) ± 0.01 Q1: 2.66, Q3: 2.67 CV: 0.39%	1.3/**1.1** (6) ± 0.7 Q1: 0.8, Q3: 1.7 CV: 56.95%	1.7E-18/**7.2E-19** (5) ± 1.6E-18 Q1: 4.6E-19, Q3: 3.4E-18 CV: 94.83%
Limestone Jurassic	2.64/**2.66** (39) ± 0.05 Q1: 2.62, Q3: 2.68 CV: 1.98%	2.63/**2.61** (30) ± 0.04 Q1: 2.59, Q3: 2.68 CV: 1.69%	1.8/**1.1** (29) ± 1.6 Q1: 0.8, Q3: 2.6 CV: 88.61%	1.5E-15/**2.1E-18** (24) ± 5.7E-15 Q1: 8.1E-19, Q3: 9.2E-18 CV: 388.40%
Sandstone Jurassic	2.64/**2.65** (7) ± 0.02 Q1: 2.64, Q3: 2.66 CV: 0.63%	2.07/**2.08** (6) ± 0.08 Q1: 2.02, Q3: 2.13 CV: 3.77%	20.5/**20.4** (6) ± 1.8 Q1: 19.3, Q3: 21.8 CV: 8.74%	8.1E-13/**3.2E-14** (7) ± 2.0E-12 Q1: 1.8E-16, Q3: 2.7E-13 CV: 243.80%
Basaltic - andesitic dykes	2.66/**2.65** (26) ± 0.19 Q1: 2.58, Q3: 2.95 CV: 6.85%	2.68/**2.57** (22) ± 0.21 Q1: 2.56, Q3: 2.93 CV: 7.73%	1.6/**1.0** (22) ± 2.1 Q1: 0.7, Q3: 2.0 CV: 128.04%	5.6E-18/**3.7E-18** (16) ± 4.5E-18 Q1: 2.3E-18, Q3: 8.8E-18 CV: 79.44%
Marble	2.72/**2.71** (69) ± 0.10 Q1: 2.69, Q3: 2.85 CV: 3.59%	2.70/**2.69** (69) ± 0.11 Q1: 2.63, Q3: 2.80 CV: 4.06%	1.5/**0.8** (79) ± 1.7 Q1: 0.5, Q3: 1.8 CV: 117.27%	2.5E-15/**2.5E-18** (48) ± 1.2E-14 Q1: 1.1E-18, Q3: 6E-18 CV: 467.41%
Quartz veins	2.63/**2.64** (20) ± 0.03 Q1: 2.62, Q3: 2.69 CV: 1.10%	2.53/**2.57** (19) ± 0.09 Q1: 2.51, Q3: 2.58 CV: 3.64%	3.5/**2.8** (19) ± 3.0 Q1: 1.5, Q3: 4.3 CV: 85.60%	1.5E-14/**4.5E-15** (10) ± 2.2E-14 Q1: 2.5E-16, Q3: 2.7E-14 CV: 151.63%
Skarn	3.19/**3.32** (142) ± 0.51 Q1: 2.73, Q3: 3.69 CV: 15.53%	3.23/**3.26** (111) ± 0.49 Q1: 2.71, Q3: 3.57 CV: 15.14%	3.7/**2.4** (115) ± 3.9 Q1: 0.8, Q3: 4.5 CV: 103.87%	8.4E-13/**9E-18** (90) ± 8.0E-12 Q1: 2.5E-18, Q3: 4E-17 CV: 948.01%
Granitoids total	2.64/**2.65** (124) ± 0.12 Q1: 2.61, Q3: 2.67 CV: 4.39%	2.51/**2.52** (73) ± 0.18 Q1: 2.35, Q3: 2.63 CV: 6.99%	6.0/**3.6** (76) ± 4.8 Q1: 1.6, Q3: 10.7 CV: 80.26%	2.6E-16/**7.9E-18** (53) ± 1.4E-15 Q1: 2.7E-18, Q3: 5.8E-17 CV: 539.26%
Granitoids (weak - moderate alteration)	2.65/**2.65** (80) ± 0.12 Q1: 2.63, Q3: 2.68 CV: 4.53%	2.56/**2.59** (52) ± 0.18 Q1: 2.36, Q3: 2.65 CV: 6.91%	1.8/**1.6** (40) ± 1.2 Q1: 0.9, Q3: 2.5 CV: 65.85%	4.0E-17/**3.5E-18** (28) ± 1.2E-16 Q1: 1.2E-18, Q3: 7.7E-18 CV: 300.54%
Granitoids (strong alteration)	2.60/**2.62** (30) ± 0.04 Q1: 2.60, Q3: 2.64 CV: 1.50%	2.38/**2.37** (21) ± 0.07 Q1: 2.36, Q3: 2.42 CV: 2.77%	9.7/**9.7** (21) ± 2.8 Q1: 8.4, Q3: 10.9 CV: 28.68%	2.9E-17/**2.6E-17** (14) ± 2.5E-17 Q1: 4.5E-18, Q3: 4.9E-17 CV: 87.14%

arithmetic mean values in normal font, the numbers in bold represent the median, ± = standard deviation, () = number of analyzed plugs, Q1: 25% quartile, Q3: 75% quartile, ρP = particle density, ρB = bulk density, φ = porosity, K = permeability

Table A2: Thermal properties of the LHVC

Unit	λ dry [W m^{-1} K^{-1}]	λ sat [W m^{-1} K^{-1}]	α dry [10^{-6} m² s^{-1}]	α sat [10^{-6} m² s^{-1}]
Post-caldera group				
Pyroclastics, undifferentiated	0.48/**0.50** (4) ± 0.04 Q1: 0.44, Q3: 0.51	1.00/**1.01** (4) ± 0.05 Q1: 0.95, Q3: 1.03	0.37/**0.37** (4) ± 0.02 Q1: 0.35, Q3: 0.39	0.89/**0.89** (4) ± 0.05 Q1: 0.85, Q3: 0.94
Basalts	0.90/**0.92** (33) ± 0.12 Q1: 0.81, Q3: 0.98 CV: 13.77%	1.33/**1.32** (33) ± 0.20 Q1: 1.19, Q3: 1.36 CV: 14.94%	0.54/**0.54** (29) ± 0.05 Q1: 0.51, Q3: 0.57 CV: 8.94%	0.88/**0.85** (29) ± 0.17 Q1: 0.78, Q3: 0.96 CV: 19.13%
Ash fall deposits	0.39/**0.32** (6) ± 0.18 Q1: 0.58, Q3: 0.44 CV: 47.40%	1.16/**1.09** (6) ± 0.21 Q1: 1.04, Q3: 1.22 CV: 18.61%	0.37/**0.37** (5) ± 0.01 Q1: 0.36, Q3: 0.38	0.41/**0.40** (5) ± 0.02 Q1: 0.39, Q3: 0.44 CV: 5.97%
Caldera group				
Zaragoza ignimbrite	0.64/**0.64** (34) ± 0.09 Q1: 0.58, Q3: 0.70 CV: 14.10%	1.31/**1.28** (26) ± 0.18 Q1: 1.19, Q3: 1.39 CV: 13.88%	0.52/**0.51** (32) ± 0.04 Q1: 0.50, Q3: 0.55 CV: 7.24%	0.95/**0.91** (24) ± 0.20 Q1: 0.77, Q3: 1.12 CV: 21.57%
Xáltipan ignimbrite total	0.51/**0.40** (120) ± 0.41 Q1: 0.30, Q3: 0.54 CV: 79.40%	1.19/**1.26** (84) ± 0.34 Q1: 0.99, Q3: 1.40 CV: 28.56%	0.48/**0.47** (117) ± 0.22 Q1: 0.34, Q3: 0.50 CV: 46.12%	0.76/**0.66** (81) ± 0.23 Q1: 0.60, Q3: 0.90 CV: 30.53%
Xáltipan ig. (unaltered)	0.44/**0.41** (98) ± 0.18 Q1: 0.33, Q3: 0.53 CV: 40.30%	1.19/**1.24** (73) ± 0.25 Q1: 1.01, Q3: 1.39 CV: 21.04%	0.43/**0.48** (90) ± 0.10 Q1: 0.33, Q3: 0.50 CV: 22.58%	0.71/**0.66** (70) ± 0.15 Q1: 0.60, Q3: 0.87 CV: 21.21%
Xáltipan ig. (pumice)	0.17/**0.18** (13) ± 0.03 Q1: 0.15, Q3: 0.19 CV: 15.99%	0.47/**0.45** (5) ± 0.06 Q1: 0.43, Q3: 0.52 CV: 13.80%	0.39/**0.42** (18) ± 0.09 Q1: 0.30, Q3: 0.46 CV: 23.29%	0.63/**0.64** (5) ± 0.11 Q1: 0.55, Q3: 0.71 CV: 17.24%
Xáltipan ig. (altered, welded)	1.78/**1.75** (9) ± 0.14 Q1: 1.69, Q3: 1.94 CV: 7.88%	1.83/**1.82** (6) ± 0.07 Q1: 1.77, Q3: 1.91 CV: 3.64%	1.10/**1.27** (9) ± 0.32 Q1: 0.79, Q3: 1.40 CV: 29.14%	1.39/**1.39** (6) ± 0.11 Q1: 0.64, Q3: 1.51 CV: 8.08%
Pre-caldera group				
Cinder cones total	0.91/**0.86** (15) ± 0.37 Q1: 0.70, Q3: 1.23 CV: 41.10%	1.62/**1.63** (11) ± 0.09 Q1: 1.53, Q3: 1.70 CV: 5.77%	0.57/**0.61** (15) ± 0.15 Q1: 0.38, Q3: 0.64 CV: 26.81%	0.74/**0.76** (11) ± 0.09 Q1: 0.64, Q3: 0.83 CV: 12.21%
Scoria	1.07/**1.06** (11) ± 0.28 Q1: 0.84, Q3: 1.26 CV: 26.35%	1.62/**1.63** (11) ± 0.09 Q1: 1.53, Q3: 1.70 CV: 5.77%	0.65/**0.64** (11) ± 0.08 Q1: 0.60, Q3: 0.66 CV: 12.95%	0.74/**0.76** (11) ± 0.09 Q1: 0.64, Q3: 0.83 CV: 12.21%
Fallout deposits	0.48/**0.46** (4) ± 0.22 Q1: 0.29, Q3: 0.68	-	0.36/**0.36** (4) ± 0.02 Q1: 0.34, Q3: 0.38	-
Teziutlán andesite unit total	1.32/**1.35** (112) ± 0.32 Q1: 0.99, Q3: 1.61 CV: 24.09%	1.50/**1.52** (112) ± 0.12 Q1: 1.43, Q3: 1.58 CV: 7.67%	0.82/**0.86** (110) ± 0.15 Q1: 0.73, Q3: 0.91 CV: 18.33%	1.10/**1.09** (110) ± 0.16 Q1: 0.99, Q3: 1.18 CV: 14.82%
Teziutlán and. (nonporous)	1.49/**1.56** (80) ± 0.18 Q1: 1.32, Q3: 1.64 CV: 12.36%	1.52/**1.54** (80) ± 0.13 Q1: 1.43, Q3: 1.60 CV: 8.26%	0.83/**0.86** (80) ± 0.10 Q1: 0.77, Q3: 0.89 CV: 12.31%	1.14/**1.14** (78) ± 0.17 Q1: 1.06, Q3: 1.23 CV: 15.27%
Teziutlán and. (porous)	0.89/**0.90** (32) ± 0.10 Q1: 0.82, Q3: 0.97 CV: 11.52%	1.47/**1.48** (32) ± 0.08 Q1: 1.43, Q3: 1.54 CV: 5.14%	0.81/**0.74** (30) ± 0.24 Q1: 0.58, Q3: 1.03 CV: 29.58%	1.00/**1.00** (32) ± 0.06 Q1: 0.95, Q3: 1.04 CV: 5.70%
Cuyoaco andesite unit	1.46/**1.47** (47) ± 0.26 Q1: 1.24, Q3: 1.73 CV: 17.90%	1.67/**1.63** (38) ± 0.21 Q1: 1.52, Q3: 1.75 CV: 12.64%	0.84/**0.86** (48) ± 0.10 Q1: 0.78, Q3: 0.92 CV: 11.95%	1.38/**1.38** (38) ± 0.18 Q1: 1.26, Q3: 1.48 CV: 12.98%
Basement				
Limestone Cretaceous	2.74/**2.73** (327) ± 0.55 Q1: 2.44, Q3: 2.93 CV: 20.11%	3.03/**2.93** (272) ± 0.58 Q1: 2.64, Q3: 3.34 CV: 19.23%	1.45/**1.35** (324) ± 0.46 Q1: 1.21, Q3: 1.54 CV: 31.57%	1.72/**1.56** (264) ± 0.59 Q1: 1.32, Q3: 1.93 CV: 34.52%
Chert nodules	3.26/**2.90** (16) ± 1.04 Q1: 2.67, Q3: 4.27 CV: 31.81%	4.11/**3.27** (17) ± 1.57 Q1: 2.91, Q3: 5.73 CV: 38.19%	1.54/**1.23** (17) ± 0.52 Q1:1.13, Q3: 2.13 CV: 33.75%	1.91/**1.80** (17) ± 0.83 Q1: 1.21, Q3: 2.32 CV: 43.68%
Shales Cretaceous	2.18/**2.12** (7) ± 0.30 Q1: 1.92, Q3: 2.27 CV: 13.60%	2.29/**2.13** (7) ± 0.39 Q1: 2.09, Q3: 2.26 CV: 17.25%	1.80/**1.80** (6) ± 0.09 Q1: 1.73, Q3: 1.87 CV: 4.75%	1.64/**1.65** (6) ± 0.06 Q1: 1.60, Q3: 1.69 CV: 3.52%
Limestone Jurassic	2.66/**2.68** (38) ± 0.23 Q1: 2.48, Q3: 2.84 CV: 8.65%	2.76/**2.66** (36) ± 0.32 Q1: 2.49, Q3: 3.08 CV: 11.76%	1.60/**1.50** (36) ± 0.34 Q1: 1.28, Q3: 1.95 CV: 21.41%	1.95/**1.69** (30) ± 0.75 Q1: 1.44, Q3: 2.50 CV: 38.66%
Sandstone Jurassic	1.38/**1.38** (6) ± 0.16 Q1: 1.28, Q3: 1.53 CV: 11.29%	2.28/**2.29** (6) ± 0.12 Q1: 2.20, Q3: 2.39 CV: 5.21%	0.88/**0.88** (6) ± 0.05 Q1: 0.84, Q3: 0.92 CV: 5.36%	1.89/**1.77** (6) ± 0.41 Q1: 1.61, Q3: 2.17 CV: 21.58%
Basaltic - andesitic dykes	1.71/**1.70** (22) ± 0.32 Q1: 1.47, Q3: 1.99 CV: 18.90%	1.86/**1.65** (26) ± 0.57 Q1: 1.53, Q3: 1.99 CV: 30.51%	0.88/**0.89** (20) ± 0.11 Q1: 0.79, Q3: 0.97 CV: 12.57%	1.12/**0.91** (24) ± 0.39 Q1: 0.83, Q3: 1.48 CV: 34.78%
Marble	3.10/**3.22** (65) ± 0.60 Q1: 2.51, Q3: 3.64 CV: 19.29%	3.52/**3.42** (65) ± 0.77 Q1: 2.78, Q3: 4.45 CV: 21.85%	1.52/**1.37** (62) ± 0.60 Q1: 1.15, Q3: 1.64 CV: 39.66%	3.01/**2.75** (61) ± 1.39 Q1: 1.85, Q3: 3.99 CV: 46.19%
Quartz veins	5.25/**5.21** (20) ± 0.61 Q1: 4.77, Q3: 5.80 CV: 11.65%	5.85/**5.78** (20) ± 0.79 Q1: 5.20, Q3: 6.49 CV: 13.44%	4.30/**3.92** (19) ± 1.08 Q1: 3.41, Q3: 5.36 CV: 25.19%	3.95/**3.50** (20) ± 1.31 Q1: 2.92, Q3: 5.18 CV: 33.16%
Skarn	3.23/**3.42** (127) ± 0.77 Q1: 2.62, Q3: 3.82 CV: 23.71%	3.44/**3.48** (126) ± 0.93 Q1: 2.87, Q3: 4.11 CV: 26.91%	1.81/**1.55** (123) ± 0.63 Q1: 1.32, Q3: 2.27 CV: 34.17%	2.25/**2.27** (117) ± 0.78 Q1: 1.63, Q3: 2.69 CV: 34.58%
Granitoids total	2.00/**1.97** (121) ± 0.50 Q1: 1.68, Q3: 2.28 CV: 25.19%	2.35/**2.24** (102) ± 0.59 Q1: 1.95, Q3: 2.57 CV: 25.31%	1.09/**1.08** (120) ± 0.26 Q1: 0.95, Q3: 1.18 CV: 23.91%	1.61/**1.40** (102) ± 0.79 Q1: 1.08, Q3: 1.73 CV: 49.28%
Granitoids (weak - moderate alteration)	2.13/**2.06** (81) ± 0.39 Q1: 1.84, Q3: 2.28 CV: 18.43%	2.31/**2.27** (68) ± 0.41 Q1: 2.06, Q3: 2.41 CV: 17.93%	1.14/**1.11** (77) ± 0.21 Q1: 1.03, Q3: 1.20 CV: 30.15%	1.69/**1.54** (62) ± 0.68 Q1: 1.30, Q3: 1.81 CV: 40.15%
Granitoids (strong alteration)	1.90/**1.64** (30) ± 0.62 Q1: 1.43, Q3: 2.50 CV: 32.71%	2.58/**2.73** (26) ± 0.92 Q1: 1.78, Q3: 3.28 CV: 35.60%	1.07/**1.00** (33) ± 0.32 Q1: 0.91, Q3: 1.18 CV: 30.15%	1.65/**1.26** (30) ± 1.03 Q1: 1.08, Q3: 1.52 CV: 62.35%

arithmetic mean values in normal font, the numbers in bold represent the median, ± = standard deviation, () = number of analyzed plugs, Q1: 25% quartile, Q3: 75% quartile, λ = thermal conductivity, α = thermal diffusivity, dry or sat = analyzed under dry or saturated conditions

Table A3: Compressional and shear wave velocities of the LHVC

Unit	V$_P$ dry [m s^{-1}]	V$_P$ sat [m s^{-1}]	V$_S$ dry [m s^{-1}]	V$_S$ sat [m s^{-1}]
Post-caldera group				
Pyroclastics, undifferentiated	1615/**1605** (4) ± 85 Q1: 1539, Q3: 1701 CV: 5.25%	2637/**2633** (4) ± 145 Q1: 2506, Q3: 2771	946/**925** (4) ± 66 Q1: 897, Q3: 1016	1040/**1036** (4) ± 125 Q1: 926, Q3: 1158
Basalts	3770/**3674** (38) ± 689 Q1: 3177, Q3: 4325 CV: 18.29%	5521/**5573** (36) ± 866 Q1: 5046, Q3: 6009 CV: 15.69%	2216/**2183** (36) ± 385 Q1: 1919, Q3: 2541 CV: 17.36%	3362/**3276** (34) ± 554 Q1: 2924, Q3: 3890 CV: 16.47%
Ash fall deposits	1938/**1886** (4) ± 240 Q1: 1740, Q3: 2190	2222/**2219** (4) ± 273 Q1: 1962, Q3: 2485	1286/**1312** (4) ± 170 Q1: 1115, Q3: 1432	1402/**1348** (4) ± 235 Q1: 1218, Q3: 1639
Caldera group				
Zaragoza ignimbrite	2311/**2356** (34) ± 306 Q1: 2108, Q3: 2485 CV: 13.26%	3119/**3002** (31) ± 642 Q1: 2708, Q3: 3271CV: 20.58%	1414/**1433** (32) ± 153 Q1: 1289, Q3: 1478 CV: 10.85%	1881/**1777** (29) ± 390 Q1: 1642, Q3: 1964 CV: 20.75%
Xáltipan ignimbrite total	1945/**1756** (117) ± 613 Q1: 1432, Q3: 2391 CV: 31.51%	2461/**2295** (81) ± 742 Q1: 2055, Q3: 2726 CV: 30.14%	1194/**1075** (114) ± 379 Q1: 886, Q3: 1472 CV: 31.75%	1458/**1378** (78) ± 416 Q1: 1215, Q3: 1686 CV: 28.52%
Xáltipan ig. (unaltered)	1773/**1628** (92) ± 525 Q1: 1382, Q3: 2134 CV: 29.60%	2371/**2256** (68) ± 616 Q1: 2071, Q3: 2685 CV: 25.98%	1088/**985** (89) ± 334 Q1: 850, Q3: 1343 CV: 30.64%	1479/**1380** (71) ± 425 Q1: 1239, Q3: 1710 CV: 28.72%
Xáltipan ig. (pumice)	2437/**2466** (18) ± 482 Q1: 2012, Q3: 2934 CV: 19.76%	2080/**2047** (7) ± 372 Q1: 1742, Q3: 2517 CV: 17.86%	1490/**1523** (18) ± 283 Q1: 1245, Q3: 1735 CV: 18.96%	1247/**1210** (7) ± 239 Q1: 982, Q3: 1468 CV: 19,16%
Xáltipan ig. (altered, welded)	2945/**3004** (7) ± 286 Q1: 2883, Q3: 3214 CV: 9.72%	3936/**3959** (6) ± 794 Q1: 3325, Q3: 4697 CV: 20.16%	1766/**1784** (7) ± 191 Q1: 1720, Q3: 1887 CV: 10.82%	2332/**2343** (6) ± 438 Q1: 1919, Q3: 2796 CV: 18.79%
Pre-caldera group				
Cinder cones total	3260/**3649** (15) ± 1089 Q1: 1673, Q3: 3979 CV: 33.40%	4195/**4351** (13) ± 1057 Q1: 4045, Q3: 4996 CV: 25.18%	1946/**2261** (15) ± 616 Q1: 1094, Q3: 2361 CV: 31.65%	2664/**2792** (13) ± 666 Q1: 2478, Q3: 3189 CV: 24.99%
Scoria	3880/**3880** (11) ± 270 Q1: 3640, Q3: 4090 CV: 6.95%	4584/**4444** (11) ± 510 Q1: 4068, Q3: 5198 CV: 11.12%	2297/**2289** (11) ± 151 Q1: 2126, Q3: 2445 CV: 6.58%	2907/**2852** (11) ± 330 Q1: 2590, Q3: 3202 CV: 11.35%
Fallout deposits	1556/**1532** (4) ± 88 Q1: 1487, Q3: 1648 CV: 5.66%	2058 (2)	984/**975** (4) ± 96 Q1: 897, Q3: 1079	1326 (2)
Teziutlán andesite unit total	3787/**3879** (138) ± 1204 Q1: 2828, Q3: 4706 CV: 31.80%	5341/**5425** (117) ± 1022 Q1: 4708, Q3: 6219 CV: 19.13%	2200/**2286** (132) ± 683 Q1: 1666, Q3: 2738 CV: 31.04%	3168/**3213** (114) ± 619 Q1: 2758, Q3: 3730 CV: 19.53%
Teziutlán and. (nonporous)	4125/**4384** (101) ± 1145 Q1: 3417, Q3: 4981 CV: 27.75%	5476/**5556** (89) ± 1050 Q1: 4729, Q3: 6404 CV: 19.17%	2407/**2561** (95) ± 639 Q1: 1969, Q3: 2850 CV: 26.55%	3259/**3285** (86) ± 622 Q1: 2842, Q3: 3764 CV: 19.08%
Teziutlán and. (porous)	2863/**2972** (37) ± 826 Q1: 2056, Q3: 3667 CV: 28.86%	4908/**5196** (28) ± 799 Q1: 4362, Q3: 5545 CV: 16.28%	1667/**1762** (37) ± 474 Q1: 1211, Q3: 2106 CV: 28.44%	2889/**3009** (28) ± 523 Q1: 2513, Q3: 3394 CV: 18.23%
Cuyoaco andesite unit	4142/**4029** (48) ± 1039 Q1: 3253, Q3: 5027 CV: 25.08%	5280/**4893** (37) ± 1314 Q1: 4114, Q3: 6559 CV: 24.89%	2457/**2377** (48) ± 602 Q1: 1984, Q3: 2906 CV: 24.48%	3083/**2972** (37) ± 775 Q1: 2413, Q3: 3806 CV: 25.13%
Basement				
Limestone Cretaceous	5310/**5298** (380) ± 1223 Q1: 4459, Q3: 6118 CV: 23.03%	7175/**7171** (275) ± 1446 Q1: 6311, Q3: 8230 CV: 20.16%	3118/**3058** (368) ± 731 Q1: 2615, Q3: 3535 CV: 23.44%	4271/**4317** (272) ± 835 Q1: 3824, Q3: 4856 CV: 19.54%
Chert nodules	5806/**5813** (18) ± 828 Q1: 5348, Q3: 6339 CV: 14.25%	8142/**8251** (15) ± 1148 Q1: 7248, Q3: 9172 CV: 14.10%	3532/**3588** (18) ± 639 Q1: 3048, Q3: 3889 CV: 18.10%	4763/**4849** (15) ± 718 Q1: 4092, Q3: 5361 CV: 15.07%
Shales Cretaceous	2826/**2469** (7) ± 1015 Q1: 2104, Q3: 3551 CV: 35.92%	3573/**3210** (7) ± 1190 Q1: 2534, Q3: 4162 CV: 33.31%	1467/**1365** (6) ± 322 Q1: 1258, Q3: 1624CV: 21.97%	1973/**2058** (6) ± 404 Q1: 1529, Q3: 2322 CV: 20.45%
Limestone Jurassic	5057/**4834** (38) ± 872 Q1: 4384, Q3: 5800 CV: 17.23%	6358/**6360** (34) ± 1156 Q1: 5734, Q3: 7308 CV: 18.19%	3057/**2953** (36) ± 638 Q1: 2583, Q3: 3329 CV: 20.88%	3779/**3760** (32) ± 742 Q1: 3218, Q3: 4490 CV: 19.64%
Sandstone Jurassic	2300/**1959** (7) ± 1048 Q1: 1758, Q3: 2084 CV: 45.56%	3119/**3150** (6) ± 401 Q1: 2778, Q3: 3472 CV: 12.85%	1380/**1200** (7) ± 417 Q1: 1178, Q3: 1366 CV: 30.20%	1828/**1850** (6) ± 245 Q1: 1648, Q3: 2044 CV: 13.37%
Basaltic - andesitic dykes	4538/**4461** (20) ± 999 Q1: 3975, Q3: 5150 CV: 22.02%	5842/**5938** (20) ± 833 Q1: 5559, Q3: 6031 CV: 14.25%	2692/**2702** (20) ± 542 Q1: 2493, Q3: 3004 CV: 20.13%	3557/**3553** (20) ± 508 Q1: 3363, Q3: 3668 CV: 14.28%
Marble	4028/**3697** (85) ± 1268 Q1: 3031, Q3: 5078 CV: 31.48%	6698/**6581** (67) ± 1690 Q1: 5304, Q3: 7964 CV: 25.22%	2262/**2141** (84) ± 628 Q1: 1749, Q3: 2760 CV: 27.74%	3864/**3826** (66) ± 1069 Q1: 2971, Q3: 4761 CV: 27.66%
Quartz veins	3588/**3683** (20) ± 752 Q1: 3143, Q3: 4222 CV: 20.96%	5481/**5598** (20) ± 1658 Q1: 4186, Q3: 6377 CV: 30.26%	2120/**2081** (20) ± 418 Q1: 1864, Q3: 2522 CV: 19.74%	3181/**3378** (20) ± 857 Q1: 2477, Q3: 3716 CV: 26.94%
Skarn	4627/**4570** (146) ± 1123 Q1: 3779, Q3: 5319 CV: 24.28%	6326/**6297** (133) ± 1372 Q1: 5661, Q3: 7130 CV: 21.69%	2704/**2639** (141) ± 656 Q1: 2189, Q3: 3208 CV: 24.27%	3742/**3752** (130) ± 815 Q1: 3328, Q3: 4261 CV: 21.78%
Granitoids total	3920/**3815** (124) ± 1172 Q1: 2986, Q3: 4719 CV: 29.91%	5122/**5176** (107) ± 1482 Q1: 3918, Q3: 6034 CV: 28.93%	2382/**2303** (122) ± 732 Q1: 1806, Q3: 2765 CV: 30.74%	3052/**3094** (105) ± 939 Q1: 2375, Q3: 3593 CV: 30.78%
Granitoids (weak - moderate alteration)	4352/**4302** (80) ± 1115 Q1: 3495, Q3: 5158 CV: 25.61%	5714/**5653** (66) ± 1407 Q1: 4860, Q3: 6424 CV: 24.63%	2659/**2556** (79) ± 700 Q1: 2195, Q3: 3173 CV: 26.32%	3420/**3415** (64) ± 882 Q1: 2905, Q3: 3908 CV: 25.80%
Granitoids (strong alteration)	3360/**3279** (31) ± 684 Q1: 2954, Q3: 3728 CV: 20.36%	4514/**4723** (31) ± 970 Q1: 3771, Q3: 5284 CV: 21.49%	2025/**1957** (31) ± 414 Q1: 1771, Q3: 2300 CV: 20.46%	2737/**2806** (31) ± 608 Q1: 2305, Q3: 3192 CV: 22.20%

arithmetic mean values in normal font, the numbers in bold represent the median, ± = standard deviation, () = number of analyzed plugs, Q1: 25% quartile, Q3: 75% quartile, V$_P$ = P-wave velocity, V$_S$ = S-wave velocity, dry or sat = analyzed under dry or saturated conditions

Table A4: Rock compressibility, magnetic susceptibility, specific and volumetric heat capacity of the LHVC

Unit	ß [PSI]	X [10^{-3} SI]	cp [J kg^{-1} K^{-1}]	VHC [J m^3 K^{-1}]
Post-caldera group				
Pyroclastics, undifferentiated	3.3E-04	3.977/**3.758** (3) ± 0.448	883 (1)	1306 (1)
Basalts	1.3E-05	1.356/**1.357** (18) ± 0.534 Q1: 0.997, Q3: 1.586 CV: 39.39%	753/**758** (5) ± 51 Q1: 701, Q3: 801 CV: 6.74%	1698/**1663** (5) ± 98 Q1: 1612, Q3: 1802 CV: 5.77%
Ash fall deposits	4.2E-04	-0.004/**-0.009** (4) ± 0.016 Q1: -0.014, Q3: 0.013	862 (1)	1034 (1)
Caldera group				
Zaragoza ignimbrite	1.4E-04	1.098/**0.842** (15) ± 0.586 Q1: 0.630, Q3: 1.555 CV: 53.34%	766/**776** (3) ± 21	1248/**1164** (3) ± 176
Xáltipan ignimbrite total	2.6E-04	0.441/**0.310** (50) ± 0.431 Q1: 0.095, Q3: 0.778 CV: 97.72%	762/**750** (7) ± 38 Q1: 740, Q3: 803 CV: 4.95%	992/**931** (9) ± 348 Q1: 842, Q3: 1151 CV: 35.07%
Xáltipan ig. (unaltered)	2.9E-04	0.495/**0.325** (41) ± 0.446 Q1: 0.089, Q3: 0.963 CV: 90.14%	767/**763** (4) ± 28 Q1: 742, Q3: 796	975/**931** (7) ± 147 Q1: 842, Q3: 1044 CV: 15.03%
Xáltipan ig. (pumice)	6.3E-04	0.115/**0.117** (8) ± 0.032 Q1: 0.086, Q3: 0.131 CV: 27,91%	778 (2) ± 50	408 (1)
Xáltipan ig. (altered, welded)	6.2E-06	0.874 (1)	707 (1)	1697 (1)
Pre-caldera group				
Cinder cones total	5.8E-05	0.773/**0.644** (7) ± 0.330 Q1: 0.618, Q3: 1.008 CV: 42.61%	747/**761** (3) ± 32	1349/**1520** (3) ± 312
Scoria	3.1E-05	0.598/**0.639** (5) ± 0.090 Q1: 0.528, Q3: 0.647 CV: 15.02%	765 (2) ± 6	1530 (2) ± 14
Fallout deposits	5.3E-04	1.211 (2) ± 0.287	710 (1)	989 (1)
Teziutlán andesite unit total	5.7E-06	6.092/**5.697** (80) ± 2.852 Q1: 4.081, Q3: 7.822 CV: 46.82%	765/**766** (15) ± 40 Q1: 751, Q3: 784 CV: 5.25%	1963/**2044** (15) ± 148 Q1: 1844, Q3: 2058 CV: 7.52%
Teziutlán and. (nonporous)	1.8E-06	6.995/**6.524** (55) ± 2.859 Q1: 5.322, Q3: 8.223 CV: 40.88%	762/**765** (10) ± 46 Q1: 744, Q3: 786 CV: 6.09%	2035/**2044** (11) ± 92 Q1: 1991, Q3: 2078 CV: 4.52%
Teziutlán and. (porous)	2.7E-05	4.105/**4.111** (25) ± 1.551 Q1: 2.767, Q3: 5.243 CV: 37.78%	772/**774** (5) ± 27 Q1: 749, Q3: 794 CV: 3.34%	1767/**1761** (4) ± 59 Q1: 1714, Q3: 1826
Cuyoaco andesite unit	2.9E-06	2.367/**2.471** (23) ± 1.269 Q1: 0.956, Q3: 2.961 CV: 53.63%	752/**744** (7) ± 26 Q1: 728, Q3: 766 CV: 3.51%	1941/**1924** (7) ± 127 Q1: 1817, Q3: 2002 CV: 6.53%
Basement				
Limestone Cretaceous	8.6E-07	0.162/**-0.004** (193) ± 0.634 Q1: -0.026, Q3: 0.021 CV: 391.76%	807/**814** (32) ± 31 Q1: 785, Q3: 825 CV: 3.79%	2159/**2162** (32) ± 127 Q1: 2095, Q3: 2246 CV: 5.87%
Chert nodules	3.0E-07	-0.029/**-0.032** (15) ± 0.012 Q1: -0.033, Q3: -0.0267 CV: 40.95%	814 (2) ± 30	2157 (2) ± 138
Shales Cretaceous	1.6E-06	0.056/**0.051** (7) ± 0.010 Q1: 0.049, Q3: 0.058 CV: 17.59%	780 (1)	2068 (1)
Limestone Jurassic	8.7E-07	0.038/**0.001** (25) ± 0.115 Q1: -0.003, Q3: 0.019 CV: 306.01%	829/**823** (6) ± 40 Q1: 809, Q3: 847 CV: 4.77%	2171/**2155** (5) ± 108 Q1: 2080, Q3: 2271 CV: 4.98%
Sandstone Jurassic	6.0E-05	0.067/**0.006** (6) ± 0.157 Q1: -0.014, Q3: 0.125 CV: 232.56%	739 (1)	1524 (1)
Basaltic - andesitic dykes	9.1E-07	11.270/**4.199** (14) ± 12.410 Q1: 2.909, Q3: 26.52 CV: 110.05%	757 (2) ± 55	2088 (2) ± 312
Marble	9.8E-07	0.124/**-0.027** (41) ± 0.498 Q1: -0.034, Q3: 0.008 CV: 402.46%	853/**836** (9) ± 45 Q1: 825, Q3: 859 CV: 5.25%	2318/**2269** (9) ± 123 Q1: 2208, Q3: 2435 CV: 5.32%
Quartz veins	3.3E-06	0.349/**0.136** (19) ± 0.713 Q1: 0.052, Q3: 0.350 CV: 204.11%	760/**763** (4) ± 13 Q1: 746, Q3: 771 CV: 1.75%	1941/**1937** (4) ± 51 Q1: 1895, Q3: 1991
Skarn	1.6E-06	94.120/**3.920** (62) ± 190.800 Q1: 1.756, Q3: 102.800 CV: 202.72%	742/**740** (11) ± 26 Q1: 746, Q3: 763 CV: 3.51%	2399/**2477** (12) ± 333 Q1: 2028, Q3: 2629 CV: 13.89%
Granitoids total	5.1E-06	4.363/**3.331** (60) ± 4.457 Q1: 0.301, Q3: 6.402 CV: 102.15%	775/**787** (15) ± 54 Q1: 749, Q3: 809 CV: 6.91%	1901/**1920** (26) ± 123 Q1: 1798, Q3: 1979 CV: 6.48%
Granitoids (weak - moderate alteration)	1.2E-06	5.206/**3.573** (38) ± 4.878 Q1: 1.738, Q3: 6.795 CV: 93.70%	769/**779** (12) ± 57 Q1: 733, Q3: 793 CV: 7.39%	1956/**1972** (9) ± 174 Q1: 1811, Q3: 2065 CV: 8.90%
Granitoids (strong alteration)	1.2E-05	0.036/**0.026** (12) ± 0.048 Q1: -0.0068, Q3: 0.085 CV: 135.70%	795/809 (3) ± 38	1931/**1948** (4) ± 100 Q1: 1828, Q3: 2016

arithmetic mean values in normal font, the numbers in bold represent the median, ± = standard deviation, () = number of analyzed plugs, Q1: 25% quartile, Q3: 75% quartile, ß = compressibility, cp = specific heat capacity, VHC = volumetric heat capacity, X = magnetic susceptibility

Appendix B – Additional Information on Data Processing

Table B1: Empirical relationships used for temperature and pressure correction of thermal properties and sonic wave velocities

Parameter	Type of correction	Reference	Rock type
Thermal conductivity	Temperature	Vosteen and Schellschmidt (2003)	Sedimentary, magmatic and metamorphic rocks
		Chen et al. (2021)	Volcanic rocks
	Pressure	Abdulagatov et al. (2006) Abdulagatova et al. (2009)	Sandstone, limestone, intrusive rocks
Thermal diffusivity	Temperature	Vosteen and Schellschmidt (2003)	Sedimentary, magmatic and metamorphic rocks
		Durham et al. (1987)	Volcanic rocks
Specific heat capacity	Temperature	Vosteen and Schellschmidt (2003)	Sedimentary, magmatic and metamorphic rocks
Sonic wave velocities	Temperature and pressure	Qi et al. (2020)	Carbonates
		Hughes and Maurette (1957) and Birch (1961)	Magmatic and intrusive rocks
		Vinciguerra et al. (2005)	Tuff

Table B1 provides an overview of the empirical relationships that were applied for the temperature and pressure correction of thermal conductivity, thermal diffusivity, specific heat capacity and sonic wave velocities. These relationships are based on laboratory experiments of the respective parameter at elevated temperature and/or pressure conditions. Here we present the correction function for thermal conductivity of sedimentary rocks as an example to explain the procedure. The effect of temperature on thermal conductivity was calculated using the following equations:

$$\lambda\,(0) = 0.54 \cdot \lambda(25) + \tfrac{1}{2}\sqrt{1.16 \cdot \left(\lambda(25)\right)^2 - 0.39 \cdot \lambda(25)} \tag{12}$$

$$\lambda\,(T) = \frac{\lambda\,(0)}{0.99 + T \cdot (0.0034 - 0.0039/\lambda\,(0))} \tag{13}$$

where $\lambda\,(0)$ is the normalized thermal conductivity at 0 °C, $\lambda\,(25)$ is the measured thermal conductivity at 25 °C, and $\lambda\,(T)$ is the thermal conductivity at temperature T in °C. Abdulagatova et al. (2009) fitted their experimental data to the following empirical equations:

$$\lambda\,(T, P) = \lambda_\infty \exp\left(-\frac{P_0}{P}\right) + \lambda_0 (P = 0.1, T) \tag{14}$$

$$\lambda_\infty(T) = a_0 + a_1 T + a_2 T^2 \tag{15}$$

$$\lambda_0 (P = 0.1, T) = (C + DT)^{-1} \tag{16}$$

where the values of parameters $a_0 = 1.7358 \times 10^{-2}$, $a_1 = 1.0272 \times 10^{-3}$, $a_2 = -8.1 \times 10^{-7}$, C = 0.30532, D = 0.2302×10^{-3}, P_0 = atmospheric pressure and P = pressure at reservoir depth. Based on the results presented in Abdulagatova et al. (2009) the following equation was derived to calculate the effect of pressure on thermal conductivity:

$$\lambda(P) = (-1E - 10) \cdot P^4 + (1E - 07) \cdot P^3 - (4E - 05) \cdot P^2 + 0.0074 \cdot P + \lambda \tag{17}$$

where $\lambda(P)$ is the thermal conductivity at reservoir pressure, λ = thermal conductivity at laboratory conditions and P is the respective pressure at reservoir depth.

Appendix C – Additional Data to Chapter 5 (Reservoir Samples)
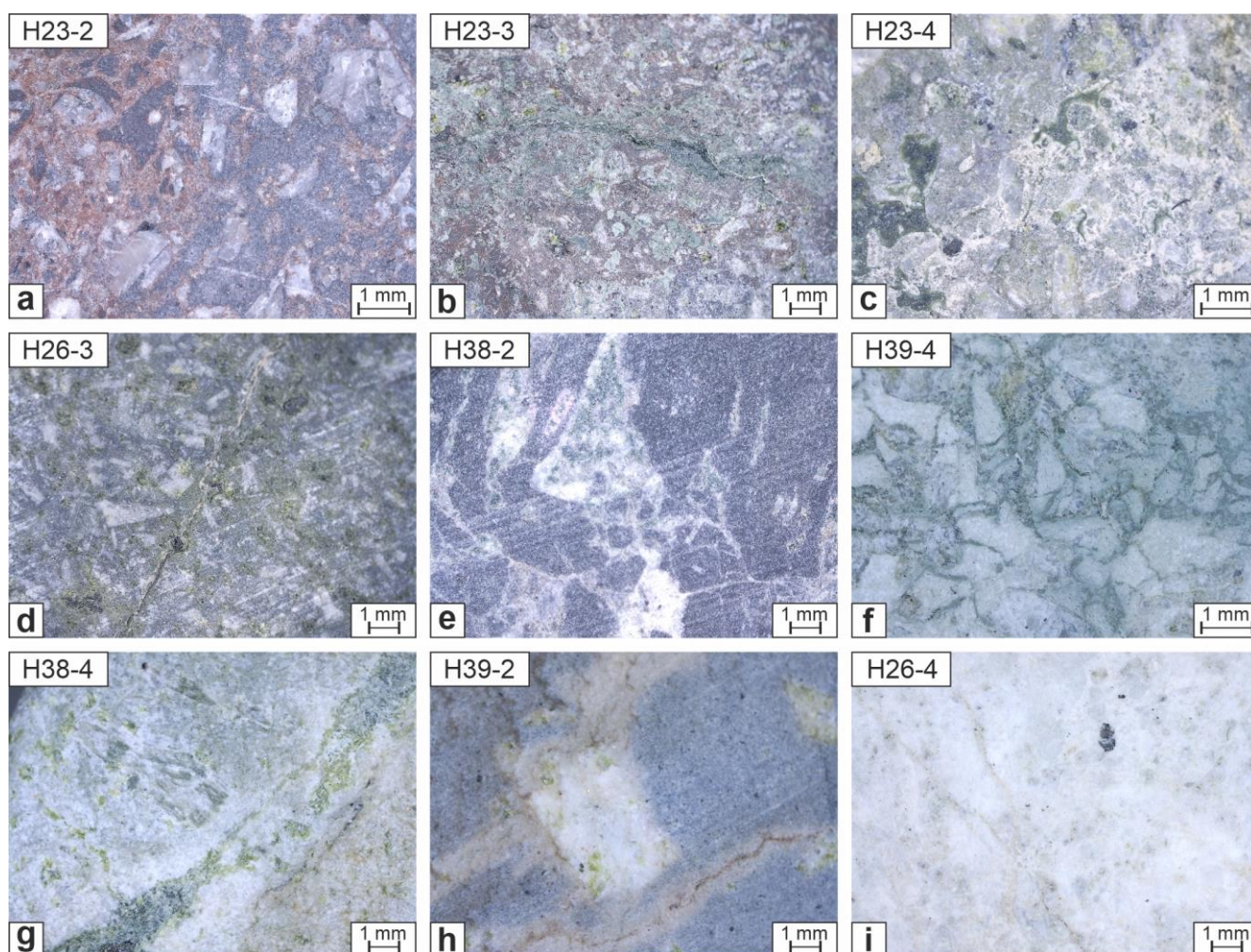
Figure C1: Micro-capture photographs of selected reservoir samples showing the impact of hydrothermal alteration, brecciation, and fracturing at the cm-scale.
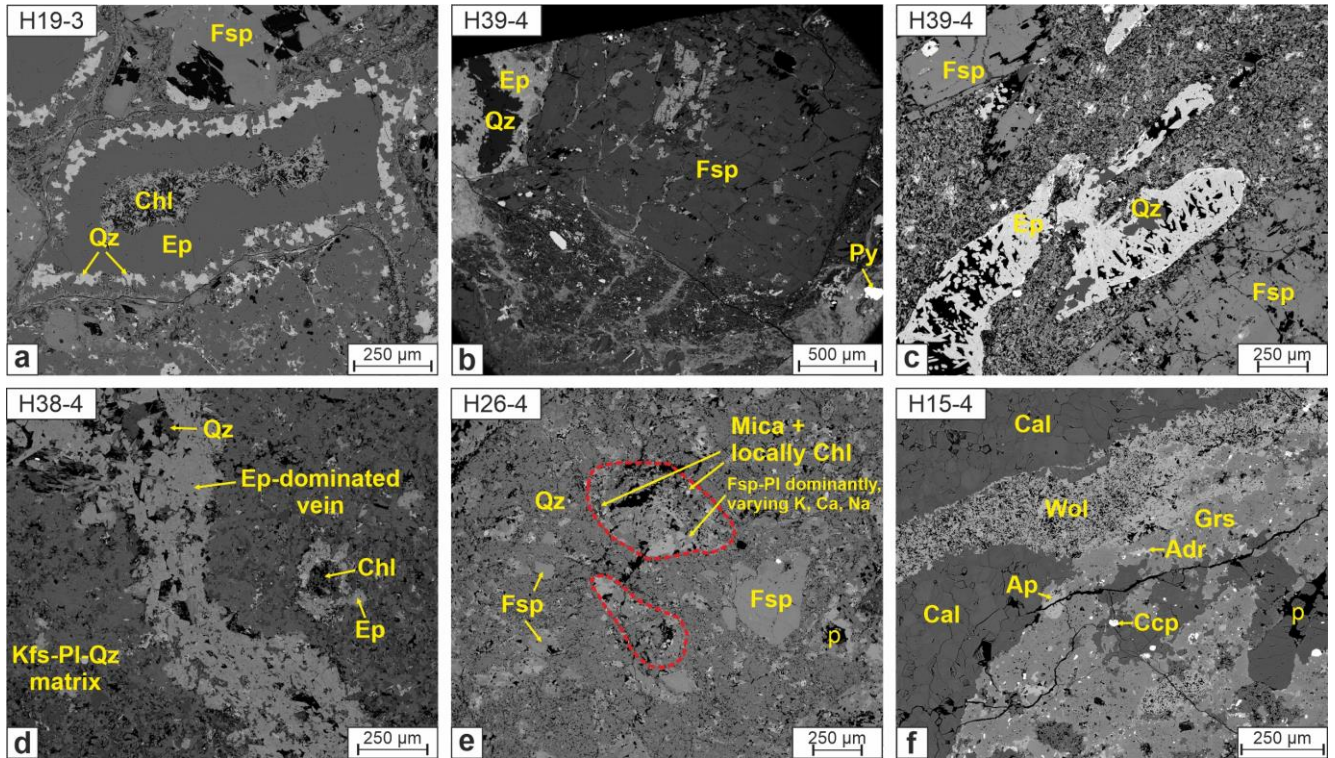
Figure C2: SEM images showing (a) amygdales filled with chlorite, epidote, and quartz, (b) alteration rims near larger felspar phenocrysts, (c-d) epidote s. l. and quartz filling vugs (c) and veins (d), and pervasive silicification and relicts of phenocrysts in andesitic lavas. (f) metasomatic vein in fractured marble with wollastonite, garnet and apatite. Note the abundance of secondary porosity (black) in (c) to (f). Abbreviations: Adr = andradite, Ap = apaite, Cal = calcite, Ccp = chalcopyrite, Chl = chlorite, Ep = epidote, Fsp = feldspar, Grs = grossular, Kfs = K-feldspar, p = pores, Pl = plagioclase, Py = pyrite, Qz = quartz, Wol = wollastonite.
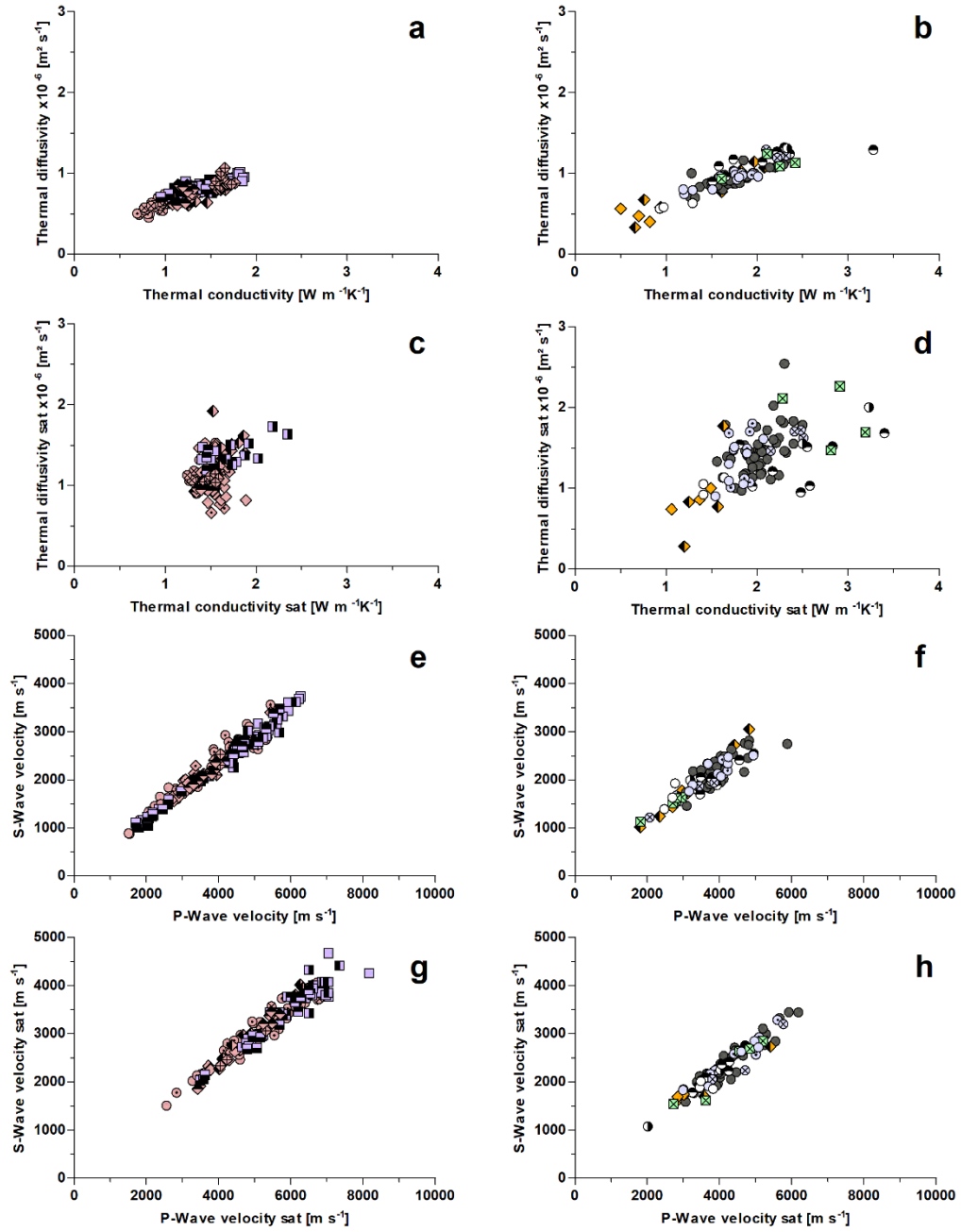
Figure C3: Cross-plots of thermal conductivity, thermal diffusivity, P-wave and S-wave velocities analyzed under dry and saturated conditions. See legend in Figs. 45 and 46.

Table C1: Geographic coordinates of the outcrop samples

Sample ID	Unit	Latitude dec deg (WGS84)	Longitude dec deg (WGS84)
LH8		19.804628	-97.305636
LH9		19.80378	-97.315324
LH10 - LH12		19.798628	-97.313116
LH13 - LH14	Teziutlán andesite unit	19.703344	-97.198453
LH15 - LH17	(1.44–2.65 Ma)	19.687336	-97.206481
LH29 - LH30		19.781882	-97.498057
RLM1 - RLM3		19.662437	-97.169278
RLM9		19.669266	-97.166532
LH33 - LH35		19.538136	-97.64261
LH40		19.621165	-97.61248
LH41	Cuyoaco andesite unit	19.630453	-97.611294
LH50 - LH51	(8.9–10.5 Ma)	19.712052	-97.633049
LH72		19.603134	-97.61642
OLH1		19.602048	-97.618647

Table C2: Sample depth and lithological interpretation of the reservoir samples

Sample ID	Well	Depth [m bgl]	Lithological interpretation
H7-x	H7	2300	Marble
H13-1	H13	1200	Mafic lava
H13-3	H13	2414	Marble
H15-1	H15	1250	Andesitic lava
H15-4	H15	1970	Marble
H18-1	H18	796	Mafic lava
H18-3	H18	1750	Andesitic lava/breccia
H18-4	H18	2900	Skarn
H19-1	H19	981	Rhyolitic lava
H19-2	H19	1300	Andesitic lava
H19-3	H19	1769	Basaltic - andesitic lava
H20-4	H20	1400	Andesitic lava
H22-x	H22	663	Ignimbrite/andesite breccia
H23-1	H23	673	Ignimbrite/andesite breccia
H23-2	H23	1200	Andesitic lava
H23-3	H23	1924	Andesitic lava
H23-4	H23	2495	Andesitic lava
H24-1	H24	1008	Trachyandesitic lava
H24-3	H24	2294	Andesitic lava (partially silicified)
H24-4	H24	2844	Skarn
H25-3	H25	2300	Andesitic lava
H26-1	H26	350	Ignimbrite
H26-2	H26	1200	Trachyandesitic lava
H26-3	H26	1810	Basaltic - andesitic lava
H26-4	H26	2000	Silicified lava
H27-1	H27	1110	Andesitic lava
H27-3	H27	2048	Andesitic lava
H28-1	H28	1250	Basaltic - andesitic lava
H28-2	H28	2002	Silicified lava
H38-1	H38	1100	Basaltic - andesitic lava
H38-2	H38	1500	Andesitic lava
H38-4	H38	1950	Andesitic lava
H39-1	H39	1200	Andesitic lava
H39-2	H39	1650	Andesitic lava (partially silicified)
H39-3	H39	1800	Andesitic lava
H39-4	H39	2100	Andesitic lava
H40-1	H40	1612	Andesitic lava

Table C3: Overview of published rock property data with respect to hydrothermal alteration

Lithology	Study area	O/R	A	ρ_B [g cm^{-3}]	ϕ [%]	K [m^2]	λ [W m^{-1} K^{-1}]	α [10^{-6} m^2 s^{-1}]	Ref.
Andesitic lava	MX	O	U	2.31/**2.40** (19) ± 0.19	14.0/**11.6** (19) ± 6.4	3.2E-13/**2.7E-14** (14) ± 4.7E-13			1
Andesitic lava	MX	O	U	2.31/**2.40** (9) ± 0.28	14.5/**10.6** (9) ± 9.1	1.9E-13/**6.1E-14** (9) ± 2.1E-13			5
Scoracious andesitic lava	MX	O	U	1.42/**1.43** (4) ± 0.03	46.6/**46.7** (4) ± 1.3	4.4E-13/**4.4E-14** (4) ± 4.2E-13			5
Andesite	WI	O	U	2.61/**2.64** (210) ± 0.3	5.3/**3.9** (46) ± 12.0	2E-14/**6E-18** (46)	1,62/**1.68** (50) ± 0.62	0.84/**0.88** (25) ± 0.24	10
Andesite	WI	O	W - M	2.42/**2.49** (33) ± 0.5	10.7/**4.6** (19) ± 18.0	8E-15/**4E-15** (17)	1,52/**1.65** (25) ± 0.56	0.72/**0.75** (14) ± 0.24	10
Andesite	WI	O	S	2.05/**2.00** (6) ± 0.1	26.0/**25.8** (4) ± 1.4	1E-13/**2E-14** (4)	1,71/**1.66** (9) ± 0.35	0.97/**0.92** (6) ± 0.37	10
Andesitic lava	LAIA	O	M -S		10.9/**8.5** (12) ± 8.7	9.1E-18/**5.2E-19** (10) ± 1.7E-17			12
Effusive lavas, tuff, tuffites	R	O+R	S	2.57 (74) ± 0.23	5.6 (74) ± 5.3				2
Effusive lavas, tuff, tuffites	R	O+R	S	2.42 (17) ± 0.26	14.0 (17) ± 9.0				2
Effusive lavas, tuff, tuffites	R	O+R	S	1.59 (40) ± 0.46	40.0 (40) ± 16.7				2
Effusive lavas, tuff, tuffites	R	O+R	S	1.9 (29) ± 0.33	33.0 (29) ± 11.0				2
Effusive lava	R	O+R	U	2.69 (28) ± 0.21	4.9 (28) ± 6.2				2
Tuff	R	O+R	U	1.47 (66) ± 0.63	44.3 (66) ± 19.4				2
Andesite breccia	NZ	R	M - S	2.66/**2.66** (12) ± 0.02	1.7/**1.7** (12) ± 0.2				4
Rotokawa andesite	NZ	R	M - S	2.51/**2.53** (15) ± 0.07	7.7/**6.8** (15) ± 2.6				4
Rotokawa andesite	NZ	R	M - S	2.50/**2.53** (52) ± 0.07	8.7/**7.6** (52) ± 2.6	3.8E-17/ **3.0E-17** (30) ± 3.2E-17			3
Rotokawa andesite	NZ	R	M - S	2.41/**2.42** (10) ± 0.10	11.7/**9.8** (15) ± 3.5				9
Rotokawa andesite	NZ	R	M	2.48/**2.48** (10) ± 0.02	8.8/**8.7** (10) ± 0.8	2.4E-18/ **2.4E-18** (10) ± 1.1E-18			11
Rotokawa andesite	NZ	R	H	2.29/**2.29** (10) ± 0.02	15.7/**15.6** (10) ± 1.7	3.5E-16/ **3.1E-16** (10) ± 2.5E-16			11
Spa andesite	NZ	R	W	2.25/**2.37** (24) ± 0.23	12.1/**9.5** (24) ± 12.0	2.0E-16/ **4.4E-17** (24) ± 4.8E-16	1.30/**1.32** (24) ± 0.28	0.78/**0.74** (24) ± 0.16	6
Spa andesite breccia	NZ	R	S	1.67/**1.71** (12) ± 0.18	39.1/**38.7** (12) ± 5.3	5.9E-15/**1.9E-15** (12) ± 1.0E-14	0.75/**0.71** (12) ± 0.20	0.68/**0.68** (12) ± 0.16	6
Andesitic lava (Tauhara)	NZ	O	U	2.32 (3) ± 0.01	10.1 (3) ± 3.2	5E-16 (3) ± 2E-16	1.61 (3) ± 0.22	1.07 (3) ± 0.12	8
Dacitic lava (Tauhara)	NZ	O	U	2.37 (5) ± 0.01	10.8 (5) ± 0.3	8E-16 (5) ± 9E-16	1.18 (5) ± 0.04	0.84 (5) ± 0.07	8
Rhyolitic lava (Rotorua)	NZ	O	U	1.96 (16) ± 0.18	23.1 (16) ± 7.3	2E-13 (16) ± 4E-13	1.04 (16) ± 0.17	0.83 (16) ± 0.09	8
Whakapapa andesitic lava	NZ	O	M - S		4.2/**4.4** (8) ± 0.6	7.0E-17/**4.6E-17** (8) ± 5.5E-17			7
Whakapapa andesitic lava	NZ	O	U		19.4/**16.9** (19) ± 8.9	6.4E-12/ **4.3E-14** (19) ± 1.1E-11			7

Abbreviations: O = outcrop samples, R = reservoir samples, A = alteration intensity, U = unaltered, W = weak, M = moderate, S = strong, LAIA = Lesser Antilles Island arc (Carribean Sea), MX = Mexico, NZ = New Zealand, R = Russia, WI = West Indies volcanic zone. References: 1 - Heap et al. (2014), 2 - Frolova et al. (2014), 3 - Siratovich et al. (2014), 4 - Wyering et al. (2014), 5 - Farquharson et al. (2015), 6 - Mielke et al. (2015), 7 - Heap and Kennedy (2016), 8 - Mielke et al. (2016), 9 - Siratovich et al. (2016), 10 - Navelot et al. (2018), 11 - Mordensky et al. (2019b), 12 - Delayre et al. (2020).
Arithmetic mean values in normal font, the numbers in bold represent the median, ± = standard deviation, () = number of analyzed plugs, ρ_P = particle density, ρ_B = bulk density, ϕ = porosity, K = permeability, λ = thermal conductivity, α = thermal diffusivity.

Table C3 continuation: Overview of published rock property data with respect to hydrothermal alteration

Lithology	Study area	O/R	A	cp [J kg^{-1} K^{-1}]	V$_P$ [m s^{-1}]	V$_S$ [m s^{-1}]	X [10^{-3} SI]	Ref.
Andesitic lava	MX	O	U		3135/**2690** (35) ± 971	1275/**1250** (25) ± 115		1
Andesitic lava	MX	O	U					5
Scoracious andesitic lava	MX	O	U					5
Andesite	WI	O	U	760/**750** (28) ± 60	4627/**4589** (34) ± 1679		13.92/ **11.60** (41)	10
Andesite	WI	O	W - M	890/**890** (16) ± 140	3947/**4490** (16) ± 2000		13.34/ **11.97** (23)	10
Andesite	WI	O	S	920/**970** (6) ± 186	1668/**1837** (5) ± 1081		5.99/ **0.09** (7)	10
Andesitic lava	LAIA	O	M -S					12
Effusive lavas, tuff, tuffites	R	O+R	S		4650 (74) ± 1330			2
Effusive lavas, tuff, tuffites	R	O+R	S		3800 (17) ± 828			2
Effusive lavas, tuff, tuffites	R	O+R	S		1000 (40) ± 1166			2
Effusive lavas, tuff, tuffites	R	O+R	S		2300 (29) ± 951			2
Effusive lava	R	O+R	U		4760 (28) ± 1506			2
Tuff	R	O+R	U		1830 (66) ± 1202			2
Andesite breccia	NZ	R	M - S		4204/**4163** (12) ± 119	2457/**2428** (12) ± 96		4
Rotokawa andesite	NZ	R	M - S		4164/**4154** (15) ± 188	2552/**2550** (15) ± 102		4
Rotokawa andesite	NZ	R	M - S		4011/**4021** (52) ± 230	2510/**2534** (22) ± 133		3
Rotokawa andesite	NZ	R	M - S					9
Rotokawa andesite	NZ	R	M		3995/**3985** (10) ± 106	2106/**2117** (10) ± 258		11
Rotokawa andesite	NZ	R	H		3604/**3616** (10) ± 181	1899/**1920** (10) ± 121		11
Spa andesite	NZ	R	W	748/**740** (24) ± 85				6
Spa andesite breccia	NZ	R	S	680/**662** (12) ± 113				6
Andesitic lava (Tauhara)	NZ	O	U	580 (3) ± 25	3700 (3) ± 824	2400 (3) ± 400		8
Dacitic lava (Tauhara)	NZ	O	U	530 (5) ± 35	2200 (5) ± 200	1400 (5) ± 200		8
Rhyolitic lava (Rotorua)	NZ	O	U	490 (16) ± 75	2000 (16) ± 851	1300 (16) ± 608		8
Whakapapa andesitic lava	NZ	O	M - S					7
Whakapapa andesitic lava	NZ	O	U					7

Abbreviations: O = outcrop samples, R = reservoir samples, A = alteration intensity, U = unaltered, W = weak, M = moderate, S = strong, LAIA = Lesser Antilles Island arc (Carribean Sea), MX = Mexico, NZ = New Zealand, R = Russia, WI = West Indies volcanic zone. References: 1 - Heap et al. (2014), 2 - Frolova et al. (2014), 3 - Siratovich et al. (2014), 4 - Wyering et al. (2014), 5 - Farquharson et al. (2015), 6 - Mielke et al. (2015), 7 - Heap and Kennedy (2016), 8 - Mielke et al. (2016), 9 - Siratovich et al. (2016), 10 - Navelot et al. (2018), 11 - Mordensky et al. (2019b), 12 - Delayre et al. (2020).
Arithmetic mean values in normal font, the numbers in bold represent the median, ± = standard deviation, () = number of analyzed plugs, V$_P$ = P-wave velocity, V$_S$ = S-wave velocity, cp = specific heat capacity, X = magnetic susceptibility.

Appendix D – Additional Data to Chapter 5 (Geochemistry)

Table D1: Major (wt%) and trace element (ppm) concentrations of the outcrop and reservoir samples

Sample ID	Unit/Depth	SiO₂	TiO₂	Al₂O₃	Fe₂O₃	MnO	MgO	CaO	Na₂O	K₂O	P₂O₅	Ba	Nb	Sr	Zr
LH8	Teziutlán	53.15	1.57	17.73	9.38	0.14	4.60	7.90	3.45	1.38	0.35	446	13	428	162
LH9	Teziutlán	57.04	1.43	17.51	7.78	0.11	2.84	6.67	3.47	1.89	0.34	564	15	454	161
LH11+12	Teziutlán	55.37	1.01	19.64	6.49	0.09	2.16	9.15	3.99	1.66	0.17	601	nd	630	246
LH13	Teziutlán	56.06	1.54	18.58	6.34	0.28	2.82	5.92	3.27	2.61	0.44	871	21	427	267
LH16	Teziutlán	56.88	1.29	17.07	7.63	0.14	3.28	6.03	3.14	2.67	0.35	717	21	420	255
LH29	Teziutlán	61.67	0.71	17.88	5.34	0.07	2.14	5.28	3.84	1.56	0.18	479	nd	517	94
RLM3	Teziutlán	56.56	1.40	16.85	8.08	0.13	3.17	7.19	3.22	2.23	0.37	551	14	434	207
RLM9	Teziutlán	60.82	0.98	17.65	5.29	0.09	1.97	5.08	3.19	3.42	0.29	671	16	377	243
LH34	Cuyoaco	61.32	0.75	17.94	5.28	0.10	2.12	4.79	3.77	1.61	0.20	638	10	496	103
LH41	Cuyoaco	64.99	0.79	16.65	4.90	0.06	0.94	5.11	4.28	1.89	0.20	607	nd	601	279
LH51	Cuyoaco	66.79	0.45	17.37	3.31	0.06	1.03	4.48	4.14	1.24	0.13	305	10	625	80
LH72	Cuyoaco	63.00	0.75	17.97	5.22	0.08	1.91	4.92	4.02	1.61	0.19	422	10	514	111
OLH1	Cuyoaco	65.07	0.76	16.82	5.01	0.07	1.08	4.64	4.22	1.93	0.20	647	nd	620	294
H13-1	1200	53.41	1.47	17.98	8.19	0.14	5.61	6.91	4.58	0.72	0.38	nd	nd	414	200
H15-1	1250	61.79	0.97	16.86	4.74	0.08	3.09	4.27	4.16	2.13	0.36	851	28	372	274
H18-1	796	56.75	1.26	19.52	4.68	0.03	4.71	5.91	3.36	1.17	0.33	564	nd	381	178
H18-3	1750	60.90	1.28	18.70	5.85	0.10	1.88	4.01	3.90	2.06	0.45	699	35	296	474
H18-4	2900	68.72	0.23	16.15	2.07	0.04	0.09	0.73	6.50	2.92	0.06	851	21	59	378
H19-1	981	77.19	0.11	13.48	1.05	0.01	0.61	0.38	3.62	3.42	0.01	nd	14	17	126
H19-2	1300	59.37	1.12	17.52	5.33	0.14	2.35	7.15	3.60	2.65	0.43	672	21	347	392
H19-3	1769	55.87	1.27	17.08	9.33	0.13	5.44	5.00	3.77	1.21	0.51	170	21	406	244
H20-4	1400	56.44	1.10	18.67	5.63	0.07	4.64	4.67	4.84	2.18	0.41	699	21	414	333
H23-1	673	57.59	1.27	18.16	6.71	0.10	4.26	6.53	3.92	1.08	0.32	511	14	372	192
H23-2	1200	55.56	1.52	20.11	5.99	0.10	2.36	6.66	4.97	1.86	0.62	537	21	448	333
H23-3	1924	56.12	1.26	18.78	7.43	0.08	5.68	5.10	3.74	1.02	0.55	152	21	474	289
H23-4	2495	53.53	1.39	20.64	7.56	0.07	5.10	5.52	4.03	1.34	0.51	116	21	507	311
H24-1	1008	61.57	1.07	18.18	4.96	0.10	2.23	2.88	4.74	1.63	0.46	116	14	254	311
H24-3	2294	66.73	0.37	13.94	2.28	0.07	1.92	10.29	1.75	2.21	0.17	555	21	330	170
H24-4	2844	69.64	0.14	12.06	2.29	0.18	2.22	8.24	3.30	1.71	0.06	358	21	211	67
H25-3	2300	62.97	0.67	17.44	3.54	0.06	2.83	3.47	5.15	1.72	0.30	573	14	355	192
H26-1	350	69.78	0.63	16.06	2.98	0.05	0.95	2.17	4.23	2.73	0.17	573	14	194	289
H26-2	1200	63.39	1.04	17.14	4.81	0.12	1.74	3.33	5.93	1.89	0.41	663	14	296	311
H26-3	1810	56.04	1.27	18.67	7.48	0.09	4.01	5.62	4.21	1.79	0.44	690	14	431	229
H26-4	2000	73.49	0.15	16.04	1.25	0.08	1.02	1.21	2.96	3.51	0.09	466	21	93	89
H27-1	1110	61.34	1.36	18.00	6.00	0.09	1.88	3.84	5.08	1.56	0.56	743	28	338	407
H27-3	2048	65.62	0.89	18.00	2.13	0.05	1.21	2.25	4.69	3.70	0.55	nd	nd	25	400
H28-1	1250	56.16	1.12	17.76	5.82	0.14	5.33	7.18	4.36	1.49	0.40	179	21	440	326
H28-2	2002	76.31	0.10	15.60	0.95	0.03	2.46	0.79	1.63	1.96	0.03	269	28	51	67
H38-1	1100	54.66	1.44	21.39	6.97	0.14	3.67	5.51	3.67	1.74	0.53	197	28	516	326
H38-2	1500	57.77	1.55	20.34	5.90	0.09	2.38	3.28	5.55	2.23	0.61	224	49	321	637
H38-4	1950	58.72	0.77	18.14	5.44	0.08	3.80	6.72	3.97	0.37	0.46	134	nd	829	104
H39-1	1200	52.27	1.52	19.09	7.64	0.13	4.59	9.74	3.45	0.45	0.36	nd	nd	474	200
H39-2	1650	70.43	0.39	16.75	1.36	0.05	0.65	1.15	6.71	2.17	0.13	484	21	135	392
H39-3	1800	63.00	1.08	18.11	4.62	0.07	2.41	4.03	4.69	1.10	0.31	116	21	406	281
H39-4	2100	59.33	1.16	19.66	5.76	0.09	2.91	4.21	4.10	1.76	0.37	779	21	423	333
H40-1	1612	54.65	1.04	16.12	6.23	0.18	4.94	11.83	2.32	1.05	0.35	233	nd	769	259

Values normalized to 100; SiO₂ to P₂O₅ in wt%, Ba to Zr in ppm, nd = not detected, depth in m bgl

Table D1 continuation: Rare earth element concentrations (ppm) of the reservoir and outcrop samples

Sample ID	Unit/Depth	La	Ce	Pr	Nd	Sm	Eu	Gd	Tb	Dy	Ho	Er	Tm	Yb	Lu
LH8	Teziutlán	34.97	86.23	9.26	36.07	7.48	2.40	7.28	1.08	6.35	1.21	3.39	0.49	3.17	0.46
LH9	Teziutlán	30.58	65.16	8.07	29.22	12.95	1.80	6.10	0.88	5.08	0.97	2.77	0.39	2.57	0.38
LH11+12	Teziutlán	26.05	56.37	5.43	24.52	8.30	1.27	4.04	0.58	3.32	0.65	1.79	0.24	1.67	0.24
LH13	Teziutlán	48.53	125.53	11.88	46.81	9.33	2.65	8.26	1.18	6.57	1.27	3.44	0.49	3.17	0.46
LH16	Teziutlán	55.82	119.31	13.48	52.35	10.43	2.87	9.62	1.37	7.53	1.47	4.13	0.57	3.74	0.55
LH29	Teziutlán	41.03	66.92	9.68	37.17	7.07	1.96	6.50	0.95	5.09	0.96	2.56	0.36	2.29	0.35
RLM3	Teziutlán	46.46	108.20	11.94	46.77	9.65	2.58	8.85	1.28	7.38	1.41	3.90	0.56	3.57	0.52
RLM9	Teziutlán	49.01	116.11	12.36	46.69	9.26	2.45	8.16	1.20	6.91	1.32	3.79	0.52	3.53	0.52
LH34	Cuyoaco	22.41	46.89	5.31	21.86	8.79	1.24	3.98	0.57	3.19	0.62	1.76	0.25	1.68	0.25
LH41	Cuyoaco	17.98	36.05	4.56	18.04	7.79	1.17	3.22	0.44	2.41	0.44	1.24	0.17	1.12	0.16
LH51	Cuyoaco	15.01	32.67	4.07	15.62	6.72	0.97	2.57	0.33	1.81	0.32	0.90	0.13	0.82	0.12
LH72	Cuyoaco	33.00	70.69	8.41	33.26	6.28	2.00	5.61	0.78	4.07	0.77	2.09	0.28	1.77	0.26
OLH1	Cuyoaco	19.30	44.33	5.14	20.34	9.61	1.36	3.90	0.54	3.07	0.56	1.54	0.22	1.42	0.21
H13-1	1200	29.30	90.22	8.75	34.49	7.84	2.66	7.58	1.14	6.70	1.34	3.76	0.53	3.51	0.51
H15-1	1250	43.82	106.34	10.91	41.48	7.83	2.30	6.89	0.97	5.35	1.05	2.95	0.42	2.78	0.41
H18-1	796	24.17	70.54	6.26	24.87	5.12	1.83	4.71	0.73	4.26	0.80	2.30	0.33	2.13	0.31
H18-3	1750	54.12	126.05	13.12	49.80	9.39	2.57	8.50	1.23	6.96	1.37	3.88	0.55	3.73	0.55
H18-4	2900	51.96	125.20	12.95	48.81	9.71	2.12	9.07	1.46	9.03	1.86	5.52	0.84	5.55	0.84
H19-1	981	42.43	92.83	9.13	29.97	5.76	0.68	4.98	0.80	4.94	0.97	2.92	0.45	3.11	0.46
H19-2	1300	57.89	136.46	13.99	52.09	9.99	2.81	8.57	1.24	7.02	1.34	3.93	0.57	3.68	0.54
H19-3	1769	49.32	123.22	12.19	48.29	9.27	2.76	8.30	1.17	6.58	1.24	3.45	0.50	3.09	0.46
H20-4	1400	48.16	110.48	11.65	47.13	8.79	2.39	7.51	1.06	5.94	1.14	3.24	0.44	2.91	0.44
H23-1	673	28.77	70.69	7.16	29.74	6.00	1.78	5.69	0.83	4.82	0.94	2.68	0.36	2.38	0.35
H23-2	1200	47.54	117.55	11.87	49.00	9.31	2.62	8.15	1.14	6.32	1.19	3.31	0.45	2.86	0.42
H23-3	1924	45.38	115.12	11.34	48.17	8.98	2.50	7.88	1.11	6.06	1.14	3.19	0.42	2.81	0.40
H23-4	2495	47.31	115.39	12.20	51.21	9.65	2.62	8.35	1.16	6.41	1.19	3.38	0.43	2.84	0.42
H24-1	1008	45.92	109.48	11.71	48.94	9.61	2.72	8.95	1.32	7.69	1.50	4.31	0.60	3.92	0.60
H24-3	2294	35.65	78.88	7.54	27.81	4.90	1.31	4.26	0.64	3.63	0.72	2.13	0.30	2.03	0.31
H24-4	2844	19.07	45.08	4.14	15.74	3.27	0.96	3.12	0.50	3.01	0.58	1.70	0.23	1.59	0.24
H25-3	2300	36.93	82.64	7.99	31.00	5.48	1.69	4.77	0.65	3.73	0.70	2.02	0.28	1.83	0.28
H26-1	350	43.12	101.71	9.50	37.51	6.78	1.74	6.10	0.90	5.31	1.04	3.08	0.44	2.99	0.45
H26-2	1200	48.72	115.52	12.12	51.78	9.83	2.86	9.38	1.35	7.81	1.53	4.41	0.61	3.96	0.58
H26-3	1810	36.86	91.22	9.04	39.07	7.35	2.16	6.66	0.94	5.35	1.01	2.86	0.38	2.49	0.37
H26-4	2000	35.40	86.91	7.48	24.64	4.82	1.36	4.16	0.65	3.86	0.74	2.17	0.33	2.26	0.34
H27-1	1110	55.11	130.92	14.53	53.50	10.87	2.97	9.63	1.37	7.71	1.47	4.19	0.59	3.90	0.57
H27-3	2048	49.89	118.91	13.22	49.42	9.96	2.78	8.86	1.28	7.34	1.40	4.05	0.57	3.75	0.55
H28-1	1250	49.16	116.54	12.28	45.54	9.20	2.85	7.86	1.11	6.20	1.18	3.38	0.48	3.11	0.46
H28-2	2002	25.48	60.32	5.84	18.33	3.85	1.18	3.45	0.56	3.31	0.64	1.86	0.28	1.89	0.27
H38-1	1100	51.66	127.49	13.99	51.33	10.66	3.24	9.65	1.36	7.76	1.48	4.19	0.58	3.79	0.54
H38-2	1500	77.97	174.12	20.44	75.10	15.33	3.69	13.42	1.87	10.66	2.00	5.67	0.80	5.26	0.75
H38-4	1950	37.56	105.03	10.60	39.69	8.01	2.78	6.93	0.95	5.25	0.98	2.75	0.40	2.59	0.38
H39-1	1200	32.09	95.76	8.83	33.50	7.41	2.70	6.98	1.02	5.90	1.12	3.12	0.43	2.84	0.40
H39-2	1650	52.28	121.14	14.80	51.48	11.59	3.04	10.78	1.62	9.71	1.90	5.57	0.81	5.49	0.79
H39-3	1800	47.17	122.04	13.50	47.13	10.37	3.19	9.02	1.29	7.18	1.34	3.80	0.53	3.49	0.50
H39-4	2100	48.77	130.68	14.11	48.02	10.65	3.24	9.56	1.36	7.78	1.47	4.22	0.60	3.98	0.58
H40-1	1612	51.21	129.51	13.16	51.85	10.04	3.25	8.71	1.22	6.82	1.26	3.53	0.49	3.22	0.47

Table D2: Chemical indices of the outcrop and reservoir samples

Sample ID	Unit/Depth [m bgl]	CIW	CIA	PIA	CCPI	AI
LH8	Teziutlán	61.0	58.2	59.0	53.5	34.5
LH9	Teziutlán	63.3	59.3	60.6	49.3	31.8
LH11+12	Teziutlán	59.9	57.0	57.8	37.8	22.5
LH13	Teziutlán	66.9	61.2	63.5	48.1	37.1
LH16	Teziutlán	65.1	59.0	61.1	52.5	39.4
LH29	Teziutlán	66.2	62.6	64.2	43.2	28.9
RLM3	Teziutlán	61.8	57.1	58.4	50.1	34.2
RLM9	Teziutlán	68.1	60.2	63.2	44.9	39.5
LH34	Cuyoaco	67.7	63.8	65.6	44.5	30.3
LH41	Cuyoaco	63.9	59.6	61.1	36.3	23.2
LH51	Cuyoaco	66.8	63.8	65.2	31.7	20.8
LH72	Cuyoaco	66.8	63.0	64.7	42.5	28.3
OLH1	Cuyoaco	65.5	60.9	62.7	38.7	25.4
H13-1	1200	61.0	59.6	60.0	53.0	35.5
H15-1	1250	66.7	61.5	63.6	46.6	38.3
H18-1	796	67.8	65.1	66.4	49.1	38.8
H18-3	1750	70.3	65.2	67.8	47.5	33.2
H18-4	2900	69.1	61.4	64.6	21.2	29.4
H19-1	981	77.1	64.5	71.5	28.0	50.2
H19-2	1300	62.0	56.7	58.1	39.9	31.7
H19-3	1769	66.1	63.1	64.4	61.2	43.1
H20-4	1400	66.3	61.5	63.4	50.5	41.7
H23-1	673	63.5	61.2	62.0	49.6	33.8
H23-2	1200	63.4	59.9	61.1	40.0	26.6
H23-3	1924	68.0	65.6	66.8	58.3	43.1
H23-4	2495	68.4	65.4	66.9	55.5	40.3
H24-1	1008	70.5	66.3	68.5	46.7	33.6
H24-3	2294	53.7	49.4	49.3	24.8	25.6
H24-4	2844	51.1	47.7	47.3	27.0	25.4
H25-3	2300	66.9	62.8	64.6	41.1	34.5
H26-1	350	71.5	63.8	67.6	36.2	36.6
H26-2	1200	64.9	60.6	62.2	39.6	28.1
H26-3	1810	65.5	61.6	63.2	52.2	37.1
H26-4	2000	79.3	67.6	75.0	33.9	52.1
H27-1	1110	66.9	63.2	64.8	44.9	27.8
H27-3	2048	72.2	62.8	67.3	31.0	41.5
H28-1	1250	60.6	57.7	58.5	47.8	37.1
H28-2	2002	86.6	78.1	84.9	57.9	64.6
H38-1	1100	70.0	66.2	68.2	52.0	37.1
H38-2	1500	69.7	64.8	67.2	46.5	34.3
H38-4	1950	62.9	62.1	62.4	44.9	28.0
H39-1	1200	59.1	58.3	58.6	46.5	27.7
H39-2	1650	68.0	62.5	65.0	19.2	26.4
H39-3	1800	67.5	64.8	66.1	43.0	28.7
H39-4	2100	70.3	66.1	68.3	49.3	35.9
H40-1	1612	53.2	51.5	51.6	42.7	29.7

Table D3: Cross-correlations of selected major, trace and rare earth elements

	SiO₂	TiO₂	Al₂O₃	Fe₂O₃	MnO	MgO	CaO	Na₂O	K₂O	P₂O₅	Ba	Nb	Sr	V	Zn	Zr	La	Ce	Pr	Nd	Sm	Eu	Gd	Tb	Dy	Ho	Er	Tm	Yb	Lu
SiO_2	1.00																													
TiO_2	-0.91	1.00																												
Al_2O_3	-0.73	0.83	1.00																											
Fe_2O_3	-0.92	0.89	0.65	1.00																										
MnO	-0.52	0.39	0.04	0.55	1.00																									
MgO	-0.80	0.61	0.43	0.79	0.44	1.00																								
CaO	-0.63	0.39	0.06	0.51	0.69	0.60	1.00																							
Na_2O	-0.06	0.18	0.29	0.03	-0.17	-0.29	-0.45	1.00																						
K_2O	0.67	-0.53	-0.35	-0.69	-0.44	-0.75	-0.60	0.12	1.00																					
P_2O_5	-0.79	0.88	0.78	0.76	0.31	0.47	0.27	0.23	-0.35	1.00																				
Ba	0.20	-0.11	-0.13	-0.24	-0.24	-0.44	-0.19	0.25	0.52	-0.20	1.00																			
Nb	-0.15	0.28	0.31	0.13	0.09	-0.01	-0.03	0.00	0.01	0.31	-0.10	1.00																		
Sr	-0.79	0.59	0.46	0.72	0.50	0.72	0.72	-0.17	-0.77	0.55	-0.35	0.07	1.00																	
V	-0.83	0.58	0.53	0.72	0.40	0.90	0.35	-0.05	-0.71	0.19	-0.49	-0.25	0.78	1.00																
Zn	-0.41	0.36	0.12	0.58	0.38	0.37	0.18	0.10	-0.27	0.42	-0.13	0.07	0.24	0.19	1.00															
Zr	-0.30	0.49	0.52	0.24	0.02	-0.16	-0.17	0.59	0.19	0.56	0.16	0.58	-0.02	-0.36	0.16	1.00														
La	-0.19	0.34	0.39	0.18	0.02	-0.20	-0.21	0.48	0.26	0.50	-0.01	0.56	0.05	-0.40	0.21	0.89	1.00													
Ce	-0.34	0.48	0.51	0.33	0.11	-0.06	-0.11	0.47	0.09	0.59	-0.05	0.51	0.21	-0.29	0.27	0.87	0.96	1.00												
Pr	-0.29	0.44	0.50	0.27	0.07	-0.11	-0.16	0.53	0.10	0.56	-0.07	0.55	0.15	-0.29	0.22	0.89	0.96	0.98	1.00											
Nd	-0.42	0.55	0.57	0.40	0.13	0.01	-0.08	0.56	0.02	0.67	-0.08	0.46	0.24	-0.21	0.29	0.90	0.94	0.96	0.97	1.00										
Sm	-0.41	0.55	0.58	0.38	0.14	0.00	-0.09	0.58	-0.03	0.63	-0.11	0.49	0.22	-0.14	0.26	0.88	0.90	0.95	0.98	0.98	1.00									
Eu	-0.63	0.70	0.69	0.57	0.35	0.27	0.17	0.43	-0.34	0.73	-0.22	0.50	0.50	0.29	0.29	0.88	0.87	0.93	0.96	0.96	0.99	1.00								
Gd	-0.40	0.55	0.58	0.38	0.15	-0.02	-0.11	0.62	-0.05	0.60	-0.08	0.46	0.19	-0.09	0.27	0.88	0.87	0.93	0.96	0.96	0.99	0.90	1.00							
Tb	-0.32	0.47	0.52	0.31	0.11	-0.09	-0.17	0.65	0.01	0.51	-0.04	0.43	0.10	-0.08	0.24	0.87	0.85	0.90	0.94	0.93	0.97	0.86	0.99	1.00						
Dy	-0.25	0.41	0.47	0.24	0.07	-0.16	-0.23	0.68	0.05	0.43	-0.01	0.41	0.02	-0.08	0.22	0.85	0.83	0.87	0.91	0.89	0.95	0.81	0.97	0.99	1.00					
Ho	-0.21	0.36	0.42	0.20	0.05	-0.20	-0.26	0.71	0.09	0.38	0.04	0.38	-0.03	-0.09	0.20	0.84	0.80	0.84	0.88	0.86	0.92	0.77	0.95	0.98	1.00	1.00				
Er	-0.15	0.30	0.38	0.14	0.01	-0.25	-0.29	0.71	0.14	0.33	0.07	0.36	-0.08	-0.12	0.17	0.83	0.79	0.82	0.87	0.84	0.89	0.73	0.93	0.97	0.99	1.00	1.00			
Tm	-0.07	0.22	0.31	0.06	-0.03	-0.32	-0.34	0.70	0.19	0.24	0.10	0.35	-0.14	-0.18	0.16	0.79	0.77	0.80	0.84	0.79	0.85	0.67	0.89	0.94	0.97	0.98	0.99	1.00		
Yb	-0.02	0.17	0.27	0.01	-0.06	-0.35	-0.37	0.70	0.22	0.19	0.12	0.35	-0.18	-0.21	0.11	0.78	0.76	0.78	0.82	0.77	0.83	0.64	0.87	0.92	0.96	0.98	0.99	1.00	1.00	
Lu	0.00	0.14	0.24	0.00	-0.08	-0.37	-0.38	0.71	0.25	0.17	0.14	0.32	-0.20	-0.24	0.12	0.77	0.76	0.77	0.81	0.76	0.81	0.61	0.85	0.91	0.94	0.97	0.98	0.99	1.00	1.00

Table D4: Concentration changes in % of major and trace elements of the reservoir samples

Sample ID	SiO$_2$	TiO$_2$	Al$_2$O$_3$	Fe$_2$O$_3$	MnO	MgO	CaO	Na$_2$O	K$_2$O	P$_2$O$_5$	Ba	Nb	Sr	Zr
H13-1	-6.6	18.4	0.7	116.3	8.7	95.1	3.9	32.8	-66.8	20.8	nd	nd	-10.1	-2.2
H15-1	8.0	-21.5	-5.6	67.4	-43.0	7.6	-35.8	20.8	-2.0	14.1	38.9	68.4	-19.3	34.0
H18-1	-0.8	1.8	9.3	66.5	-78.7	63.9	-11.1	-2.6	-46.1	7.0	-7.9	nd	-17.4	-13.1
H18-3	6.5	3.4	4.7	83.0	-22.4	-34.5	-39.7	13.1	-5.6	42.6	14.1	110.6	-35.8	131.8
H18-4	20.2	-81.3	-9.6	29.4	-68.8	-97.0	-89.0	88.6	34.2	-81.7	38.9	26.3	-87.2	84.7
H19-1	35.0	-91.4	-24.6	15.0	-90.9	-78.9	-94.3	5.1	57.2	-96.2	nd	-15.8	-96.3	-38.4
H19-2	3.8	-9.6	-1.9	75.7	6.5	-18.3	7.4	4.5	21.7	37.4	9.7	26.3	-24.8	92.0
H19-3	-2.3	2.6	-4.4	132.5	-1.1	89.3	-24.8	9.3	-44.3	64.4	-72.2	26.3	-11.9	19.5
H20-4	-1.3	-11.3	4.5	80.0	-46.0	61.5	-29.8	40.5	-0.1	31.0	14.1	26.3	-10.1	63.0
H23-1	0.7	2.6	1.6	95.3	-24.7	48.1	-1.8	13.6	-50.6	0.9	-16.6	-15.8	-19.3	-5.8
H23-2	-2.9	22.9	12.6	85.1	-27.8	-17.8	0.1	44.1	-14.8	97.0	-12.3	26.3	-2.8	63.0
H23-3	-1.9	1.3	5.1	105.5	-37.6	97.6	-23.4	8.5	-53.0	74.9	-75.1	26.3	2.7	41.3
H23-4	-6.4	12.0	15.5	107.4	-43.7	77.5	-17.0	17.0	-38.4	63.1	-81.0	26.3	10.1	52.1
H24-1	7.7	-13.3	1.8	70.4	-24.0	-22.3	-56.7	37.7	-25.0	46.4	-81.0	-15.8	-45.0	52.1
H24-3	16.7	-70.3	-22.0	32.4	-44.5	-33.1	54.6	-49.2	1.6	-45.9	-9.3	26.3	-28.4	-16.7
H24-4	21.8	-88.8	-32.5	32.5	36.9	-22.9	23.8	-4.2	-21.7	-81.1	-41.5	26.3	-54.1	-67.4
H25-3	10.1	-45.8	-2.4	50.2	-52.1	-1.5	-47.8	49.6	-20.9	-4.2	-6.4	-15.8	-22.9	-5.8
H26-1	22.0	-49.2	-10.1	42.3	-65.8	-66.8	-67.4	22.7	25.4	-44.6	-6.4	-15.8	-57.8	41.3
H26-2	10.8	-16.2	-4.0	68.3	-11.0	-39.6	-50.0	72.1	-13.3	32.0	8.2	-15.8	-35.8	52.1
H26-3	-2.0	2.6	4.5	106.2	-29.3	39.4	-15.5	22.2	-18.0	41.9	12.6	-15.8	-6.4	12.3
H26-4	28.5	-88.2	-10.2	17.7	-36.9	-64.5	-81.8	-14.0	61.3	-72.8	-24.0	26.3	-79.8	-56.5
H27-1	7.3	9.8	0.8	85.2	-30.8	-34.7	-42.3	47.4	-28.6	78.1	21.4	68.4	-26.6	99.2
H27-3	14.7	-27.9	0.7	30.2	-65.0	-57.9	-66.1	35.9	70.1	75.9	nd	nd	-94.5	95.6
H28-1	-1.8	-9.9	-0.6	82.6	3.4	85.5	7.9	26.4	-31.8	28.8	-70.8	26.3	-4.6	59.4
H28-2	33.4	-91.6	-12.7	13.5	-76.4	-14.3	-88.2	-52.6	-9.9	-90.4	-56.1	68.4	-89.0	-67.4
H38-1	-4.4	16.1	19.7	98.9	3.4	27.9	-17.2	6.4	-20.1	69.2	-67.8	68.4	11.9	59.4
H38-2	1.0	24.7	13.8	83.7	-34.6	-17.0	-50.7	61.0	2.3	93.8	-63.4	194.8	-30.3	211.5
H38-4	2.7	-38.1	1.5	77.3	-38.4	32.1	0.9	15.2	-83.1	47.4	-78.1	nd	79.8	-49.3
H39-1	-8.6	22.6	6.8	108.5	0.4	59.8	46.4	0.1	-79.2	13.7	nd	nd	2.7	-2.2
H39-2	23.1	-68.4	-6.3	19.3	-65.8	-77.3	-82.7	94.7	-0.4	-58.7	-21.0	26.3	-70.6	92.0
H39-3	10.2	-12.9	1.4	65.6	-46.8	-16.2	-39.5	36.1	-49.3	-2.0	-81.0	26.3	-11.9	37.6
H39-4	3.7	-6.1	10.0	81.8	-28.5	1.1	-36.7	19.0	-19.3	18.5	27.2	26.3	-8.3	63.0
H40-1	-4.5	-16.3	-9.7	88.4	33.1	71.9	77.9	-32.6	-51.6	11.2	-62.0	nd	67.0	26.8

nd = not detected

Table D4 continuation: Concentration changes in % of REE of the reservoir samples

Sample ID	La	Ce	Pr	Nd	Sm	Eu	Gd	Tb	Dy	Ho	Er	Tm	Yb	Lu
H13-1	-29.5	-3.0	-14.8	-13.7	-15.8	18.2	3.1	7.0	11.1	15.5	16.8	16.9	18.3	17.1
H15-1	5.5	14.4	6.3	3.8	-15.9	2.5	-6.3	-9.1	-11.3	-9.4	-8.4	-7.0	-6.3	-5.5
H18-1	-41.8	-24.1	-39.0	-37.7	-45.0	-18.4	-35.9	-31.8	-29.3	-30.8	-28.6	-27.0	-28.1	-27.7
H18-3	30.2	35.6	27.9	24.7	0.9	14.4	15.6	15.2	15.5	18.1	20.5	22.4	25.8	26.5
H18-4	25.0	34.6	26.2	22.2	4.4	-5.8	23.4	37.4	49.8	60.5	71.5	85.2	87.3	92.6
H19-1	2.1	-0.2	-11.1	-25.0	-38.1	-69.8	-32.3	-24.8	-18.1	-15.9	-9.3	-1.6	5.0	6.9
H19-2	39.3	46.8	36.3	30.4	7.3	25.3	16.5	16.6	16.4	15.8	21.9	25.1	24.1	24.4
H19-3	18.7	32.5	18.7	20.9	-0.4	23.0	12.9	10.0	9.2	6.8	7.0	9.6	4.1	6.9
H20-4	15.9	18.8	13.5	18.0	-5.6	6.6	2.1	-0.6	-1.4	-1.5	0.6	-3.8	-1.7	2.2
H23-1	-30.8	-24.0	-30.2	-25.6	-35.6	-20.8	-22.5	-22.3	-20.0	-18.8	-16.9	-20.0	-19.8	-18.7
H23-2	14.4	26.4	15.7	22.6	0.0	16.5	10.9	6.9	4.8	3.0	2.6	-1.5	-3.4	-3.1
H23-3	9.2	23.8	10.5	20.6	-3.5	11.3	7.2	4.5	0.6	-1.3	-1.1	-7.5	-5.3	-7.9
H23-4	13.8	24.1	18.9	28.2	3.7	16.8	13.6	9.1	6.4	3.3	5.0	-4.0	-4.1	-3.7
H24-1	10.5	17.7	14.1	22.5	3.3	21.3	21.7	23.6	27.5	29.4	33.7	32.7	32.2	37.2
H24-3	-14.2	-15.2	-26.5	-30.4	-47.3	-41.9	-42.1	-40.1	-39.8	-37.9	-33.8	-33.8	-31.5	-27.6
H24-4	-54.1	-51.5	-59.7	-60.6	-64.8	-57.5	-57.6	-53.3	-50.0	-49.9	-47.2	-48.8	-46.2	-45.4
H25-3	-11.1	-11.1	-22.1	-22.4	-41.2	-24.5	-35.2	-38.6	-38.2	-39.3	-37.4	-37.5	-38.2	-36.3
H26-1	3.8	9.4	-7.5	-6.1	-27.2	-22.4	-17.0	-15.0	-11.9	-10.0	-4.5	-2.7	0.8	4.3
H26-2	17.2	24.2	18.1	29.6	5.6	27.4	27.6	27.0	29.6	32.5	36.9	34.5	33.6	34.4
H26-3	-11.3	-1.9	-12.0	-2.2	-21.0	-4.0	-9.4	-11.7	-11.2	-12.3	-11.2	-16.3	-15.9	-15.9
H26-4	-14.8	-6.5	-27.1	-38.3	-48.3	-39.3	-43.5	-38.5	-35.9	-36.1	-32.7	-28.1	-23.6	-22.2
H27-1	32.6	40.8	41.5	33.9	16.8	32.2	30.9	28.2	28.0	27.1	30.0	30.0	31.5	31.2
H27-3	20.0	27.9	28.8	23.7	7.0	23.8	20.6	20.1	21.7	20.7	25.7	26.2	26.6	25.8
H28-1	18.3	25.3	19.7	14.0	-1.2	26.7	7.0	4.6	2.8	2.3	4.8	5.5	4.9	5.0
H28-2	-38.7	-35.1	-43.1	-54.1	-58.6	-47.4	-53.1	-47.7	-45.1	-44.6	-42.2	-39.1	-36.1	-37.7
H38-1	24.3	37.1	36.3	28.5	14.6	44.2	31.3	27.9	28.7	27.9	30.0	28.6	27.9	25.4
H38-2	87.6	87.3	99.2	88.0	64.8	64.4	82.5	75.7	76.9	73.2	75.9	76.3	77.3	72.5
H38-4	-9.6	13.0	3.2	-0.7	-14.0	23.7	-5.8	-11.1	-12.9	-15.2	-14.5	-12.6	-12.5	-12.6
H39-1	-22.8	3.0	-13.9	-16.1	-20.4	20.2	-5.1	-3.9	-2.1	-3.2	-3.1	-4.0	-4.3	-8.3
H39-2	25.8	30.3	44.2	28.9	24.5	35.5	46.6	52.7	61.1	64.2	72.9	78.7	85.3	82.6
H39-3	13.5	31.3	31.5	18.0	11.4	42.0	22.7	21.0	19.1	15.7	17.9	18.2	17.9	14.7
H39-4	17.4	40.5	37.5	20.2	14.5	44.1	30.0	27.6	29.1	27.3	30.9	32.6	34.4	32.9
H40-1	23.2	39.3	28.2	29.8	7.9	44.9	18.5	15.0	13.1	8.8	9.7	9.3	8.6	8.7

Table D5: P-values obtained during Kruskal-Wallis Tests

Tests	La	Ce	Pr	Nd	Sm	Eu	Gd	Tb	Dy	Ho	Er	Tm	Yb	Lu
Cuyoaco vs. Teziutlán	**0.0153**	**0.0329**	**0.0192**	**0.0447**	0.2775	0.0722	**0.0187**	**0.0083**	**0.0084**	**0.0068**	**0.0070**	**0.0071**	**0.0051**	**0.0054**
Cuyoaco vs. Reservoir	**0.0009**	**0.0003**	**0.0014**	**0.0022**	0.4355	**0.0056**	**0.0022**	**0.0014**	**0.0009**	**0.0007**	**0.0005**	**0.0004**	**0.0003**	**0.0003**
Teziutlán vs. Reservoir	0.5662	0.2026	0.6214	0.4091	0.5343	0.4415	0.7472	0.9319	0.8203	0.8402	0.7122	0.6670	0.7311	0.7120
Cuyoaco vs. R. argillic	**0.0062**	**0.0029**	**0.0095**	**0.0056**	0.4903	**0.0145**	**0.0078**	**0.0047**	**0.0031**	**0.0021**	**0.0013**	**0.0007**	**0.0006**	**0.0006**
Teziutlán vs. R. argillic	0.8719	0.4173	0.9222	0.4681	0.6296	0.5446	0.8661	0.9961	0.8738	0.8412	0.6995	0.5560	0.6217	0.5859
Cuyoaco vs. R. propylitic	**0.0002**	**0.0001**	**0.0003**	**0.0006**	0.1744	**0.0010**	**0.0007**	**0.0006**	**0.0005**	**0.0005**	**0.0004**	**0.0005**	**0.0004**	**0.0005**
Teziutlán vs. R. propylitic	0.2442	**0.0478**	0.2080	0.1563	0.8511	0.1205	0.3520	0.5532	0.4869	0.5519	0.4815	0.5468	0.6162	0.6116
Cuyoaco vs. silicification/skarn	0.0610	0.0769	0.1212	0.2345	0.6434	0.4668	0.1526	0.0872	0.0723	0.0582	**0.0450**	**0.0358**	**0.0265**	**0.0275**
Teziutlán vs. silicification/skarn	0.6467	0.7884	0.4623	0.4315	0.0958	0.2793	0.3802	0.3859	0.4437	0.4623	0.5493	0.6246	0.6378	0.6393

numbers in bold = significant differences, R = reservoir samples (for input data please refer to Table D1)

Significance levels:
ns   P > 0.05
*   P ≤ 0.05
**   P ≤ 0.01
***   P ≤ 0.001
****   P ≤ 0.0001

Additional information on the laboratory measurements

Petrographic and SEM analyses were performed at the British Geological Survey and TU Darmstadt. SEM analyses at BGS were performed using a FEI Quanta 600 SEM with an Oxford Instruments X-Max detector (SDD) for Energy Dispersive Spectrometry (EDS), running with Oxford Instruments INCA (v4) software. The SEM was operated at: 20 kV accelerating voltage, approximately 5 nA beam current; and an acquisition time of 60 seconds per spot was used. EDS process time of 4 resulted in dead-times of < 45%. Use of Backscattered SEM imaging (i.e., BSEM) aided phase identification, with EDS analysis providing quantification of phase compositions. SEM analyses at TU Darmstadt were carried out using an EDAX FEI Quanta 200F SEM running with EDAX Genesis software. The SEM was operated in low vacuum mode with a pressure of 0.8 mbar, 15 kV voltage and approximately 5 nA spot size. EDS processing with 1000 counts per 30 seconds resulted in a dead-time of 30–50%. BGS: Figs. 40h, 40o, 40p and Fig. 41k, Fig. C2; TU Darmstadt: Fig. 40l.

Appendix E – Publications and Additional Data

Appendix E is provided on the CD-ROM attached to the back of this dissertation.

List of Publications

Peer-reviewed journal articles

2022   **Weydt, L. M., Lucci, F., Lacinska, A., Scheuvens, D., Carrasco-Núñez, G., Giordano, G., Rochelle, C. A., Schmidt, S., Bär, K., and Sass, I.:** The impact of hydrothermal alteration on the physiochemical characteristics of reservoir rocks: the case of the Los Humeros geothermal field (Mexico), Geothermal Energy, 10, 20(2022), 49 pp., 2022.

Weydt, L. M., Bär, K., and Sass, I.: Petrophysical characterization of the Los Humeros geothermal field (Mexico): From outcrop to parametrization of a 3D geological model, Geothermal Energy, 10, 5(2022), 48 pp., 2022.

2021   **Weydt, L. M., Ramírez-Guzmán, Á. A., Pola, A., Lepillier, B., Kummerow, J., Mandrone, G., Comina, C., Deb, P., Norini, G., González-Partida, E., Avellán, D. R., Macías, J. L., Bär, K., and Sass, I.:** Petrophysical and mechanical rock property database of the Los Humeros and Acoculco geothermal fields (Mexico), Earth System Science Data, 13, 571–598, 2021.

2018   **Weydt, L. M., Bär, K., Colombero, C., Comina, C., Deb, P., Lepillier, B., Mandrone, G., Milsch, H., Rochelle, C. A., Vagnon, F., and Sass, I.**: Outcrop analogue study to determine reservoir properties of the Los Humeros and Acoculco geothermal fields, Mexico, Adv. Geosci., 45, 281–287, 2018.

Weydt, L. M., Heldmann, C.-D. J., Machel, H. G., and Sass, I.: From oil field to geothermal reservoir: assessment for geothermal utilization of two regionally extensive Devonian carbonate aquifers in Alberta, Canada, Solid Earth, 9, 953–983, 2018.

Non-peer-reviewed articles

2020   **Willson, G. L., Weydt, L. M., Bär, K., Sass, I., and Machel, H. G.:** Geothermal Potential of the Rimbey-Meadowbrook Reef Trend in Alberta, Canada, Geothermische Energie, 94, 29, Bundesverband Geothermie e.V., 8–10, ISSN 0948-6615, 2020.

Peer-reviewed conference proceedings

2022   **Rallo, R., Carbonari, R., Ton, D., Ashari, R., Ashok, P., Bonneville, A., Bour, D., Cladouhos, T., Garrison, G., Horne, R., van Oort, E., Petty, S., Rallo, R., Schultz, A., Sørlie, C. F., Thorbjornsson, I. O., Uddenberg, M., and Weydt, L.:** A Probabilistic Approach to Model and Optimize Geothermal Drilling, Proceedings 47th Workshop on Geothermal Reservoir Engineering, Stanford University, Stanford, California, 07.02–09.02.2022, SGP-TR-223, 12 pp., 2022.

2021   **Carbonari, R., Ton, D., Bonneville, A., Bour, D., Cladouhos, T., Garrison, G., Horne, R., Petty, S., Rallo, R., Schultz, A., Sørlie, C. F., Thorbjornsson, I. O., Uddenberg, M., and Weydt, L.:** First year report of EDGE project: An International Research Coordination Network for Geothermal Drilling Optimization Supported by Deep Machine Learning and Cloud Based Data Aggregation, Proceedings 46th Workshop on Geothermal Reservoir Engineering, Stanford University, Stanford, California, 15.02–17.02.2021, SGP-TR-218, 11 pp., 2021.

Weydt, L. M., Bär, K., and Sass, I.: Petrophysical reservoir characterization of the Los Humeros and Acoculco geothermal fields, Mexico, Proceedings World Geothermal Congress 2020+1, Reykjavik, Iceland, April–October 2021, 8 pp., 2021.

2021	**Weydt, L. M., Wilson, G., Bär, K., Heldmann, C.-D., Machel, H. G., and Sass, I.:** Geothermal assessment of regionally extensive Upper Devonian carbonate aquifers in Alberta, Canada, Proceedings World Geothermal Congress 2020+1, Reykjavik, Iceland, April–October 2021, 10 pp., 2021.
	Rochelle, C., Lacinska, A., Kilpatrick, A., Rushton, J., Weydt, L. M., Bär, K., and Sass, I.: Evidence for fracture-hosted fluid-rock reactions within geothermal reservoirs of the eastern trans-Mexico volcanic belt, Proceedings World Geothermal Congress 2020+1, Reykjavik, Iceland, April–October 2021, 11 pp., 2021.
	Sass, I., Weydt, L. M., Götz, A. E., Machel, H. G., and Heldmann, C.-D.: Geothermal Reservoir Analogues on a Continental Scale Western Canadian Sedimentary Basin versus Northern Alpine Molasse Basin, Proceedings World Geothermal Congress 2020+1, Reykjavik, Iceland, April–October 2021, 9 pp., 2021.

Non-peer-reviewed conference proceedings

2021	**Weydt, L. M., Wilson, G., Heldmann, C.-D., Machel, H. G., and Sass, I.:** Geothermal assessment of the Upper Devonian carbonate aquifer systems in the Alberta Basin, Canada, Geoconvention 2021 Virtual Event, Calgary, Alberta, Canada, 13.09–5.09.2021, 5 pp., 2021.

Oral and poster presentations

2022	**Weydt, L., and Sass, I.:** The MalVonian project, Workshop Geothermal Potential of Volcanic Belts, Virtual Event, University of Calgary, Canada, 28.04.2022, 2022.
	Rallo, R., Carbonari, R., Ton, D., Ashari, R., Ashok, P., Bonneville, A., Bour, D., Cladouhos, T., Garrison, G., Horne, R., van Oort, E., Petty, S., Rallo, R., Schultz, A., Sørlie, C. F., Thorbjornsson, I. O., Uddenberg, M., and Weydt, L.: A Probabilistic Approach to Model and Optimize Geothermal Drilling, Proceedings 47th Workshop on Geothermal Reservoir Engineering, Stanford University, Stanford, California, 07.02–09.02.2022, 2022.
2021	**Weydt, L. M., Wilson, G., Heldmann, C.-D., Machel, H. G., and Sass, I.:** Geothermal assessment of the Upper Devonian carbonate aquifer systems in the Alberta Basin, Canada, Geoconvention 2021 Virtual Event, Calgary, Alberta, Canada, 13.09–15.09.2021, 2021.
	Weydt, L., Bär, K., and Sass, I.: Petrophysical reservoir characterization of the Los Humeros geothermal field (Mexico): from outcrop analogue analysis to parametrization of a 3D geological-geothermal model, 12th European Geothermal PhD Days, Online, CY Cergy Paris Université, France, 15.02–16.02.2021, 2021.
	Carbonari, R., Ton, D., Bonneville, A., Bour, D., Cladouhos, T., Garrison, G., Horne, R., Petty, S., Rallo, R., Schultz, A., Sørlie, C. F., Thorbjornsson, I. O., Uddenberg, M., and Weydt, L.: First year report of EDGE project: An International Research Coordination Network for Geothermal Drilling Optimization Supported by Deep Machine Learning and Cloud Based Data Aggregation, Proceedings 46th Workshop on Geothermal Reservoir Engineering, Stanford University, Stanford, California, 15.02–17.02.2021, 2021.

2020   **Peters, E., Candela, T., Lepillier, B., Hofmann, H., Deb, P., Kruszewski, M., Wheeler, W., Bastesen, E., Trumpy, E., Weydt, L., Bär, K., Sass, I., and Van Wees, J.-D.:** Estimation of geothermal potential for Enhanced Geothermal System taking into account geological uncertainty and the risk of induced seismicity: a case study in Acoculco, Mexico, 8th European Geothermal Workshop, Online, 07.10–08.10.2020, 2020.

Weydt, L. M., Lucci, F., Carrasco-Núñez, G., Giordano, G., Lacinska, A., Rochelle, C., Bär, K., and Sass, I.: Petrophysical reservoir characterization of the Los Humeros geothermal field (Mexico): comparison of outcrop analogues and reservoir formations. Potsdam, GEMex Final Conference, GFZ, Potsdam, Germany, 18.02–19.02.2020, 2020.

Lacinska, A., Rochelle, C., Kilpatrick, A., Weydt, L. M., Bär, K., and Sass, I.: Fracture-hosted fluid-rock reactions within geothermal reservoirs of the eastern Trans-Mexican Volcanic Belt. Potsdam, GEMex Final Conference, GFZ, Potsdam, Germany, 18.02–19.02.2020, 2020.

2019   **Willson, G. L., Weydt, L. M., Bär, K., Sass, I., and Machel, H. G.:** Geothermal Potential of Upper Devonian Carbonate Aquifer Systems of the Southwestern Rimbey-Meadowbrook Reef Trend in the Western Canada Sedimentary Basin, Alberta, Canada, Der Geothermiekongress 2019, München, Deutschland, 19.11–22.11.2019, 2019. First price Sciencebar award

Weydt, L. M., Bär, K., and Sass, I.: Thermo- and petrophysical rock properties of the Los Humeros geothermal field (Mexico): from outcrop analogue analysis to parametrization of a 3D geological-geothermal model, Der Geothermiekongress 2019, München, Deutschland, 19.11–22.11.2019, 2019.

Weydt, L. M., Bär, K., and Sass, I.: Thermo- and petrophysical rock properties of the Los Humeros geothermal field (Mexico): comparison of outcrop analogues and reservoir formations, 7th European Geothermal Workshop, Karlsruhe, Deutschland, 08.10–11.10.2019, 2019.

Weydt, L. M., Bär, K., and Sass, I.: Assessment for geothermal utilization of the Upper Devonian Leduc and Nisku Formation in the Alberta Basin, Canada, 7th European Geothermal Workshop, Karlsruhe, Deutschland, 08.10–11.10.2019, 2019.

2018   **Weydt, L. M., Bär, K., and Sass, I.:** New insights on geothermal rock properties of the Los Humeros geothermal field, Mexico, 6th European Geothermal Workshop, Strasbourg, France, 10.10–11.10.2018, 2018.

Weydt, L. M., Bär, K., and Sass, I.: Outcrop analogue study to determine reservoir properties of the Los Humeros and Acoculco geothermal fields, Mexico, European Geosciences Union General Assembly 2018, Vienna, Austria, 08.04–13.04.2018, 2018.

Weydt, L. M., Heldmann, C.-D., Machel, H. G., and Sass, I.: First assessment for geothermal utilization of two regionally extensive Devonian carbonate aquifers in Alberta, Canada, European Geosciences Union General Assembly 2018, Vienna, Austria, 08.04–13.04.2018, 2018.

2017   **Qin, Y., Schill, E., Weydt, L. M., Bär, K., Sass, I., and Pérez-Florez, M. A.:** Concept of Gravimetric Exploration of Enhanced and Super-Hot Geothermal Systems in Acoculco and Los Humeros (Mexico), 5th European Geothermal Workshop, Karlsruhe, 12.10–13.10.2017, 2017.

Weydt, L. M., Bär, K., and Sass, I.: Outcrop analogue study to determine petrophysical properties of the Los Humeros and Acoculco geothermal fields, Mexico, 5th European Geothermal Workshop, Karlsruhe, 12.10–13.10.2017, 2017.

2016   **Weydt, L. M., Machel, H. G., and Sass, I.:** Analogue Study of Geothermal Properties of the Rimbey-Meadowbrook Reef Trend in the Alberta Basin, Canada, Der Geothermiekongress 2016, Essen, 29.11–01.12.2016, 2016.